NASA SP-304

FLUID MECHANICS, ACOUSTICS, AND DESIGN OF TURBOMACHINERY

Part II

A symposium held at
THE PENNSYLVANIA STATE UNIVERSITY
University Park, Pennsylvania
August 31–September 3, 1970

DEPARTMENT OF THE NAVY · UNITED STATES OF AMERICA

NATIONAL AERONAUTICS AND SPACE ADMINISTRATION

FLUID MECHANICS, ACOUSTICS, AND DESIGN OF TURBOMACHINERY

Part II

NASA SP-304

FLUID MECHANICS, ACOUSTICS, AND DESIGN OF TURBOMACHINERY

Part II

A symposium held at The Pennsylvania State University,
University Park, Pennsylvania, August 31 to September 3, 1970,
and sponsored by the National Aeronautics and Space Administration,
The Pennsylvania State University, and the U.S. Navy

Edited by
B. LAKSHMINARAYANA
The Pennsylvania State University

W. R. BRITSCH
NASA Lewis Research Center

W. S. GEARHART
The Pennsylvania State University

Scientific and Technical Information Office 1974
NATIONAL AERONAUTICS AND SPACE ADMINISTRATION
Washington, D.C.

GENERAL CHAIRMAN

B. Lakshminarayana	The Pennsylvania State University

SESSION CHAIRMEN

J. H. Horlock	Cambridge University, England
H. Marsh	Cambridge University, England
J. P. Johnston	Stanford University
J. W. Holl	The Pennsylvania State University
M. Sevik	The Pennsylvania State University
L. H. Smith	General Electric Company
M. J. Hartmann	NASA Lewis Research Center
R. E. Henderson	The Pennsylvania State University

ORGANIZING COMMITTEE MEMBERS

W. R. Britsch	NASA Lewis Research Center
W. S. Gearhart	The Pennsylvania State University
R. E. Henderson	The Pennsylvania State University
J. W. Holl	The Pennsylvania State University
J. H. Horlock	Cambridge University, England
M. Sevik	The Pennsylvania State University
L. H. Smith	General Electric Company
N. F. Wood	The Pennsylvania State University

For sale by the Superintendent of Documents
U.S. Government Printing Office, Washington, D.C. 20402
Price $3.80 (paper cover) Stock Number 3300-00583
Library of Congress Catalog Card Number 72-600087

PREFACE

The present status of fluid mechanics, in particular the fluid mechanics of turbomachines, is much like a flexible montage: It consists partly of derived theoretical expressions and partly of expressions obtained through insight, but to a far greater degree the montage consists of the empirical results derived from the hard-earned experimental data that also serve as the bond for the montage. This montage stems from our inability to solve the complex equations governing real fluid flow for all but the simplest problems. The nature of their nonlinearity in the general case precludes any closed-form solution. Unfortunately, the flow of fluids in turbomachines requires the solution to these equations in their most complex form. Even with our modern computers, the time required to solve this set of equations is prohibitive from the monetary viewpoint. Their manual solution has never been considered practical.

Engineers, physicists, and mathematicians have all imposed many simplifying assumptions to gain some knowledge of the behavior of fluids. Engineers and physicists found this approach necessary to solve practical flow problems confronting them. Mathematicians used this approach to obtain a whole series of elegant *closed-form* solutions to simplified, usually steady state, inviscid and incompressible, fluid-flow problems. These mathematical solutions are in many cases excellent approximations to the real flows and are used as the starting point for analysis of most real flow problems. But now our needs extend far beyond these simplified solutions and also beyond the ability of the theorist to provide a true solution within the imposed limitations of time and cost. The need for speed on the one hand and for precision on the other has created separated branches for the experimental and the theoretical approaches to fluid mechanics.

The need for the rapid development of modern gas turbines and rocket engines to satisfy our expanding needs for communication and transportation has necessitated quick answers, whether approximate or exact, to many questions long extant and some new ones. The need for answers has been on the one hand useful in narrowing the gap between the mathematician and the fluid dynamicist, but on the other hand it has forced a division of fluid dynamics into several disciplines and subgroups within them. Research is now being conducted on specialized problems in the realms of subsonic, transonic, supersonic, and hypersonic flows; viscous, boundary-layer, and secondary flows, two-phase flow and cavitation; laminar and turbulent flows and flow stability; steady and nonsteady flows and noise; and flows in cascades, compressors, and turbines. Solutions to any of the specialized problems in each of these disciplines are certainly contributing to a better understanding of fluid flow. The superposition of all these separate solutions cannot describe the flow of real fluids in a complex flow field because in many instances the assumptions as to flow conditions and boundary conditions will be inconsistent and incompatible.

In the development of a turbomachine, the fluid dynamic designer must sift through the results obtained in the various disciplines and determine which are applicable. All his knowledge and skills are required to reassemble these separate flow pictures artfully in an iterative process to define the desired blade shapes. He is painfully aware that all his efforts can at best give him only reasonable assurance that his design goal can be met and that final blade adjustments or even the need for some redesign will be determined in the laboratory. The theorist is in a similar position. He must use the empirical results first to guide and justify the simplifying assumptions to obtain a tractable set of equations and then again to check the accuracy of his solutions against the experimental results.

Obviously, theory, design, and experiment are interdependent; so too are the several disciplines of fluid mechanics. Major advances in the design of turbomachines can only be obtained through constant interchange of knowledge among specialists in all these facets of fluid mechanics. This conference was designed to promote just such an exchange of ideas. Its dedication to Dr. George F. Wislicenus is in recognition of his continuing efforts to narrow the gaps between those interested in the theoretical, the design, and the experimental phases of flow in turbomachines and of his efforts to make us all aware of developments in the other disciplines.

Credit for the conception, structure, and organization of this conference goes primarily to Dr. Lakshminarayana, who devoted considerable time and effort beyond his normal duties to bring this meeting to a successful conclusion. Arrangements for the symposium were efficiently handled by Professors N. F. Wood and W. S. Gearhart, Betty Beckwith, and Maude Gagorik.

Many thanks to Jack Suddreth, Nelson Rekos, and Dr. Robert Levine of NASA Headquarters, to Irving Johnsen of the NASA Lewis Research Center, and to Dr. Ralph D. Cooper of the Office of Naval Research for their considerable effort and support toward making this conference possible.

The committee extends its thanks to The Pennsylvania State University for hosting this conference; to the Office of Naval Research for providing travel for the overseas participants; and to NASA for its financial support. We wish to thank Dean N. J. Palladino for his continued encouragement of this conference and Dr. A. O. Lewis for his enjoyable and enlightening after-dinner presentation "From Bakewell to Buxton—The Engineer A Humanist." Above all many thanks and much credit are due the session chairmen, who had the primary responsibility for inviting the papers for their sessions, and to the authors and the discussors without whose contribution this conference would not have been possible.

WERNER R. BRITSCH

CONTENTS

*Part I**

SESSION I

THEORETICAL PREDICTION OF TWO-DIMENSIONAL AND THREE-DIMENSIONAL FLOWS IN TURBOMACHINERY

Chairmen: J. H. Horlock and H. Marsh

---

* *Sessions I, II, and III are presented under separate cover.*

SESSION II

TWO- AND THREE-DIMENSIONAL VISCID FLOWS

Chairman: J. P. Johnston

SESSION III

CAVITATION

Chairman: J. W. Holl

Part II

SESSION IV
UNSTEADY FLOW AND NOISE
Chairman: M. Sevik

SESSION V
TURBOMACHINERY DESIGN
Chairman: L. H. Smith

SESSION VI

PUMPING MACHINERY FOR AEROSPACE APPLICATIONS

Chairman: M. J. Hartmann

SESSION VII

TURBOMACHINERY FOR MARINE PROPULSION

Chairman: R. E. Henderson

SESSION IV

Unsteady Flow and Noise

Chairman: **M. SEVIK**

Sources of Sound in Fluid Flows

J. E. FFOWCS WILLIAMS

Imperial College
London, England

This paper describes some features of a flow that produce acoustic radiation, particularly when the flow is turbulent and interacting with solid surfaces such as turbine or compressor blades. Early theoretical ideas on the subject are reviewed and are shown to be inadequate at high Mach number. Some recent theoretical developments that form the basis of a description of sound generation by supersonic flows interacting with surfaces are described.

At high frequencies the problem is treated as one of describing the surface-induced diffraction field of adjacent aerodynamic quadrupole sources. This approach has given rise to distinctly new features of the problem that seem to have bearing on the radiating properties of relatively large aerodynamic surfaces.

At low speeds, for fixed geometry, the acoustic power output from turbomachinery increases in proportion to the square of mechanical power. This variation obviously cannot be continued to indefinitely high powers since the acoustic loss would soon exceed the available energy supply. The mechanism of fan noise generation must therefore change its character at high speed, and the critical point seems to be reached when the blade tip speed exceeds the sonic velocity.

Observationally, the change becomes apparent in several distinct ways, one of the most striking being the appearance of the "buzz-saw" phenomenon, a noise characterized by multiple harmonics of the disk rotation frequency. At these high speeds, shock waves form, and the radiation field can hardly remain linear. On the other hand, it seems that the essential features of buzz-saw noise can be explained on the basis of linear theory alone and that nonlinearity is essential only in effecting minor modifications of amplitude. The first part of this paper sets down the central points of the arguments leading to a prediction of the buzz-saw phenomenon from purely linear theory.

The second part of this paper outlines some ideas on how the sound problem changes fundamentally at high speeds because of an inevitable wavelength contraction to a condition where the wavelength cannot be large in comparison with surface dimensions. This noncompactness makes the high-speed problem quite different in nature from that with which we are familiar at low speed. The radiated power is seen to be a decreasing function of jet power, for given geometry. At high speed, the noncompact sources are not so clearly related to the unsteady (or even steady) lift on the surfaces, so there must be some doubt as to the relevance of attempts to eliminate the unsteady forces to the high-speed fan noise problem.

SOURCES OF SOUND AT DISK ROTATION FREQUENCIES

The sound of an N-bladed fan is not always confined to harmonics of the blade-passage frequency $N\Omega$. There is, inevitably, some residual component at the disk rotation frequency Ω that can be attributed to the fact that the blades are not positioned in a completely regular array around the supporting disk and cannot support identical aerodynamic loads, both because of the slight irregularity of support and because of slight geometrical variation from one blade to another. It is known that, when blades travel at supersonic speeds, buzz-saw noise at harmonics of the disk rotation frequency becomes very intense and can become the dominant sound. By precisely what mechanism is this low-frequency sound generated? Is the mechanism essentially nonlinear, and why is the mechanism relatively stronger at supersonic speeds? On the basis of linear theory it is obviously not directly attributable to variations of blade size, incidence, or camber. Each of these effects produces an irregularity in the time history of the sound field that is harmonic on the fundamental rotation frequency of the disk but random on the blade frequency. However, these effects that bring about variations in loading from one blade to another are virtually independent of blade speed; thus the relative level of disk frequency noise to blade frequency noise arising from this cause would be independent of speed, a feature distinctly contrary to observations of the buzz-saw phenomenon. On the other hand, the variation in phase caused by slight circumferential variation of blade support can, on the basis of purely linear theory, induce an effect consistent with observation. This effect becomes more important at supersonic speeds because the frequency spectrum then contains much energy at very short wavelengths; on this short scale, the slight positional irregularities appear very significant. This effect can be quantified as follows.

Consider an N-bladed disk rotating at an angular frequency Ω. The pressure field generated by the motion will be at harmonics of this frequency because, when all effects of turbulence are discarded, the field is repeated on each rotation of the disk. If the geometry were ideally precise, the sound field would also be repeated at intervals corresponding to the blade-passage frequency. We denote this hypothetical time history of the field at any point by $g(t)$, and this signal could be Fourier-analyzed into discrete frequency components:

$$g(t) = \sum_n G_n e^{inN\Omega t} \tag{1}$$

Now suppose that the blades are identical but are positioned in a slightly irregular way around the disk circumference. The time history might then be denoted by $g(t+\epsilon)$, where ϵ is a small stochastic function of time on the interval corresponding to disk rotation but is exactly repeated every period. The signal $g(t+\epsilon)$ can be expanded in a Taylor series about $\epsilon=0$, and, for sufficiently small ϵ, the real signal can be represented by

$$g(t+\epsilon) = g(t) + \epsilon g'(t) \tag{2}$$

$g(t)$ is periodic at the blade frequency, but the second term is not, being periodic at intervals of disk rotation frequency only. Consequently, the real signal is made up of the discrete frequency part of the ideal case, plus a small subharmonic part, smaller by a factor of order

$$\overline{(\epsilon^2)}^{1/2} nN\Omega \tag{3}$$

than the nth harmonic of the tone at the blade-passage frequency $N\Omega$. The frequency $nN\Omega$ is the ratio of the amplitude of g' to that of g. At higher frequencies, the expansion of equation (2) fails and the situation becomes quite different. The spectrum $\mathcal{G}(\alpha)$ can then be obtained by the Fourier transformation.

$$\mathcal{G}(\alpha) = \frac{1}{2\pi} \int g(t+\epsilon) e^{-i\alpha t}\, dt$$

$$= \frac{1}{2\pi} \int \sum_n G_n e^{inN\Omega(t+\epsilon) - i\alpha t}\, dt \tag{4}$$

The phase factor, $nN\Omega(t+\epsilon)$, is now a rapidly varying function of t, so that the integral may be evaluated by the method of stationary phase to give

$$\mathcal{G}(\alpha) = \frac{1}{2\pi} \sum_p \sum_n \sum_m \frac{G_n \exp\left[i(t_p + 2m\pi/\Omega)(nN\Omega - \alpha) + inN\epsilon\Omega\right]}{(nN\Omega\epsilon''/2\pi)^{1/2}} \tag{5}$$

where $\sum_p$ signifies summation over all stationary points occurring in the interval $(0, 2\pi/\Omega)$, and ϵ, ϵ'' are evaluated at the stationary points t_p.

The sum over m forms a delta function so that

$$\mathcal{G}(\alpha) \sim \frac{1}{2} \sum_p \sum_n \frac{G_n e^{-i\alpha t_p}}{(nN\Omega\epsilon''/2\pi)^{1/2}} \delta\left(\sin \frac{\pi\alpha}{\Omega}\right) \tag{6}$$

$$\sim \frac{1}{2\pi} \sum_p \sum_n G_n \left(\frac{2\pi\Omega}{nN\epsilon''}\right)^{1/2} \delta(\alpha - m\Omega) \tag{7}$$

(Note that $e^{im\Omega}t_p =$ constant.)

This spectrum is a series of discrete components at harmonics of the disk rotation frequency Ω and is utterly independent of the blade-passage frequency. Furthermore, the levels of the discrete tones are independent of the harmonic number, a feature often observed in buzz-saw situations. It seems paradoxical that it is only when the basic waveform contains high enough frequencies that $nN\Omega\epsilon$ is large that the low-frequency spectrum can become significant. This fact is a reflection of the need that the waveform possess sharp corners, necessitating high frequencies in the spectral decomposition before small errors in phase in $g(t+\epsilon)$ can materially affect the waveform. Where this is so, the phase variation is random enough for there to be no blade-passage frequency harmonics in the spectrum, and the sound is composed of harmonics of the disk rotation frequency alone. The spectrum is the characteristic of that measured if a definite interval of white noise is repeated harmonically, as it would be in a short loop of taped noise continuously playing on a recorder. That spectrum is an infinite series of equal-strength tones of the loop frequency.

The most significant effect of supersonic motion is that "sharp-cornered" shock waves are formed, making the basic Fourier synthesis of the wave contain very high frequencies. This effect, coupled with slight phase variations due to irregularities of blade positioning, can evidently bring about the array of low-frequency tones that constitute buzz saw.

The essential element of the buzz-saw phenomenon seems to be a phase randomization of the elementary blade-passage signals. This effect is inevitable because of slight manufacturing imperfections leading to errors in circumferential positioning. It is also an effect that can arise from nonlinear effects resulting from blades of slightly varying geometry, for the higher pressure regions would tend to travel relatively faster than the low-amplitude signal to induce phase variations away from the rotor disk.

SOURCES OF BROADBAND SOUND AT HIGH SPEED

Random broadband noise in any turbomachine is caused by some form of turbulence. Steady flow distortions cause broadband noise only indirectly by bringing about turbulence in some part of the machine. The inlet flow into the machine may be turbulent, so that the aerodynamic loading of the blades is made stochastic, and sound of continuous frequency content is then inevitable. Sound generated in this way can appear relatively discrete only if successive blades experience nearly identical loading histories, as they would if a large sausage-shaped turbulent eddy were being absorbed by a fan over a significant fraction of a disk revolution. Ffowcs Williams and Hawkings (ref. 1) show that the bandwidth of the blade-passage tone generated in such a situation is the reciprocal of the number of blades subjected to the distortion field of a single eddy.

At low speeds the random noise is due almost entirely, apart from small (in air) displaced inertia terms, to the unsteady forces on a blade. These forces can be computed by the method of Sears and von Kármán (ref. 2), a method which regards the flow as incompressible. The motions bringing about the unsteady forces are virtually decoupled from the small sound field at low Mach number. At higher Mach number, the coupling is immensely improved, and it is no longer possible to determine the blade loading independently of the sound field; neither is the blade load itself the source of the field. The computation of the field centered on the blades is then properly posed as a diffraction problem, where the incident field is specified with the object of determining the scattered waves. Of course, once conditions are known on the bounding surfaces, the linear radiation field is determined.

Miles (ref. 3) gives many relevant references and describes the field induced by a thin supersonic aerofoil entering a sharp-edged gust. This solution can serve as the Green's function to generate the scattered field for arbitrary two-dimensional incident flow. At first sight, quite a different viewpoint must be taken of the sound generated by turbulence arising on the rapidly moving blading, but in fact recent developments bring the two situations very close together. We consider here blading that moves in a uniform stream.

It is known that in coordinates moving with the stream sound is generated and propagates according to Lighthill's inhomogeneous wave equation

$$\frac{\partial^2\rho}{\partial t^2}-c^2\nabla^2\rho\equiv\Box^2\rho=\frac{\partial^2 T_{ij}}{\partial x_i\partial x_j} \tag{8}$$

T_{ij} is only nonzero effectively in a confined region of space where turbulence is present. The boundary conditions under which equation (8) is to be solved usually take the form of a constraint that the normal velocity in the fluid is equal to that of the bounding solid surface, together with a radiation condition. The noise problem is then posed as that of finding the solution to equation (8) with T_{ij}, a specification of the driving turbulence, known.

It is troublesome to have the boundary conditions specified on a moving surface, so there is some benefit to accrue from a selection of a new coordinate system fixed relative to the surfaces. Unfortunately, the wave operator is not invariant to a Galilean transformation, so the benefit of easily specified boundary conditions is bought at the expense of a more intractable governing equation. This difficulty can be overcome for steadily moving surfaces by the use of a Lorentz transformation that slightly distorts the geometry of the boundaries. However, if the surfaces are thin planes parallel to the flow, the complication in the Lorentz frame is minimal, and the high-speed surface problems can then be reduced to elementary low-speed examples. This scheme can be used, for example, to study sound diffraction from a thin-walled pipe, with flow on both sides of the wall. It is also the scheme by which Berman has been successful in posing the general aerodynamic noise problem for steadily moving surfaces. The results of this approach reproduce the conclusions reached by Ffowcs Williams and Hawkings for steady motion (ref. 4). However, their results are applicable to arbitrary motion, so they are more suitable as a basis from which to discuss the issues arising in turbomachinery noise, where rapid rotary accelerations are inevitable.

The solution to equation (8) can be written in a useful form as long as all source distributions are compact. That is, all surface and eddy sizes must be very much smaller than any wavelength in the radiation field. That solution is given in equation (7.4) of Ffowcs Williams and Hawkings (ref. 4):

$$4\pi c^2(\rho-\rho_0)(\mathbf{x},t)=\frac{\partial^2}{\partial x_i\partial x_j}\left[\frac{Q_{ij}+\rho_0 v_i v_j V_0}{r\,|1-M_r|}\right]-\frac{\partial}{\partial x_i}\left[\frac{P_i+\rho_0\dot{v}_i V_0}{r\,|1-M_r|}\right] \qquad (9)$$

Q_{ij} is the integrated stress tensor, v_i the surface velocity, V_0 the volume displaced by the surfaces, and P_i the force exerted by the surface on the fluid. The field is driven by a dipole system of strength equal to the body force excess over that required to change the displaced momentum and by a quadrupole made up in part by the integrated turbulence stress tensor and in part by the surface Reynolds stresses. $|1-M_r|$ is the Doppler factor by which the length scale in the sound field is reduced because of source motion at Mach number M_r toward the field point $\mathbf{x}$.

At low speeds, the dipole term is dominant, as can be seen from the usual estimating procedure of setting the force proportional to ρU^2L^2 (L being a characteristic source length) and the integrated Reynolds stress to ρU^2L^3. The source radiates a field of wavelength λ, and the operator $\partial/\partial x_i$ changes the magnitude of the differentiated quantity by a factor of order λ^{-1}. According to equation (9), the magnitude of the quadrupole field is, therefore,

$$c^2\rho \sim \frac{\rho U^2 L^3}{r\,|\,1-M_r\,|}\cdot\frac{1}{\lambda_0^2\,|\,1-M_r\,|^2} = \rho U^2\left(\frac{L}{r}\right)\left(\frac{L}{\lambda}\right)^2 |\,1-M_r\,|^{-1} \qquad (10)$$

while that of the dipole-induced field is

$$c^2\rho \sim \frac{\rho U^2 L^2}{r\,|\,1-M_r\,|}\cdot\frac{1}{\lambda_0\,|\,1-M_r\,|} = \rho U^2\left(\frac{L}{r}\right)\left(\frac{L}{\lambda}\right) |\,1-M_r\,|^{-1} \qquad (11)$$

λ_0 is the wavelength emitted by the source at rest, and $\lambda = \lambda_0\,|\,1-M_r\,|$ is the wavelength at convection Mach number M_r.

The quadrupole is negligible evidently only as long as $L/\lambda \ll 1$, as it always is in the regime where equation (9) is relevant. Then, the dominant source term is the force exerted by the fluid on the surface, and the job of quieting a low-speed fan is essentially one of reducing the level of the unsteady forces on the fan surfaces. Not so when $L/\lambda < \not\sphericalangle 1$, as is inevitably the case because of the Doppler contraction and the tendency for the wavelength to vary inversely with fan speed. The general solution to equation (8) was rewritten by Ffowcs Williams and Hawkings in a form suitable for the noncompact distribution, and for the special case of steady high-speed motion this equation becomes

$$4\pi c^2(\rho-\rho_0)(\mathbf{x},t) = \int_{\bar\Omega,\tau} \frac{\partial^2 T_{rr}}{\partial r^2}\,\frac{c\,d\bar\Omega\,d\tau}{r}$$

$$+\int_{\Gamma,\tau}\left\{\operatorname{div}\left[\mathbf{m}\rho\cot\theta(u_r^2-c^2)\right]+\cos\theta\,\frac{\partial T_{rr}}{\partial r}\right\}\frac{c\,d\Gamma\,d\tau}{r\sin\theta} \qquad (12)$$

where the suffix r is the tensor component in the direction of radiation (in a frame moving with the fluid), $\bar\Omega$ is the surface $r=$ constant, Γ is the curve of intersection of $\bar\Omega$ with the boundary surface S, $\mathbf{m}$ is a unit vector normal to Γ in S, and θ is the angle between the surface normal and the radiation direction. τ is a time variable.

The usual dimensional analysis of this equation shows that both the noncompact quadrupoles and surface dipoles radiate fields of comparable magnitude, of order

$$c^2\rho \sim \rho U^2\,\frac{c\tau}{r} \qquad (13)$$

where τ is the coherent radiating lifetime of a source. For steady fields, this lifetime is infinite and leads to the shock fields of steady supersonic flow. For the broadband noise, however, the time is the inverse frequency L/U, so that at high speeds the broadband noise amplitude is

$$c^2\rho \sim \rho U^2 \left(\frac{L}{r}\right) M^{-1} \tag{14}$$

This is initially the same magnitude as that of the steady pressure waves radiated from a blade in rapid supersonic motion, but the steady field is not subjected to the same geometrical spreading law.

Equation (12) makes it clear that the fluctuating force on the blade does not appear explicitly as a source term. In place of the surface stress we have the Reynolds stress gradient, which is the same term as that responsible for volume sound. Also, the lifetime of the source appears directly in the field strength, so that the random field would be quieter if the turbulent eddies were made to lose their coherence more quickly.

A point that is perhaps worth making also is that at the high supersonic speeds the noise seems to increase in direct proportion to thrust and that the noise per unit power is a decreasing function of speed.

The differences that feature in the high-speed noise are due entirely to the inevitable contraction in wavelength to a point where sound is no longer easily distinguishable from the driving unsteady flow. Then the process of attempting a specification of surface conditions in the absence of sound, followed by a prediction of the sound field from these estimated boundary values, fails. The problem has become inevitably one of diffraction, where both surface loads and the radiated sound must be estimated together. This procedure is only in its early stages in the study of aerodynamic noise, but already effects are being predicted quite contrary to the qualitative ideas one gathers from extrapolating known results for compact source distributions. The most readily measured property of noise is the variation in energy level with increasing speed. Compact quadrupoles and dipoles have a U^8 and U^6 variation, respectively, while both have a U^2 variation in the noncompact condition. Away from these limits, one can observe a very wide range of velocity indices resulting from the scattering of the quadrupole field by noncompact surfaces. No doubt this work is relevant to the broadband noise inside fan systems wherever the fan chord exceeds the radiated wavelength. However, the ideas discussed here have yet to be applied to that situation.

REFERENCES

1. Ffowcs Williams, J. E., and D. L. Hawkings, Theory Relating to the Noise of Rotating Machinery. *J. Sound Vib.*, Vol. 10, No. 1, 1969, p. 10.
2. Sears, W. R., and T. von Kármán, Aerofoil Theory for Non-Uniform Motion. *J. Aeron. Sci.*, Vol. 5, 1938, p. 379.
3. Miles, J. W., *The Potential Theory of Unsteady Supersonic Flow.* Cambridge U. Press, 1959.
4. Ffowcs Williams, J. E., and D. L. Hawkings, Sound Generation by Turbulence and Surfaces in Arbitrary Motion. *Proc. Roy. Soc.* (*London*), Series A, Vol. 264, 1969, p. 321.

DISCUSSION

J. VRANA (McGill University): It is interesting to note the comment by Dr. Ffowcs Williams that nonlinearity need not be invoked to explain the occurrence of combination noise. Let us face it, the nonlinearity is there; that is the way shock waves propagate.

In thinking about the phenomenon, I was intrigued by the small effects of attempts to make the blading as uniform as possible. Could the bunching of shock waves be an inherent instability of certain flow fields, where, for instance, a shock displaced slightly forward would "lose" more expansion Mach waves behind it than it gained in front (speaking in the 2–D blade-to-blade terminology of the compressor designer), thereby increasing in strength and moving further forward to a new stable position? Blading imperfections would then merely act as triggers for this departure from periodicity.

T. G. SOFRIN AND G. F. PICKETT (Pratt & Whitney Aircraft): Professor Ffowcs Williams has presented a linear theory explaining the generation of tones at harmonics of engine rotation frequency. Although he shows that these tones may be produced by small circumferential variations in shock spacing, the lack of a mechanism to account for evolution of greater proportions of extra tones with increasing distance is a significant limitation. The probe data outlined in our paper clearly show that small circumferential variations in shock spacing are amplified because of the nonlinear nature of the propagating shock waves, and we contend that this is the dominant factor in the distribution of the power in the direct rotor field throughout the harmonics of engine rotation frequency.

FFOWCS WILLIAMS (author): Mr. Vrana suggests an interesting possibility, and I know that some people have been working on the stability of the shock train although I haven't myself. I think it's quite likely that it has an important bearing on this problem, but if this is just simply an instability issue, I can't really see why the experiments show that the signature is exactly the same every time the disk goes around. Your comment about the nonlinearity being there anyway: Of course it's there. But it's certainly not necessary to "buzz saw." You could get buzz saw for vanishingly low amplitude at supersonic speeds. That was the point I was making.

The information given by Mr. Sofrin and Mr. Pickett is a very convincing account of the observation that, in their experiment, nonlinear effects are very important. They are likely important in all real engine situations where buzz-saw noise is observed. The point I make, however, is that buzz saw is also inevitable for arbitrarily small amplitude. The linear theory I describe shows how blade spacing errors will account for a buzz-saw phenomenon, but I have no doubt that, in the experiment reported, the main phasing errors were induced by nonlinear effects. However, nonlinearity is not *essential* to the occurrence of buzz saw.

Multiple Pure Tone Noise Generated by Fans at Supersonic Tip Speeds[1]

T. G. SOFRIN AND G. F. PICKETT

Pratt & Whitney Aircraft
Division United Aircraft Corporation

The existence of clusters of pure tones at integral multiples of shaft speed has been noted for supersonic-tip-speed operation of fans and compressors. A continuing program to explore this phenomenon, often called combination-tone noise, has been in effect at Pratt & Whitney Aircraft (P&WA) for several years. This paper reviews the research program, which involves a wide range of engines, compressor rigs, and special apparatus. Elements of the aerodynamics of the blade-associated shock waves are outlined and causes of blade-to-blade shock inequalities, responsible for the multiple tones, are described in some detail. Some of the data presented were obtained under sponsorship of the Federal Aviation Agency.

Multiple pure tone sound, frequently called combination-tone and "buzz-saw" noise, characterizes the spectra of turbofan inlet radiation fields at supersonic-tip-speed operation. Before discussing the high-speed regime, however, some relevant background information concerning subsonic-tip-speed fan noise will be mentioned.

Instances of discrete tones other than blade-passage harmonics have been noted in the inlet spectra of turbofan engines since the time of the first aircraft compressor noise studies. In those very early 1960's, when blade-passing frequency whine was the outstanding engine noise problem, such "extra frequencies" were called "subharmonics" and were dismissed from the mainstream of research activities. With continuing time and effort, a clear understanding of blade frequency noise was achieved. The growing evidence for the prevalence of extra frequencies could no longer be ignored, and they became the subject of increasing attention. A simple

---

[1] The authors acknowledge the cooperation of the Federal Aviation Agency, under whose sponsorship portions of the data presented here were obtained.

sorting test based on whether or not these frequencies remained fixed integral orders (multiples) of shaft rotation rate served a useful classifying purpose.

Examples of strong acoustic signals with nonintegral orders are aeolian tones and edge tones caused by oscillating flows over structural elements in the fan air passages. Such small-scale items as instrumentation probes, bosses, and sheet metal seams could excite substantial acoustic vibrations and in fact did so on more occasions than one would care to recall. Figure 1 shows some of the early P&WA laboratory models used for the study of aeolian and cavity tones in airflow duct sections. As has subsequently been pointed out (ref. 1), the duct modes can couple with the triggering mechanism to sustain intense fields. Despite such complexity, solution of many of these types of extra-frequency problems is a matter of careful attention to detecting and removing disturbances in and along the engine flow passages.

A more subtle category of extra-frequency compressor sounds includes cases of subsonic-tip-speed, two-stage fans with spectra having several integral order tones. The essential feature of these spectra, which clued discovery of the generating mechanism, is that the predominant orders are arranged in arithmetic sequence. The sequence may be broken occasionally and may contain a very few misfits, but the main sequence difference equals the difference in the number of rotating blades of the two fan stages. Figure 2 shows a pair of order diagrams for experimental engines run in 1961. By plotting narrow-band spectral components against engine shaft speed, frequencies that are related to speed by a factor or "order" are recognized by falling upon radial lines. Figure 2*a* pertains to a turbofan having 35 first-stage blades and 42 blades in the second stage, a difference of 7 blades. Lines of constant order have been labeled and the concentration of data points along lines separated by 7 orders is striking. In figure 2*b*, corresponding groupings for an experimental fan with 35 and 32 blades are seen along order lines separated by 3 units.

The sequence of important order lines in these and other instances of two-stage fans suggested that a common generating mechanism was responsible for many cases of extra-frequency spectra and that both rotors were mutually involved. From that point on it was quite straight-forward to show that the extra frequencies are generated when a rotor-stator interaction mode at some blade-passage harmonic of one rotor is scattered by the other rotor. This scattering, now called "secondary interactions" in multistage compressors, transforms acoustic energy in the frequency domain as well as effecting mode conversion. Mode conversion at fixed frequency is a result of stator scattering; frequency shifts require a rotating scatterer. The allowable orders in a two-stage fan are given by integral linear combinations of the blade numbers; i.e., $[k_1B_1+k_2B_2]$. Whether an allowable secondary interaction exists in significant strength (some are on

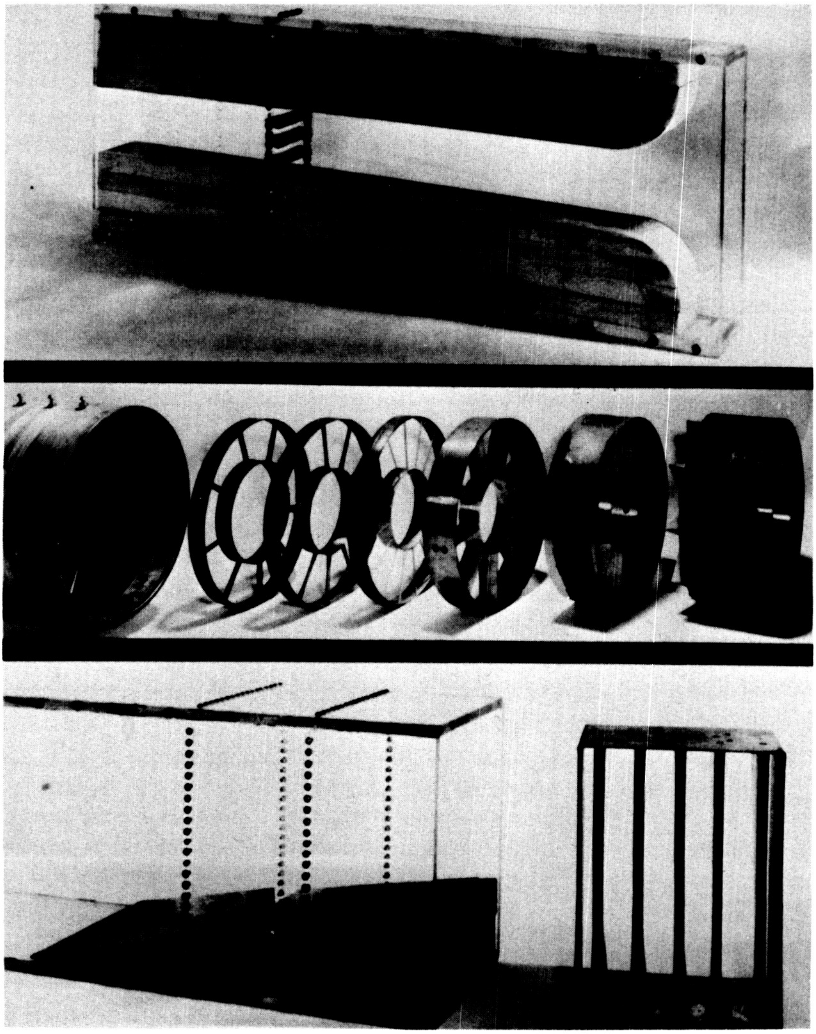

FIGURE 1.—*Apparatus used in studies of aeolian and cavity tones.*

occasion actually greater than blade-passage harmonics!) depends on many factors, including considerations of cutoff ratios of both the secondary interaction and the primary rotor-stator "generator" mode.

Secondary interactions are mentioned here because they provide one of the first cases where the phrase "combination tone" was applied to a powerplant noise. This expression was also chosen to refer to multiple pure tone supersonic noise, in preference to "buzz saw," on the basis of

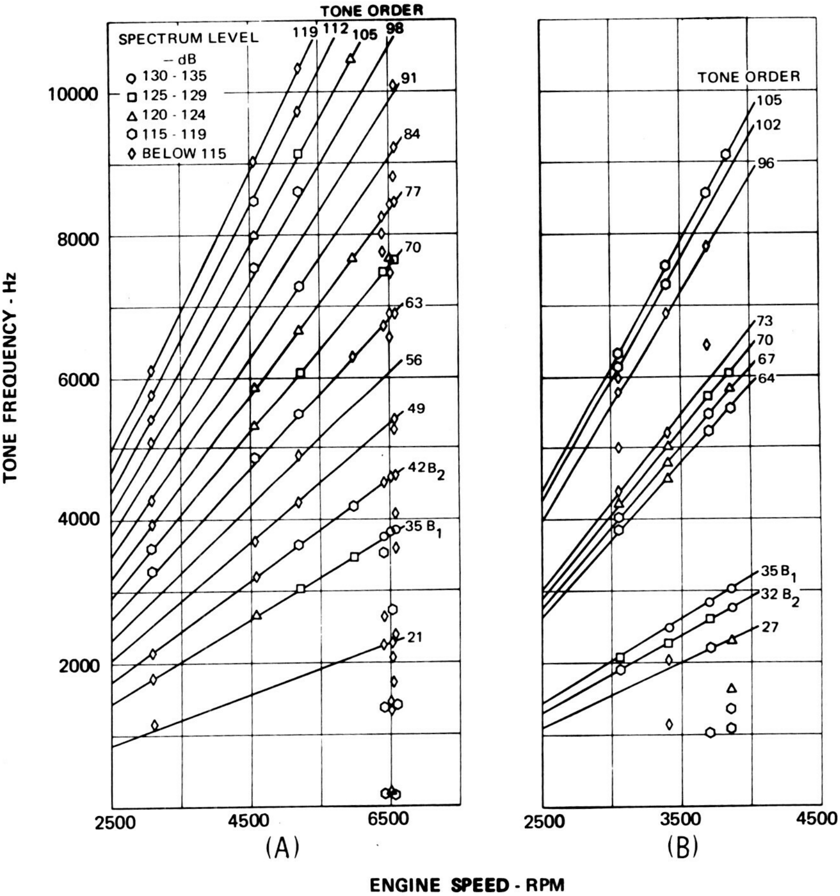

FIGURE 2.—*Combination tones at subsonic rotor speeds due to secondary interactions.*

psychoacoustic considerations that will be discussed presently. A further purpose of including some of the investigations into extra-frequency engine noise is to show the rather wide range of phenomena that can be made understandable by application of linear acoustic theory. Despite these instances of success, linear acoustic theory proved unable to account for the characteristics of supersonic-tip-speed combination tones. Detailed experimental studies have revealed the fundamental nonlinear nature of the supersonic case.

PSYCHOACOUSTIC FACTORS

An unusual feature of combination-tone noise is that its spectrum is, as a matter of natural course, much less annoying to the listener than would be the case if the transformation of energy from blade-passage harmonics failed to occur. Probably the most common examples of reducing annoyance by spreading line spectra are the irregularly spaced blade arrangements used in automotive cooling fans and the irregular tread patterns used for snow tires. This spectral control feature resurfaces every so often in the literature (refs. 2, 3, 4), but the example involved here with supersonic fan multiple-tone noise is the first known reported instance of its occurrence in machinery as a natural outcome rather than as a deliberate design feature.

At the time when blade-vane interaction noise at subsonic rotor speed was the central power plant noise problem, two psychoacoustically oriented programs were instituted to explore the possibilities for reduction of compressor-whine annoyance. One program was based on using controlled off-synchronization of the speeds of the four engines so that the airplane far-field spectra contained blade-passage components, combining in a typical sequence as, for example, 2000, 2100, 2200, and 2300 Hz and harmonics of these. The nonlinear characteristics of the human ear are

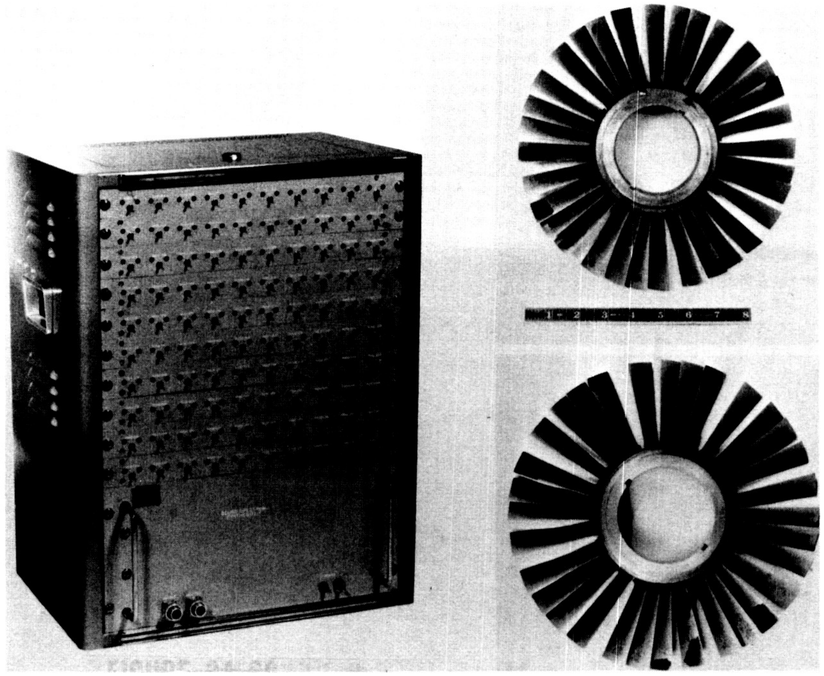

a.—*Sound-spectrum synthesizer.* b.—*10-inch-diameter asymmetric rotors.*

FIGURE 3.—*Equipment for tone-spectrum evaluation.*

such as to supply perceptions of many extra tones that are linear combinations of these basic frequencies. Stevens (ref. 5) discusses these phenomena, employing the apt term "combination tone." Where several signals separated by a common difference (e.g., 100 Hz) are presented to the ear, reinforcement of the low-frequency first-order difference tones (100, 200, 300 Hz, etc.) is especially pronounced, giving the impression of a much lower pitched sound than is actually implied by the physical spectrum. Psychoacoustic tests were conducted using a spectrum synthesizer with 100 controllable frequency outputs, as shown in figure 3*a*. This program was suspended when analysis of flight operational considerations contraindicated use of the complex engine speed control required.

A more straightforward scheme for spectral spreading was explored in model form using unequally spaced blade arrangements (ref. 10), as illustrated in figure 3*b*. This program was also dropped because of other conflicting engine requirements, although, as noted earlier, the concept has many working applications in current use.

There are indications that the spectra of combination-tone noise in supersonic rotors are subject to some measure of control. For this reason, as well as the need to predict "perceived noisiness" more reliably than current rating systems can accomplish, extensive psychoacoustic studies are required. A facility for testing multiple subjects simultaneously in exceptionally uniform sound fields has been recently developed and is shown in figure 4.

FIGURE 4.—*Psychoacoustic test facilities.*

HISTORICAL INFORMATION

As far as we have determined, the first reported incident of supersonic combination-tone noise appeared more than a decade ago in an internal report on an experimental engine (ref. 6). Conclusion number six states, "Engine noise had an odd quality . . . which was best described as sounding like a buzz saw. It was generally considered to be a less annoying sound than the compressor blade passing noise at lower thrust settings." At the time of these remarks, when no theory of compressor noise existed and when a "fix" for the acute blade-passage noise of the JT3D turbofan then entering service was being urgently sought, it is somewhat ironic to have uncovered a glimpse of a phenomenon that would assume practical significance at a later date.

By 1964, uprated engine modifications and advanced experimental prototypes were appearing with higher fan tip speeds. Reports of unusual inlet noises began to grow. Finally, full-scale inlet noise measurements on a run of several engines, together with high-operating-speed data on a single-stage compressor rig, provided the necessary information. Narrowband spectral analysis clearly and consistently showed a plurality of tones at multiples of shaft rotational frequency and linked their appearance with the onset of supersonic rotor tip speed. Compressor noise theory, by now reasonably developed, indicated that these integral order tones were linked with rotor blade inequalities. Since the phenomena occurred even with rotors having new, closely uniform blades, it was also clear that some sort of aerodynamic amplification was involved, whereby small geometric blade-to-blade variations were transformed into very substantial nonuniformities in the pressure fields rotating with the blades.

In 1965 design work was progressing on a new generation powerplant, the JT9D, which incorporated all known fan noise reduction features in the basic configuration (ref. 7). Interaction noise had been designed out of the powerplant, but at supersonic tip speeds, where no method other than absorbing lining was available to attenuate the propagating pressure field of the rotor, it had originally been feared by some that the direct rotor field would generate an objectionable siren-like noise. However, the test information related above, supplemented by noise data on a related larger turbofan, indicated that combination-tone noise rather than blade-passage noise would be radiated from the inlet at high powers. A significant body of information thus indicated that we could reasonably expect to avoid this piercing blade-passage whine problem. Early in 1966, tests of a prototype JT9D confirmed this fortunate state; the concept behind asymmetric fans had finally reached practicable embodiment with the natural, small blade-to-blade nonuniformities of aircraft rotors operating at supersonic tip speeds.

Disclosure of combination-tone noise as an inherent characteristic of supersonic-tip-speed operation was made in a pair of 1966 survey papers (refs. 8, 9). Studies to advance the understanding of this noise and to explore methods for its control were pursued. Extensive use was made of the 28-in.-diameter single-stage compressor rig shown in figure 5. Internal traversing of the inlet of this rig revealed the blade-tip shock patterns and gave definitive evidence of the nonlinear behavior involved in supersonic combination-tone noise. Many of the detailed noise characteristics learned in these programs were described by J. D. Kester in 1969 (ref. 10) and were also disclosed in a short motion picture released in 1968 (ref. 11).

Several compressor rigs and many engines have been used to establish the current state of understanding. The wide-scale range of equipment used is highlighted in figure 6*a*. Posed in the inlet of an experimental full-scale flight-test JT9D engine is a wind-tunnel-model-powered nacelle designed for installation aerodynamic programs. Its 4-in.-diameter fan, capable of spinning at 80 000 rpm design speed, develops a tip Mach number of 1.3. Noise data were obtained with a high-frequency microphone system, recorded at high speed on magnetic tape, and played back at ¼ speed through a narrow-band wave analyzer. A sample inlet noise spectrum is shown in figure 6*b*. The prevalence of multiple pure tones may be noted and compared with the full-scale JT9D inlet noise spectrum of figure 6*c*. This model program provided convincing evidence for the reliability of scaling to blade Mach number, a principle of acoustic testing

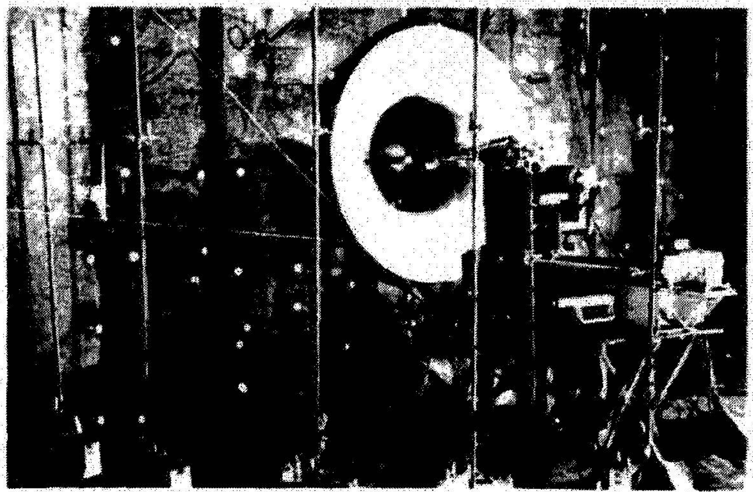

FIGURE 5.—*28-inch-diameter compressor rig.*

a.—*JT9D and scale-model powered nacelle.*

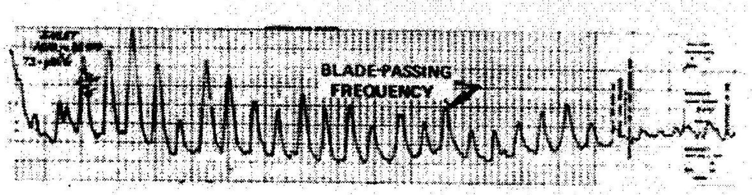

b.—*Scale-model spectrum—[illegible]-inch diameter.*

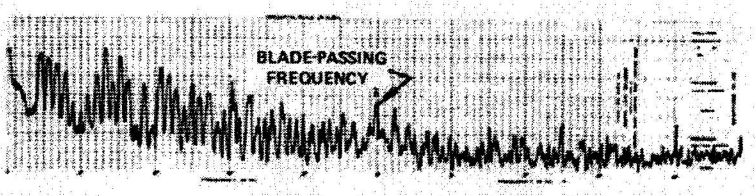

c.—*JT9D spectrum—92-inch diameter*

FIGURE 6.—*Effect of fan diameter on combination-tone noise.*

that had been stated explicitly for subsonic compressor operation by Wells and McGrew (ref. 12).

A supersonic cascade wind tunnel was used in a program to explore the consequences of various blade nonuniformities upon cascade shock-wave variations (refs. 13, 14). Figure 7 gives a view of the installation and a Schlieren photograph of the shock structure taken during operation with a uniform reference configuration.

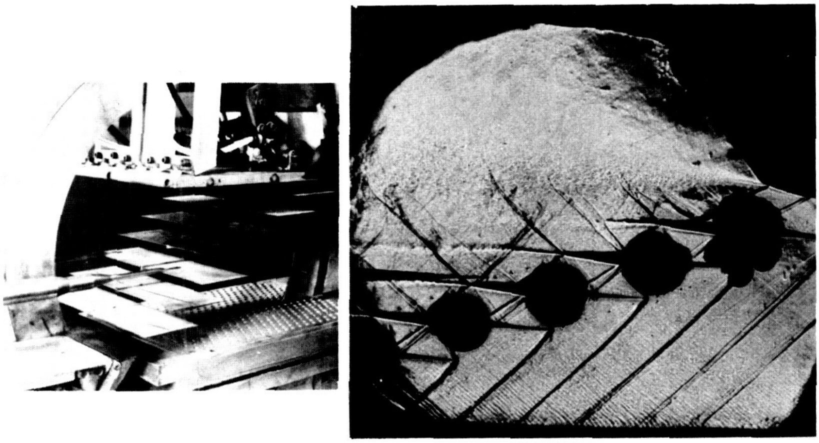

a.—*Cascade arrangement.* b.—*Schlieren photograph.*

FIGURE 7.—*Supersonic cascade tunnel.*

To supplement full-scale engine studies of combination-tone noise with a variety of blade designs and flexible test programs, a new single-stage fan rig has been developed (ref. 15). As seen in figure 8, the rig is installed in an outdoor stand where reliable far-field noise surveys are made and where inlet traversing equipment can be emplaced quickly for very near field data acquisition.

As is true in the linear cases of compressor noise phenomena, the three-dimensional nature of the inlet geometry presents complications in the nonlinear domain of supersonic fan noise. Radial or spanwise variations in the aerodynamic characteristics of the flow very near the rotor face, as well as acoustic field variations symptomatic of higher radial mode structure farther out the inlet, raise significant obstacles to theoretical and experimental studies alike. A simplified basis for further study would be established if it could be demonstrated in a narrow annulus inlet that the power in predominantly blade-passage harmonics in the very near shock field of the rotor were transformed into multiple tones at shaft rotation harmonics, as occurs in conventional fan inlets.

A short program has been conducted recently under Federal Aviation Agency sponsorship to determine if combination-tone noise is developed in a narrow annular inlet region (ref. 16). By inserting a sleeve spaced concentrically in the inlet of the 28-in.-diameter rig (figure 9), a narrow annulus was formed within which the outboard blade shock field could travel. Confined between the closely spaced (1-$\frac{1}{2}$ in.) walls, shock structure in the very near field of the rotor evolved into the characteristic form of combination-tone noise as the pattern spiraled forward. Figure 9*b* shows typical combination-tone results obtained several inches from the rotor in the annulus.

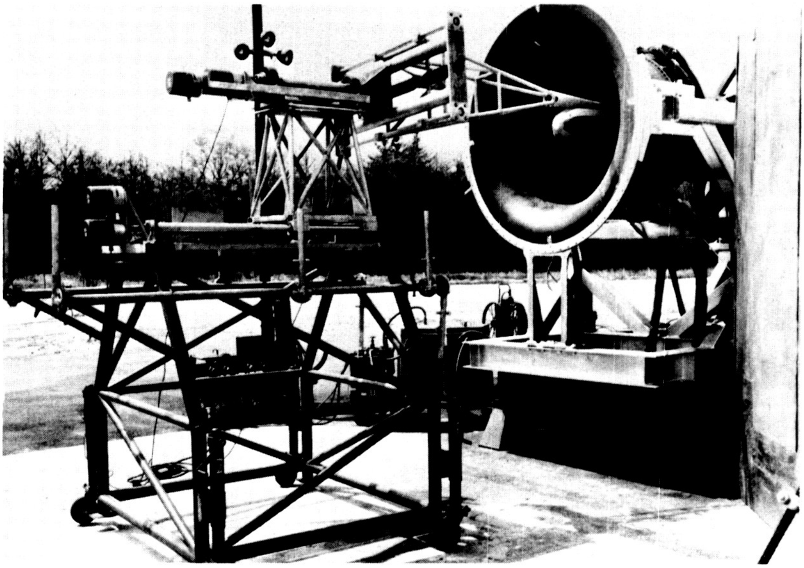

FIGURE 8.—*52-inch-diameter fan rig.*

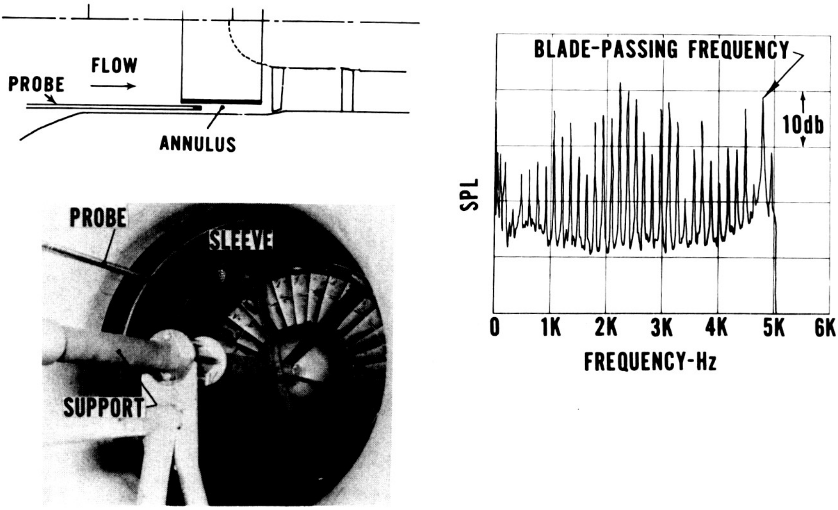

a.—*Annulus and probe.* b.—*Spectrum inside annulus.*

FIGURE 9.—*Combination-tone development in narrow-annulus inlet.*

These tests confirmed that combination-tone studies could indeed be made on a two-dimensional basis and that no essential features are lost by ignoring radial complications. Accordingly, consideration is currently being given to possible fabrication and use of a special narrow annulus rig or rotating annular cascade (figure 10) in future studies.

COMBINATION-TONE CHARACTERISTICS

The essential features of combination-tone noise, based on the work reported by J. D. Kester (ref. 10) and on additional programs, are summarized below, prior to an aerodynamic explanation of the shock-wave evolution responsible for this noise.

At supersonic tip speeds, shock waves form at the rotor blade tips. Because of small blade-to-blade irregularities, the shocks display slight nonuniformity of amplitude and spacing. Probe microphone measurements taken very close to the leading edge plane of the rotor reveal that these irregularities are small compared to their average values. Typical data for the very near field (figure 11*a*) show the essential uniformity of pressure signature, repetitive at blade-passage frequency. The corresponding spectrum confirms the visual impression, extra harmonics of shaft rotational rate being at least 20 dB below blade-passage levels. Parenthetically, these small traces of extra orders are also present in the subsonic spectra of actual fans.

Only when the pressure sensor is drawn farther away from the rotor do the characteristics of combination-tone phenomena appear. The rotor signature exhibits relatively more blade-to-blade irregularity. At this distance the shock pattern, locked to and spinning with the rotor, assumes

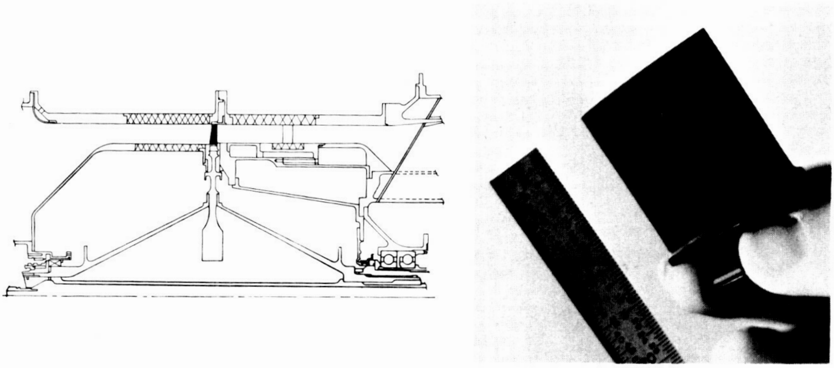

a.—*Sketch of rotating annular cascade.*

b.—*Blade for rotating annular cascade.*

FIGURE 10.—*Rotating annular cascade rig.*

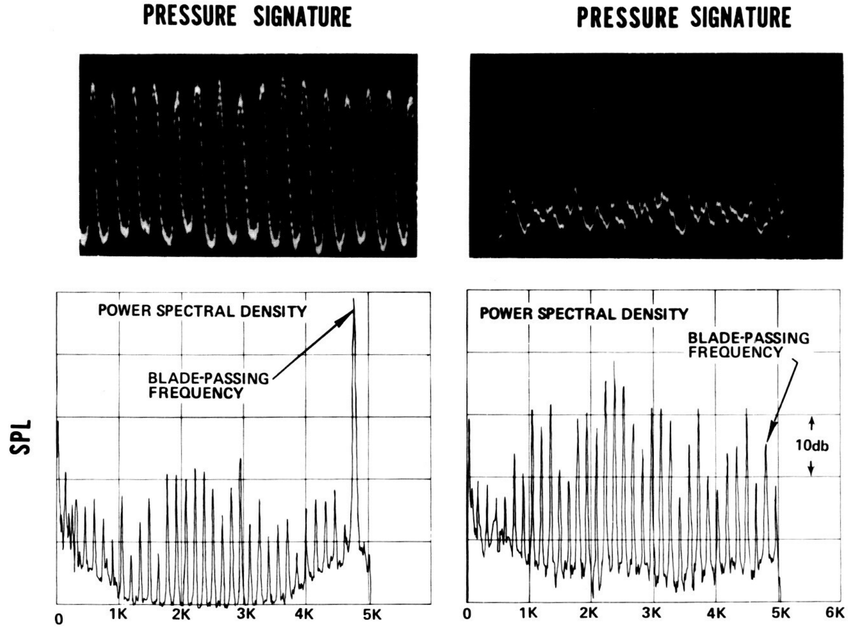

a.—*Uniform very near field.* b.—*Combination-tone field.*

FIGURE 11.—*Waveforms and spectra in combination-tone development.*

different features around its perimeter. Correspondingly, the extra frequencies present in the spectrum have levels that are no longer negligible relative to blade-passage harmonics. At stations still farther from the rotor plane (figure 11*b*), the rotating pressure field has lost most if not all of its original repetitive blade imprint, and its spectrum is overwhelmingly multiple pure tone. This sequence portrays the complete evolution of the combination-tone pattern; further probe travel discloses no essential novelty.

The earliest studies of combination-tone structure inside a fan inlet drew heavily on instrumentation systems and concepts that had previously proved successful in explaining the nature of compressor noise at subsonic rotor speeds. In that field it is expedient to work with such concepts of linear analysis as spectral parameters (e.g., amplitude and phase of blade-passage frequency) and duct characteristic functions (circumferential and radial modes). These techniques have limited value for examining combination-tone behavior. Examination of the *unfiltered* pressure signature in the course of axial traversing shows the complex evolving progression of the train of unequal shocks. Filtering techniques in frequency and resolution into modal components actually obscure the clear information in the pressure-time signature. No amount of spectral information can substitute for witnessing the overtaking and merging of shocks when seeking understanding of combination-tone generation.

In supersonic rotors having subsonic exit flow relative to the blades, the shock structure producing combination-tone noise is restricted to the regions ahead of the rotor. The effects of inlet guide vanes noted to date are largely predictable: Preswirl lowers the resultant flow speed entering the fan and defers the onset of shock behavior. Guide vanes may affect the transmission of the combination-tone wave field as they do blade-passage noise, in a manner described by Mani, Horvay, and others (ref. 17). However, guide vanes reintroduce the prime source of blade-vane interaction noise.

Combination-tone noise has been successfully reduced by sound-absorbing liners (figure 12). Because the shock-wave field is confined to the vicinity of the inlet wall rather than distributed radially inward to the rotor hub, a short treatment length is more effective for the attenuation of combination-tone noise than it would be for interaction noise.

AERODYNAMIC THEORY—IDEAL, UNIFORM FANS

Having illustrated the essential features of combination-tone noise with examples from several rigs and engines, we will investigate in more detail that region ahead of the rotor called the transition zone, where sound power is transferred from blade-passing frequency into other harmonics of engine rotation frequency. We shall first consider the shock-wave behavior ahead of an ideal, symmetrical fan and then extend the results to actual fans.

A theoretical investigation using shock-wave theory is somewhat complicated by the low supersonic regime in which most fans operate and the three-dimensional nature of the flow. It is possible, however, using the methods of finite-amplitude wave theory as developed by Whitham (ref. 18) and Lighthill (ref. 19), and extended by Blackstock (ref. 20), Morfey (ref. 21), and Fink (ref. 22), to obtain the asymptotic behavior of two-dimensional steady shock waves from cascades.

Applying finite-amplitude wave theory to an isolated airfoil in supersonic flow, the leading-edge shock wave decays eventually as the inverse square root of distance from the airfoil and is of parabolic locus (ref. 19 sec. 9). The distance from the airfoil for which this solution is valid varies with the free-stream Mach number and the leading-edge thickness for the flow regime considered. If this airfoil is now assembled in a two-dimensional cascade, it can be seen from figure 13 that the shock wave from that airfoil will be intersected by or will eventually meet the expansion-wave region of the preceding blade. The fields are illustrated for straight- and curved-blade entrance profiles in figures 13*a* and 13*b*.

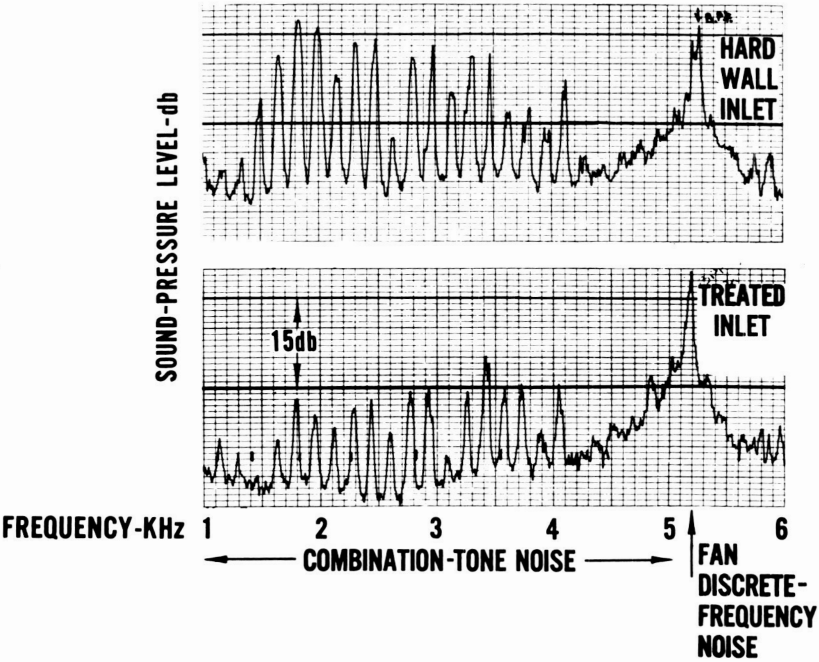

FIGURE 12.—*Effects of sound-absorbing inlet liner on combination-tone noise.*

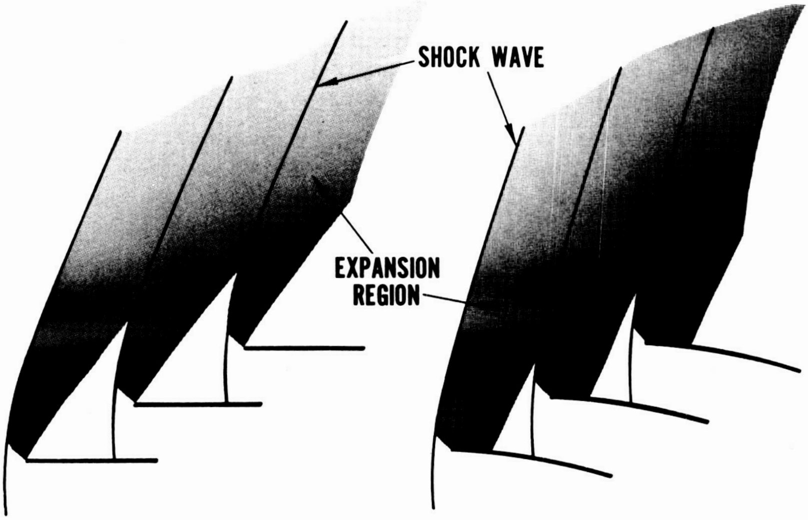

a.—*Straight entrance-region blades.* b.—*Curved entrance-region blades.*

FIGURE 13.—*Shock patterns for uniform blade cascades.*

Shock waves that are both preceded and followed by expansion waves were first investigated by Whitham (ref. 18); he found that the shock strength at large distances varied as the inverse first power of distance, converging to a line parallel with the free-stream Mach lines. Subsequent investigation by Blackstock (ref. 20) and Morfey (ref. 21) confirmed these results. Specifically, the shock strength at large distances, x, was shown to be

$$\frac{\Delta P}{P_0}=\frac{2\gamma}{\gamma+1}\frac{\lambda}{x}(\sin \varphi-M_x) \tag{1}$$

where λ is the gap between shocks, P_0 is the ambient pressure, M_x is the axial Mach number, φ is the angle between the free-stream Mach wave and the axial direction, and γ is the ratio of specific heats. Notice that equation (1) is independent of the initial amplitude of the shocks and that it does not contain any dissipative terms. This latter consideration is a restriction of the validity of equation (1) for very large distances when the shock strength is so small as to make dissipative terms comparable with nonlinear, steepening effects.

It can be concluded that the shock waves ahead of an ideal fan will initially advance on the expansion regions of preceding blades and their strength will decay as the inverse square root of distance from the fan. At distances of the order of one blade gap, where the expansions preceding and following the shocks are comparable,[2] the shocks will no longer advance on the expansion regions of the preceding blades, and their amplitude will decay more like the inverse first power of distance.

The conclusions were validated in the two-dimensional field of the narrow-annulus test mentioned earlier in the paper. The annulus was probed with a $\frac{1}{8}$-in. B&K microphone so that the strength of the average[3] shock wave could be measured as a function of distance ahead of the fan. The results for three operating points of the compressor are presented in figure 14. The pressure rise across the average shock is normalized by its value at the first measuring point ahead of the rotor, and lines with slopes of $-\frac{1}{2}$ and -1, corresponding to inverse square-root and inverse first-power decay respectively, are superimposed upon the measured data with evident fit. The change from $1/\sqrt{x}$ to $1/x$ decay is seen to occur around 2.5 in., which is slightly less than one blade gap.

---

[2] That is to say, the areas preceding and following the shock on a pressure-time curve are comparable. Lighthill (ref. 19) illustrates similar situations in his treatment of plane shock-wave formation (sec. 7) that can be extended to include the development of nonplane shock waves (sec. 9).

[3] The data, taken on an actual fan, naturally reflect blade-to-blade inequalities. It was necessary to process these data so that the behavior of the corresponding uniform, ideal case could be inferred.

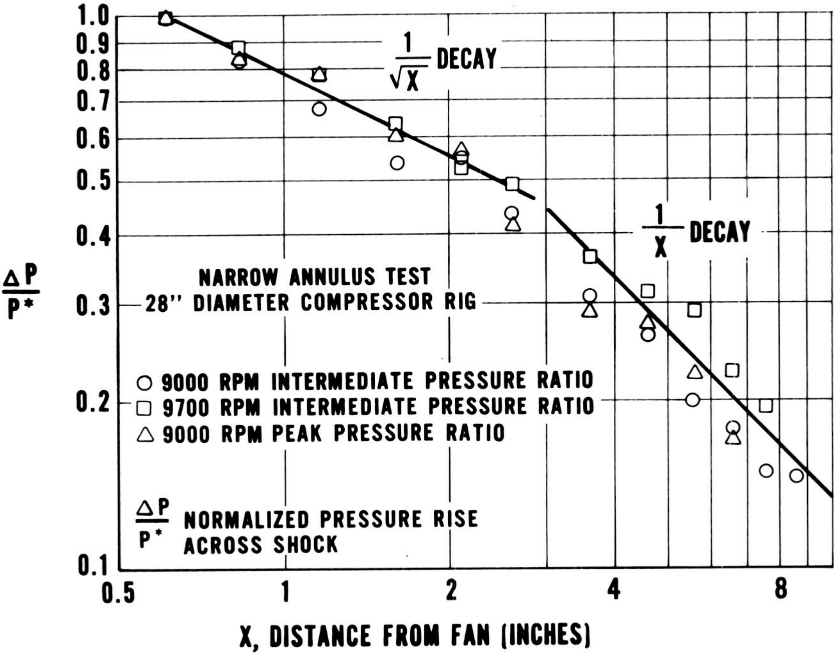

FIGURE 14.—*Changing rate of shock-wave decay.*

Figure 15 shows the development of the waveform from an ideal, symmetrical fan at distances of $\frac{1}{4}$, $\frac{1}{2}$, and 1-$\frac{1}{2}$ tip chords ahead of the rotor. At the $\frac{1}{4}$- and $\frac{1}{2}$-chord locations, it can be seen that the shock fronts have not caught up with the expansion regions of the preceding blades and thus still decay as $1/\sqrt{x}$. At the 1-$\frac{1}{2}$-chord position, the expansion regions preceding and following the shocks are comparable, and subsequent shock decay varies as $1/x$.

It is now possible to infer some of the details of the evolution of the shocks ahead of real fans containing nonuniformities and to explain how the sound power at blade-passing frequencies is transformed into harmonics of engine rotation frequency.

AERODYNAMIC THEORY—REAL FANS

In all real fans, small nonuniformities within manufacturing tolerances are present or are created by routine wear in service. These blade-to-blade nonuniformities are reflected in supersonic operation by variations in shock strengths and associated expansion regions. Very close to the blades, however, the nature of the nonuniformity closely preserves regularity of

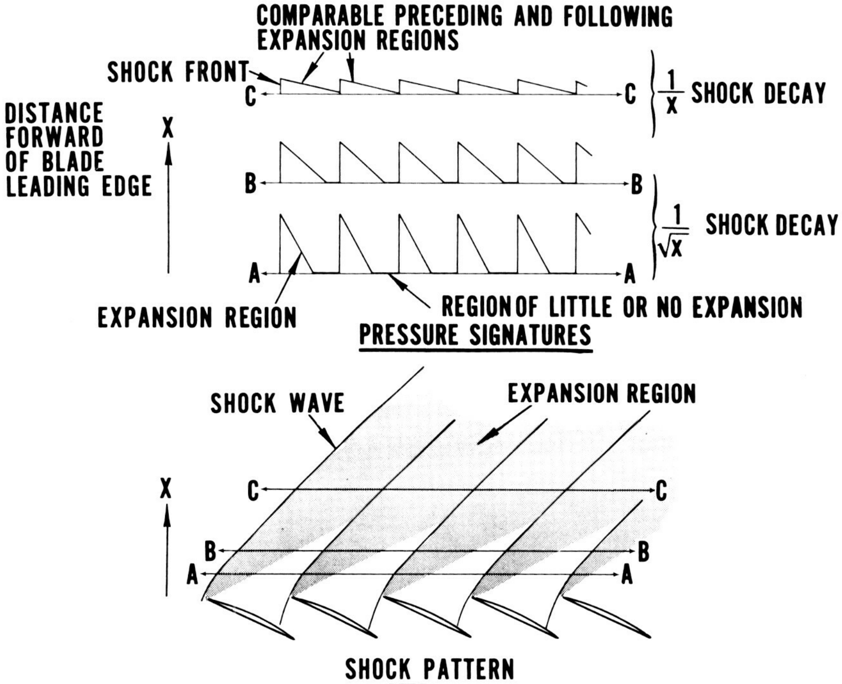

FIGURE 15.—*Shock-wave pattern from a uniform fan.*

interval between shocks. A Fourier analysis of waveforms produced by such rotating shock-wave patterns has been investigated as a particular case of a general analysis of time- and amplitude-modulated waves (ref. 22). An important result of this investigation is that the expected power spectrum depends critically upon variations of the intervals between shocks and only slightly upon variations in shock strength. Therefore, since the variance in interval between shocks is small close to the fan, most of the sound power will be concentrated at blade-passing frequency even if there are appreciable variations in shock strength. Probe data taken very close to a variety of fans confirms this spectral characteristic, the power at blade-passing frequency being as much as 20 dB greater than the power in other engine harmonics.

Now, this picture changes as the shock waves spiral upstream in the inlet. Because there are variations in shock strength, the stronger shocks advance on the weaker ones and the intervals between them become noticeably irregular, causing the combination tones to emerge. In this region of the duct, the shocks from each blade will behave more like isolated shocks, being influenced only slightly by the other blades, and will decay in amplitude as the inverse square root of distance. The irregularities are enhanced when each shock encroaches on the expansion region of the preceding blade, and begins to decay more nearly as the inverse first power of distance. Because of the existing irregularities, this change in decay will occur at different points in the inlet for each shock. Thus, until all the shocks are decaying as the inverse first power, there is a region in the inlet where essentially two different types of decay mechanism are present. The intervals between the shocks will change appreciably in this region since some shocks will be advancing upon the expansion regions of the preceding blades while others will already be converging toward their respective asymptotes. As all the shocks approach their asymptotes, there will be no further changes in shock intervals. When dissipative forces have produced acoustic waves, noise radiates to the far field with no further exchange of power among the tones. Figure 16 illustrates, for a cascade, the various stages of shock-wave evolution. It may be seen how the essentially uniform pattern very close to the rotor is transformed into one containing marked irregularities.

Figures 17, 18, and 19, showing the inlet-duct pressure signatures of three different fans, illustrate various aspects of shock-wave decay considered in this section. High-frequency-response pressure transducers, flush-mounted in the inlet of an experimental JT9D engine, produced the waveforms in figure 17. It is clear that the shock waves close to the fan are not preceded by expansions until about the $\frac{3}{4}$-tip-chord position forward of the rotor. At this point, an irregular sawtooth waveform has developed.

Figure 18 displays waveforms obtained by probing the inlet of a 52-in.-diameter fan rig. An arrow draws attention to the evolution of a particular shock at various axial positions. It is both preceded and followed by stronger shocks, the following one overtaking the reference shock 8 in. ahead of the fan. The combined shock is then indicated by the arrow and its subsequent decay proceeds as the inverse first power of distance. This latter decay is consistent with theory since at 8 in. the combined shock has comparable preceding and following expansion regions.

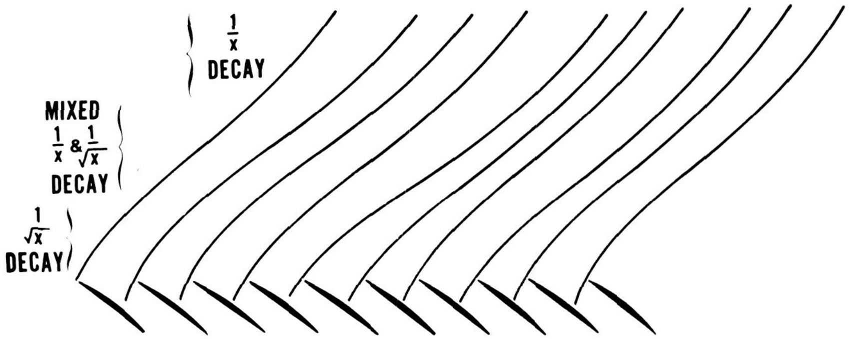

FIGURE 16.—*Shock-wave pattern from an actual fan.*

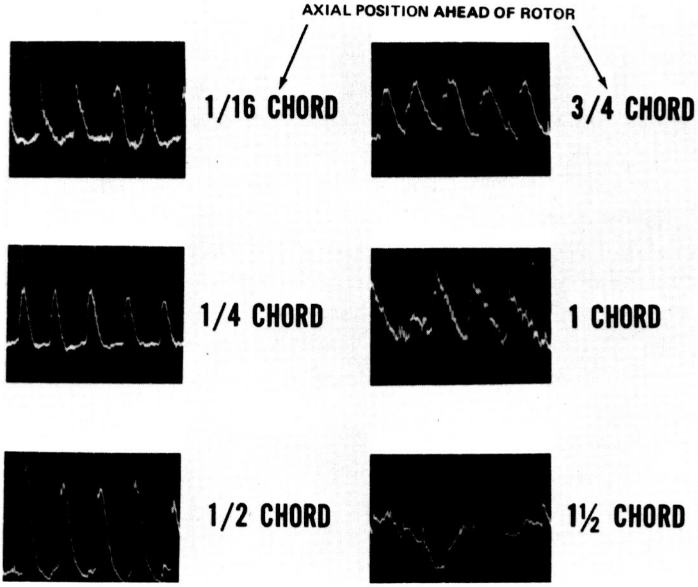

FIGURE 17.—*Blade-pressure signatures—experimental JT9D.*

The development of the three shocks ahead of the arrow is of interest also because they combine after 16 in. to produce a single shock that is seen to be approaching an acoustic waveform after 28 in. At 32 in., a typical shock-free, acoustic waveform can be seen, and it may be assumed that little or no subsequent transfer of sound power between the combination tones will take place.

Extensive data have been acquired on the 28-in.-diameter rig, which has been referred to frequently here. Sample waveform patterns for a blade configuration in this rig are shown in figure 19. One region of waveform is called to attention by an arrow, showing the behavior of a weaker shock decaying between two stronger shocks. Here again may be seen examples of how the nonlinear aerodynamic behavior of shock waves accounts for combination-tone noise.

SUMMARY

It has been shown theoretically and experimentally how finite-amplitude wave theory can account for the transfer of sound power from blade-passage harmonics into harmonics of engine rotation frequency. This transfer, occurring in the inlet forward of a supersonic rotor, produces noise with a multiple-tone spectrum and a deep, distinctive sound, characteristic of combination-tone noise.

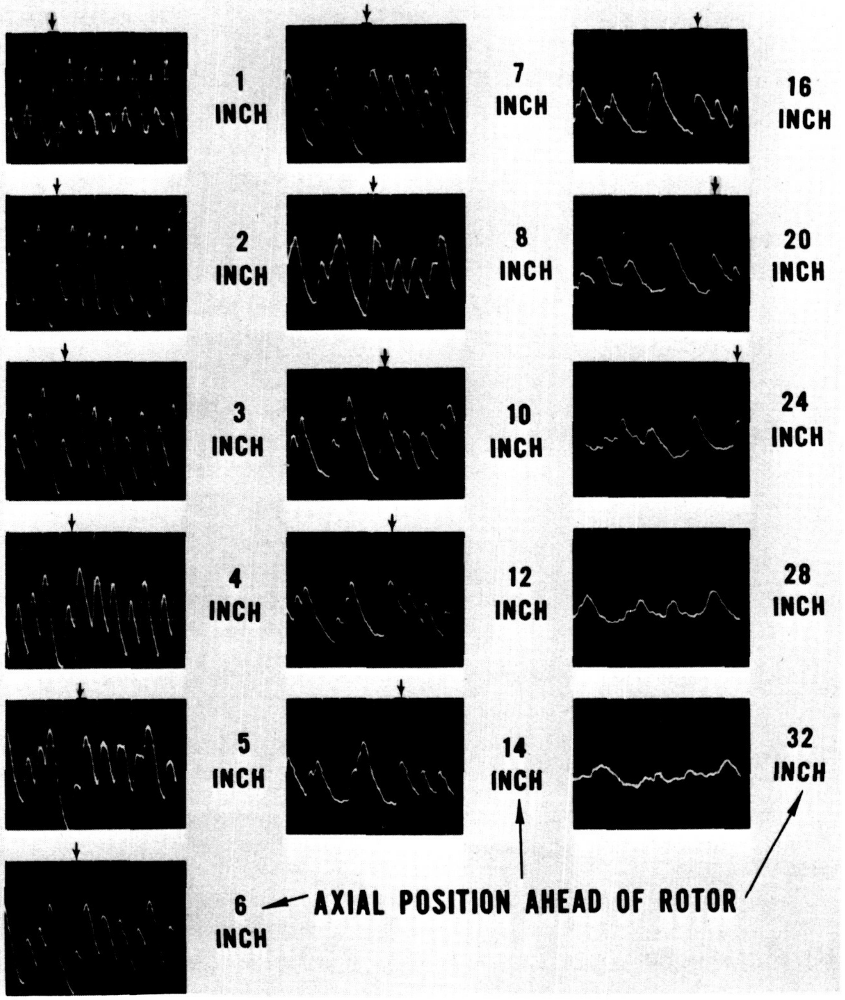

FIGURE 18.—*Blade-pressure signatures—52-inch-diameter fan.*

The work reported here and recent appearances of other accounts in the literature (refs. 24, 25) provide interesting examples of significant progress in aircraft noise reduction. Combination-tone noise is neither a new phenomenon nor has it suddenly become more severe. However, a new generation of high-bypass-ratio engines is appearing with important improvements in jet exhaust roar and fan interaction discrete noise. These reduced levels of previously dominant engine sources have unmasked combination-tone noise as a target of renewed noise reduction efforts.

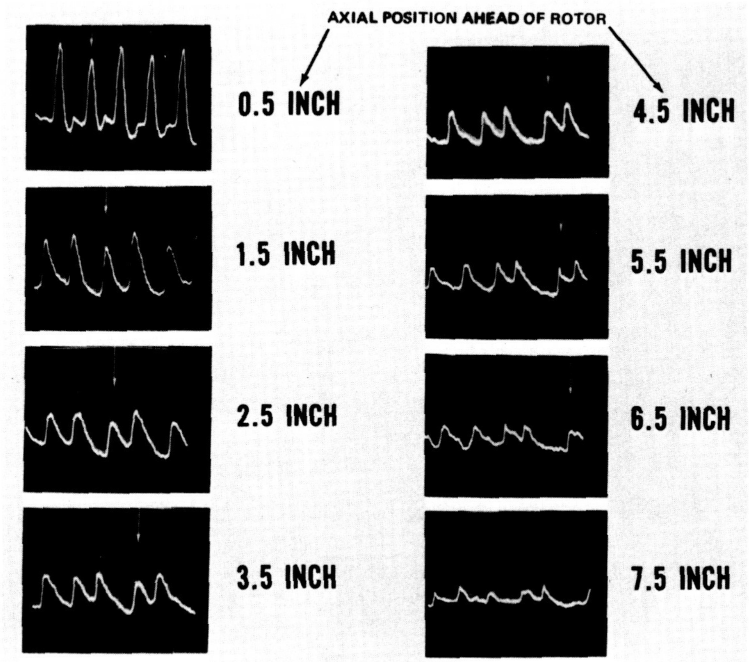

FIGURE 19.—*Blade-pressure signatures—28-inch-diameter fan.*

ACKNOWLEDGMENT

It is a pleasure to acknowledge the cooperation of the Federal Aviation Agency, under whose sponsorship portions of the data presented here were obtained.

REFERENCES

1. PARKER, R., *Discrete Frequency Noise Generation Due to Fluid Flow Over Blades, Supporting Spokes, and Similar Bodies.* ASME Paper 69–WA/GT–13, November 1969.
2. CARUSO, W. J. ET AL., *Turbo-Machine Blade Spacing with Modulated Pitch.* U.S. Patent 3,006,603, October 31, 1961.
3. VARTERASIAN, J. H., Math Quiets Rotating Machines. *J. SAE,* Vol. 77, No. 10, October 1969.
4. MELLIN, R. C., AND G. SOVRAN, *Controlling the Tonal Characteristics of Aerodynamic Noise Generated by Fan Rotors.* ASME Paper 69–WA/FE–23, November 1969.
5. STEVENS, S. S., AND H. DAVIS, Aural Harmonics and Combination Tones. *Hearing,* Chapter 7, John Wiley & Sons, Inc., 1938.
6. KESTER, J. D., *X–283–2 Inlet and Exhaust Noise.* Pratt & Whitney Aircraft, Internal Document, January 19, 1960.

7. KESTER, J. D., AND T. G. SLAIBY, *Designing the JT9D Engine to Meet Low Noise Requirements for Future Transports.* SAE Preprint 67–0331, 1967.
8. SOFRIN, T. G., AND J. C. MCCANN, *High Bypass Ratio Engine Noise.* International Conference on the Reduction of Noise and Disturbance Caused by Civil Aircraft, Paper INC/C1/P15 (London) November 1966.
9. SOFRIN, T. G., AND J. C. MCCANN, *Pratt & Whitney Aircraft Experience in Compressor Noise Reduction,* Acoust. Soc. Am., Paper 2D2, November 1966.
10. KESTER, J. D., Generation and Suppression of Combination Tone Noise From Turbofan Engines. *Proc. AGARD Fluid Dynamics Panel,* Paper 19 (Saint-Louis, France), May 1969.
11. *Noise Reduction Progress at Pratt & Whitney Aircraft.* Motion Picture Section, P&WA, 1968.
12. WELLS, R. J., AND J. M. MCGREW, *Model Freon Compressor for Acoustic Investigations,* Technical Report FAA–ADS-47, June 1965.
13. FINK, M. R., *Upstream Supercritical Flow Pattern of a Supersonic Cascade with Misaligned Blades.* United Aircraft Research Laboratories, Internal Report, January 9, 1967.
14. FINK, M. R., AND H. K. TAKVORIAN, *Effects of Blade Misalignment on the Flow Pattern Upstream of a Supersonic Cascade.* United Aircraft Research Laboratories, Internal Report, January 1968.
15. WARDEN, C. A., *High Bypass Ratio Fan Noise Research Test Vehicle.* AIAA Paper 69–492, June 1969.
16. *Compressor Noise Research.* Contract DOT–FA–69WA–2045, Federal Aviation Agency, 1969.
17. MANI, R., AND G. HORVAY, Sound Transmission Through Blade Rows. *J. Sound Vib.,* Vol. 12, No. 1, 1970, pp. 59–83.
18. WHITHAM, G. B., *The Flow Pattern of a Supersonic Projectile (Appendix).* Comm. on Pure and Applied Math, Vol. V, No. 3, August 1952, pp. 301–348.
19. LIGHTHILL, M. J., Viscosity Effects in Sound Waves of Finite Amplitudes. *Surveys in Mechanics, G. I. Taylor 70th Anniversary Volume,* Cambridge U. Press, 1956, pp. 250–351.
20. BLACKSTOCK, D. T., Connection Between the Fay and Fubini Solutions for Plane Sound Waves of Finite Amplitude. *J. Acoust. Soc. Am.,* Vol. 39, No. 6, June 1966, pp. 1019–1026.
21. MORFEY, C. L., A Review of the Sound-Generating Mechanisms in Aircraft-Engine Fans and Compressors, Aerodynamic Noise. *Proc. AFOSR–UTIAS Symposium (Toronto),* Toronto U. Press, 1969, pp. 299–330.
22. FINK, M. R., *Predicted Noise Decay of Transonic Compressors with Sharp Leading Edges.* United Aircraft Research Laboratories, Report UAR–J173, July 1970.
23. PICKETT, G. F., *The Prediction of the Spectral Content of Combination Tone Noise.* To be presented at the AIAA 7th Propulsion Joint Specialist Conference, June 14–18, 1971.
24. PHILPOT, M. G., *The Buzz-Saw Noise Generated by a High Duty Transonic Compressor,* ASME Paper 70–GT–54, May 1970.
25. HAWKINS, D. L., *Multiple Tone Generation by Transonic Compressors.* Symposium on Aerodynamic Noise, U. Tech., Loughborough, England, September 1970.

DISCUSSION

J. E. FFOWCS WILLIAMS (Imperial College, London, England): I completely agree that the shock formation and steepening is a nonlinear process and I find your model completely consistent. However, there's one point that I would like to make and that is that I would argue that it is possible to get buzz saw even if you were to devise a supersonic fan with very small perturbations in pressure across the blades. And I would just take you up on the point you made at the beginning of your talk where you said, "We surely don't make fans that chaotic in spacing." But what is the measure of whether the error is large or small? It isn't on any absolute geometric scale.

The point I am stressing is that for a small error in blade positioning, it wouldn't matter at all, as long as the pressure signature was slowly varying on that scale. But if the signature is varying rapidly on that scale it would matter. In this case, if you've got supersonic flow, the pressure would rise abruptly. There will be a sort of a step wave, and, if you would misposition that step by any error, however small, the result would inevitably give rise to some buzz-saw noise.

I agree that your situation is entirely nonlinear. So for you to quote your experiments as evidence on my hypothetical linear supersonic fan problem isn't really to the point.

C. L. MORFEY (Southampton University): Referring to figure 11 where you show the very near field compared with the far field after the shocks are developed, the first question is whether the base lines are the same on these two figures. Second, I wonder if you could give us any guidance as to why it is we often see a peak in the envelope of these plots at roughly half the blade-passing frequency? This seems to be a common feature of some of your spectrographs. If the baseline is the same in figure 11*a* and figure 11*b*, then it shows your levels at about one-half blade-passing frequency have increased.

R. D. WELLIVER (The Boeing Co.): In all this discussion, there's just one point that I think gets lost a little bit that I would like to make. We've done a number of fan experiments in fans that run at supersonic tip speeds and when we think of the buzz saw being created by the nonuniformity of the blade or things of this nature, one thing comes to mind that's become very clear in many of our experiments, and that is that the magnitude of the buzz-saw levels as combination tones varies considerably with the blade loading. If we consider a fan running at a constant speed across the fan operating map from the maximum air flow to the surge line for a given speed, the Mach number really doesn't change too much since the inlet relative Mach number of the fan varies very little. If you look at the vector diagrams, obviously the absolute Mach number as well as the inlet relative Mach number for a high-speed fan doesn't vary too much, and yet if we measure the noise and look at the spectrum, across the speed line, we find that the buzz-saw noise could vary as much as 20 dB for a high-speed fan. It sometimes goes from disappearing perhaps at some lower loading to be very dominant. Now, I didn't change the speed, I didn't really change the Mach number, and I didn't change the blading obviously as I moved across the speed line, and so this is a question which I've certainly had and I think some explanation of this phenomenon is required.

SOFRIN AND PICKETT (authors): In reply to Professor Ffowcs Williams, we agree that combination-tone noise would be generated for the hypothetical linear supersonic fan problem. It would differ, however, from combination-tone noise produced from actual fans in two important ways: Firstly, the power at the harmonics of engine rotation frequency would not be comparable to blade passage harmonics and also there would be no transfer of power among the harmonics as a function of distance forward of the fan. These characteristics of combination-tone-noise generation can be explained only by using a nonlinear model.

With reference to Dr. Morfey's questions, figure 11 shows the differences in spectrum shapes at two axial locations in the inlet and was not prepared to compare the spectra at the two locations on a quantitative basis. He observes correctly that the envelope of the tones seems to peak at roughly half of blade-passing frequency. The reasons for the typical envelope shapes are discussed in reference 23.

Concerning the question of effect of blade loading on combination-tone noise as raised by Mr. Welliver, a reexamination of our results has confirmed that, over the operating range available on the rigs and engines reported in our paper, the spectra shape can often change, but the total energy contained in the tones remains effectively the same.

Broadband Sound Radiated from Subsonic Rotors[1]

C. L. MORFEY

Institute of Sound & Vibration Research
University of Southampton, England

Recent theoretical work on sound sources in subsonic turbomachinery is applied to the correlation of axial-flow fan and compressor noise measurements. Correlations are presented for directivity and sound-power spectra associated with broadband noise. A simple explanation is given to account for the relative amounts of sound power transmitted upstream and downstream from a single-stage fan.

The mechanisms of sound generation in subsonic turbomachinery are understood in principle and have been documented in a recent paper by the author (ref. 1). Current fundamental research is now aimed at describing the unsteady flow within the machine with sufficient accuracy that the relative importance of the various mechanisms can be assessed. Existing noise measurements are unfortunately not matched by the necessary unsteady aerodynamic measurements; in this situation, positive identification of mechanisms is clearly not possible. Any correlation of data with mean-flow measurements will remain of doubtful generality until the gap is closed.

If a particular noise-generation mechanism is put forward as a hypothesis, however, theory can provide considerable guidance in the correlation of measurements. Even though only mean-flow aerodynamic measurements are available, the relevant unsteady-flow components can be related to the steady flow by similarity arguments. Considerable success has been achieved in this way in jet noise correlation, following the initial work of Lighthill (ref. 2); the same approach is adopted in this paper for broadband fan noise.

---

[1] The cooperation of Rolls-Royce Limited in supplying data is gratefully acknowledged. The initial calculations were carried out by R. Snow, B.A.C. Acoustics Laboratory, Weybridge, while at I.S.V.R., Southampton University.

Following the studies by Smith and House (ref. 3) and Morfey and Dawson (ref. 4) on aircraft-engine fan and compressor noise, further data on broadband noise have become available covering a range of axial-flow machines (table I). These are reported by Snow in reference 5, which gives details of measurement and analysis techniques and forms the basis of the present study.

In the sections that follow, various aspects of the noise measurements—sound-power spectrum shapes and levels, directivity patterns and the ratio of downstream to upstream radiated power—are discussed and correlated with mean-flow data. The theory on which the correlations are based has been developed where necessary in the appendixes.

CORRELATION OF BROADBAND POWER SPECTRUM SHAPES

The correlation of broadband sound-power spectra is approached in two stages. First, a frequency parameter is sought that brings the different spectra into line horizontally; then, for a fixed value of the frequency parameter, normalized values of sound-power spectral density are plotted versus Mach number. This is the same general procedure as was followed by Smith and House (ref. 3), although the details differ.

Nondimensional Frequency Parameter

Given a characteristic length scale L, a nondimensional frequency parameter can be formed either as a Strouhal number fL/U, where U is a characteristic velocity, or as the ratio fL/c $(=L/\lambda)$. These are related by the Mach number U/c.

We start by choosing a length scale, leaving till later the choice between U and c as velocity scales. It is expected that the spectrum of broadband sound radiated from a rotor-stator stage will depend on the scale of turbulence in the rotor wake. This in turn is related to the rotor wake-momentum thickness, as Mugridge has shown (ref. 6).

A possible length scale is therefore $b_R C_D$ (equal to twice the momentum thickness), where b_R is the first-rotor chord and C_D is the profile drag coefficient. This may conveniently be estimated in terms of the irreversible temperature rise ΔT_{irr} through the first rotor (ref. 7):

$$b_R C_D \doteq \frac{(\Delta T)_{\text{irr}}}{T_{01}} \cdot \frac{2\, d_R \cos \beta_2}{(\gamma-1) M_R^2} \qquad (1)^2$$

In equation (1), $d_R \cos \beta_2$ represents the rotor wake spacing and M_R is the relative Mach number at the rotor exit.

---

[2] $(\Delta T)_{\text{irr}}$ is assumed small compared with the stagnation temperature T_{01} at exit from the first rotor.

TABLE I.—*Summarized Compressor Information*

	Type of machine	First rotor			Design point		Blade numbers		
		Hub-tip ratio	Diameter (in.)	Mid-Rad. chord, (in.)	Mass flow (lb/s)	Speed (rev/min)	IGV	R1	S1
		(entry)							
A	2-stage fan	0.36	45	5.145	370	6 500	24	23	50
B	4-stage fan	0.36	52	4.041	475	5 450	----	35	52
C_1	7-stage	0.56	25	1.553	84	10 120	37	31	38
C_2	7-stage	0.56	25	1.553	84	10 020	85	31	38
D	8-stage	0.50	17.4	1.680	52	13 760	28	29	28
E	1-stage fan	0.55	24.5	1.815	79	8 550	43	31	50

For the engines tested, information was available on the overall isentropic efficiency η_n and hence on the irreversible temperature rise $(1-\eta_n)(\Delta T_0)_n$ over all n stages. Neglecting stator losses and apportioning the irreversible temperature rise equally between the n rotors gives as a rough estimate

$$(\Delta T)_{\text{irr}} \doteq \frac{1}{n}(1-\eta_n)(\Delta T_0)_n \tag{2}$$

Combining equations (1) and (2) gives a length scale L, defined as

$$L = \frac{2(1-\eta_n)(\Delta T_0)_n}{n(\gamma-1)T_{01}M_R^2} \cdot d_R \cos \beta_2 \tag{3}$$

which because of its link with the wake-momentum thickness should reveal any variations in the eddy scale leaving the first rotor.

This length scale is used below to obtain an empirical collapse of broadband spectrum shapes, with one modification: The rotor relative Mach number is taken for convenience as the inlet (rather than the exit) value. Midradius values are used throughout.

Collapse of Spectrum Shapes

Figure 1 shows, for each engine separately, the collapse of inlet sound-power spectra obtained with $L/\lambda = F$ as frequency parameter. Somewhat surprisingly, this is a good deal better than the collapse obtained with the Strouhal-type parameter F/M_R. Note that the spectra are plotted in constant-percentage-bandwidth form (i.e., the vertical scale is proportional to $f(dW/df)$); the peak occurs around $F = 0.1$ to 0.2 in each case. No correction has been made for atmospheric attenuation; the greatest measuring distance was 32 feet.

In figure 2 the mean spectrum shapes from the different engines are superimposed; the broken line for engine B indicates that the horizontal positioning of the spectrum is uncertain since the efficiency had to be estimated from other data. For comparison, figure 2 also shows the mean spectrum shape obtained by Smith and House (ref. 3) for broadband compressor noise at the position of maximum sideline OASPL; the peak has been placed at $F = 0.16$ to line up with the present data.[3]

A mean line based on figure 2 lies within 5 dB of most of the data points. Some of the scatter is doubtless due to errors both in sound-power measurement and in the aerodynamic data used for forming the frequency parameter; but the present scheme cannot account for genuine variations in spectrum shape.

---

[3] This implies a value of C_D between 0.1 and 0.2 for the compressors plotted in figure 12 of reference 3.

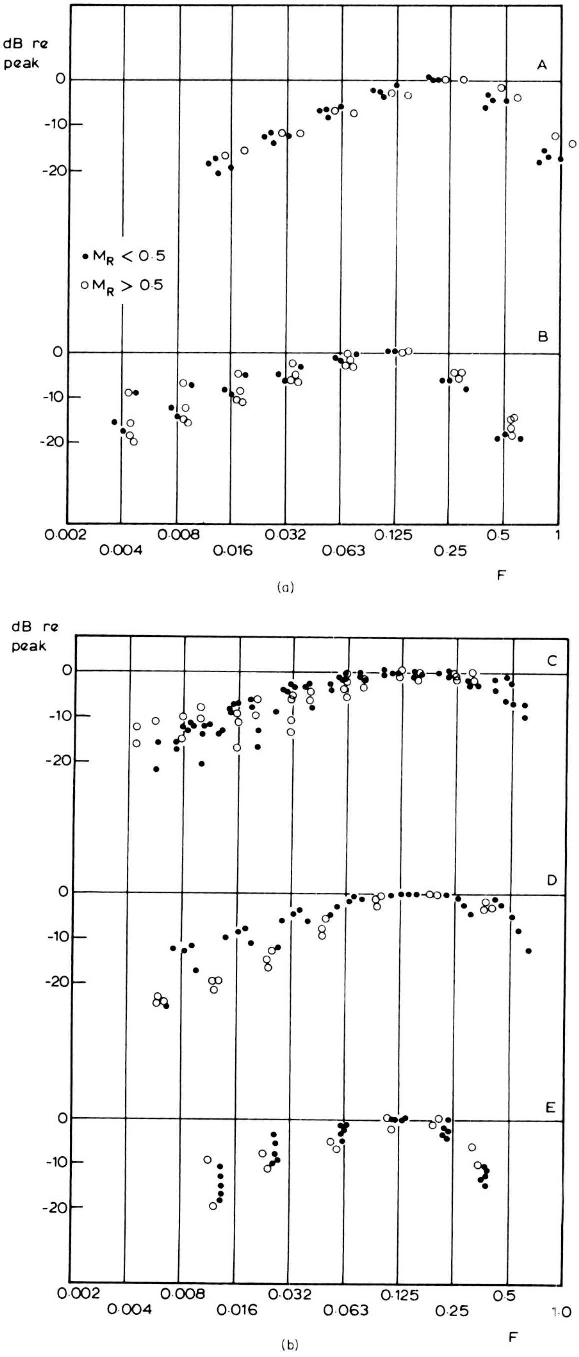

FIGURE 1.—*Spectrum shape correlation—broadband sound power radiated from inlet.*

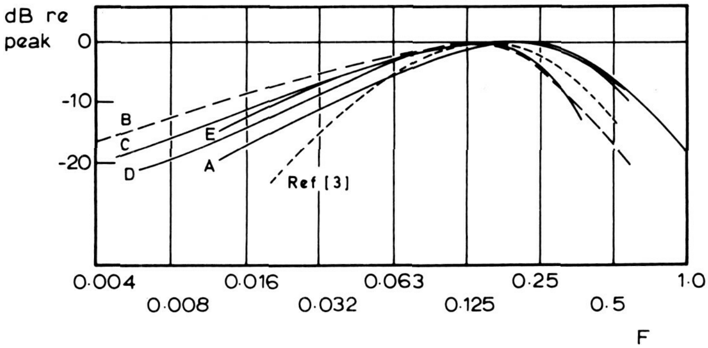

FIGURE 2.—*Mean spectrum shapes for all engines (constant-percentage bandwidth).*

CORRELATION OF ABSOLUTE LEVELS

The next stage in the data correlation process is to collapse the sound-power spectrum levels for a given value of the frequency parameter. This will be done with the aid of a simplified analytical model that predicts the sound-power variation with Mach number, blade area, and other principal factors. A nondimensional sound-power parameter is obtained in which these factors are normalized out; it is found to be constant within ±5 dB for all the engines measured, up to a rotor inlet Mach number of 0.6.

Nondimensional Sound-Power Parameter

The broadband sound-power spectrum generated by a single rotor-stator stage is related in Appendix I to the characteristics of the rotor wake turbulence. The analysis is highly simplified, its purpose being to predict the main trends so that these can be normalized out from the data. The analysis is based on the following assumptions:

(1) Broadband noise is generated by turbulence from one blade row, entering the row immediately downstream and setting up lift fluctuations on the downstream blades. Only the axial component of the lift fluctuations is taken into account in calculating the sound output (this point will be mentioned again below).

(2) Blade profiles are assumed acoustically compact. (This is a rather crude assumption since the ratio of axial chord to wavelength is of order 1 at the peak of the spectra in figure 1. The effect of noncompact blade profiles on sound radiation requires investigation.)

(3) The axisymmetric rotor-stator geometry is replaced by a two-dimensional model based on mean-radius conditions, and the spanwise

extent of the model is taken as being large compared with the sound wavelength.

(4) The flow is subsonic with $M^2 \ll 1$.

The results of the analysis are summarized in equations (15) and (16) of Appendix I. These involve the unknown quantities l_c (spanwise integral length scale of turbulence) and C_D (rotor-blade drag coefficient), besides the turbulence intensity parameter α. However, if we assume $l_c \propto b_R C_D$, as Mugridge's experiments (ref. 6) indicate, and replace $b_R C_D$ by L as in the previous section, we get the following relationship between the sound-power spectrum and aerodynamic parameters:

$$\frac{f}{\rho c^3 S_R}\,\frac{dW}{df} \propto {M_R}^5 \left(\frac{f d_R}{c}\right)^{-2} \sigma_S\, f(\beta_2,\alpha_1)\cdot\alpha \begin{pmatrix} F^3 \\ \\ F^2 \end{pmatrix} \tag{4}$$

The left-hand side of equation (4) is itself a nondimensional form of the sound-power spectrum; it will be divided by the first four factors on the right-hand side to produce a normalized power parameter.

For this preliminary study, it was considered an advantage to base the normalization solely on rotor parameters; σ_S is therefore replaced by the rotor solidity σ_R, and α_1 is replaced by β_2. Furthermore the C_L term in $f(\beta_2,\alpha_1)$ is neglected. The resulting nondimensional sound-power parameter is

$$G = \frac{dW}{df}\cdot\frac{f^3\, {d_R}^2 \csc^4 \beta_2}{\rho c^5 S_R' {M_R}^5} \tag{5}$$

Here $S_R' = \sigma_R S_R$ denotes the rotor blade area (span×chord×number of blades). All the quantities that make up G, apart from the sound-power spectrum itself, are generally known at the design stage of a fan or compressor.

As in the previous section, the correlation that follows is based on the relative Mach number at the rotor inlet.[4]

Sound Power Data Correlation

Values of G for $F = 0.16$—corresponding approximately to the peak of the constant-percentage-bandwidth spectra in figure 1—are plotted versus the rotor inlet relative Mach number in figure 3. The data points represent inlet-radiated broadband sound from the six different engines in table I, each run over a range of speeds.

---

[4] Note that for a given F value, $G \propto {M_R}^{-1}$; so the value of G is not very sensitive to the exact definition of M_R, provided the same definition is used in both F and G.

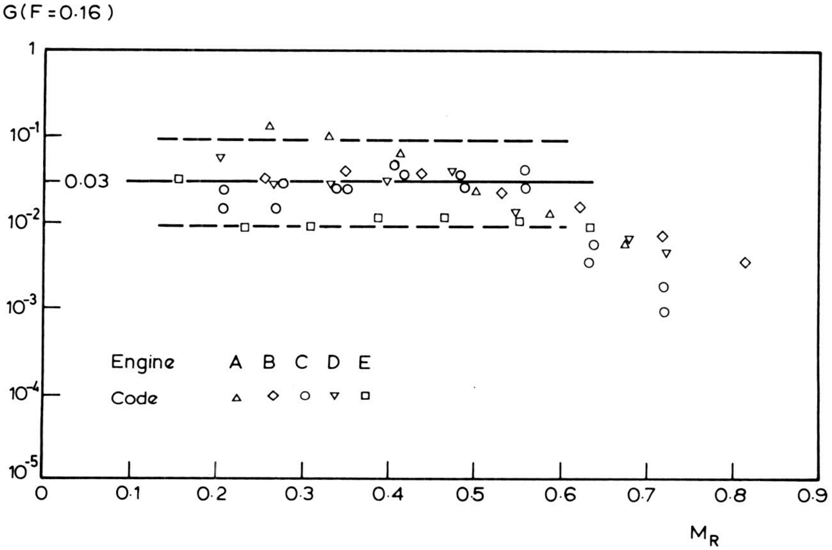

Figure 3.—*Sound-power parameter based on peak of spectrum, versus first-rotor inlet relative Mach number.*

Ideally the sound power from each stage would be correlated separately when dealing with a multistage machine. However, there is no way in which the broadband sound output from separate stages can be distinguished when only the total sound output has been measured, as has been done here. The inlet sound-power measurements from the multistage machines (A, B, C, D) have therefore been combined with first-stage rotor parameters to give a value of G. Such a normalization procedure leaves the number of stages unaccounted for, so it is interesting that the single-stage fan tends to fall at the bottom of the scatter band in figure 3 (i.e., about 5 dB below most of the multistage points).

Below $M_R = 0.6$, almost all the points lie within ±5 dB of the constant value $G = 0.03$; this collapse is encouraging in view of the small number of variables included in the definition of G. Furthermore, the tendency to remain constant over this range of Mach number supports the theoretically predicted M_R^5 variation (see equation (4)).[5]

---

[5] Note that if the frequency spectrum scaled on relative velocity, rather than the sound speed as indicated in figure 1, the right-hand side of equation (4) for $l_c \ll \lambda$ would be proportional to M_R^6 rather than M_R^5. Although Strouhal number scaling—and hence an M_R^6 dependence for compact sources—is commonly assumed for sound radiation from fluctuating forces of aerodynamic origin, we have shown ("Correlation of Broadband Power Spectrum Shapes") that it does not fit the present data.

Above $M_R = 0.6$, figure 3 shows a falloff in G with increasing M_R; this amounts to roughly 10 dB at $M_R = 0.7$ and is similar to the flow effect found by Smith and House (ref. 3).

DIRECTIVITY OF INLET-RADIATED SOUND

The directivity of broadband inlet-radiated sound is discussed in reference 8; the opportunity is taken here to present an updated correlation due to Snow (ref. 5). In the light of these results, a hypothesis is put forward to account for the directional radiation of broadband sound at high frequencies.

Multistage Data Correlation

Figures 4a and 4b show the directivity index,[6] plotted versus angle from the inlet axis, for five different multistage fans and compressors ($n = 2$ to 8). The parameter is ka, where a is the rms first-rotor radius; each ka curve is based on a number of engine speeds.

At a nondimensional frequency of $ka = 4$, the curves for the various engines collapse within $1\frac{1}{2}$ dB. They also agree fairly closely (up to 60°) with the theoretical curve in figure 5. The latter is taken from reference 8 and represents a spatially random source distribution; the departure from a uniform field shape is due to duct cutoff effects.

At $ka = 16$, the same theoretical model predicts a fairly flat directivity curve, with a slight dip at 90° (fig. 5); but the measured curves fall off a good deal more sharply away from the axis. The departure from the random-source model is still more pronounced at $ka = 63$. In fact, the model predicts hemispherically uniform radiation in the high-frequency limit ($ka = \infty$), while the measured radiation patterns become progressively more directional with increasing frequency above $ka = 4$ and apparently tend toward a $\cos^2 \psi$ directional distribution.[7]

Optical Model for High-Frequency Directivity

A clue to the observed directivity along the axis at high frequencies ($ka = 16$ and above) is provided by closer examination of figure 4. There is a significant trend at 90° for the directivity index to vary according to the number of stages: The higher the number, the larger the dip at 90°. An optical model, outlined below, suggests that reflection of sound by upstream blade rows could account for the observed directivity patterns.

---

[6] Based on the upstream hemisphere ($\psi = 0°$ to $90°$); thus omnidirectional radiation has a directivity index of 3 dB.

[7] It is interesting that this is the distribution which corresponds to fluctuating forces oriented in the axial direction.

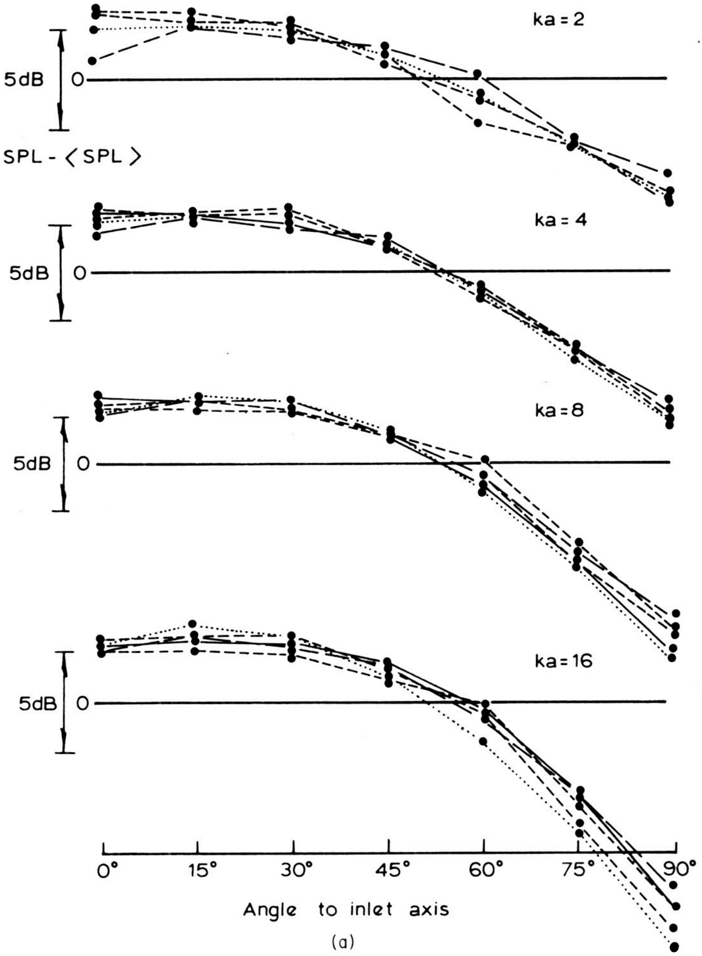

FIGURE 4a.—*Narrowband directivity index measurements for inlet radiation from multistage fans and compressors (frequency band width: 5 percent).*

In a multistage machine, sound generated by the second and subsequent stages must travel through the first stage before it can escape from the inlet. The transmission process is represented in figure 6 by rays that are reflected from the blade surfaces in the same way as light from a mirror; this optical model becomes valid at high frequencies, where the sound wavelength is short compared with the blade chord and spacing.

Referring to figure 6, rays incident on the stator within the shaded band will be reflected back in the downstream direction. The same applies to the rotor, so in this two-dimensional picture the radiation transmitted

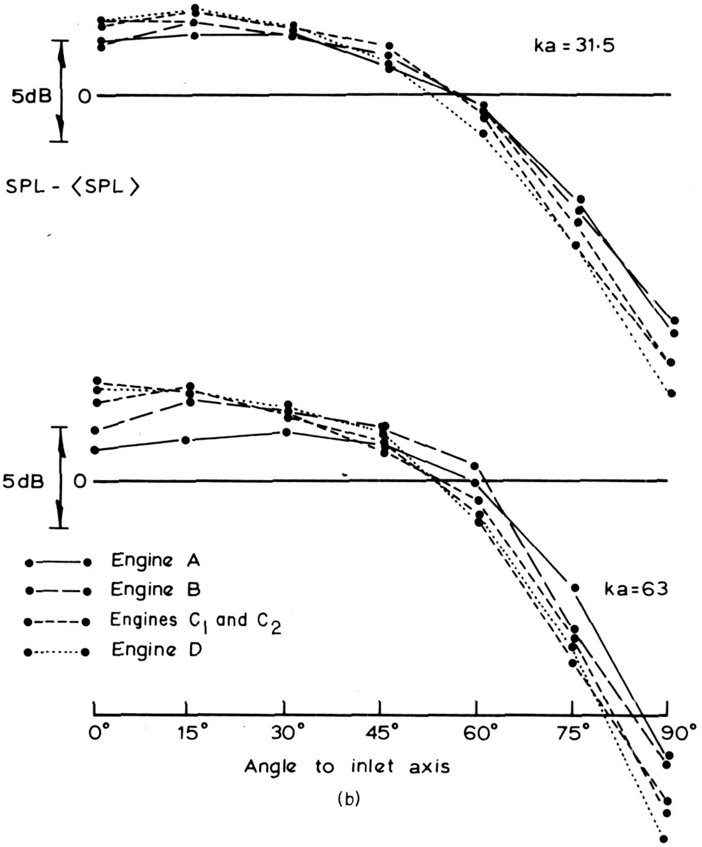

FIGURE 4b.—*Narrowband directivity index measurements for inlet radiation from multistage fans and compressors (frequency bandwidth: 5 percent).*

upstream is confined to a wedge of included angle $\pi-2(\alpha_2'+\beta_2')$.[8] Returning to the three-dimensional geometry of the actual rotor-stator stage, the optical model clearly predicts a reduction of transmitted intensity at 90° (compared with the axial direction) due to upstream blade rows.

This effect probably accounts for at least part of the observed directivity of inlet-radiated noise at $ka=16$ and above. The similarity in figure 4 between the fans A (two-stage) and B (four-stage) may be connected with the absence of IGV's in the latter.

---

[8] An interesting point is that, if the rotor and stator blade angles add up to more than 90° (which is unusual in aircraft-engine fans and compressors), the model predicts zero sound transmission through this stage.

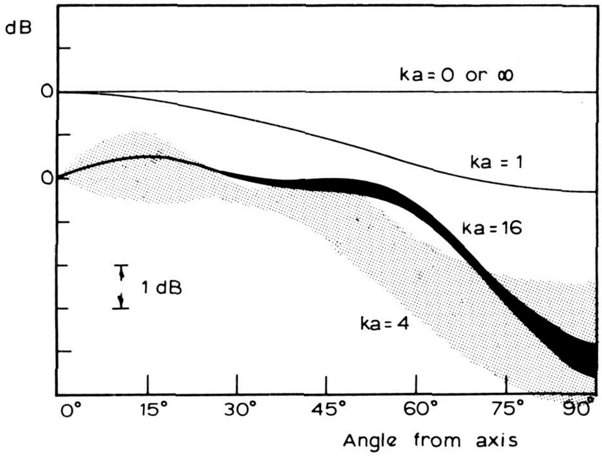

FIGURE 5.—*Theoretical directivity index based on random source model, for* ka = *0 to ∞. Bands indicate hub-tip ratio range 0.3–0.5.*

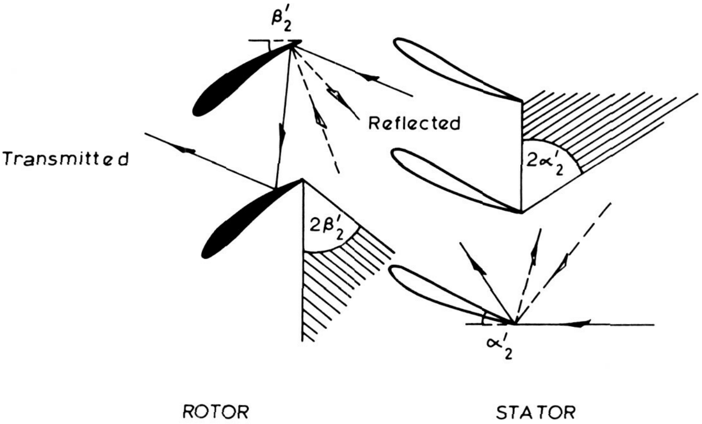

FIGURE 6.—*High-frequency sound transmission through blade rows.*

EFFECTS OF SOURCE MOTION AND MEAN FLOW

The relative amounts of broadband sound power escaping from the exhaust and inlet of a single-stage fan have been studied by Smith and House (ref. 3); they show an empirical correlation with the relative Mach number through the rotor. The same measurements have been reanalyzed for this study to give the downstream/upstream power ratio in narrow frequency bands. The tendency reported in reference 3 for more sound power to travel downstream is verified, but it appears to be restricted to high frequencies (above 2 kHz). The high-frequency data are compared below with the predictions of a theoretical model that accounts for source motion and mean flow.

Theoretical Prediction of Downstream/Upstream Energy Split

The single blade-row model of Appendix III gives an estimate of the sound-power spectrum radiated downstream and upstream due to broadband blade forces. Provided the blades are not highly staggered (mean relative flow angle less than 30°), the downstream/upstream power ratio can be approximated to first order in Mach number by

$$\frac{1+\frac{3}{4}M_x}{1-\frac{3}{4}M_x} \tag{6}$$

The total sound-power spectrum (inlet+exhaust) is unaffected by flow to this approximation.

The energy split predicted by Appendix III actually depends on the shape of the radiated power spectrum, and equation (6) is strictly valid only for a flat spectrum of sound power in constant-percentage bands. Furthermore, the analysis is based on the assumption that many modes contribute to the sound-power spectrum at the frequency concerned. These considerations limit the application of equation (6) to frequencies around the peak of the constant-percentage-bandwidth spectrum.

Comparison of Theory with Experimental Data

Figure 7 shows the downstream/upstream power ratio for engine E, measured at three different frequencies (3.8, 7, and 11.5 kHz) over a range of axial Mach numbers. The constant-percentage broadband spectrum peaks at around 4 to 7 kHz at all speeds.

Although the data are scattered, there is a definite trend toward increasing power ratios with increasing axial Mach number, a finding which agrees fairly well with equation (6) (shown on fig. 7 as a solid line).

CONCLUSIONS

(1) Measurements of inlet-radiated broadband power spectra from a range of fans and compressors show a collapse of spectrum shape based on the estimated first-rotor wake-momentum thickness (figs. 1 and 2).

(2) A simplified model of broadband sound-power generation has been used to establish the main factors determining the radiated power, leading to the definition of a nondimensional sound-power parameter in which these factors are normalized out.

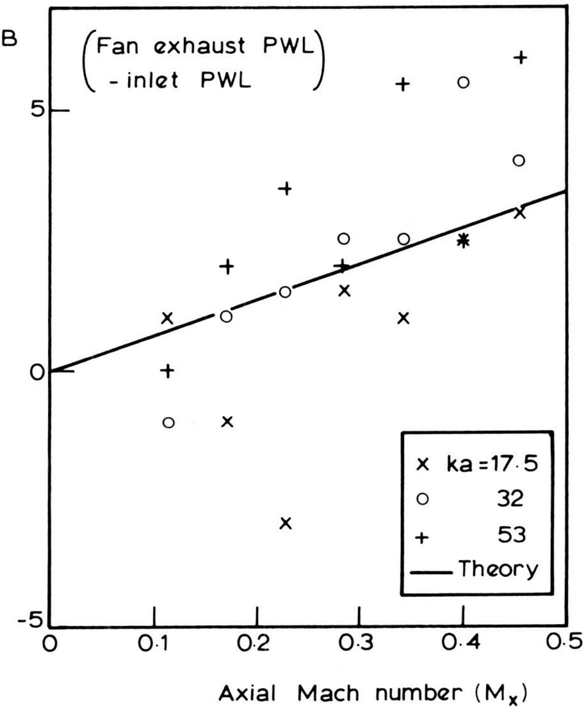

FIGURE 7.—*Ratio of exhaust to inlet sound power in narrow frequency bands—single-stage fan.*

(3) Plotting the peak (constant-percentage) power spectrum levels in normalized form collapses the data within 5 dB (fig. 3). Below a rotor relative Mach number of 0.6, the nondimensional power parameter is approximately independent of Mach number; above 0.6 there is a noticeable falloff, similar to the flow effect found by Smith and House (ref. 3).

(4) The single-stage fan levels tend to fall at the bottom of the scatter band; i.e., about 5 dB below most of the multistage points. This may well be a stage-number effect; figure 14 of reference 3 predicts differences of this order between single- and multi-stage machines over the relative Mach number range concerned (0.2 to 0.6). The difference largely disappears if the exhaust-radiated power is included in the single-stage data.

(5) Inlet directivity measurements in narrow frequency bands show a consistent trend toward more directional radiation at higher frequencies (fig. 4), which becomes more marked the larger the number of fan or compressor stages. The high-frequency beaming along the axis is, if anything, more pronounced at low engine speeds (jet noise obscures the pattern at the highest speeds) and thus cannot be explained in terms of refraction. Transmission through upstream blade rows provides a qualitative explanation.

(6) For a single-stage fan, the ratio of exhaust to inlet sound power has been measured in narrow frequency bands. Around the peak of the constant-percentage broadband power spectrum, the trend of the measurements agrees with the ratio $[1+(\frac{3}{4}M_x)]/[1-(\frac{3}{4}M_x)]$ theoretically predicted for low-stagger blade rows (fig. 7).

LIST OF SYMBOLS

a, a_0	rms radius, outer radius of annulus
b	blade chord
C_D, C_L	blade drag, lift coefficients
d	tangential spacing of blades
F	frequency parameter (L/λ)
f	frequency
$f(\beta_2,\alpha_1)$	defined in equation (9)
G	sound-power parameter, equation (5)
g	frequency exponent, equation (23)
I	acoustic intensity
k	acoustic wavenumber (ω/c)
k_y, k_z	turbulence wavenumber components (tangential, spanwise)
L	length scale, equation (3)
L_x	axial blade force per unit span
l_c	spanwise correlation length of turbulence, equation (11)
M_R, M_t	rotor Mach numbers (relative, tangential)
M_x, M_θ	flow Mach numbers (axial, peripheral)
(m,n)	annulus mode numbers (circumferential, radial)
n	number of stages in machine
S	area of duct cross section
S_R, S_R'	rotor disk area, blade area
T, T_0	absolute temperature, stagnation value
$(\Delta T_0)_n$	overall stagnation temperature rise
W, dW/df	sound power, spectral density
w	defined in equation (19)
α	turbulence intensity parameter, equation (13); axial wavenumber parameter, Appendix III
α, α'	stator flow angle, blade angle
β, β'	rotor relative flow angle, blade angle
γ	specific-heat ratio
ϵ	ratio of tangential to axial force at outer wall of duct
η_n	overall isentropic efficiency
λ	sound wavelength
ρ	fluid density
σ	blade-row solidity

ψ	angle from duct axis
ω	radian frequency (relative to swirl in Appendix IV)
ω_0, ω'	radian frequency in fixed, rotor reference frames

Subscripts

R, S	rotor, stator
1, 2	inlet, exit values for blade row
$\langle\ \rangle$	denotes time average

APPENDIX I

Generation of Broadband Acoustic Energy

Broadband noise generation is here attributed to the interaction between flow turbulence and the fan or compressor blades. More specifically, the process of sound generation at subsonic speeds is viewed in two stages: Turbulent flow produces lift fluctuations on a row of blades, and the lift fluctuations give rise to sound radiation. We shall consider the particular case where the turbulence is produced by the row of blades immediately upstream, although this is not the only possibility. The following analysis is designed to give guidelines for data correlation and is by no means a complete description of the complex processes involved.

Periodic Interaction Theory

A relatively simple case of rotor-stator interaction is that associated with the mean rotor-wake profile. Reference 1 gives the sound intensity, at any multiple of blade-passing frequency, due to a uniform axial force L_x per unit span on each stator blade at that frequency:

$$I \doteq \frac{\langle L_x^2 \rangle}{4\rho c\, d_S^2} \quad \text{(single mode, well above cutoff)} \tag{7}$$

Equation (7) is based on a two-dimensional model and assumes low-Mach-number flow. With the same assumptions, the mean-square harmonic force is given by an extension of the Kemp-Sears analysis (refs. 1 and 9) as

$$\langle L_x^2 \rangle \doteq \frac{\pi}{2} K_w \frac{\rho^2 c^5 b_S}{\omega} \sigma_R^2 C_D^2 M_R^5 f(\beta_2, \alpha_1) \tag{8}$$

where K_w is a factor allowing for the downstream decay of the rotor wakes and

$$f(\beta_2,\alpha_1) = \tan^2 \alpha_1 \frac{\cos \beta_2}{\cos \alpha_1} \cdot \sin^2 (\beta_2+\alpha_1) \cdot \left[1 - \frac{C_L}{\pi} \cot (\beta_2+\alpha_1) \right]^2 \tag{9}$$

Note that the drag coefficient C_D refers to the rotor blades, and the lift coefficient C_L to the downstream stator blades. The blade-row geometry is shown in figure 8.

Application to Broadband Turbulence

The single-mode, single-frequency results given above correspond to a rotor-wake pattern that is sinusoidal in the tangential direction (i.e., single k_y wave number), uniform in the spanwise direction ($k_z=0$), and carried round with the rotor. To deal with incident turbulence that has a continuous range of wave numbers and frequencies, we use the wave-number-frequency spectrum $E(k_y, k_z, \omega)$ of the fluctuating velocity entering the stator. Only velocity components parallel to the rotor wakes (i.e., streamwise relative to the rotor) are considered here.

Figure 9 shows which regions of the turbulence spectrum give rise to propagating acoustic modes. The criterion for propagation is that for a given radian frequency ω the interaction wave number—whose components are $(k_y+2\pi s/d_S, k_z)$, where $s=\pm 1, \pm 2$, etc.—should be less than the acoustic wave number $k=\omega/c$. The contributing regions in the (k_y, k_z)

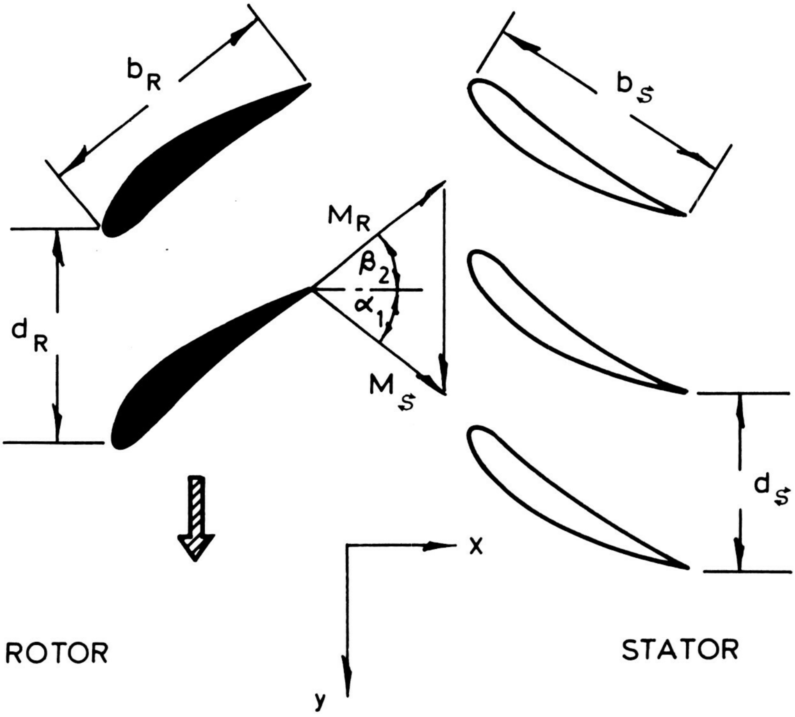

FIGURE 8.—*Geometry of rotor-stator stage.*

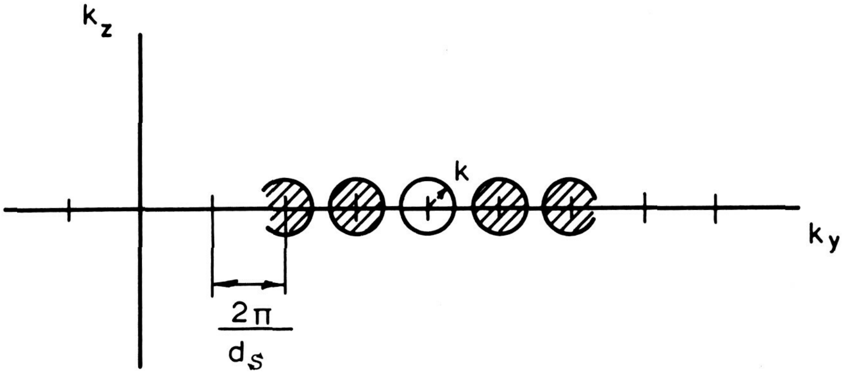

FIGURE 9.—*Regions of* (k_y,k_z) *wave-number spectrum of turbulence which contribute to sound radiation at frequency* ω.

plane are therefore circles of radius k; these overlap if the stator blades are spaced further apart than the acoustic wavelength, and are distinct regions if $d_S < \lambda/2$.

In either case, the equivalent of the mean-square harmonic wake velocity in the previous section is an integral of the wave-number spectrum over all the contributing regions. However, exact correspondence occurs only in the center of each circle; departure from two-dimensionality and proximity to cutoff introduce a weighting factor for points away from the center proportional to the axial wave number of the radiated sound[9] and, hence, proportional to the height of the hemisphere with the circle as base.

We make the following assumptions in order to estimate the wave-number integral: (1) The variation of $E(k_y,k_z,\omega)$ is small over an interval $2\pi/d_S$ in k_y; (2) the variation with k_z is small over the contributing region $(|k_z|<k)$. Thus

$$E(k_y,k_z,\omega) \doteq E(k_y,0,\omega)$$

This implies that the integral length scale l_c (see below) is small compared with λ.

With these approximations, and taking account of the weighting factor mentioned above, the contributing region of the (k_y,k_z) turbulence spectrum is estimated as

$$\frac{2}{3}\pi k^2 \cdot \frac{d_S}{2\pi} \cdot 2 \int_{-\infty}^{\infty} E(k_y,0,\omega)\, dk_y \tag{10}$$

(Note factor 2 for + and − frequencies.)

---

[9] This is an acoustic coupling factor for axial forces (see ref. 10, sec. 6.4). The aerodynamic effect of finite k_z on the fluctuating lift is shown in Appendix II to be unimportant.

If the integral length scale l_c in the spanwise direction is defined by

$$l_c = 2\pi E(k_y,0,\omega) \bigg/ \int_{-\infty}^{\infty} E(k_y,k_z,\omega)\, dk_z \tag{11}$$

and the dependence of l_c on k_y is neglected, expression (10) may be written as

$$\frac{1}{6\pi} k^2\, d_S l_c G(\omega) \tag{12}$$

In the above expression

$$G(\omega) = 2\int_{-\infty}^{\infty} dk_y \int_{-\infty}^{\infty} dk_z E(k_y,k_z,\omega)$$

is the single-sided ω-spectral density of the velocity fluctuations entering the stator. A nondimensional measure of $G(\omega)$ is provided by the ratio α of $\omega G(\omega)$ to the mean-square fundamental[10] component of the rotor-wake velocity defect:

$$\alpha(\omega) = \omega G(\omega) \cdot \frac{2}{c^2 \sigma_R{}^2 C_D{}^2 M_x{}^2} \tag{13}$$

It follows from equations (12) and (13) that, in order to apply the periodic-wake analysis to the present problem, it is simply necessary to replace K_w in equation (8) by

$$\frac{1}{6\pi} k^2\, d_S l_c \cdot \frac{\alpha}{\omega} \tag{14}$$

This, with equation (7), gives the acoustic intensity per unit bandwidth due to axial lift forces on the stator blades as

$$\frac{dI}{d\omega} = \frac{1}{48} \alpha \rho c^2 l_c \sigma_S \sigma_R{}^2 C_D{}^2 M_R{}^5 f(\beta_2,\alpha_1) \tag{15}$$

with $l_c \ll \lambda$.

The opposite extreme to equation (15) is obtained when the spanwise integral length scale is greater than λ; a similar analysis then gives

$$\frac{dI}{d\omega} = \frac{\pi}{32} \alpha \rho c^3 \cdot \frac{1}{\omega} \sigma_S \sigma_R{}^2 C_D{}^2 M_R{}^5 f(\beta_2,\alpha_1) \tag{16}$$

with $l_c > \lambda$.

---

[10] i.e., with period equal to the rotor blade space.

Radiation from Turbulent Boundary-Layer Pressure Fluctuations

In the preceding analysis, blade lift fluctuations are attributed to incident turbulence. An alternative cause of lift fluctuations is the unsteady pressure field set up by the blade's own turbulent boundary layer and wake. This mechanism was recognized by Kramer (ref. 11), and a quantitative estimate of the sound radiation was made by Sharland (ref. 12) using theoretical ideas put forward by Lilley (ref. 13). In fact the simplified sound power parameter, equation (5), used to correlate the data does not distinguish between the two mechanisms. The question, whether the rotor-generated turbulence radiates by interaction with the rotor or the downstream stator, is therefore left open.

APPENDIX II

Three-Dimensional Effects on Fluctuating Lift

Mugridge (ref. 6) has estimated the fluctuating lift per unit span on a two-dimensional airfoil in a three-dimensional convected gust pattern by considering a single radian frequency ω and spanwise wavenumber k_z. The case $k_z=0$ corresponds to Sears' two-dimensional analysis (ref. 9).

The mean-square fluctuating lift is approximately equal to the two-dimensional mean-square lift multiplied by a correction factor

$$\left(1+\frac{p^2}{n^2+2/\pi^2}\right)^{-1}$$

with $p^2+n^2<4$, where $n=\omega b/2U$ (i.e., the reduced frequency) and $p=\frac{1}{2}k_z b$.

Since $p/n=k_z U/\omega$, and we are interested only in values of k_z less than k for sound radiation, it follows that over this range $p<Mn$ with $M=U/c$. This limits the correction factor above to between $\frac{1}{2}$ and 1 for subsonic flow.

For high gust wavenumbers, a more accurate value of the correction factor is available from an independent analysis by Filotas (ref. 14); it is

$$\frac{2}{\pi p}\,(1+p^2/n^2)^{-1/2}$$

with $p^2>4$, $n>1$.

Large values of p will be associated in the present problem with acoustic wavelengths that are small compared with the blade chord (i.e., high frequencies). However, the acoustic representation of the blade as a line force breaks down in this region.

APPENDIX III

Downstream/Upstream Energy Split from an Isolated Blade Row

Apart from any reflecting surfaces upstream or downstream, a rotating blade row is expected to radiate different amounts of sound power in the upstream and downstream directions. Both the source motion and mean flow contribute to this effect, which applies both to discrete-frequency[11] and broadband radiation. The following analysis deals with the broadband case.

For this purpose the blade row is modeled by a force distribution at one cross section of a uniform axisymmetric duct. The local force per unit area has components (f_x, f_θ, f_r) in the axial, tangential, and radial directions, and we assume for simplicity that

$$f_\theta = \epsilon \left(\frac{r}{a_0} \right) f_x \tag{17}$$

with $f_r = 0$. (a_0 is the outer radius of the annular cross section.) A swirling mean flow in the duct is modeled by a uniform axial Mach number M_x together with a solid-body rotation.

The analysis starts from the result derived in reference 16, section 4, for single-frequency excitation in a single (m,n) duct mode. This gives the downstream (W_+) and upstream (W_-) sound power in terms of the axial-force modal amplitude $\bar{F}_x$, as

$$W_\pm(m,n) = \frac{1}{8} \frac{\omega_0}{\omega} \frac{|\bar{F}_x|^2 S}{\alpha \rho c} A_\pm$$

and

$$A_\pm = \left[\frac{\pm\alpha - M_x + (\omega_0/\omega)(m\epsilon/w)(1 - M_x^2)}{1 \mp \alpha M_x} \right]^2 \tag{18}$$

Here α is the axial wavenumber parameter, defined in equation (24) below; $\omega_0 = wc/a_0$ is the fixed-frame radian frequency, and ω is the corresponding frequency relative to the swirl. Equation (18) is valid over the whole frequency range above mode cutoff.

Frequency Relationships

If the swirl angular velocity is Ω in the θ direction, ω is related to ω_0 by

$$\omega = \omega_0 - m\Omega \qquad (m = \text{circumferential mode number})$$

---

[11] The discrete-frequency case has been studied theoretically and checked against experimental data by Mani (ref. 15).

Thus

$$\frac{\omega}{\omega_0}=1-\frac{m}{w}M_\theta \tag{19}$$

where

$$w=\frac{\omega_0 a_0}{c} \qquad \text{(based on fixed-frame frequency)}$$

and

$$M_\theta=\frac{\Omega a_0}{c}$$

is the peripheral swirl Mach number.

Similarly the radian frequency ω' in the rotor frame of reference is related to ω_0 by

$$\frac{\omega'}{\omega_0}=1-\frac{m}{w}M_t \tag{20}$$

where M_t is the rotor tip Mach number.

Broadband Excitation

Since ω_0 and ω' are related by a constant factor for a given m value, the single-frequency sound-power result (eq. (18)) can be generalized to broadband excitation by the substitutions

$$\left.\begin{aligned}\tfrac{1}{2}\,|\,\bar{F}_x\,|^2 &\rightarrow \omega' G_x(\omega')\\ W_\pm(m,n) &\rightarrow \omega_0\,\frac{dW_\pm(m,n)}{d\omega_0}\end{aligned}\right\} \tag{21}$$

Thus

$$\frac{dW_\pm(m,n)}{d\omega_0}=\frac{1}{4}\,\frac{S}{\alpha\rho c}\,\frac{\omega'}{\omega}\,G_x(\omega')\cdot A_\pm \tag{22}$$

If the force spectral density $G_x(\omega')$ varies as $(\omega')^g$, equation (22) can be written as

$$\frac{dW_\pm(m,n)}{d\omega_0}=\frac{1}{4}\,\frac{S}{\alpha\rho c}\left(\frac{\omega}{\omega_0}\right)^{-1}\left(\frac{\omega'}{\omega_0}\right)^{g+1}G_x(\omega_0)\cdot A_\pm \tag{23}$$

Cutoff Condition

We consider only $(m,0)$ modes, for which

$$\alpha \doteq \left[1-(1-M_x^2)\left(\frac{mc}{a_0\omega}\right)^2\right]^{1/2} \tag{24}$$

Cutoff occurs when

$$\left(\frac{mc}{a_0\omega}\right)^2(1-M_x^2)=1$$

i.e., from equation (19),

$$\left(\frac{m}{w}\right)^2(1-M_x^2)=\left(1-\frac{m}{w}M_\theta\right)^2$$

Thus the propagation range is given by

$$\frac{-M_\theta-(1-M_x^2)^{1/2}}{1-M^2}\leq\frac{m}{w}\leq\frac{-M_\theta+(1-M_x^2)^{1/2}}{1-M^2} \tag{25}$$

with $M^2=M_x^2+M_\theta^2$. Modes within this range will propagate along the duct; modes outside the range make no contribution to the sound power in the present model.

The substitution

$$\frac{m}{w}=\frac{-M_\theta}{1-M^2}+\frac{(1-M_x^2)^{1/2}}{1-M^2}\sin\phi \tag{26}$$

gives the propagation range in terms of ϕ as $-\frac{1}{2}\pi\leq\phi\leq\frac{1}{2}\pi$. Also, α is given by

$$\alpha=\frac{\omega_0}{\omega}(1-M^2)^{1/2}(1-M_x^2)^{1/2}\cos\phi \tag{27}$$

Summation over Propagating Modes

The total sound power per unit bandwidth $dW_\pm/d\omega_0$, radiated in either direction, is found by summing the contributions given by equation (22) for all propagating modes. Two simplifying assumptions are introduced at this point.

(1) The excitation spectral density G_x is taken as the same for all $(m,0)$ modes and as zero for all higher order radial modes. Although it would probably be more realistic to assign equal excitation to all modes regardless of radial order, the exclusion of higher order modes is not expected to alter the downstream/upstream energy split significantly.

(2) The propagation range is assumed to contain a large enough number of $(m,0)$ modes that the discrete summation over integer m values can be replaced by integration over a continuous range. The multimode sound power in either direction is then

$$\left.\begin{aligned} \frac{dW_\pm}{d\omega_0} &\doteq \int_{m_1}^{m_2} \frac{dW_\pm(m,0)}{d\omega_0}\,dm \\ &= \frac{w(1-M_x^2)^{1/2}}{1-M^2} \int_{-\pi/2}^{\pi/2} \frac{dW_\pm(m,0)}{d\omega_0} \cos\phi\cdot d\phi \end{aligned}\right\} \qquad (28)$$

The integral over ϕ in equation (28) is a function of ϵ, M_x, M_θ, and M_t; it can be evaluated using equations (18), (23), (26), and (27). A particularly simple result, valid for low Mach numbers, is obtained by neglecting squares and higher powers of the various Mach numbers; to this accuracy,

$$\frac{dW_\pm}{d\omega_0} \doteq \frac{1}{4}\frac{S}{\rho c} w\, G_x(\omega_0)$$

$$\cdot \left\{\tfrac{1}{2}\pi\,(1+\epsilon^2) \mp \frac{4}{3}\left[(1-\epsilon^2)\,M_x + \epsilon\,M_\theta + (g+1)\,\epsilon M_t\right]\right\} \qquad (29)$$

Special Case: Force Perpendicular to Relative Mean Flow

If the fluctuating blade forces act in the lift direction (i.e., perpendicular to the relative flow), then

$$\epsilon = \cot\beta_m = \frac{M_x}{M_t - M_\theta} \qquad (30)$$

where β_m is the mean relative flow angle referred to the axis. Combining this relation with equation (29), and taking the exponent g as -2, gives

$$\frac{dW_+/d\omega_0}{dW_-/d\omega_0} \doteq \frac{1+(8/3\pi)M_x\cos^2\beta_m}{1-(8/3\pi)M_x\cos^2\beta_m} \qquad (31)$$

The assumption $g=-2$ corresponds, according to equation (29), to a flat spectrum of sound power in constant-percentage bands.

A noteworthy feature of equation (31) is that, provided β_m is not more than 30°, the downstream/upstream sound power ratio is almost independent of β_m and can be approximated by

$$\frac{1+\frac{3}{4}M_x}{1-\frac{3}{4}M_x} \qquad (32)$$

In other words, the energy split is determined solely by the axial Mach number and is the same for both rotating and stationary blades, provided the relative flow angles are not too large.

REFERENCES

1. MORFEY, C. L., *Sound Generation in Subsonic Turbomachinery.* ASME Paper 69-WA/FE-4, 1969. (See *Trans. ASME, J. Basic Eng.*, Vol. 92D, 1970, p. 450.)
2. LIGHTHILL, M. J., On Sound Generated Aerodynamically: I. General Theory. *Proc. Roy. Soc.* (*London*), Series A, Vol. 211, 1952, p. 564.
3. SMITH, M. J. T., AND M. E. HOUSE, Internally Generated Noise From Gas Turbine Engines: Measurement and Prediction. *Trans. ASME, J. Eng. for Power*, Vol. 89A, 1967, p. 177.
4. MORFEY, C. L., AND H. DAWSON, *Axial Compressor Noise: Some Results From Aero-Engine Research.* Bristol-Siddeley Engines Ltd., TRH 107, 1966.
5. SNOW, R., M.S. thesis, Inst. Sound and Vib. Res., Southampton U., 1970.
6. MUGRIDGE, B. D., Ph.D. dissertation, Southampton U., 1970. (See *J. Sound Vib.*, Vol. 18, 1971, p. 475.)
7. LIEBLEIN, S., AND W. H. ROUDEBUSH, *Theoretical Loss Relations for Low-Speed Two-Dimensional-Cascade Flow.* NACA Technical Note 3662, 1956.
8. MORFEY, C. L., A Review of the Sound-Generating Mechanisms in Aircraft-Engine Fans and Compressors. *Proc. UTIAS/AFOSR Symposium on Aerodynamic Noise*, H. S. Ribner, ed., Toronto U. Press, 1969, p. 299.
9. KEMP, N. H., On the Lift and Circulation of Airfoils in Some Unsteady-Flow Problems. *J. Aero. Sci.*, Vol. 19, 1952, p. 713.
10. MORFEY, C. L., Rotating Pressure Patterns in Ducts: Their Generation and Transmission. *J. Sound Vib.*, Vol. 1, 1964, p. 60.
11. KRAMER, M., The Aerodynamic Profile as Acoustic Noise Generator. *J. Aero. Sci.*, Vol. 20, 1953, p. 280.
12. SHARLAND, I. J., Sources of Noise in Axial Flow Fans. *J. Sound Vib.*, Vol. 1, 1964, p. 302.
13. LILLEY, G. M., *On the Vortex Noise From Airscrews, Fans and Compressors.* Rolls Royce Ltd., Noise Panel Report, 1961.
14. FILOTAS, L. T., Response of an Infinite Wing to an Oblique Sinusoidal Gust. *Basic Aerodynamic Noise Research*, I. R. Schwartz, ed., NASA SP-207, 1969.
15. MANI, R., Discrete Frequency Noise Generation From an Axial Flow Fan Blade Row. *Trans. ASME, J. Basic Eng.*, Vol. 92D, 1970, p. 37.
16. MORFEY, C. L., Ph.D. dissertation, Southampton U., 1970. (see *J. Sound Vib.*, Vol. 14, 1971, p. 37.)

DISCUSSION

M. V. LOWSON (Loughborough University, England): This interesting paper by Dr. Morfey raises a number of points which deserve further discussion. It is assumed in the paper that shed turbulence is the principal source of broadband noise radiation. While this is certainly an important contributor, other sources can also give rise to broadband noise. The turbulence in the inlet boundary layer of a jet engine is probably much larger, in both scale and level, than that of the standard equilibrium boundary layer, and also interacts with the highest speed part of the rotor near the tip. Indeed the tip itself can be regarded as running in a stalled condition, and the direct self-induced radiation at the tip could well be large. Definitive measurements of inlet turbulence levels and spectra are badly needed to illuminate this problem.

The empirical correlation on momentum thickness demonstrated by Morfey offers some evidence in favor of the dominance of shed turbulence effects, but it should be pointed out that, because all engines are designed to similar rules, empirical parameters tend to move together. Thus there is some danger in inferring source mechanisms from the success of empirical collapses.

The measured high-frequency beaming of the broadband noise is an interesting effect, particularly since it is more pronounced than predicted by the theory. A possible reason for this is that the theoretical estimates ascribe too high a level to the higher order circumferential and radial modes. The actual source strength must fall off smoothly toward the tip and this would cause a lower level of the higher order radial modes than the rectangular distribution assumed. Since it is these higher order modes which cause the radiation normal to the axis, a somewhat lower level of sideline radiation than that of the present theory can be anticipated.

As a final point, I wonder if Dr. Morfey would care to indicate his present thoughts on the likely relative significance of the dipole and quadrupole source mechanisms for broadband noise radiation.

M. E. HOUSE (Southampton University): Dr. Morfey is well recognized for his theoretical contribution to the problems of turbomachinery noise, and indeed his paper presented at the 1969 Winter Annual Meeting of ASME held at Los Angeles, California (ref. 1), contains a very full treatment of subsonic rotor-stator interaction noise in terms of steady-state parameters. I must confess, however, to being a little disappointed that that paper offered no experimental verification.

His present paper extends the concepts to the case of random or broadband sound, and here I am pleased to note that experimental data are included.

I have little or no comment to make on the derivations in the paper or the appendixes since they follow logically from the basis and assumptions stated by Dr. Morfey. My main concern lies within these assumptions.

First, I would like to comment on sound-power normalization. As for discrete tones, there are numerous mechanisms which one can postulate as giving rise to random noise from compressors. While I, myself, and others, have pointed to the likely dominances of one or another mechanism for a particular class of machine operating in particular circumstances, it is unlikely that this will hold universally. Rather there will be transition regimes in which a given mechanism gives way to a stronger one. Evidence of this is well known in the case of transonic compressor discrete tone noise when conditions are reached where rotor-associated force fields may propagate and dominate the conventional rotor-stator interaction tones. Dr. Morfey has elected to inspect the broadband noise from a wide range of compressors (table I of his paper) in terms of frequency scaling using a length scale associated with the rotor blade momentum thickness. The sound-power level normalizing technique he uses is also heavily dependent upon the mechanism of lift fluctuations over blade surfaces caused by turbulence wakes from upstream rows.

While this approach might be realistic for multistage compressors (say three stages and above), work done over the last 2 to 3 years at Rolls-Royce (ref. D–1) indicates that for subsonic single-stage fans, at least, other mechanisms can and do strongly influence the radiated sound characteristics. These include blade interactions with the turbulence structure of the intake flow. I would not, therefore, expect Dr. Morfey's normalizing functions to cope with both multi- and single-stage machines, and perhaps this is another reason for the tendency of the engine E data to fall at the lower scatter band.

Another subject I wish to discuss is frequency resolution of data. The data in figure 2 of reference 5 used by Morfey were frequency-analyzed using 100-Hz Spectral Dynamics equipment with approximately 2-second averaging (from the 15 ips recorded data on a 30-in. tape loop).

It is interesting to inspect such data with even greater resolution and averaging. An example is the Rolls-Royce Conway compressor noise for a well-subsonic operating condition, as shown in figure D–1, where 20-Hz Spectral Dynamics equipment was used with 7-second averaging. Besides the "sum-and-difference" tones of the type noted by Crigler, et al. (ref. D–2), the signal clearly contains a large range of tones at compressor

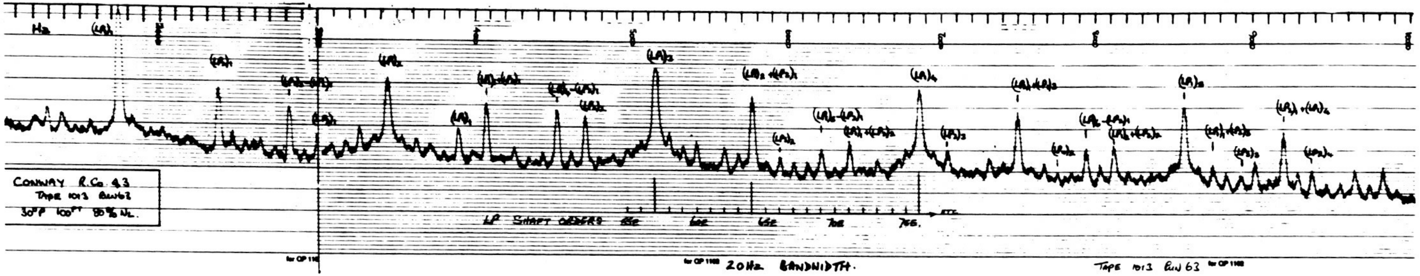

FIGURE D-1.—*20-Hz constant bandwidth spectrum of typical subsonic multistage compressor forward arc noise.*

shaft orders. Most of these protrude less than 5 dB and hence would appear much as the data of Snow (ref. 5) when resolved to only 100 Hz. The data for engines—A, B, C, and D being of 5-percent bandwidth—would also fail to resolve adequately the compressor shaft order signals.

Although I do not agree that the sound-power level data collapse obtained by Morfey is a significant improvement on past attempts, his correlation does, however, seem reasonable. Nevertheless I feel that in view of my comments above this can only be fortuitous. The directivity data collapse, is, however, surprisingly good and I wonder whether Dr. Morfey would agree that this could be due to a much closer association with discrete tone characteristics than he had assumed.

Finally, I would like to comment on Dr. Morfey's optical model for high-frequency directivity. A marked difference noted in directivity between the single-stage data and the remaining engines is interesting. Dr. Morfey has developed a simple optical model to explain this, but I wonder if he has attempted to use the approaches of Kaji and Mani (refs. 15, D–3). The neglect of flow-associated effects on the propagation of sound through blade rows seems unwarranted and I feel that one needs an integral approach to the problems of Dr. Morfey's sections entitled "Optical Model for High-Frequency Directivity" and "Effects of Source Motion and Mean Flow." I also feel that the effect of blade spanwise twist cannot be ignored since conditions may not be such as to prevent transmission over the entire compressor annulus.

R. MANI (University of Massachusetts): The paper is an elegant contribution to the broadband noise problem in turbomachines. It should prove particularly useful as a guide to experimental work. In contrast to earlier works on the subject, while the author uses similarity arguments as the need arises, there is a welcome emphasis on use of first principles in computing the sound power, directivity, energy split, etc. The following are some more specific comments:

(1) In the theoretical development the effect of longitudinal (chordwise) velocity fluctuation is included resulting in a C_L term in $f(\beta_2, \alpha_1)$. In computing the sound-power parameter G, the C_L term was dropped. Now in the Smith-House paper, the authors explain the higher normalized sound power at part speed as due to the cascade operating at lower incidence angle and hence in regimes of higher lift-curve slope. The Smith and House argument is based on quasi-steady, real fluid effects and I wonder if the retention of the C_L term in $f(\beta_2, \alpha_1)$ does not provide a more natural explanation, based on unsteady airfoil theory, of the trends observed by Smith and House.

(2) With regard to the optical model for transmission through blade rows, the mechanism by which a blade row produces reflected and transmitted waves is different from the one suggested by figure 6. The blade

row behaves like a pair of line diffraction gratings coupled by parallel-plate waveguides. The reflected and transmitted waves have orientations given by the Tyler-Sofrin formula that the tangential wave number k_y of these waves differs from that of the incident wave by an integer multiple of $(2\pi/d)$, being the tangential spacing of the blade row. Thus blade rows of completely different stagger angles but of the same tangential spacing would give the same orientations of reflected and transmitted waves. Actually, at high frequencies the effects are more complex than at low frequencies since several higher order transmitted and reflected waves are produced. Based on some calculations that I have done on this problem, I did conclude that the author's surmise, to wit that the acoustic energy transmission coefficients are low in the incidence regions shown shaded in figure 6, is probably correct. I believe, however, that the mechanism involved here is that the degradation of acoustic energy to wake kinetic energy (always present in such a problem when moving medium effects are involved) is high in these incidence regimes at high frequencies.

(3) To students of the theoretical aspects of the subject, attention is specially directed to the appendixes, where considerations involved in the transition from the discrete-frequency to the continuous-spectrum case are comprehensively dealt with.

(4) I agree with the author's approach of gradually building the refinements into the analysis. Examples are extension of the Kemp-Sears work to include chordwise velocity fluctuations and the effect of the cutoff weighting factor on the acoustic efficiency of axial fluctuating forces, etc. Perhaps the author will agree that there are further refinements not mentioned here which could be significant. Two examples with regard to sound-power estimation are that tangential fluctuating forces would make a contribution near cutoff and, secondly, work on estimation of unsteady blade forces suggests that Kemp-Sears type estimates are rather inadequate near cutoff.

MORFEY (author): The discussers raise a number of interesting points and I am grateful for their comments. Since the questions mainly fall in the three categories used by Mr. House, I have grouped my replies under these headings.

I will first address the subject of sound-power normalization. The fact that the single-stage fan (E) falls on the lower edge of the scatter band (fig. 3) might well be accounted for by a difference in source mechanisms, as Mr. House suggests. Figure 2 shows that, compared with the multistage machines, the mean spectrum shape for engine E is deficient at high frequencies.

Dr. Mani's point about the C_L effect in $f(\beta_2,\alpha_1)$ deserves further study. Retention of the C_L term would raise the normalized level of engine E at maximum speed by around 5 dB. Because this machine is a single-stage fan, however, the correction may not be much different over the whole speed range. Probably a more important reason for the failure to follow a V^6 speed variation (as noted in ref. 3) is the breakdown of Strouhal number scaling in the frequency spectrum.

Dr. Lowson's final question is also relevant to the normalization procedure. A comparison of the dipole and quadrupole mechanisms—with a number of simplifying assumptions—has been made for the related problem of an isolated rotor in nonuniform flow (see Paper D3, Loughborough Symposium on Aerodynamic Noise, September 1970). If one adopts the Kemp-Sears method (ref. 9) of calculating the unsteady blade forces, the comparison shows that dipole noise is likely to predominate unless the rotor pressure ratio exceeds 1.1. However, this conclusion may have to be modified as theory and experiment yield more data on the interaction of blade rows with turbulent flow.[12]

The second subject I will reply to is frequency resolution of the data. This is a key question which has not been satisfactorily resolved in published data, and the danger of even 100-Hz bandwidth analysis is well illustrated by the Conway spectrum. In fact the engine E data used in the paper were analyzed initially at 20 Hz, and no shaft order tones were detectable at this bandwidth. Nevertheless, the possibility remains that the spectra consist of overlapping peaks centered at multiples of shaft rotation frequency. These peaks would arise, of course, from irregularities in blade geometry or spacing round the rotor disk.

Mr. House suggests that such "semiordered" noise would show a better directivity collapse than true broadband noise; but the evidence from tone radiation patterns (ref. 8) indicates that the more ordered the source the less correlation there is between engines.

Finally, I wish to reply to comments made concerning the optical model for high-frequency directivity. It would be interesting to take Dr. Mani's theory on sound transmission through blade rows and apply it at very high frequencies. I would expect, as he suggests, that the wave theory would support the trend predicted by the optical model. If this is the case, it might be worth extending the optical model to include the effects of flow and blade twist, as indicated by Mr. House.

---

[12] (Note added in proof) Substantial advances have been made, since this paper was presented, in understanding the radiation of sound from blades in turbulent flow. Reference D-4 gives an updated review of the situation; it is arguable that the spectrum collapse on L/λ should be replaced by a collapse on rotor chord/wavelength.

REFERENCES

D-1. Barry, B., and C. J. Moore, *Subsonic Fan Noise*. Paper to be presented at Symposium on Aerodynamic Noise, Loughborough U., England, September 14–17, 1970. (See *J. Sound Vib.*, Vol. 17, 1971, p. 207)

D-2. Crigler, J. L., W. L. Copeland, and G. J. Morris, *Noise Studies to Evaluate Effects of IGV-Rotor Spacing*. NASA TN D-4690, 1968.

D-3. Kaji, S., *Axial-Flow Compressor Noise*. Ph.D. dissertation, Tokyo U., 1969. (See *J. Sound Vib.*, Vol. 11, 1970, p. 355)

D-4. Morfey, C. L., Rotating Blades and Aerodynamic Sound. *J. Sound Vib.*, Vol. 28, 1973, p. 587.

Sound Radiation from a Subsonic Rotor Subjected to Turbulence

M. Sevik

The Pennsylvania State University

The broadband sound radiated by a subsonic rotor subjected to turbulence in the approach stream has been analyzed. The power spectral density of the sound intensity has been found to depend on a characteristic time scale—namely, the integral scale of the turbulence divided by the axial flow velocity—as well as several length-scale ratios. These consist of the ratio of the integral scale to the acoustic wavelength, rotor radius, and blade chord. Due to the simplified model chosen, only a limited number of cascade parameters appear. Limited comparisons with experimental data indicate good agreement with predicted values.

The noise radiated by rotating machinery is known to consist of a broadband, random signal on which are superimposed a number of discrete peaks. These characteristics of the radiated noise spectrum have been observed on a wide range of turbomachinery such as aircraft compressors (refs. 1, 2, 3), turbines (ref. 4), fans (ref. 5), and marine propulsors.

The discrete peaks, which are due to mutual interference effects between blade rows, were of greatest concern as a cause of public annoyance and were the first to be investigated (refs. 6, 7, 8). This source of sound is now well understood and its reduction has met with a certain measure of success (ref. 10).

Broadband radiation has received relatively little attention in aircraft applications. The vibratory forces generated by turbulence, however, were of considerable interest in certain naval applications since marine propellers operate well within the boundary layer of a ship's hull. In this case, the length scales of the turbulence and the propeller are of comparable magnitudes, and, hence, strong thrust and torque fluctuations can arise (ref. 11).

The random pressure fluctuations within a turbomachine which give rise to broadband radiation are due to the following phenomena:

(1) Turbulence in the approach stream generated, for instance, by upstream blade rows or by the combustion system.

(2) Boundary layer turbulence at the duct walls.

(3) Vortex shedding from the blade trailing edges.

(4) Random variations of the tip vortex strength.

Sharland (ref. 5), Smith and House (ref. 3), and Smith and Bushell (ref. 4) conclude from their measurements that the major source of broadband, random noise in compressors and turbines is turbulence in the approach stream. This has also been found to be the case in marine propulsors (ref. 11), although vortex shedding from the blade trailing edges can—under certain conditions—become the dominant source over a range of frequencies.

In this paper, the sound radiated from a rotor subjected to turbulence in the approach stream, at subsonic speeds, will be considered.

CORRELATION OF PRESSURE FLUCTUATIONS

Curle (ref. 12) and Doak (ref. 13) have shown that the dipole radiation from a turbulent flow containing rigid surfaces can be expressed in terms of the distribution of fluctuating pressures acting over the surfaces. In order to calculate the characteristics of these pressures, imagine the rotor blades to be subdivided into an arbitrarily large number of surface elements. The fluid velocity is measured with respect to a coordinate system α' $(\alpha'=1', 2', 3')$ that is fixed in space (fig. 1). An unprimed system α $(\alpha=1, 2, 3)$ is fixed to the rotor and is so oriented that one of its axes coincides with the centerline of the rotor shaft.

The time-dependent pressures acting on the various surface elements are related by virtue of spatial and temporal correlation of the velocity fluctuations in the approach stream as well as by virtue of induction effects that take place between adjacent blade elements. The acoustic radiation depends on the correlation area for the pressure-difference fluctuations; because of induction effects this area may differ considerably from the correlation area of the turbulence.

Since the physical quantities involved in this problem are tensors, the index notation—including the summation convention in the case of repeated indices—constitutes the most convenient choice. Superscripts are used to denote the direction along one of the coordinate axes, whereas subscripts are used to denote the rotor blade element involved. For example, $u_k^\beta(\tau')$ denotes the component of the fluctuating velocity at time τ' in the direction β of the rotating reference frame at the blade element k. Similarly, $F_{ik}^{\alpha\beta}(t,\tau')$ denotes the aerodynamic force acting on the ith blade element in the direction α at the instant of time t caused by a velocity fluctuation of unit magnitude in the direction β to which the kth

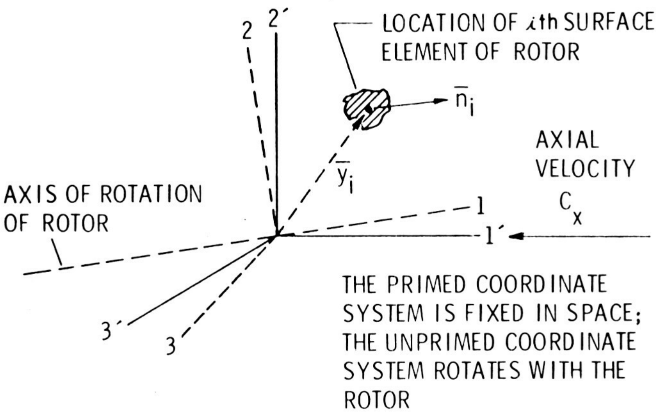

FIGURE 1.—*Coordinate system.*

blade element was subjected at the instant of time τ'. Finally, $\ell_i^\alpha(t)$ indicates the aerodynamic force acting on the ith blade element at time t in the direction α. In terms of these quantities, and neglecting higher order terms, the lift force is given by

$$\ell_i^\alpha(t) = \int_{-\infty}^{t} F_{ik}^{\alpha\beta}(t,\tau')u_k^\beta(\tau')\,d\tau' \tag{1}$$

where

$$\alpha,\ \beta = 1,\ 2,\ 3$$

$$i,\ k = 1,\ 2,\ \ldots\ n$$

with

$$\tau' \leq t$$

In most cases, the aerodynamic force tensor is time-invariant, and equation (1) can be written as a convolution integral:

$$\ell_i^\alpha(t) = \int_{0}^{\infty} F_{ik}^{\alpha\beta}(t)u_k^\beta(t-\tau)\,d\tau \tag{2}$$

where

$$\tau = t - \tau' \geq 0$$

Since the aerodynamic forces $\ell_i^\alpha(t)$ are random functions, they are determined statistically by the complete system of joint-probability distributions of the values of the functions at any n values of t, where n may take any integral value. From an engineering standpoint, the correlation tensor $\langle \ell_i^\alpha(t)\ell_j^\beta(t+\tau)\rangle$ and its Fourier transform are the most significant quantities. In forming average values of the forces and fluid velocities, we assume that the random processes are stationary and ergodic. The mathematical expectation

$$\left.\begin{aligned} E[\ell_i{}^{\alpha}(t)\ell_j{}^{\beta}(t+\tau)] &= \lim_{T\to\infty}\frac{1}{T}\int_0^T \ell_i{}^{\alpha}(t)\ell_j{}^{\beta}(t+\tau)\,dt \\ &= \Phi_{lilj}^{\alpha\beta}(\tau) \end{aligned}\right\} \tag{3}$$

can be expressed in terms of the aerodynamic force functions and the velocity fluctuations in the form

$$\left.\begin{aligned} \Phi_{lilj}^{\alpha\beta}(\tau) &= \int_0^\infty F_{ik}{}^{\alpha\gamma}(\tau_1)\,d\tau_1\int_0^\infty F_{jr}{}^{\beta\delta}(\tau_2)\,d\tau_2 \\ &\quad\times\lim_{T\to\infty}\frac{1}{T}\int_0^\infty u_k{}^{\gamma}(t-\tau)u_r{}^{\delta}(t+\tau-\tau_2)\,dt \\ &= \int_0^\infty F_{ik}{}^{\alpha\gamma}(\tau_1)\,d\tau_1\int_0^\infty F_{jr}{}^{\beta\delta}(\tau_2)\,d\tau_2 R_{kr}{}^{\gamma\delta}(\tau) \end{aligned}\right\} \tag{4}$$

$R_{kr}{}^{\gamma\delta}(\tau)$ is the velocity correlation tensor for the points located at $\mathbf{y}_k$ and $\mathbf{y}_r$, respectively. The spectrum tensor of the force fluctuations can now be found by taking the Fourier transform of the correlation tensor:

$$\left.\begin{aligned} G_{lilj}^{\alpha\beta}(\omega) &= \frac{1}{\pi}\int_{-\infty}^\infty \Phi_{ij}{}^{\alpha\beta}(\tau)[\exp i\omega\tau]\,d\tau \\ &= \int_0^\infty F_{ik}{}^{\alpha\gamma}(\tau_1)[\exp i\omega\tau_1]\,d\tau_1\int_0^\infty F_{jr}{}^{\beta\delta}(\tau_2)\,[\exp(-i\omega\tau_2)]\,d\tau_2 \\ &\quad\times\frac{1}{\pi}\int_{-\infty}^\infty R_{kr}{}^{\gamma\delta}(\tau)[\exp(-i\omega\tau)]\,d\tau \\ &= [H_{ik}{}^{\alpha\gamma}(\omega)]^*[H_{jr}{}^{\beta\delta}(\omega)]G_{kr}{}^{\gamma\delta}(\omega) \end{aligned}\right\} \tag{5}$$

where $H(\omega)$ represents the aerodynamic frequency response function, $G_{kr}{}^{\gamma\delta}(\omega)$ is the spectrum tensor of the turbulence, and $i=\sqrt{-1}$.

APPLICATION TO A ROTOR

As an illustration, consider a rotor placed in a flow containing homogeneous and isotropic turbulence. In this case, the velocity correlation tensor can be expressed in terms of the distance r between two points in the flow field and the mean square value of the velocity fluctuations u^2 as follows:

$$R_{kr}{}^{\alpha\beta}(r)=u^2\left[-\frac{1}{2r}\,r^\alpha r^\beta\,\frac{\partial f}{\partial r}+\left(f+\frac{1}{2}\,r\,\frac{\partial f}{\partial r}\right)\delta^{\alpha\beta}\right] \tag{6}$$

where $\delta^{\alpha\beta}$ is the Kroenecker delta. The coefficient of longitudinal correlation f can be approximated by an exponential function; namely

$$f(r)=\exp\left(-\frac{r}{\Lambda_f}\right) \tag{7}$$

where Λ_f is the integral scale of the turbulence. Furthermore, the velocity correlation tensor is approximated by

$$R_{kr}{}^{\alpha\beta}(r)\cong\left[\exp\left(-\frac{q}{\Lambda_f}\right)\right]R_{kk}{}^{\alpha\beta}(c_x\tau) \tag{8}$$

where $q=|\mathbf{y}_k-\mathbf{y}_r|$ is the distance between blade elements k and r.

We now calculate the spectrum tensor of the force fluctuations normal to the plane of the rotor. In equation (5), α and β are both assigned the value 1, which corresponds to the direction normal to the rotor disk. The indices γ and δ take the values 1 and 2 only, since axis 3 coincides with the spanwise axis of a blade. From equation (8) the velocity correlation tensor has the components

$$\left.\begin{aligned}
R_{kr}{}^{11}(r)&=u^2\exp\left\{-\left(\frac{c_x\tau}{\Lambda_f}+\frac{q}{\Lambda_f}\right)\right\}\\
R_{kr}{}^{22}(r)&=u^2\left(1-\frac{1}{2}\,\frac{c_x\tau}{\Lambda_f}\right)\exp\left\{-\left(\frac{c_x\tau}{\Lambda_f}+\frac{q}{\Lambda_f}\right)\right\}\\
R_{kr}{}^{12}(r)&=R_{kr}{}^{21}(r)=0
\end{aligned}\right\} \tag{9}$$

where c_x is the axial velocity, as shown in figure 2.

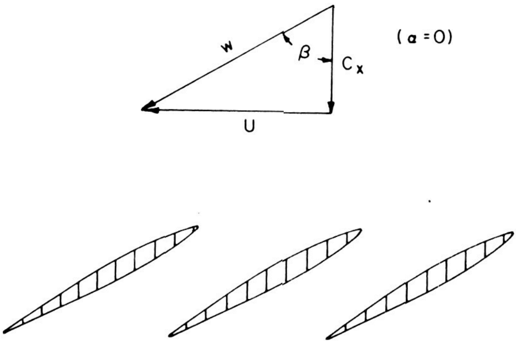

FIGURE 2.—*Velocity diagram for an axial flow pump or compressor stage.*

The Fourier transforms of these correlation functions can readily be calculated:

$$\left.\begin{aligned}
G_{kr}{}^{11}(\omega) &= \frac{2}{\pi}\,u^2\left[\frac{\dfrac{c_x}{\Lambda_f}}{\left(\dfrac{c_x}{\Lambda_f}\right)^2+\omega^2}\right]\exp\left(-\frac{q}{\Lambda_f}\right)\\[2ex]
G_{kr}{}^{22}(\omega) &= \frac{2}{\pi}\,u^2\left[\frac{\dfrac{c_x}{\Lambda_f}}{\left(\dfrac{c_x}{\Lambda_f}\right)^2+\omega^2}\right]\left\{1+\frac{1}{2}\left[\frac{\left(\dfrac{c_x}{\Lambda_f}\right)^2-\omega^2}{\left(\dfrac{c_x}{\Lambda_f}\right)^2+\omega^2}\right]\right\}\exp\left(-\frac{q}{\Lambda_f}\right)
\end{aligned}\right\} \qquad (10)$$

The spectrum tensor of the force fluctuations therefore reduces to

$$\begin{aligned}
G_{1i1j}^{11}(\omega) &= [H_{ik}{}^{11}(\omega)]^*[H_{jr}{}^{11}(\omega)]G_{kr}{}^{11}(\omega)\\
&\quad +[H_{ik}{}^{12}(\omega)]^*[H_{jr}{}^{12}(\omega)]G_{kr}{}^{22}(\omega)
\end{aligned} \qquad (11)$$

The simplest expression for the aerodynamic response function is that of Sears (ref. 14). This expression is based on two-dimensional, incompressible, thin-airfoil aerodynamics and ignores mutual interference between blade elements. The task of establishing aerodynamic response functions for cascades is yet to be accomplished. Recent experiments that have been performed at Pennsylvania State University, however, show that strip theory gives satisfactory predictions providing the value of the local lift slope is appropriately corrected. This correction consists in replacing the value of the lift slope—which is equal to 2π in Sears' equation—by the steady-state local value. In terms of Sears function, the values of $H(\omega)$ are given by

$$\left.\begin{aligned}
H_{ii}{}^{11}(\omega) &= H_i(\omega)\ \sin^2\beta_i\\
H_{ii}{}^{12}(\omega) &= \tfrac{1}{2}H_i(\omega)\ \sin 2\beta_i
\end{aligned}\right\} \qquad (12)$$

where

$H(\omega)$	$2\pi\rho w b\delta r K(\kappa)$
$K(\kappa)$	Sears function
κ	$\dfrac{\omega b}{w}$

$2b$	blade chord
δr	spanwise distance along the blade
w	relative fluid velocity
β	angle between the flow relative to the blade and the axial direction, as shown in figure 2.

We can further simplify our final expression if $H(\omega)$ is chosen as the mean value for the entire blade span. In this case

$$\frac{1}{n^2}\sum_{i=1}^{n}\sum_{j=1}^{n}H_i^*(\omega)H_j(\omega)\cong H^*(\omega)H(\omega)=|H(\omega)|^2\cong(2\pi w\rho b)^2\frac{1}{(1+2\pi\kappa)}\delta r_i\delta r_j \tag{13}$$

The spectrum of the total normal force driving the rotor can now be found from equation (11), using equations (10), (12), and (13). It has the form

$$G(\Gamma)=\pi(\rho c_x^2R^2)^2\left(\frac{2bB}{R}\frac{u}{c_x}\right)^2\left(\frac{1}{1+\phi^2}\right)f(\Gamma)\,S\left(\frac{R}{\Lambda_f}\right) \tag{14}$$

where $\phi=c_x/U$ is the flow coefficient, B is the number of rotor blades, and u/c_x is the turbulence level in the approach stream.

The function $S(R/\Lambda_f)$ represents a "correlation area" and is given by

$$S\left(\frac{R}{\Lambda_f}\right)=\frac{1}{B^2R^2}\int\int\exp\left(-\frac{q}{\Lambda_f}\right)dr_i\,dr_j;\qquad q=|\mathbf{r}_i-\mathbf{r}_j| \tag{15}$$

The integration is performed from the hub radius r_h to the tip radius R. This function has been plotted in figure 3 for rotors having various numbers of blades and hub-to-tip ratios.

The frequency dependence of the total force driving the rotor is given by $f(\Gamma)$, which has the form

$$f(\Gamma)=\left(\frac{1}{1+e\Gamma}\right)\left(\frac{1}{1+\Gamma^2}\right)\left(C+\frac{1-\Gamma^2}{1+\Gamma^2}\right) \tag{16}$$

where

$$\Gamma=\frac{\omega\Lambda_f}{c_x}$$

$$e=\pi\frac{2b}{\Lambda_f}\cos\beta$$

$$C=2\left(1+\frac{1}{\phi^2}\right)$$

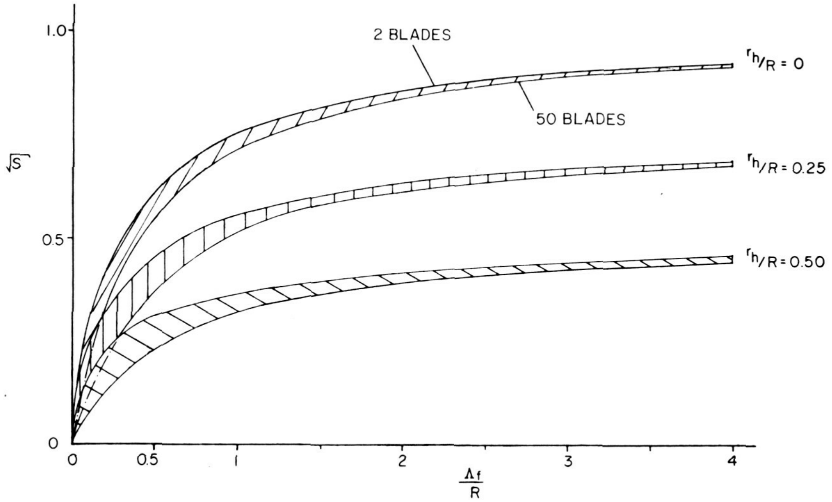

FIGURE 3.—*"Correlation area" in the spectrum function of the axial force.*

EXPERIMENTAL INVESTIGATIONS

To verify the theory, an experiment was conducted in the water tunnel of the Ordnance Research Laboratory at Pennsylvania State University (ref. 11). This tunnel has a test section that is 4 ft in diameter and 14 ft in length. Velocities as high as 80 fps can be achieved, and the static pressure can be varied from 3 to 60 psia. The settling section of the tunnel contains a honeycomb of large length-to-diameter ratio that reduces the turbulence level in the test section to about 0.1 percent.

A propeller was used for this investigation. The propeller had 10 blades with a constant chord length of 1 in. and a radius of 4 in. The design static thrust coefficient based on propeller disc area is 0.183, and the advance ratio at the design thrust coefficient is 1.17. The propeller and its installation in the water tunnel are shown in figure 4.

A special balance was designed for measuring the unsteady thrust force of the propeller. The arrangement used is shown in figure 5. A piezoelectric crystal is mounted in a steel cup at the end of the propeller shaft. After assembly, the cup is positioned by means of set screws until the hemispherical ball bonded to the crystal lies on the exact center line of the shaft, thus minimizing the crystal's response to bending distortions of the shaft caused by hydrodynamic moments acting on the propeller. The frequency response and the linearity of the balance are shown in figure 6.

During the tests, turbulence was generated by means of grids mounted 20 mesh sizes upstream of the propeller. Two grids were used with mesh

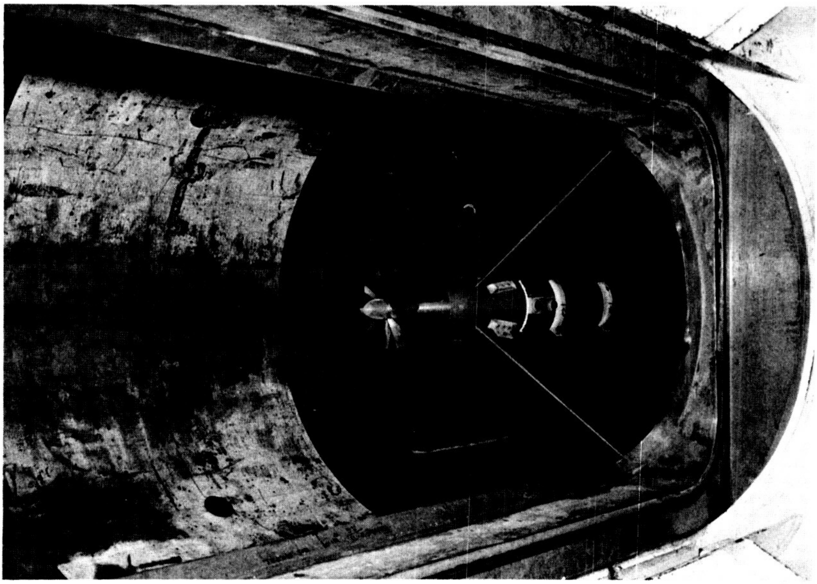

Figure 4.—*Experimental propeller and balance housing in the water-tunnel test section.*

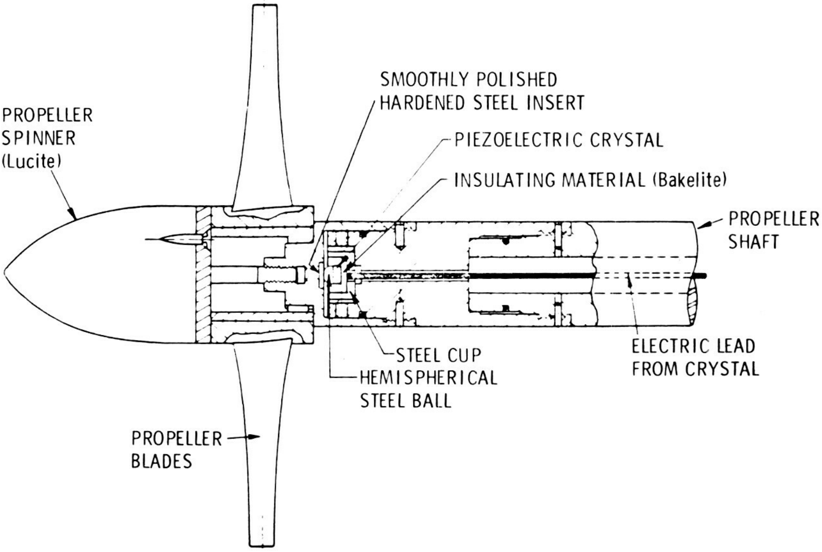

Figure 5.—*Unsteady force balance.*

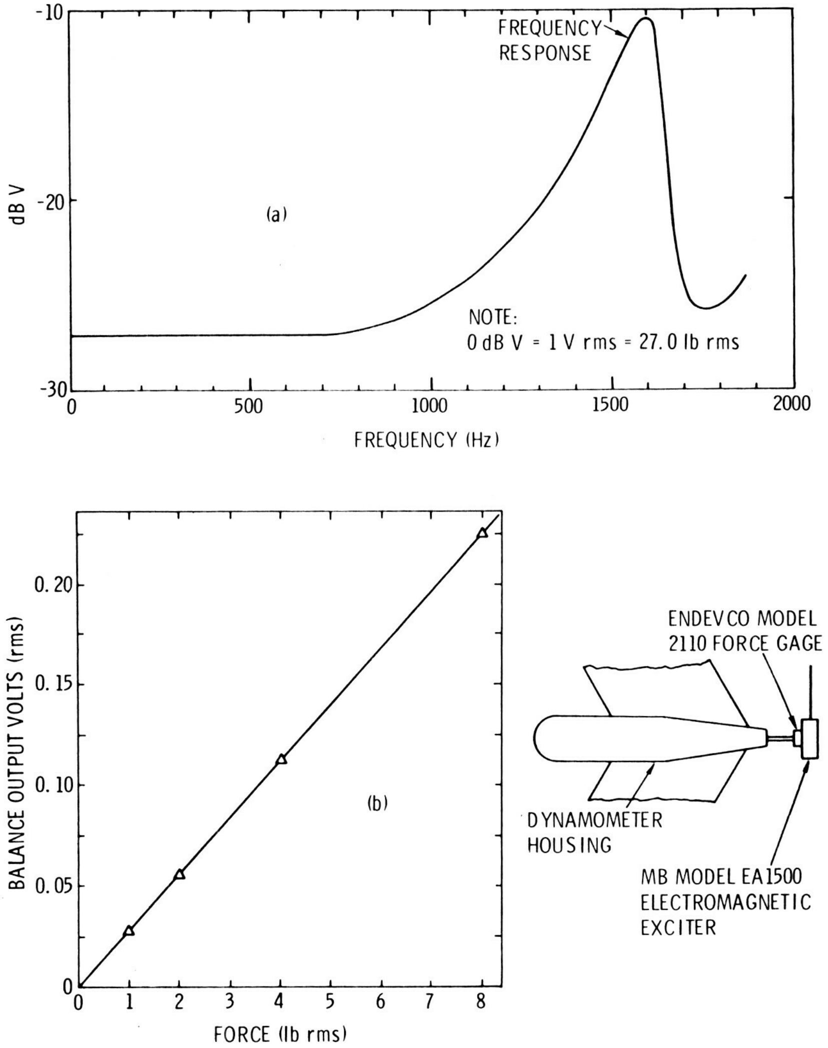

FIGURE 6.—*Frequency response and linearity of balance.*

sizes of 4 in. and 6 in., respectively. The first had a solidity of 0.34 and was fabricated with $\frac{3}{4}$-in.-diameter rods. The second had a solidity of 0.27 and consisted of $\frac{7}{8}$-in.-diameter rods. Figure 7 shows a view of the propeller taken from a position upstream of the 4-in. grid in the water tunnel.

The measurements are compared in figure 8 with theoretical predictions. The "humps" in the measured spectrum occur at blade passage frequency.

FIGURE 7.—*Downstream view of propeller through the 4-inch grid.*

SOUND RADIATION FROM A ROTOR

The statistical measure of greatest engineering interest is the power spectral density of the sound pressure fluctuations. This is related to the power spectral density of the force fluctuations by a Green's function $g(\mathbf{x},\mathbf{y};\omega)$ as follows:

$$P(\mathbf{x};\omega) = \sum_{i=1}^{n} \sum_{j=1}^{n} g^{*}(\mathbf{x},\mathbf{y}_i;\omega)\, g(\mathbf{x},\mathbf{y}_j;\omega)\, G^{11}_{lilj}(\omega) \qquad (17)$$

If the rotor is housed in a duct, the radiation into the free field will be affected by the characteristics of sound propagation in the duct and by its intake geometry. These effects have been considered by Tyler and Sofrin (ref. 6), as well as by Morfey (ref. 15), for pure tone radiation.

In order to simplify the present problem, the Green's function chosen will be that of a dipole whose axis is normal to the rotor plane. Comparison of predicted acoustic power with experimental measurements on ducted fans will still be possible in cases where the dimension of the duct is comparable with, or greater than, the quarter wavelength of the sound generated. The appropriate Green's function for the far field is given by

$$g(\mathbf{x},\mathbf{y}_j;\omega) = -\frac{ik\cos\theta}{4\pi r}\{\exp ikr\}\{\exp[-ikr_j\cos(\varphi_j-\varphi)\sin\theta]\} \qquad (18)$$

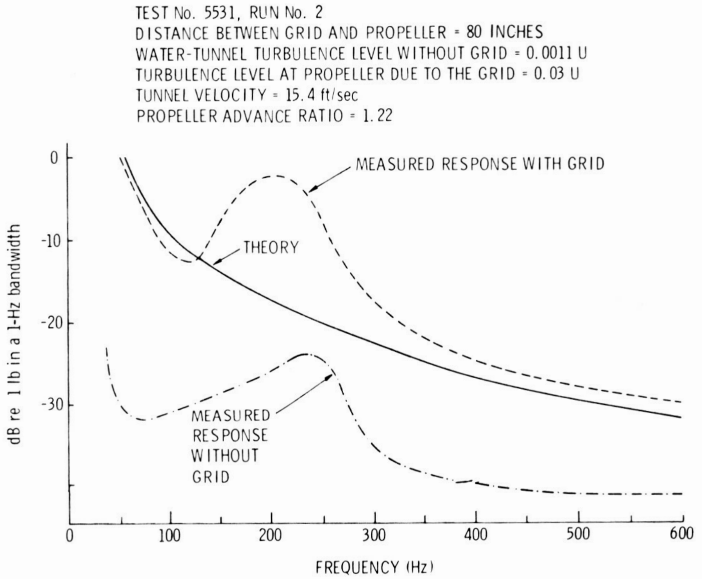

a.—*4-inch grid mesh.*

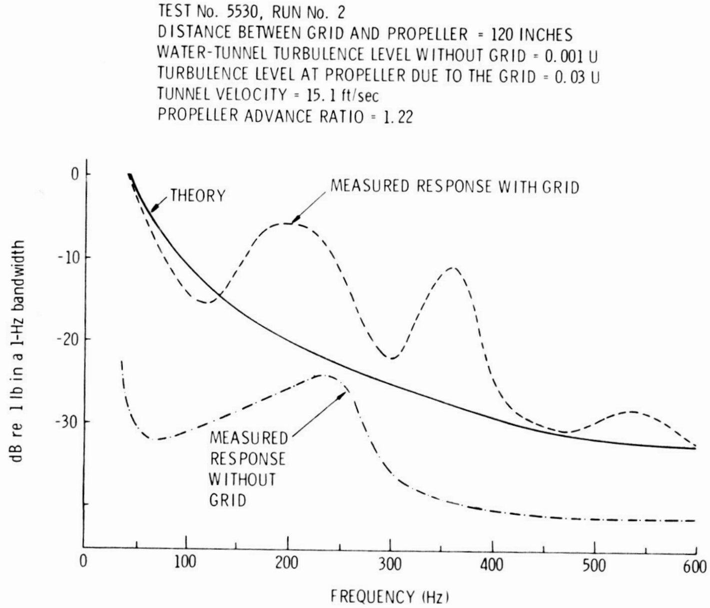

b.—*6-inch grid mesh.*

FIGURE 8.—*Power spectral density of the propeller response.*

where $k=\omega/c$. The polar coordinates used in this equation are defined in figure 9.

A further restriction is imposed by the requirement that the eddies be compact on a wavelength scale so that retarded time changes will be negligible. This implies that the acoustic wave length λ must be much larger than the integral scale Δ_f.

The spectral density of the sound intensity at $\mathbf{x}$ follows from equations (17) and (18):

$$I(\mathbf{x};\Gamma)=\frac{\pi^2}{4r^2}\left(\frac{u}{c_x}\right)^2 M^3\left[1-\left(\frac{r_h}{R}\right)^2\right]^2\left(\frac{\rho c_x{}^3R^2}{1+\phi^2}\right)\left(\frac{R}{\Lambda_f}\right)^2 g(\Gamma)F\left(\theta,\frac{R}{\Lambda_f},kR\right) \tag{19}$$

where $M=c_x/c$ is the axial flow Mach number and $g(\Gamma)=\Gamma^2 f(\Gamma)$.

In deriving the function F, it is assumed that the solidity of the rotor is such that it can be treated acoustically as a disk. This implies that the acoustic wavelength must be much larger than the blade chord and the blade spacing. Under these conditions F has the form

$$F\left(\theta,\frac{R}{\Lambda_f},kR\right)=\frac{\cos^2\theta}{2\pi^2\left[1-\left(\frac{r_h}{R}\right)^2\right]^2 R^4}\int_{r_h}^{R}\int_0^{2\pi}\exp\left\{-\frac{R}{\Lambda_f}(Q^2+Z^2)^{1/2}\right\}$$

$$\times[J_0(kRQ\sin\theta)+J_0(kRZ\sin\theta)]r_i\,dr_i\,d\varphi_i\,r_j\,dr_j\,d\varphi_j \tag{20}$$

where J_0 denotes Bessel functions and r_h denotes the hub radius. The quantities Q and Z are measured on the rotor disk and are given by

$$Q=\frac{1}{R}\,(r_i\cos\varphi_i-r_j\cos\varphi_j)$$

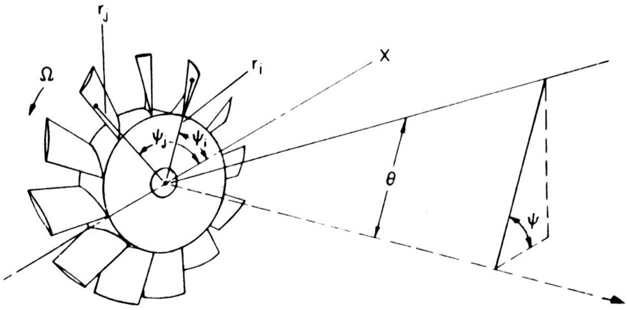

FIGURE 9.—*Polar coordinate system.*

$$Z=\frac{1}{R}\,(r_i \sin \varphi_i - r_j \sin \varphi_j)$$

Finally, the intensity can be integrated over a large spherical surface to yield the spectral density of the sound power:

$$\frac{dW}{d\Gamma}=\pi^3\left(\frac{u}{c_x}\right)^2 M^3\left(\frac{\rho c_x{}^3R^2}{1+\phi^2}\right)\left(\frac{R}{\Lambda_f}\right)^2\left[1-\left(\frac{r_h}{\mathrm{R}}\right)^2\right]^2 g(\Gamma)F_1\left(\frac{R}{\Lambda_f},\,kR\right) \quad (21)$$

where

$$F_1\left(\frac{R}{\Lambda_f},\,kR\right)=\int_0^{\pi/2} F\left(\theta,\,\frac{R}{\Lambda_f},\,kR\right)\sin\theta\,\cos^2\theta\,d\theta$$

The function F_1 has been calculated numerically and is plotted in figure 10 for a range of values of kR and R/Λ_f.

As an example, the theory has been applied to the following case:

Rotor hub-to-tip radius ratio $\frac{r_h}{R}=0.5$

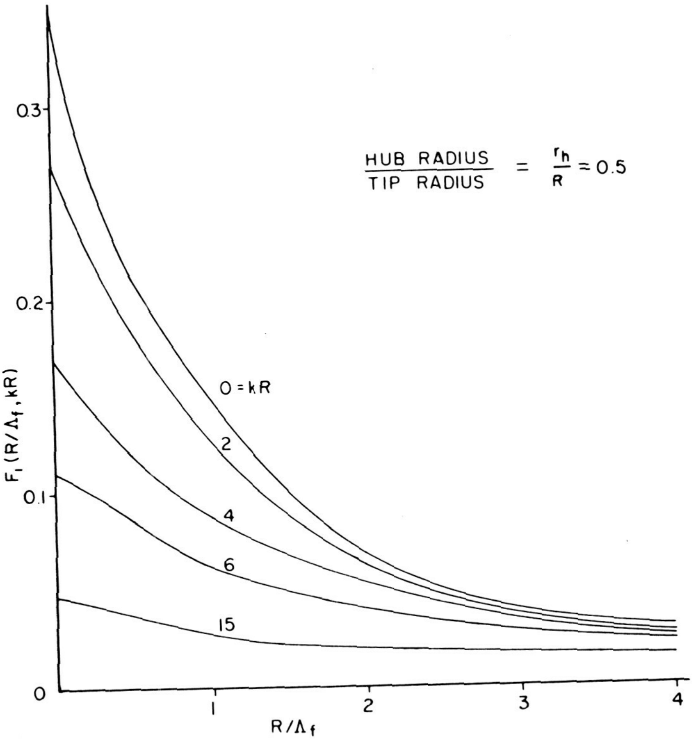

FIGURE 10.—*Radiation function in the spectral density of the sound power.*

Flow coefficient $\phi = 0.64$

Axial flow Mach number $M = 0.25$

Ratio of integral scale to tip radius $\frac{\Lambda_f}{R} = 0.5$

This choice of Λ_f corresponds to the span of the blades. The resulting spectrum is shown in figure 11. The vertical scale is proportional to $\Gamma(dW/d\Gamma)$; i.e., a constant-percentage bandwidth, and the horizontal scale consists of the ratio of the integral scale Λ_f to the sound wavelength λ. The peak of the spectrum occurs at a value of $\Lambda_f/\lambda = 0.16$. The predicted spectrum level becomes inaccurate at values of $\Lambda_f/\lambda \geq 0.25$ since the integral scale of the turbulence and the wavelength of the sound become of comparable magnitude. A much more rapid, exponential decrease in the value of $\Gamma(dW/d\Gamma)$ than indicated in figure 11 would be expected.

The directivity of the sound pressure is illustrated in figure 12, which shows that the sound becomes progressively less directional as the integral scale Λ_f decreases.

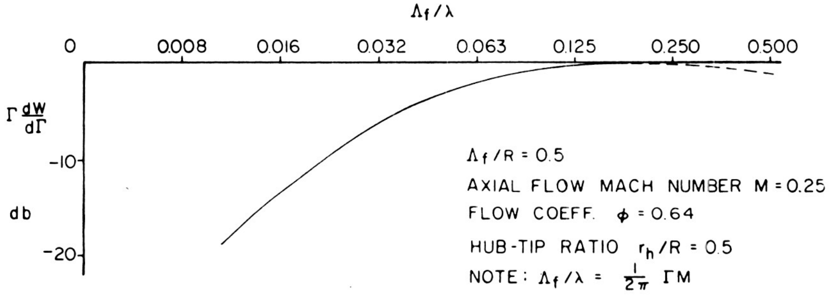

FIGURE 11.—*Broadband sound-power spectrum.*

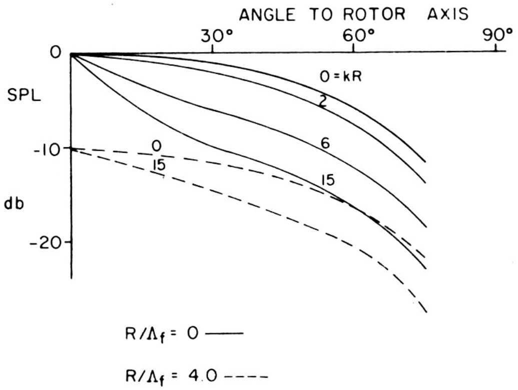

FIGURE 12.—*Directivity of sound radiation.*

SUMMARY AND CONCLUSIONS

Broadband sound radiation from turbomachinery appears to be mainly due to turbulence in the approach stream. This turbulence may be generated by one of several mechanisms such as upstream blade rows or, in the case of turbines, the combustion system.

As a preliminary step in the calculation of the power spectral density of the radiated sound pressure, the spectrum tensor of the axial force fluctuations acting on a rotor have been found. These have been expressed in terms of aerodynamic response functions and the correlation tensor of the turbulence. At the present time, there is little information concerning the characteristics of the turbulence in turbomachinery. Also, expressions for the aerodynamic response functions are limited to two-dimensional, incompressible, thin-airfoil theory. Research in both areas is desirable. In order to make further progress and establish the general characteristics of the radiated sound, a simple case was considered. The turbulence in the approach stream was chosen to be isotropic and homogeneous, and the spectrum of the total force normal to a rotor disk was calculated. The predicted spectrum levels were compared with experimental results obtained on a 10-bladed propeller subjected to grid turbulence. Good agreement was observed.

The power spectral density of the sound intensity and of the sound power were next calculated. The spectrum depends on a number of parameters, such as the turbulence level, a characteristic time scale consisting of the ratio of the integral scale of the turbulence divided by the axial flow velocity, and characteristic length scales such as the ratio of the integral scale of the turbulence to the acoustic wavelength, the radius of the rotor, and the blade chord.

Due to the simplicity of the model used, only a limited number of cascade parameters enter the equations. In a more complete description, additional cascade parameters—such as the solidity and stagger angle—would also appear. As an example, the broadband sound-power spectrum for a turbomachinery rotor was calculated and plotted in figure 11. A flow coefficient of 0.64, a hub-to-tip ratio of 0.50, and an axial flow Mach number of 0.25 were chosen. The broadband sound power radiated has been estimated at 140 dB re 10^{-12} watts for a turbulence level of 5 percent of the axial velocity.

LIST OF SYMBOLS

B	number of blades on rotor
$2b$	blade chord
C	cascade parameter defined in equation (16)

c	speed of sound
c_x	axial flow velocity
e	cascade parameter defined in equation (16)
F	aerodynamic force function, defined in equation (1)
f	coefficient of longitudinal correlation of the turbulence
$G(\omega)$	spectrum function
$H(\omega)$	aerodynamic frequency response function
$K(\kappa)$	Sears function
k	acoustic wave number
ℓ	local lift force
M	Mach number of axial flow
n	number of blade elements
Q,Z	projections of q on the x and y axes, respectively
q	distance between blade elements
R	tip radius of rotor
r	distance, as variously defined
r_h	hub radius of rotor
t,T	time
U	tangential velocity of rotor
u	fluid velocity
W	sound power
w	flow velocity relative to the blades
$\mathbf{x},\mathbf{y}$	position vectors

Greek Letters

β	angle between the flow relative to the blade and the axial direction
Γ	frequency parameter, defined in equation (16)
Φ	correlation function
ϕ	flow coefficient, defined in equation (14)
κ	reduced frequency parameter in Sears function
Λ_f	integral length scale of the turbulence
λ	wavelength of the acoustic radiation
τ	time
θ,φ	position angles in polar coefficient
ω	angular frequency

APPENDIX: TABLE OF RADIATION FUNCTION[1]

$F(\theta, \frac{R}{\Lambda_f}, kR)$, defined by equation (20)

θ	kR	$\frac{R}{\Lambda_f} \to 0$	0.5	1.0	2.0	4.0
0°	0	1.0	0.620	0.408	0.208	0.088
	2	1.0	0.620	0.408	0.208	0.088
	4	1.0	0.620	0.408	0.208	0.088
	6	1.0	0.620	0.408	0.208	0.088
	15	1.0	0.620	0.408	0.208	0.088
30°	0	0.750	0.461	0.305	0.155	0.066
	2	0.640	0.410	0.275	0.145	0.064
	4	0.420	0.289	0.210	0.121	0.059
	6	0.250	0.194	0.151	0.100	0.054
	15	0.100	0.084	0.068	0.051	0.035
60°	0	0.250	0.155	0.101	0.052	0.022
	2	0.160	0.108	0.076	0.043	0.020
	4	0.071	0.055	0.044	0.031	0.017
	6	0.055	0.042	0.033	0.023	0.014
	15	0.022	0.017	0.014	0.011	0.008
90°	0	0	0	0	0	0
	2	0	0	0	0	0
	4	0	0	0	0	0
	6	0	0	0	0	0
	15	0	0	0	0	0

---

[1] This table applies to a hub/tip ratio of 0.50.

REFERENCES

1. Bragg, S. L., and R. Bridge, Noise from Turbojet Compressors. *J. Roy. Aeron. Soc.*, Vol. 68, No. 637, January 1964.
2. Copeland, W. L., and J. L. Crigler, *Noise Studies of Inlet-Guide-Vane—Rotor Interaction of a Single-Stage Axial-Flow Compressor.* NASA TN D-2962, September 1965.
3. Smith, M. J. T., and M. E. House, Internally Generated Noise from Gas Turbine Engines. Measurement and Prediction. *Trans. ASME, J. of Eng. Power*, April 1967, pp. 177–190.
4. Smith, M. J. T., and K. W. Bushell, *Turbine Noise—Its Significance in the Civil Aircraft Noise Problem.* ASME Paper 69–WA/GT–12, presented at the ASME Winter Annual Meeting (Los Angeles), November 16–20, 1969.
5. Sharland, I. J., Sources of Noise in Axial Flow Fans. *J. Sound Vib.*, Vol. 3, 1964, pp. 302–322.
6. Tyler, J. M., and T. G. Sofrin, Axial Flow Compressor Noise Studies. *Trans. SAE*, 1962, pp. 309–332.
7. Morfey, C. L., *Sound Generation in Subsonic Turbomachinery.* ASME Paper 69–WA/FE–4, presented at the ASME Winter Annual Meeting (Los Angeles), November 16–20, 1969.
8. Mani, R., *Discrete Frequency Noise Generation From an Axial Flow Fan Blade Row.* ASME Paper 69–FE–12, presented at the ASME Applied Mechanics and Fluids Engineering Conference (Evanston, Ill.), June 16–18, 1969.
9. Lipstein, N. J., and R. Mani, *Experimental Investigation of Discrete Frequency Noise Generated by Unsteady Blade Forces.* ASME Paper 69–WA/FE–22, presented at the ASME Winter Annual Meeting (Los Angeles), November 16–20, 1969.
10. Kramer, J. J., B. R. Leonard, and C. E. Feiler, *Low-Noise Propulsion Systems for Subsonic Transports.* ASME Paper 69–WA/GT–7, presented at the ASME Winter Annual Meeting (Los Angeles), November 16–20, 1969.
11. Sevik, M., *The Response of Propulsors to Turbulence.* Presented at the 7th Symposium on Naval Hydrodynamics (Rome), 1968.
12. Curle, N., The Influence of Solid Boundaries Upon Aerodynamic Sound. *Proc. Roy. Soc.* (*London*), Series A, Vol. 231, 1955, pp. 505–514.
13. Doak, P. E., Acoustic Radiation from a Turbulent Fluid Containing Foreign Bodies. *Proc. Roy. Soc.* (*London*), Series A, Vol. 254, 1960, p. 129.
14. Sears, W. R., Some Aspects of Non-Stationary Air Foil Theory and Its Practical Application. *J. Aeron. Sci.*, Vol. 8, No. 3, January 1941.
15. Morfey, C. L., Broadband Sound Radiated from Subsonic Rotors. To be presented at the Internationsl Symposium on the Fluid Mechanics and Design of Turbomachinery (Penn State U.), August 31–September 3, 1970.

DISCUSSION

R. MANI (University of Massachusetts): It would seem from your description of the experimental apparatus that you have turbulence scales which are quite large compared to the propulsor size. It has been shown that you should get a predominance of blade-passage tones. If the eddies are really of substantial size, I do not really see how you would only get a broadband spectrum.

SEVIK (author): I believe that you are referring to a paper by Ffowcs Williams and Hawkings in which they show that blade-passage tones will also occur when the inflow is turbulent. They indicate that the bandwidth of the spectrum will be inversely proportional to the number of blades which are subject to the distortion field of a single eddy. Our test results do indeed show a "bump" around blade-passage frequency, which corresponds to their prediction. The bandwidth of the bump is about 40 cps, in agreement with their expression. Unfortunately, we also discovered after the tests that we had a blade resonance in the same frequency range and hence that there were two possible contributors to the energy. I agree that my theoretical approach does not predict the tones, but only the broadband energy.

Compressibility Effects in the Kemp-Sears Problem[1]

RAMANI MANI

University of Massachusetts

The effects of including compressibility in the Kemp-Sears problem of aerodynamic interference between moving blade rows are examined. Methods of linearized, subsonic, plane, unsteady flow are adopted. The major new effect is that a resonance appears at certain combinations of flow Mach number, tip Mach number, and blade vane ratios. The resonance is at exactly the Tyler-Sofrin cutoff condition for rotor-stator interaction. At such conditions the unsteady lift on a blade row due to externally imposed nonstationary upwash vanishes. However, the resonance appears to be very sharp and seems to be more significant as an indication that around this condition the unsteady lift changes very rapidly.

This paper is concerned with unsteady blade forces developed on an axial compressor blade row due to unsteady periodic wave disturbances. The applications discussed pertain to unsteady disturbances produced on a blade row due to steady-state lifts of adjacent rows moving past the row of interest and due to viscous wakes shed by upstream rows.

The framework for the analytical approach to the solution of this complex problem is contained in two pioneering papers by Kemp and Sears (refs. 1, 2). Kemp and Sears adopt the representation of blade wheels as infinite cascades of two-dimensional airfoils. They consider a typical airfoil in the blade row on which unsteady forces are to be calculated as an isolated airfoil in linearized, unsteady, incompressible flow. This isolated airfoil is subject to unsteady disturbances from various sources. Reference 1 considers nonstationary upwash due to translation of steady-state design fields of an adjacent row. In this case the effect of a row upon

---

[1] The author gratefully acknowledges substantial assistance rendered during the course of this work by Dr. T. C. Liu. Many thanks are also due to N. J. Lipstein and I. H. Edelfelt of the General Electric Research and Development Center. The work was supported financially by the assessed funds program of the G.E. Research and Development Center.

an adjacent row downstream of it and the nonstationary upwash due to the "inviscid" wakes is included. Reference 2 considers nonstationary upwash due to viscous wakes shed by an upstream row. In this paper two refinements are considered. First, a typical airfoil of the row on which we wish to calculate the unsteady blade forces is regarded as a member of an isolated, infinite *cascade* of airfoils rather than as an isolated airfoil. Second, in calculating both the nonstationary upwash and the unsteady forces we include compressibility effects. Methods for linearized, subsonic, plane, compressible unsteady flow are adopted. For the present, we have not included nonstationary upwashes due to "inviscid" wakes. The motivation for incorporating these refinements is simply that in most present-day applications where unsteady blade forces in fans and compressors are of interest, the Mach numbers of the flow are too high for compressibility effects to be negligible.

Consider an isolated, infinite flat-plate cascade of identical airfoils spaced s apart whose chord lengths have been normalized to unity and with flow at Mach number M through the cascade. M is restricted to $M<1$ (subsonic flow through the blade passages). The problem is to calculate the unsteady lift on a typical blade of such a cascade due to a known nonstationary upwash on it where the time-dependence of the nonstationary upwash is of simple harmonic type. The nonstationary upwash will later be related to the translation of adjacent steady-state design fields and to viscous wakes shed by an upstream row. Due to the symmetry of the cascade the nonstationary upwash on the nth blade is essentially the same as on the zeroth blade, except for a phase difference factor of $\exp(jn\gamma)^2$, where we will later relate γ to the aerodynamic parameters.

The method of solution adopted is the method of distributed singularities and singular integral equations. An $x-y$ coordinate system is used as shown in figure 1. Let ξ denote the running coordinate on the zeroth blade that runs from $-\frac{1}{2}$ to $\frac{1}{2}$. Let the unsteady lift distribution on the zeroth chord be denoted by $F(\xi)e^{j\omega t}$. Let $K_v(x,\xi)$ denote a kernel function that gives the nonstationary upwash at the point $(x,0)$ on the zeroth blade due to an infinite row of equal oscillating forces of unit strength with phase shift γ located at ξ and its corresponding points; i.e., at

$$\xi+ns\sin(\alpha_s),\ ns\cos(\alpha_s)$$

where $n=0, \pm 1, \pm 2, \ldots$, etc. $K_v(x,\xi)$ is known since it is merely the sum of upwash contributions due to unit forces of known phase and location. Let $v_d(x)e^{j\omega t}$ be the known nonstationary upwash due to the adjacent rows. Then the boundary condition that the velocity normal to

---

[2] $j=\sqrt{-1}$

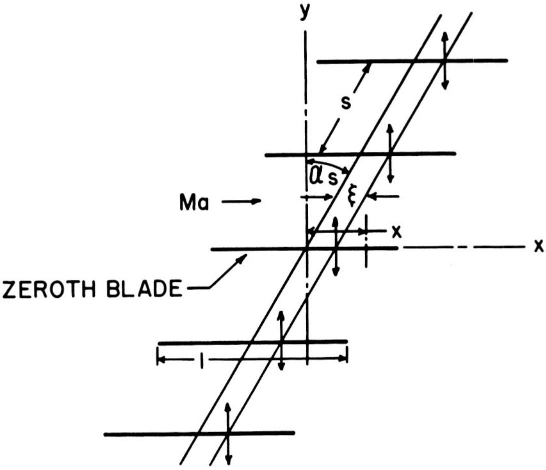

FIGURE 1.—*Coordinate system.*

the blade chords be zero leads to the integral equation:

$$\int_{-1/2}^{1/2} F(\xi) K_v(x,\xi)\, d\xi = -v_d(x) \ldots \tag{1}$$

where $K_v(x,\xi)$ and $v_d(x)$ are known. Only $F(\xi)$ is unknown, and, after solving equation (1), the total unsteady lift is found from

$$(\text{total lift}) = \int_{-1/2}^{1/2} F(\xi)\, d\xi \tag{2}$$

$K_v(x,\xi)$ has a singularity; i.e., a term as $1/(x-\xi)$; hence, equation (1) constitutes a singular integral equation for the force distribution. There are two other requirements on $F(\xi)$: first, that it vanish at the trailing edge $\xi=\frac{1}{2}$ (the Kutta-Joukowski condition), and, second, that it have a square-root singularity at the leading edge; i.e., the force distribution tends to ∞ as $\xi \rightarrow -\frac{1}{2}$ as $1/\sqrt{\xi+\frac{1}{2}}$.

CALCULATION OF KERNEL FUNCTION

The physical significance of the kernel function $K_v(x,\xi)$ is repeated: It is the upwash at point $(x,0)$ on the zeroth blade due to an infinite row of unit forces located at

$$\xi + ns \sin(\alpha_s),\ ns \cos(\alpha_s)$$

with $n=0, \pm 1, \pm 2, \ldots$, etc., where the phase of the oscillating force on the nth blade is related to that on the zeroth blade by a factor $\exp(jn\gamma)$.

In the derivation of the kernel function we have relied heavily on a recent paper by Kaji and Okazaki, who treat an analogous problem (ref. 3). We are especially indebted to their repeated and ingenious use of the Poisson summation formula to switch from infinite series of Hankel functions to infinite series of exponential functions. In view of their paper, we omit many of the details of the derivation of the kernel function and follow Kaji's notation.

The first step is to note that the nonstationary upwash $V_n(x,0,t)$ at $(x,0)$ due to a force of complex strength $\exp(jn\gamma)$ located at $[\xi+ns\sin(\alpha_s),\ ns\cos(\alpha_s)]$ is as follows.

Let $k=\omega/a$, $\beta=\sqrt{1-M^2}$, $\rho=$density of uniformly flowing medium, $a=$speed of sound, $x_n=x-\xi-ns\sin(\alpha_s)$, $y_n=-ns\cos(\alpha_s)$, and $x_n'=x'-\xi-ns\cos(\alpha_s)$. Then

$$V_n(x,0,t)=e^{j\omega t}e^{jn\gamma}\left(\frac{k\beta}{4j\rho Ma}\exp\left(j\frac{kMx_n}{1-M^2}\right)\right.$$

$$\times\left\{-x_nH_1^{(2)}\frac{\left(\frac{\omega}{\beta^2a}\sqrt{x_n^2+\beta^2y_n^2}\right)}{\beta^2\sqrt{x_n^2+\beta^2y_n^2}}-\frac{j}{\beta^2M}H_0^{(2)}\right.$$

$$\left.\times\left[\frac{\omega}{\beta^2a}(x_n^2+\beta^2y_n^2)^{1/2}\right]\right\}-\frac{k^2\exp\left(-j\frac{k}{M}x_n\right)}{4jM^2\rho\beta Ma}$$

$$\left.\times\int_{-\infty}^{x_n}\exp\left[j\frac{kx_n'}{M(1-M^2)}\right]H_0^{(2)}\left(\frac{\omega}{\beta^2a}\sqrt{x_n'^2+\beta^2y_n^2}\right)dx\right)$$

(3)[3]

and

$$\left.K_v(x,\xi)=\sum_{n=-\infty}^{\infty}V_n(x,0,t)\right\}\qquad(4)$$

The above expression for V_n may be deduced from equations (8) and (11), section 14.3, of Y. C. Fung's "An Introduction to the Theory of Aeroelasticity." Thus,

---

[3] $H_0^{(2)}$ and $H_1^{(2)}$ are Hankel functions of the second kind of orders 0 and 1, respectively.

$$K_v(x,\xi) = \frac{jk}{4\pi\rho\beta^2 Ma} \exp\left\{j\left[\frac{kM(x-\xi)}{1-M^2} - P\delta\right]\right\}$$

$$\times\left[\frac{\ell(x-\xi)}{2w}\left(2\pi + s\bar{P}\sin(\alpha_s)I_1 - \frac{\ell s \sin(\alpha_s)}{2w} I_2\right)\right.$$

$$\left. + \frac{j(1-M^2)}{M^2}\left(\frac{\pi M I_3}{\sqrt{1-M^2}} + I_4\right)\right] \tag{5}$$

where

$$P = \frac{-2(x-\xi)\sin(\alpha_s)\pi}{s[1-M^2\cos^2(\alpha_s)]}$$

$$\delta = \frac{1}{2\pi}\left[\gamma - \frac{ksM\sin(\alpha_s)}{(1-M^2)}\right]$$

$$\ell = \frac{k}{\sqrt{1-M^2}}$$

$$\bar{P} = \frac{-2\pi\sin(\alpha_s)}{s[1-M^2\cos^2(\alpha_s)]}$$

and

$$w = \frac{ks\sqrt{1-M^2\cos^2(\alpha_s)}}{2\pi(1-M^2)}$$

$$\bar{\eta} = \frac{2\pi}{s}\,\frac{\sqrt{1-M^2}\cos(\alpha_s)}{[1-M^2\cos^2(\alpha_s)]}$$

and

$$\eta = \bar{\eta}\,|\,x-\xi\,|$$

and

$$I_1 = \frac{j}{\pi\omega\eta}\sum_{n=-\infty}^{\infty} H_1^{(2)}\,\frac{[w\sqrt{(2\pi n+P)^2+\eta^2}]}{[(2\pi n+P)^2+\eta^2]^{1/2}}\exp[j(2\pi n+P)\delta] \tag{5a}$$

$$I_2 = \sum_{-\infty}^{\infty}\frac{(2\pi n+P)H_1^{(2)}}{\sqrt{(2\pi n+P)^2+\eta^2}}[w\sqrt{(2\pi n+P)^2+\eta^2}]\exp[j(2\pi n+P)\delta] \tag{5b}$$

$$I_3 = \sum_{-\infty}^{\infty} H_0^{(2)}[w\sqrt{(2\pi n+P)^2+\eta^2}]\exp[j(2\pi n+P)\delta] \tag{5c}$$

I_4 represents the contribution from the integral term in equation (3); we give below the transformed form of it after application of the Poisson summation formula:

$$I_4=\ell\sum_{-\infty}^{\infty}\frac{\exp\left[jnP-\eta\sqrt{(\delta-n)^2-w^2}\right]}{\sqrt{(\delta-n)^2-w^2}\left[j(n-\delta)\bar{P}+j\dfrac{k}{M(1-M^2)}+\eta\sqrt{(\delta-n)^2-w^2}\right]}$$

for $(x-\xi)<0$. (5*d*)

$$I_4=\ell\sum_{-\infty}^{\infty}\frac{\exp\left[jnP-\eta\sqrt{(\delta-n)^2-w^2}\right]}{\sqrt{(\delta-n)^2-w^2}\left[j(n-\delta)\bar{P}+j\dfrac{k}{M(1-M^2)}-\eta\sqrt{(\delta-n)^2-w^2}\right]}$$

$$+\frac{2\eta\exp\left[jP\delta-j\dfrac{k(x-\xi)}{M(1-M^2)}\right]}{\left[(n-\delta)\bar{P}+\dfrac{k}{M(1-M^2)}\right]^2+\bar{\eta}^2\left[(\delta-n)^2-w^2\right]}$$

for $(x-\xi)>0$.

For $x\neq\xi$, the expressions for I_1, I_2, and I_3 may be transformed by Poisson's summation formula as under

$$I_1=\frac{j}{\pi w\eta}\sum_{-\infty}^{\infty}\exp\left[jnP-\eta\sqrt{(\delta-n)^2-w^2}\right] \tag{5a}$$

$$I_2=\frac{1}{\pi w}\sum_{-\infty}^{\infty}\frac{(n-\delta)}{\sqrt{(\delta-n)^2-w^2}}\exp\left[jnP-\eta\sqrt{(\delta-n)^2-w^2}\right] \tag{5b}$$

$$I_3=\frac{j}{\pi}\sum_{-\infty}^{\infty}\frac{1}{\sqrt{(\delta-n)^2-w^2}}\exp\left[jnP-\eta\sqrt{(\delta-n)^2-w^2}\right] \tag{5c}$$

The expressions for I_1, I_2, and I_3 diverge as $x\to\xi$ in equations (5*a*), (5*b*), and (5*c*), or as P, $\eta\to 0$, which is merely the indication of the $1/|x-\xi|$ and $\log|x-\xi|$ types of singularities in $K_v(x,\xi)$. To locate these singularities, we examine the small value expansions of the Hankel functions as follows.

$$H_0^{(2)}(x)\sim-\frac{2j}{\pi}\log(x)+\left[1-\frac{2j}{\pi}(\gamma_0-\log 2)\right]$$

where $\gamma_0=0.5772=$ Euler's constant and $H_0^{(2)}(x)\sim 2j/\pi x$. With the aid of the above it is easily shown that

$$K_v(x,\xi)-\frac{jk}{4\pi\rho\beta^2Ma}\left[\frac{2j\beta^3}{k(x-\xi)}+\frac{2\sqrt{1-M^2}}{M}\log\left(|x-\xi|\right)\right]=K_r(x,\xi) \tag{6}$$

is regular as $x\rightarrow\xi$. This motivates writing

$$K_v(x,\xi)=K_r(x,\xi)-\frac{\beta}{2\pi\rho Ma(x-\xi)}+j\frac{k\log\left(|x-\xi|\right)}{2\pi\rho\beta M^2a} \tag{7}$$

Finally, let

$$f(x)=\frac{-2\rho Ma}{\beta}v_d(x) \tag{8}$$

Equation (1) now reads as

$$\int_{-1/2}^{1/2}\frac{F(\xi)}{\pi}\left[\frac{2\rho M\dot{a}\pi}{\beta}K_r(x,\xi)+\frac{jk\log\left(|x-\xi|\right)}{M(1-M^2)}-\frac{1}{(x-\xi)}\right]d\xi=f(x) \tag{9}$$

CALCULATION OF UPWASH DUE TO TRANSLATION OF ADJACENT STEADY-STATE FIELDS

Potential Interaction

The problem of potential interaction (see fig. 2) is to calculate the nonstationary upwash on line AB due to steady-state design lifts on a blade row on the right-hand side, which translates downward at a certain speed corresponding to a tip Mach number M_t. In a linearized treatment, clearly the stagger (α_r) and Mach number M_r of flow through the adjacent row are related to M_t, M, and α_s by

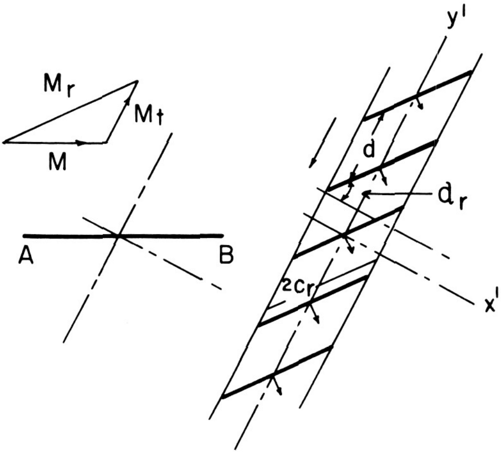

FIGURE 2.—*Geometry of adjacent row.*

$$\alpha_r = \tan^{-1}\left[\frac{M_t + M \sin(\alpha_s)}{M \cos(\alpha_s)}\right]$$

and

$$M_r = \sqrt{M_t^2 + M^2 + 2M_t M \sin(\alpha_s)}$$

Let $W_r = aM_r$. We first find the solution for velocity components u' and v', parallel to the x'-y' coordinate system of figure 2, due to equally spaced concentrated unit forces at the origin and its corresponding points as shown in figure 2. (Note that the blade exerts a force on the fluid equal and opposite to the force exerted by the fluid on the blade.) We use a frame of reference fixed with respect to the translating blade row so that we have a steady-state problem. We have to consider the effect of a sum of forces:

$$\mathbf{1} \sum_{n=-\infty}^{\infty} \delta(x')\,\delta\left(y' - 2n\frac{d}{2}\right)$$

where **1** denotes a unit force vector and δ stands for the Dirac delta function. By using a result on page 68 of reference 4 concerning the sum of an infinite row of equally spaced delta functions, we find that the above is clearly equal to

$$\frac{\mathbf{1}}{d}\,\delta(x')\left[1 + 2\sum_{n=1}^{\infty} \exp\left(j\,\frac{2\pi n y'}{d}\right)\right]$$

since our use of complex forms always implies that real parts are to be taken. The linearized equations of motion and continuity are

$$\rho\left(\frac{\partial u'}{\partial x'} + \frac{\partial v'}{\partial y'}\right) + W_r\left[\cos(\alpha_r)\frac{\partial \rho'}{\partial x'} + \sin(\alpha_r)\frac{\partial \rho'}{\partial y'}\right] = 0 \qquad (10a)$$

$$\cos(\alpha_r)\frac{\partial u'}{\partial x'} + \sin(\alpha_r)\frac{\partial u'}{\partial y'}$$

$$= -\frac{1}{\rho W_r}\frac{\partial p'}{\partial x'} + \frac{\sin(\alpha_r)\,\delta(x')}{\rho d W_r}\left[1 + 2\sum_{1}^{\infty} \exp\left(j\,\frac{2\pi n y'}{d}\right)\right] \qquad (10b)$$

and

$$\cos(\alpha_r)\frac{\partial v'}{\partial x'} + \sin(\alpha_r)\frac{\partial v'}{\partial y'}$$

$$= -\frac{1}{\rho w_r}\frac{\partial p'}{\partial y'} - \frac{\cos(\alpha_r)\delta(x')}{\rho d W_r}\left[1 + 2\sum_{1}^{\infty} \exp\left(j\,\frac{2\pi n y'}{d}\right)\right] \qquad (10c)$$

In what follows we omit the y' independent term in the force since it gives a stationary upwash (cf. p. 591 of ref. 1). In equations (12*a*), (12*b*), and (12*c*), ρ' and p' stand for small perturbations of the density and pressure. Eliminating p' from equations (10*b*) and (10*c*) we derive

$$\left[\cos(\alpha_r)\frac{\partial}{\partial x'}+\sin(\alpha_r)\frac{\partial}{\partial y'}\right]\left[\frac{\partial u'}{\partial y'}-\frac{\partial v'}{\partial x'}-\frac{2\delta(x')}{\rho W_r d}\sum_1^\infty \exp\left(j\frac{2\pi n y'}{d}\right)\right]=0$$

Since u', v', and the delta function term vanish far from the blade row,

$$\frac{\partial u'}{\partial y'}-\frac{\partial v'}{\partial x'}=\frac{2\delta(x')}{\rho W_r d}\sum_1^\infty \exp\left[j\frac{2\pi n y'}{d}\right] \tag{11}$$

(Kutta-Joukowski Law).

Next we eliminate the force terms in equations (12*b*) and (12*c*); assuming an isentropic relation between p' and ρ', we obtain:

$$\frac{\partial u'}{\partial x'}\left[1-M_r^2\cos^2(\alpha_r)\right]+\frac{\partial v'}{\partial y'}\left[1-M_r^2\sin^2(\alpha_r)\right]$$

$$=M_r^2\sin(\alpha_r)\cos(\alpha_r)\left[\frac{\partial u'}{\partial y'}+\frac{\partial v'}{\partial x'}\right] \tag{12}$$

(modified continuity equation).

Using equations (11) and (12), single equations for u' and v' may be obtained that may be solved by requiring that u' and v' vanish as $x'\rightarrow\pm\infty$. We omit the details and give the result.

$$u' \text{ for } x'\gtrless 0=-\frac{1}{\rho d W_r}\frac{\left[j\sqrt{1-M_r^2}\pm M_r^2\sin(\alpha_r)\cos(\alpha_r)\right]}{1-M_r^2\cos^2(\alpha_r)}$$

$$\times\sum_1^\infty \exp\left(j\frac{2\pi n y'}{d}\right)$$

$$\times\exp\left\{\frac{2\pi n x'\left[jM_r^2\sin(\alpha_r)\cos(\alpha_r)\mp\sqrt{1-M_r^2}\right]}{d(1-M_r^2)\cos^2(\alpha_r)}\right\} \tag{13a}$$

Similarly:

$$v' \text{ for } x'\gtrless 0=\frac{\mp 1}{\rho d W_r}\sum_{n=1}^\infty \exp\left(j\frac{2\pi n y'}{d}\right)\exp\left\{\frac{2\pi n x'}{d\left[1-M_r^2\cos^2(\alpha_r)\right]}\right.$$

$$\left.\times\left[jM_r^2\cos(\alpha_r)\sin(\alpha_r)\mp\sqrt{1-M_r^2}\right]\right\} \tag{13b}$$

The upwash normal to line AB (fig. 2) is

$$v_d = v' \cos(\alpha_s) - u' \sin(\alpha_s) \tag{13c}$$

Thus v_d for $x' \gtrless 0$ is

$$\frac{\mp 1}{\rho d W_r}\left[\cos(\alpha_s) - \frac{M_r^2 \sin(\alpha_r)\cos(\alpha_r)\sin(\alpha_s)}{1-M_r^2\cos^2(\alpha_r)} \mp \frac{j\sin(\alpha_s)\sqrt{1-M_r^2}}{1-M_r^2\cos^2(\alpha_r)}\right]$$

$$\times \sum_1^\infty \exp\left(j\frac{2\pi n y'}{d}\right)\exp\left[\frac{2\pi n x'}{d}\,\frac{jM_r^2\sin(\alpha_r)\cos(\alpha_r) \mp \sqrt{1-M_r^2}}{1-M_r^2\cos^2(\alpha_r)}\right] \tag{13d}$$

The effect of distributed loading on a finite chord may be estimated by integrating the results of equation (13*d*) over the finite chord. We again omit the details since the derivation is very similar to that outlined on pages 589 through 590 of reference 1. Noting that these upwash fields translate with respect to the adjacent rows, one readily obtains the nonstationary upwash on the adjacent rows.

Viscous Wake Interaction

The form of the nonstationary upwash contributed by the viscous wake intraction mechanism was assumed to be the same as in reference-2. The pertinent equation giving the upwash is equation (28) of reference 2.

FINAL FORMULATION OF INTEGRAL EQUATION (9) AND METHOD OF SOLUTION

From figure 3, clearly the frequency ω of unsteady lift is $(2\pi n/d)M_t\,a$ and thus $k = \omega/a = (2\pi n/d)M_t$. In what follows we consider each harmonic n separately. The phase lag γ is discussed on page 592 of reference 1. It is easily shown that

$$\gamma = 2\pi n\left(\frac{s}{d}\right)$$

Assume for $F(\xi)$ the form

$$A_0 \cot\left(\frac{\phi}{2}\right) + \sum_1^N A_n \sin(n\phi)$$

where $\xi = -\frac{1}{2}\cos\phi$, $\phi = 0$ at the leading edge, and $\phi = \pi$ at the trailing edge.

All the above terms are zero at the trailing edge (Kutta condition), and the series has the usual square-root singularity at the leading edge. $A_0, A_1, A_2 \ldots A_n$ are, of course, unknown. We let $x = -\frac{1}{2}\cos\theta$ so that $\theta = 0$ corresponds to $x = -\frac{1}{2}$ and $\theta = \pi$ corresponds to $x = \frac{1}{2}$ and denote by

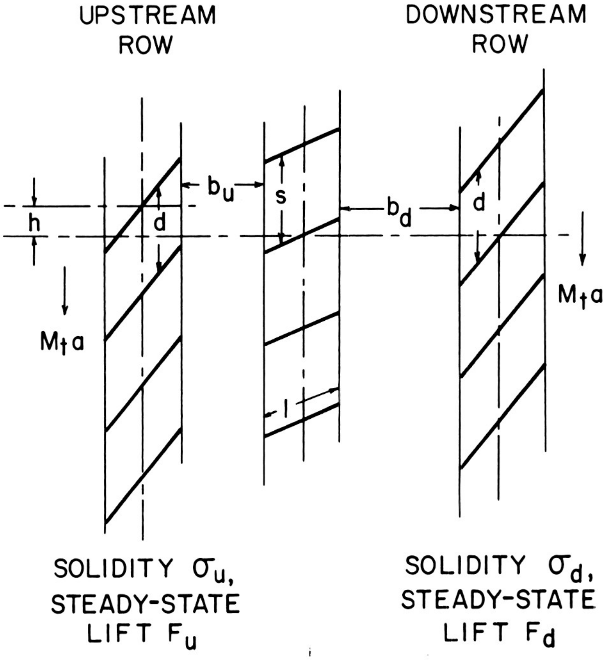

FIGURE 3.—*Sketch for potential interaction due to two adjacent rows.*

$$G(n,\theta)=\int_0^\pi \cos\,(n\phi)K_r(x,\xi)\;d\phi$$

where $n=0,\,1,\,\ldots\,,\,N+1$.

The $G(n,\theta)$ will be evaluated numerically by Simpson's rule and will present no difficulties since $K_r(x,\xi)$ is bounded. Then it is easily shown by using the results of equations (16), (17), and (18) of the appendix that equation (9) may be written as

$$A_0\left\{\tfrac{1}{2}[G(0,\theta)+G(1,\theta)]\,\frac{-\beta}{2\rho Ma}-\frac{jk(\log 2+\frac{1}{2}\cos\theta)}{2\rho\beta M^2a}\right\}$$

$$+A_1\left\{\tfrac{1}{4}[G(0,\theta)-G(2,\theta)]+\frac{\beta\cos\theta}{2\rho Ma}-\frac{jk}{4\rho\beta M^2a}\left[\log 2-\frac{\cos\,(2\theta)}{4}\right]\right\}$$

$$+\sum_{n=2}^{N}A_n\left\{\tfrac{1}{4}[G(n-1,\theta)-G(n+1,\theta)]+\frac{\beta\cos\,(n\theta)}{2\rho Ma}\right.$$

$$\left.-\frac{jk}{8\rho\beta M^2a}\left[\frac{\cos\,(n-1)\,\theta}{n-1}-\frac{\cos\,(n+1)\,\theta}{n+1}\right]\right\}=f(x)$$

The above equation holds for $0 \leq \theta \leq \pi$, and the method of collocation of points involves satisfying the above equation exactly for $(N+1)$ equally spaced values of θ between 0 and π and thus deriving $(N+1)$ simultaneous equations for $A_0, A_1, \ldots, A_N$, which may be solved by matrix inversion.

The net lift is

$$\int_{-1/2}^{1/2} F(\xi)\, d\xi = \frac{\pi}{2}\left(A_0 + \frac{A_1}{2}\right)$$

and the magnitude of unsteady lift is the amplitude of $\pi/2[A_0 + (A_1/2)]$.

NUMERICAL DETAILS AND TYPICAL RESULTS

The unsteady lift distribution was assumed to have the form of an $(M+1)$ term series. The check on whether the chosen M is satisfactory is whether the terms $A_0, A_1, \ldots, A_M$ resulting from the solution of the simultaneous equations (14) converge rapidly enough. Judging from the calculations performed in this paper, the value of M to be used increases with the Mach number of the flow through the blade passages. Up to a Mach number of about 0.5, $M=7$ suffices. Between Mach numbers of 0.5 and 0.8, $M=11$ suffices. Beyond a Mach number of 0.8 it seems necessary to use $M=15$ to get good convergence. The use of the present analysis for Mach numbers close to unity is not very valid anyway because for such high Mach numbers the convected wave equation (from which eq. (3) is derived) is not a valid linearized equation for describing the nonsteady flow.

In figure 4 we have plotted results for potential interaction[4] on a row with flow at a Mach number of 0.1 due to a row downstream. This case should be analogous (owing to the low Mach numbers) to a case calculated in figure 5 of reference 1. The Kemp-Sears results and results of this paper compare reasonably well.

A similar check with the Kemp-Sears results is obviously desirable for viscous wake interaction. In reference 2, in the interest of obtaining a closed-form solution, the upwash used to calculate the unsteady lift is taken at selected points on the airfoil. Two sets of results pertaining to a stator rotor sequence as sketched in figure 5, one corresponding to the upwash at quarter chord from the leading edge and another corresponding to the upwash at quarter chord from the trailing edge, are presented in table 1 of reference 2. The methods used in this paper make such an

---

[4] For all potential interaction calculations reported in this paper (Figs. 4, 6*a*, 7*b*) the steady lift distribution is assumed to be of the flat-plate type (see p. 594 of ref. 1).

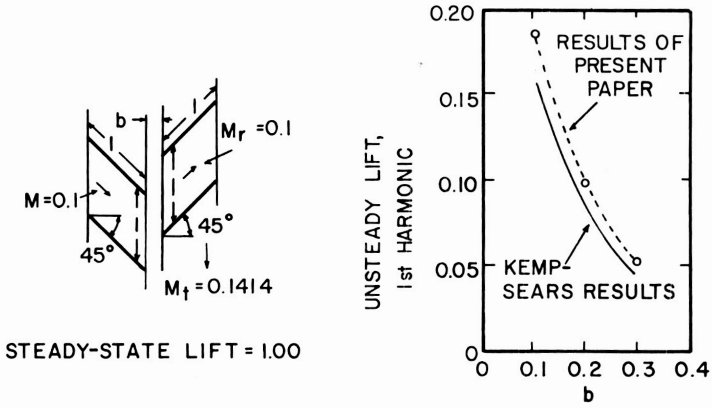

Figure 4.—*Potential interaction due to downstream row. Comparison with Kemp-Sears (reference 1).*

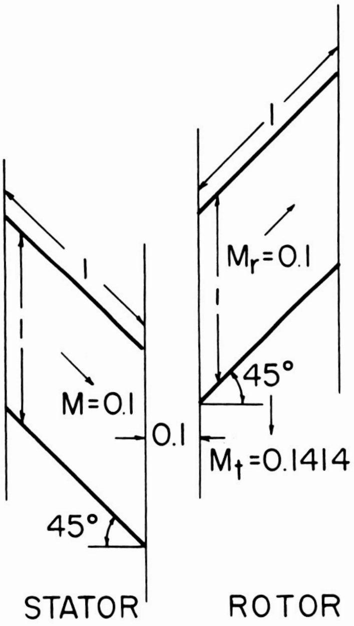

Figure 5.—*Stator rotor sequence used to compare results for viscous wake interaction with Kemp-Sears (reference 2).*

approximation unnecessary; our results are compared with the Kemp-Sears results in table I below. The calculations in this paper are again for a row with flow at a Mach number of 0.1.

From table I it is seen that the first harmonic results compare well if Kemp-Sears results corresponding to an upwash at a quarter chord from the leading edge are used.

In figure 6*a* we have plotted results for unsteady lift assuming the velocity triangles of figure 4 to be linearly scaled up in Mach number. This could be representative of changes in unsteady lift as one runs up a fan or compressor on a constant loadline.

The forms for I_2, I_3, and I_4 obtained by the use of the Poisson summation formula (eqs. 5*b*, 5*c*, and 5*d*) indicate that if, for any integer m,

$$(\delta-m)^2-\omega^2=0\ldots \tag{14}$$

then I_2, I_3, and $I_4\rightarrow\infty$. Since $K_v(x,\xi)$ in equation (1) involves I_2, I_3, and I_4, this means that if equation (14) is satisfied then $K_v(x,\xi)\rightarrow\infty$. The only way in which one can obtain a bounded $v_d(x)$ under the condition that $K_v(x,\xi)\rightarrow\infty$ in equation (1) is to have $F(\xi)\rightarrow 0$. Thus the resonance condition denoted by equation (14) is one for which the unsteady blade forces vanish. Physically this condition arises when purely transverse waves are produced in the blade passages (i.e., waves traveling only in the tangential direction). At this resonance condition, waves emitted from one surface, say the upper surface of a blade, travel transversely and arrive at the lower surface of an adjacent blade with the time of travel being such that the incident wave phase is exactly antiphase (i.e., with a phase difference of some odd integer multiple of 180°) with the phase of

TABLE I.—*Viscous Wake Interaction*[1]

Kemp-Sears results				Results of present paper		
Harmonic number	C_D	Upwash evaluated at	C_L	Harmonic number	C_D	C_L
1	0.01	Q.C. from L.E.	0.029	1	0.01	0.029
		Q.C. from T.E.	0.023			
	0.02	Q.C. from L.E.	0.057		0.02	0.05757
		Q.C. from T.E.	0.045			

Q.C. = quarter chord, C_D = profile drag coefficient, L.E. = leading edge, T.E. = trailing edge, C_L = coefficient of unsteady lift.

[1] Comparison with Kemp-Sears results for case sketched in figure 5.

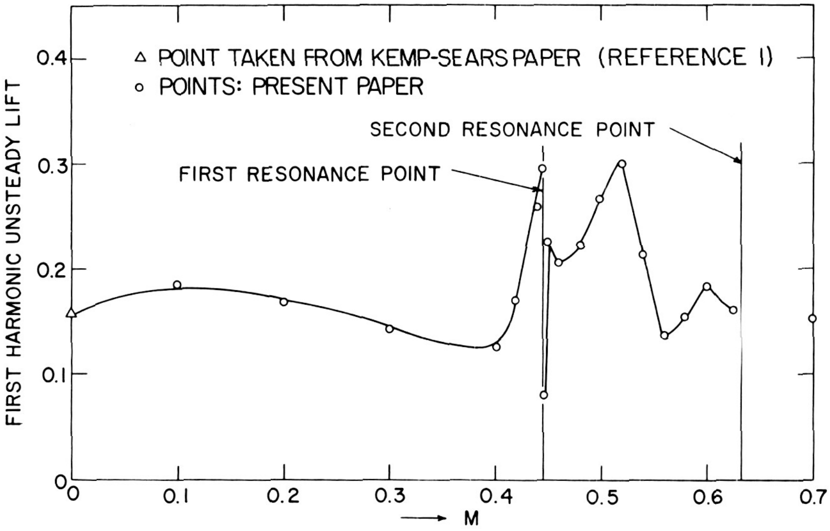

FIGURE 6a.—*Potential interaction for dynamically similar velocity triangles. Effect of Mach number.*

the sources on the lower surface of this adjacent blade. This phase cancellation prevents development of any unsteady lift.

The resonance condition of equation (14) may be rewritten in terms of tip Mach numbers and flow Mach numbers as

$$M_t=\left(1-\frac{md}{s}\right)[\pm\sqrt{1-M^2\cos^2(\alpha_s)}-M\sin(\alpha_s)] \qquad (15)$$

For velocity triangles of the type shown in figure 4, $M_t=M\sqrt{2}$, $\alpha_s=-45°$, and the solution of (15) yields resonant Mach numbers of

$$M=\frac{(m-1)}{\sqrt{m^2+1}}$$

where m is a positive integer. The first significant resonant Mach number M is thus

$$M=\frac{1}{\sqrt{5}}=0.447$$

and the second is

$$M=\frac{2}{\sqrt{10}}=0.632$$

These two ordinate lines (corresponding to $M=0.447$ and 0.632) are shown in figure 6*a* as first and second resonance points. As can be noted, the resonance is extremely sharp in that the approach of the unsteady lift to zero as $M \rightarrow 1/\sqrt{5}$ is extremely sharp, being represented by an almost vertical drop in figure 6*a*.

The results of figure 6*a* suggest that the resonance, while undoubtedly denoting a point of zero unsteady lift, is much too sharp to have practical significance as a condition of low unsteady lift. However, the resonance points do have considerable significance (as may be observed from fig. 6*a*) as delineating rather different families of variations of unsteady lift with Mach number.

A similar result is shown by Kaji and Okazaki in reference 3. They consider in reference 3 the effect of a flat-plate cascade with flow on an incident sound wave as shown in figure 6*b*. An unsteady force distribution on the blades to cancel the velocities induced by the incident sound wave is sought as the solution to an integral equation of the same type as equation (1). Later the effect of the unsteady force distributions is integrated to obtain far-field pressure (sound) waves in the transmitted and reflected regions. The cascade in figure 6*b* behaves as a diffraction grating with respect to the incident sound wave. One propagating reflected and one propagating transmitted wave are always produced by the interaction of the incident sound wave and the blade row. The reflected wave corresponds to a specular reflection of the incident wave by the blade row,

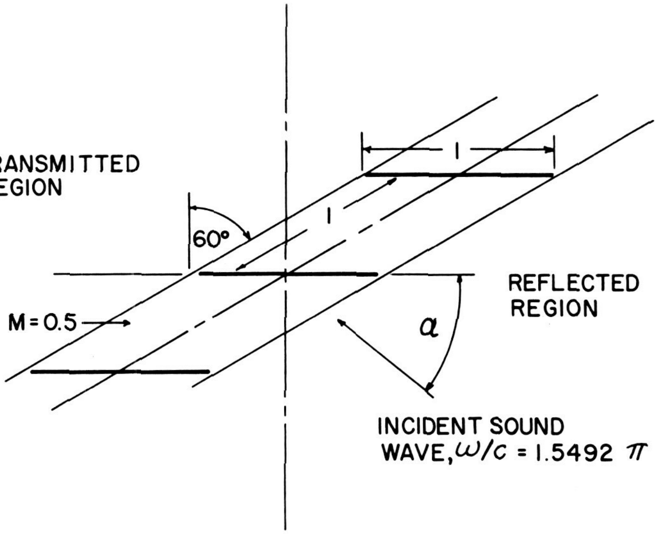

FIGURE 6b.—*Configuration of cascade whose results are shown in figure 6c of reference 3.*

and the transmitted wave has the same orientation as the incident wave. The basic transmitted wave, produced under all circumstances, is denoted by the authors of reference 3 as a $\nu=0$ mode[5] in figure 5 of their paper (the upper half of which is reproduced as fig. 6*c* in this paper). Higher order modes are also produced if, for the interaction of the incident wave and the blade row, more than one resulting mode is above "cutoff." In figure 6*c*, for α less than about 40°, a basic transmitted mode (labeled $\nu=0$) and a higher order mode (labeled $\nu=-1$) are produced. For α greater than 40°, the basic transmitted mode and a higher order mode (labeled $\nu=+1$) are produced. The pressure transmission coefficient is the ratio of amplitude of transmitted wave to the amplitude of incident wave. The ordinate around $\alpha=40°$ in figure 6*c* represents a resonant condition of the type of equation (14). In the example of figure 6*c*, the orientation of the higher order transmitted wave undergoes an abrupt change as one passes across the resonant incidence angle. Note how the pressure transmission

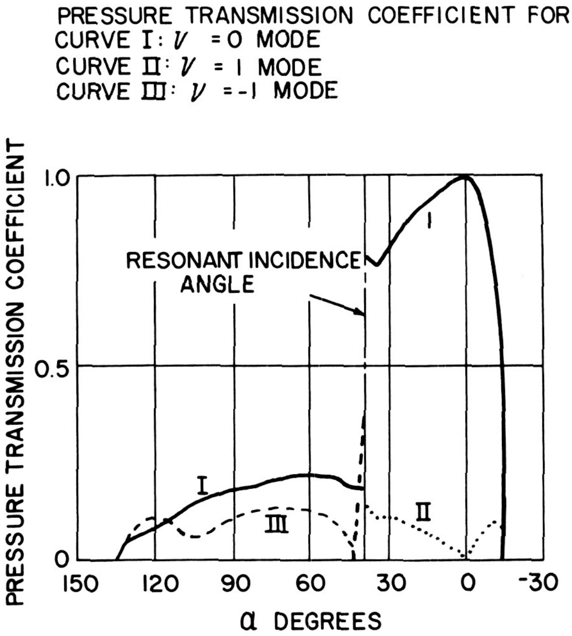

FIGURE 6c.—*Curve from upper half of figure 5 of reference 3.*

---

[5] Corresponds to $m-1=0$ in this paper.

coefficient associated with the basic transmitted wave ($\nu=0$ mode) undergoes an abrupt change as one crosses over the resonant incidence angle.

This type of resonance effect was apparently first observed by Runyan, Woolston, and Rainey (ref. 5). Their concern was with the effect of wind-tunnel walls on the lift forces developed by an oscillating wing in two-dimensional subsonic compressible flow. The resonance phenomenon was experimentally confirmed by these authors.

In view of the very rapid change of events just around resonance, it might appear worthwhile to attempt an analytical solution of equation (1) close to resonance. However, McCune, in a different context, has examined the merits of replacing cylindrical wave functions (which should be employed in a proper three-dimensional analysis) by two-dimensional approximation in such problems (ref. 6). He shows clearly that such an approximation breaks down precisely at these resonance frequencies. Thus, it seems of dubious advantage to pursue the cascade plane analysis any further near resonance. Finally, one may easily show that the resonance conditions are precisely the conditions at which successive rotor-stator interaction modes of the classical Tyler-Sofrin analysis (ref. 6) are cut off. Thus the cutoff frequencies introduced by Tyler and Sofrin as delineating regimes of acoustic propagation or decay of successive interaction modes are seen to play an important role in the estimation of the unsteady blade force problem.

From equation (13*d*), one notices that the exponential decay rate of the potential flow field of an adjacent row is altered from its incompressible value by the factor

$$\frac{\sqrt{1-M_r^2}}{1-M_r^2\cos^2(\alpha_r)}$$

To show the effect of this factor, we have plotted the decay of unsteady lift with spacing for $\alpha_r=0$, 45°, and 60° in figure 7.

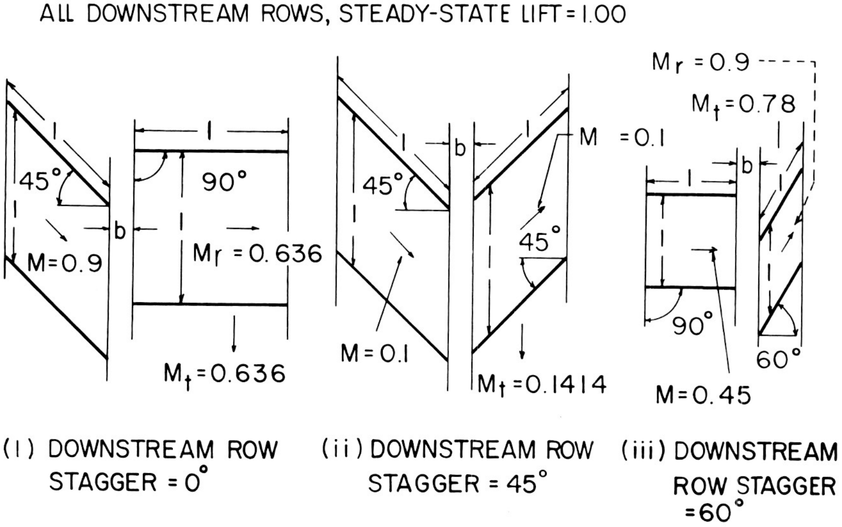

FIGURE 7a.—*Effects of stagger angle on decay of potential flow fields—configurations considered.*

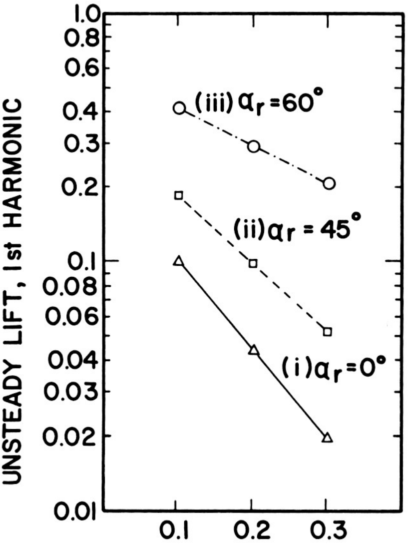

FIGURE 7b.—*Effects of stagger angle on decay of potential flow fields—results for unsteady lift for configurations of figure 7a.*

APPENDIX

Two well-known principal value integrals are

$$\frac{1}{\pi}\int_0^\pi \left[\frac{\cos(n\phi)\,d\phi}{\cos(\phi)-\cos(\theta)}\right]=\frac{\sin(n\theta)}{\sin\theta}\ldots \tag{16}$$

and

$$\frac{1}{\pi}\int_0^\pi \frac{\sin(n\phi)\sin(\phi)\,d\phi}{\cos(\theta)-\cos(\phi)}=\cos(n\theta)\ldots \tag{17}$$

An expansion of $jk\ (\log|x-\xi|)/2M(1-M^2)$ convergent for $x\neq\xi$ or $\theta\neq\phi$ is

$$\frac{-jk}{M(1-M^2)}\left[\log(2)+\sum_1^\infty \frac{\cos(n\theta)\cos(n\phi)}{n}\right]\ldots \tag{18}$$

REFERENCES

1. Kemp, N. H., and W. R. Sears, Aerodynamic Interference Between Moving Blade Rows. *J. Aeron. Sci.*, Vol. 20, No. 9, September 1953, p. 585.
2. Kemp, N. H., and W. R. Sears, The Unsteady Forces Due to Viscous Wakes in Turbomachines. *J. Aeron. Sci.*, Vol. 22, No. 7, July 1955.
3. Kaji, S., and T. Okazaki, *Study on Plane Sound Waves Passing Through a Compressor Blade Row.* Paper F-5-1, presented at Sixth International Congress on Acoustics (Tokyo), August 21–28, 1968.
4. Lighthill, M. J., *Fourier Analysis and Generalized Functions.* Cambridge U. Press, 1962.
5. Runyan, H. L., D. S. Woolston, and A. G. Rainey, *Theoretical and Experimental Investigation of the Effect of Tunnel Walls on the Forces on an Oscillating Airfoil in Two-Dimensional Subsonic Compressible Flow.* NACA Report 1262, 1955.
6. McCune, J. E., The Transonic Flow Field of an Axial Compressor Blade Row. *J. Aeron. Sci.*, Vol. 25, 1958, pp. 616–626.
7. Tyler, J. M., and T. G. Sofrin, Axial Compressor Noise Studies. *Trans. SAE*, Vol. 70, 1962, pp. 309–332.

DISCUSSION

A. ABDELHAMID (Carleton University): I would like to comment on the effect of the blade being in a row or being isolated and on whether it's a first- or a second-order effect. I believe it's a second-order effect because the steady vorticity on the blades of the same row as the blade that you are considering will not contribute to the contour it imposes.

J. E. FFOWCS WILLIAMS (Imperial College of Science): It seems to me that when you have this guaranteed repetitive system you must generate a resonance. You've got to pick them up somehow. My point of concern is the way in which the boundary conditions are put in. There are difficulties concerned in judgments, and these turn up when the resonant wave fronts are going at a parallel, one normally observes. Now if they're going parallel to the surface, the procedure to adopt is one to control the velocity on the surface. If one asks what pressure is required on that surface to bring about a control on the velocity, it turns out to be infinite by the way his blade is set, so a more realistic boundary condition for any practical system would be a pressure-release condition.

MANI (author): Two points have been raised in the discussion period. The first concerns the proper boundary condition to be used near the resonant (cutoff) frequency. The author agrees that if very large pressures result the assumption of perfectly rigid blades is not a suitable one and should be replaced perhaps by an impedance condition. It is worth reiterating, however, that from the point of view of the isolated two-dimensional cascade model's representativeness of the actual situation in the turbomachine, it would not be worthwhile to pursue matters much further in the cascade plane near cutoff. The effect of adjacent blade rows, open-end terminations, and three-dimensional effects become all-important at this condition.

The second pertains to the effect of adjacent blade rows. It should be noted that estimates of effect of adjacent rows as carried out in the original Kemp-Sears papers is not entirely sufficient. Kemp and Sears assumed the fluid to be incompressible and, with this assumption, all nonaxisymmetric flow patterns exhibit exponential axial decay. When the fluid is regarded as compressible, some of these flow patterns (those above cutoff) exhibit no axial decay and hence the treatment of the problem on the basis of isolated blade rows subject to given external upwash becomes questionable.

SESSION V

Turbomachinery Design

Chairman: L. H. SMITH

Impeller Blade Design Method for Centrifugal Compressors

Willem Jansen and Andreas M. Kirschner

Northern Research and Engineering Corporation

The design of a centrifugal impeller must yield blades that are aerodynamically efficient, easy to manufacture, and mechanically sound. The blade design method described here satisfies the first two criteria and with a judicious choice of certain variables will also satisfy stress considerations. The blade shape is generated by specifying surface velocity distributions and consists of straight-line elements that connect points at hub and shroud. The method may be used to design radially elemented and backward-swept blades. The background, a brief account of the theory, and a sample design are described in this paper.

The design of impeller blades is a difficult task due to the fact that, ideally, three separate and equally important requirements must be satisfied. The first requirement is that the impeller provide acceptable distributions of relative velocity on both driving and trailing surfaces of the blades in order to minimize the possibility of flow separation and the accompanying loss in performance. In addition, the selected blade shape must be such that it can be manufactured accurately and economically by means of automated fabrication procedures. Finally, the blades should be designed so as to keep the stresses at a safe level, eliminating the possibility of excessive distortion or fracture occurring during operation.

For many applications, these three requirements are somewhat incompatible. For example, it is possible to define a blade shape which theoretically would give ideal velocity distributions throughout. However, it is often the case that such a shape is virtually impossible to fabricate in any reasonable manner. Therefore, any practical design method must involve some reasonable compromises with regard to the conflicting requirements. The method described in this paper, the prescribed loading method, is intended specifically to produce impeller designs which satisfy the aerodynamic and manufacturing requirements mentioned above.

Although the method does not include stress considerations explicitly, an intelligent choice of inputs to the method and a careful examination of the results obtained will enable safe designs to be produced with a moderate amount of effort.

AERODYNAMIC CONSIDERATIONS

Losses in a centrifugal compressor are generally caused by boundary-layer and separated flow developments in the impeller and their subsequent effects in the diffuser. The development of the boundary layers and separated flows is directly a result of the velocity distributions along the blade, hub, and shroud surfaces. There are four important parameters associated with the velocity distribution that affect the boundary-layer behavior. They are

(1) The streamwise velocity reduction. This velocity gradient is also recognized as being the main variable that affects boundary-layer behavior in two-dimensional flows.

(2) The reduction and increase in turbulence intensity along the suction and pressure blade surfaces, respectively. This enhances flow separation along the suction surface due to partial laminarization. The change in turbulence intensity is directly related to the differences in suction and pressure surface velocities or loading (ref. 1).

(3) The influx of flow along the blade surfaces from one streamtube (a thin annular channel containing the primary flow) to the next caused by secondary flow. This flow usually consists of low-momentum fluid; the boundary layers are more susceptible to separation when they contain a large amount of low-momentum flow. The differential loading of one streamtube compared to the next is directly related to the development of secondary flows (ref. 2).

(4) The higher flow losses of the shroud streamtube caused by clearance effects. These losses cause a pressure drop which leads to flow separation. Increased work input will offset the rise in pressure losses (ref. 3).

Extensive experimental research is currently being carried on to measure these effects and refine relevant theories.

The method should therefore be capable of generating a blade surface for which the following items are specified:

(1) The streamwise velocity distribution. This quantity is controlled by both the hub and shroud contours and the blade loading.

(2) The difference in suction and pressure surface velocity (or loading) to minimize the turbulence attenuation at the suction surface.

(3) The difference between the work addition to a streamtube near the hub and that near the shroud to minimize the transport of low-momentum flow by the secondary flow phenomenon.

(4) The higher work input into the flow in the shroud streamtube to offset the clearance losses.

From an aerodynamic point of view, it is thus desirable to specify a velocity distribution along the pressure and suction surfaces of the blade such that the generation of separated flows is kept to a minimum. This general principle would lead to a blade defined by a set of streamlines whose individual loading schedule is controlled by the designer.

MANUFACTURING AND GEOMETRICAL CONSIDERATIONS

The ideal blade which would be composed of an arbitrary number of individually loaded streamlines represents a very general three-dimensional blade surface. It is questionable whether such a blade could be economically produced with the required accuracy. Impeller casting patterns are very difficult to manufacture, particularly when the surface of the blade has an arbitrary shape, when close tolerances have to be maintained, or when the impeller size is small. A more desirable blade shape is one defined by straight-line elements; such a shape facilitates setting up the pattern and allows close tolerances to be maintained.

The machining of an arbitrary blade surface would generally be impossible because of the extreme local curvature of the blade surface. At best, the tool would have point contact only and too much time would be required to machine away all the filler material. A more appropriate machining method is one where the cutter has line contact and hence large cutting rate. However, the blade shape must still be restricted to moderate inclinations against normals to the hub surface to avoid tool interferences.

In summary, from manufacturing considerations, a blade shape consisting of straight-line elements on both surfaces is preferred. The thickness distribution of the blades is then necessarily restricted to a constant taper between hub and shroud, and the camber line surface of the blades will also consist of straight-line elements.

Since the camber-line surface is defined by a set of streamlines with controlled individual loading, the number of streamlines for which loading can be controlled and still yield a straight-line element camber surface is limited. In general, the individual streamlines form curves in space and a straight line can only connect a maximum of three curves in space. Consequently, a straight-line element blade can be constructed when the loading of three streamlines is specified. These streamlines are assumed to be those adjacent to the shroud and the hub and an intermediate one.

This specification is considered adequate aerodynamically, and the ruled blade surface is accepted as a balanced compromise.

There are three general categories of blades which can be defined by straight-line elements. These are termed radial, axial, and arbitrary blades. The first two blade types are characterized by the fact that the angular orientations of the line elements defining their camber surfaces are fixed by the nature of the blades; that is, in the radial direction and axial direction, respectively. As a result, the angular orientation (θ) can be prescribed along only one streamline; the obvious choice is the shroud streamline where the flow conditions are critical.

The arbitrary type of blade is characterized by the general and usually unspecified orientations of the line elements (except those at the leading and trailing edges which are usually radial elements) defining the camber surface. The procedure followed in designing an arbitrary blade involves, in general, the loading of the three streamlines in an appropriate manner. The orientation of each blade element is then determined by requiring that the straight line pass through each of the three space curves defined by the loaded streamlines.

In some cases when for an arbitrary blade the loading is specified at three streamlines, the resulting blades may still exhibit a large variation in circumferential angle between the hub and shroud streamlines which would be unsatisfactory from manufacturing or stress considerations; that is, the blade would have excessive lean throughout its length. This difficulty was recognized during the development of the procedure and special provisions were introduced in the procedure to circumvent this by specifying at the outset the desired distribution of line element orientation and by prescribing the loading along the shroud streamline only.

REQUIRED AND GENERATED INFORMATION

The prescribed loading method can be utilized to design an impeller when its rotative speed, flow, average efficiency, overall geometry (that is, hub and shroud coordinates, distribution of blade thickness along hub and shroud, location of leading and trailing edge, number of blades, and exit blade angles), desired swirl distribution at inlet, and angular momentum distribution at discharge are given. The designer must also specify any one of four possible types of loading distribution:

(1) Linear loading from inlet to discharge (fig. 1*a*).
(2) Double linear loading from inlet to discharge (fig. 1*b*).
(3) Double linear loading from inlet to discharge, maximum loading near leading or trailing edge (fig. 1*c*).
(4) General loading distribution (fig. 1*d*).

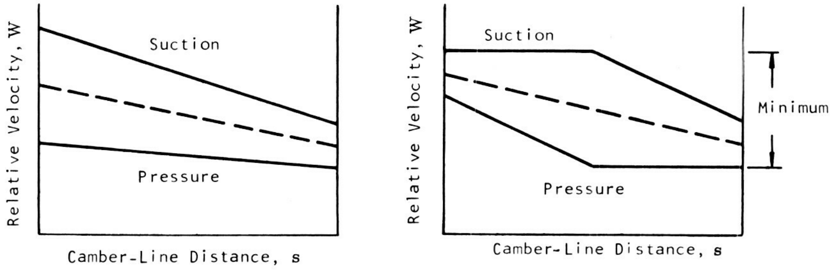

a.—*Linear loading.*

b.—*Double linear loading.*

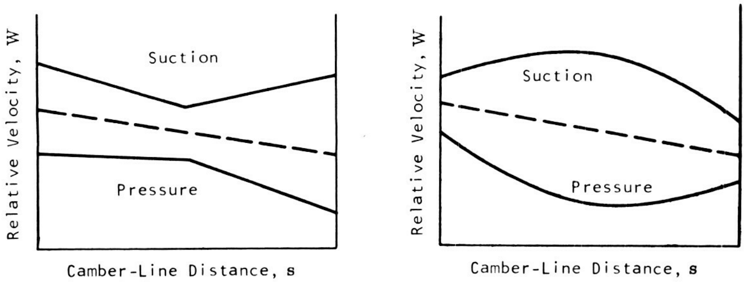

c.—*Inverse double linear loading.*

d.—*General loading.*

FIGURE 1.—*Available options of loading distributions.*

The choice of a preferable loading is difficult to make, since practically no systematic experiments have been performed to determine the relative merits of possible loadings. It is suggested that in most applications either a constant linear loading distribution, thereby minimizing secondary flows (ref. 4), or a double linear loading, minimizing the streamwise velocity reduction, will be quite satisfactory. Figure 2 shows these two loadings superposed.

The results of the calculation are a full description of the blade surface in cylindrical coordinates and the associated thickness distribution.

LIMITATION OF THE BLADE DESIGN METHOD

The prescribed loading method can be used to design radial, axial, and "arbitrary" blade shapes whose surfaces are defined by straight-line elements. However, there are a number of limitations incorporated in this approach. These limitations are discussed briefly below. In some cases

FIGURE 2.—*Linear and double linear loading superposed.*

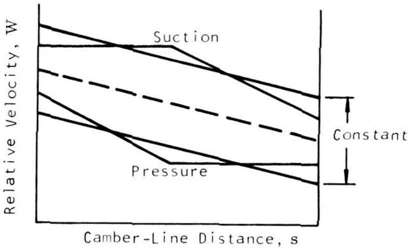

these limitations are not serious; in others some additional effort is necessary before the generated blading can be produced.

Thickness Distribution

The generated blade shapes are restricted to having trapezoidal thickness distributions; i.e., constant taper along any line element between hub and shroud. An exponential thickness distribution may be preferred when blade stresses are an important design consideration. This alteration may be made by adding or subtracting thickness from the generated surface; no appreciable change in aerodynamic variables is expected when thickness changes are kept moderate.

Blade Shape Restrictions

One fairly important limitation of the prescribed loading method as applied to arbitrary blades is that it is possible to obtain unusual shapes which may be difficult to manufacture or which would not be expected to be capable of withstanding the operating stresses. Such a blade shape may result from different loading requirements at the hub and shroud streamtube. This blade can be redesigned by specifying a new and more desirable straight-line orientation. For this case the blade loading at the shroud is still specified as before, but now the blade loading at the hub and the intermediate streamline can no longer be specified. The sample case is an illustration of this procedure.

Leading Edge Geometry

The method generates the blade shape near the leading edge such that the flow enters at zero incidence. However, when the relative inlet Mach number is high, this may not result in an optimum blade shape. Therefore, separate procedures are necessary to design a blade leading edge capable of efficiently handling supersonic flows.

Hub and Shroud Contours

A complete aerodynamic impeller passage design method would include a provision for automatically adjusting the hub and shroud contours to give a linear or any other prescribed distribution of average relative velocity. Due to the phenomenon of slip, the average relative velocity near the trailing edge decreases and then rises. In order to straighten out this distribution, the blade height of the impeller near the tip becomes larger at higher radii, which is usually unacceptable. Considerable effort has been expended to incorporate this design feature, but it was found that hub and shroud contours which yield a linear relative velocity distribution are in general not acceptable, and this hub-shroud contour generation procedure was abandoned.

Trailing Edge Flow

The specified blade loading does not vanish near the trailing edge as is required from the Kutta or "slip" conditions. However, appropriate steps are taken in the analysis to satisfy the Kutta condition, thereby overriding the specified blade loading over the last 10 percent of the blade chord. In addition, the procedure adjusts the loading such that the specified amount of work will still be imparted to the flow.

GENERAL THEROY OF PRESCRIBED LOADING METHOD

The overall procedure used in designing an impeller by the method of prescribed loading involves the following four basic steps:

(1) An initial estimate is made of the meridional velocities in the impeller passage as described below.

(2) The meridional velocities are then used in loading the required number of streamlines in the prescribed manner.

(3) A blade surface the shape of which conforms to loaded streamlines is developed.

(4) A detailed analysis of the flow field in the impeller with the developed blade surface is performed.

The procedure, starting with the loading of the streamlines, is repeated with the new estimates of the flow field obtained in the detailed analysis. Experience has shown that two repetitions of the procedure are sufficient to ensure convergence. This is defined as occurring when the estimated flow field used in loading the streamlines and defining the blade shape is approximately the same as that obtained in the subsequent detailed analysis. The various steps involved in the design procedure are discussed below in more detail.

INITIAL VELOCITY ESTIMATE

The distributions of meridional velocity along the shroud, hub, and intermediate streamlines are required for use in the loading procedure.

Initial estimates of these distributions are obtained by means of the one-dimensional analysis. First, a number of normals are constructed which are normal to both the hub and shroud at the points of intersection. These normals to the hub and shroud are circular arcs.

Neglecting curvature effects, the mean meridional velocity at a normal is given by the continuity equation

$$C_{m,m}=\frac{\dot{m}}{2\pi r_m n \rho_m} \tag{1}$$

The density ρ_m is a function of the mean meridional velocity, $C_{m,m}$, and equation (1) is solved by an iterative procedure using compressible flow equations to relate static density to total temperatures and pressures. The values of $C_{m,m}$ calculated in this manner are taken as the initial estimates of the meridional velocities along the intermediate streamline.

If it is assumed that zero circulation exists in an area bounded by two adjacent normals and the hub and shroud streamlines, the following expression relating $C_{m,s}$ and $C_{m,h}$ can be derived.

$$C_{m,h}\,dm_h=C_{m,s}\,dm_s \tag{2}$$

If the additional assumption is made that the quantity $\rho_m C_m r$ varies linearly with normal length between hub and shroud, then for constant density

$$C_{m,m}r_m=\tfrac{1}{2}(C_{m,h}r_h+C_{m,s}r_s) \tag{3}$$

A rearrangement and simultaneous solution of equations (2) and (3) results in the following explicit relations for $C_{m,s}$ and $C_{m,h}$.

$$C_{m,s}=\frac{2(r_m/r_h)C_{m,m}}{(r_s/r_h)+(dm_s/dm_h)} \tag{4}$$

$$C_{m,h}=\frac{dm_s}{dm_h}\,C_{m,s} \tag{5}$$

The derivatives dm_s/dm_h are obtained from the ratio of meridional length between two normals at hub and shroud. The initial estimates of the meridional velocities at the calculation stations along the hub and shroud are then obtained from the latter two equations along with the intermediate values, $C_{m,m}$.

STREAMLINE LOADING PROCEDURE

At the outset of the procedure for loading a streamline, the meridional coordinates (r,z), figure 3, of a number of points or calculation stations along the streamline and the values of meridional velocity (C_m) at these

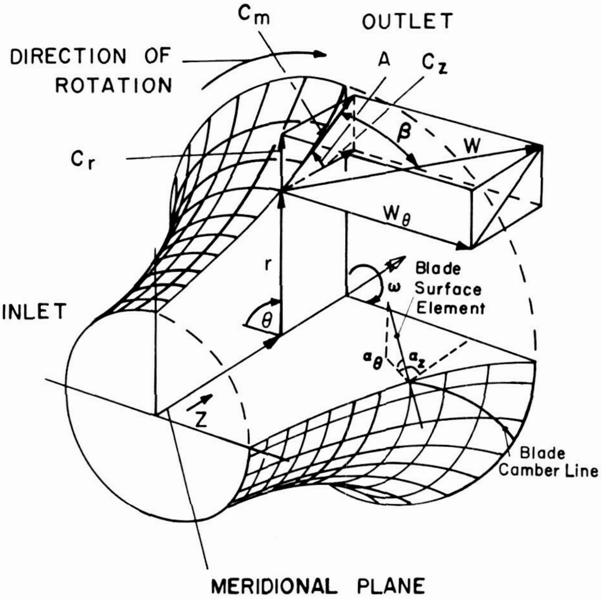

FIGURE 3.—*Nomenclature of relative flow and blade-element geometry in a centrifugal compressor.*

points are known from the results of the previous steps in the design method. First, the distribution of angular momentum is calculated from the given loading distribution $W_t - W_d$ from

$$\frac{d(rC_\theta)}{ds} = \frac{Z}{2\pi}\,(W_t - W_d) \tag{6}$$

where s is the camber-line length and Z the number of blades.

Assuming for the moment that the blade camber-line distance from the leading edge is also known at each point, then the swirl can be distributed in the specified manner and a value of rC_θ can be computed anywhere along the streamline. Combined with the meridional velocity distribution, sufficient information is then available to construct the velocity triangle and evaluate the flow angle (β) at each calculation station from

$$\beta = \tan^{-1}\left(\frac{C_\theta - r\omega}{C_m}\right) \tag{7}$$

In the above description of the loading procedure, it was assumed that the blade camber-line distance from the leading edge was known at each calculation station. In actual fact, this is not the case at the outset of the procedure. Therefore, this quantity must be determined iteratively. The initial estimate of the blade camber-line distance is taken as the meridional arc length from the leading edge. The streamline is then loaded in the manner described to obtain values of β along the streamline. The angular coordinate (θ) of the blade at each station is obtained by integrating the calculated β-distribution as follows:

$$\theta = \int_{m_1}^{m} \frac{\tan \beta}{r}\, dm \tag{8}$$

In this integration, θ is arbitrarily initialized to be zero at the trailing edge point on the shroud. Finally, the three-dimensional coordinates (r,z,θ) of the blade camber line are used to compute the camber-line distance at each point. The procedure is repeated using the calculated values of camber-line distance as the new estimates. This is done until the estimated and calculated values of the total blade camber-line distance from leading edge to trailing edge are the same. An additional iteration on the distribution of angular momentum is necessary when geometrical constraints require the relative streamline to pass through a given angular interval. Such conditions arise whenever the blade surface is to be determined from the loading specification on more than one streamline. The requirement follows from the stipulation that all streamlines intersect with an initial and final straight-line blade element.

The relative streamline coordinates that result from a specified loading distribution and the meridional velocity distribution define the blade camber line for an infinite number of blades. A modification of this camber line is introduced to account for flow deviation associated with a finite number of impeller blades (i.e., slip). For the major part of the blade passage, the average flow direction is assumed to coincide with that of the blade camber line. In the latter third of the blade passage, a progressive degree of deviation is assumed to occur. At the impeller discharge the amount of deviation is equivalent to the slip.

BLADE CONSTRUCTION

The third major step in the procedure is the synthesis of a mean blade surface from the three camber lines that have been generated in the previous step and the two line elements at the leading and trailing edge.

The general procedure for constructing a line element is illustrated in figure 4 which shows three general space curves and an initial element intersecting each of them. The incremental arc length, Δs_i, along the first curve from the initial line element is chosen arbitrarily to provide the origin of the adjacent element which is to be constructed. The incremental arc lengths, Δs_j and Δs_k, represent the distances from the initial element to the points of intersection of the adjacent element with the remaining two curves. It can be shown that the distance ratios defining the adjacent

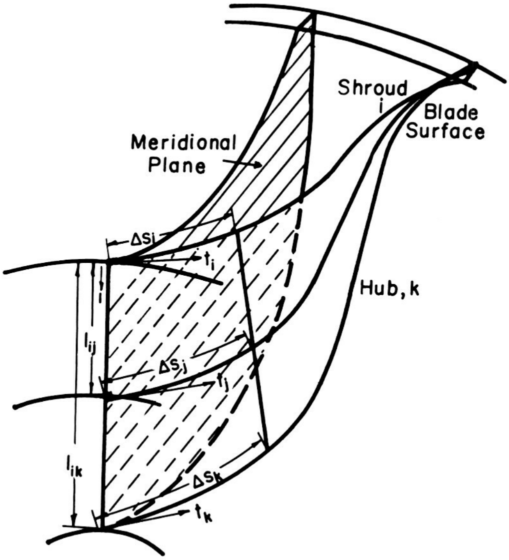

FIGURE 4.—*Vector representation of the straight-line element surface.*

line element are given by the following expressions:

$$\frac{\Delta s_j}{\Delta s_i}=\left(\frac{l_{ik}-l_{ij}}{l_{ik}}\right)\cdot\left(\frac{\mathbf{t}_k\cdot(\mathbf{t}_i\times\mathbf{l})}{\mathbf{t}_k\cdot(\mathbf{t}_j\times\mathbf{l})}\right)\tag{9a}$$

$$\frac{\Delta s_k}{\Delta s_i}=\left(\frac{l_{ik}-l_{ij}}{l_{ij}}\right)\cdot\left(\frac{\mathbf{t}_j\cdot(\mathbf{t}_i\times\mathbf{l})}{\mathbf{t}_j\cdot(\mathbf{t}_k\times\mathbf{l})}\right)\tag{9b}$$

These relations are based on the property of ruled surfaces by which the infinitesimal displacement of a straight-line element is related to vectors which are tangent to the surface at different points on the line element.

In the above equations, the unit vector, **l**, represents the direction of the initial line element from the first curve, and **t** is the unit tangential vector of each curve at the point of intersection as shown in figure 4. The value of **t** is found from differentiation of the previously defined camber line with respect to the distance s measured along it.

The procedure for defining the camber surface of the blade is begun by generating on the loaded shroud streamline between the leading and trailing edge a number of equally spaced points representing the origins of the line elements to be constructed. Starting from the leading edge element, the points of intersection of the next line with the intermediate and hub streamlines are determined by computing the incremental arc lengths along these curves with equations (9a) and (9b). The construction procedure is performed in a stepwise fashion with the generation of each line element being the basis for the generation of the next one until the trailing edge is reached. This process is necessarily an iterative one, since initially the exact values of **t** and **l** are not known.

As has been pointed out before, the method for constructing a blade surface from three streamlines in space may lead to undesirable geometries. If this occurs, the case may be redesigned by specifying the orientation of the straight-line elements in advance in terms of two angles, α_θ and α_z, in addition to the loading distribution along the shroud line.

The straight line and its normal projection on the meridional plane include an angle of lean or dihedral (α_θ) as shown in figure 3. The angle between the projection and the impeller axis defines the slope (angle α_z) of the straight-line element. The described definition of blade element orientation leads naturally to the following often used special blade surfaces:

(1) The radial element blade surface is determined by a camber line through which radial line elements are drawn to define the surface. The elements are sloped vertically without lean ($\alpha_\theta = 0$, $\alpha_z = 90°$).

(2) The axial element blade surface is determined by axial line elements originating from a camber line. These elements are sloped horizontally without lean ($\alpha_\theta = 0$, $\alpha_z = 0$).

(3) The arbitrary blade surface is defined by straight-line elements emanating with arbitrary orientation from a camber line. The elements may have slope and lean ($\alpha_\theta \neq 0$, $\alpha_z \neq 0$).

The camber surface and the given distribution of normal blade thickness along the hub and shroud contour determine the suction and pressure surface of the blade. At each point of intersection of camber line and straight-line element, the normal thickness is interpolated from the given data and one-half of this value is applied in each direction of the local normal to the mean blade surface to define points on the outer blade surfaces. The remainder of these outer surfaces is again described by straight-line elements joining corresponding hub and shroud points. For purposes of the following flow analysis, the blade geometry is defined by a matrix of discrete point coordinates and tangential blade thicknesses on the straight-line elements of the mean blade surface. The interpolation of blade thicknesses and subsequent conversion to tangential thickness requires the determination of the local normal to the mean blade surface. On straight-line elements this normal vector is a linear combination of the known normal vectors at the hub and shroud points of the element. During the flow analysis, planar interpolation of the blade geometry is used for any blade point not explicitly located on a specified straight-line element.

DETAILED FLOW ANALYSIS

The final step in the blade design procedure is an analysis of the flow field that corresponds to the designed impeller blade passages. The analysis serves to reevaluate the meridional flow field from which the blade shape has evolved, by means of prescribed loading distributions on one or more streamlines. Three cycle iterations of the blade design are usually sufficient to achieve convergence on the meridional velocity distribution.

The most convenient way of expressing the governing equations is in so-called streamline coordinates. These coordinates lie in a meridional plane (see fig. 3). A set of fictitious streamlines is defined as the intersections of annular stream surfaces and the meridional plane. The stream surface itself is obtained by rotating the actual streamline for the infinite-number-of-blades solution around the axis.

Using the distance along streamlines (the meridional distance), m, and the distance normal to the streamlines, n, as coordinates, the governing equations reduce to the following:

(1) The normal momentum equation, a differential equation which primarily determines the distribution of meridional velocity along normals.

(2) The continuity equation, an integral equation which primarily determines the position of the streamlines along normals for a given meridional velocity distribution.

(3) The conservation of angular momentum equation (upstream and downstream of the wheel) or the Euler work equation (within the wheel), which is an algebraic equation applied along streamlines between normals.

(4) The energy equation, an algebraic relation between the change in stagnation enthalpy and the energy input along streamlines.

(5) The equivalent of the streamwise momentum equation, an algebraic relation which primarily determines total pressure loss along streamlines.

These equations are generally expressed in two slightly different forms depending upon whether the flow region considered is inside or outside the blade passage. In addition, for gases, the equation of state provides the necessary relationship between fluid properties. The remaining equations, including the many useful relations derivable from the equation of state and the definitions of stagnation properties, are well known and not presented here. Detailed discussions of this flow analysis method may be found in references 3, 5, and 6.

Briefly, the solution procedure is an iterative one which involves first estimating the positions of the streamlines throughout the flow field, solving the normal momentum equation and the continuity equation simultaneously along each normal (using other equations to relate flow properties on each streamline to those of the upstream normal), revising the estimate of streamline positions, and repeating the process until convergence on the streamline position is obtained. The solution so obtained is based on the assumption that the flow is everywhere parallel to the blade surfaces and, in effect, accomplishes the determination of appropriate streamtube widths throughout the flow field from which the meridional velocities are determined by the use of quasi-one-dimensional flow relationships.

SAMPLE IMPELLER DESIGN

The blade design method is illustrated by a sample case with the following design specifications:

Rotational speed	27 900 rpm
Design mass flow	4.61 lbm/sec
Inlet total pressure	14.7 psia
Inlet total temperature	528° R
Discharge total temperature	708° R
Impeller isentropic efficiency	0.945
Impeller discharge blade angle	$-25°$
Impeller inlet hub radius	1.5 in.
Impeller inlet shroud radius	3.33 in.
Impeller discharge radius	5.08 in.
Impeller discharge width	0.539 in.
Impeller axial length	2.75 in.
Leading edge element orientation	$\alpha_z = 90°$ $\alpha_\theta = 0$
Trailing edge element orientation	$\alpha_z = 0$ $\alpha_\theta = -30°$
Blade number	16
Blade thickness along the shroud	0.05 in.
Average blade thickness along the hub	0.15 in.

The impeller hub and shroud contours are shown in figure 5. An arbitrary mean blade surface of unspecified blade element orientation was selected for the initial design. The loading distribution along the shroud streamline was chosen for minimum diffusion on the blade suction and pressure surfaces. This loading schedule is as shown in figure 1*b*. Along the hub and an intermediate streamline, a linear loading schedule was maintained as shown in figure 1*a*. At the blade inlet this loading was adjusted to meet the geometrical constraint that all three streamlines should pass through the initial straight-line element at the leading edge and the final line element at the trailing edge.

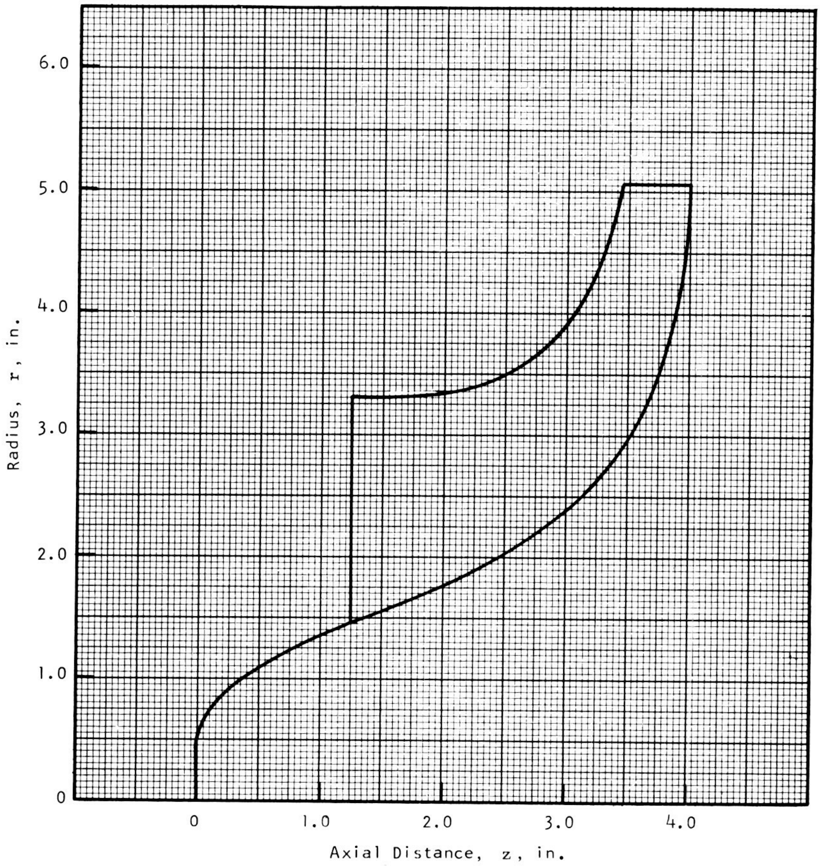

FIGURE 5.—*Impeller contours for the datum stage (25-degree backslope impeller).*

Figure 6 shows the blade element orientation resulting from the initial design. The leading edge blade element is radial while a negative or forward lean, α_θ, is indicated in the inducer region. The blade lean reverses its sign toward the middle of the blade and has a negative or forward lean of 30° at the trailing edge as prescribed. Blade element slope, α_z, varies uniformly from vertical at the leading edge to horizontal at the trailing edge.

Several design considerations led to a revision of the blade element orientation. A first concern arose from blade root bending stresses at the inducer inlet. The subject impeller forms a basic design standard in a series of research compressors that represent systematic variations of design parameters. For this reason, a simpler variation of blade element orientation was selected for the impeller by specifying zero blade lean throughout and a variation of slope as shown in figure 6. This design

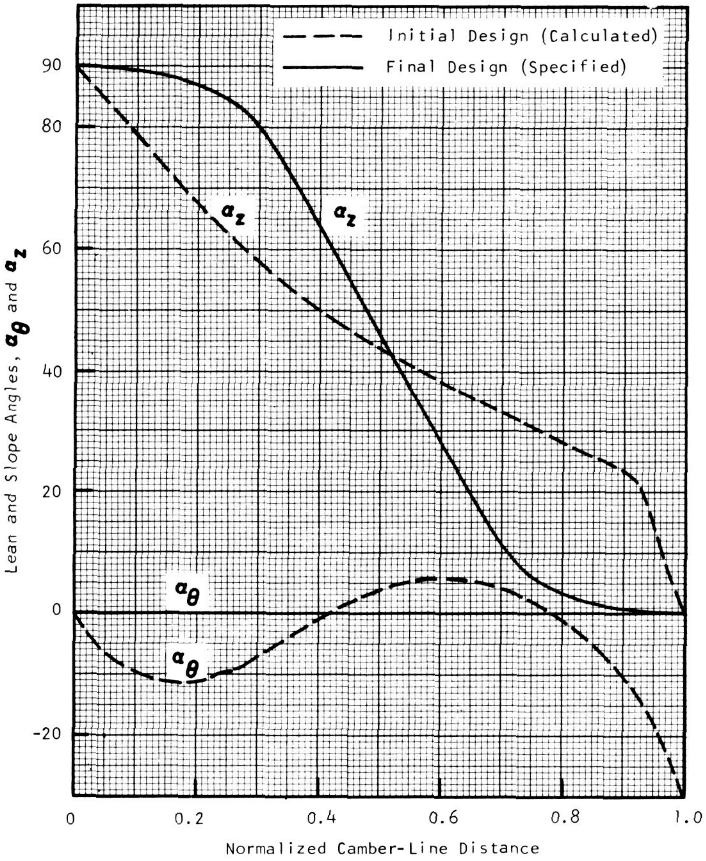

FIGURE 6.—*Blade-element orientation for sample impeller design.*

modification eliminated blade root bending stresses in the inducer and the originally calculated negative blade lean, α_θ, at the impeller exit.

The final velocity distributions on the blade surfaces are shown for the shroud streamtube in figure 7. The velocity variation along the shroud was not affected by the revised distribution of blade element orientation, since the loading schedule on the shroud streamline was not altered. Within the numerical accuracy of this application, the loading along the shroud streamtube varies in the prescribed manner. A suitable modification of the hub and shroud contour would have produced a more linear variation of the average relative velocity and a resemblance to the idealized velocity distributions of figure 1, but the present distribution was considered satisfactory.

The final velocity variation along the hub streamtube as shown in figure 8 was not significantly affected by the revised orientation of blade

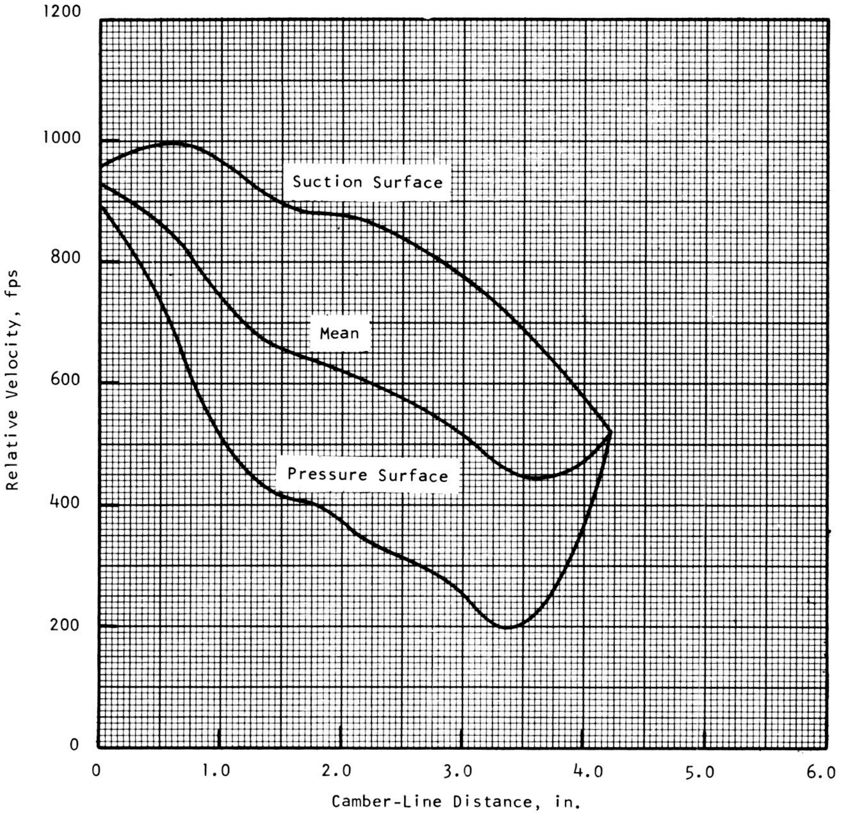

FIGURE 7.—*Design-point blade-surface-velocity distributions for sample impeller (shroud streamtube).*

elements, although blade loading was increased along the forward portion of the hub camber line. The large variation in average relative velocity along the hub could be reduced by modification of the hub contour but was considered acceptable in its present form.

CONCLUSIONS AND RECOMMENDATIONS

The impeller blade design method has been utilized to generate impellers with 0°, 25°, 45°, and 55° backslope at the trailing edge. Some of these designs were cast and others machined, but due to the straight-line element principle the manufacturing of these designs was relatively straightforward. The test results of these designs showed that their aerodynamic performance was very satisfactory. Dynamic and static pressure measurements have shown that the actual surface velocity distributions agree

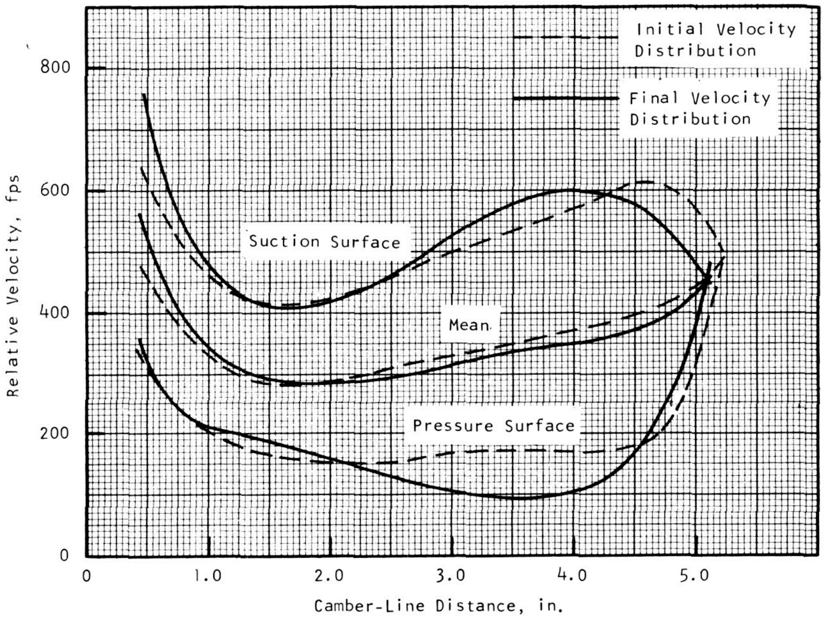

FIGURE 8.—*Design-point blade-surface-velocity distributions for impeller (hub streamtube).*

closely with those calculated with the prescribed loading procedure as described above.

The method involves a large and complicated set of calculation steps which are not presented here; these steps are computerized so that a solution is readily obtainable.

There are two areas where future activities in impeller blade design are essential. The first is linking the velocity distribution along the blade surfaces at different streamlines to the impeller and impeller-induced diffuser losses. When this link is established, there is more confidence that a specified velocity distribution will achieve low impeller losses. The second area is the attenuation of impeller losses by various boundary-layer treatments such as suction, blowing, split blades, tandem blades, and wall treatment. Both areas are currently under investigation in various research establishments.

A logical extension of the present method is to generate directly from the computer program a paper tape to be used in a numerically controlled five-axis milling machine for manufacturing impellers which cannot be easily cast at present (i.e., titanium).

LIST OF SYMBOLS

A	Angle between meridional velocity and impeller axis, deg
C	Absolute velocity, ft/sec
$\mathbf{l}$	Vector tangent to line element, ft
$\dot{m}$	Mass flow rate, lbm/sec
m	Streamline meridional distance, ft
n	Distance along normal to meridional streamline (positive in direction of increasing radius), ft
r	Radius, ft
s	Camber-line distance, ft
$\mathbf{t}$	Vector tangent to streamline, ft
t	Blade thickness, ft
W	Relative velocity, ft/sec
Z	Number of blades
z	Axial distance, ft
α	Angle of blade surface orientation, deg
β	Relative angle from meridional plane (positive in direction of wheel rotation); when overscored ($\bar{\beta}$), signifies flow angle, deg
θ	Cylindrical coordinate angle around z-axis (positive in direction of rotor rotation), deg
ρ	Density, lbm/ft^3
ω	Angular velocity, rad/sec

Subscripts

1	Impeller inlet
2	Impeller exit
d	Pressure surface
h	Hub
m	Meridional value
m,m	Mid-passage meridional value
r	Radial direction
s	Shroud
t	Suction surface
z	Axial direction
θ	Tangential direction

REFERENCES

1. Hill, Philip G., and I. Man Moon, *Effects of Coriolis on the Turbulent Boundary Layer in Rotating Fluid Machines.* MIT Gas Turbine Lab Report No. 69, June 1962.
2. Moore, John, *The Development of Turbulent Boundary Layers in Centrifugal Machines.* MIT Gas Turbine Lab Report No. 99, June 1969.

3. Jansen, W., A Method for Calculating the Flow in a Centrifugal Impeller When Entropy Gradients Are Present. *Internal Aerodynamics* (*Turbomachinery*), Inst. Mech. Engrs. (London), 1970, pp. 133–146.
4. Dallenbach, F., The Aerodynamic Design and Performance of Centrifugal and Mixed-Flow Compressors. *Centrifugal Compressors,* Technical Progress Series, Vol. 3, Soc. Automotive Engrs., December 1961.
5. Stockman, N. O., and J. L. Kramer, *Method for Design of Pump Impellers Using a High Speed Digital Computer.* NASA TN D-1562, 1963.
6. Jansen, W., Flow Analysis in Francis Water Turbines. *Trans. ASME, J. Eng. Power,* Series A, Vol. 89, No. 3, July 1967, pp. 445–451.

DISCUSSION

F. DALLENBACH (Consultant, U.S. Army): The authors present a method whereby the blade shape may be determined by specifying the blade loading distribution along the flow path. Starting with a prescribed meridional shape, the meridional velocities are computed along the shroud and hub by assuming that zero vorticity exists along the streamline normals and that the quantity $\rho C_m r$ varies linearly with normal length between hub and shroud. These assumptions are incorrect, since the vorticity along the normals in general is not zero but varies with the normal distance and the normal gradient of the quantity $\rho C_m r$ is not constant. The resulting meridional velocities must therefore be considered quite approximate and, in fact, may be in considerable error from the correct values.

The relative flow angle β is computed by prescribing the blade loading along a particular streamline as a function of the camber-line length s. The angular momentum rC_θ is then readily calculated. However, until the relationship between the camber-line length s and the meridional length m is established, the angle β cannot be determined.

The solution of the camber-line length as a function of the meridional length leads to the solution of a nonlinear differential equation in which the overall camber-line length is a variable. The final solution which may be obtained by numerical methods must satisfy the given overall meridional length. This procedure is very time consuming.

If, instead of specifying the blade loading distribution along the camber-line length, the angular momentum rC_θ is specified along the meridional length, the angle β may be directly computed and the blade-to-blade velocities readily determined along the meridional and camber-line lengths. This procedure requires little time and affords a ready means of adjusting the blade loading in the event the first trial does not give the desired result.

By specifying blade loading distributions along the shroud and hub contours, the total angular displacement between inlet and exit is determined from the distribution of the blade angle (not the flow angle). As pointed out by the authors, the total angular displacement for the shroud and hub should be essentially the same in order that the leading edge should be a straight radial line. The problem of specifying blade loading distributions for both the shroud and hub contours for backward curved impellers is that the angular displacements of the shroud and hub are, in general, not equal. The authors recognize this and point out that adjustments of the shroud and hub blade loadings are required to satisfy equal angular displacement but they do not treat in any detail what compromises are necessary.

The authors' proposal to generate the impeller blade surfaces by straight lines connecting the hub and shroud is quite practical and, indeed, is being done today where such impellers are machined on a five-axis milling machine.

The authors' discussion of the impeller design philosophy is very well presented and they are to be commended for presenting this paper covering a new design approach for centrifugal impellers.

D. G. WILSON (Massachusetts Institute of Technology): This is a request for further information about the actual boundary-layer behavior on the tested impellers. It is stated that measurements of pressure distributions have shown good agreement with predictions, and this agreement is very heartening for proponents of analytical design methods. It would be very helpful to be shown the measurements.

In particular, such a demonstration of success would help to quiet a strong criticism of theoretical methods of design of centrifugal compressors. It is easy to show that, unless the radial velocity at outlet is made unacceptably high, the mean velocity through a centrifugal compressor with near-radial blades must undergo a deceleration which in two-dimensional flow would result in separation. Conditions must therefore be worse for the pressure surface than for the mean, and worse at the hub than at the shroud. Figures 7 and 8 confirm these rather obvious statements. But flow analysis by these methods is useless once separation has taken place. Do the authors agree? Does separation take place near enough to the impeller outlet that neither the work output (slip factor) nor the impeller efficiency is greatly affected? Even so, the pressure distributions would be strongly, if locally, affected. Or do the secondary flows, instead of causing earlier separation as one might imagine, thin down the important parts of the boundary layer and concentrate all the low-momentum fluid in one noncritical location?

I believe that the significance of these questions is that, although many previous tests on centrifugal compressors using flow visualization of various types have shown serious flow breakdown which has often been ascribed to secondary flows, none of these impellers, to my knowledge, was designed in the first place to have the kind of controlled velocity distributions which it has been the aim of the authors to produce. They are to be congratulated on a stimulating paper.

H. D. LINHARDT (Airco Cryogenics): The authors are to be congratulated for reporting on their continued effort in the development of aerodynamic impeller design methods for centrifugal compressors. Since the complex flow field of centrifugal and, in particular, high pressure ratio centrifugal compressors is not completely understood yet and does not lend itself to rigorous analytical treatment, approximate solutions and/or analysis of assumed flow fields are being utilized for most compressor designs. The authors' suggested loading technique, which lacks experimental foundation and physical understanding of the impeller flow, falls into the latter category of approximate solutions. The application to practice of the authors' method requires a large and complicated set of calculation steps (the authors neglected to present and discuss the equations) which can only be handled by a computer with a large storage capacity. I am sure continued experimental and analytical effort will eventually refine the proposed technique, thus providing a reasonable design of centrifugal compressors of moderate or medium pressure ratio.

Considering industrial applications, one should not forget or underestimate the classic hydraulic approach as outlined in reference D–1. The advantage of the "Conformal Transformation Technique" is that the designer can prescribe the blade loading according to his personal understanding of the anticipated flow and his experience with manufacturing of similar machines. In addition, a clear picture of the impeller passage can be readily obtained, which allows application of basic diffusion and boundary layer stability analysis. The conformal transformation or geometric technique has been applied successfully in the past to industrial pumps and rocket type turbopumps and presents a good and rapid design tool for custom-engineered industrial process compressors. As a matter of fact, the conformal transformation technique has recently been computerized at Airco and successfully applied to medium and high pressure ratio industrial compressors. For this purpose the computer-generated blade coordinates were punched on a paper tape which has been utilized for automatic machining of impeller passages with a tape controlled machine. For example, figure D–1 shows a high specific speed, mixed flow, 2:1 pressure ratio, 5000-horsepower process compressor that achieved 86-percent efficiency at design point and exhibited a wide flow range due to the 35° back-swept design.

JANSEN AND KIRSCHNER (authors): Mr. Dallenbach raised three points, and they are discussed below.

The meridional velocities calculated by assuming zero vorticity are those used as the first values in an iterative scheme. As is pointed out in the text, subsequent velocities in the iteration are determined by a detailed flow analysis of the type described in references 3, 4, 5, or 6. We agree that the initial estimates are quite approximate, but the final velocities are accurate.

We agree that the procedure for loading the blade along the camber line is very time-consuming, since again an iterative scheme is required.

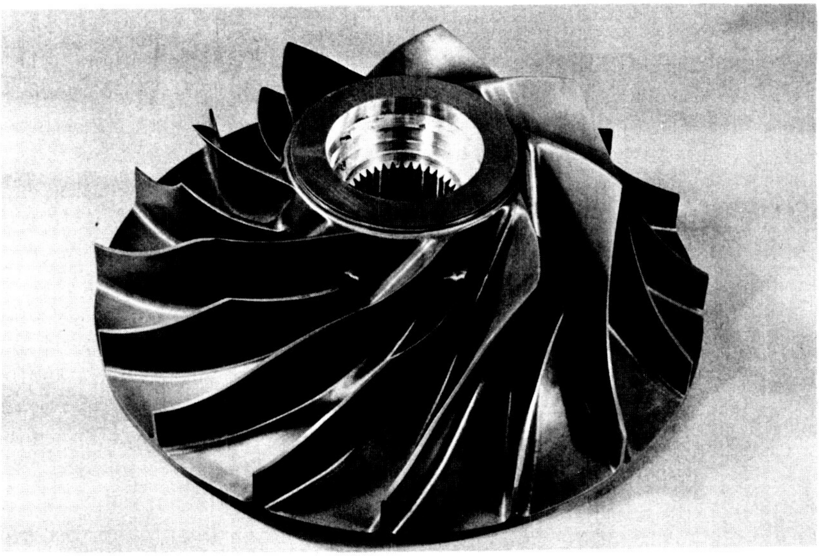

FIGURE D-1.—*5000-horsepower compressor wheel.* (*Airco Cryogenics*)

However, the velocity distribution along the blade length (and not that along the meridional length) is the item to be controlled, since it governs the boundary-layer characteristics and secondary flows. Thus, a technically superior procedure was preferred over a method which yielded a shorter computer running time.

The compromise which has to be accepted when the blade orientation (α_θ and α_z) is specified is that the velocity distribution along the hub and an intermediate streamtube cannot be specified. However, the shroud streamtube velocity distribution should still be specified.

Professor Wilson asks valid questions about the applicability of theoretical methods to centrifugal impeller design. What the present paper attempts is to bridge the gap between research and design. From research we know that boundary-layer separation more than anything else will generate large losses. Also from research we have identified the significant flow mechanisms that govern separation in impellers. Each of these flow mechanisms may be controlled by manipulation of the flow field and this paper provides a procedure by which this may be accomplished and which yields a producible impeller. It is true that more research is needed to associate one flow field with a superior impeller performance, but current work at various establishments, including the authors' own firm, has uncovered some definite trends in velocity distributions (in addition to those associated with limiting the inlet to discharge relative velocity ratio) which improve impeller performance.

The usefulness of the procedure is further exemplified by considering the correlation between calculated and measured results. Figures D–2 and D–3 show the calculated and superposed measured velocities along the shroud streamtube for an impeller with 50° backslope generating a pressure ratio of 2.4 at an rpm of 28 000. The impellers for figures D–2 and D–3 are similar in all aspects, except that the exit width for the case of figure D–3 is 13 percent less than that for figure D–2. The measured data shown are reduced from measurements of average static pressures and dynamic pressures taken along the shroud, together with total pressure traverses at the impeller discharge. The agreement between calculated and measured data is reasonable in the initial 60 percent of the blade passage. After this point, the measured velocities are higher, which indicates that the flow is separated. The actual passage flow is compared with the calculated flow in figure D–4. By prescribing a more reasonable

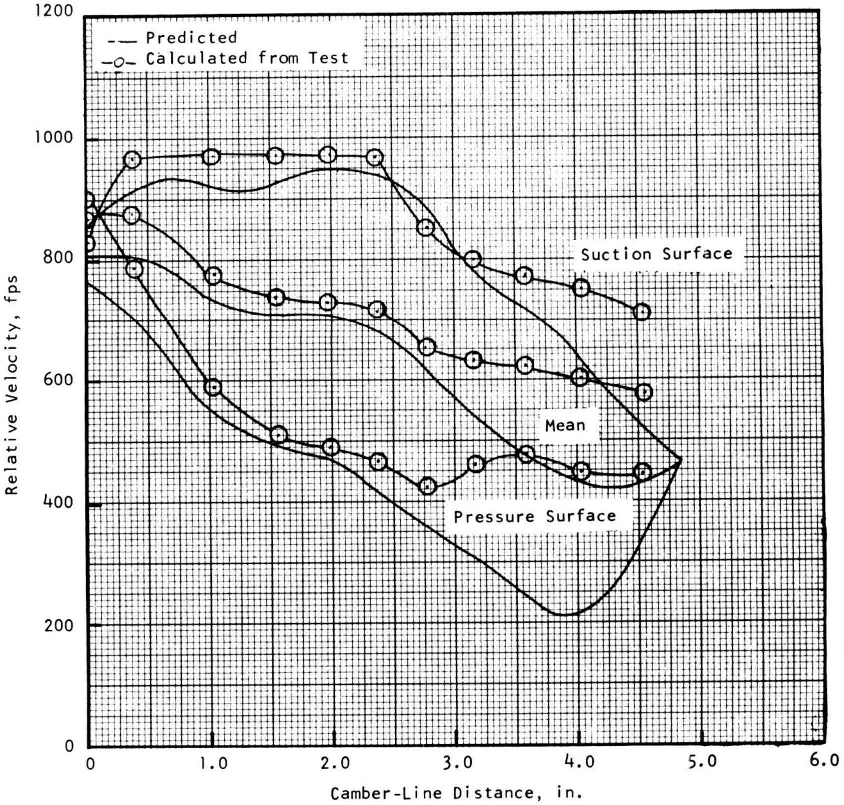

FIGURE D–2.—*Comparison of calculated and measured blade-surface-velocity distribution along the shroud for 50-degree backslope impeller (separation starts at a camber-line distance of 2.9 inches).*

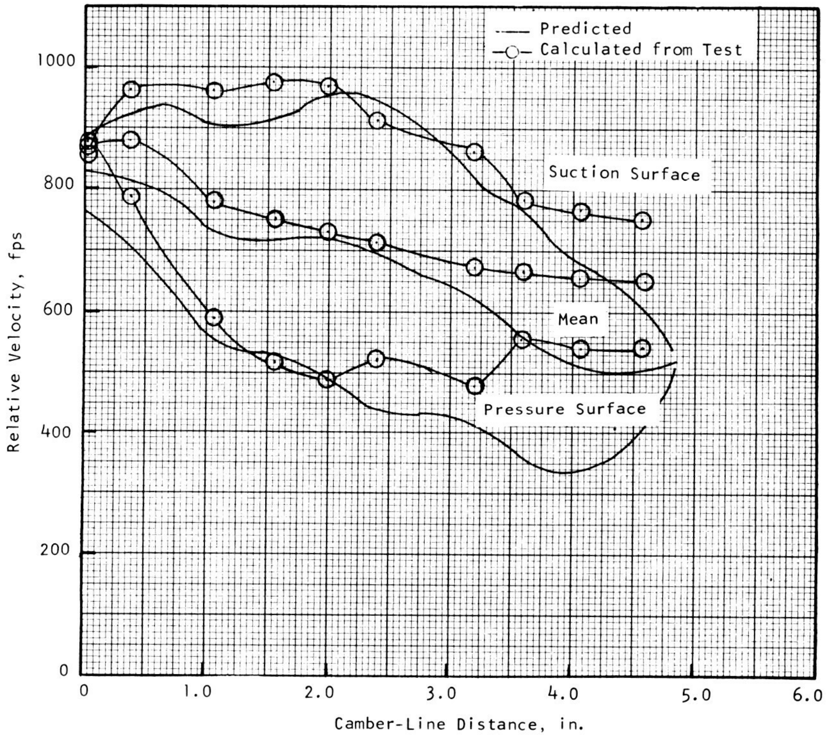

FIGURE D-3.—*Comparison of calculated and measured blade-surface-velocity distribution along the shroud for 50-degree backslope impeller (separation starts at camber-line distance of 3.2 inches; impeller width is 0.87 times that of fig. D-1).*

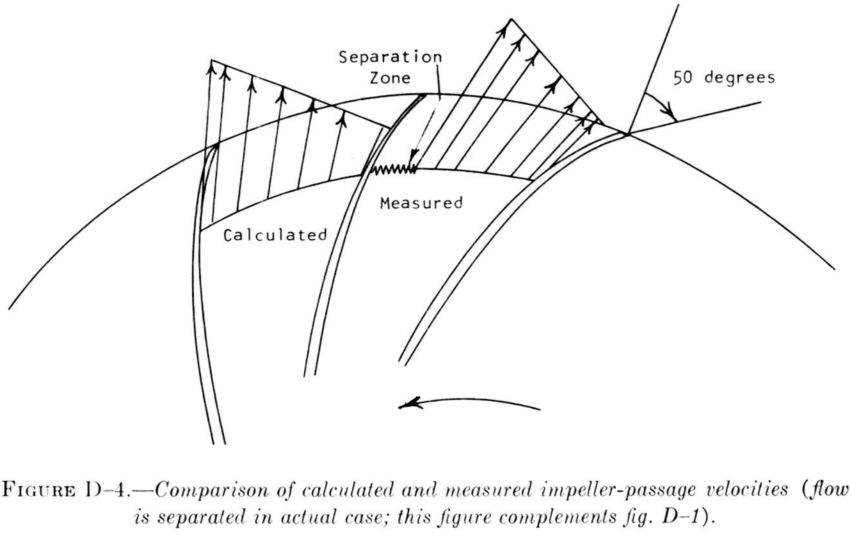

FIGURE D-4.—*Comparison of calculated and measured impeller-passage velocities (flow is separated in actual case; this figure complements fig. D-1).*

velocity distribution, a new impeller can now be designed with the procedure. The occurrence of separation can thus be delayed or eliminated in the new impeller, ensuring higher efficiencies.

The writers appreciate Dr. Linhardt's comments and interpret his discussion as a brief outline of an alternative blade design method.

REFERENCE

D–1. WISLICENUS, G. F., *Fluid Mechanics of Turbomachines*, Vol. II, Dover Publications (New York), 1965, p. 582.

Calculation of Flow Distribution in Large Radius Ratio Stages of Axial Flow Turbines and Comparison of Theory and Experiment[1]

JOSEF HERZOG

General Electric Company

This paper describes a method of calculating stage parameters and flow distribution of axial turbines. The governing equations apply to space between the blade rows and are based on the assumption of rotationally symmetrical, compressible, adiabatic flow conditions. Results are presented for stage design and flow analysis calculations. Theoretical results from the calculation system are compared with experimental data from low pressure steam turbine tests.

Modern steam turbines expand water vapor in 20 to 25 stages from a pressure of 3400 psia, 1050° F to about 0.80 psia, 94° F and handle thereby an 1800:1 increase in volume flow. Subdivision of the steam path into high pressure, intermediate pressure, and low pressure cylinders[2] makes the magnitude of pressure, temperature, and specific volume changes technically acceptable within each of the three units. The large volume flows at the low pressure end are handled by adding the appropriate number of low pressure turbines.

We will discuss one step in the steam path layout of such a low pressure turbine: the method of determining blade flow angles and calculating flow distribution in a sharply divergent, locally transonic flow field (ref. 1).

Comparison of analytical predictions with low pressure test turbine results is the second subject of this paper. The calculation method is based on the well known "streamline curvature method" assuming rotationally symmetrical flow. The resulting circumferentially averaged information is used as a basis for the profile design.

---

[1] The author gratefully acknowledges the contributions of a great number of colleagues and expresses appreciation to Mr. J. E. Fowler and to the General Electric Company for permitting this publication.

[2] A "cylinder" designates a separate housing.

DERIVATION OF WORKING EQUATIONS AND CALCULATION PROCEDURE

The equations of motion and the continuity equation are transformed from a cylindrical coordinate system into a system with the stream function and the axial distance as independent variables. The meridional streamlines, along which the stream function is a constant, are approximated by polynomials. These transformed equations and an assumed isentropic pressure density relationship in stream direction allow determination of the axial velocity derivative and the pressure gradient in a radial direction at any axinormal plane (called "station") outside a blade row. Derivation of the equations is given and one cycle of an iterative solution is discussed in this section.

The Euler equations for steady state inviscous rotationally symmetrical flow without body forces in a cylindrical coordinate system,

$$\left.\begin{aligned} uu_r+wu_z-\frac{v^2}{r}&=-\frac{1}{\rho}P_r\\ uv_r+wv_z+\frac{uv}{r}&=0\\ uw_r+ww_z&=-\frac{1}{\rho}P_z \end{aligned}\right\} \qquad (1)^3$$

and the equation of continuity

$$(\rho ur)_r+(\rho wr)_z=0 \qquad (2)$$

are transformed into the ψ,z plane. P designates the static pressure and ρ the fluid density. Coordinate system and velocity components are shown in figure 1. ψ is a stream function defined by the differential expression

$$d\psi=2\pi\rho rw\cdot dr-2\pi\rho ru\cdot dz=\psi_r\cdot dr+\psi_z\cdot dz \qquad (3)$$

Setting $u=w\sigma$ (σ being the streamline slope in the meridional plane) and $v=\Gamma/r$, $2\pi=k$, leads to the following set of equations in the ψ,z plane:

$$\frac{1}{kr}(\sigma w)_z-\frac{\Gamma^2}{wkr^4}=-P_\psi \qquad (4)$$

$$\Gamma_z=0 \qquad (5)$$

---

[3] Partial derivatives are indicated by the coordinate subscripts.

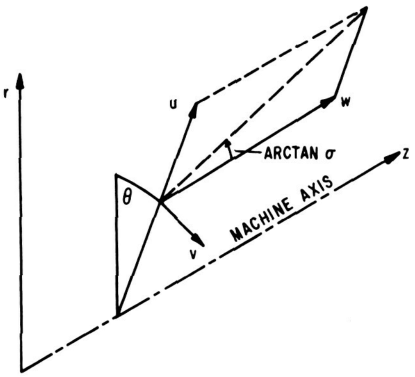

FIGURE 1.—*Coordinate system and velocity components.*

$$ww_z - kr\sigma wP_\psi = -\frac{1}{\rho}P_z \tag{6}$$

$$k\rho^2 r^2 w^2 \sigma_\psi + \rho(wr)_z + wr\rho_z = 0 \tag{7}$$

Equations (4), (5), and (6) combined yield the Bernoulli equation in differential form along a streamline

$$\left[\frac{1}{2}\left(\frac{\Gamma}{r}\right)^2 + \frac{w^2}{2}(1+\sigma^2)\right]_z + \frac{1}{\rho}P_z = 0 \tag{8}$$

Equation (4) is used for the calculation of the radial pressure distribution by iteration. In order to do this, w_z is determined from equation (7) and equation (8), assuming isentropic expansion along a streamline and known streamline shape.

$$w_z = \frac{1}{\left[1 - \frac{w^2\rho(1+\sigma^2)}{\gamma P}\right]}\left[\frac{w^2\rho\sigma}{\gamma P}\left(w\sigma_z - \frac{\Gamma^2}{wr^3}\right) - k\rho r w^2 \sigma_\psi - \frac{w\sigma}{r}\right] \tag{9}$$

Equations (4) and (9), applying to the fluid motion at any axial station i, (fig. 2), are supplemented by the energy equation that is valid along any streamline (ψ_j=constant) and links up thermodynamically with station $i-1$.

$$W_i^2 = (K1)W^2_{i-1} + (K2)\frac{2\gamma_{i-1}P_{i-1}}{(\gamma_{i-1}-1)\rho_{i-1}}\left[1 - \left(\frac{P_i}{P_{i-1}}\right)^{(\gamma_{i-1}-1)/\gamma_{i-1}}\right] + \omega_i^2(r_i^2 - r^2_{i-1}) \tag{10}$$

W is the total velocity relative to the blade row at which exit station i is located. $K1$ and $K2$ are the carryover and reaction coefficients, denoting fraction of upstream kinetic energy and reaction energy accounting for

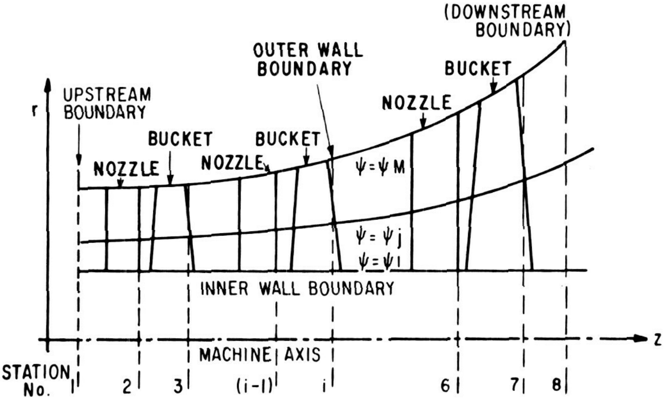

FIGURE 2.—*Grid for setup of calculation.*

the kinetic energy at station i, respectively. ω is the wheel speed and γ the specific heat ratio of the medium.

The shape of the streamlines σ and σ_z is approximated by piecewise polynomial curve fit such that

$$\sigma = AR + B \tag{11}$$

$$\sigma_z = CR + D \tag{12}$$

The coefficients of matrices A and C are functions of spacing of stations. Those of matrices B and D are functions of spacing and streamline slopes at upstream and downstream boundaries. R is the radius matrix. Only one matrix inversion is necessary at the beginning of iterations. σ_ψ is found by numerical differentiation.

Equations (4), (9), (10), (11), and (12), equation of state or steam tables, and relations for velocity triangles are the basic equations used in the iteration at a station. This system can be solved either in a design mode or in an analysis mode for each station.

The interchangability of modes permits steam path design to proceed through both new and available cascade components, besides the usual routine layout of all new stages or the analysis of an existing turbine at arbitrary flow conditions.

The sequence of calculations for a design iteration is sketched in the following:

Assume station i is to be iterated. Having just passed station $i-1$, gas conditions, velocities, and streamline shape are known as functions of ψ_j and z_{i-1}. Slopes σ_{ij} and their derivatives σ_{zij}, and $\sigma_{\psi ij}$ are determined from respective matrices. Reaction and carryover coefficients may be calculated internally or given by input.

Next follows determination of w_{zij} (eq. (9)) pressure derivative $P_{\psi ij}$ (eq. (4)) and the pressure distribution

$$P_{ij}=P_{i1}+\int_{\psi_{\text{root}}}^{\psi} P_{\psi}\,d\psi \tag{13}$$

P_{i1} is the known root pressure at station i.

From the known pressure ratio and upstream data at station $i-1$, total velocity W_{ij} relative to blade row at station i can be determined from equation (10), and the static enthalpy h_{ij} can also be calculated. Gas specific volume is either calculated from gas law or found from computerized steam tables. An alternate simplified calculation, including the wet region, is possible using gas laws and variable specific heat ratio by numerically differentiating steam table values.

The axial velocity component, w_{ij}, derived from local velocity triangles and given Γ_{ij}/Γ_{i1} distribution, is used to force

$$r_0^2-r_{\text{root}}^2=2\int_{\psi_{\text{root}}}^{\psi_{\text{tip}}}\frac{d\psi}{k\rho w} \tag{14}$$

to approach a given value of $r_{\text{tip}}^2-r_{\text{root}}^2$ by rotating the total velocity vector W_{i1} at the root such that the modified root axial velocity is given by

$$w_{i1_{\text{mod}}}=w_{i1}\cdot\frac{r_0^2-r_{\text{root}}^2}{r_{\text{tip}}^2-r_{\text{root}}^2} \tag{15}$$

and by adjusting Γ_{i1} accordingly.

A new radius distribution,

$$r_{ij}=\sqrt{r_{i1}^2+2\int_{\psi_{\text{root}}}^{\psi_j}\frac{d\psi}{k\rho w}} \tag{16}$$

is finally calculated using a modified axial velocity,

$$w_{ij_{\text{mod}}}=w_{ij}+(w_{i1_{\text{mod}}}-w_{i1})\text{DC} \tag{17}$$

(DC = Damping Constant.)

Convergence is checked by comparing radii, slopes σ, and slope derivative σ_{ψ} based on the new radii with those computed in the previous iteration. Depending on these checks, the described iteration is either repeated or the system moves on to the next station. This process goes on until the downstream boundary is reached. The system will either return to the upstream boundary for a new iteration loop or move to answer calculations, depending on an overall streamline radius convergence criterion.

NUMERICAL EXAMPLES

Design Calculation

In a design case, the whole low pressure turbine is calculated in one or two sections. In the latter case an overlay is made at the joining stations in order to ensure streamline as well as thermodynamic continuity. Design information for one stage out of several calculated is shown in figures 3 through 6.

Figure 3 shows sin α (α is the nozzle exit angle) versus radial height and the partial derivative of sin α with respect to z at constant radius. The latter information allows one to account for nonradial trailing edges and other small axial adjustments during the course of design. Figure 4 relates the relative bucket entrance angle and its derivative with respect to z, and figure 5 describes the sine of the relative bucket exit angle γ and its derivative with respect to z as a function of the radius. Finally, in figure 6, the absolute stage exit angle versus radius is given. This information is the basis for the next step in designing the blade sections. Additional information such as pressure, velocity, Mach number distribution, and streamline shape is available, serving as a guide in the successive progress of a low pressure turbine layout.

Analysis of Test Conditions and Comparison of Theoretical Data with Laboratory Measurements

Calibration of the outlined procedure is of most interest. The calculation system is used for this purpose in its analysis mode to make predictions of pressure distributions, flow distributions, and flow angles at any station based on given turbine geometry, estimated efficiency, root

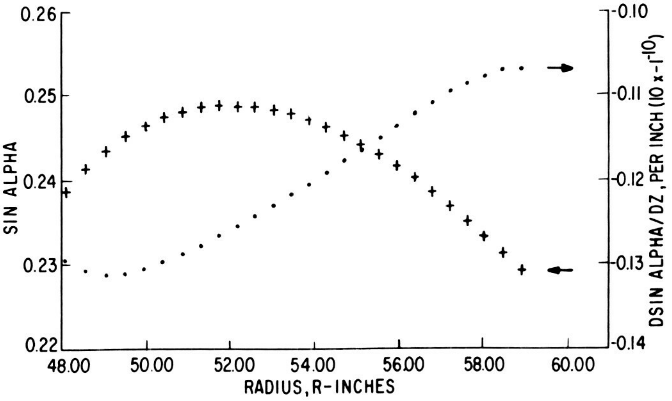

FIGURE 3.—*Design information: sine of nozzle exit angle and its derivative versus radius.*

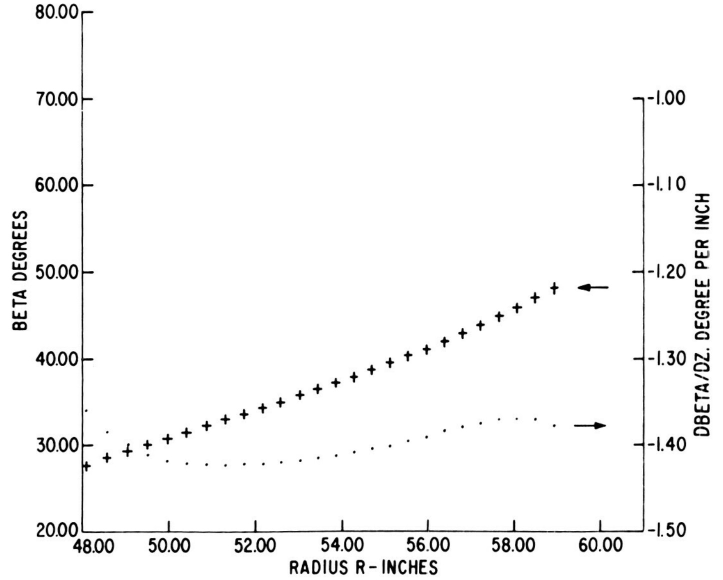

FIGURE 4.—*Design information: relative bucket entrance angle and its derivative versus radius.*

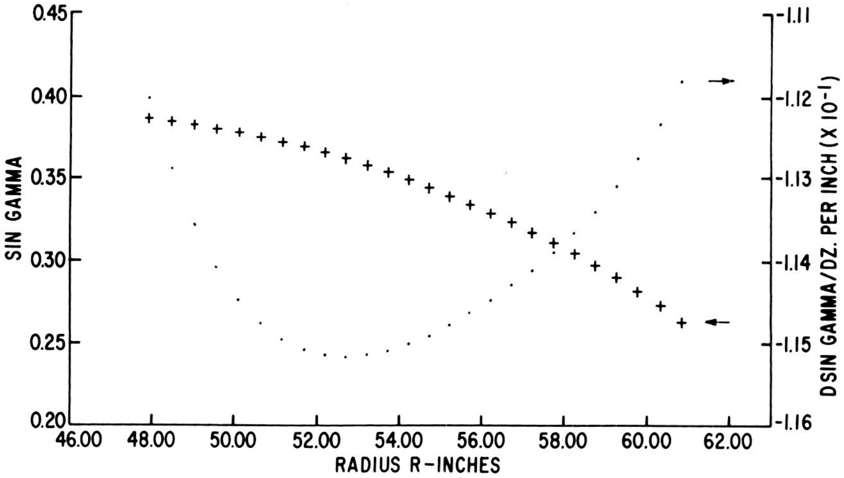

FIGURE 5.—*Design information: sine of relative bucket exit angle and its derivative versus radius.*

stage exit pressures, upstream and downstream conditions, and total flow. These predictions are compared with available traverse data behind the second, third, and fourth stage of a test turbine. Since most of the test data were accumulated under off-design conditions due to high initial

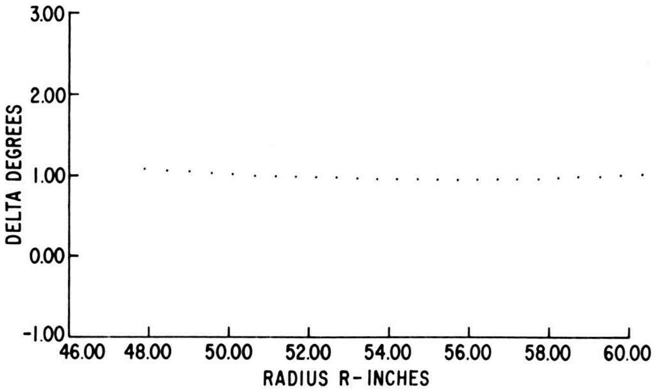

FIGURE 6.—*Design information: absolute stage leaving angle.*

superheat necessary for temperature traverses, the comparison makes for an especially good test of the capabilities of the analysis mode.

The test data presented here was obtained in the low pressure turbine test facility in the Product Development Laboratory of the Large Steam Turbine Department of General Electric Company. A detailed description of this facility is given in reference 2. The last four stages of a 30-in. low pressure turbine were tested. A cross section of the test turbine showing location of pressure taps (P), and temperature sensors (T), as well as traverse locations behind the second, third, and fourth stage is exhibited in figure 7. Figure 8 is a photo of the test rotor.

Test data (circles) and theoretical predictions (full lines) are plotted versus the respective radius ratio in figures 9 through 13.

Figures 9 and 10 present traverse data behind exit from stage number two. There is maximum discrepancy in the static pressure readings of 0.18 psia or a 2.5 percent deviation in absolute pressure level. The absolute leaving angle is negative due to lower than design velocity ratios. Calculated angles are too large, on the average by 7.8°, when the effect of tip leakage is discarded. The deviation in both graphs is in the same direction.

Comparisons of conditions at the third stage exit are shown in figures 11 and 12. The measured axial velocity decreases towards the tip less rapidly than indicated by the analysis. The leaving angle is again negative, indicating that the direction of the tangential leaving velocity is opposite to direction of wheel rotation. Calculations show angles larger on the average by 2.5°.

Average carryover and reaction coefficients were used in the calculations of the second and third stage results. In the analysis of the last stage, an estimated nozzle efficiency and the known stage streamline efficiency were used for an approximation of the bucket efficiency. The

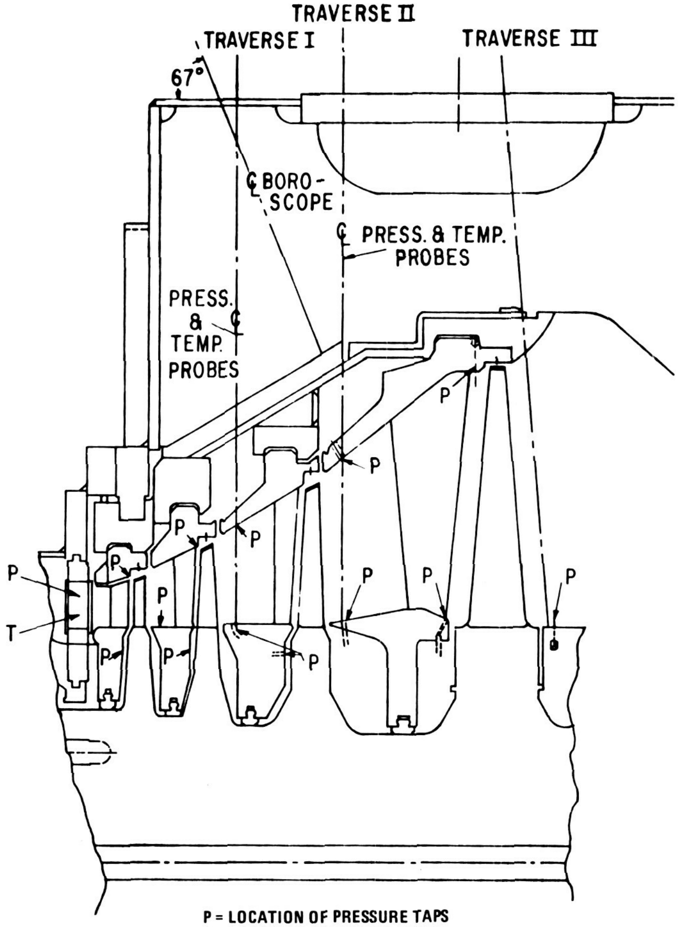

FIGURE 7.—*Cross section through test turbine.*

graph in figure 13 compares predicted and measured axial velocity distribution on a dimensionless basis.

Finally, we want to call attention to the different flow regimes that do occur in different portions of a large radius ratio low pressure steam turbine stage. The absolute velocity entering the stator is well subsonic, while the stator exit velocity ranges from supersonic at the root to subsonic at the tip as shown by the Mach number plot in figure 14. The relative exit velocities at the rotor change from transonic velocities near the root to supersonic velocities along the outer portion of the bucket. The calculation system discussed is able to analyze these stages.

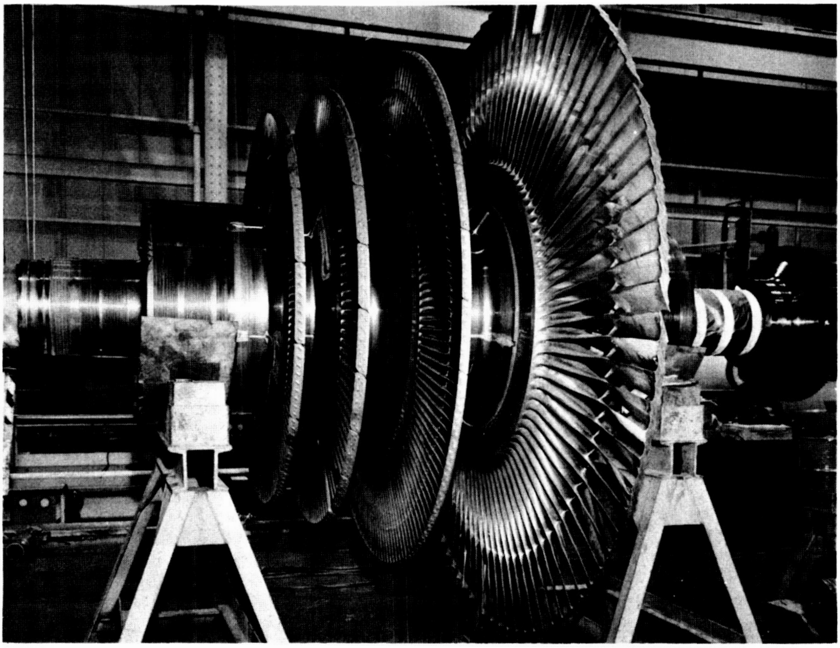

FIGURE 8.—*Thirty-inch LSB test turbine rotor.*

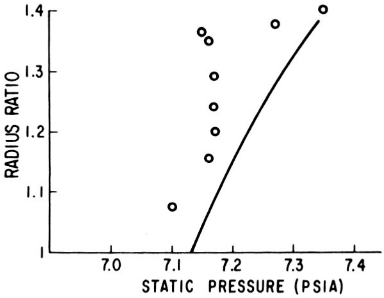

FIGURE 9.—*Comparison of predicted and measured static pressure distribution at exit of stage 2.*

FIGURE 10.—*Comparison of predicted and measured absolute leaving angle at the exit of stage 2.*

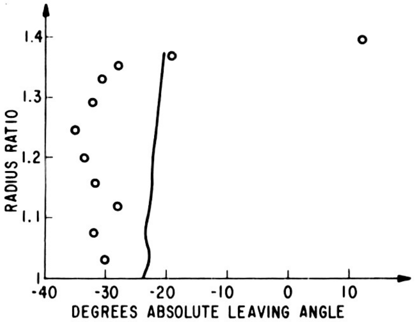

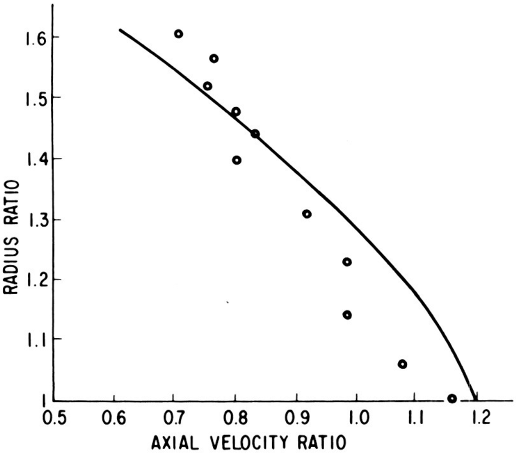

FIGURE 11.—*Comparison of predicted and measured axial velocity distribution at the exit of stage 3.*

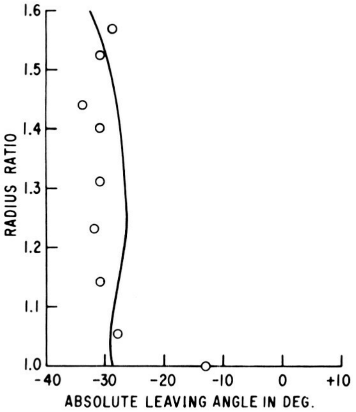

FIGURE 12.—*Comparison of predicted and measured absolute leaving angle at exit of stage 3.*

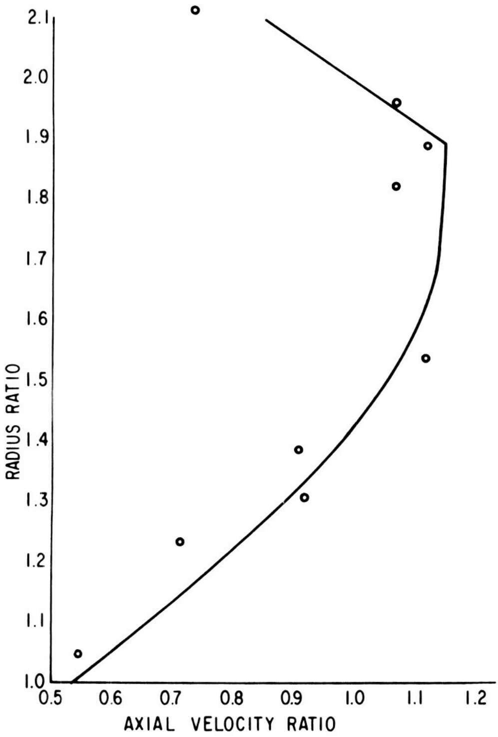

FIGURE 13.—*Comparison of predicted and measured axial velocity distribution at exit of last stage.*

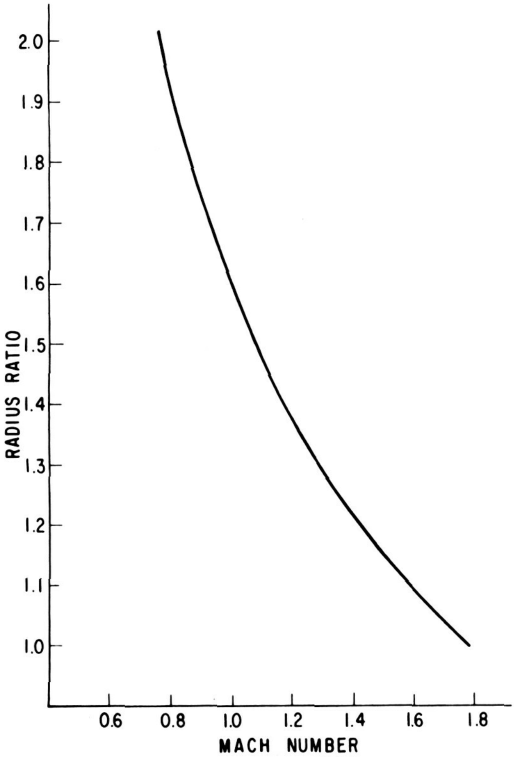

FIGURE 14.—*Mach number distribution at last stage nozzle exit.*

CONCLUSIONS

The system described has proved to be a reliable design tool. Its simple structure allows updating of the system by input of experimental data derived from tests in air and steam. The analysis mode is helpful in interpretation of test evidence. Comparison of analysis with test data shows that the system overshoots traverse data at the second stage traverse, while third and fourth stage traverses are predicted well. The match of static pressure and leaving angle depend very much on the effective nozzle areas. Differences in the axial velocity distributions can be reduced by taking account of radial bucket efficiency distribution.

REFERENCES

1. FOWLER, J. E., AND E. H. MILLER, *Some Aspects of Development of Efficient Last Stage Buckets for Steam Turbines.* ASME Paper 69–WA/Pwr–11.
2. DOWNS, J. E., AND K. C. COTTON, *Low Pressure Turbine Testing.* ASME Paper 58–SA–38.

DISCUSSION

G. K. SEROVY (Iowa State University): The author has presented a method for solution of a most difficult problem. The basic approach, as indicated by the author, is not new. It has been used to attack both design and analysis problems in axial-flow compressors, as reported independently by Smith and by Novak in ASME papers several years ago. Another closely related method was described by Renaudin and Somm of the Brown Boveri Company at a Symposium on Flow Research on Blading held in Baden, Switzerland, in 1969. The authors of earlier papers as well as this one have all succeeded in handling a very complicated situation in numerical analysis which has been encountered by all those who attempt to iterate on stream-surface shapes, especially when the flow is of a transonic character.

It would be helpful in evaluating the paper and results if the author could tell us something about the initial conditions assumed at the upstream boundary. Also he must have in his solution system some method for making an initial guess at the shapes and locations of the ($\psi =$ constant) lines. How is this done?

In the case of axial-flow compressor calculations, it has been possible to improve solutions for the design case by using stations located inside the blade rows. It has always seemed probable to this observer that the blade-to-blade flow problem in turbines has been under control, so that such solutions (intra-blade stations) might be very feasible for steam turbines.

One might also take a certain amount of fiendish pleasure in noting that the "turbine crowd" has a most serious problem in accounting for end wall flows. We have this problem in equal or greater quantity in the "compressor crowd" and it is to be hoped that we can cooperate in developing consistent procedures for doing a better job in these regions. Mr. Herzog deserves our thanks for giving us a clear outline of his method, supported by comparison with experimental radial surveys.

H. D. LINHARDT (Airco Cryogenics): I understand the turbine you have discussed is operating under wet steam conditions in the last stage. Could you please define what are the wet steam conditions in the last stage, what is the percentage of wetness and how does the performance change when operating under wet conditions? It would be interesting to know what kind of design procedure you use and what the condensate droplet sizes are in the last stage. How do you correlate performance and erosion phenomena with droplet size?

R. M. HEARSEY (Ohio State University Research Foundation): I wonder if you have considered modifying your procedure slightly from what I understand it to be to include the possibility of the calculation stations being nonradial, which would appear to allow you to calculate velocity distributions rather closer to the blade edges.

C. FARN (Westinghouse Research and Development): What kind of loss criteria did you use in the computation, especially for the last stage?

You only use two axial stations per stage. I always wonder whether this is accurate enough.

Is this a design program or performance program? If it's a design program, what design parameters are you specifying?

HERZOG (author): The initial conditions assumed to be given at the upstream boundary are the axial location of the station, the stagnation pressure and stagnation enthalpy, as well as the radius and slope at each streamline. Total conditions can vary from streamline to streamline.

The initial guess at shape and location of the (ψ=constant) lines is made by subdividing the flow path into a given number of equal area filaments at each station. This provides a complete radius matrix that is used to determine initial matrices for streamline slope σ_{ij} and slope derivative σ_{zij}.

Introduction of intra-blade stations is desirable and expected to improve accuracy of shape and location of the (ψ=constant) lines. As of now, we use only three stations per stage. Additional stations can be introduced into the vaneless portions of a stage. Use of nonradial stations is not planned at this time. Information needed along nonradial contours such as blade trailing edges are determined from information at the radial station which is modified by linear extrapolation either in streamline or in axial direction.

The program is mainly used as a design tool for large radius ratio steam turbines; we specify, in addition to upstream conditions, the inner and outer wall shape, blade spacing in axial direction, axial energy and reaction distribution at blade roots, and the stage total flow, wheel speed, and pressure distribution at the turbine exit. Existing components may be incorporated in new designs.

Steam entering the last stage under discussion is about 3½ percent wet and leaves the stage at about 10 percent wet.

The performance of the turbine deteriorates with increase in initial moisture content. This effect is shown in figure D–1, which was taken from reference 2. This graph displays the change in turbine efficiency

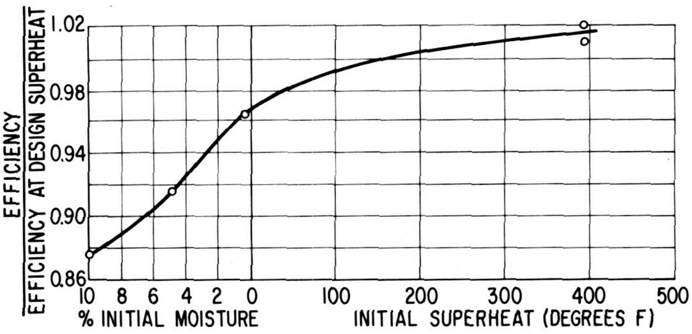

Figure D–1.—*Change of turbine group efficiency with change of initial steam wetness.*

with the change of the initial moisture content at the inlet of a four stage low pressure test turbine. In the range of super-heated inlet condition only part of the turbine is running on wet steam. We did not measure drop sizes in the turbine. Size measurements in a shock tunnel indicated an initial drop dimension, after spontaneous condensation took place, of submicron size. It is believed that these small drops do not cause erosion and that most of the damage is done by much larger "secondary drops" torn off the partition trailing edges. We are not aware of any laws correlating performance and erosion phenomena with drop size.

Transonic Compressor Technology Advancements

WILLIAM A. BENSER

NASA-Lewis Research Center

This paper discusses the highlights of the NASA program on transonic compressors. Effects of blade shape and throat area on losses and flow range are discussed. Some effects of casing treatment on stall margin are presented. Results of tests with varying solidity are also presented. High Mach number, highly loaded stators are discussed and some results of stator hub slit suction are presented.

For turbojet and turbofan aircraft propulsion applications, lightweight, compact, efficient fans and compressors are essential. These requirements have led to the selection of axial-flow type components for most aircraft propulsion systems. At the present time, axial-flow fans and compressors have been developed to a point where improvements in efficiency are not easily achieved. Therefore, the goal of much of the research and development effort is to reduce size and weight without sacrificing efficiency. Present-day supersonic aircraft propulsion systems must also be capable of operating with rather severe distortions of total pressure at the fan or compressor inlet. This stresses the requirement of broad stall-free range of operation. Therefore, reductions in fan or compressor size or weight must be compatible with operating range requirements of specific applications.

The objective of this paper is to review some of the approaches to reduced size and weight and to discuss some of the recent advances in fan and compressor technology that may contribute to improved designs. This paper is not intended to be an exhaustive report on new technology, but will consider some of the advances considered to be significant.

APPROACHES TO REDUCED SIZE AND WEIGHT

Fan or compressor size is significant from the standpoint of compactness, as related to installation problems, and is also significant because of the direct relationship of size on weight. Reductions in size can be achieved by reduced diameter and/or reduced length. Reduced diameter requires increased flow per unit of annulus area or more effective flow area per unit of diameter. Current practice already is quite advanced with regard to flow capacity, so that only limited gains can be made in this area. Reduced length can be achieved by reducing the length of each stage or by reducing the number of stages. Reduced length per stage or increased blade aspect ratio is an effective way of achieving reduced weight. Unfortunately, this approach leads to severe mechanical and aeroelastic problems as well as to severe limitations in attainable flow range. Both of these problem areas are being studied, but to date no major breakthrough has been achieved. This leaves increased pressure ratio per stage as the most promising technique of achieving more compact compressors.

Reductions in compressor weight can, of course, be achieved by reductions in weight per unit size as well as by reductions in compressor size. Reductions in weight per unit size, however, are achieved through improvements in materials or in mechanical design concepts rather than through aerodynamic advancements and will not be considered in this paper.

Increases in stage pressure ratio can be achieved by increasing the tip speed of the rotor or by increasing blade loading. The effectiveness of these two approaches to increasing stage pressure is shown in figure 1. In this figure, pressure ratio is plotted versus rotor tip speed with rotor tip loading as a parameter. Tip loading is expressed in terms of tip diffusion factor, D_{rt}. This plot is based on the assumption of zero pre-whirl at the rotor inlet.

Figure 1 shows that pressure ratio increases can be achieved either by increased loading or by increased tip speed. Maximum gains obviously come from increasing both loading and tip speed. An increase in loading at a given tip speed does not increase the relative inlet Mach number, but increased losses and reduced range of operation may result from the increased diffusion. Increases in tip speed at a given level of loading, of course, result in increased Mach numbers relative to the rotor blading. This may also adversely affect efficiency and range of operation. With zero inlet swirl, the tip relative Mach number at 1000 feet per second tip speed will be on the order of 1.1 and at 1600 feet per second it will be on the order of 1.6. Pre-swirl can, of course, be used to reduce the rotor tip relative Mach number, but this will reduce the attainable pressure ratio for a given tip diffusion factor and will also increase the stator Mach numbers.

In addition to rotor Mach numbers and loading, consideration must be given to stator parameters which are usually critical at the hub. Figure 2 shows variations in stator hub Mach number and stator hub diffusion factor as functions of rotor tip speed with rotor tip diffusion factor as a

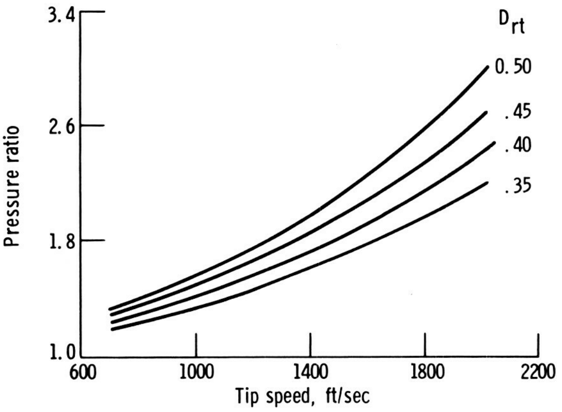

FIGURE 1.—*Effect of tip speed and blade loading on rotor pressure ratio.*

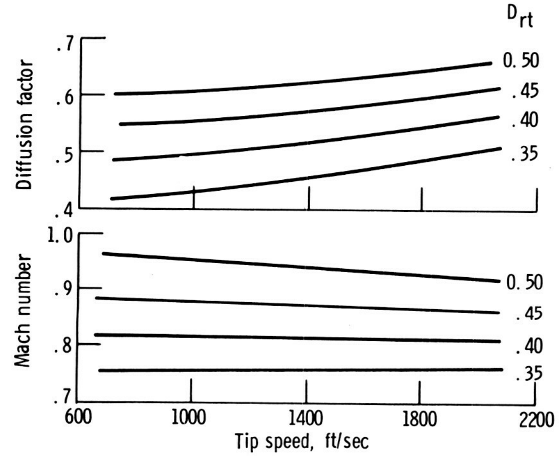

FIGURE 2.—*Effect of rotor tip speed and loading on stator hub loading and Mach number.*

parameter. Stator hub Mach number increases appreciably with increased rotor tip loading at a given tip speed, but is nearly constant with increased tip speed at a fixed level of rotor loading. The stator hub diffusion factor increases at about the same rate as the rotor tip diffusion factor when speed is held constant. Only small increases in stator hub diffusion factor are obtained when tip speed is increased at a constant value of rotor tip loading.

From figures 1 and 2 it is evident that increasing tip speed at a given level of rotor loading requires only the solution of the problem of increased rotor relative Mach numbers, provided, of course, that limiting values of rotor loading are not adversely affected by increased Mach number. Increases in rotor loading, however, result in stator Mach number and loading problems as well as in increased rotor problems. Simply counting problems would indicate that the simplest approach would be to just increase tip speed to attain higher stage pressure ratio. The relative effort required to achieve acceptable performance as well as other design requirements, however, may make the route of high loading, low speed more profitable. Maximum gains are made by increasing both rotor tip speed and loading. Therefore, studies of both increased loading and increased Mach numbers for rotors and stators are required. Studies of the effects of increased loading and/or increased Mach numbers must include evaluation of attainable flow range or stall margin as well as attainable efficiencies. If flow range limitations are severe, it may be necessary to operate the compressor at reduced pressure ratio and efficiency to provide sufficient stall margin. Such restrictions could limit the gains attainable from increased loading or tip speed.

NASA ROTOR PROGRAM

As a part of the overall NASA compressor research program, a number of axial-flow stages have been designed, built, and tested either in-house or by contract to investigate the effects of high loading and high tip speed on performance. Figure 3 shows the range of loadings and wheel speeds studied to date. In this figure, individual stages are plotted at design values of tip speed and tip diffusion factor. The pressure ratios are not exact because of three-dimensional effects and loss gradient effects, but this plot does indicate the range of conditions covered to date. The solid symbols represent subsonic stages. The two lower speed subsonic stages had no inlet guide vanes and the remaining three utilized inlet guide vanes.

These subsonic stages were aimed at investigation of boundary layer control schemes such as slotted blading and are included here just to define the complete scope of the NASA program. Transonic stages cover a range of tip speeds from 1000 to 1600 feet per second and rotor tip *D*-factors from 0.35 to slightly over 0.5. Most of these transonic stages were designed to investigate blade shapes for high relative Mach numbers.

Design speed maximum efficiencies and the corresponding pressure ratios for these stages are given in figure 4. This figure shows that, in general, maximum efficiency decreases only slightly with speed. The peak efficiency for the 1600-feet-per-second rotor is 0.89. The pressure ratio at that operating point is slightly over 2.0. At the other extreme of the curve is a very highly loaded rotor designed for a tip speed of 1000 feet per second. This rotor has a maximum efficiency of about 0.93 at a pressure ratio of 1.5.

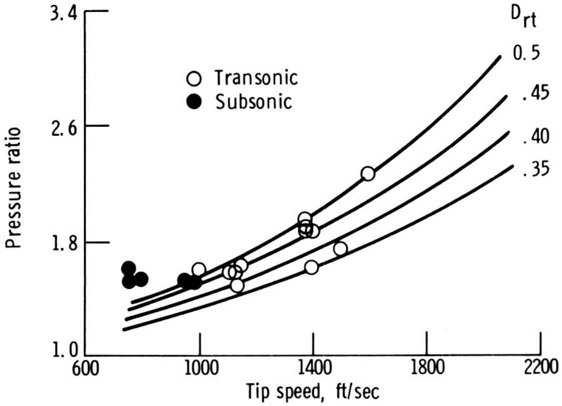

FIGURE 3.—*Rotors tested in NASA program.*

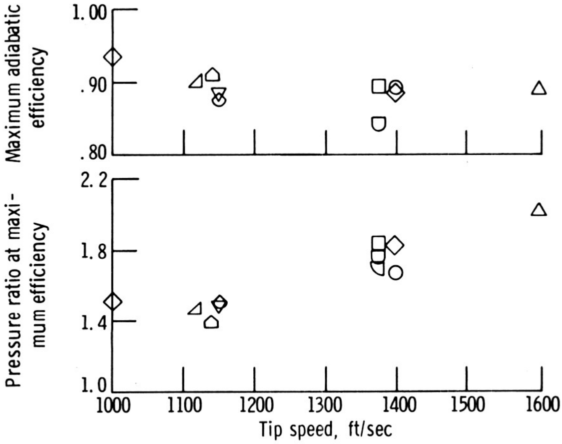

FIGURE 4.—*Experimental rotor performance at design tip speed.*

TRANSONIC BLADE SHAPES

The early transonic axial-flow compressors used double circular arc blade sections. For relative inlet Mach numbers above 1.2, however, this type of blade section was relatively inefficient. An analysis of passage shock losses for this type of blade (ref. 1) indicated that a passage shock could be assumed which was normal to the mean flow path and extended from the leading edge of one blade to the suction surface of the adjacent blade (fig. 5). Shock loss could be approximated by the loss across a normal shock at a Mach number equal to the average of the upstream

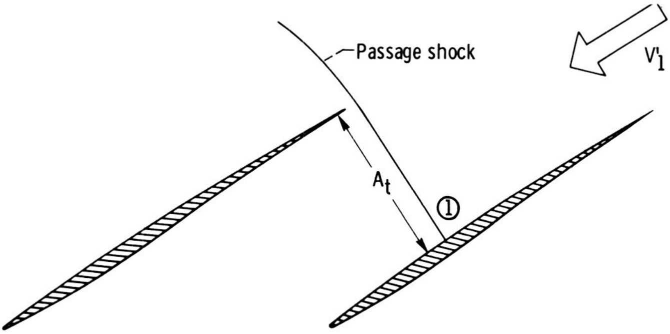

FIGURE 5.—*Typical transonic rotor blade section. Design criteria: minimum suction surface Mach number,* M_1'*; minimum throat area,* A_t.

Mach number and the Mach number at the intersection of the passage shock and the blade suction surface. This passage shock loss in some cases was over half of the total measured loss. For a given inlet relative Mach number, it is obvious that the suction surface Mach number must be reduced if shock losses are to be minimized.

The suction surface Mach number at point 1 in figure 5 is a function of the inlet relative Mach number and the amount of turning from the inlet free stream direction to the suction surface flow direction at point 1. Therefore, low shock losses require minimum suction surface turning upstream of the shock intersection point. As the suction surface turning is reduced, however, the passage throat area indicated as A_t in figure 5 decreases. Sufficient throat area must exist so as to pass the required mass flow. Otherwise, the passage will choke and the blade will be forced to operate at a positive incidence angle. This will increase the suction surface turning and the magnitude of passage shock loss. Therefore, the minimum suction surface turning must be consistent with a ratio of throat area to critical area, A_t/A^*, which is slightly greater than 1. The loss across the passage shock must be included in the determination of the critical area, A^*.

Based on the concept of minimum suction surface turning consistent with adequate throat area, most of the blade profiles for the rotors shown in figure 4 were composed of multiple circular arcs; that is, the pressure and suction surfaces of the forward or supersonic section of the blade are circular arcs with relatively small curvatures. The suction and pressure surfaces of the rear or subsonic portion of the blade are also circular arcs with relatively larger curvatures.

The preceding is a simplified discussion of the critical factors of supersonic blade shape and throat area requirements. In the actual case, blade blockage, streamline convergence in the radial direction, upstream extended compression or expansion wave effects, and boundary layer blockage must be evaluated. These factors are discussed in some detail in reference 2.

EFFECT OF THROAT AREA RATIO

As a part of an investigation of the effect of blade shape on performance, three rotors designed for a tip speed of 1400 feet per second were built and tested. The design speed performance and critical design parameters for these rotors are shown in figure 6. Rotor *1B* was designed for a tip diffusion factor of 0.35 and a small supersonic turning on the suction surface. The estimated suction surface Mach number at the shock point was 1.49 and the ratio of throat area to critical area was 1.08. This critical area ratio accounted for radial streamline convergence and for shock losses but did not account for boundary layer growth on the flow surfaces or any other losses. Rotor *2B* was designed for a tip diffusion factor of 0.45, an estimated maximum suction surface Mach number of 1.51, and

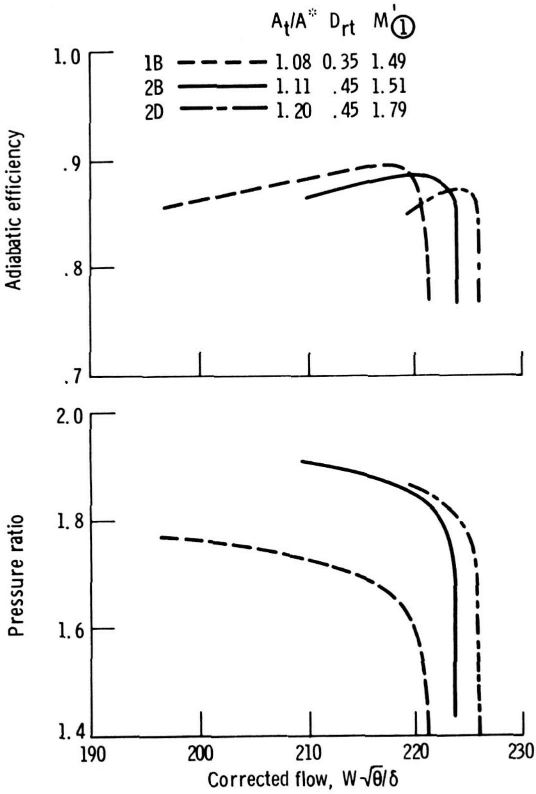

FIGURE 6.—*Effect of throat area ratio on rotor performance. Design speed.*

a critical area ratio of 1.11. Rotor 2*D* was also designed for a tip diffusion factor of 0.45, but had an estimated maximum suction surface Mach number of 1.79 and a critical area ratio of 1.2. Additional details on the design and performance of these rotors are given in reference 3.

Comparison of the maximum efficiencies for these three rotors (fig. 6) shows that rotor 1*B* is about one point better than rotor 2*B* and two points better than rotor 2*D*. The design inlet relative Mach number is the same for all three rotors; the suction surface Mach numbers for rotors 1*B* and 2*B* are comparable, whereas the suction surface Mach number for rotor 2*D* is appreciably higher. It may be surmised that the differences in efficiency between rotors 1*B* and 2*B* may be due to the decrease in subsonic diffusion as a result of lower blade loadings and that the differences between rotors 2*B* and 2*D* may be due to differences in shock losses as a result of a lower average shock Mach numbers.

A rather surprising difference in performance of these three rotors is the difference in stable operating range. The minimum flow for each rotor represents the point of initiation of rotating stall. As can be seen from figure 6, rotor 1*B* has the largest flow range, rotor 2*B* the next largest, and rotor 2*D* the smallest range. There appears to be a direct relationship between range and critical area ratio. A possible explanation for this range effect is based on the theory that the shock-boundary layer interaction at the existing values of suction surface Mach number are sufficiently high that flow separation must occur downstream of the shock. The passage velocity in the region of the shock probably accelerates to sonic levels. The larger the throat area ratio, the larger the extent of the separated region, and the more critical the flow reattachment and subsonic diffusion process. Therefore, a critical area ratio just sufficient to pass the mass flow not only results in a lower shock loss, but also improves the subsonic diffusion process. Therefore, gains in both efficiency and flow range are obtained.

It should be noted that the degree of supersonic suction surface turning consistent with flow choking is a function of relative inlet Mach number. For low Mach numbers, a fairly large turning is required; for a relative inlet Mach number on the order of 1.4, the suction surface turning can be practically zero, and, for still higher relative inlet Mach numbers, reverse turning can be used. This critical area variation with inlet Mach number, of course, means that the throat area ratio can only be optimized for design speed. The variation of efficiency with speed for these three rotors is shown in figure 7. At design speed and at 110 percent of design speed, the rotor with the smaller critical area ratio is most efficient. At 90 percent of design speed all three rotors have about the same maximum efficiency and at lower speeds the rotors with the larger throat areas have the best efficiency. Therefore, selection of throat area ratio will be dependent on the particular application. If maximum efficiency at design

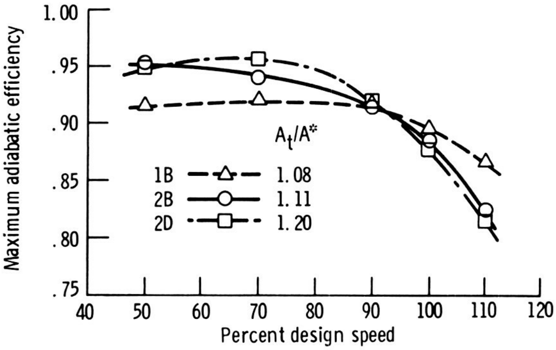

FIGURE 7.—*Effect of rotative speed on maximum efficiency.*

speed is of prime importance, the throat area ratio should be near 1.0. If, however, high efficiency at part speed is more significant, larger throat area ratios are desirable. The lowest area ratio for these studies was 1.08, but other rotors have been designed for area ratios of 1.03 to 1.05. (The deviation from a value of 1.00 is an allowance for boundary layer blockage.)

EFFECT OF CASING TREATMENT

In order to be useful for most turbojet engine applications, compressor stages must have appreciable stall-free-flow range and must be tolerant of severe distortions of inlet pressure. For example, the *2B* stage of figure 6 could be marginal from a range standpoint. Furthermore, most high aspect ratio stages have exhibited insufficient flow range for most applications. During tests of tip boundary layer control on a high aspect ratio rotor blade row (ref. 4), it was discovered that appreciable gains in flow range could be achieved by use of porous material over the rotor blade tips. Figure 8 shows the effect of this treatment on a highly loaded, 1375-feet-per-second rotor tested by NASA. The solid curves show the performance and stall limit for tests with a solid casing; the dashed curves are for the same rotor with casing treatment. In this case, the treatment consisted of 310 slots which were 0.070 inches wide, 0.30 inches deep, about a half blade chord long, and cut at approximately the angle of the blade tip as shown in the sketch in figure 8. As can be seen, this casing treatment had an extremely large effect on the rotor stall margin and did not seriously affect the rotor pressure ratio or maximum efficiency. Other configurations of porous casing also gave appreciable gains in flow range, but some had more adverse effects on pressure ratio and efficiency. The mechanism by which these range improvements are obtained is not understood, but they offer great potential as a means of attaining broad

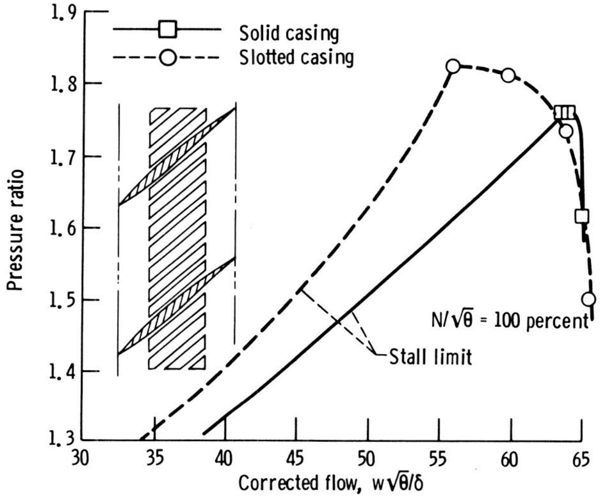

FIGURE 8.—*Effect of rotor casing treatment on stall limit.*

range for highly loaded transonic stages. Such treatments have been applied to complete stages, but have not been tried on multistage fans or compressors yet.

EFFECT OF SOLIDITY ON ROTOR PERFORMANCE

The preceding discussion has considered the losses associated with the supersonic portion of the transonic blade. In another phase of the NASA program, the effects of solidity on subsonic diffusion were considered. For this study, blade rows with tip solidities of 1.1, 1.3, and 1.5, were designed, built, and tested. All three rotors were designed for a tip speed of 1375 feet per second. The variation of basic blade shape is shown in figure 9 along with the design speed performance. As shown in the sketch, the forward or supersonic portions of the blade were the same and solidity was increased by extending the rearward or subsonic portion of the blade. All three rotors were designed for an overall pressure ratio of 1.65, and the camber of the rearward portion of the blade was selected accordingly. Tip section diffusion factors varied from 0.47 to 0.50.

Examination of the performance plots of figure 9 shows that the peak pressure ratio increased with increased solidity. The variation of adiabatic efficiency shows the high solidity rotor with a maximum efficiency of 0.89 at a pressure ratio of 1.82 to be the most efficient.

These data show the maximum efficiency of the 1.3 solidity rotor to be slightly lower than that for the 1.1 solidity rotor. This is believed to be a result of differences in midspan vibration dampers. The dampers on the

1.3 solidity rotor were very thick and poorly streamlined compared to those for the other two rotors. With comparable dampers, it is believed that the 1.3 solidity rotor maximum efficiency would fall between those for the other two rotors. These data clearly show the advantages of high solidity for highly loaded transonic rotors.

Based on conventional correlations of loss parameter versus diffusion factor for rotor tip sections, a lower value solidity would be expected to be optimum. To study this in more detail, existing data were reviewed to determine the influence of solidity on rotor blade tip losses. Conventional plots of loss parameter versus diffusion factor were made in which ranges of solidity were isolated. Figure 10 is such a plot for tip section data. Nominal values of solidity on the order of 0.6, 1.0, and 1.4 are indicated by different symbols. The loss parameter values plotted are

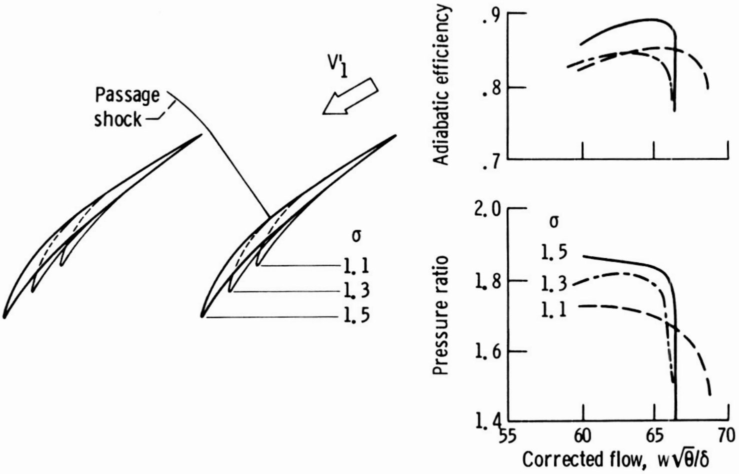

FIGURE 9.—*Effect of solidity on transonic rotor performance. Design speed.*

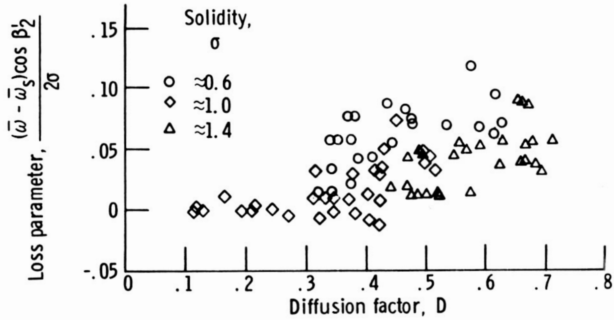

FIGURE 10.—*Effect of solidity on rotor tip loss parameter.*

the profile loss parameters obtained by subtracting estimated shock losses from the total measured losses. As usual for this type of data, there is an appreciable scatter. There is a definite trend, however, for the low solidity data to concentrate near the top of the band and the high solidity data near the bottom of the band for diffusion factors above 0.4.

Based on this data review, one might conclude that the correlation of loss parameter against solidity is not valid and that either solidity should not be included in the loss parameter or the exponent should be much larger than −1. Other forms of loss correlations have been tried with only limited success. Perhaps one source of difficulty is the lack of sufficient data from designs which are truly comparable. Most of the very low solidity data of figure 10 were obtained by simply removing vanes from rotors designed for higher solidities. Therefore, current concepts of optimized blade shape were not incorporated in the low solidity configurations. Secondary flow losses are a significant part of the losses in the rotor tip region, and the influence of these losses on the effects of solidity are probably not adequately accounted for in the existing correlations. It is obvious that much more study is required before solidity can be optimized for a given application. Rotor data as presented in figure 9, however, strongly indicate performance advantages for high solidities for highly loaded transonic rotors.

HIGH MACH NUMBER STATORS

As shown in figure 2, highly loaded rotor stages will result in highly loaded, high Mach number stators. NASA has an active program on high Mach number stators which applies the same principles of minimum shock loss and controlled passage throat area discussed for rotors. Initially this program consisted of a study of a family of transonic stators (ref. 5). Current effort consists of design and test of stators to match research rotors. A typical radial variation of loss parameter for a transonic stator from reference 5 is shown in figure 11. For this particular point, the Mach number varied from 0.8 at the tip to 1.0 at the hub and the hub diffusion factor was on the order of 0.65. From this figure it is evident that hub and tip losses are extremely high for this level of loading and inlet Mach number.

Figure 12 indicates the relative magnitude of the effects of Mach number and diffusion factor. This is a plot of loss parameter and diffusion factor versus inlet Mach number for the stator hub section. These data are also from reference 5. The solid curve represents total loss parameter and the dotted curve represents profile loss parameter. This profile loss parameter is obtained by substracting an estimated shock loss from the measured total losses. Stator diffusion factor is plotted as the dot-dashed

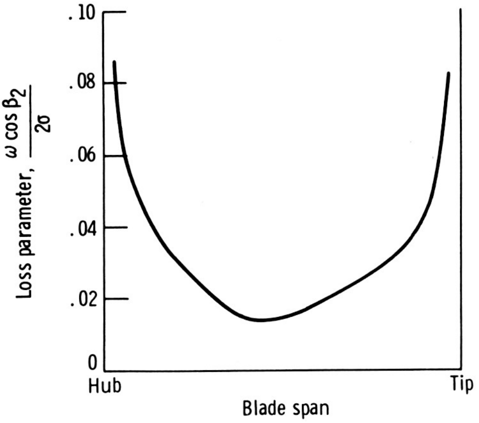

FIGURE 11.—*Radial distribution of stator loss. Inlet Mach number, 0.8 to 1.0; hub diffusion factor, 0.65.*

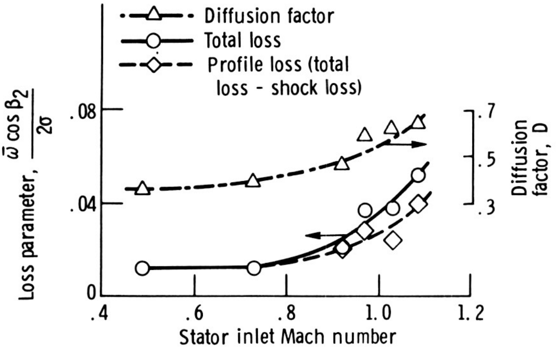

FIGURE 12.—*Effect of Mach number on stator loss.*

curve. As can be seen, an increase in stator Mach number is accompanied by an increase in diffusion factor. A comparison of the profile loss and total loss shows that at an inlet Mach number of 1.00, about 20 percent of the loss is estimated to be due to shock loss; the rest must be attributed to loading. At higher Mach numbers a larger proportion of the loss can be attributed to the effect of Mach number.

Several methods of reducing stator end losses through boundary layer control may prove profitable. One method is that of corner slit suction as reported in reference 6. This is shown schematically in figure 13. The suction slit is located at the intersection of the suction surface and the annulus wall. For this test, the slit was located at the hub end of the stator, extended from 15 to 85 percent of blade chord, and was 0.017 inches wide. The objective of this corner suction was to reduce corner flow separation and thus reduce losses. Results in terms of loss parameter versus span are also shown in figure 13. The circles show losses with the slits plugged, and the diamonds show losses with a slit flow of 0.2 percent of the total flow. Test conditions were a stator hub Mach number of 0.9 and a hub diffusion factor of 0.64. As can be seen, the application of this limited amount of slit suction appreciably reduced the losses in the hub region.

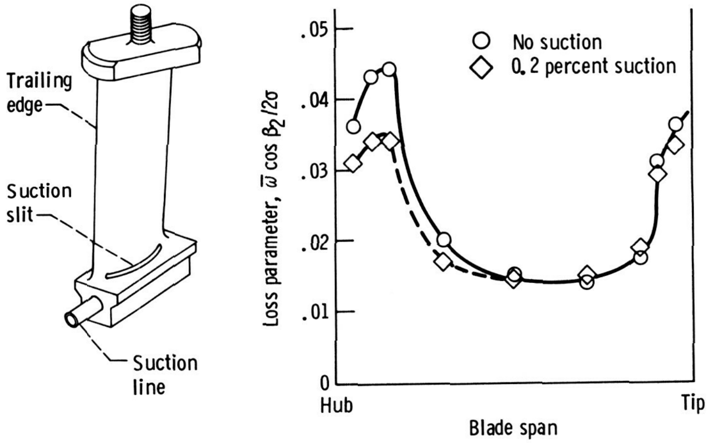

FIGURE 13.—*Effect of slit suction on stator losses. Stator hub Mach number, 0.9; hub diffusion factor, 0.64.*

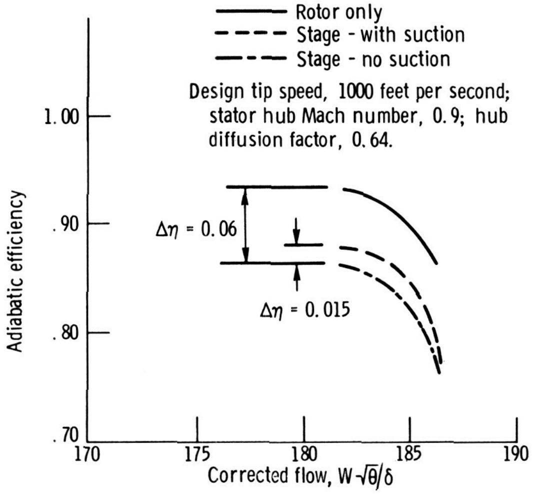

FIGURE 14.—*Effect of stator slit suction on stage performance. Design tip speed, 1000 feet per second; stator hub Mach number, 0.9; hub diffusion factor, 0.64.*

The effect of this stator loss reduction on stage efficiency is shown in figure 14. This particular stage is a highly loaded, low tip speed stage such as might be applied to a low noise, high bypass ratio fan engine. Design tip speed was 1000 feet per second, pressure ratio was 1.50, stator hub inlet Mach number was 0.9 and stator hub diffusion factor was 0.64. The solid curve is rotor efficiency, the dot-dashed curve is stage efficiency with no slit suction, and the dashed curve is stage efficiency with slit suction. This figure shows that the loss across the stator with no slit suction results in a 6-point drop in stage efficiency. Application of stator hub slit suction of 0.2 percent of total flow results in a gain of 1 to $1\frac{1}{2}$ points in stage efficiency. These data clearly show the need for efficient stators for highly loaded compressor stages.

SUMMARY REMARKS

To achieve light-weight, compact fans and compressors for advanced aircraft propulsion systems, it is desirable to obtain axial-flow compressor stages with increased pressure ratio per stage. Stage pressure ratio can be increased by increasing rotor tip speed, by increasing blade loading, or by some combination of these increases. Increased rotor tip speed at a given loading level increases the rotor relative Mach number, but has little effect on stator Mach number or loading. Increased rotor loading, however, results in increases in both stator Mach number and loading.

Very good efficiencies have been achieved for high tip speed transonic rotors by utilizing proper control of suction surface curvature and blade section throat area. Minimum curvature on the forward portion of the suction surface has been used to minimize shock losses. The minimum permissible curvature in this region is limited by choking requirements downstream of the passage shock. Choking limits change with tip speed, so that designs with throat areas near the limit at design speed will show maximum efficiency at design speed but be less efficient at lower speeds than designs with a larger margin from choke. Therefore, selection of the optimum throat area ratio will depend on the requirements of any particular application. Designs with minimum throat area margins also seem to exhibit maximum stall-free operating ranges.

Large gains in flow range without severe penalties in performance have been achieved by use of porous casing treatment over single rotor blade rows.

Increased solidity appears to have a beneficial effect for highly loaded transonic rotors. Highly loaded transonic stators have shown extremely high losses in the blade end regions. Limited tests with slit suction at the junction of the stator suction surface and the hub annulus wall have shown appreciable performance gains for relatively small suction flows.

LIST OF SYMBOLS

A_t	Blade passage throat area
A^*	Critical area
C	Blade chord
D	Diffusion factor
M	Mach number
S	Blade spacing
U_t	Rotor tip speed
β_2	Exit flow angle
η	Adiabatic efficiency
σ	Blade row solidity
$\bar{\omega}$	Loss coefficient

Subscripts

rt	Rotor tip
sh	Stator hub

Superscripts

$'$	Relative to the rotor blade

REFERENCES

1. Schwenk, Francis C., George W. Lewis, and Melvin J. Hartmann, *A Preliminary Analysis of the Magnitude of Shock Losses in Transonic Compressors.* NACA RM E57A30, 1957.
2. Reddy, J. L., and J. F. Klapproth, *Advanced Fan Development for High Bypass Engines.* AIAA, Paper 68–563, June 1968.
3. Gostelow, J. P., K. W. Krabacher, and L. H. Smith, Jr., *Performance Comparisons of High Mach Number Compressor Rotor Blading.* NASA CR–1256, 1968.
4. Koch, C. C., *Experimental Evaluation of Outer Case Blowing or Bleeding of Single Stage Axial Flow Compressor*, Part VI, Final Report. NASA CR–54592, April 1970.
5. Keenan, M. J., and J. A. Bartok, *Experimental Evaluation of Transonic Stators.* Report PWA-3470, Pratt & Whitney Aircraft, NASA CR–72298, 1969.
6. Peacock, R. E., *Flow Control in Corners of Cascades.* Report ARC–27291, Aeronautical Research Council, Great Britain, October 8, 1965.

DISCUSSION

C. C. KOCH (General Electric Co.): As Mr. Benser discusses in his paper, significant improvements in compressor stall margin have been obtained by the use of porous casing treatments. Although these effects have been observed for some time (e.g., a casing treatment configuration that increased the stall margin of a centrifugal compressor was demonstrated and patented by the General Electric Company in 1945; ref. D–1), our understanding of them is based primarily on empirical results. Several hypotheses do exist concerning the physical processes by which casing treatment increases stall margin, but one must agree with Mr. Benser's conclusion that at present the mechanism is not adequately understood. However, it is likely that more insight into the casing treatment mechanism may result from greater understanding of the growth of casing boundary layers and the stability of these boundary layer flows as the stall limit is approached.

The photograph in figure D–1 is presented in the hope that it may contribute to this understanding. Lamp black and oil patterns on plexiglas rotor casing sections of a four-stage, low-speed research compressor are shown. In this figure the rotor moves from left to right and the through-flow is downward. On each window there are two crayon lines that indicate the leading-edge and trailing-edge planes of the rotor blades. At certain places crayon marks also indicate the trailing edges of upstream stator vanes. It can be seen that the flow direction in the rotor tip clearance region is primarily circumferential, but near the leading edge there is a through-flow component, while in the rear portions of the blades the flow frequently has an upstream component. These flows tend to coalesce at a location in the front half of each blade row. The pattern shown occurred when the compressor was near stall; with more open throttle positions the line of coalescence was further aft. This indicates that the extent of axial back flow increases in the casing boundary layer as a machine is throttled toward stall. Casing boundary layer measurements taken upstream and downstream of the third rotor confirm this and indicate that the displacement thickness of the axial-velocity casing boundary layer increases rapidly as stall is approached.

If, in fact, the growth and ultimate breakdown of the region of coalesced boundary layer flow were the cause of stall, then the above observations suggest that casing treatment may delay stall by reducing back flows or by preventing the forward movement of the coalesced region.

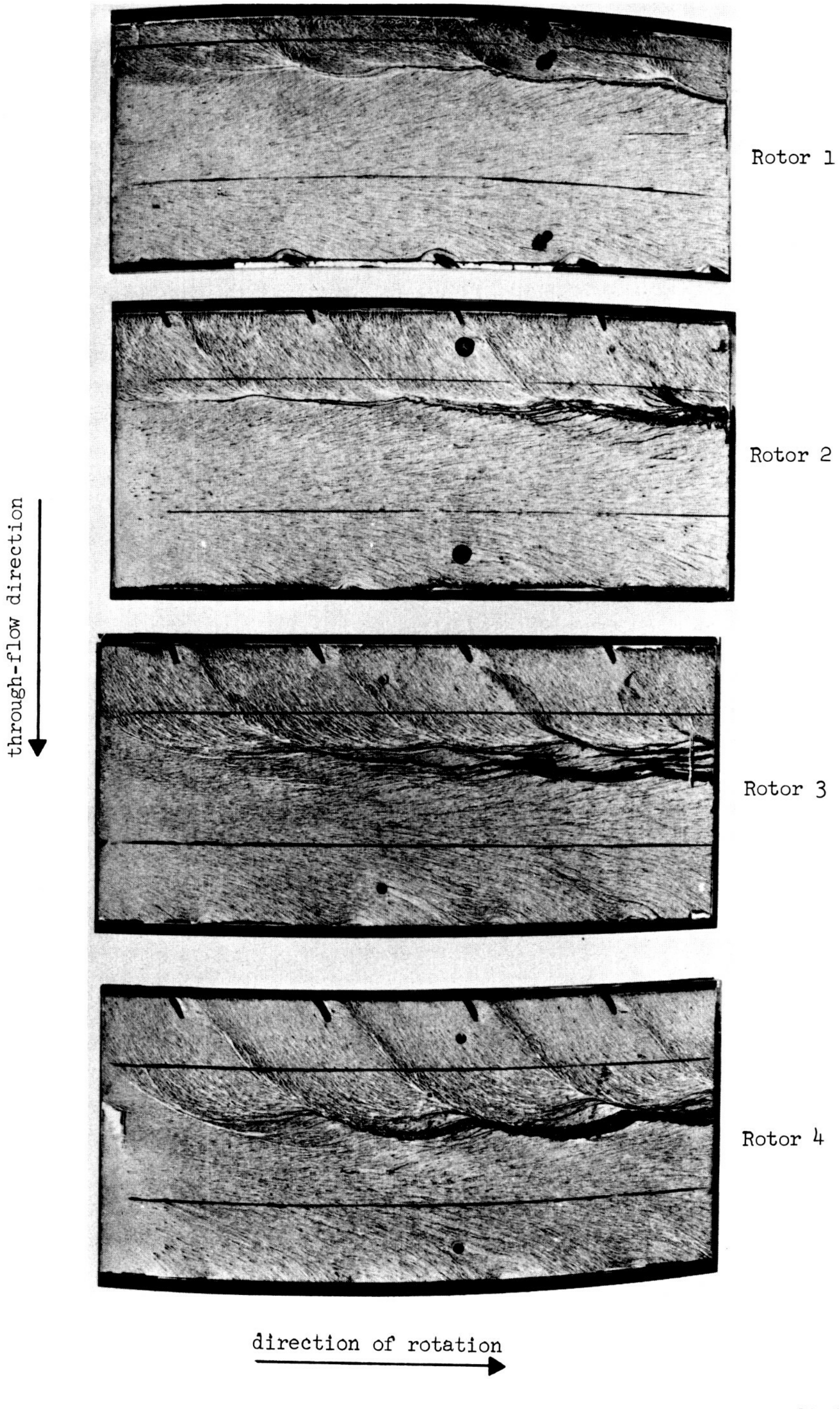

FIGURE D-1.—*Boundary layer flow visualization in rotor tip region using lamp black and oil.*

M. J. KEENAN (Pratt & Whitney): Mr. Benser presents a concise summary of the most significant results obtained in recent NASA investigation of high loading and high tip speed on compressor performance. The relationship between rotative speed (or Mach number) and critical area ratio is particularly interesting. The trend toward higher efficiency at high speeds and lower efficiency at part speed with decreasing area ratios is very strong in the 1600-ft/sec rotor described in reference D–2. This rotor was designed with $A_t/A^*=1.04$ for sections having supersonic relative Mach numbers. The small throat areas, obtained with negative front camber near the tip, forced the rotor to operate at high incidence and high loss at part speed. At a tip speed equivalent to 114-percent design speed in figure 7, this rotor reached its maximum efficiency, 0.890. Its peak efficiency at 800 ft/sec tip speed was 0.863, 2.7 percent lower than at design speed, and 9 percent lower than that of the $A_t/A^*=1.2$ rotor (2*D*) at the same tip speed.

High Mach number stator tests (ref. 5) showed similar results. Multiple circular arc and double circular arc stators were designed with the same incidence angles, but reduced front camber gave the multiple circular arc designs smaller throat areas. These multiple circular arc stators had a clear performance advantage at high Mach numbers, but averaged slightly higher losses at lower Mach numbers.

These data, in themselves, are not conclusive but appear to be an extension of Mr. Benser's observations on the effect of throat area on performance. They indicate a need for further analysis along the lines presented in reference D–3, in which bow wave losses are related to off-design incidence angles, leading to improved loss models.

E. BOXER (NASA Langley Research Center): The Lewis Research Center's compressor research program you have outlined is both comprehensive and well ordered. I have just one question to ask and several comments to make. The question concerns the curves presented in the first two slides. For the ordinate scale to be meaningful, it is necessary to know the assumed value of hub-tip radius ratio, tip solidity, radial distribution of both loss coefficient and work, and the maximum value of tip turning angle or annulus contraction through the rotor. Can they be provided?

The advantages of pursuing a compressor research program based essentially upon tests of rotors or complete stages are self-evident, in that the performance maps obtained are valid, containing as they do the three-dimensional effects of off-design operation, secondary and boundary layer flows, and shock-boundary layer interactions which are only qualitatively predictable. Unfortunately, with this approach, even with peripheral sensors, there is a lack of detailed knowledge of the fluid behavior within the blade passage. Without such knowledge, extrapolation of compressor performance into regions beyond current experience is subject to wide deviations. In addition, for a series of research rotors designed for a given task, it is almost impossible to vary one significant design parameter without subtle changes in other variables which may have an appreciable effect upon the reported trends. For example, the stated influence of throat area ratio upon maximum efficiency at off-design speeds, based upon the data of figure 7, ignores the variation in relative turning angle and overall annular area contraction between rotors 2*B* and 2*D* (which are identical except for meanline shape) with that of rotor 1*B*. It appears likely that throat area ratio is only one of several geometric variables responsible for the observed trend and may not be the principal responsible variable. In fact, rotors 2*B* and 2*D*, which have the greatest divergence in design throat area ratio, are remarkably similar in their speed-efficiency relationship, whereas rotor 1*B* exhibits a distinctly different slope with only a third of the throat area change from that of rotor 2*B* as compared to rotors 2*B* and 2*D*.

To make the NASA-Lewis program more meaningful to compressor designers and to permit extrapolation for conditions beyond the scope of rotor tests, I feel that more fundamental experimental studies should complement the program. A recent paper (ref. D–4) indicates that with careful attention to small details supersonic cascade data can correlate with rotor data. I would suggest that a useful adjunct to a well-rounded program would be a continuation of supersonic cascade testing.

F. GILMAN (Worthington): It may be of interest to this audience to know that Dr. Wislicenus was one of the first to suggest that transonic and supersonic axial-flow compressors could have practical value and were worthy of investigation. The wheel which Dr. Wislicenus designed for transonic relative flow had a 10-inch tip diameter and a constant 7$\frac{1}{8}$-inch hub diameter. The five blades of this impeller were milled with straight helical surfaces on their pressure faces and single-circular-arc profiles for suction faces. An overall compressor efficiency of 78 percent was obtained with a tip velocity of 1050 feet per second, and the pressure ratio at best efficiency was 1.30. Stable operation extended between 60 and 90 CFS. Discovery of the workability of this transonic range in 1946 was new and interesting and formed the basis for a later three-stage transonic axial-flow test program at Worthington.

BENSER (author): The assumptions used in the calculations of figures 1 and 2 were as follows:

(1) Hub-tip ratio at the rotor inlet equal 0.5
(2) Constant work input from root to tip
(3) Constant polyhopic efficiency of 0.9 root to tip
(4) Axial velocity ratio of 1 across the rotor blade row
(5) Simple radial equilibrium

(6) Rotor tip solidity equal 1.5
(7) Axial velocity equal 600 ft/sec
(8) Zero inlet whirl

The analysis based on these assumptions is extremely simplified and is used to indicate trends rather than to define exact values of design or performance parameters. A more complete analysis of the effects of variations of design variables is given in reference D–5.

As stated by Mr. Boxer, it is extremely difficult to isolate the effects of variations of a single parameter by comparison of test results from single rotors or single stages, because variations cannot be restricted to a single parameter. By such comparisons, however, it is hoped that some empirical design rules can be derived which will lead to improved design control. The throat area ratio concept is such an empirical rule which has currently been applied to designs with considerable success. The data of figures 6 and 7 show the effect of throat area ratio on efficiency and range. Rotor and stator data discussed by Mr. Keenan as well as other NASA data substantiate the trends shown in these figures.

The flow processes within transonic axial-flow compressor blade rows are extremely complex and our design concepts, which are essentially axisymmetric approaches, are certainly limited where strong shocks exist in the blade-to-blade planes. Supersonic cascades may be useful in studying details of flow in the blade-to-blade plane. More detailed flow measurements within the rotating blade row would also be helpful. To date, the NASA Lewis research has been concentrated on single rotor and single stage tests. The NASA rotor and stage program has been supplemented by theoretical studies, but no supersonic cascade tests have been run.

In our attempts to determine the mechanism by which casing treatment improves stall margin, we have postulated many models, as Mr. Koch has stated. To date, no single model has been found which explains all of the results obtained. This may be due to the fact that we have not as yet set up the proper model, or it may be due to the fact that there is more than one mechanism involved. Many empirical rules for casing treatment have been evolved, but more understanding of the phenomenon is necessary in order to optimize designs for any given application.

REFERENCES

D–1. McMahan, K. D., and N. P. Bailey, *Centrifugal Compressor.* U.S. Patent 2,453,524, application date May 31, 1945.

D–2. Sulam, D. H., M. J. Keenan, and J. T. Flynn, Data and Performance, Multiple Circular Arc Rotor. *Single Stage Evaluation of Highly-Loaded High-Mach-Number Compressor Stages, Part II,* NACA CR 72694, 1970.

D-3. Miller, G. R., and M. J. Hartmann, *Experimental Shock Configurations and Shock Losses in a Transonic-Compressor Rotor at Design Speed.* NACA RM E58A14b.

D-4. Mikolajczak, et al., ASME paper 70-GT-79. Presented in Brussels in the spring of 1970.

D-5. Miller, M. L., and A. C. Bryans, *Parametric Study of Advanced Multistage Axial-Flow Compressors.* NASA CR 797.

Blade Selection for a Modern Axial-Flow Compressor

L. C. WRIGHT

AiResearch Manufacturing Company

In spite of the high-speed digital computer, no theoretical procedure for solving the real, three-dimensional, compressible flow, cascade problem yet appears imminent. However, under the pressure of engineering necessity, a practical, sophisticated combination theoretical and empirical design approach has evolved which utilizes a quasi-three-dimensional calculation procedure (the combination of essentially 2 two-dimensional procedures). The following is a satisfactory list of steps which have led to successful designs.

(1) Selection of the average pressure ratio and temperature rise or efficiency per stage (from past experience or literature)
(2) Definition of the span-wise variation of pressure ratio and loss or efficiency (from experience or literature)
(3) Under the assumption of axial symmetry, solution of the radial component of the equations of motion, yielding the blade row inlet and outlet velocity diagrams
(4) Selection or calculation of the two-dimensional blade sections to match the velocity diagrams determined in (3)

This paper is primarily concerned with (4): the methods used in the past, those presently in use, and some possible innovations which might extend the achievements of this approach to still higher performance levels.

A short summary of the published cascade data most used in this country is given along with some speculation on the type of design approach and blade section design concepts which might provide the next improvements in compressor technology.

The success of an axial-flow compressor design depends upon the proper execution of several steps. Assuming that the secondary flows, loss variations, and boundary layer growths are properly accounted for; that the ultimate loading limits are not exceeded; and that the axisymmetric calculation of blade row inlet and outlet velocity diagrams are correctly performed, the achievement of design point operation depends entirely on the proper selection of blade shapes. However, other factors such as Mach number and proximity of the selected design point to the ultimate loading limits may determine range of operation or off-design performance levels. Range of operation is, of course, important in high pressure ratio, multistage, engine compressors in that it may not be possible to operate the compressor through the midspeed regions to reach the design point without mechanical aids (e.g., bleed and/or variable vanes). Neglecting for the moment these considerations, which constitute more properly a study for off-design performance prediction, the process of blade shape selection is examined.

Three related approaches to cascade selection are theoretically possible.

(1) The purely experimental approach which relies entirely on the use of experimental results from identical cascades to satisfy the velocity diagrams calculated

(2) A purely analytical procedure whereby blade shapes are calculated from the theoretical cascade and viscous flow equations

(3) A semiempirical procedure which utilizes experimental data together with the theoretically derived functional relations to relate the cascade parameters (solidity, angle of attack, stagger angle, cascade turning, airfoil thickness, etc.)

Each approach has its advantages and disadvantages. The purely empirical approach (1) is most limited because it requires huge amounts of data to duplicate any design situation which might arise. However, if the proper data can be located (in literature or from in-house test programs) it provides a nerve-soothing assurance when expensive engine programs are contemplated. The purely theoretical approach (2) is ideal in all aspects except that of implementation. As of now, it is not possible to solve such real flow problems as those posed by today's practical turbomachinery designs. The final and almost universally used procedure (3) provides the optimum combination of assurance and range of application. Further, it allows encroachment into the more complex and comprehensive realm of the purely theoretical. The insertion of experimentally derived coefficients into the intractable theoretical relations provides a design capability which can, with continuing research, approach arbitrarily close to the generality offered by the purely theoretical.

CRITERIA FOR BLADE SECTION SELECTION

In the design of modern flight-type, axial-flow blade rows, size and weight are inevitably important. Assuming that a respectable efficiency could be maintained, it would then appear that only highly loaded, high Mach number sections are of current importance. However, there are many cases, such as the latter stages in multistage compressors, where

Mach numbers are moderate (due to the temperature rise) and incidence angle range requirements dictate moderate dimensionless loading as defined by D-factor and $\Delta P/q$. Moreover, the stator vanes in all current high-performance, flight-type compressors fit this description fairly closely. Consequently, blade sections which can operate with very low losses under these conditions are vitally important. Such sections exist in the empirical cascade domain. The NACA 65-series blower blade sections (or variations of these) have proved near optimum for this application (refs. 1, 2, and 3).

The NACA 65-series cascade data in its original form (ref. 1), in the form of carpet plots (ref. 2), or as replotted by Mellor's charts (ref. 3) constitute the most widely published cascade data available in America. Mellor's presentation, in particular, gives these experimental cascade results in a convenient form for designers.

It should be noted that the referenced NACA cascade data, whatever the presentation form, are two-dimensional data, while the designer is usually faced with a distinctly three-dimensional flow problem. Consequently, precautions should be taken to ensure that the cascade data are applied to sections which have the same effective circulation, considering both changes in radius between the section leading edge and trailing edge and inlet/exit annulus area ratio. Factors to be considered in adapting the two-dimensional cascade data to the three-dimensional compressor problem will be discussed in a later section.

PROCEDURES FOR VARIOUS BLADE SECTION DESIGNS

Depending on the type of cascade selected, the designer has various loosely established procedures for effecting his design. Table I summarizes the Mach number ranges in which the modern aerodynamic designer must work and the generally acceptable cascade types for each range.

Experience has shown that the simple expedient of selecting cascade sections according to these broad overlapping Mach number ranges essentially eliminates the possibility of designs with inherently improper section types.

65-Series Thickness Distribution on Circular Arc Meanline

Sections consisting of circular arc meanlines with 65-series thickness distributions are commonly and successfully used in the low-to-moderate Mach number range ($M \leq 0.78$). For these sections, empirical incidence and deviation angle rules usually replace the strict application of the NACA cascade data.

TABLE I.—*Mach Number Range—Blade Section Type Correlation*

Category number	Design point inlet Mach number	Recommended section types
1	$M \leq 0.78$	NACA 65-series blades, circular or parabolic arc meanlines
2	$0.70 \leq M \leq 1.20$	Double circular arc sections
3	$1.10 \leq M \leq 1.50$	Arbitrary straight leading edge sections, specially designed sections, multiple circular sections
4	$M > 1.50$	Special normal shock-free sections

Figure 1 shows the standard cascade parameters. Blade geometry is usually defined by the blade profile, the stagger or chord angle λ, camber angle φ, and the blade row solidity σ (see table of symbols). Also illustrated are the important aerodynamic parameters such as the cascade inlet velocity W_1, the flow inlet angle β_1', the outlet velocity W_2, the outlet flow angle β_2', and the blade deviation angle $\delta°$.

The blade resulting from the application of the 65-series thickness distribution (see table I, ref. 1) to a circular arc meanline is a hybrid. Consequently, some means of determining the blade setting and blade camber is required. In order to permit some use of the cascade data from reference 1, an equivalence has been established between the NACA $(a=1)$ (uniformly loaded) meanline and the circular arc meanline. This process is described in reference 4 and the actual equivalence is presented in figure 2 along with some other useful geometrical relations. It is now possible to obtain reasonable setting angles for the hybrid section from the experimental 65-series cascade data given in references 1 through 3.

For practical compressor blade (or vane) designs using this type section, it may be more prudent to use the store of single stage blade element performance data of the type published in many NACA references; e.g., references 4 through 6. These reports present, for a range of geometrical conditions, experimental blade element data which relate element loss coefficient and deviation angle as functions of blade element incidence angle. These are precisely the parameters which must be set by the designer to implement his design. These data have been used for blade setting with excellent results in spite of the differences in thickness distribution between the hybrid and the biconvex sections. The acceptability of the procedures just described is implied by the results shown in reference 7.

Reference 7 presents a comparison of the performance of the British NGTE circular arc meanline (10C4/30C50) sections with the equivalent

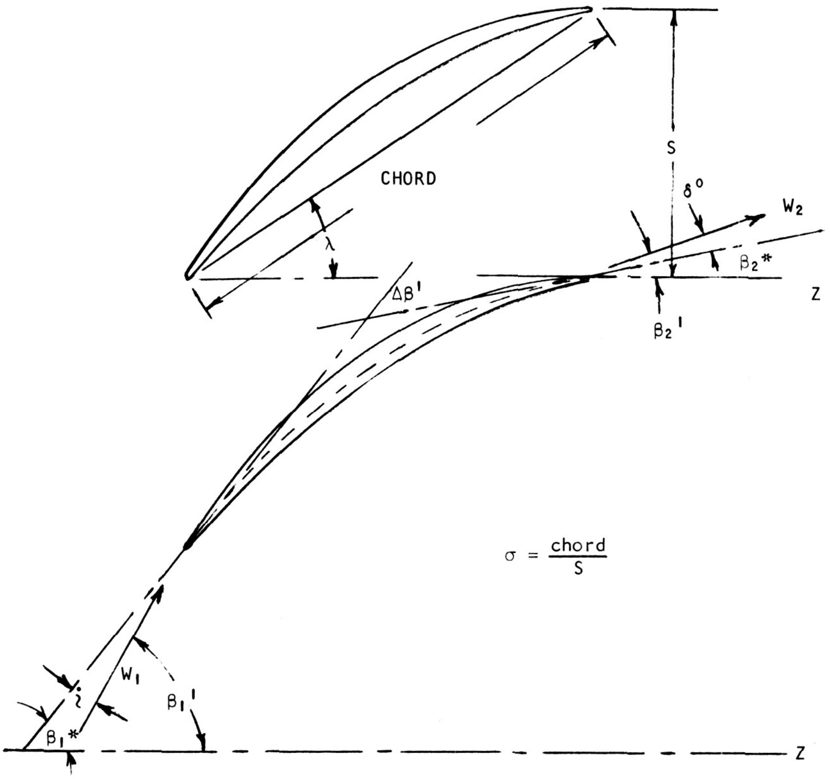

FIGURE 1.—*Standard cascade parameters.*

NACA 65 $(12A_{10})$ 10 section. The relatively small turning angle differences (approximately 3° maximum) between the NGTE and NACA tabulations appear to result from the fact that porous cascade tunnel walls were used for the NACA section while the NGTE used solid walls. Loss variation, surface velocities, and turning angles are shown to be very similar when tested under the same conditions. The surface pressure distributions indicate a slightly higher critical Mach number for the NACA sections.

The deviation angles for the hybrid sections have been shown to correlate well with Carter's deviation angle rule (ref. 8). Carter's rule gives the deviation angle as a function of turning angle, cascade solidity, and a parameter m in the following relation.

$$\delta^\circ = m\frac{\varphi}{\sqrt{\sigma}} \tag{1}$$

The parameter m is given in figure 3 and may be expressed closely as a function of the blade stagger angle λ by the following expression:

$$m = .216 + .000875\lambda + .00002625\lambda^2 \tag{2}$$

where λ is in degrees.

The hybrid section is not recommended for design Mach numbers above 0.78 and hence choking considerations are not too vital in general. However, because the operating conditions in many multistage units may

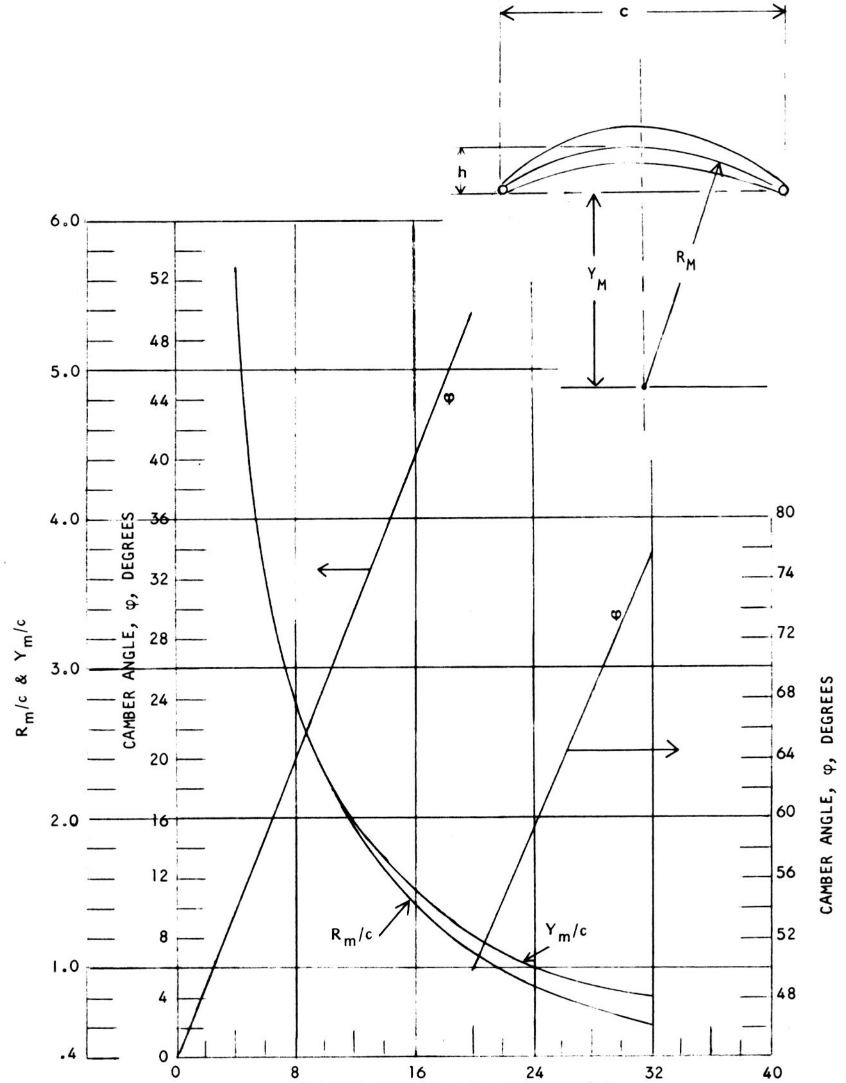

FIGURE 2.—*Equivalence between circular arc meanline camber and the NACA* (a = *1*) *lift coefficient.*

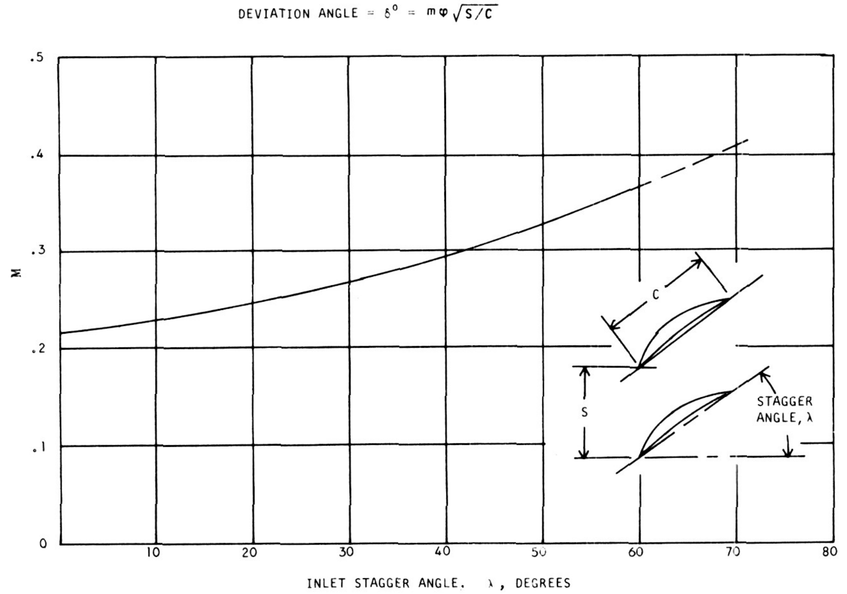

FIGURE 3.—*Carter's rule for deviation angle at optimum incidence for compressor cascades using circular-arc camber lines (ref. 8).*

undergo large swings from design, the critical Mach number (Mach number where the suction surface velocity first reaches unity) and the cascade choking inlet incidence Mach number should be determined.

Standard 65-($a = 1$ Meanline) Section

The 65-series blades of reference 1 were derived to be used directly in the design of cascades in category 1, Table I. These data have been used with contemporary success in the design of both single and multistage compressors (refs. 9 and 10).

The cascade summary of either of the 65-series data formulations (refs. 1 through 3) could be used in the design procedure for the standard sections. The cascade data of reference 1, which was obtained by holding the flow angle and varying the cascade angle, has been cross plotted in reference 3 to permit a more convenient section selection procedure. Referring to figure 4, the inlet and outlet flow angles β_1 and β_2 constitute the abscissa and ordinate, respectively. Lines of constant stagger angle λ and angle of attack α are also shown. The inlet and exit flow angles may now be taken from the velocity diagrams resulting from the radial equilibrium calculations and located on a plot of the type of figure 4 for an acceptable solidity and lift coefficient. The criterion for acceptance of these parameter values is a combination of the desired location of the

β_1,β_2 intersection in the experimentally defined useful range between the positive (stalling) angle of attack and the negative (choking) value on the desired solidity figure. The blade sections to match the stagger, solidity, angle of attack, camber and percent thickness may then be defined as shown in reference 1.

The results of reference 9 provide a clear indication that the pure 65-series ($a=1$ meanline) sections may still be appropriately used in category 1 ($M \leq 0.78$). It is primarily for simplicity that the circular arc meanline has largely replaced the original ($a=1$ meanline) calculated for uniform chordwise loading.

It is currently common practice to use the 65-series thickness distribution for stator sections whether ($a=1$) or circular arc meanlines are

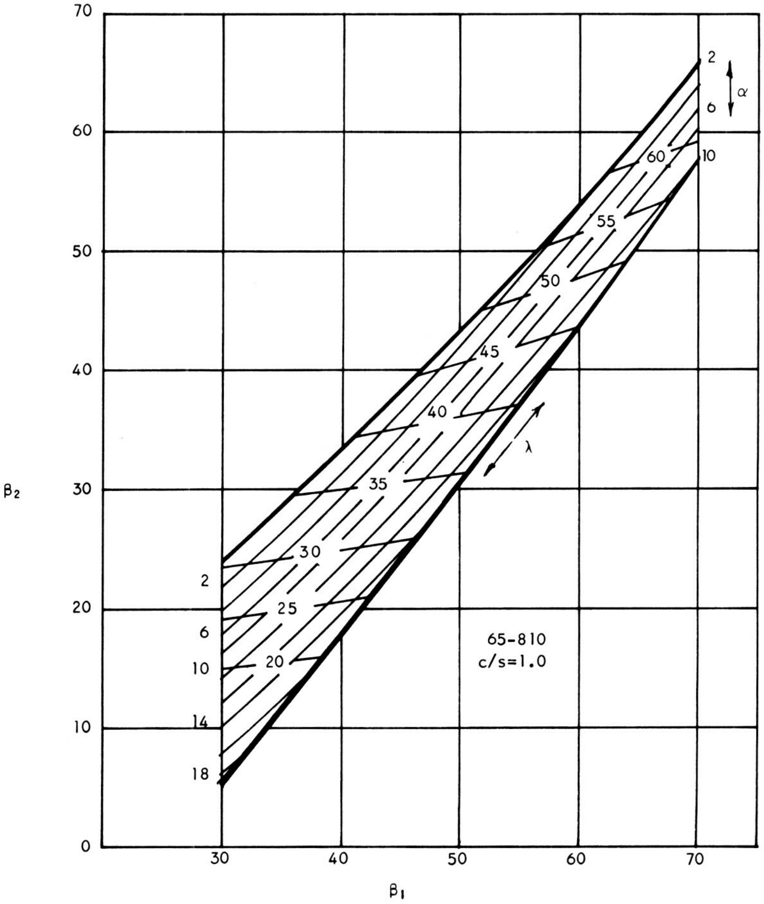

FIGURE 4.—*Typical representation of the Mellor (ref. 3) display of the NACA 65-series cascade data.*

used. There is some indication that sections using a 65-series thickness distribution, particularly in the section nose region can tolerate a wider range of incidence regardless of the meanline to which it is applied. Accordingly, the procedure for defining the leading edge nose radius illustrated in figure 5 has been used for sections which have symmetrical thickness about the meanline. The smaller radius represents the lower limit on the leading edge dimensional tolerance. The radius of the larger circle represents the upper tolerance limit on leading edge diameter. A smooth fairing from the smaller circle to the basic contour at four large diameters downstream of the leading edge completes the blade section. Although the fairing illustrated using the small circle is preferred, the difficulty of maintaining accurate dimensions on these very small leading edge dimensions make anything between and including the two contours illustrated acceptable.

Double Circular Arc and Other Circular Arc Meanline Sections

In the early 1950's, the NACA set out to provide experimental blade element design data for transonic blade sections via single stage compressor tests (ref. 11). These are the sections designated in table I as most satisfactory for category 2. Early NACA transonic, single stage tests (e.g., ref. 12) had demonstrated good performance with double circular arc sections (sections composed of two circular arcs of different radii intersecting at two points). Moreover, these sections were simple, easy to manufacture, and possessed the characteristics which appeared analytically desirable for transonic blades. Hence the NACA program of transonic compressor element design data accumulation utilized these sections.

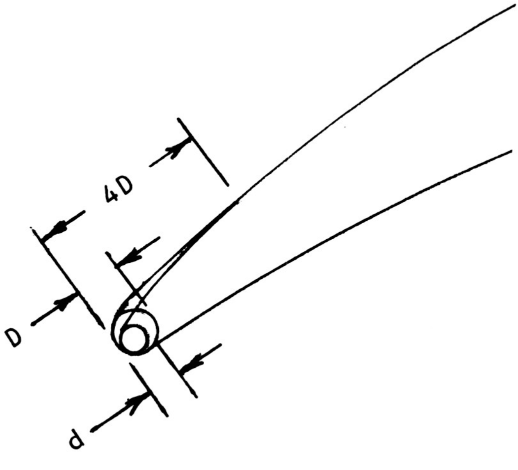

FIGURE 5.—*Application of blade leading edge tolerance.*

In a sense, this program constituted a departure from the original concept of a quasi-three-dimensional design procedure wherein 2 two-dimensional calculations (in the radial-axial plane and the tangential plane) were combined to define the entire flow field. Actually, compressor element performance data, as tabulated by NASA, reflect many phenomena which do not originate in the two-dimensional flow field. Therefore, in an inadvertent way, such effects as secondary flow, boundary layer centrifugation, tip clearance vorticity, wall boundary layer, and annulus convergence are confounded in the single stage element data with the true cascade variations. Under these conditions the true relations between the cascade parameters are not easily isolated. Even so, blade rows of a sufficient range of radius ratios, Mach numbers, stagger angles, camber angles, solidities, and thickness were tested to provide the designer with a suitable model for almost any configuration he contemplated designing. (See refs. 4, 5, 6, 11, 12, 13, and 14.) In addition, several analyses and correlations (refs. 15 through 18) provided aid in interpreting and adapting the cascade data substitutes obtained from the single stage tests to actual design problems. In spite of the obvious confounding of two- and three-dimensional effects, the results of using these data in industrial transonic compressor design must be considered highly successful.

In England, Andrews (ref. 19) investigated the circular arc sections in a 2-dimensional cascade tunnel. These results demonstrated clearly that the basic double circular arc sections could provide highly satisfactory transonic blades. The designer was now able to cross check the single stage elements data (obtained from single stage tests) with that from circular arc sections in 2-dimensional cascades.

The double circular arc has been closely associated with the transonic compressor from its inception. This fact is clearly illustrated by reference 20 in which the highlights of the transonic compressor development are summarized. R. O. Bullock discusses the various NACA investigations designed to illuminate the phenomena involved in transonic compression and make more general the cascade design data obtained.

With the advent of the transonic stages and the single stage element data the presentation format was altered from, for example, the cascade results of reference 1. A typical plot of element data for a single section taken from reference 5 is shown in figure 6. Here the design parameters loss coefficient $\bar{\omega}$, deviation angle δ°, D-factor, blade row inlet relative Mach number M_1', element efficiency η, work coefficient $\Delta H/U_t^2$ and axial velocity ratio C_{z_2}/C_{z_1} are given as functions of the independent variable incidence angle i. Such data are extremely useful in predicting the actual performance to be expected in a real design once certain similarity criteria (e.g., loading, solidity, stagger angle, and Mach number) have been satisfied.

The work of Lieblein (ref. 21) gave a significant tool to the transonic compressor field in its formulation of a loss criterion. Although the correlation of the large store of available loss data against a diffusion parameter D showed a high degree of scatter, a rational and useful basis for loss projection was created.

Chapter VII of reference 22, on blade element flow in annular cascades, provides some basic information on the correction and use of available blade element data on a generalized basis. In particular, it provides losses and curves for conversion of two-dimensional incidence and deviation angle data for use in annular cascades, considering both Mach number and radial position in the annulus of the element under consideration.

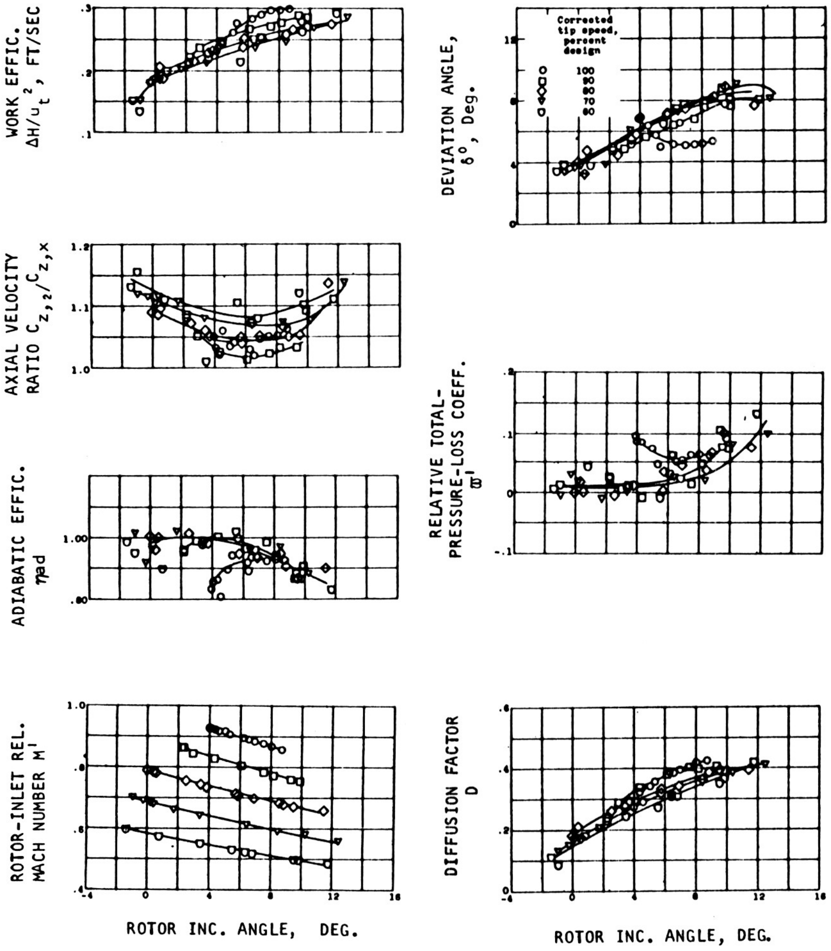

FIGURE 6.—*Typical presentation format for single-stage element data (ref. 5).*

One of the early multistage transonic compressors was the 1954 NACA 5-stage for which design and experimental evaluation are recounted in references 23 through 26. This compressor, which utilized an engine as a source of drive power, had all circular arc meanline sections and each of its five stages operated with transonic inlet relative velocity. A basic objective of this program was demonstration of the practicality of staging high pressure ratio transonic stages. The results from this program provided a large amount of information on the interaction of transonic stages and essentially verified the plausibility of the blade element or annular cascade approach as well as the utility of double circular arc and circular arc meanline sections.

With the velocity diagrams known and a section type selected, the empirical element data such as loss and deviation angle versus incidence angle data just discussed (e.g., ref. 22), permit the straightforward design of compressors in Mach number category 1.

Arbitrary or Multiple Circular Arc Sections

It has been demonstrated that cascade losses go up as Mach number exceeds the section critical Mach number. However, for rotors these losses are largely compensated for by the increased work generated by the higher wheel speed. Hence, for Mach numbers up to approximately 1.10 to 1.20, little, if any, penalty in rotor efficiency is experienced. At blade relative Mach numbers somewhere above 1.1 for the current state of the art, efficiency begins to drop in spite of the increase in useful work with the double circular arc or circular arc meanline sections. Detail study of the passage flow phenomena indicated that the Mach numbers at which the tip passage shocks occurred were high enough to cause, for the first time, nonnegligible shock losses as well as secondary losses resulting from shock separation of the boundary layer.

Some experimental studies utilizing high-frequency response probes showed clearly the mechanism of the rotor tip shock structures (Ref. 15). From this understanding evolved a better picture of the type of blade which would minimize these shock losses at a given Mach number and increase the tip speed and hence Mach numbers and pressure ratio before the efficiency would begin to drop. Generally, it became clear that curvature of the suction surface of the blades between the leading edge and the final, strong shock generated Prandtl-Meyer expansions, increasing the preshock inlet Mach numbers appreciably. Apparently, reduction in this curvature or leading edge camber would lower the preshock Mach number and reduce losses. The rotor of reference 27 demonstrated that this did in fact occur. A major effort was made in this rotor to balance the dimensionless static pressure rise between the rotor and stator. However, perhaps a more important feature was the design procedure which yielded a very small blade leading edge camber. The resulting rotor demonstrated a very creditable peak design speed efficiency of 0.89 at a pressure ratio of 2.12 in spite of a design tip relative Mach number of 1.48.

Subsequently, many investigators devised design procedures which guaranteed a blade of zero or near zero camber in the supersonic region of the blade (see fig. 7). The design techniques included the solution of the radial equilibrium equations inside the blade row and "tailoring" the blade to the relative flow direction throughout the blade row (see ref. 28).

The benefits of blade sections with uncambered supersonic regions are now generally accepted and substantial effort has been devoted to

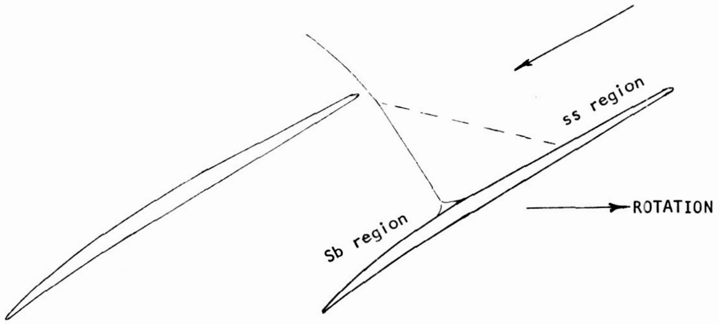

a.—*Arbitrary sections with uncambered leading edge.*

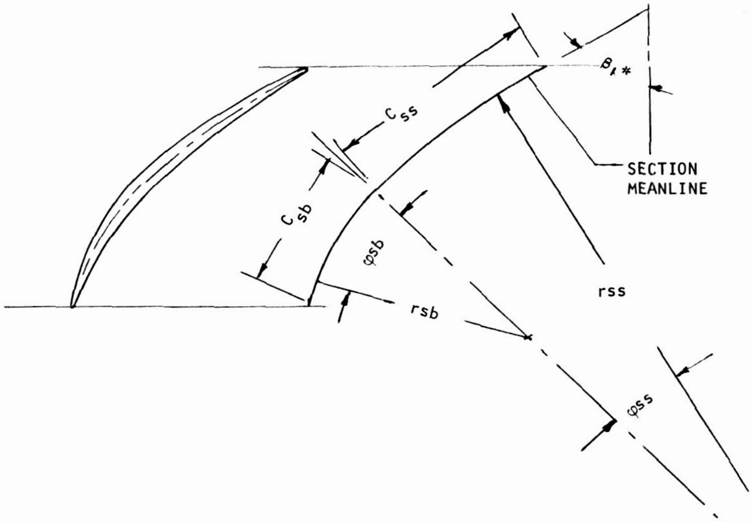

b.—*Multiple circular arc section.*

FIGURE 7.—*Typical transonic blade sections with uncambered leading edge.*

systematizing such sections (see ref. 29). The selected sections of reference 29 are defined by multiple circular arcs. The meanlines of these sections are made up of two circular arcs with mutual tangents at their juncture (see fig. 7*b*). The larger radius arc forms the leading edge (supersonic) portion of the blade while the smaller arc constitutes the rearward (subsonic) portion. It is concluded in reference 29 that the optimum blade achieves the best balance between the supersonic shock losses and the subsonic diffusion losses. The ratio of the leading edge (supersonic region) camber to the total blade camber is called the camber ratio. This ratio provides a parameter to which systematic changes may be made to achieve the optimum loss balance.

Reference 3 reports the experimental performance from four multiple circular arc rotors designed and investigated by General Electric under NASA contract. The results appear significant, varying in such a manner as to verify the loss mechanism hypothesized for transonic blades. It can, therefore, be concluded that the multiple circular arc section shape format does provide a satisfactory cascade base for systematic variation of the geometric and hence aerodynamic properties.

Moderate Supersonic Mach Number Sections

Supersonic compressors have been seriously considered in America since the early 1940's. As conceived at that time, the supersonic rotor would consist of a row of blades comprising a series of rotating supersonic diffusers. The blade relative inlet velocity was supersonic along the entire blade span and a strong shock was stabilized in each passage (refs. 31 and 32). That this somewhat idealized concept did not yield an immediately practical engine compressor is probably primarily due to the shock boundary layer interaction, the radially nonconstant angles and velocity at the rotor inlet, and the difficulty in satisfying simultaneously radial equilibrium and the shock equations as well as other real flow effects.

Most blade sections were developed using a two-dimensional method of characteristics which did not rely at all on cascade data. The principal outputs to date from the U.S. supersonic compressor programs have been, first, the feasibility demonstration, and, second, provision of detail insight into the flow phenomena associated with transonic compressors.

Today there is a renewed interest in supersonic compressors for various applications. However, the concepts are more mature and the requirements more demanding. Considerable interest is focussed on the potential of rotors which utilize high tip speeds and weak oblique shocks which do not diffuse through Mach 1.0 in the tip regions where shock losses could be large. Possible advantages of this type rotor include the possibility of high pressure ratio, uniformly loaded rotors with low radius ratios, and good efficiency along the entire blade span. Also, current high bypass ratio fan engines are usually restricted to low rpm by fan tip speed while the smaller diameter fan turbine has many stages to compensate for its low tip speed.

The type of blade sections required for this category 4 type of supersonic compressor are not yet generally defined. These sections will probably require a more intimate mingling of the two- and three-dimensional flow calculations than previous compressor types utilized. In order to avoid the strong shocks at the design point, the passage through flow areas must be carefully controlled, and the old procedures for section layouts (probably not on constant radius surfaces) utilizing a supersonic method of characteristics will probably be required. As always, the stream surfaces will reflect the radial equilibrium equations.

OTHER CASCADE CONSIDERATIONS

In the application of either two-dimensional design rules or cascade data to the design of real compressor blades, most often the stream surface intersects the blade leading edge at one radius and intersects the trailing edge at another. As previously stated, blade sections defined on such surfaces should be related to true two-dimensional sections on the basis of equivalent circulation. The following expressions define $\beta'_{2,e}$ and $\beta_{2,e}$ the equivalent (two-dimensional cascade) trailing edge angles for a rotating and a stationary blade section, respectively.

$$\left.\begin{aligned}\tan \beta'_{2,e} &= \frac{r_2 C_{z2}}{r_1 C_{z_1}} \tan \beta_2 + \frac{U_1}{C_{z_1}}\left[1-\left(\frac{r_2}{r_1}\right)^2\right] \\ \tan \beta_{2,e} &= \frac{r_2 C_{z2}}{r_1 C_{z_1}} \tan \beta_2\end{aligned}\right\} \tag{3}$$

These angles represent the three-dimensional blade (or vane) discharge angles which would give the same circulation as the actual section along the actual stream surface but with constant radius and axial velocity. The use of these discharge angles permits the direct application of two-dimensionally derived incidence or deviation angles or cascade data.

The angles β and β' are defined as $\tan^{-1} C_u/C_z$ and $\tan^{-1} W_u/C_z$, respectively, and neglect the radial components of velocity. It therefore became necessary to make geometrical corrections to the blade angles β when sections are defined on cylindrical surfaces and the blade elements are neither radial nor normal to the axis (see Appendix B of ref. 36), and radial velocity components exist.

The final expression for the corrected blade angle on the cylindrical surface is given as

$$\tan \beta(\text{corrected}) = \frac{\tan \varphi \tan \epsilon + \dfrac{\tan \beta}{\cos \varphi}}{1 - \tan L \tan \epsilon} \tag{4}$$

In the case where the element is normal to the axis (sweep angle $L=0$) the considerably simpler expression which follows may be derived for the corrected β.

$$\tan \beta(\text{corrected}) = \tan \beta - \tan \varphi \tan \epsilon \tag{5}$$

It can be seen that for large hub slopes and lean angles a substantial correction is required for the blade tangent angle on the cylindrical surface. This complication may be eliminated by laying the blade out on a stream surface. The stream surface can usually be assumed to be a conical surface with little error. A procedure and the computer program for defining double and multiple circular arc blades on conical surfaces are given in reference 33. The procedure is designed to preserve the rate of change of surface angle with distance on the specified conical surface. From these calculated sections, new sections outlined by the intersections of plane surfaces with the blade which results from the conical surface profiles are defined. The area, center of area, and moments of inertia are computed for use in the blade stress analysis. The program also can be made to give any degree of tilt (tangential lean) desired for stress reasons.

Once the blade sections are completely defined and stacked, the section layouts together with the stream surface traces in the radial-axial plane permit the determination of the cascade throat areas. With these data the blade choking incidence angles may be determined. It is important to compare the section choking incidences with the selected design values and ascertain that some margin (e.g., 2° to 6°, depending on the design) exists between choke and design.

Some other miscellaneous considerations include the importance of blade surface finish and trailing edge thickness. These topics are covered in references 34 and 35. Indications are that for a trailing edge thickness up to 30 percent of the maximum thickness, no increase in loss with thickness has been observed for compressor cascades. The case for surface finish is less conclusive. There have been indications from time to time that, under some conditions of low Reynolds number and/or high Mach number operation, some surface roughness is beneficial. The conclusions in reference 35 are that nothing is gained by using finishes better than 40 microinches root-mean-square for conventional compressors.

Multistage Example

The range of section types used in current jet engine turbomachinery is illustrated by a typical multistage mix in figure 8. A high performance,

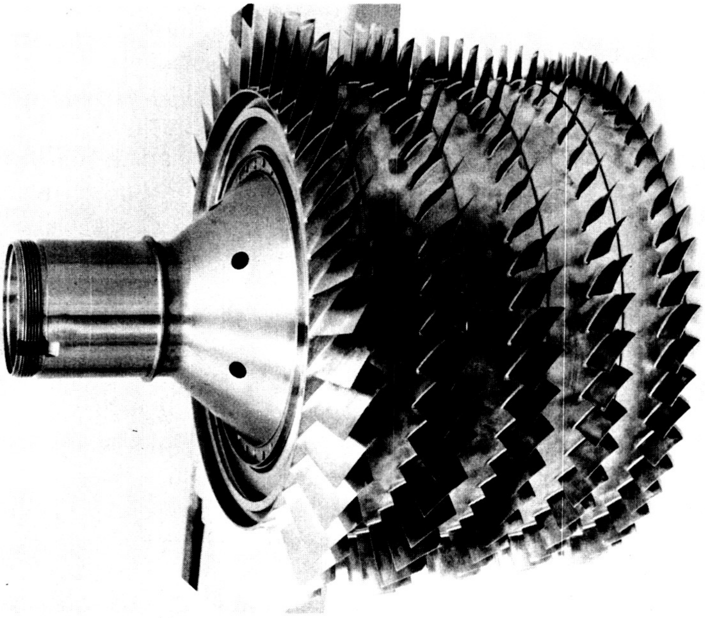

FIGURE 8a.—*High-performance five-stage compressor rotor.* (*AiResearch Manufacturing Division, Garrett Corporation*)

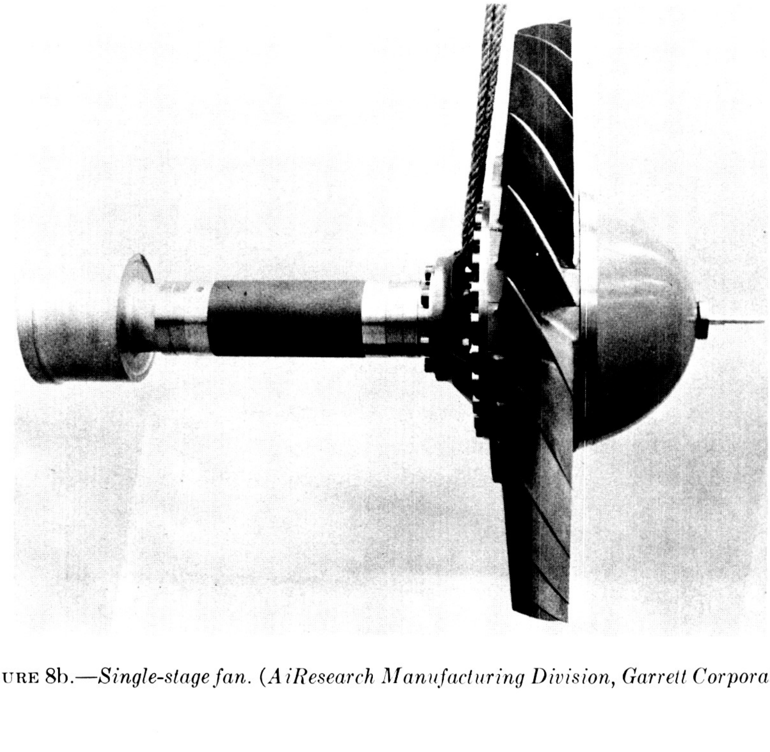

FIGURE 8b.—*Single-stage fan.* (*AiResearch Manufacturing Division, Garrett Corporation*)

5-stage compressor rotor is shown in figure 8*a*. Rotor 1 has special or arbitrary sections; all stators are circular arc meanlines with 65-series thicknesses. Rotors 2 through 5 utilize double circular arc sections. The single stage fan shown in figure 8*b* gave efficiencies in the high eighties at a design speed pressure ratio of 1.6. The sections varied from the arbitrary, uncambered leading edge region at the tip to a near circular arc meanline hub.

CONCLUDING REMARKS

The preceding remarks constitute a highly condensed and heavily referenced summary of the methods of cascade selection and design available today to the practical compressor aerodynamicist. Throughout the entire field, the emphasis has been, and still is, on the semiempirical approach. For the designer who dedicates himself to understanding the fundamental phenomena involved in cascade flow, the methods described can be used quite successfully. Beyond this, possibilities for future improvement in cascade performance appear abundant, and it is largely from this source that large gains in future turbine engines will probably come.

LIST OF SYMBOLS

C	Absolute velocity, ft/sec
c	Blade chord
D	Dimensionless loading parameter, $\left(1-\frac{W_2}{W_1}\right)+\frac{R_2C_{u_2}-R_1C_{u_1}}{2R\sigma W_1}$
ΔH	Enthalpy rise, ft-lb/slug
h	Blade camber
i	Incidence angle, $\beta_1'-\beta_1^*$, degrees (see fig. 1)
L	Blade sweep angle in plane of blade leading edge, degrees
M	Mach number
$\Delta P/q$	Dimensionless static pressure rise coefficient
R_m	Blade mean camber-line radius, inches
R_m/c	Blade mean camber-line radius normalized by blade chord
U	Wheel speed, ft/sec
W	Velocity relative to rotor, ft/sec
Y_m	Distance from center of meanline circle to chord
Y_m/c	Distance from center of meanline circle to chord normalized by blade chord
α	Angle between the flow direction and the blade chord, degrees

β	Angle measured from axial, $\tan \frac{C_u}{C_z}$, degrees
δ°	Deviation angle $\beta_2' - \beta_2^*$, degrees (see figure 1)
ϵ	Blade lean angle, degrees
σ	Solidity, blade chord/blade spacing
φ	Camber angle, $\beta_2^* - \beta_1^*$, degrees
$\bar{\omega}$	Total pressure loss coefficient

Superscripts

$*$	Geometrical
$'$	Relative to the rotor

Subscripts

e	Equivalent
m	Mean
sb	Subsonic
ss	Supersonic
t	Tip
u	Tangential component
z	Axial component
1	Blade row inlet
2	Blade row outlet

REFERENCES

1. Herrig, L. Joseph, James Emery, and John R. Erwin, *Systematic Two-Dimensional Cascade Tests of 65-Series Compressor Blades at Low Speeds.* NACA RM L51G31, September 1951.
2. Felix, Richard A., *Summary of 65-Series Compressor-Blade Low-Speed Cascade Data by Use of the Carpet-Plotting Technique.* NACA RM L54H18a, November 2, 1954.
3. Mellor, G., *The Aerodynamic Performance of Axial Compressor Cascades With Application to Machine Design.* MIT Gas Turbine Lab Report No. 38, 1957.
4. Schwenk, Francis C., Seymour Lieblein, and George W. Lewis, Jr., Blade-Row Performance of Stage With Transonic Rotor and Subsonic Stators at Corrected Tip Speeds of 800 and 1000 Feet Per Second. *Experimental Investigation of Axial-Flow Compressor Inlet Stage Operating at Transonic Relative Inlet Mach Numbers, Part III,* NACA RM E53G17, September 18, 1953.
5. Tysl, Edward R., and Francis C. Schwenk, Blade-Element and Over-All Performance at Three Solidity Levels. *Experimental Investigation of a Transonic Compressor Rotor With 1.5-inch Chord Length and Aspect Ratio of 3.0, Part III,* NACA RM E56D06, August 17, 1956.
6. Montgomery, John C., and Frederick W. Glaser, Stage and Blade-Element Performance. *Experimental Investigation of a 0.4 Hub-Tip Diameter Ratio Axial-Flow Compressor Inlet Stage at Transonic Inlet Relative Mach Numbers, Part II,* NACA RM E54I29, January 10, 1955.

7. Felix, Richard A., and James C. Emery, *Comparison of Typical National Gas Turbine Establishment and NACA Axial-Flow Compressor Blade Sections in Cascade at Low Speed.* NACA TN 3937, March 1957.
8. Carter, A. D. S., *The Low Speed Performance of Related Airfoils in Cascade.* Report No. R55, British N.G.T.E., September 1949.
9. Voit, Charles H., Donald C. Guentert, and James F. Dugan, *Performance of High-Pressure-Ratio Axial-Flow Compressor Using Highly Cambered NACA 65-Series Blower Blades at High Mach Numbers.* NACA RM E50A09, March 28, 1950.
10. Johnson, Irvine A., Aerodynamic Design. *Investigation of a 10 Stage Subsonic Axial Flow Research Compressor, Part I,* NACA RM E52B18, 1952.
11. Lewis, George W., Jr., Francis C. Schwenk, and George K. Serovy, Design, Overall-Performance And Stall Characteristics. *Experimental Investigation of a Transonic Axial-Flow-Compressor Rotor With Double-Circular-Arc Airfoil Blade Sections, Part I,* NACA RM E53L21a, April 5, 1954.
12. Lieblein, Seymour, George W. Lewis, Jr., and Donald M. Sandercock, Overall Performance of Stage With Transonic Rotor and Subsonic Stators up to Rotor Relative Inlet Mach Number of 1.1. *Experimental Investigation of an Axial-Flow Compressor Inlet Stage Operating at Transonic Relative Inlet Mach Numbers, Part I,* NACA RM E52A24, 1952.
13. Robbins, W. H., and F. W. Glaser, *Investigation of an Axial-Flow-Compressor Rotor With Circular-Arc Blades Operating up to a Rotor-Inlet Relative Mach Number of 1.22.* NACA RM E53D24, 1953.
14. Wright, L. C., and W. W. Wilcox, First-Rotor Blade-Element Performance. *Investigation of a Two-Stage Counter Rotating Compressor, Part II,* NACA RM E56G09, 1956.
15. Miller, Genevieve, and M. J. Hartman, *Experimental Shock Configurations and Shock Losses in a Transonic Compressor Rotor at Design Speed.* NACA RM E58A14b, 1958.
16. Schwenk, F. C., G. W. Lewis, and M. J. Hartman, *A Preliminary Analysis of the Magnitude of Shock Losses in Transonic Compressors.* RM E57A30, 1957.
17. Lieblein, Seymour, *Loss and Stall Analysis of Compressor Cascades.* ASME Paper No. 58–A–91, 1958.
18. Lieblein, Seymour, *Incidence and Deviation-Angle Correlations for Compressor Cascades.* ASME Paper No. 59–A–171, 1959.
19. Andrews, S. J., *Tests Related to the Effect of Profile Shape and Camber Line on Compressor Cascade Performance.* Report No. R60, British N.G.T.E., October 1949.
20. Bullock, R. O., *Critical Highlights in the Development of the Transonic Compressor.* ASME Paper No. 60–WA–290, 1961.
21. Lieblein, Seymour, Francis C. Schwenk, and Robert L. Broderick, *Diffusion Factor for Estimating Losses and Limiting Blade Loadings in Axial-Flow-Compressor Blade Elements.* NACA RM E53D01, June 8, 1953.
22. *Aerodynamic Design of Axial-Flow Compressors.* NASA SP–36, 1965.
23. Sandercock, Donald M., Karl Kovach, and Seymour Leiblein, Compressor Design. *Experimental Investigation of a Five-Stage Axial-Flow Research Compressor With Transonic Rotors in All Stages, Part I,* NACA RM E54F24, 1954.
24. Kovach, Karl, and Donald M. Sandercock, Compressor Overall Performance. *Experimental Investigation of a Five-Stage Axial-Flow Research Compressor With Transonic Rotors in All Stages, Part II,* NACA RM 54G01, 1954.

25. Sandercock, Donald M., and Karl Kovach, Interstage Data and Individual Stage Performance Characteristics. *Experimental Investigation of a Five-Stage Axial-Flow Research Compressor With Transonic Rorots in All Stages, Part III,* NACA RM E56G24, 1956.

26. Sandercock, Donald M., Blade Element Performance. *Experimental Investigation of a Five-Stage Axial-Flow Research Compressor With Transonic Rotors in All Stages, Part IV,* NACA RM E57B12, May 7, 1957.

27. Klapproth, John F., John J. Jacklitch, and Edward R. Tysi, *Design and Performance of a 1400-Foot-Per-Second Tip-Speed Supersonic Compressor Rotor.* NACA RM E55A27, April 11, 1955.

28. Wright, L. C., and R. A. Novack, *Aerodynamic Design and Development of the General Electric CJ805-23 Aft Fan.* ASME Paper No. 60–WA–270, 1960.

29. Seyler, D. R., and L. H. Smith, Jr., Design of Rotor Blading. *Single Stage Experimental Evaluation of High Mach Number Compressor Rotor Blading, Part I,* NASA CR 54581, G.E. R66FPD321, April 1, 1967.

30. Gostelow, J. P., K. W. Krabacher, and L. H. Smith, Jr., *Performance Comparisons of High Mach Number Compressor Rotor Blading.* NASA CR-1256, December 1968.

31. Kantrowitz, Arthur, and Coleman du P. Donaldson, *Preliminary Investigation of Supersonic Diffusers.* NACA ACR L5D20, 1945.

32. Kantrowitz, Arthur, *The Supersonic Axial-Flow Compressor.* NACA TR 974.

33. Crouse, James E., David C. Janetzke, and Richard E. Schwirian, *A Computer Program for Composing Compressor Blading from Simulated Circular Arc Elements on Conical Surfaces.* NASA TN D-5437, September 1969.

34. Moses, J. J., and G. K. Serovy, *Some Effects of Blade Trailing Edge Thickness on Performance of a Single-Stage Axial-Flow Compressor.* NACA RM E51E28, October 26, 1951.

35. Moses, J. J., and G. K. Serovy, *Effect of Blade-Surface Finish on Performance of a Single-Stage, Axial-Flow Compressor.* NACA RM E51C09, April 16, 1951.

36. Tysl, Edward, R., Francis C. Schwenk, and Thomas B. Watkins, Design, Over-All Performance, and Rotating-Stall Characteristics. *Experimental Investigation of a Transonic Compressor Rotor With a 1.5-Inch-Chord Length and an Aspect Ratio of 3.0, Part I,* NACA RM E54L31, 1955.

DISCUSSION

L. H. KING AND A. C. BRYANS (General Electric Co): The author has presented a comprehensive summary of various design approaches used to select blading for axial-flow compressors. This paper will be a valuable reference for the compressor designer.

The author offered one practical comment on 65-series thickness distribution blading that should be qualified. The statement that the leading edge shape cannot be obtained consistently in manufacturing and therefore would justify allowing a tolerance band is valid. However, the magnitude of the variation between the lower and upper tolerance limit must be specified and then types of acceptable nose profiles defined within these limits. Since the paper does not deal with the problem of blading tolerance limits, it seems inappropriate to introduce this unqualified comment.

The writers' experience with small axial compressor blading has shown that tolerance specification and manufacturing control are important aspects of the designer's role in obtaining the desired performance levels.

The tip region of transonic rotors still requires a great deal of study before we can adequately determine the flow field. The present paper makes reference to the procedure of designing at axial stations within the blade row. L. H. Smith's paper (ref. D–1) develops rigorously such a procedure, dealing therein with the effects arising from blade-to-blade variations which do not exist in a true axisymmetric field. Dr. Smith indicates that these perturbation effects are analogous to Reynolds stresses in turbulence theory. We are concerned that current practice still continues to use a linear distribution to represent the blade-to-blade variation in the force field when we know that shocks must result in some radical departure from this idealized situation. The normal concept that a blade row is equivalent to a force field and this force field, in turn, is equivalent to a vorticity distribution requires that the correct vorticity be used to define the blade. We would suggest some research into the significance of the rate of change of vorticity as it affects the flow field in the supersonic regime. We would further suggest that the mathematical model used to represent the shock structure in this region be checked for radial equilibrium.

D. M. SANDERCOCK (NASA Lewis Research Center): The author has presented a very useful summary of blade sections currently used in blade designs and their general areas of applicability.

There is one additional point of interest regarding the multiple circular arc blade shape. The use of low turning in the forward portion of the blade section does indeed tend to lower the shock inlet Mach number and presumably the shock losses. However, the amount of fluid turning upstream of the shock also affects the throat area of the blade passage, which must be large enough to pass the required mass flow. Thus, the throat area requirement can place some restrictions on the amount of turning that can be assigned to the inlet portion of a blade section. Also, there is a line of reasoning that indicates that close control of the throat area along the blade span may have a more significant effect on overall blade losses and stable operating range than that realized from minimizing blade passage shock loss. Mr. Benser, in his paper "Transonic Compressor Technology Advancements," discusses the effects of throat area observed from experimental data from transonic blade rows over a range of blade speeds.

For the cases of high solidity stator blade sections, added turning is sometimes introduced in the forward portion of the blade section in order to attain required throat areas to pass the mass flow.

R. M. HEARSEY (Ohio State University Research Foundation): Have you considered selecting cascade solidity by means of the total pressure loss parameter/diffusion factor relationship presented in Figure 203 of NASA SP 36?

WRIGHT (author): It is true, as Mr. Sandercock states, that the leading edge camber of transonic, multiple-circular-arc sections has a pronounced effect on blade throat area. Of course, so do the blade thickness and the convergence of the annular stream tubes. It would be interesting to compare the performance of blades designed for the same inlet velocity diagram and with the same throat area obtained via different combinations of the three variables: camber, thickness, and annular convergence. It is my unverified opinion that the best performance (and the maximum choking flow) will result for the configuration yielding the most uniform throat flow. I don't believe that this would be the blade with the more cambered leading edge because its integrated ρV would include some supersonic suction surface values and some subsonic pressure surface values and the variations between.

It is my opinion, further, that a straight leading edge blade with a higher design incidence will also yield a more uniform throat than a curved inlet blade and hence a lower suction surface Mach number at the normal shock for peak efficiency operation. The existence of a stronger expansion around the suction surface of the leading edge following the sonic velocity point, which in turn follows the leading edge stagnation point, is believed to be preferable to the later suction surface expansions of the curved section for the same reason (throat uniformity). Hence, until further proof is offered, I believe that the throat area requirements must be satisfied, but with minimum blade suction surface curvature.

On the leading edge tolerance discussed by Messrs. Bryans and King, I simply offer this for what it is worth to the reader. We at AiResearch have noticed what I take to be an advantage, particularly with respect to stalling incidence, of the asymmetric leading edge contour. And, inasmuch as some manufacturing tolerances are required, this approach offers the potential of converting a problem area into an advantage.

With regard to the rotor internal calculations, it is well known that the force field created by the blade sections is not rigorously represented by linear cross channel gradients. Further, the rigorous calculation of the rotor internal flow configurations requires complete departure from the quasi-three-dimensional procedures (a radial-axial plane flow based on axial symmetry plus the 2-*D* blade flow) which have traditionally, and perhaps surprisingly, yielded satisfactory performance and reasonable checks of rotor outlet distributions for moderate supersonic Mach number levels. Even neglecting the formation of the secondary flow vortices which in real life are extremely difficult to avoid, the stream surfaces between the hub and tip shrouds will not be axisymmetric surfaces. A qualitative approach to minimizing these perturbations from axial symmetry would be the use of very high solidity. The rationale would be similar to that by which the assumption of infinite solidity was used in early cascade theory in order to drop derivatives in the tangential direction.

I agree with Mr. King and Mr. Bryans that some research aimed at a closer approach to the rigorous representation of the supersonic flow field in a high Mach number rotor would be a worthwhile undertaking. The most practical fallout from this research would probably be the derivation of some analytical expressions for the radial accelerations caused by the shocks and the resulting warped, equilibrium shock.

Relating to Mr. Hearsey's question, and as commented by Mr. Benser, my experience is that the NASA SP36 figure 203 gives solidities somewhat lower than the optimum for transonic blades at optimum incidence. We have used this approach on stators in particular where the inlet Mach numbers are low.

REFERENCES

D-1. Smith, L. H., Jr., *The Radial-Equilibrium Equation of Turbomachinery.* ASME 65-WA/GTP-1.

SESSION VI

Pumping Machinery for Aerospace Applications

Chairman: **M. J. HARTMANN**

Axial Pumps for Propulsion Systems

M. C. HUPPERT AND K. ROTHE

Rocketdyne
A Division of North American Rockwell Corporation

A historical review of the axial-flow hydrogen pumps developed by Rocketdyne is presented. The design features and the performance data obtained during the course of these programs as well as the engine problems caused by the pump characteristics are discussed.

The design and development of axial-flow hydrogen pumps was initiated in 1957 by a contract awarded to Rocketdyne by Air Research and Development Command of the United States Air Force. The pump, designated Mark 9, consists of a high head inducer and six identical axial stages. This configuration was used to supply hydrogen for nuclear rocket reactor tests (December 1963 through April 1965; see ref. 1) in single-mode and dual-mode (parallel flow) feed-system configurations. The basic pump configuration with one more axial stage was used in the NASA J–2 (LH_2–LOX) rocket engine developed for the Apollo space program. During the initial development phase of the J–2 engine, NASA sponsored the design and experimental evaluation of four axial-stage configurations designed for higher blade loading than that used in the Mark 9 staging. The results of this stage program were used to design the Mark 26 pump for use with an uprated J–2 engine.

In response to the need for increased flow and head requirements for the evaluation of advanced reactor configuration (ref. 1), Rocketdyne designed the Mark 25 axial-flow pump. The flowrate was increased by 50 percent and the head rise by 25 percent, compared to the Mark 9 pumps.

MARK 9 TURBOPUMP

The Mark 9 turbopump consists of an inducer and six identical axial stages (fig. 1). The pump has a four-bladed inducer with four splitter vanes. The six axial stages have 17 rotor blades and 42 stator blades each.

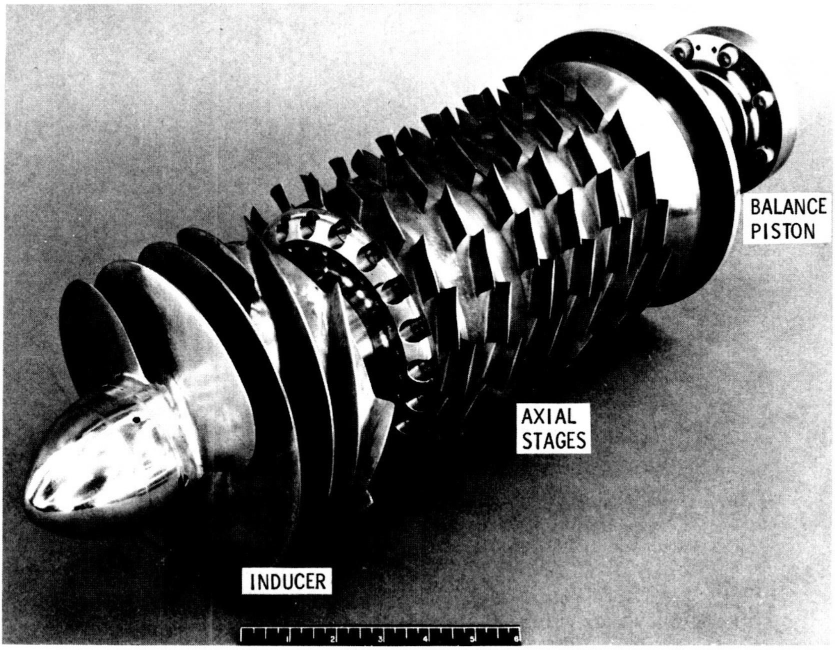

FIGURE 1.—*Mark 9 pump rotor.*

The last rotor is not followed by a stator and discharges directly into a vaned volute. The pump was designed to run at 34 000 rpm and produce 50 000 feet of head at a flowrate of 10 600 gal/min. The inducer produces 10 000 feet of head, and the remaining 40 000 feet is developed by the six axial stages. Mark 9 testing was initiated in 1958.

MARK 15 PUMP

The Mark 15 liquid hydrogen pump is used on the J–2 engine in the Saturn V vehicle that launches the Apollo spacecraft to the moon. Five engines are used on the second stage and one on the third. The blade sections of the Mark 15 pump are identical to those of the Mark 9. The Mark 15 has seven stages of axial-flow blading instead of six, as used in the Mark 9 pump. Figure 2 shows a layout of the Mark 15 turbopump. The rotating assembly is mounted on two bearings with the turbine overhung; this allows both bearings to be located within the pump under similar load and environmental conditions. Both bearings are cooled and lubricated with liquid hydrogen. The bearing coolant liquid leaves the main passage at the entrance to the volute and passes through a self-positioning balance piston that nulls all the end thrust of the rotating

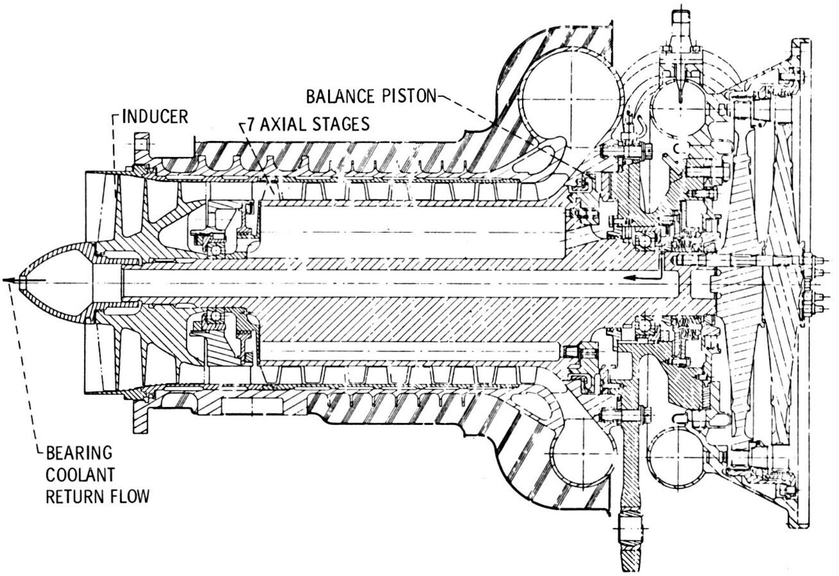

FIGURE 2.—*J-2 (Mark 15) fuel turbopump.*

assembly. The flow then splits. A portion of it passes through the rear bearing, then through radial holes to the center of the shaft and out the front spinner nut; the remaining flow passes through the outer portion of the drum, through the front bearing and bearing support, and joints the mainstream at the inducer exit. The flowrate through each bearing is approximately 10 gpm of the total balance piston flow (45 gpm). The angular contact ball bearings are made of 440C stainless steel and have Armalon (glass-filled Teflon) cages. Bearing DN values are approximately 1.7×10^6 maximum. The pump must operate satisfactorily for a total of 3750 seconds with single-run times of up to 500 seconds. This life must be in addition to any "green run" or acceptance testing required. These total life requirements are approximately 6000 seconds.

The pump has a tip diameter of 7.25 inches, runs at 25 000 rpm, and produces 38 330 feet of head at 8580 gpm flow. The inlet and outlet pressures are 30 and 1247 psia, respectively. The pump absorbs 8145 horsepower under nominal conditions. Figure 3 shows a nondimensional performance map of the pump. Note that the pump has an abrupt stall, the head dropping to approximately 84 percent of the peak value; this is not too different from the nominal operating head ($\psi = 1.697$). (The overall head coefficient ψ of the seven-stage pump plus inducer is referenced to the tip diameter. The inducer head coefficient is $\psi_{\text{ind}} = 0.222$.) The efficiency is on the low side because of the balance piston flow losses and the losses through the bearings. Figure 4 shows the velocity diagram for the axial-flow blading.

Cavitation performance of the Mark 15 pump at 25 750 rpm (slightly lower than nominal) is shown in figure 5. Note that the head stays almost constant as the net positive suction head (NPSH) is reduced until the pump abruptly cavitates. Figure 6 shows the results of more than 50 such tests on 15 production pumps and 2 R&D pumps. The average line through these points is a least-squares fit. Standard deviation from the

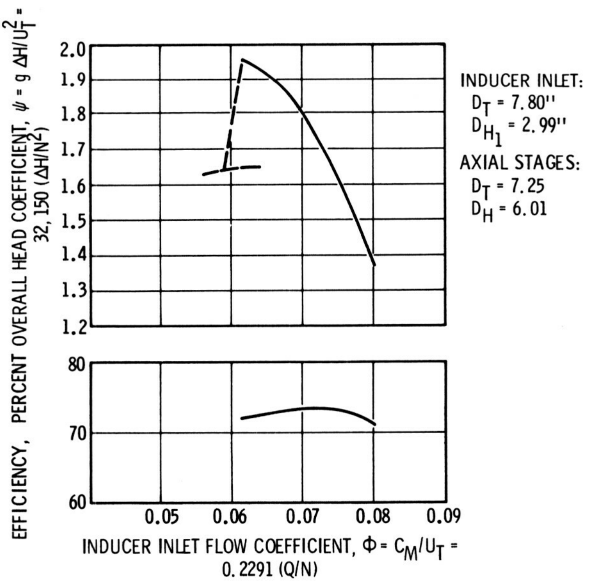

FIGURE 3.—*Mark 15 pump performance.*

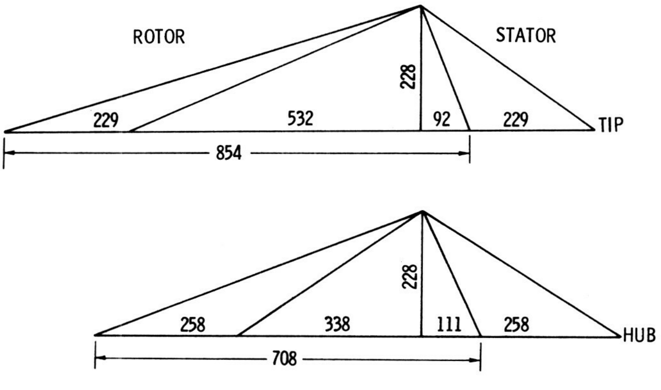

FIGURE 4.—*Mark 9 and J–2 fuel pump axial-stage vector diagram.*

average is 14.6 feet and the 2σ variation is 27.2 feet, which band encloses all the points. A scattering of points is to be expected because vapor pressure is determined from an inlet line temperature measurement and Bureau of Standards charts for parahydrogen; a temperature error of 0.1° is equivalent to a difference in vapor pressure of 10 feet of hydrogen. At design conditions, the suction specific speed of the pump in liquid hydrogen is 103 000. The test technique used in obtaining the pump suction performance, as shown in Figures 5 and 6, neglects considerations

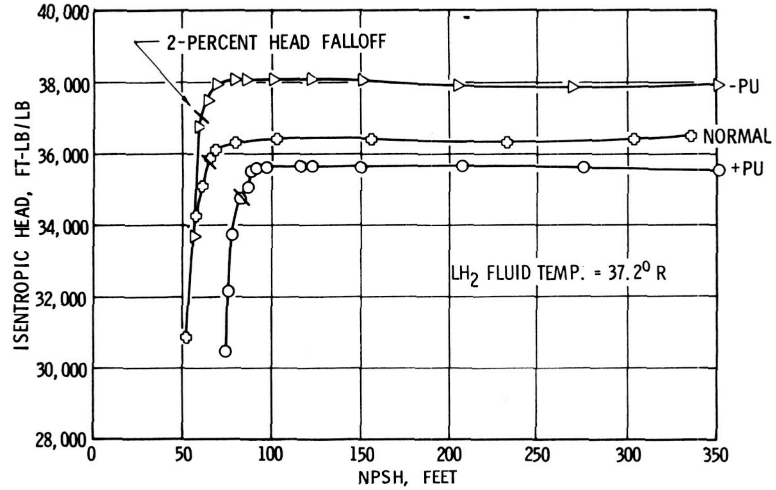

FIGURE 5.—*Typical J–2 fuel pump cavitation tests in liquid hydrogen.*

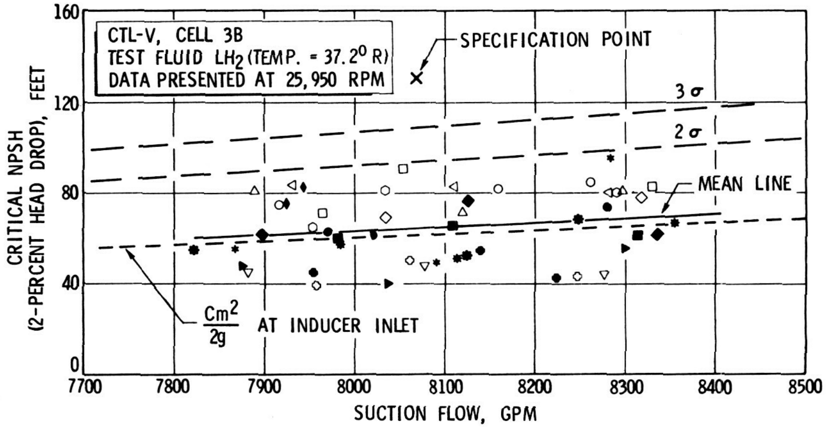

FIGURE 6.—*J–2 Fuel pump suction performance in liquid hydrogen.*

of two-phase flow at the pump inlet. When the NPSH is equal to the duct velocity head, the duct wall static pressure corresponds to the fluid vapor pressure as indicated by the duct temperature measurement. The quality (vapor fraction) of the duct flow can only be determined from the duct measurements if the fluid stagnation temperature or enthalpy is also known. Subsequent test programs in which more complete instrumentation was used indicated that the pump was capable of ingesting two-phase flow. The vapor fraction ingested for various pump inlet stagnation temperatures and flows is shown in figure 7.

STAGE LOADING ADVANCEMENT PROGRAM

Under the sponsorship of NASA, Rocketdyne conducted an R&D effort to determine the upper limit of hydrodynamic loading that could be accepted by an axial-flow pump stage without serious performance penalty. Four sets of blades were designed, each with a symmetrical velocity diagram at the hub. The pumps were designated *A*, *B*, *C*, and *D* (fig. 8) with diffusion factors at the hub of 0.58, 0.64, 0.68, and 0.72, respectively. Each pump had four stages of blading. The test results, which include volute losses, in the air rig (ref. 2) along with a four-stage pump with Mark 9 blading are shown in figure 9 through 13. All pumps

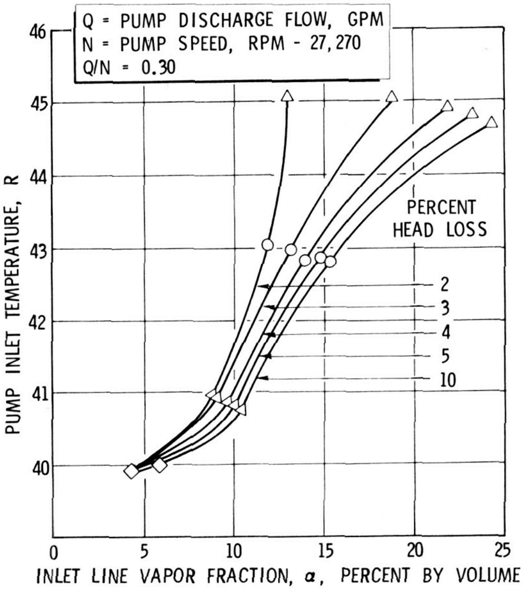

FIGURE 7.—*Mark 15 hydrogen pump performance with two-phase inlet flow.*

had the same design inducer inlet flow coefficient (0.10). It can be seen from the results that each pump produced a progressively higher head while losing stall margin. Also, the drop in head as the pump stalled became progressively greater, the head of the *D*-bladed pump dropping to 55 percent of its peak value. A study of the data indicated that each pump stalled when the average retardation factor (ratio of relative exit to relative entrance velocities) was reduced to 0.5 or when the maximum diffusion factor climbed to a value of 0.75.

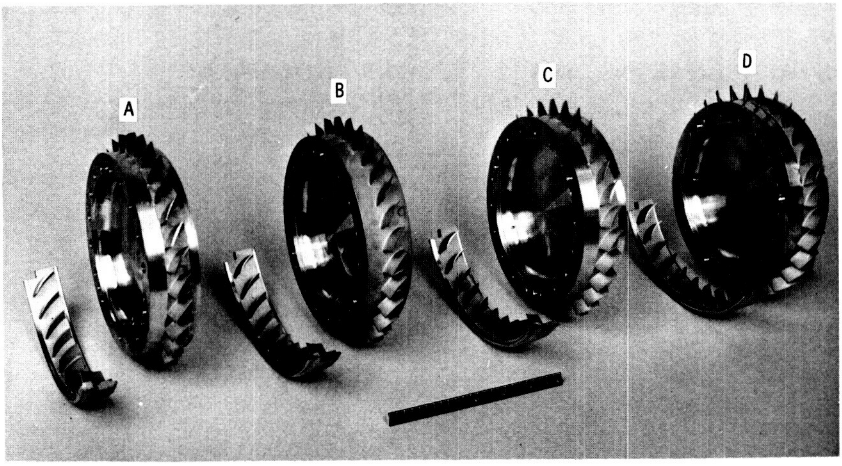

FIGURE 8.—A, B, C, *and* D *rotors with stator segments.*

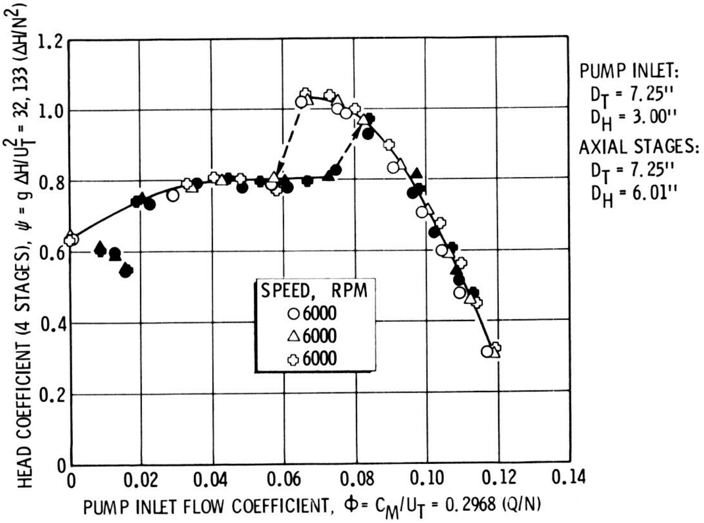

FIGURE 9.—*Four-stage pump performance, Mark 9 blading.*

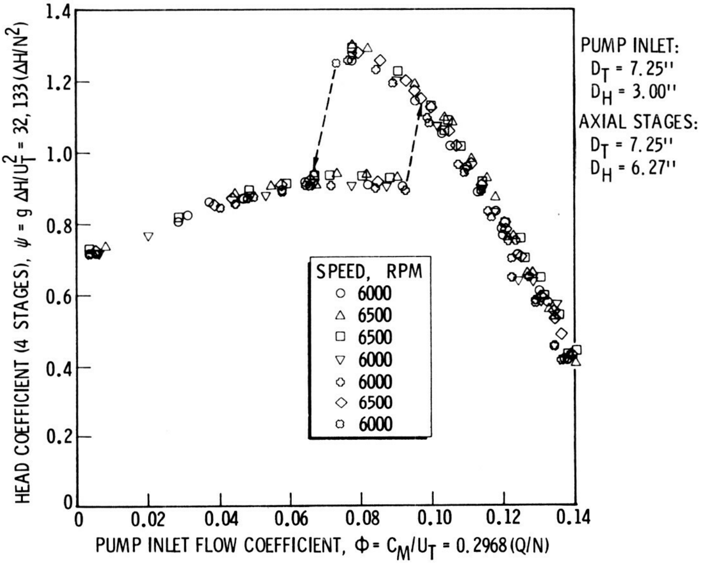

FIGURE 10.—*Four-stage pump performance, "A" blading.*

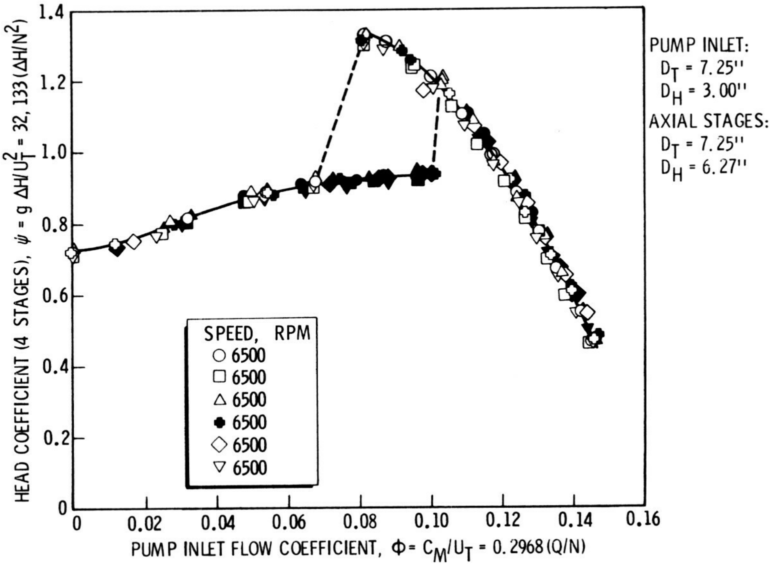

FIGURE 11.—*Four-stage pump performance, "B" blading.*

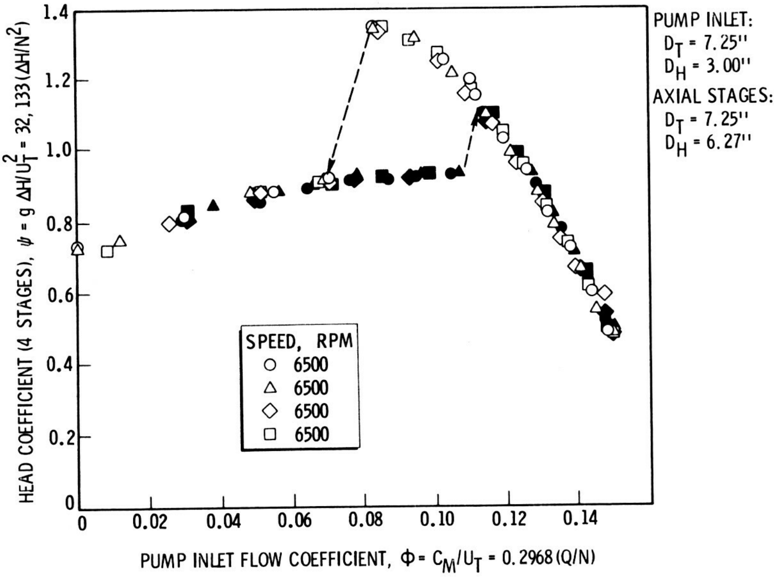

FIGURE 12.—*Four-stage pump performance, "C" blading.*

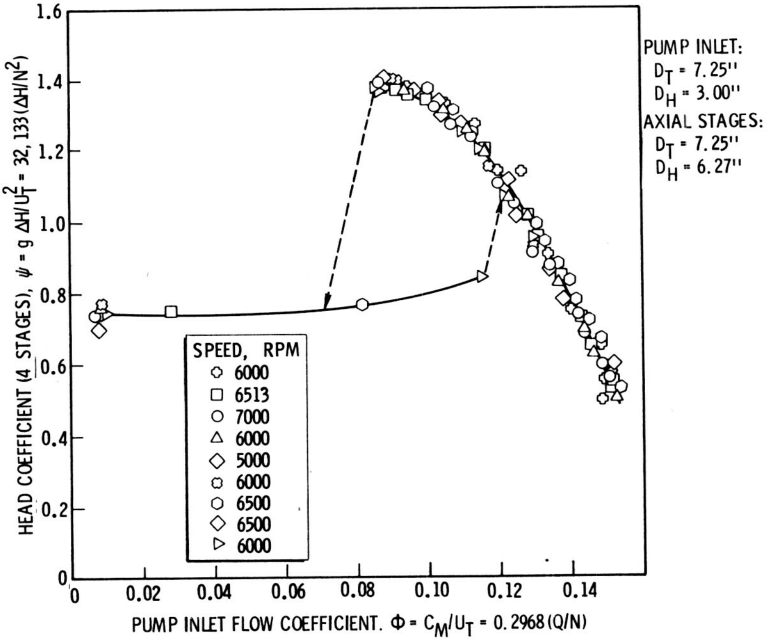

FIGURE 13.—*Four-stage pump performance, "D" blading.*

MARK 26 PUMP

The Mark 26 pump was, in effect, a Mark 15 pump configuration with *D*-blading. It also consisted of an inducer plus seven axial stages. It was designed as a possible replacement for the Mark 15 pump in case there was a substantial uprating of the J–2 engine. The Mark 26 was tested in 1965 and gave the performance shown in figure 14. It performed as predicted from the four-stage configuration data and produced a head coefficient at stall inception of 2.864, as compared to 1.955 for the Mark 15, an increase of 46.5 percent. Its efficiency was slightly higher. It also had a deeper stall, the head in stall being about 70 percent of the peak value.

MARK 25 PUMP

The Mark 25 pump was designed to meet uprated conditions not obtainable with the Mark 9. The design flowrate was increased by about 50 percent and the head by 25 percent. The passage height (annular flow area) was also decreased to increase the axial velocity to a value of half the blade speed at the mean diameter. This is, theoretically, the optimum value for maximum efficiency. Moreover, the increase in axial velocity produced a diagram that permitted higher head per stage with the same

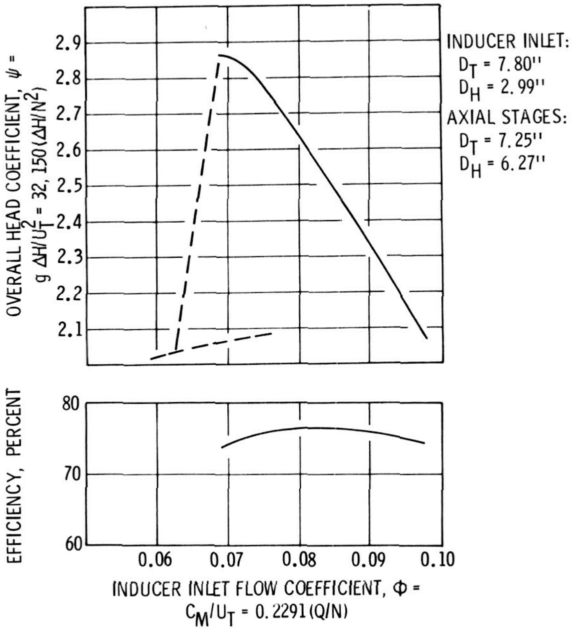

FIGURE 14.—*Mark 26 pump performance.*

blade loading (diffusion factor). The pump was designed to give a stall margin of 25 percent; this resulted in a value of 0.63 for the retardation factor and 0.55 for the diffusion factor at the mean diameter. The resultant velocity diagram is shown in figure 15. It was desired that the Mark 25 be capable (from the blade stress standpoint) of running at a substantially higher speed than the Mark 9; therefore, blades with relatively large chords and cross-sectional areas were used. Only four axial stages were required. The overall pump head coefficient, however, was comparable to that of the Mark 15, as can be seen from figure 16. This pump also had a deep stall, the head falling to 60 percent of its peak value. A photograph of the Mark 25 rotor is shown in figure 17.

WATERJET PUMP

The Mark 25 design has recently been used as a model for a waterjet pump for ship propulsion. In a waterjet system, the pump efficiency is very important; therefore, a strong effort was made to obtain high efficiency. To accomplish this, the backflow through the rotor was eliminated, as was the balance piston. In addition, the stator shrouds were removed. The discharge scroll, a source of losses, was eliminated and axial stators were used in its place to provide axial flow to the nozzle and steering device. The resultant pump was tested in an accurately calibrated water rig. The results of the test are shown in figure 18; it can be

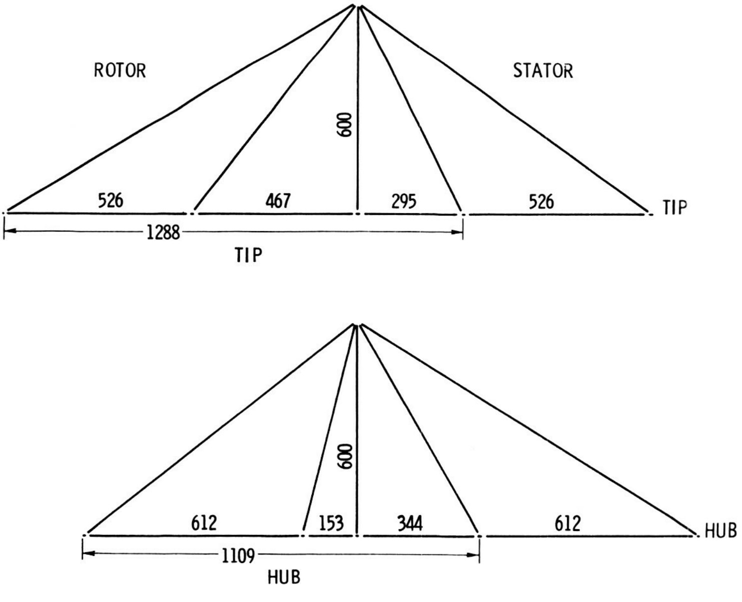

FIGURE 15.—*Mark 25 axial-stage vector diagram.*

seen from the curve that a peak efficiency of 90 percent was obtained and that the pump head coefficient was approximately 15 percent higher than that obtained with the Mark 25 pump.

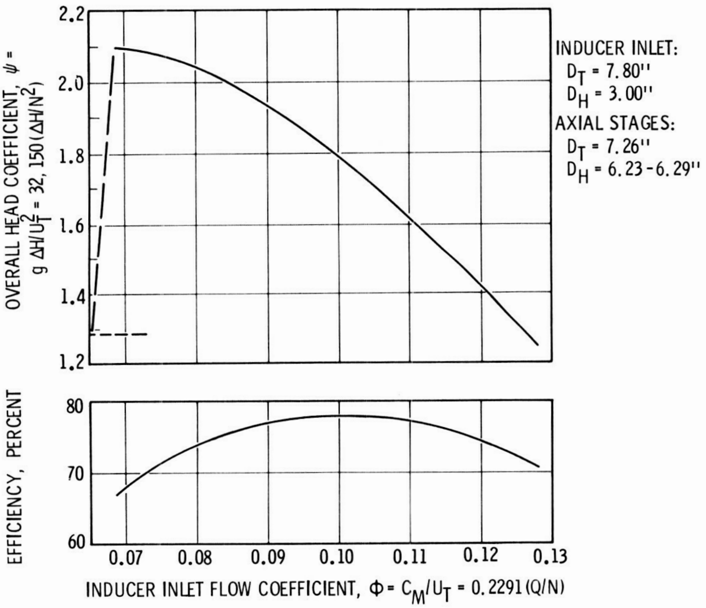

FIGURE 16.—*Mark 25 pump performance.*

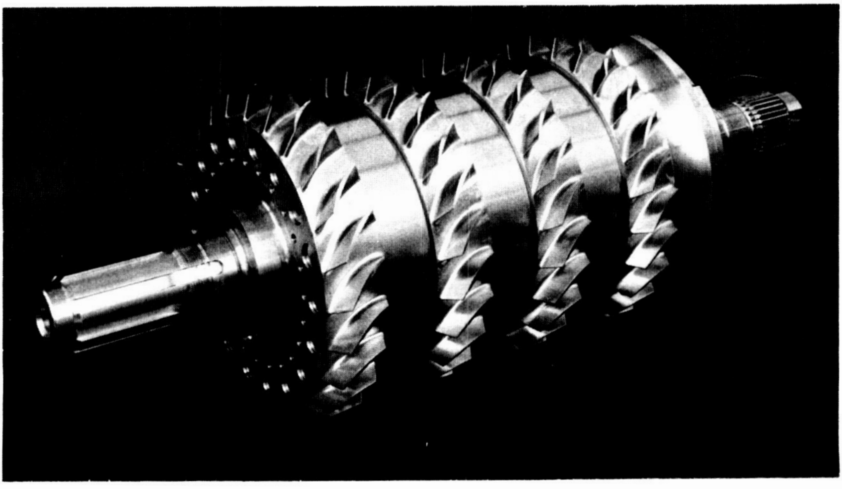

FIGURE 17.—*Mark 25 rotor.*

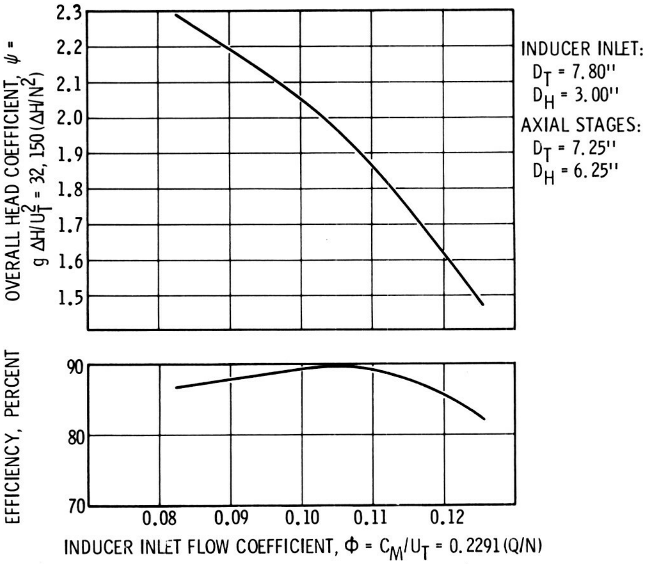

FIGURE 18.—*Mark 25 pump performance as a water-jet pump.*

EFFECT OF MARK 15 PUMP PERFORMANCE ON THE J–2 ENGINE SYSTEM

Axial-flow pumps have always performed satisfactorily on engines under steady-state conditions. However, early in the J–2 program, many problems were encountered with the proper sequencing of events during the engine start transient.

The J–2 engine system consists of dual series turbopumps driven by hot gas supplied by a bootstrapping gas generator. The initial start is supplied by high-pressure hydrogen gas, followed by bootstrapping operation to mainstage. Engine control during the start transient is accomplished with the use of a LOX turbine bypass valve and a programmed opening for the main oxidizer valve.

During the early stage of the development, excessive gas generator temperature, fuel pump stall, and discharge pressure decay, as well as rough thrust chamber combustion at very low chamber pressure levels was experienced. The solution to these problems required a thorough understanding of the different component characteristics.

As already mentioned, an interesting feature of the J–2 engine is the use of two independent turbopumps. This introduces a degree of freedom in terms of relative pump speeds. During the hydrogen gas spin portion of the start, the power distribution between the two turbines tends to increase the LOX turbopump speed more rapidly than the fuel turbopump speed. After completion of the hydrogen gas spin, the combustion in the gas generator is initiated and the power distribution starts favoring the fuel turbine. During the gas spin portion, the higher LOX pump speed results in an increased LOX flow that produces a higher head demand on the fuel pump and tends to drive the fuel pump toward stall. To compensate for this, it was necessary to use a LOX turbine gas bypass system, which allows a portion of the spin gases to bypass the LOX turbine and reduce its speed to be compatible with the fuel turbopump. During engine thrust buildup, the fuel pump operating point must be kept away from the stall line throughout the entire start. It is Rocketdyne's practice to consider any start during which the stall line is crossed as a failure even though no hardware damage may result. The start sequence which has evolved is as follows:

(1) The main fuel valve is opened to allow a small amount of fuel to flow through the pump and thrust chamber to ensure that liquid hydrogen is in the pump at the time the spin gases are released.
(2) The gas spin valve is opened and the fuel pump is accelerated to approximately 11 000 rpm and the LOX pump to 4500 rpm.
(3) The main LOX valve opens approximately 14 degrees thus allowing the LOX dome to be filled and main propellant ignition established.
(4) The gas generator valves open and engine bootstrapping begins.
(5) The turbopumps are continuously accelerated and the main LOX valve gradually ramps to full open.

Figure 19 shows a typical engine start superimposed on a Mark 15 fuel pump map. The entire length of the line is traversed in about 2½ seconds. It can be seen that during the spin bottle blowdown the pump moves toward the stall line and then loops away from it. Also, when the dome of the thrust chamber is primed with LOX and chamber ignition occurs, there is another movement toward the stall line. Finally, the movement of the main oxidizer valve (MOV) brings the path closer to stall.

DESIGN CONSIDERATIONS

The axial pump design process is directed to achieve a configuration that will satisfy design requirements and will also operate within the constraints imposed by other components of the turbopump assembly. Thus, the pump design cannot be divorced from the design of components such as the drive turbine, inducer, bearings, and seals.

The hydrodynamic design consists of the proper selection of the fluid velocity diagrams and the blading. The design must assure the required fluid turning with a minimum of pressure losses. Structural adequacy is achieved by maintaining the operating stresses within the limits of the

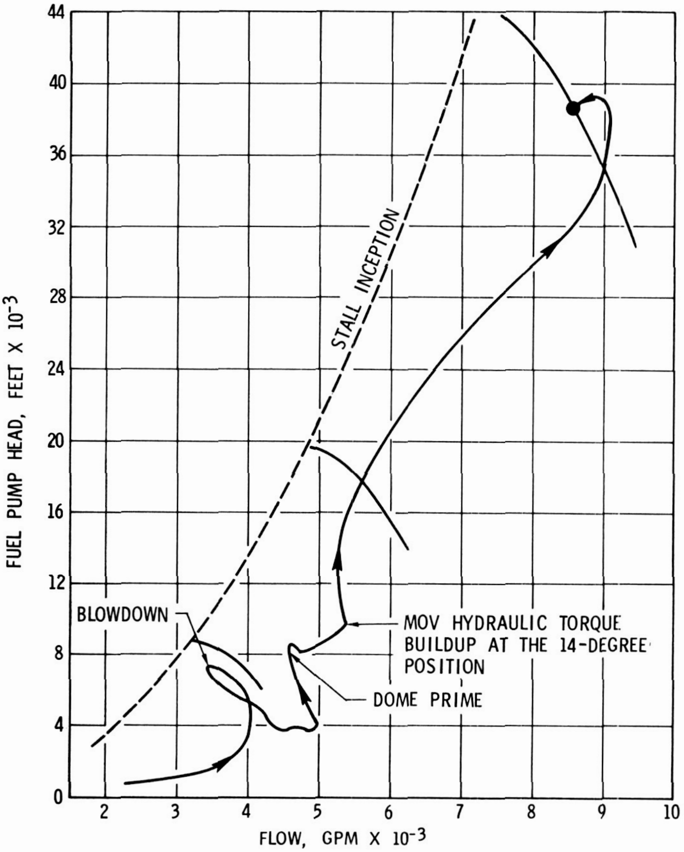

FIGURE 19.—*Pump start transient with J–2 engine.*

materials used. Major areas of concern include fatigue failures of the blading and excessive elastic deflections of the housing and rotor assemblies rather than Major areas of concern include fatigue failure in the blading housing and rotor deflection.

The dynamic behavior of the turbopump rotor has received attention in rocket engine design and development programs. In particular, the critical speeds associated with bearing stiffness have resulted in development problems. The use of duplex ball bearings or roller bearings to achieve turbopump operation free of shaft critical speeds is the safest design policy.

Stage Hydrodynamic Design

The procedure used in the hydrodynamic design of axial pumps has generally followed axial-flow compressor design practice (ref. 3). The three-dimensional flow problem is approximated by assuming axisymmetric flow. Radial variations in flow are approximated from continuity, energy addition, and radial equilibrium considerations consistent with the axisymmetric flow assumption. Flow losses are estimated from cascade data and flow loss correlations, such as those presented in references 4 and 5.

The diffusion factor has been used successfully (ref. 3) as a measure of blade loading and as a correlation parameter for blade profile loss data. For a symmetrical velocity diagram, the diffusion factor (DF) is related to the ideal head coefficient, ψ_i, and flow coefficient, ϕ, as follows:

$$DF=\frac{\psi_i}{2\sigma\sqrt{\phi^2+\left(\frac{1+\psi_i}{2}\right)^2}}+1-\frac{\sqrt{\phi^2+\left(\frac{1-\psi_i}{2}\right)^2}}{\sqrt{\phi^2+\left(\frac{1+\psi_i}{2}\right)^2}}$$

This relationship is shown graphically in figure 20. Rocketdyne experience

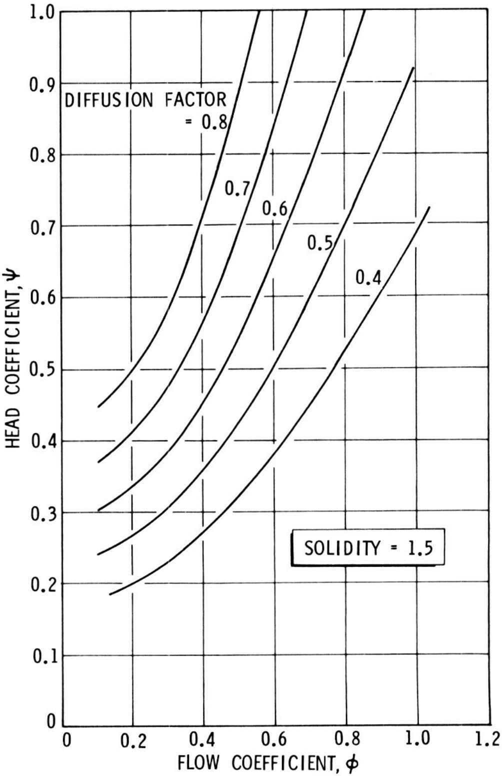

FIGURE 20.—*Effect of flow coefficient on head coefficient for constant diffusion factor.*

with six axial-stage designs has indicated that stage stall occurs at a diffusion factor value of approximately 0.75. The diffusion factor, however, is determined from the vector diagrams rather than the blade surface velocity distribution which determines boundary layer growth and separation. Consequently, any relationship between diffusion factor and stall could not apply to all blade profile types. Generally speaking, however, the larger the design diffusion factor, the smaller the stall margin.

Blade Profiles

Research and development of blading for axial-flow compressors has produced considerable data on so-called standard profiles. These include the NACA 65-series, British C-series, and double-circular-arc profiles. Nonstandard profile shapes with the maximum thickness moved beyond the 50-percent chord point may have reduced maximum surface velocity. Such shapes have a lower cavitation number and are particularly advantageous for high-solidity applications (ref. 6). Table I shows the profiles and design parameters used in these four pump designs. The Mark 9 and Mark 25 pumps incorporated nonstandard blading. The blading was designed by an iterative process in which the blade surface velocities were computed by the stream filament theory discussed in reference 3. The general criterion was that the suction surface velocity should not exceed 1.2 times the relative inlet velocity. A sample profile is shown in figure 21, and its computed surface velocity in figure 22. A design incidence angle of zero was used; the deviation angle was estimated by the procedure presented in reference 3. The A, B, C, and D were the double-circular-arc-type blading. In general, the effort required to design the nonstandard profile is deemed to be worthwhile.

ACKNOWLEDGMENT

The data concerning the development of the first axial pump used in rocket engine systems were made available by the Power Systems Divisions of North American Rockwell, who pioneered this pump type under the sponsorship of NASA.

The authors wish to express their thanks to the engineers who participated in this development. Special acknowledgment is given to Dr. George Wislicenus who, as consultant, contributed substantially to the success of these programs.

TABLE I.—*Profile Design Parameters*

Unit		Profile type	Chord		Maximum thickness to chord ratio		Solidity		Camber		Stagger	
			Hub	Tip	Hub	Tip	Hub	Tip	Hub	Tip	Hub	Tip
Mark 9	Rotor	Nonstandard	1.37	1.36	0.09	0.05	1.21	1.05	18.5	12.0	61.9	67.9
	Stator		0.87	0.98	0.117	0.065	1.9	1.8	40.0	40.0	38.0	35.3
Mark 15–F	Rotor				Same as Mark 9							
	Stator											
Mark 25	Rotor				Same as E							
	Stator											
Mark 26	Rotor				Same as D							
	Stator											
A	Rotor	Double-Circular-Arc	0.923	0.892	0.140	0.051	1.37	1.14	38.7	21.36	40.35	54.39
	Stator		1.00	0.924	0.120	0.050	1.4	1.31	36.9	34.8	37.38	40.35

B	Rotor	Double-Circular-Arc	0.912	0.872	0.138	0.052	1.34	1.11	43.1	24.9	39.05	53.75
	Stator		0.99	0.860	0.121	0.054	1.31	1.3	39.4	39.4	35.12	38.99
C	Rotor	Double-Circular-Arc	0.899	0.852	0.14	0.054	1.33	1.09	46.0	27.1	38.0	53.15
	Stator		0.980	0.850	0.122	0.054	1.30	1.29	43.0	43.1	34.1	37.85
D	Rotor	Double-Circular-Arc	0.909	0.836	0.132	0.062	1.33	1.06	50.0	28.9	36.5	52.55
	Stator		0.875	0.874	0.123	0.058	1.33	1.29	47.8	46.1	34.1	36.85
E	Rotor	Nonstandard	1.667	1.268	0.104	0.081	1.9	1.28	45.9	29.1	30.0	41.0
	Stator		1.538	1.394	0.085	0.089	1.7	1.6	35.1	36.0	41.1	38.9

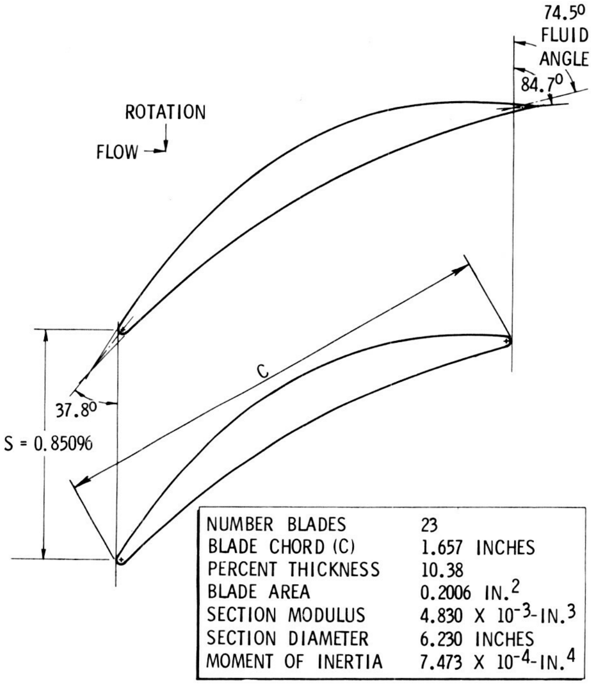

FIGURE 21.—*Mark 25 rotor blade, hub.*

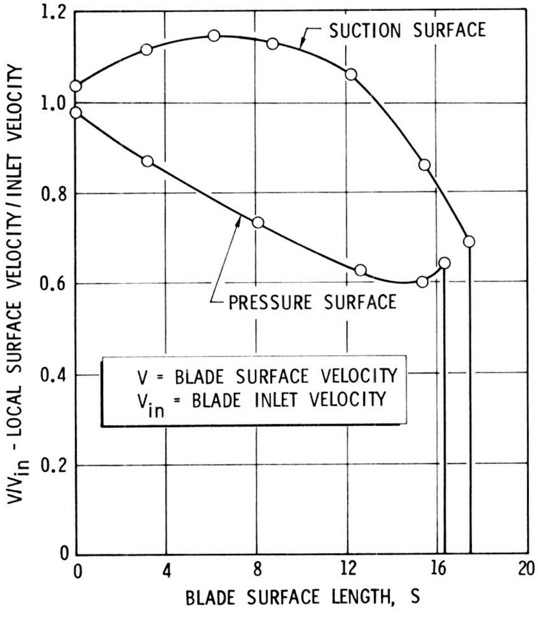

FIGURE 22.—*Mark 25 blade surface velocity ratio (rotor hub).*

LIST OF SYMBOLS

C	Blade chord length, inches
C_M	Meridional velocity, ft/sec
DF	Diffusion factor (defined in text)
D_H	Hub diameter, inches
DN	Bearing speed parameter, bore diameter (mm) × rotational speed (rpm)
D_T	Tip diameter, inches
g	Gravitational constant, ft/sec^2
ΔH	Pump developed head, ft-lb/lb
N	Pump rotational speed, rpm
Q	Pump volumetric flow, gpm
s	Blade spacing, inches
U_T	Tangential velocity at tip, ft/sec
ϕ	Flow coefficient, defined as C_M/U_T
σ	Solidity, defined as C/s
ψ	Head coefficient, defined as $g\Delta H/U_T{}^2$

REFERENCES

1. Gunn, S. V., and C. Dunn, Feed Systems and Nozzles for Phoebus Reactor Experiments. *J. Spacecraft Rockets*, Vol. 6, No. 7, 1969, pp. 769–777.
2. King, J. A., Testing Pumps in Air. *Trans. ASME, J. Eng. Power*, Ser. A, Vol. 90, No. 2, 1968, pp. 97–105.
3. *Aerodynamic Design of Axial Flow Compressors*, NASA SP–36, 1965.
4. Axial Cascade Technology and Application to Flow Path Designs; Part 1, Axial Cascade Technology. *Trans. ASME, J. Eng. Power*, 1968.
5. Lieblein, S., Loss and Stall Analysis of Compressor Cascades. *Trans. ASME, J. Basic Eng.*, Ser. D, Vol. 81, No. 3, 1959.
6. Taylor, W. E., T. H. Murrin, and R. M. Colombo, Systematic Two-Dimensional Cascade Tests. *Multiple Arc Hydrofoils*, NASA CR–72499, Vol. 2.

DISCUSSION

G. K. SEROVY (Iowa State University): Reference 3 is given as the source of some of the design procedures used for all of the Rocketdyne pumps. It would keep the record clear if some added comments could be made about both the velocity diagram computations and the selection of blading.

Were the rotors for these stages all designed for a constant actual or a constant ideal head rise along the radius (hub to tip) or was some other variation of energy transfer specified? Is the incidence angle defined with reference to the blade mean camber line or with respect to the blade suction surface (as in some compressor applications)? Did the deviation angles estimated include any arbitrary corrections, such as the $\delta_c - \delta_{2-D}$ given in reference 3, or were the two-dimensional correlations used without correction? Could the authors give the average rotor and stator tip clearances used, and could they say something about the axial spacings between blade rows?

These questions are asked not in a critical sense, but mainly to get some significant data on record. A number of years ago, many of us in reporting experimental results on axial-flow compressors failed to give or record important design data. As a consequence, the value of the experiments has been somewhat diminished. The data developed in the Rocketdyne work should be supported by the most complete design information that is possible to obtain.

L. H. SMITH (General Electric Co.): I was interested in your comment that the hub tip diameter ratio of 0.83 was high enough to be of concern to you; whereas, in the axial-flow compressor field, we go above $\frac{9}{10}$ in our rear stages without feeling that we suffer a great deal in efficiency so long as the ratio of clearance to blade height is kept small. You mentioned also in your comments that you recognized clearance was quite important, and I wondered if you would be good enough to tell us what the clearance levels were in these pumps that you had given this data for. One further comment: The Mark 25 had very impressive efficiency; it was almost 90 percent in a flow coefficient that was just over $\frac{1}{10}$. I looked at the photograph of the rotor, and it appears that the stator vanes have shroud at their inner diameter; at least there appear to be recesses in the rotor drum. Was this, in fact, the case? I presume these were well sealed if this was the case.

F. GILMAN (Worthington Corp.): Have you given any thought to the improvement in range? For example, the Westinghouse Company was able to completely suppress the disturbance which came from stall in their blowers. This was done by putting a divider between the flow which approached the outer tips of the impeller and that which approached further in. More recently, Worthington Company has been able to cut out the stall on their axial-flow blower by merely putting holes in the shroud at the proper places. I think there are many ways by which the stall range of axial-flow machines could be improved.

HUPPERT AND ROTHE (authors): The authors agree wholeheartedly with Mr. Serovy's comment that the value of experimental data is enhanced when supported by design information.

The rotors used in the experimental study were designed for a constant ideal head rise from hub to tip. The Mark 15 inducer, however, had radial blade elements, while the Mark 25 inducer is designed for constant head. The incidence angle is defined with reference to the mean camber angle and, for the deviation angle, Carter's rule without corrections was used. The Mark 25 pump was designed using Howell's modification of Carter's rule as presented in reference D–1.

During the development phase of the Mark 15 pump, which has a hub-to-tip ratio of 0.83 for all seven stages, it was observed that, due to tip clearance variations, pump head and efficiency varied from pump to pump. These variations had to be reduced in order to satisfy the engine specifications. Therefore, the following procedure was established: The pump was installed in the component test facility which is capable of operating at speeds higher than design speed while pumping liquid hydrogen. The tolerances of the rotor, stator, and housing are theoretically set such that when running with about 10-percent overspeed the rotor blade tips "kiss" the housing. This results in a close clearance under design point operating speed conditions, and performance repeatability from pump to pump is assured. Taking into account eccentricity, the resulting rotor tip running clearance tolerances are between 0.0041 and 0.0196, and the radial stator tip running clearance lies between 0.033 and 0.0177. Notice that the stator clearance is larger; no "run-in" is required to assure performance repeatability, as was confirmed by experimental studies during which the stator clearance was changed.

The axial blade spacing was set to $0.0785^{+0.022}_{-0.000}$ following the rotor and $0.1199^{+0.022}_{-0.040}$ following the stator. These spacings were set by the desire to obtain the shortest and lightest pump. No tests were conducted to assess the effect of different spacings.

The Mark 25 pump has stator shrouds, as correctly observed by Mr. Smith. In this case shrouds were used to preclude blade failure due to fatigue combined with the relatively high blade hydraulic loading. The clearance between the shrouds and the rotor drum is $0.017^{+0.002}_{-0.000}$ on the diameter. The overall efficiency obtained is 78 percent (fig. 17). This efficiency includes volute and axial thrust balance piston losses.

Later, the Mark 25 was used as the basis for a waterjet pump. Since the efficiency of this pump was of prime importance for the planned application, the pump was redesigned to minimize all parasitic losses; the shrouds were removed and a smooth cylindrical rotor drum was used. The axial thrust balance piston necessary when operating with hydrogen-lubricated bearings was eliminated, and oil-lubricated bearings carrying the axial rotor loads were installed. Furthermore, closely controlled seals were used to minimize the leakage losses, and the volute was eliminated and replaced by a nozzle which converted the pump pressure measured at the last rotor exit into velocity. The result of these changes was that a peak efficiency of 90 percent measured at the exit of the last rotor was reached (fig. 19). Mr. Smith pointed out that in axial-flow compressors, a hub-to-tip ratio of 0.9 or higher is used in the rear stages without a substantial efficiency loss as long as the clearance-to-blade height ratio is kept small. We agree and the results of the waterjet pump, which has a hub-to-tip ratio of 0.85, confirm this. It must, however, be kept in mind that, when pumping liquid, all stages have the same hub-to-tip ratio and it is rather difficult to maintain close clearances with high-horsepower, high-speed pumps when pumping cryogenics, as demonstrated by the elaborate procedure which was used for the Mark 15 production. At this point, we would like to correct a misunderstanding. In all pump performance graphs in the paper the flow coefficient is referenced to the pump inlet (that is, to the inducer inlet), while the repeating axial stages are designed for a higher flow coefficient (fig. 4 and fig. 16).

Figure 4, representing the Mark 15 axial stage vector diagram, shows a lower flow coefficient than figure 16 which represents the Mark 25. The reason for the selection of the lower flow coefficient is that 12 years ago, when the Mark 15 was designed, we were concerned about first axial stage stator cavitation and the possibility that high hub-to-tip ratios might impair the obtainable efficiency. Therefore, an asymmetrical vector diagram was selected with low stator velocities and a relatively low axial through-flow velocity to obtain maximum blade height. Experience later showed that this concern was not justified, which led to the design of the Mark 25.

Mr. Gilman's suggestion to widen the operating range by suppressing the disturbance generated by pump stall is appreciated. The importance of this idea is especially evident in light of the facts illustrated in figure 19. During our experimental studies, we found that the tip clearance was critical to stall margin. The smaller the clearance the greater the margin. Currently, Rocketdyne is working on improvement in range for multistage axial pumps with constant blade height on a research basis. The results of the first tests are encouraging, but not yet conclusive, and it is too early to comment on these results at this time.

To date, axial pumps for rocket engine application have only been used when pumping liquid hydrogen. They cannot be recommended for liquid oxygen, since any rubbing of rotating members against stationary parts has to be avoided; hence, the rotor tip clearances have to be relatively large, resulting in a corresponding loss in efficiency.

When comparing design features and test results of cryogenic rocket engine pumps with compressors, it must be kept in mind that the power concentration of rocket pumps (ratio of densities of the fluid to be pumped) is considerably higher. Another difference lies in the fact that the bearings are always "lubricated" with the fluid to be pumped. To obtain sufficient bearing life, it is necessary to balance the axial rotor thrust with a balance piston, which results in additional efficiency losses. The overall rocket engine pump efficiencies will, therefore, always be below the values normally obtainable in commercial applications.

Figure 7 shows the two-phase flow test results of the Mark 15 hydrogen pump. When compared to the vapor swallowing capability of the Mark 25, which was tested at NRDS, the Mark 15 shows a relatively low two-phase flow capability. The reason is that the bearing coolant flow in the Mark 15 design is returned to the pump inlet (fig. 2) where it enters in gaseous form, thus reducing the capability of pumping additional gas. The test of the Mark 25 at NRDS used a separate system for the bearing coolant flow.

Any rocket engine optimization study confronts the designer with the question of which pump type—axial or centrifugal—should be selected. The simplicity of the housing structure and the high efficiency obtainable with an axial pump are attractive features.

The waterjet pump for a captured air bubble boat is a perfect example for an axial pump application since high efficiency, moderate pressure, and minimum diameter are required. A gas generator cycle rocket engine, however, is not sensitive to efficiency. The pump type selection, therefore, has to be based more on packaging, weight, and cost considerations. In general, the axial pump is the preferable solution for a single operating point hydrogen pump design with moderate discharge pressures and high efficiency requirements. The centrifugal pump is the preferable solution for all engine applications requiring throttling. An exception to this general rule is the single operating point high pressure preburner cycle engine. Pump discharge pressures on the order of 7000 psi combined with maximum efficiency represent the optimum solution. To supply 7000 psi, the axial pump becomes very long, having many stages. Controlling the tip clearance becomes a problem (as well as performance repeatability from pump to pump) which in turn results in an efficiency loss. The compactness of the centrifugal pump and the insensitivity to clearance changes when shrouded impellers are used makes this pump the superior solution.

In conclusion, the authors wish to thank the discussors for their consideration and thoughtful comments which form an appreciated supplement to the paper.

REFERENCES

D–1. Horlok, T. H., Axial Flow Compressors. *Fluid Mechanics and Thermodynamics,* 1958, p. 58.

Centrifugal Pumps for Rocket Engines

W. E. CAMPBELL AND J. FARQUHAR

NERVA Rocket Operations[1]
Aerojet Nuclear Systems Company

The use of centrifugal pumps for rocket engines is described in terms of general requirements of operational and planned systems. Hydrodynamic and mechanical design considerations and techniques and test procedures are summarized. Some of the pump development experiences, in terms of both problems and solutions, are highlighted.

The centrifugal pump has been an important element of the history of pump-fed liquid propellant rocket engines. The use of this type of pump is the resultant of its relative simplicity and reliability, wide operating flow range, and adequate performance. Additionally, at the outset of the rocket program, centrifugal pumping system experience was available from the commercial pumping industry.

Successful development of centrifugal pumping systems, however, has not been without some dramatic problems. These problems have been due mostly to the difficult application parameters, such as

(1) A wide variety of design requirements—flow rate, head rise, and fluid characteristics
(2) The importance of very low suction pressure
(3) The importance of high efficiency while achieving high stage head rise
(4) The effects of unknown or difficult-to-handle cryogenic, corrosive, and low-density pumping fluids
(5) Very rapid start, shutdown, and flow change transients

---

[1] The Nuclear Engine for Rocket Vehicle Application Program (NERVA) is administered by the Space Nuclear Propulsion Office, a joint office of the U.S. Atomic Energy Commission and the National Aeronautics and Space Administration. Aerojet-General Corporation, as prime contractor for the engine system, and Westinghouse Electric Corporation, as subcontractor for the nuclear subsystem, are developing a nuclear propulsion system for deep space travel.

The solutions of these problems resulted in improved analytical techniques for hydrodynamic and mechanical design, a partial understanding of such hydrodynamic/mechanical interactions as axial thrust and blade stresses, new and interesting fabrication and materials technology, and effective development test techniques.

The intent of this paper is to orient the reader to the general requirements for, and experience gained from, rocket engine pumps already operational and currently being designed; to summarize the hydrodynamic and mechanical design considerations and techniques and test procedures employed; and to highlight the development experience in terms of both problems and solutions.

Primary emphasis centers on the pumps designed and developed by Aerojet-General Corporation, but the general discussions of requirements, sizes, materials, and fabrication methods reflect the experience of other companies as known by the authors.

GENERAL REQUIREMENTS

Flow Rate and Variations

Rocket engine centrifugal pumps have been developed for flow rates as low as 10 gpm and as high as 25 000 gpm, with the preponderance of systems operating in the 1000–10 000 gpm range. Earlier ballistic missiles, being essentially fixed thrust systems, required a flow-coefficient range up to only ±10 percent; some space vehicle systems need a thrust variation (throttling) of 10:1, while others have to develop a "pump-out" capability (the ability to continue to deliver full engine flow for full thrust engine operation after a failure of one of the two parallel turbopumps). These requirements result in a flow-coefficient[2] shift of 65 percent for the throttling case and 2:1 for the pump-out case. Table I summarizes the important parameters of the pumps utilized in some well-known rocket engines.

Head or Pressure Rise and Variations

Head or pressure requirements likewise vary considerably; very large head rises are required for low-density liquid hydrogen. Rocket pumps have been built for pressure rises ranging from 700 psi to about 5000–6000 psi; corresponding head-rise values of 1500 to 12 000 ft for conventional density fluids and 20 000 to nearly 200 000 ft for hydrogen are seen in these applications. The earlier ballistic missiles required small variations

---

[2] Defined at end of paper.

of pressure—only enough to cover engine tolerance effects, say ±10 percent; the more recent throttleable systems require a delivered pressure variation of 10:1.

Specific Speed

Specific speeds for the pumps in operating systems have ranged from 500 to 2000 (rpm, gpm, ft units); the majority lie between 600 and 1500. These unfavorably low values are dictated by high head rise, low suction pressure speed limits, and mechanical speed limits of the drive system.

NPSH/NPSP

A tank NPSH (net positive suction head) of zero (i.e., the ability to pump saturated fluid at the inlet to the pump suction line) is becoming a popular criterion for liquid hydrogen systems and has been demonstrated with inducers adaptable to centrifugal pumps. For other fluids such as liquid oxygen, kerosene, and the storable propellants, NPSH values have ranged from 20 ft to 130 ft for current systems. Conventional suction specific speeds being achieved with acceptably low cavitating head losses (2 percent or less) are about 35 000 (rpm, gpm, ft units).

Fluids

A fairly large variety of conventional and unconventional propellants and testing fluids have been handled, as summarized in table II.

Duration/Number of Starts

The duration or life required of rocket pumps is low: ballistic-missile pumps operate for 2 to 5 minutes; space vehicular pumps for 1 to 10 minutes. Newer applications, such as the nuclear and chemical space shuttles, may require multimission usage cycles up to 20 minutes in duration for a usable life of 10 hours. The number of operational cycles has varied from 1 to current requirements of perhaps 100. Testing has typically been conducted on several multiples of these operating times, but the accrual of more than a few hours operating time on a single unit has been rare.

DESIGN CONSIDERATIONS AND TECHNIQUES

Types of Systems

Various pump and drive arrangements have been used and are being portrayed in conceptual designs of new systems. The drive systems for the main propellant pumps have been limited exclusively to gas turbines.

TABLE I.—*Summary of Characteristics—Typical Rocket Engine Pumps*

Pump	Flow rate (gpm)	Head rise (ft)	Shaft speed (rpm)	SHP	Impeller OD (in.)	Pump fluid	Impeller description	Housing description
Titan I fuel first stage	1 642	2 758	8 814	1 734	10.06	RP–1	Aluminum forging—machined	Aluminum casting—volute
Titan I oxidizer fist stage	2 629	1 494	7 979	1 770	10.06	LO_2	Aluminum forging—machined	Aluminum casting—volute
Titan I fuel second stage	659	2 985	24 888	697	4.695	RP–1	Aluminum forging—machined	Aluminum casting—volute
Titan I oxidizer second stage	1 108	1 548	8 831	756	9.00	LO_2	Aluminum forging—machined	Aluminum casting—volute
Titan II fuel first stage	2 234	3 273	8 800	2 295	10.86	A–50	Aluminum forging—machined	Aluminum casting—volute
Titan II oxidizer first stage	2 695	1 640	8 008	2 146	9.635	N_2O_4	Aluminum forging—machined	Aluminum casting—volute
Titan II fuel second stage	896	2 988	22 830	856	5.035	A–50	Aluminum forging—machined	Aluminum casting—volute
Titan II oxidizer second stage	1 006	1 717	8 100	899	8.825	N_2O_4	Aluminum forging—machined	Aluminum casting—volute

J–2 oxidizer	3 000	2 400	8 000	3 000	10	LO_2	Aluminum casting—shrouded	Aluminum casting—volute
J–2S fuel	10 000	50 000	28 000	9 500	11.5	LH_2	Titanium forging—machined, shrouded	Aluminum casting—rolled over volute
M–1 oxidizer	19 000	3 400	3 650	27 000	29	LO_2	Aluminum forging—machined	304L–SS casting—rolled over volute and diffuser
F–1 fuel	15 000	6 000	6 000	27 000	23.3	RP–1	Aluminum casting—machined, shrouded	Aluminum casting—volute, double discharge
F–1 oxidizer	24 000	3 600	6 000	37 000	19.5	LO_2	Aluminum casting—machined, shrouded	Aluminum casting—volute, double discharge
CENTAUR fuel	195.7	29 000	28 600	568	--------	LH_2	Aluminum castings—mounted back-to-back—back shrouded	Aluminum casting—volute, and diffusers
CENTAUR oxidizer	185.3	840	11 400	90.4	--------	LO_2	Stainless forging—shrouded	Aluminum casting—volute, and diffuser
NERVA (I)	7 850	33 100	22 800	7 180	12.25	LH_2	Aluminum forging—machined	Aluminum casting—volute, diffuser

TABLE II.—*Summary of Typical Pumping Fluids*

Fluid	Symbol	Specific gravity	Temperature, °F	Character
Liquid oxygen	LO_2	1.15	−297	Corrosive, explosive
Liquid hydrogen	LH_2	0.07	−423	Cryogenic, low density
Kerosene	RP–1	0.80	70	Easy to handle
Nitrogen tetroxide	N_2O_4	1.45	70	Toxic, corrosive
Aerozyne-50 (½ UDMH/½ hydrazine)	A–50	0.90	70	Toxic
Liquid nitrogen	LN_2	0.80	−320	Cryogenic, easy to handle (substitute test fluid)
Water	H_2O	1.0	70	Substitute test fluid

The pump rotors are supported on shafts carried on rolling-element bearings cooled by propellant or lubricated by specially supplied oil. Figures 1a through 1e illustrate the typical pump and drive arrangements.

Early configurations were typified by single-stage pumps running at suction-pressure-limited speeds, with one or both propellant pumps driven in parallel through a speed reducing gearbox by a common turbine (Titan I, Atlas, Thor, Titan II). The first operational hydrogen/oxygen engine, RL–10 (used on Centaur), employed a two-stage direct-driven hydrogen pump and an LO_2 pump gear driven by the same turbine. This system also employed remote (tank mounted) electric-motor-driven boost pumps. The F–1 engines for Saturn IC utilize in-line low-speed (6000 rpm) single-stage, suction-pressure-limited kerosene and LO_2 pumps direct driven by a common turbine on a single shaft. J–2 and M–1 (200 000-lb and 1 500 000-lb thrust hydrogen/oxygen engines) introduced the separate direct-drive pump concept for each propellant. In these engines, the high-speed hydrogen pump and the lower-speed oxygen pump were each driven at moderate speed. An updated version of the J–2 engine utilizes a hydrogen pump with a very high-work axial stage in series with a single centrifugal stage to deliver a pressure rise of 2000 psi.

Current conceptual designs for high thrust chamber pressure space shuttle engines utilize boost pumps (low-speed inducers) to allow main pump speeds in the range of 30 000 to 40 000 rpm at low NPSH, while utilizing two or three stages to deliver a total pump pressure of 6000 psi. Current NERVA conceptual designs employ a two-stage centrifugal pump of approximately 30 000 rpm, operating at ultralow NPSP (0–2 psi). This pump will require a flow rate change of nearly 2:1 at constant pressure rise and high efficiency to provide pump-out capability to the engine, which incorporates two pumping systems in parallel.

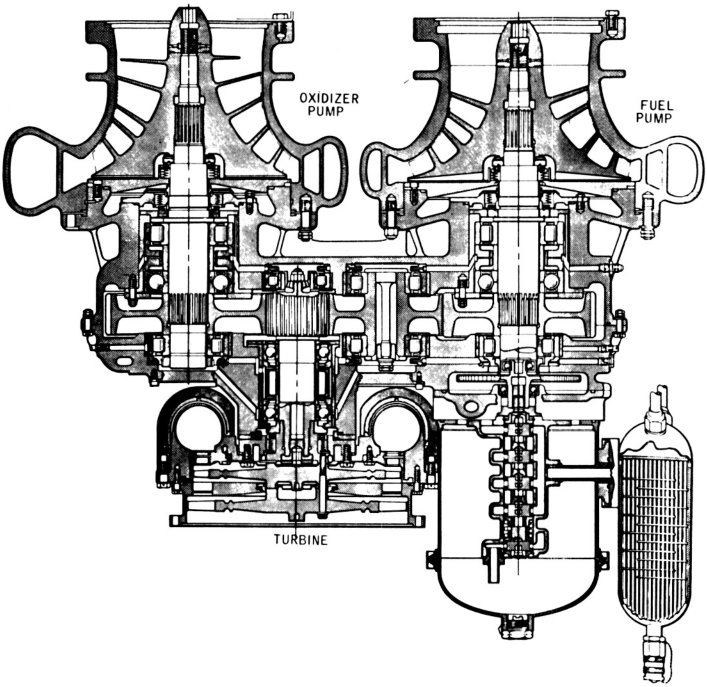

FIGURE 1a.—*Gear-box-driven system: both pumps gear-driven (Titan II).*

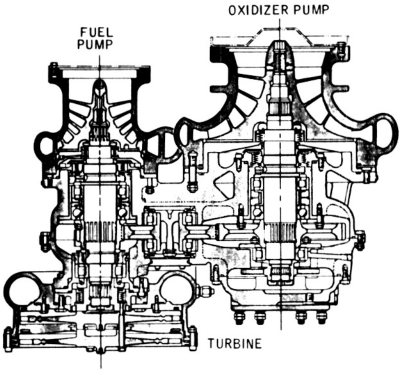

FIGURE 1b.—*Gear-box-driven system: one pump direct-driven (Titan II).*

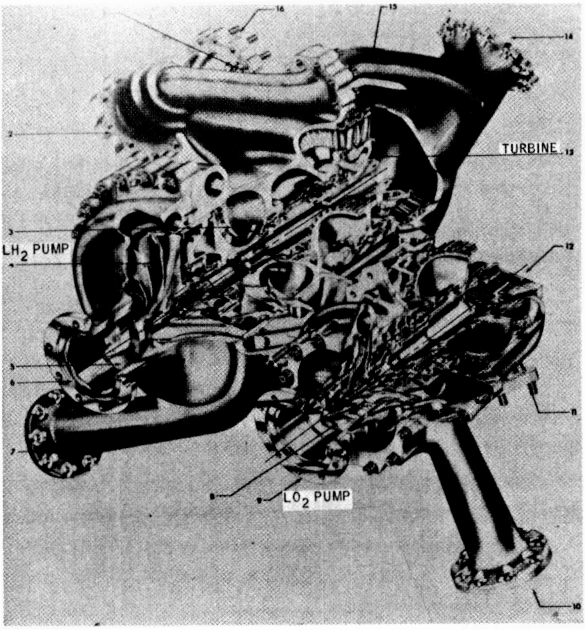

FIGURE 1c.—*Two-stage, direct-driven LH_2 pump; gear-driven LO_2 pump.*

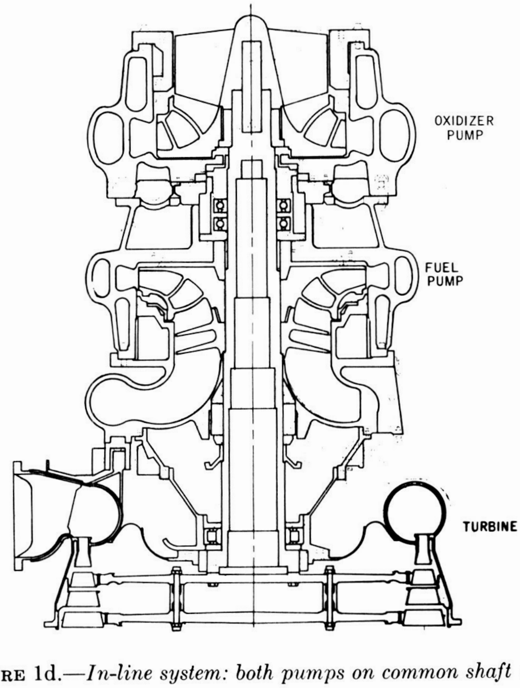

FIGURE 1d.—*In-line system: both pumps on common shaft (F-1).*

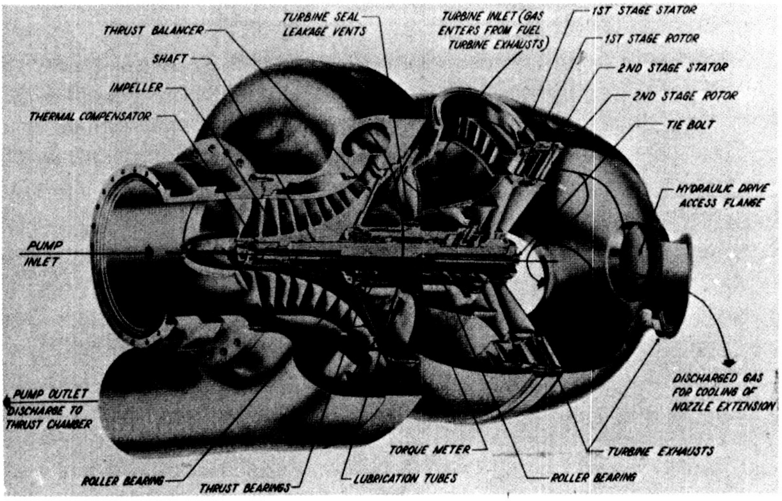

FIGURE 1e.—*Direct-driven LO_2 pump with its own turbine (M-1).*

Shaft Speed

As in most aerospace turbomachinery applications, the most important variables are speed and efficiency. Because speed influences the efficiency as well as turbopump weight, this parameter dominates the pump design. Widely varying shaft speeds have been utilized—3500 rpm to about 40 000 rpm—with the very high speeds used for the low-density hydrogen pumps. The more recent typical consideration of low-speed preinducers (separate stages preceding the main pump inlet which were previously used only on Centaur) has removed the NPSH limit on speed for current conceptual designs, resulting in the speed limit being determined by allowable stresses, gear and seal velocities, or optimum specific speed.

The $N(Q)^{1/2}$ term in the specific speed expression, $N_s = N(Q)^{1/2}/H^{3/4}$, can be used as a measure of relative speed for pumps of differing flow rates. Table I contains such data for selected rocket pumps.

The conventional suction specific speed parameter,

$$S = N(Q)^{1/2}/(\mathrm{NPSH})^{3/4},$$

is used as the index for cavitation performance of pumps. The values achieved with rocket pumps of the past 20 years have evolved from about 20 000 to 40 000. A typical empirical curve for achievable suction specific speed as a function of design inlet flow coefficient $\phi_{1t} = C_{m1}/U_{1t}$ is shown in figure 2, which also depicts a theoretical curve as derived by Brumfield (ref. 1).

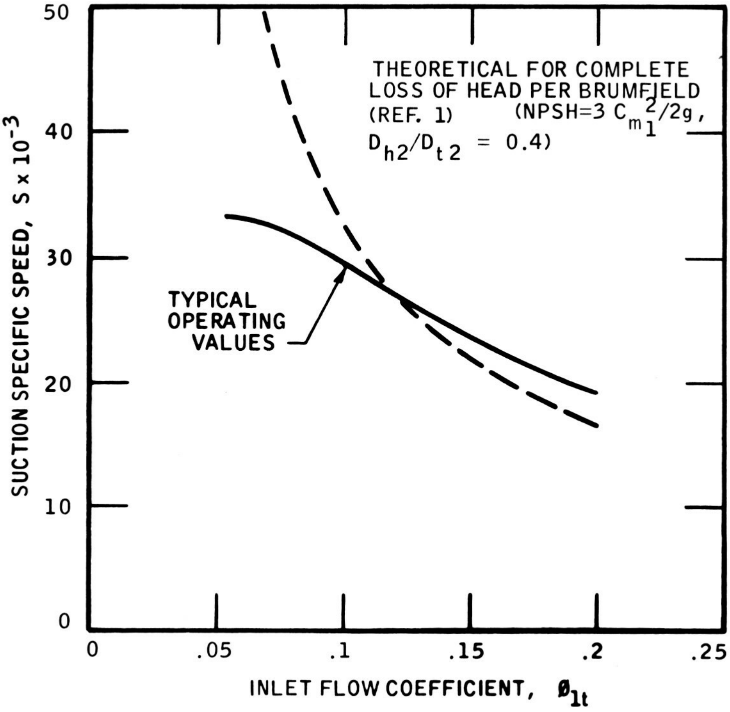

FIGURE 2.—*Specific speed as a function of inlet flow coefficient.*

The cryogenic fluids, particularly hydrogen, exhibit a "sub-cooling" effect, with the fluid having a lower effective vapor pressure because of cooling as the fluid is accelerated and vaporized in the blade passages. With liquid hydrogen, it is possible to operate without significant performance loss while ingesting two-phase flow with up to 15 percent vapor volume at the pump inlet. The extent of the subcooling effect appears to be limited by heat transfer from the bulk liquid to the vapor cavity on the blade surface. The pump speeds that are obtainable with hydrogen are apparently limited by sonic or "choking" flow considerations. Recent test results (ref. 2) indicate that with boiling hydrogen (zero quality) in a tank at 41°R, pump $N(Q)^{1/2}$ values of 2.1×10^6 are possible, provided a close-coupled, low-loss inlet system is used. At higher temperatures, higher speeds can be achieved because of additional fluid subcooling effect; conversely, lower temperatures require lower speeds. Liquid oxygen and the multi-component, mineral-base fuels (RP–1 and similar fuels), while not cryogenic, exhibit the same characteristics to a much lesser extent.

Pump Efficiency

Figure 3 shows typical design efficiency curves for rocket pumps as a function of stage specific speed and impeller size. Impeller size has been used rather than volumetric flow rate (as in the Worthington "experience" curves, ref. 3) because efficiency appears to be dependent on size for rocket pumps and because the higher $N(Q)^{1/2}$ values of rocket pumps result in smaller sizes than for a typical fixed-station pump of comparable flow rate. The inferior rocket pump efficiencies, particularly at the higher specific speeds, are attributed to the higher suction specific speeds and relatively large inlet diameters (poor geometry) of rocket-pump impellers.

Configuration Selection and Special Design Considerations

No basically new pump configurations have been used for rocket-pump design. Differences from fixed-station pumps have generally been more apparent in the values of design parameters used, due to the special considerations of the application, such as drive system and envelope limits, and ducting arrangements.

The major types of impeller and housing concepts used for commercial systems have all found use in rocket-pump applications, including the

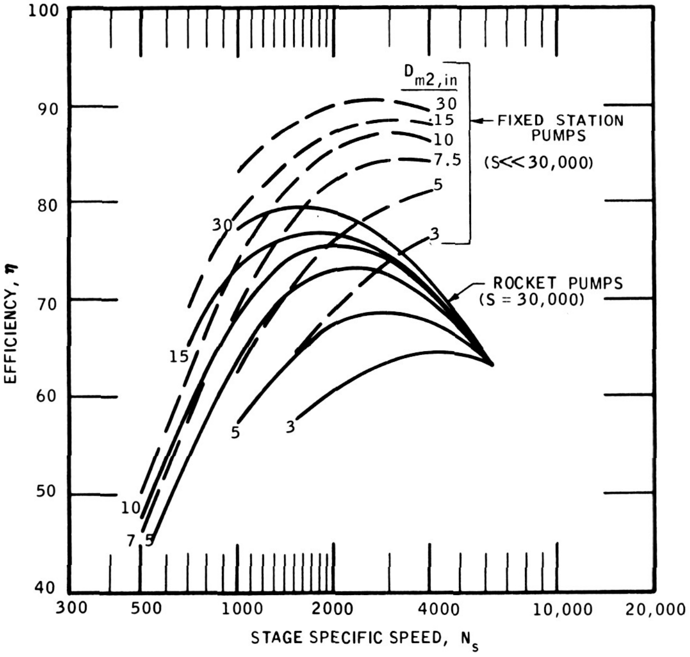

FIGURE 3.—*Efficiency as a function of stage specific speed.*

double shrouded impeller, the open impeller, the diffusion housing and the single volute, the double volute, and volute housings with various internal guide vane and splitter arrangements. Radial- and axial-flow inlet housings have been used, as well as the elbow and divided flow (or "baby pants") types of radial-flow inlet housings. The only multistage concepts have been for hydrogen applications. The Centaur (RL–10) pump is an example, the two stages being mounted with the impellers back-to-back with volute housings and an external, interstage crossover pipe.

The type of impeller and housing have often been "designer's choice" because the relative merits of each from a hydrodynamic or mechanical standpoint have not been firmly established and probably will not be in the near future. Based on one-dimensional analysis, it would appear that the open impeller is more efficient at the lower specific speeds, while the shrouded impeller is more efficient at the higher specific speeds. The same can be said of diffusion housings or vaneless volute housings (especially the double-discharge type) when compared to volute housings with internal guide vanes and impeller backvanes compared to wear rings or labyrinths.

Mechanical-design choices also are not clearly defined. A major problem area with the high-head-rise hydrogen stage is centrifugal stress in the high-tip-speed impeller. The open impeller has advantages over the shrouded impeller from a fabrication and stress standpoint, but the specific value of stage head rise at which the shrouded type can no longer be used is not easily defined. A choice the designer faces in the use of vaned housings is whether to let the vanes carry a significant portion of the separating force or to have a stiffer outer wall support the loads. The design with load-carrying vanes is lighter; however, the stress concentrations in the region of the vanes and the housing tongue are not easily defined for such a complex structure, and consequences of a miscalculation can be serious.

Hydrodynamic Design

Impeller/inducer. Conventional pump design practice has been used as the primary design technique. The one major exception is the use of empirically derived criteria such as that of figure 2 to select inlet geometry. Inducer concepts in which the blading is continuous with the main impeller, as well as concepts with separate blading incorporating a gap between the inducer and impeller, have been used. The separate-blading type exhibits better performance at higher suction specific speeds.

One-dimensional techniques are used for the flow analysis, except for the use of axisymmetric stream-filament solutions for the flow in the impeller to position the shrouds or design the through-flow profile. The results of such calculations are also used to estimate the blade surface velocity distributions, making simple assumptions for the blade-to-blade velocity distribution.

The selection of the impeller exit geometry is also based primarily on empirical data such as figure 4, which shows representative values of impeller head coefficient, $\psi = \Delta H / U_2^2/g$, as a function of specific speed at the best efficiency point.

The "area-moment" method or cascade solutions (as originally proposed by Stodola, (ref. 4) are used to estimate impeller exit-flow deviation effects. The "rule-of-thumb" that the number of impeller vanes is one-third of the discharge blade angle has been applied with fair success for rocket-pump impellers, at least at the impeller discharge. The relatively low inlet blade angles dictated by suction performance requirements result in a small number of blades at the inlet. The use of partial or splitter blades, starting one-third to three-fourths through the impeller, provides proper solidity to the high-head generation region. To simplify

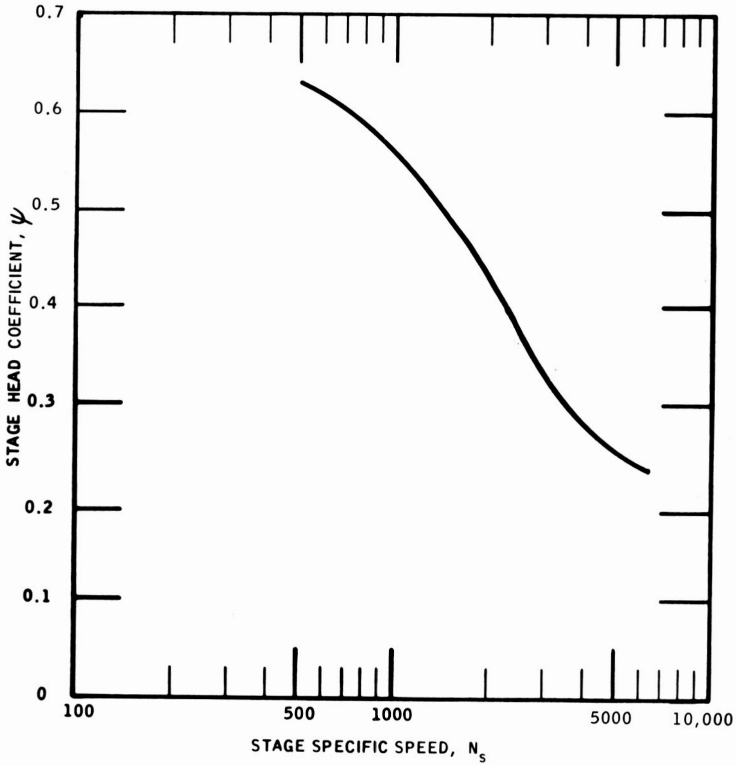

FIGURE 4.—*Stage head coefficient as a function of stage specific speed.*

machining of impellers, "straight-element" type blades are primarily used so that side-milling may be employed.

To calculate leakage through wear rings and labyrinths, methods developed for steam and gas turbines are used. For open impellers, empirical test data (such as that of fig. 5) are used to estimate the effects of clearance on pump head rise and efficiency. Figure 6 indicates the types of open impeller clearances used for rocket pumps as a function of specific speed.

Housing. One-dimensional analyses are also employed for housing design. Figure 7 shows some of the experience in terms of housing-base-circle/impeller-discharge-diameter ratio as a function of specific speed, with values of housing and diffuser-throat-velocity/base-circle-velocity ratio shown in figure 8.

For some very low specific-speed applications, very small volute and diffuser angles have been used, with the absolute flow angle of the base

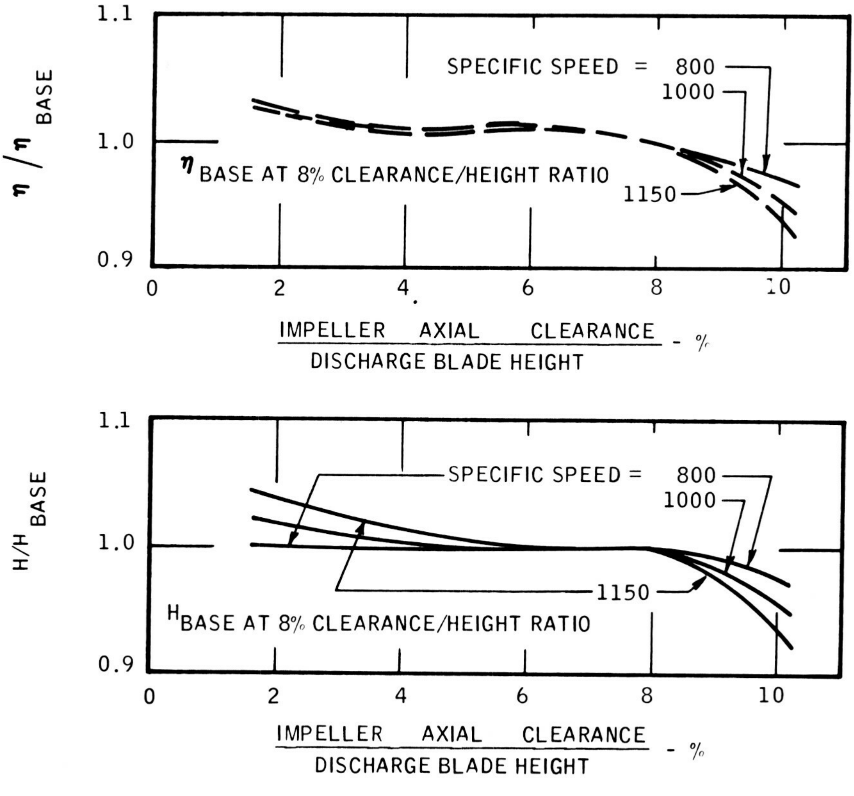

FIGURE 5.—*Head rise and efficiency as functions of clearance to blade-height ratio.*

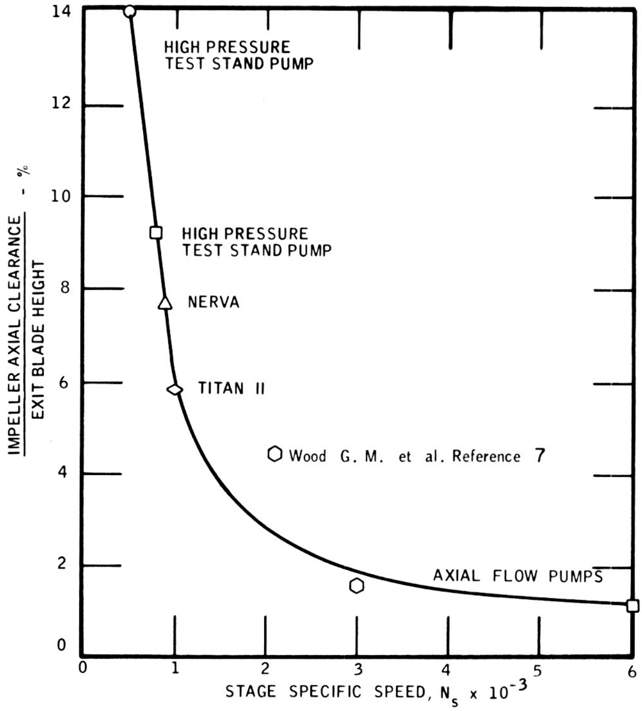

FIGURE 6.—*Clearance to blade-height ratio as a function of stage specific speed.*

circle as low as 4 or 5 degrees. Diffuser vane systems with inlet angles as low as 6 degrees have been used.

Both the cascade and channel flow approaches have been used for vane system design. For the very-low-angle vane systems, the inlet portions of the vane have a mean camber line which is close to a log spiral. This is the counterpart of the constant lead helical blade in an axial-flow system, and similar fluid-incidence/vane-angle relationships seem to apply at the minimum loss, with the minimum loss incidence angle about 40 percent of the vane angle.

Vane proportions have usually followed values given by Stepanoff (ref. 3) for chord length to spacing. With the increasing use of fabricated housings and higher strength materials, and since chord length has also been governed in many cases by structural considerations, it can be expected that somewhat shorter chord lengths and larger members of vanes may be used in the future.

Prediction of performance. One-dimensional methods supplemented with empirical data are usually used for off-design performance estimates. Simple approximations can be made of the off-design losses through

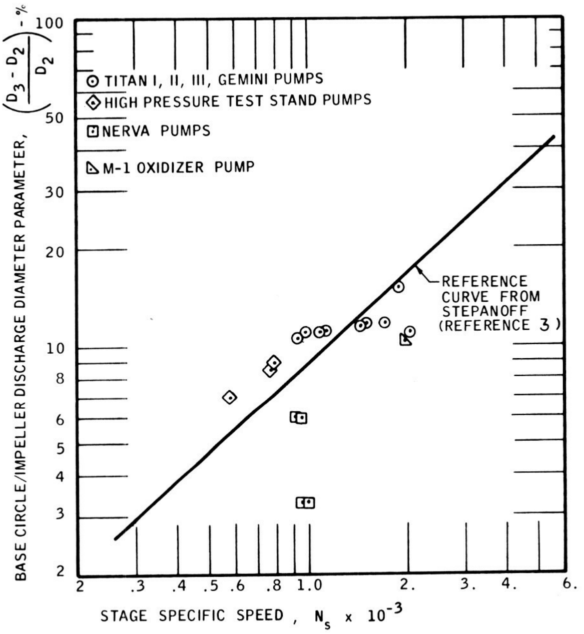

FIGURE 7.—*Housing/impeller diameter ratios versus stage specific speed.*

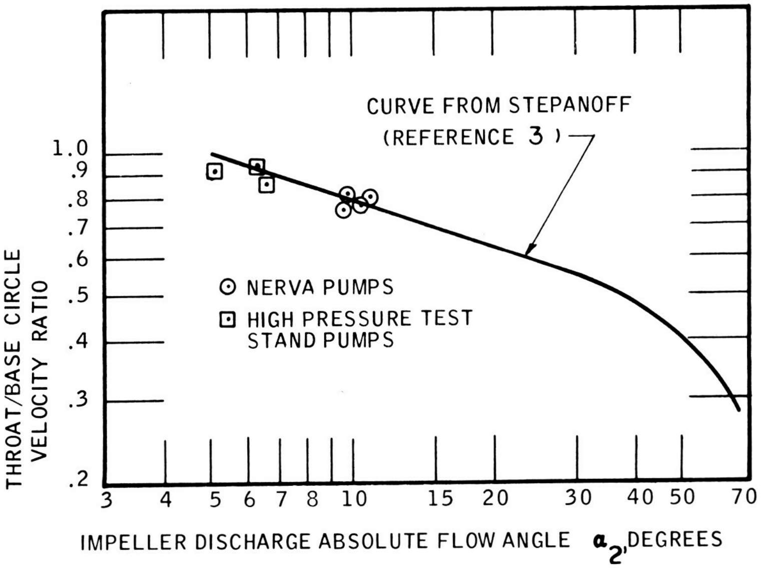

FIGURE 8.—*Housing velocity ratio versus impeller flow angle.*

blade rows, such as the assumption that losses are equal to the velocity-head difference between the off-design and the design inlet tangential velocity components.

With the advent of throttleable engine applications and redundant (two-pump) feed systems, more accurate predictions of the slope of the head-flow curve and the location of the gross flow separation point are required to ensure fluid-dynamic stability. The cascade-analysis approach appears to be more accurate than the channel-flow technique. For low-angle diffuser vanes, it has been found that the gross separation point occurs at fluid-incidence/vane-angle ratios similar to the corresponding point for the constant-lead-helix axial-flow blade; i.e., a fluid-incidence angle approximately 60 percent of the blade angle.

Axial and radial thrust. Procedures for estimating axial and radial thrust forces follow those used for fixed-station pumps. Single-discharge, double volutes with long internal splitters have been used to minimize radial thrust forces.

The most accurate method of estimating axial thrust has been to use local head-coefficient distributions as obtained for similar designs. For the higher-speed hydrogen-pump designs, it has been necessary to use single or double acting axial-clearance-compensating thrust pistons or discs because of the relatively low axial load capacity of the high-speed liquid-hydrogen cooled bearings. As pump speeds increase, it may be necessary to use such balancers for the lower-speed dense-propellant pumps.

Mechanical Design

Structural factors of safety. Since minimum weight is a prime design objective, the mechanical design of rocket pumps is based upon small structural factors of safety. The factors currently being used with the available analytical techniques are in the range of 1.10 to 1.20 for tensile yield strength and 1.2 to 1.5 for ultimate tensile strength, applied at a speed and associated pressure about 10 percent above the maximum speed to be expected in engine operation. This allows transient excursions and some adjustment in engine requirements.

Methods of analysis. The burst speed margin of the impeller disc, deflections of the disc and blade as they affect fits and clearances, blade stresses (including pressure, vibratory, and thermal loads), and housing stresses are the principal structural limits. Disc and housing stresses are calculated using finite element techniques on the digital computer. The analysis includes the magnitude and distribution (nonuniformity) of material strength and ductility and accounts for pressure, thermal, centrifugal or rotational (impeller), and flange (housing) loads, as well as stress concentrations. The criteria are acceptable tangential impeller stresses, acceptable deflections in the impeller and housing, and adequate safety margins on yield or ultimate strengths in the housing.

Blade stresses are calculated based upon centrifugal and steady-state pressure loads, cyclic pressure loads, and the effect of operation close to blade natural frequencies. Structural adequacy is determined by a comparison of calculated stresses with the allowable envelope of the modified Goodman diagram, which indicates combinations of mean and alternating stress for a given cyclic life and material.

Materials and fabrication techniques. Low-tip-speed impellers (<1000 ft/sec) are usually cast or machined (cam-generated or pattern-duplicated) from aluminum (356, Tens 50, 7075, 7079) or corrosion-resistant alloys (Monel, K-Monel).

Impellers for high-tip-speed applications (hydrogen pumps) are machined from high-strength forged material, usually alpha titanium (5 Al-2.5 Sn, ELI). Figures 9 and 10 illustrate typical unshrouded, machined impellers.

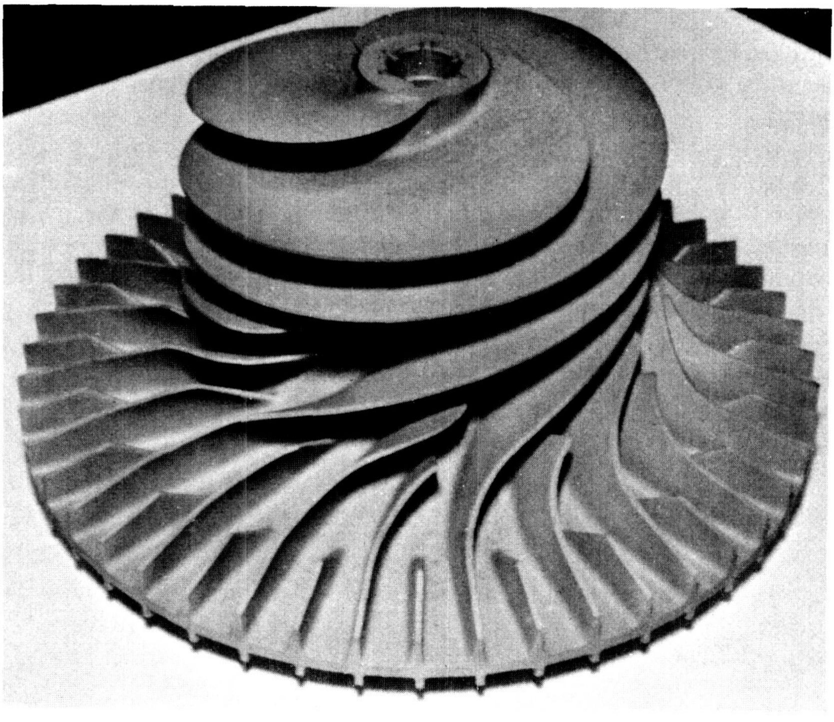

FIGURE 9.—*Typical unshrouded LH_2 pump impeller (NERVA I).*

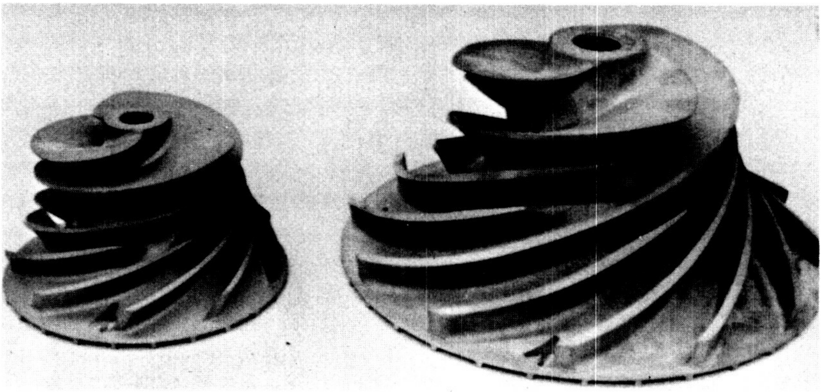

FIGURE 10.—*Typical conventional density propellant impellers* (*Titan* II).

Shrouds have been used on both the cast and machined configurations; in the latter, the shrouds are integral with the blades and are machined from both the inlet and exit ends by use of milling cutters or the EDM (electrical discharge machining) process.

Operating and burst tip speeds of at least 2000 ft/sec have been achieved with high-strength forged alloys. The ratio of strength to density favors titanium over the higher-strength Inconel and the lighter-density aluminum.

Housings are fabricated in two basic forms, either as castings or as weldments of formed elements. Both of these methods have been used for housings with and without diffuser vanes. The common materials include aluminum (Alloys 356 or Tens 50) and 300-series stainless steel for castings; and 300-series stainless, Inconel 718, and alpha titanium (5 Al–2.5 Sn) for the welded/wrought construction. The need to retain ductility for stress redistribution is an important factor, particularly in the cryogenic applications. The high-pressure systems are currently utilizing the high-strength alloys to reduce weight. Figures 11 and 12 illustrate typical housings.

Weight. The weight of rocket pumps is difficult to correlate because of a variety of design approaches and applications; since pump weight alone is not particularly meaningful, only turbopump weights are readily available. The effects of pump-shaft torque requirements on turbopump weight are shown in figure 13. The data tend to fall on a single line, regardless of whether the turbine is driving one or two pumps. The exceptions are the hydrogen pumps, which have significantly less weight for a given shaft torque.

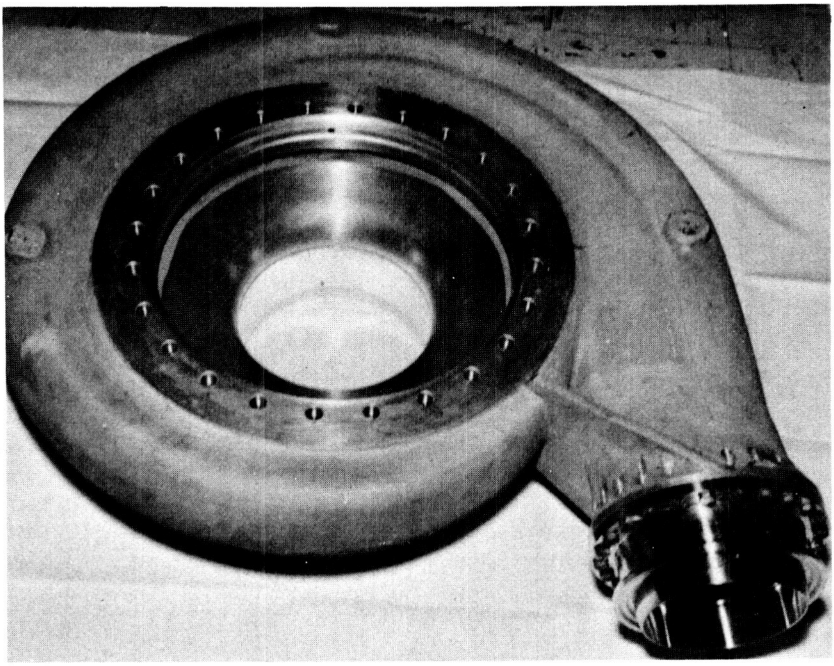

FIGURE 11.—*LH_2 pump housing with diffusers (NERVA I).*

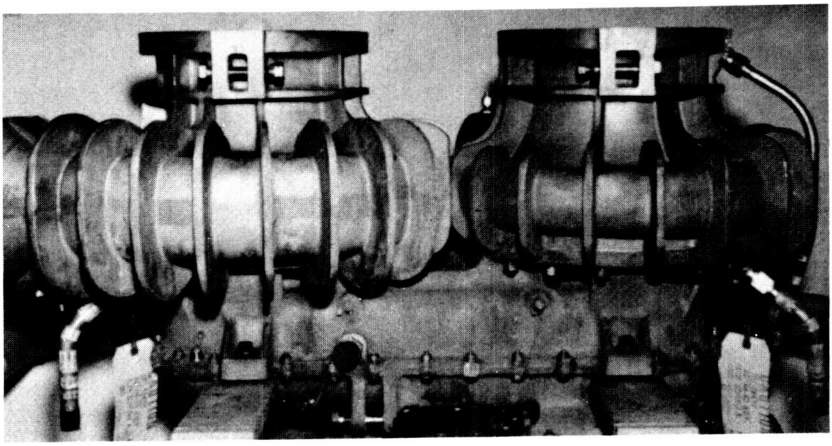

FIGURE 12.—*Typical volute housings (Titan II).*

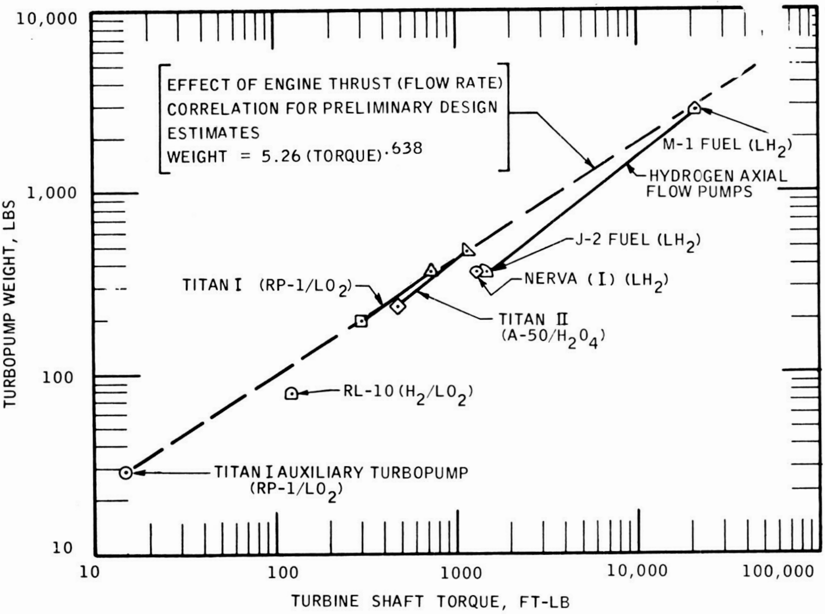

FIGURE 13.—*Turbopump weight as a function of turbine torque.*

TESTING AND DEVELOPMENT PROCEDURES

The development of rocket engine pumps has been somewhat equally concentrated between improvements of performance and mechanical integrity. Earlier systems favored achievement of safe operation over refined performance. However, the desire for better performance achieved equal status in later systems, once mechanical-design solutions were evolved for the earlier mechanical problems such as explosions, pump rubs, excessive axial and radial thrust, and impeller and housing failures. A new cycle of mechanical integrity emphasis may now be imminent with the advent of the long-duration, high-pressure cryogenic systems with stringent reliability requirements.

In contrast to the commercial pump application, rocket engine pumps are rarely an adaptation of an existing design due to significant changes in requirements from system to system. Because of this, all such pumps have required a development program. This data accrual/design adjustment cycle utilizes data from three sources: (1) component (pump only) tests, usually electric-motor driven at full or partial speed, with actual or substitute fluids (e.g., water or air); (2) turbopump (turbine-driven pump) tests at full speed, using actual or substitute fluids (water, liquid nitrogen); and (3) engine tests, at full speed with actual fluids.

The pump tests are usually of long duration and are used for mapping and wide off-design excursions without speed transient effects. Head rise and efficiency are derived as functions of flow rate and NPSH for a variety of speeds from parameters recorded at 1 to 1500 samples per second by an analog-to-digital measuring-recording system. Measurements are also made of axial thrust and shaft axial and radial displacement, as well as

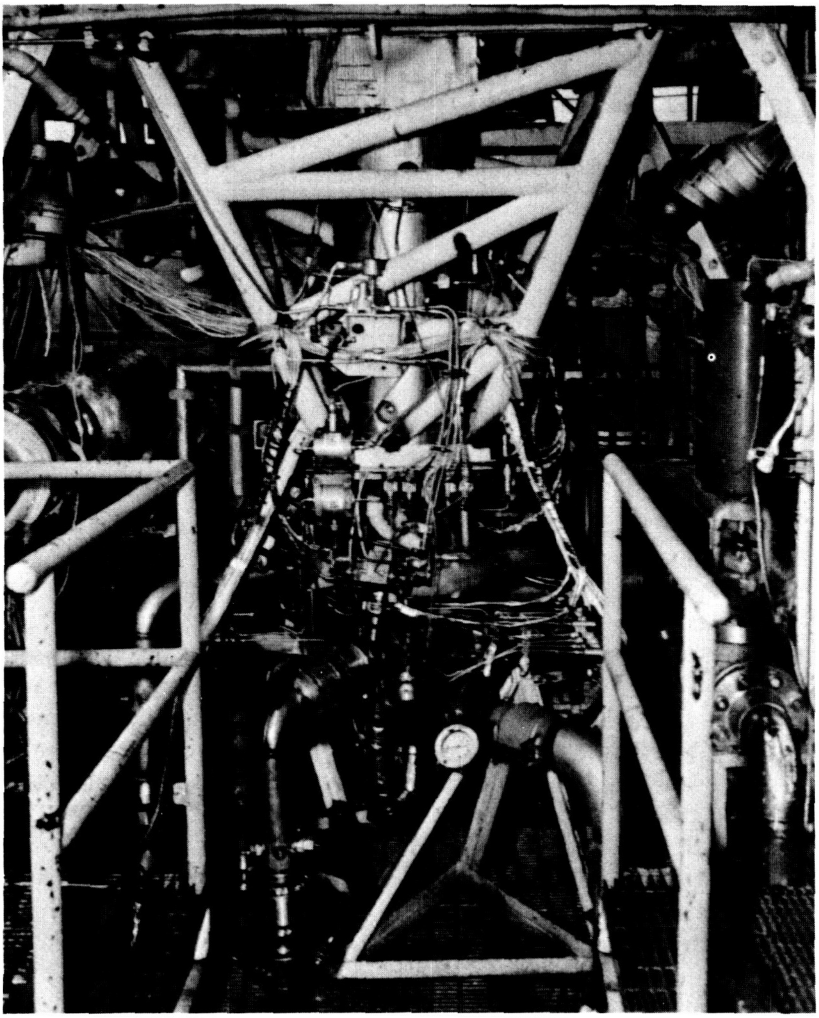

FIGURE 14.—*Typical turbopump test installation.*

velocity surveys, high-frequency pressure-oscillation surveys, and vibration monitoring. The output of this testing, during which approximately 50 to 100 parameters are typically measured, is a set of pump performance characteristic maps and a description of operating behavior.

Turbopump tests, utilizing 100 to 250 measurements, confirm performance over a more limited range of operation. This type of testing concentrates on transient behavior, verifies structural integrity, and acquires operating environment data under the more severe conditions imposed by the turbopump to support additional design analysis. Figure 14 shows a typical turbopump test installation.

Engine ground and flight tests further confirm performance, but primarily confirm or adjust start and shutdown transient effects and environmental data, such as stage or gimbaling induced pump inlet velocity distortion, stage-coupled structural oscillation (POGO) effects, and malfunction shutdown flow and speed excursions.

Most of the testing, other than that done at the pump level, is considered behavioral/interaction testing, and serves primarily to identify those areas requiring additional analysis, design refinement, or additional testing. These behavioral/interaction effects have significant impact on pump reliability, affecting both performance and mechanical integrity. Since the effects are often subtle and difficult to attack analytically, a large portion of the total testing effort is devoted to understanding these effects.

Structural testing is used to a lesser degree, but serves to further the understanding of part behavior under a simulation of imposed operating conditions. The more important structural tests are (1) housing (casing) pressure-integrity hydro-tests to confirm that burst pressure is adequately high and pressure-induced distortions are acceptable; (2) impeller-blade vibration survey tests to verify that resonant frequencies which would produce vibratory stress failures lie outside operating regions; and (3) impeller or disc spin tests to verify the structural adequacy of the impeller under the required operating tip speeds.

DEVELOPMENT EXPERIENCE HIGHLIGHTS

Problems

Most rocket pump programs have suffered their share of problems, including such vivid early experiences as LO_2 pump explosions and fires. Causes were usually found to be either contamination or severe rubbing resulting in sufficient heat to actually ignite the material, as illustrated by figure 15, an example of the results. Light rubs of the impeller in the housing, caused by shaft deflection due to combined radial and axial

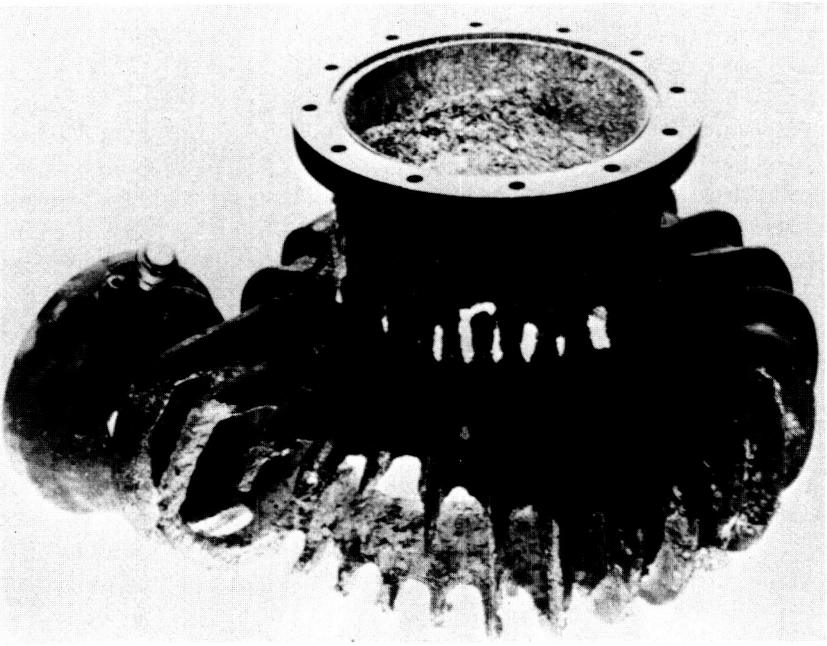

FIGURE 15.—*Results of LO_2 pump fire.*

thrust, were noncatastrophic but frustrating because of the explosion potential.

Structural failures of housings and impellers have occurred. These have most often been impeller-blade fatigue failures, usually of blade corners or tips (fig. 16 shows failure and secondary damage), and housing vane or tongue cracks at the leading or trailing edge. Housing failures were usually due to high local stress in the load-carrying tongue or vanes, together with low ductility and low strength of the cast material (fig. 17). The impeller failures have been attributed to operation at or near blade resonance and to the low stress redistribution capability of the comparatively low ductility aluminum material. The already low ductility was exaggerated by exposure to cryogenic temperatures in some of the systems. "Contamination" has also caused failures, as shown in figure 18.

A very impressive problem in a mechanical sense has been axial (end) thrust, particularly on large or high-pressure pumps. The problem rises from an inability to predict the magnitude of the small difference of the two very large pressure forces of the front and back faces of the impeller. Even with pressure survey data, errors of a few percent result in intolerable variations in net forces. Unbalanced forces of several thousand pounds have been observed on initial tests.

FIGURE 16.—*Typical impeller blade failure.*

Performance deficiencies occurred in head rise, efficiency, and low NPSH capability. The first two were the results of poor estimates and data scaling, together with improper accounting for the effects of generous clearances used to preclude rubs. Additionally, losses in the high-rate-of-diffusion impeller passages have been a reason for performance disappointments. Suction performance deficiencies occurred when pumps were operated at design (and more often at off-design) inlet flow coefficients. Mismatches of the engine operating conditions and pump performance (due to changes in both compared to initial design point assumptions) caused operation at deviations from the best efficiency point or best inlet flow coefficient.

The rapid start and shutdown transients (varying from 0.5 to 3 seconds from application of power to full speed) have caused transient axial and

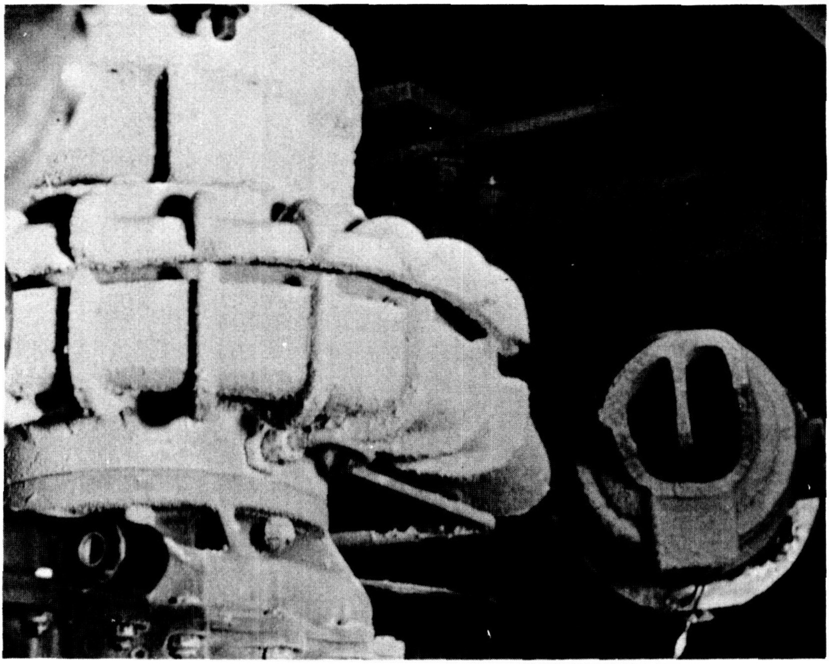

FIGURE 17.—*Pump housing rupture during cryogenic test.*

radial hydrodynamic loads and off-design fluid blade loadings, resulting in overstress and shaft deflections and rubs.

Difficulties have been experienced with cryogenic pumps in maintaining proper fits and clearances due to the large change in absolute and relative dimensions between ambient fabrication/assembly temperature and an operating temperature perhaps 500° R lower. These changes of several thousandths of an inch require detailed analysis when critical fits or clearances are selected, particularly for the transient period between ambient equilibrium and uniform operating temperature. Even the data scatter in the coefficient of thermal contraction has caused the variation of pilot diameter fits to be unacceptable.

Cavitation damage has not been a problem on operational pumps due to the short operating cycles. Some damage has been observed on both aluminum impeller blades and housing vanes; this damage has become excessive on test pumps which have been run longer than flight duration, but damage of this sort has not been observed in hydrogen pumps. Prevention of cavitation damage will be a serious consideration in the design of the currently envisioned 10-hour duty cycle systems.

During flight tests of several missiles and vehicles, conditions of longitudinal oscillation of the entire vehicles were observed. This phenomenon,

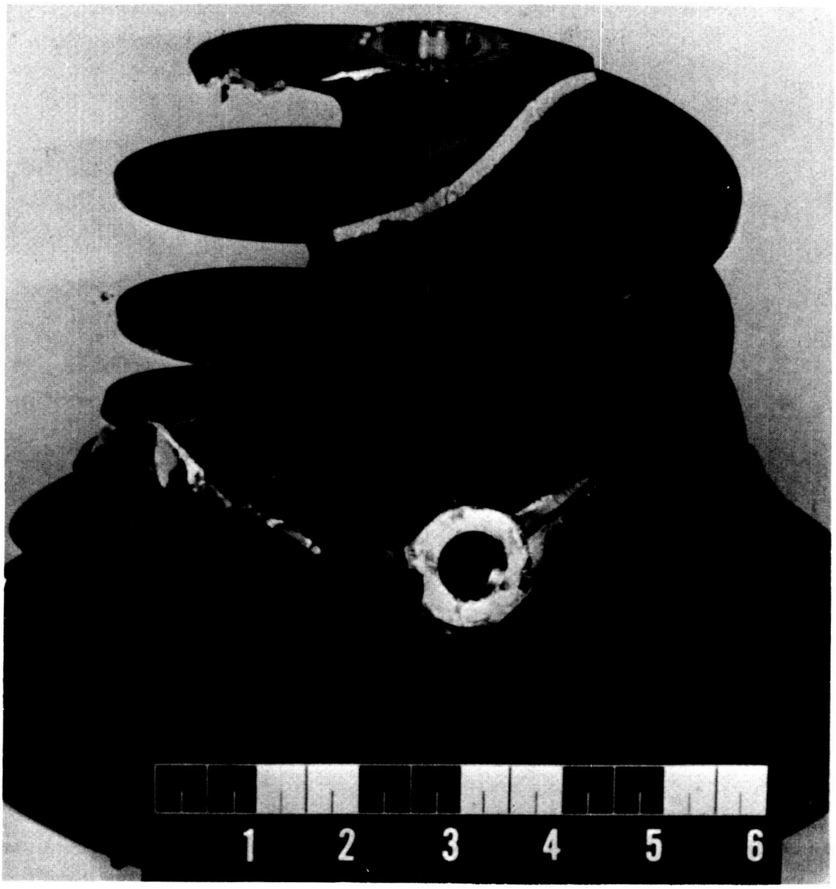

FIGURE 18.—*Results of test stand contamination.*

called POGO, is felt to be caused by a coupling of the fluid/thrust system with the structural frequency of the engine and vehicle. One of the parameters in this loop is pump "gain." Significant efforts were devoted to trying to improve suction performance (in terms of slope of the head rise versus NPSH characteristic of the pump).

Embrittlement (loss of ductility) of some materials (titanium 5 Al–2.5 Sn ELI and Inconel 718) has been recently observed in the presence of high-pressure hydrogen. This problem is not thoroughly understood but is causing concern for the highly stressed applications.

Improvements

In spite of these disappointments, successful pumps were evolved through a series of test-fail-fix steps and improvements in analysis and design techniques. When the change in difficulty of new applications did not outdistance the improvement in state-of-the-art or design capability, progress was evident.

Explosions and fires are essentially unknown in current operational LO_2 pumps. This advance has largely been the result of tremendous attention to cleanliness control; elimination of severe rubs with more rugged designs and the use of compatible and non-heat-generating materials for close clearance elements, such as wear rings, have also led to successful solutions.

Structural failures still persist. An adequate understanding of both disc and housing structural-analysis methods has been achieved largely because of the use of analytical (including finite element) techniques correlated with experimental data using strain gage and burst test information. However, blades are still a problem due to both hydrodynamic and vibratory loading. Impeller blades are virtually impossible to analyze for vibratory stresses; hydrodynamic forces are difficult to predict, and the complex blade geometry precludes translating this into a meaningful stress value. Rules of thumb based upon "this one failed—that one didn't" have been used for sizing, followed by blade shake tests and pumping tests for confirmation. Changes in environment, such as engine or turbopump testing versus pump testing, still cause surprise failures on seemingly successful configurations. However, a recently completed program (ref. 5) may furnish a tangible solution.

The lesson of low ductility has been well learned, both for housings and impellers; however, the attraction of high yield and ultimate strengths still presents a tradeoff for the use of marginal ductility (elongation between 3 percent and 10 percent). Fracture-mechanics stress-analysis techniques which treat brittle or flaw-containing material are beginning to be employed. Improvements in material fabrication methods have been noteworthy. Forgings have been produced with virtually consistent strength in all directions (no directional grain effects) or with controlled flow lines. Heat treatment intermediate through the machining process has been employed to increase strength and ductility. Aluminum castings have been much improved in quality; strength and ductility have been bettered due to careful impurity control and elaborate chilling approaches, together with the use of nondestructive and tensile tests for process development and control. Surface finish has been dramatically improved (finishes of 63 rms are now available) by the use of shell and plastic coring techniques. Welding methods (particularly electron beam) have allowed the use of both high-strength alloys (Inconel and titanium) and high stress levels, together with weight optimized shapes, in fabricated housings.

Axial and radial thrust are still problems, particularly in high-pressure systems. The axial thrust problem has become more understandable due to the accrual of test data on the pressure-area forces (measurements of pressure across front and back faces) and the net shaft thrust (force measuring sleeves in the shaft support system). The technique of wear ring diameter adjustment has been well known; back-vane trimming based upon backside vane performance (including cavitation) is reasonably well understood. Most new hydrogen pumps have abandoned thrust bearings in favor of thrust balancers.

Radial thrust remains unpredictable, particularly at wide off-design flow rates. The use of diffuser or dual exit housings has reduced the effect. For very close-clearance systems, pressure surveys from which symmetry and radial force can be inferred are useful as a development technique.

Performance improvements have been realized primarily in the ability to pump at low NPSH values. This has been most obvious in hydrogen pumps and is due not so much to particular design improvements as to the realization of the beneficial thermodynamic character of hydrogen and its somewhat homogeneous nature when boiling. Ratios of NPSH to inlet axial velocity head of 1.0 for hydrogen pumps and 3.0 for other fluids are common performance achievements. However, this entire subject is the scope of other papers and is too complex to be properly discussed here. The reduction of parasitic and leakage flows, the reduction of impeller diffusion or secondary flow losses, and the improvement of surface finishes have accounted for small efficiency improvements. Stall margins have been improved by more nearly optimum selection of housing vane geometry. However, it may be seen from the previous discussion that the rocket pump is still not competitive, from the standpoint of efficiency, with the fixed-station system.

Shaft speed and pressure rise limits have been increased, due largely to improved materials and to fabrication and design techniques. Currently proposed systems will operate at shaft speeds up to about 40 000 rpm and achievement of hydrogen pressure rise of about 6000 psi (nearly 200 000 ft) in two or three centrifugal stages is predicted. Without shrouded impellers, tip speeds are acceptable with two stages; with shrouds, three are more attractive. Experimental rotors have been run at tip speeds above 2000 ft/sec at room temperature. The increased strength at cryogenic temperature allows the use of titanium impellers at higher tip speeds.

Problems associated with rapid start/shutdown and flow change transients have been reduced by a better understanding of transient conditions and more attention to design of those features affected by transients. Better understanding has been derived by improved analytical prediction techniques, using analog computers, based largely on data acquired on routine or special-purpose development tests. Especially when correlated with applicable test data, these analytical techniques can accurately predict flow rate, speed, pressure, and suction pressure transients as functions of time during anticipated engine behavior. As an example, a special test program was recently completed to acquire transient behavior data and to refine analytical models for a dual (parallel) pumping system to prove the "pump-out" capability during highly transient operation.

Temperature effects have been adequately controlled, provided a transient heat transfer and stress/deflection/fit-clearance analysis is performed. This rather sophisticated analysis is required to preclude excessive thermal stresses and to prevent loss of critical fits or clearance (impeller-to-housing or thrust balancer-to-housing).

Achieving the elimination of cavitation damage for long duration applications remains to be proven. Initial solutions involve the use of high-strength alloys rather than aluminum, particularly for the higher-density fluid applications.

A tremendous amount of work has been devoted to elimination of POGO. The reader is referred to the literature for an overall view of the problem and its solutions.

Hydrogen embrittlement studies of high-strength alloys are now the subject of vigorous experimental investigation to determine those combinations of material, pressure, temperature, and time that cause embrittlement or reduction of strength, as well as the design values of mechanical properties that can be used. Reference 6 presents an excellent bibliography on this subject.

Testing techniques and test facilities have been improved, particularly those used for turbopump development, where a large portion of cryogenic pump development is conducted. Improvements have been mostly in the form of control systems that allow "pump designer type" data to be acquired, compared to what was formerly almost a single data-point test capability. Automatic speed and Q/N controllers have been used very successfully for pump mapping. Moderate success has been obtained with control of NPSH by means of a computerized "on-line" computation of NPSH from measured values of static pressure, temperature, and flow rate (convertible to velocity head) and control of static pressure to effect the desired NPSH. It must be noted that these are very complex facilities (as shown in figs. 19 and 20), utilizing computers for both control and data accrual-conversion, electronic control systems, and an operational crew of 30 to 60 highly skilled engineers and technicians.

CONCLUDING REMARKS

The most significant influence on the evolution of the rocket engine pump has been the evolution itself. The wide variety of design requirements from one application to another has caused *nearly every system to* *be a new product.* To maximize the performance of new designs (products), each is pushed to or beyond existing experience limits so that *improvements in the state-of-the-art are projected concurrently with the pump development.*

The wide range and combination of flow rate, head rise, and fluid properties virtually prevents accurate scaling of either performance predictions or mechanical designs; in other words almost no adaptation of existing designs has been possible. As a result, no ready set of designs or adaptable hardware has existed, and most new pump programs have gone through the entire sequence of concept selection, design, development, and qualification prior to production. This trend is expected to continue. However, either quicker product development or improved performance and reliability or both can be expected to result from the design techniques developed during the further evolution of rocket pumps and from the continued attention to the development of pump technology supporting the mainstream engine programs.

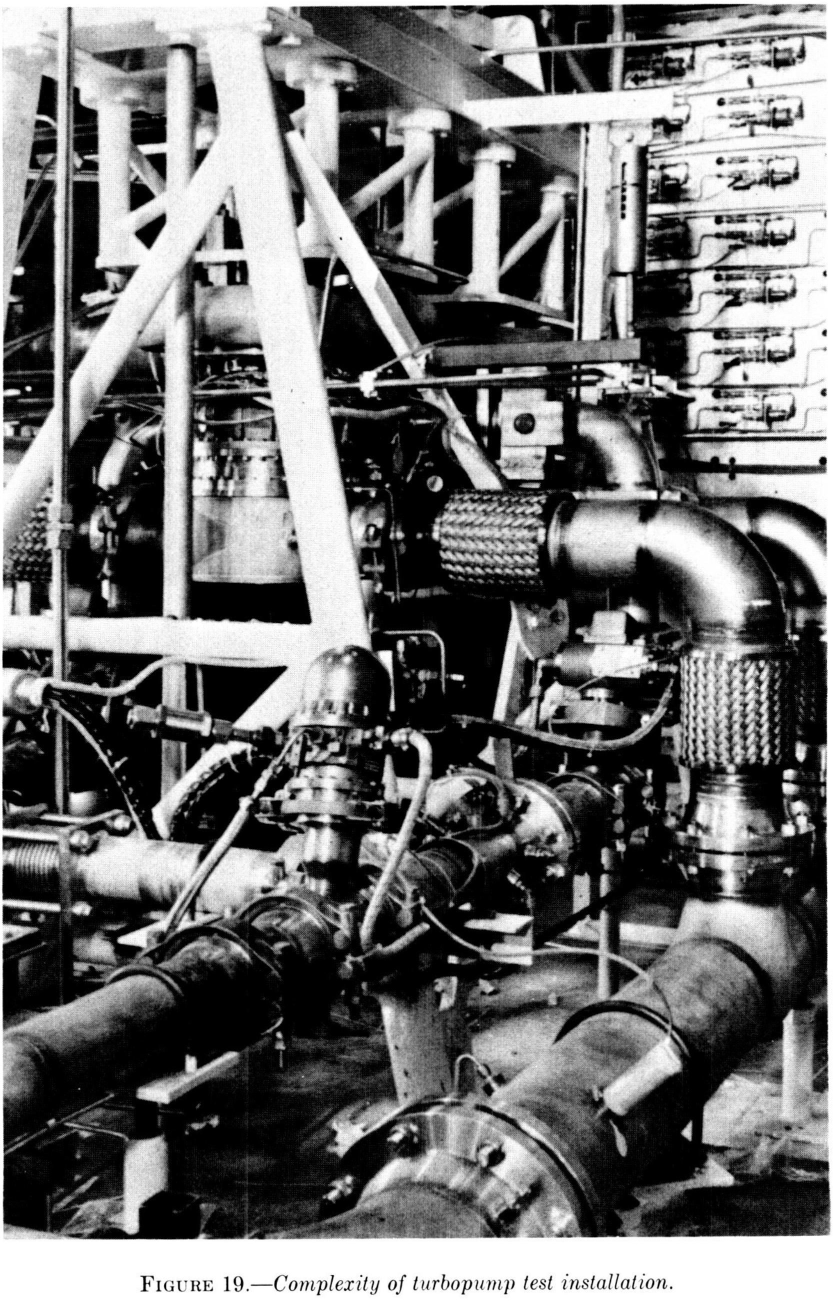

FIGURE 19.—*Complexity of turbopump test installation.*

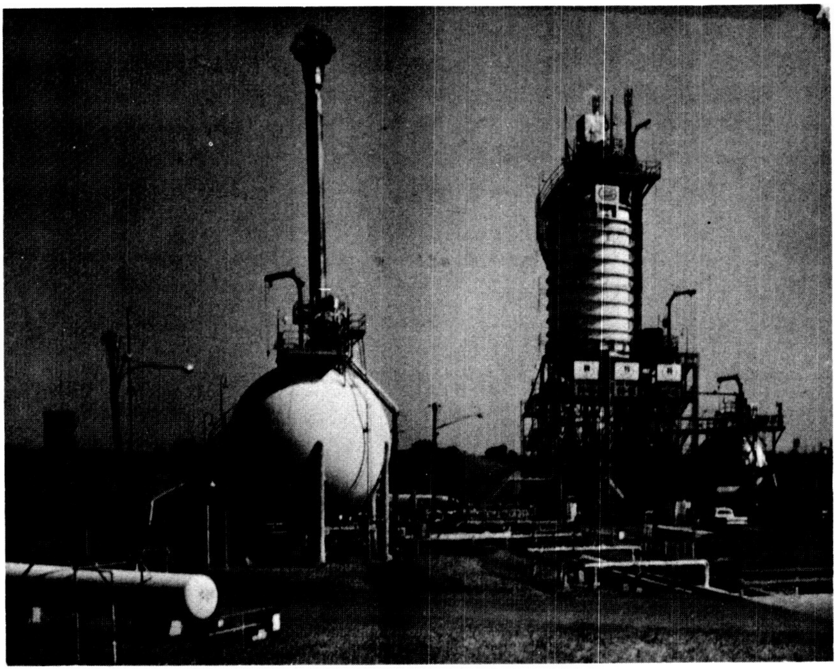

FIGURE 20.—*Typical cryogenic turbopump test facility.*

LIST OF SYMBOLS

C	Fluid absolute velocity, ft/sec
D	Diameter, bore in mm for bearings and inches for pump dimensions
F	Load, lbs
G or g	Acceleration due to gravity, ft/sec^2
H or ΔH	Pump stage head rise, ft
N	Pump speed, rpm
NPSH	Net positive suction head (fluid total head minus vapor head), ft
NPSP	Net positive suction pressure (fluid total pressure minus vapor pressure), psi
N_s	Specific speed, $NQ^{1/2}/H^{3/4}$, rpm (gpm)$^{1/2}$/(ft)$^{3/4}$
ΔP	Pressure differential, psi
Q	Pump volumetric flow rate, gpm
S	Suction specific speed, $NQ^{1/2}/NPSH^{3/4}$, rpm (gpm)$^{1/2}$/(ft)$^{3/4}$
U_t	Wheel or blade tip tangential velocity, ft/sec

$\propto$	Fluid absolute angle (measured from rotational direction), degrees
η	Pump efficiency, percent
ϕ	Flow coefficient, C_m/U_t
ψ	Stage head coefficient, $\Delta H/U_{2m}^2/g$

Subscripts

1	Inlet of impeller or inducer
2	Discharge of impeller
3	Vaned diffuser or volute throat
h	Blade hub
m	Meridional (axial plane) fluid component
t	Blade tip

REFERENCES

1. Brumfield, R. G., Optimum Design for Resistance to Cavitation in Centrifugal Pump. Memorandum, U.S. Naval Ordnance Test Station, Inyokern, California, February 1948.
2. *Results of Mark 25 Cavitation Tests.* Memorandum J–17–145–69, Los Alamos Scientific Laboratory, July 18, 1969.
3. Stepanoff, A. J., *Centrifugal and Axial Flow Pumps.* Second Ed., John Wiley and Sons, Inc. (New York), 1957.
4. Stodola, A., *Steam and Gas Turbines.* McGraw-Hill Book Co., Inc. (New York), 1927. Reprinted by Peter Smith (New York), 1945.
5. Barten, H. S., et al., *Study of Inducer Load and Stress.* PWA FR–3015, NASA CR–72514, April 2, 1969.
6. Walter, R. J., et al., "On the Mechanisms of Hydrogen-environment Embrittlement of Iron and Nickel-base Alloys". *Materials Sci. Eng.*, January 1970.
7. Wood, G. M., et al., Tip-Clearance Effects in Centrifugal Pumps. *ASME Trans.*, Paper 64 WA/FE 17, Ser. D, Vol. 87, December 1965.

Experimental and Analytical Investigation of Flow Through Rocket Pump Inducer[1]

B. LAKSHMINARAYANA

The Pennsylvania State University

A rocket pump inducer is usually an axial-flow pump runner having very high solidity and very low aspect ratio blades operating at very low coefficients. While this characteristic form is dictated by cavitation requirements, the flow is subjected to major effects of viscosity and turbulence in the flow field in the long and narrow passages between the vanes. The investigations reported in this paper are concerned with the effects of viscosity and not with the effects of cavitation.

The experimental investigations are carried out on a 3-foot-diameter model of a four-bladed inducer which is operated in air at a flow coefficient 0.065. The fluid properties are measured at the exit of the inducer using conventional and hot-wire probes. Important experimental results and the method of predicting the outlet tangential velocity and head rise are discussed in this paper.

One of the major requirements of a turbopump used in rocket application is that it should be capable of running at very high speeds, so as to minimize the size and weight of the unit and to facilitate matching with a drive turbine. The conventional pumps cavitate at suction specific speeds (SS) in excess of 8000, thus limiting the highest possible speed. The need to increase the speed led to the development of a cavitation resistance inducer which is essentially an axial-flow pump with high solidity blades used in front of the main pump. Long and narrow helical passages provide a space and time for the collapse of cavitation bubbles and for the gradual addition of energy to the fluid. Inducers are also used in water jet pumps of marine application (ref. 2). These are light and feature cavitation resistance in excess of commercial applications.

---

[1] The work reported here was done under contracts NSG537 and NGL 39–009–007 of the National Aeronautics and Space Administration, with technical management by W. R. Britsch of NASA Lewis Research Center.

The purpose of the inducer is to pressurize the flow sufficiently to enable the main pump to operate satisfactorily. The physical reasoning for the selection of such unconventional blade passages is explained by Acosta (ref. 1). These inducers have operated successfully at suction specific speeds in excess of 30 000; the test inducer described later is designed for SS = 50 000. The characteristic features of the inducers are:

(1) High solidity blading (few long-chord blades instead of many short-chord blades as in axial-flow pumps and compressors, exposing a much larger area to frictional effects)
(2) Very low flow coefficient and large stagger angles.

While the characteristic form of the inducer is dictated by cavitation requirements, the flow is subjected to major effects of viscosity and turbulence of the fluid in the long and narrow passages between the inducer vanes. The investigations reported here are concerned with the effects of viscosity and not with the effects of cavitation.

In axial-flow compressors or pumps, the secondary motions or the departure of the flow from design values are confined to fairly thin regions around the blades and near the end walls. This is not true in the case of inducers used in liquid rocket pumps. The blades of such inducers extend circumferentially over a major portion of a complete circle (fig. 1). Under

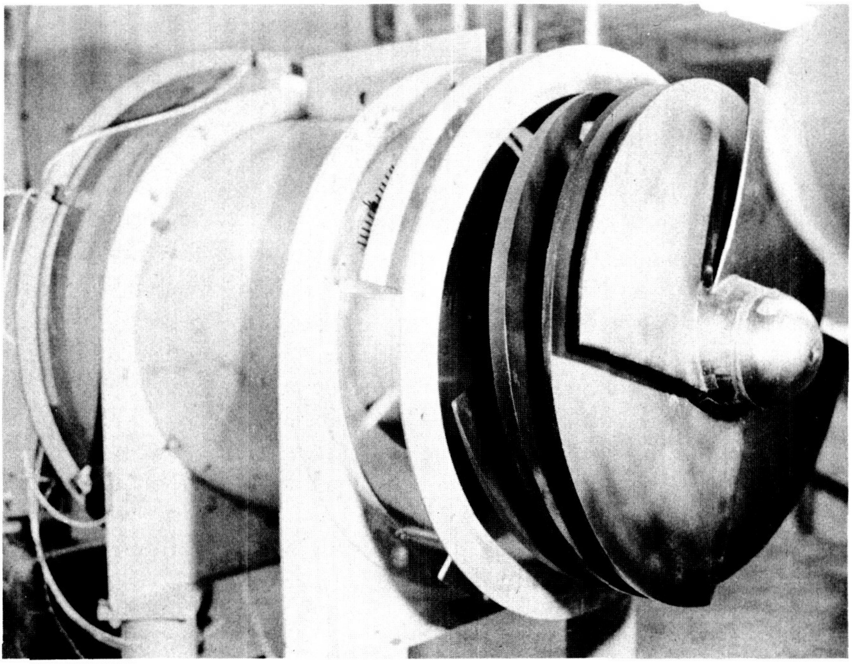

FIGURE 1.—*Photograph of the inducer (without shroud); 36-inch outside diameter, four blades.*

these circumstances, it can be estimated that the viscous effects and the consequent secondary motions are many times stronger than those encountered in other types of axial-flow machinery, and may indeed dominate the entire flow field. An understanding of such secondary motions is essential for the prediction of the efficiency and general performance of the inducer. The radial distribution of flow properties and the appropriate method of predicting them provide a further step toward the understanding of the flow through an inducer. This type of information is necessary for the analysis and design of the main pump. This is the objective of this paper.

The Department of Aerospace Engineering at The Pennsylvania State University has undertaken a systematic investigation with a view to understanding the general flow behavior and to developing flow prediction methods for inducers. A 3-foot-diameter inducer operated in air at a flow coefficient of 0.065 was built for this purpose. The following investigations, using the test rig shown in figure 2, have been completed so far:

(1) Visualization and measurement of the flow inside the passages[2] and at the exit of a four-bladed inducer. The latter measurements and an approximate analysis are reported in this paper.

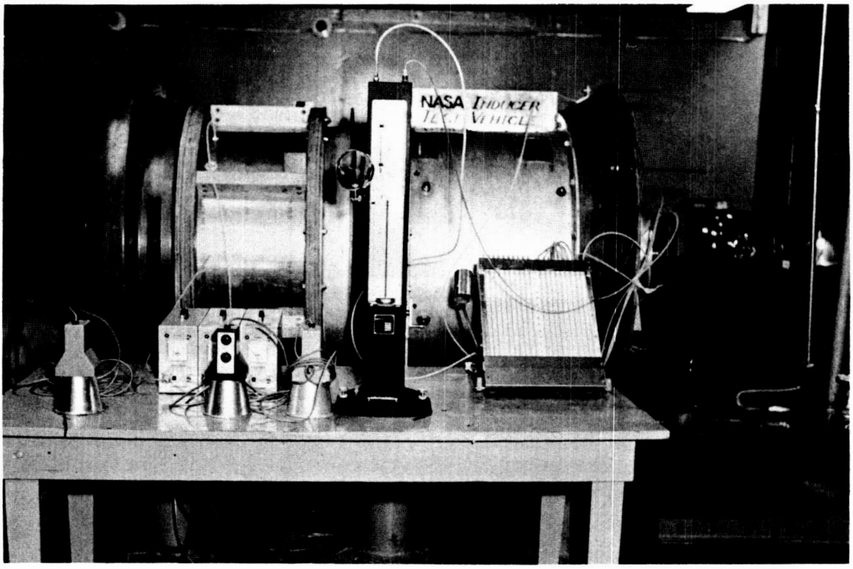

FIGURE 2.—*Test assembly.*

---

[2] These are carried out using rotating probes and pressure transfer device described in reference 20. The measurements are reported in reference 21.

(2) Three-dimensional velocity and turbulence measurements at the exit of a three-bladed inducer using hot-wire probes. Cooper and Bosch's computer program (ref. 9) is used to predict the three-dimensional inviscid effects (refs. 3 and 4).

(3) Three-dimensional turbulent boundary investigation on a single helical blade of the type used in rocket pump inducers (ref. 5).

These and future investigations to be undertaken will lead to the establishment of a theoretical model for the eventual analysis and design of turbomachinery flow dominated by secondary motions.

It is the intention of this paper to discuss the exit flow characteristics, a correlation for the frictional losses for the inducers, and an approximate analysis for the predictions of the velocity and energy distribution at the exit of the inducer. It will be shown that, while adequate information is not available to develop an exact analysis, the predictions based on loss correlations provide a method of predicting the gross behavior of the inducer.

DESIGN OF TEST INDUCER

The design of the test inducer is based on the "mean streamline" method developed by Wislicenus (ref. 6). The detailed design is described in reference 7. The overall characteristics are listed in table I.

After selecting a suction specific speed (SS) of 50 000 and head coefficient $\psi_T = 0.2$, the following parameters were derived from the design chart relating the cavitation parameters of turbomachines (fig. 259 in reference 6).

Flow coefficient, $\phi = 0.065$
Blade minimum pressure coefficient, $C_{P_{\min}} = 0.01$
$2gH_{sv}/V_z^2$

The runner is of free vortex design, producing constant head from root to tip. Using the relationship relating the stagnation head coefficient to change in tangential velocities, the inlet and outlet velocity diagrams are derived (fig. 3). The resulting runner profile is shown in figure 4. The design distribution of tangential and axial velocity components and of the stagnation and static head coefficients are shown in figures 11, 16, 18 and 20, respectively.

The design of blade sections is carried out in three steps:

(1) The mean streamline is derived from the assumed blade pressure diagram and blockage distribution as shown in figure 3. The blade pressure distribution chosen is typical of the trailing edge loaded profile which is required for this type of turbomachine and has $C_{P_{\min}} = 0.01$. In order to

account for the thickness or blockage effect of the blades, the relative velocities are varied from W_1 to W_2 along an arch-shaped curve above the nearly straight line variation that would apply to zero blade thickness. The arch-shaped curve represents an estimate of the blockage due to blade and boundary layer displacement thickness. The assumed blockage due to both effects is clearly marked in figure 3. The mean streamline for the hub and tip sections derived from the assumed pressure diagram and blockage is shown in figure 3.

(2) The departure of the camber line from the mean streamline is derived from the empirical deviation values of $\Delta\eta/L$ (nondimensionalized distance between the mean streamline and camber line measured normal to blade chord) derived by Wislicenus (ref. 6). It should be remarked here that Wislicenus' correlation for $\Delta\eta/L$ is the empirical counterpart of Ackeret's theoretical method (ref. 8). The validity of these empirical correlations for standard profiles has been established by Jakubowski (ref. 6) but its generalization to passages with nonstandard blade profiles

TABLE I.—*Inducer Characteristics*

Tip diameter		36.5 inches
Hub/tip ratio at outlet		0.5
Hub/tip ratio at inlet		0.25
Radial clearance		0.0625 inches
Suction specific speed SS (design)		50 000
Flow coefficient ($\phi = V_z/U_t$)		0.065
Blade chord	Tip ($R=1.0$)	82.96 inches
	Mid span ($R=0.75$)	63.18 inches
	Hub ($R=0.5$)	49.94 inches
Solidity	Tip ($R=1.0$)	2.86
	Mid span ($R=0.75$)	2.91
	Hub ($R=0.5$)	3.50
Number of vanes		4
Angular wrap (average)		290°
Lift coefficient of the blade based on mean velocity	Tip	0.0966
	Mid span	0.163
	Hub	0.307
Reynolds number based on tip radius		6.60×10^5
Reynolds number based on relative velocity and chord at mid radius		1.75×10^6
Maximum deviation of camber line from mean streamline$(\Delta\eta/L)_{\max}$	($R=0.5$)	0.02
	($R=0.75$)	0.01075
	($R=1.0$)	0.00637
Blade angles at inlet	($R=0.25$)	75°30′
	($R=0.625$)	83°30′
	($R=1.0$)	86°15′

All other blade angles are given in figure 6.

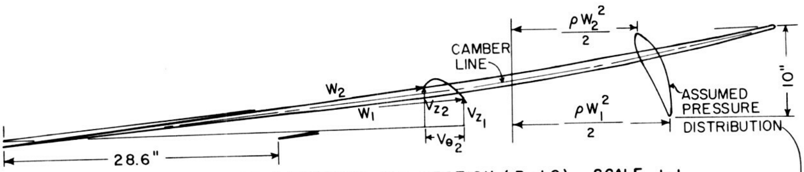

a. DEVELOPMENT OF CYLINDRICAL TIP SECTION (R = 1.0). SCALE ONE INCH

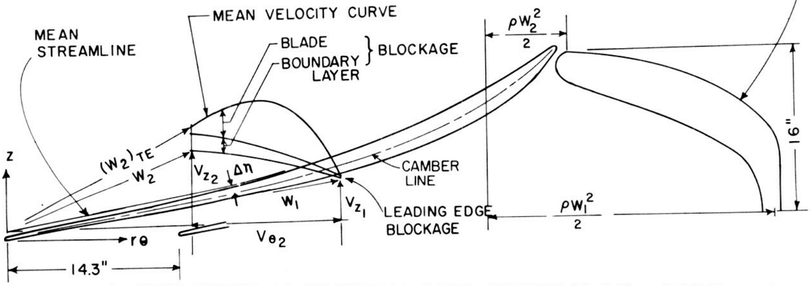

b. DEVELOPMENT OF CYLINDRICAL ROOT SECTION (R=0.5). SCALE ONE INCH

FIGURE 3.—*Design of blade profiles.*

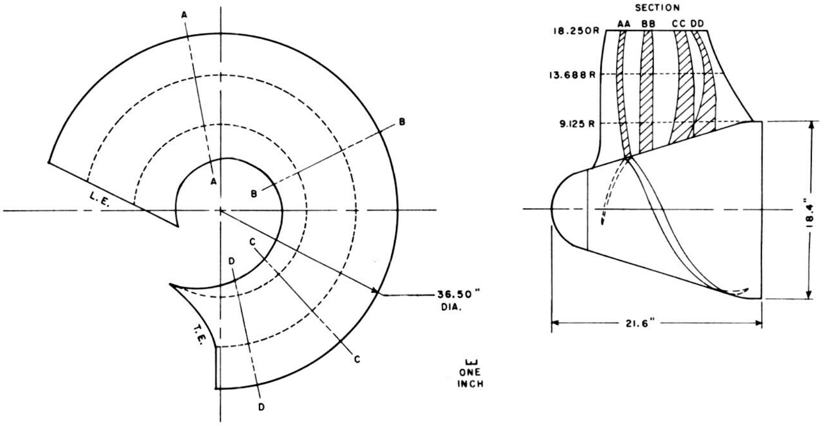

FIGURE 4.—*Axial view and circular projection of the inducer blade.*

and large stagger angle and solidities is yet to be established. The chordwise variation of $\Delta\eta/L$ assumed for this design departs from the NACA 65-series cascade data as required to obtain trailing edge loading (fig. 5). In figure 5, the notation $(\Delta\eta/L)_{\max,65}$ refers to the maximum deviation for a NACA 65-series cascade. Its value can be evaluated from the equation

$$\left(\frac{\Delta\eta}{L}\right)_{\max,65} = \left(\frac{\Delta\eta_1}{L}\right)_{\max} C_L$$

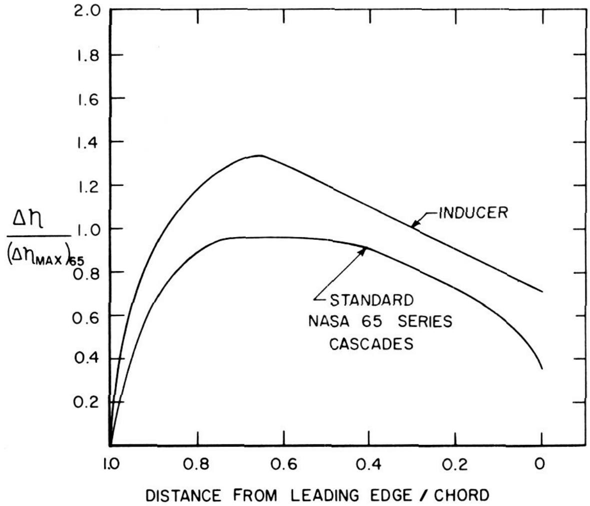

FIGURE 5.—*Assumed deviation of the camber line from the mean streamline.*

where

C_L lift coefficient

$\left(\frac{\Delta\eta_1}{L}\right)_{\max}$ maximum deviation for unit lift coefficient

Their values for various vane chord angles are plotted by Wislicenus (fig. 298, ref. 6). The value of $(\Delta\eta_1/L)_{\max}$ used for the inducer is 0.05 and the lift coefficients at various radial sections are given in table I. The camber lines so derived at hub and tip sections are shown in figure 3 and the design blade angles derived from this method are shown plotted in figure 6.

(3) The blade thickness can be derived from the assumed blockage curve (fig. 3) and the equation

$$\frac{\Delta V_z}{V_z}=\frac{t}{s}$$

where

ΔV_z perturbation in local axial velocity V_z due to blade blockage

t blade thickness in tangential direction

s blade spacing

The blade profiles so derived at hub and tip sections are shown plotted in figure 3.

FIGURE 6.—*Design blade and air angles.*

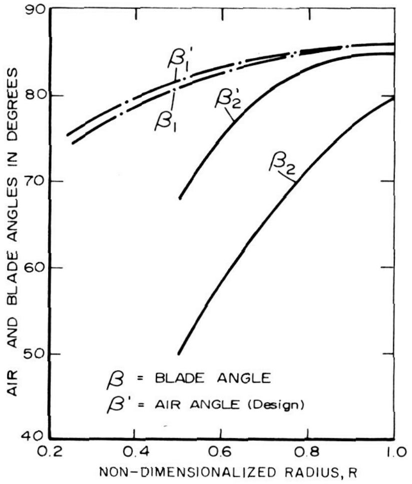

The blade section at hub ($R=0.5$), midradius ($R=0.75$) and tip sections ($R=1.0$) are designed in the manner explained above. The stacking of blade sections is carried out in much the same way as described by Wislicenus (ref. 6) and the final blade system so derived is shown in figure 4. In order to achieve reasonably constant variation in blade thickness from root to tip and smooth curvature in both chordwise and radial directions, it is sometimes necessary to change blade sections. This resulted in a slight departure from the free vortex design, especially at midradius, as shown in figures 20, 18, 16 and 11.

It should be remarked here that the Penn State inducer differs appreciably from the conventional radial blades of constant thickness (usually called flat plate inducer) used in practice. From the point of view of manufacture the radial blades are superior, but the design based on the present method should have hydrodynamically superior performance.

The blades for the inducer are of fiberglass construction, cast from suitable mold and templates. The final assembly of the test inducer, which is driven by a 5-hp variable-speed motor, is shown in figures 1 and 2. The research rotor is fitted with a pressure transfer unit which transmits pressures from a rotating blade to a stationary manometer.

APPROXIMATE THEORETICAL ANALYSIS

An attempt has been made to predict the flow properties at the exit of the inducer using a circumferentially averaged radial equilibrium equation. The three-dimensional nature of the flow and energy losses due to friction are fully recognized in deriving the circumferentially averaged radial equilibrium equation for the inducer. The inducer passages are assumed to have fully developed turbulent flow. Based on the information available in the current literature, assumptions are made for the circumferential variation of the relative tangential and radial velocities. The frictional losses accounted for in the theory are based on a friction loss coefficient (analogous to the universal friction loss coefficient derived by Blasius for pipes) derived from various inducer tests carried out at NASA Lewis Research Center, TRW Cleveland, and M.I.T. Gas Turbine Laboratory. This friction loss coefficient, which takes into account rotational effects, is valid for low flow coefficient (upstream absolute velocity/blade tip speed) or high rotation parameter (blade tip speed/upstream absolute flow). The energy losses calculated from this newly derived friction loss coefficient are in close agreement with the energy loss measured in the Penn State inducer. The radial equilibrium equation derived in this section is valid for a noncavitating inducer.

The various assumptions made in deriving the radial equilibrium equation for the inducer are given in the text in proper context. The absolute and relative tangential velocities predicted from this equation are in good agreement with the measured values (see "Experimental Results and Discussion"). The velocity profile models used in this analysis are based on the three-dimensional boundary layer investigation carried out by Lakshminarayana et al. (ref. 5) for a single blade. The viscid effects are taken into account in an approximate manner by using an empirically derived loss coefficient in the final radial equilibrium equation. The analysis considers only the perturbations caused by viscous effects. The inviscid turning effects are allowed for by taking design or the potential flow solution as the boundary conditions for the solution of the radial equilibrium equation presented in this section.

No attempt has been made to predict the axial velocity components, which are very much smaller than the tangential velocity components. This prediction should await more accurate information on the three-dimensional nature of the flow in the rotating passages.

Equations of Motion

The equations of motion governing the incompressible and steady flow inside the passages in a coordinate system rotating with an angular velocity Ω (fig. 7) are given by reference 19,

$$\nabla I = 2\mathbf{W}\times\mathbf{\Omega}+\mathbf{W}\times(\nabla\times\mathbf{W})+\mathbf{F} \tag{1}$$

$$\nabla\cdot\mathbf{W}=0 \tag{2}$$

where

$$I=\frac{P}{\rho}+\frac{W^2}{2}-\frac{\Omega^2r^2}{2} \tag{3}$$

and **F** is the frictional force per unit mass.

Since large velocity and pressure gradients exist in the case of an inducer, it is a formidable or impossible task to obtain an exact solution of equations (1) and (2). Hence, a more practical approach to satisfying the radial equilibrium equation on a circumferential average basis is employed in this paper. This technique was first employed by Ruden (ref. 10) for a compressor and later used by Smith (ref. 11) to derive a radial equilibrium equation amenable to solution by what is known as the "stream line curvature approach."

The scalar component of equation (1) in the radial direction is

$$\frac{\partial I}{\partial r}=-W_\theta\frac{\partial W_r}{r\partial\theta}-W_z\frac{\partial W_r}{\partial z}+W_\theta\frac{\partial W_\theta}{\partial r}+W_z\frac{\partial W_z}{\partial r}+\frac{W_\theta{}^2}{r}-2\Omega W_\theta+F_r \tag{4}$$

The following assumptions are made in deriving a radial equilibrium equation applicable to inducers operating at low flow coefficients.

(1) Frictional effects: The fluid friction affects the radial equilibrium equation through the terms F_r and I in equation (4). The radial component of shear stress at the blade surface is small, as indicated by Lakshminarayana's investigation (ref. 5) on a helical blade. It is recom-

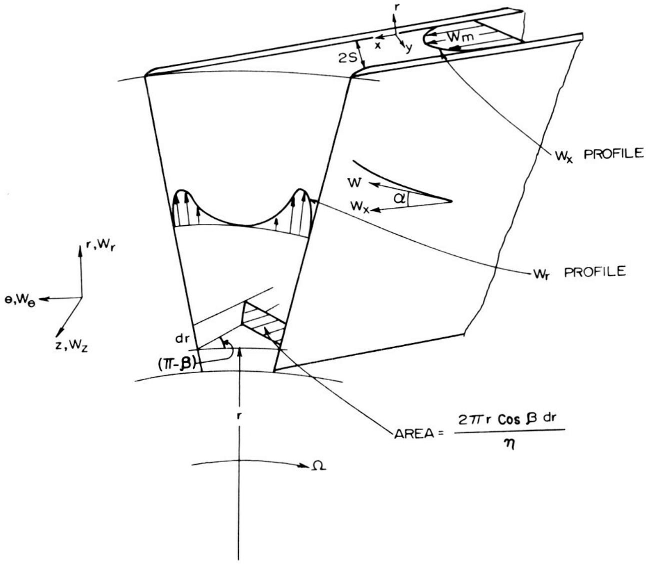

FIGURE 7.—*Notations used for inducer flow analysis.*

mended that the shear stress effect F_r be neglected in the preliminary analysis. In an inviscid flow, I is constant along a streamline. In viscid flow it can be approximated by

$$I=\frac{P}{\rho}+\frac{W^2}{2}-\frac{\Omega^2 r^2}{2}=C_1-\frac{\Delta P_0}{\rho}$$

where $\Delta P_0/\rho$ represents the stagnation pressure losses along a streamline. This term includes all losses associated with friction and turbulent mixing. In long, narrow inducer passages, this term is likely to be large. Thus,

$$\frac{\partial I}{\partial r}=-\frac{\partial}{\partial r}\left(\frac{\Delta P_0}{\rho}\right) \qquad (5)$$

(2) For inducers operating at low flow coefficients,

$$\left.\begin{aligned} &W_z \ll W_\theta \\ &\frac{\partial W_z}{\partial r} \ll \frac{\partial W_\theta}{\partial r} \end{aligned}\right\} \qquad (6)$$

(3) The flow passages are assumed to have fully developed flow and the flow properties are symmetrical about the midpassage (fig. 7). The assumptions for boundary velocity profiles are based on the investigations of reference 5 and are given by equations (12) and (13).

(4) The fluid is assumed to be guided smoothly through the channel (i.e., no flow deviation).

(5) The fluid is assumed to be single phase, incompressible and steady.

Assumptions (1) and (2) above would reduce equation (4) to

$$\underbrace{-W_\theta\frac{\partial W_r}{r\partial\theta}-W_z\frac{\partial W_r}{\partial z}}_{1}\underbrace{+W_\theta\frac{\partial W_\theta}{\partial r}}_{2}\underbrace{+\frac{W_\theta^2}{r}}_{3}\underbrace{-2\Omega W_\theta=}_{4}\underbrace{-\frac{\partial}{\partial r}\left(\frac{\Delta P_0}{\rho}\right)}_{5} \qquad (7)$$

Prior to deriving a circumferential average of the above equation, an attempt is made to present a method of evaluating the stagnation pressure loss (in relative flow) from inducer loss correlations.

Friction Loss Coefficient for a Rotating Channel with Large Rotation Parameter or Small Flow Coefficient

Since relative velocities are zero at the solid boundaries of a rotating channel, one is tempted to contemplate the behavior of the boundary layer in a frame of reference fixed to the rotor.

The fluid near the solid blade surfaces is not subjected to the same Coriolis or centrifugal forces as the main flow, and the result is that externally impressed gradients produce secondary motions inside the blade boundary layer. The additional losses associated with these secondary motions increase the frictional losses. Investigations by Spannhake (ref. 13) and Ludweig (ref. 14) indicate that the loss coefficient in such rotating channels may be several times that of an equivalent[3] stationary channel. Very little is known about the increase in friction losses due to rotation, especially the additional frictional stresses induced by Coriolis force. Systematic experimental investigations by Spannhake (ref. 13) and Ludweig (ref. 14) indicate that these frictional losses are strongly dependent on the rotation parameter. This parameter is analogous to the Rossby number used in connection with studying the effect of earth rotation on wind profile and is defined as the ratio of Coriolis to inertia force.

Since very little analytical information is available for the type of rotating channel used in the inducer, a systematic attempt is made to correlate the measurements of various investigators to derive a friction factor for inducer channels for the range of rotation parameters (inverse of flow coefficient) used in practice. The inducer data collected are from various laboratories under different flow conditions and blade configurations. The frictional losses depend on Reynolds number, velocity, dimensions of the channel, rotation parameter, and aspect ratio of the blades. Since the available experimental data on inducers are meager and the tests involve a small range of Reynolds number, no systematic approach is used to find the Reynolds number dependency on losses. First, the Blasius friction factor (λ) is determined from the equation

$$\frac{\Delta P_0}{\rho}=\frac{\lambda}{2R_N{}^{1/4}}\,\frac{L}{d_h}\,\overline{W}^2 \tag{8}$$

where

$\Delta P_0/\rho$ is the loss in stagnation pressure of the relative flow

λ is the Blasius friction factor (0.316 for a stationary channel)

R_N is the Reynolds number, Wd_h/ν (fig. 7)

d_h is the hydraulic mean diameter ($4 \times$ area/wetted perimeter)

L is the length of the channel

For an elemental blade height dr of the inducer passage at any radius r (fig. 7)

$$d_h=\frac{4(2\pi r/n)\cos\beta\, dr}{2\,dr}=4\,\frac{\pi r}{n}\cos\beta \tag{9}$$

where $\beta=f(r)$ and n is the number of passages.

---

[3] Equivalent here refers to a fully developed stationary channel having a mean velocity $\overline{W}$.

It is easy to prove that the nondimensionalized stagnation head loss coefficient in relative flow is equal to the difference between the Euler and measured head coefficient in absolute flow. Hence,

$$\psi_{\text{loss}}=\psi_E-\psi_m=\frac{2gH_{\text{loss}}}{U_t^2}=\frac{\lambda}{R_N^{1/4}}\,\frac{L}{d_h}\left(\frac{\overline{W}}{U_t}\right)^2 \qquad (10)$$

where $H_{\text{loss}}=H_E-H_M$ is the head loss due to friction in relative flow.

For any given inducer, $\psi_E-\psi_m$ can be determined from the measured stagnation pressures and tangential velocities at the exit, and, knowing the inducer geometry, values of λ can be derived at any radii. The loss factor derived from various measurements carried out at NASA Lewis Research Center, M.I.T. Gas Turbine Laboratory, and TRW Cleveland are plotted in figure 8. The sources from which these data were collected and details of the inducer configurations and flow parameters used are given in table II. The radial distribution of Blasius loss coefficient showed a systematic trend from midradius to tip; i.e., an increase in frictional losses with decreasing flow coefficient. Dependency of energy losses on hub/tip ratio is also evident from figure 8. Larger secondary losses associated with low hub-tip ratios are well known. A new friction factor λ_R is defined and all the data are replotted to derive the value of this new friction factor.

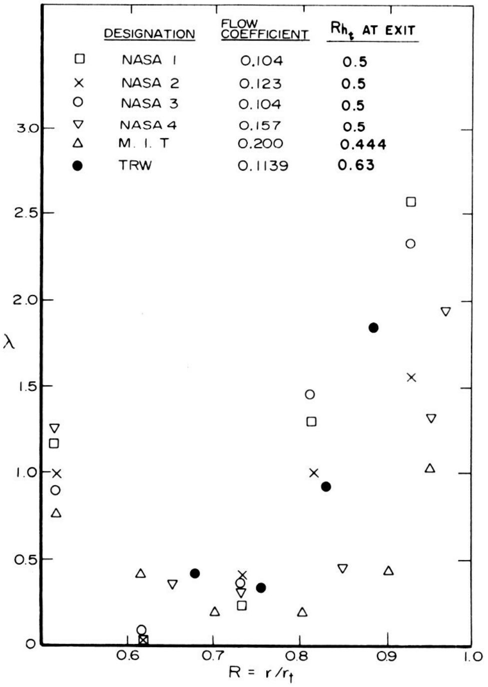

FIGURE 8.—*Radial variation of Blausius friction coefficient* (λ) *evaluated from equation (10) for various inducer configurations (table II).*

TABLE II.—*Details of the Various Inducer Configurations and Flow Parameters Used in Deriving the Friction Factors* λ *and* λ_R *(Figures 8 and 9)*[1]

Designation	Source and figure number	Outside Diameter (in.)	Number of Blades	Chord Length at the tip (in.)	RPM	Flow Coefficient at inlet	R_{ht} at exit	Reynolds number $R_N = W d_h / \nu$ at mid radius
NASA 1	Reference 17 Figures 12f and 12h	5.0	3	12.25	15 000	0.107	0.5	2.24×10^6
NASA 2	Reference 17 Figures 12f and 12h	5.0	3	12.25	15 000	0.123	0.5	2.24×10^6
NASA 3	Reference 17 Figures 14f and 14h	5.0	3	12.25	7 500	0.104	0.5	1.12×10^6
NASA 4	Reference 18 Figures 14f and 14h	5.0	3	9.62	9 000	0.157	0.5	2.44×10^6
TRW	Reference 16 Figures 4.7.3–8	4.0	3	9.4	8 000	0.1139	0.63	1.72×10^6
M.I.T.	Reference 15 Figure 15	1.8	3	4.2	10 000	0.2000	0.444	3×10^5

---

[1] All inducers listed were tested in water.

$$\psi_{\text{loss}} = \frac{2gH_{\text{loss}}}{U_t^2} = \lambda_R \frac{R_{ht}}{\phi} \frac{1}{R_N^{1/4}} \frac{L}{d_h} \left(\frac{\overline{W}}{U_t}\right)^2 \tag{11}$$

where R_{ht} is the hub/tip ratio and $H_{\text{loss}} = \Delta P_0/\rho g$.

In these calculations, local values of blade length, hydraulic diameter, blade mean angle (arc tan (tan $\beta_1 +$ tan $\beta_2)/2$), design flow coefficient, and measured local velocity (W) at the outlet are used to derive the new friction factor (λ_R) for the various inducer channels (fig. 9). It is not certain whether such a linear dependency on $\Omega r_t/W_z$ exists, but the data plotted in figure 9 seem to indicate that a relationship such as equation (11) is closely obeyed by all the inducer data plotted.

It should be remarked here that these loss correlations include mixing losses downstream of the trailing edge, since the measurements on which these loss correlations are based are taken for downstream of the inducer and not at the trailing edge.

It is suggested that a relationship such as the one discussed above be used with values of λ_R distribution shown in figure 9 for the flow coefficient ϕ ranging from 0.065 to 0.2. The largest scatter in the data is due to the M.I.T. inducer which was tested at $\phi = 0.2$. The secondary losses at the annulus and hub walls tend to be as important as secondary flow inside the blade boundary layer in such a case.

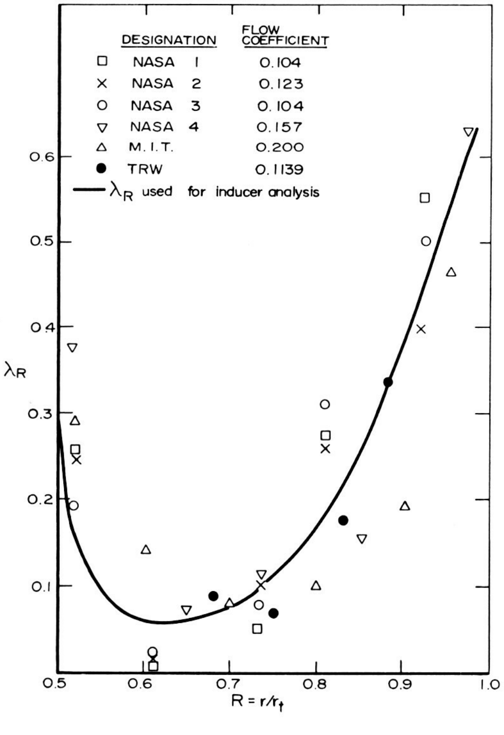

FIGURE 9.—*Radial variation of the modified friction loss coefficients* (λ_R) *calculated from equation* (*11*) *for various inducer configurations* (*table II*).

Circumferential Average of Radial Equilibrium Equation

The circumferential averaging of various terms in equation (7) is carried out under the following assumptions (fig. 7).

(1) The passages have fully developed turbulent flow and the flow properties are symmetrical about the midpassage.

(2) The velocity component parallel to the blade passage is given by

$$W_x = W_m \eta^{1/7} \tag{12}$$

where W_m is the velocity component parallel to the blade at midpassage, $\eta = y/S$, where y is the distance measured normal to the blade, $2S$ is the width of the channel (fig. 7) and x is the coordinate parallel to the blade and lying on a cylindrical surface.

(3) The radial velocity component W_r is given by reference 12,

$$W_r = W_x \tan\alpha(1-\eta)^2 = W_m \tan\alpha(\eta)^{1/7}(1-\eta)^2 \tag{13}$$

where α is the angle between the direction of the resultant velocity near the wall and W_m or angle between the limiting streamline and x direction (fig. 7). Note that W_m and α are functions of r and x only. The average of any quantity T will be denoted by a bar and is defined by

$$\overline{T} = \frac{1}{S}\int_0^s T\,dy \tag{14}$$

where $2S$ is the width of the blade passage.

Circumferential Average of Term 1 in Equation (7)

Since W_x is the velocity along x, where x is an intermediate variable and r, θ are the independent variables,

$$W_x \frac{\partial W_r}{\partial x} = W_z \frac{\partial W_r}{\partial z} + W_\theta \frac{\partial W_r}{r\partial\theta} \tag{15}$$

Now, from equation (13),

$$\frac{\partial W_r}{\partial x} = \eta^{1/7}(1-\eta)^2\left(\frac{\partial W_m}{\partial x}\tan\alpha + W_m \sec^2\alpha\,\frac{\partial\alpha}{\partial x}\right) \tag{16}$$

Hence, the circumferential average of Term 1 in equation (7) is

$$\overline{\frac{W_\theta}{r}\frac{\partial W_r}{\partial\theta} + W_z\frac{\partial W_r}{\partial z}} = \overline{W_x\frac{\partial W_r}{\partial x}}$$

$$= W_m\left(\frac{\partial W_m}{\partial x}\tan\alpha + W_m \sec^2\frac{\partial\alpha}{\partial x}\right)\int_0^1 \eta^{2/7}(1-\eta)^2\,d\eta$$

$$=0.210W_m\left(\frac{\partial W_m}{\partial x}\tan\alpha+W_m\sec^2\alpha\,\frac{\partial\alpha}{\partial x}\right) \tag{17}$$

Circumferential Average of Terms 2, 3, and 4 in Equation (7)

Since it is assumed that the fluid is smoothly guided through the passage, the circumferential average of Term 2 in equation (7) is

$$\overline{W_\theta\frac{\partial W_\theta}{\partial r}}=\int_0^1 (W_\theta)_m(\eta)^{1/7}(\eta)^{1/7}\,\frac{\partial (W_\theta)_m}{\partial r}\,d\eta=1.015\overline{W_\theta}\,\frac{\partial \overline{W_\theta}}{\partial r} \tag{18}$$

since $\overline{W_\theta}=\frac{7}{8}(\overline{W_\theta})_m$ for one-seventh profile.

Similarly,

$$\overline{W_\theta^2}=\int_0^1 W_\theta^2\,d\eta=(W_\theta)_m^2\int_0^1 \eta^{2/7}\,d\eta=1.015\overline{W_\theta}^2 \tag{19}$$

and

$$2\overline{\Omega W_\theta}=2\Omega\overline{W_\theta} \tag{20}$$

Circumferential Average and Radial Variation of the Frictional Losses in Equation (7)

Since the friction losses derived by the author (eq. 11) represent the average losses across the passage, the circumferential average of the fifth term in equation (7) is

$$\frac{\partial}{\partial r}\left(\frac{\Delta P_0}{\rho}\right)=\frac{\partial}{\partial r}\left(\lambda_R\,\frac{R_{ht}}{\phi}\,\frac{1}{R_N^{1/4}}\,\frac{L}{d_h}\,\frac{\overline{W^2}}{2}\right) \tag{21}$$

Hence, the circumferential average of the radial equilibrium equation now reads, after substituting equations (17), (18), (19), (20), and (21) in equation (7),

$$-0.210W_m\left(\tan\alpha\,\frac{\partial W_m}{\partial x}+W_m\sec^2\alpha\,\frac{\partial\alpha}{\partial x}\right)+1.015\overline{W_\theta}\,\frac{\partial\overline{W_\theta}}{\partial r}+1.015\,\frac{\overline{W_\theta}^2}{r}$$

$$-2\Omega\overline{W_\theta}+\frac{\partial}{\partial r}\left(\frac{\lambda_R}{R_N^{1/4}}\,\frac{R_{ht}}{\phi}\,\frac{L}{d_h}\,\frac{\overline{W^2}}{2}\right)=0 \tag{22}$$

Since $\overline{W_\theta}=\frac{7}{8}(W_\theta)_m=\frac{7}{8}W_m\sin\beta$, the final circumferentially averaged radial equilibrium equation valid for inducers operating at low flow coefficient is

$$\frac{-0.275}{\sin^2\beta}\,\overline{W_\theta}\left(\tan\alpha\,\frac{\partial\overline{W_\theta}}{\partial x}+\overline{W_\theta}\sec^2\alpha\,\frac{\partial\alpha}{\partial x}\right)+1.015\overline{W_\theta}\,\frac{\partial\overline{W_\theta}}{\partial r}$$

$$+1.015\,\frac{\overline{W_\theta}^2}{r}-2\Omega\overline{W_\theta}+\frac{\partial}{\partial r}\left(\frac{\lambda_R}{R_N^{1/4}}\,\frac{R_{ht}}{\phi}\,\frac{L}{d_h}\,\frac{\overline{W^2}}{2}\right)=0 \tag{23}$$

The solution of this circumferentially averaged radial equilibrium equation to derive $\overline{W_\theta}$ or $\overline{V_\theta}$ distribution along the radius is still intractable unless suitable assumptions are made for $\partial\overline{W_\theta}/\partial x$ and α. The experiment is the only source from which the values of α can be derived. The limiting streamline angle α is predictable in the case of a single rotating helical blade (ref. 5), but the values of α measured on inducer blade surfaces are found to be higher than those on a single helical blade (refs. 21 and 24). The evaluation of $\partial\overline{W_\theta}/\partial x$ could be based on either a linear variation of $\overline{W_\theta}$ along x or the inviscid solution. Once these quantities are evaluated, $\overline{W_\theta}$ or $\overline{V_\theta}$ can be predicted from equation (23) using the author's correlation for friction loss coefficient λ_R (fig. 9).

The method of predicting $\overline{W_\theta}$ or $\overline{V_\theta}$ for any given inducer geometry and flow coefficient is described in the next section.

EXPERIMENTAL RESULTS AND DISCUSSION

The four-bladed inducer described in the section on the design of the test inducer is used for the experimental investigations of the flow characteristics. The test medium is air and all the measurements are carried out at a Reynolds number (based on tip radius) of 6.6×10^5, which corresponds to 450 rpm. A throttle valve, which can be seen in figure 2, is adjusted to obtain a flow coefficient ϕ of 0.065.

The measuring stations are shown in figure 10. The exit flows were measured at stations 3, 4, 5, 6, and 7, using a stagnation probe and a tuft probe. Hot wire measurements were taken very close to the trailing edge (station 3A) to derive the average values of radial, axial, and tangential velocity components.

The outlet air angles (of the absolute flow) were measured by means of a very thin tuft probe and a sighting scope of the type used by Smith (ref. 22). Fluctuations in absolute air angles were found to be considerable, especially near the hub locations. The algebraic mean of the maximum and minimum air angles, measured by the tuft probe, was used for calculating the axial and tangential velocity components. In spite of slight inaccuracies which are discussed by McCafferty (ref. 20), much information can be gained from these stationary probe measurements. Since the flow at the exit was highly three-dimensional, the static pressures were measured at the hub and annulus walls and the radial distribution of static pressure coefficient was derived by computing the pressure gradient near the wall locations from the simplified radial equilibrium equation.

Since an accurate knowledge of the nature and magnitude of radial velocities is essential for the development of an adequate theory for predicting the flow, an attempt was made to derive the average values of all three velocity components at the exit (station 3A) using a combination

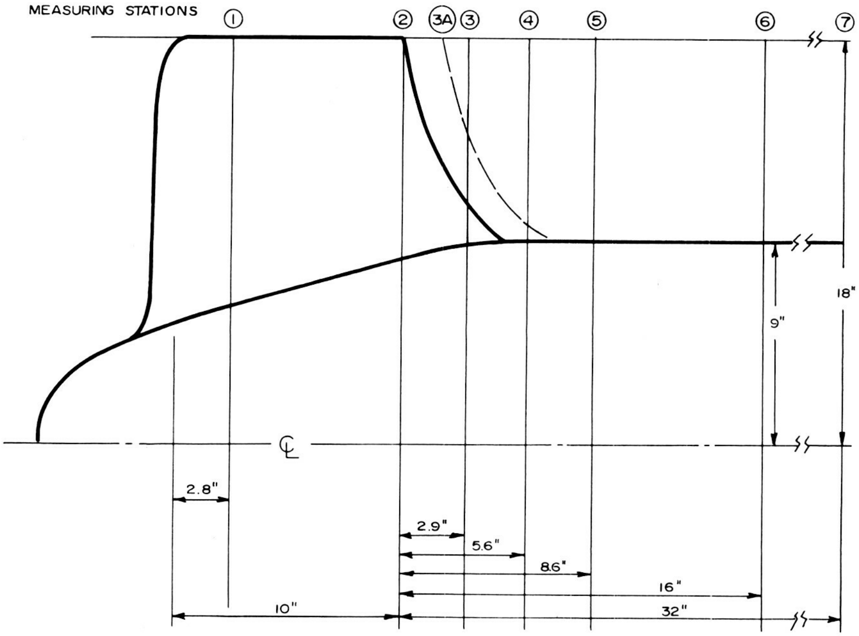

FIGURE 10.—*Location of the flow-measuring stations.*

of an X-configuration hot-wire probe plus a single sensor probe normal to the X-configuration. The probes were aligned in the three coordinate directions such that they sense the following velocity components.

$$V_{\theta z}=\sqrt{V_\theta^2+V_z^2} \tag{24}$$

$$V_{\theta r}=\sqrt{V_\theta^2+V_r^2} \tag{25}$$

$$V_{rz}=\sqrt{V_r^2+V_z^2+K^2V_\theta^2} \tag{26}$$

Since the air angles of the absolute flow are very large, a correction to the cosine law was used for the wire in the θ direction. This appears in the form of a correction factor as shown in equation (26). The value of K was derived from Schwarz and Friehe's correlations (ref. 23). For the length/diameter of the wire used in these experiments, the value of K was found to be 0.26.

The oscilloscope traces of the signal were photographed[4] to derive the blade-to-blade variation of the voltages. The hot-wire calibration curves and equations (24), (25), and (26) were then used to derive the blade-to-blade variation of V_r, V_θ, and V_z.

---

[4] The method of data processing has since been improved as indicated in reference 4.

Tangential Velocities at Exit

The absolute tangential velocities derived from pressure and angle measurements are shown plotted in figure 11 for various axial stations. The measured tangential velocities are substantially higher than the design values except near the hub. These results are consistent with the measurements reported by Sandercock et al. (ref. 17) and Soltis et al. (ref. 18). The real fluid effects combined with large radial flows that exist inside the blade passages are responsible for such a large increase in tangential velocity or head rise. Furthermore, it is also evident from figure 11 that there is a substantial change in tangential momentum as the flow proceeds downstream. Far downstream of the inducer, a "forced vortex" type of distribution exists. Such changes are due to mass flow redistribution that takes place downstream of the inducer and the mixing losses due to blade wake diffusion. The extent of mass flow redistribution can be seen from figure 16. These measurements indicate the desirability of having the inducer as an integral part of the main pump and also point out the need to take measurements close to the trailing edge in order to accurately assess the extent of real fluid effects inside the blade passages. It is quite clear that the inducer behaves like a drag or a friction pump, especially near the tip, where the head rise is imparted to the fluid by purely frictional effects.

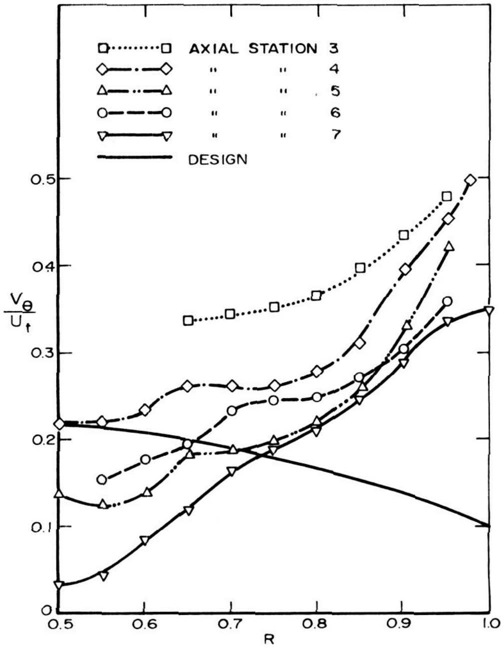

FIGURE 11.—*Radial variation of absolute tangential velocity at various axial locations.*

Even though an accurate prediction of the tangential velocity distribution is possible only by a thorough understanding of the three-dimensional boundary layer characteristics inside the passage, a qualitative estimate of the frictional effects can be made from an analysis of the type indicated in the preceding section (Approximate Theoretical Analysis).

The form of equation used for predicting the tangential velocities at the exit of the inducer is obtained by further simplification of equation (23) (by expressing $\overline{W_\theta}$ as the only dependent variable) under the following assumptions:

(1) $\overline{W_\theta}$ varies linearly with x from leading to trailing edge.

(2) Angle α between the limiting streamline and W_m varies linearly from leading edge to trailing edge, being zero at the leading edge. This trend is confirmed from the limiting streamline angle measurements reported in reference 21. Hence,

$$\frac{\partial W_\theta}{\partial x}=\frac{\overline{W_\theta}-\Omega r}{L}=\frac{\overline{W_\theta}-\Omega r}{4.5r} \tag{27}$$

where

$\overline{W_\theta}$ = relative tangential velocity at exit
$\Omega r \cong$ relative tangential velocity at inlet
L = chord length of the blade ($\cong 4.5r$ for Penn State inducer)

and

$$\frac{\partial \alpha}{\partial x}=\frac{\alpha-0}{4.5r} \tag{28}$$

where α is the angle of the limiting streamline near the trailing edge. Use of equations (27) and (28) would reduce the first term in equation (23) to

$$\frac{-\overline{W_\theta}^2}{r}\,\zeta(r)+2\overline{W_\theta}\Omega\xi(r) \tag{29}$$

where

$$\zeta(r)=\frac{0.061}{\sin^2\beta}\,(\tan\alpha+\alpha\sec^2\alpha) \tag{30}$$

$$\xi(r)=\frac{0.03\tan\alpha}{\sin^2\beta} \tag{31}$$

The friction loss term in equation (23) can be further simplified for the Penn State inducer to give

$$\frac{\partial}{\partial r}\left(\lambda_R \frac{R_{ht}}{\phi} \frac{1}{R_N{}^{1/4}} \frac{L}{d_h} \frac{\overline{W^2}}{2}\right) = \frac{\partial}{\partial r}\,(F(r\overline{W_\theta})^2)$$

$$= F'(r)\overline{W_\theta}{}^2 + 2F(r)\overline{W_\theta}\,\frac{\partial \overline{W_\theta}}{\partial r} \tag{32}$$

where

$$F(r) = \frac{1}{2}\,\frac{\lambda_R}{R_N{}^{1/4}}\,\frac{R_{ht}}{\phi}\,\frac{L}{d_h}\,\frac{1}{\sin^2\beta} \tag{33}$$

and λ_R (fig. 9), $R_N{}^{1/4}$, d_h (eq. (9)), length of the blade (L), and $\sin^2\beta$ (fig. 6) are all functions of radius at any given axial station. The variation of $F(r)$ with radius at the location of the trailing edge is plotted in figure 12. Hence, the final form of radial equilibrium equation used for predicting the relative tangential velocity at the exit of the Penn State inducer is obtained by substituting equations (29) and (32) in equation (23).

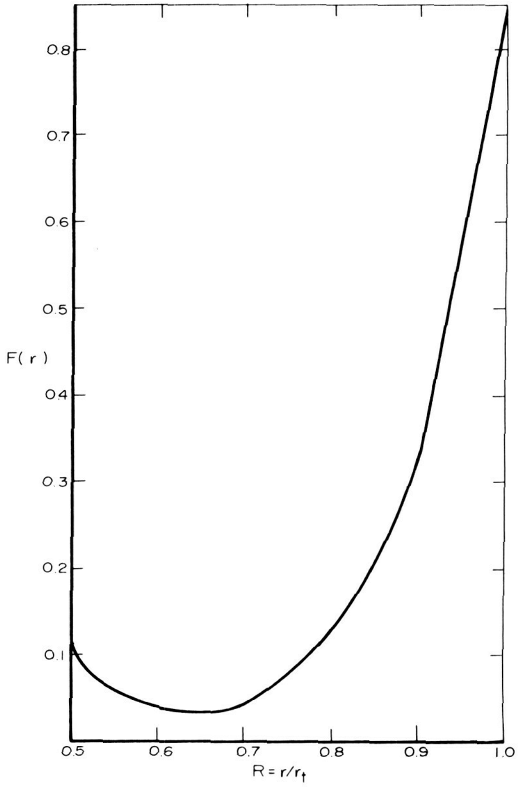

FIGURE 12.—*Radial variation of function* F(r) *(eq. (33)) for Penn State inducer.*

$$\overline{W_\theta}\frac{\partial \overline{W_\theta}}{\partial r}(1.015+2F(r))+\frac{\overline{W_\theta}^2}{r}(1.015+rF'(r)-\zeta(r))=2\Omega\overline{W_\theta}(1-\xi(r)) \tag{34}$$

where the functions $F(r)$, $\zeta(r)$, and $\xi(r)$ are defined by equations (33), (30), and (31), and $F'(r)$ is the derivative of $F(r)$ plotted in figure 12.

Equation (34) is used to predict the radial variation of mean relative tangential velocity ($\overline{W_\theta}$) at the trailing edge. In evaluating the functions $\zeta(r)$ and $\xi(r)$, information obtained by flow visualization experiments reported in reference 24 is used. Near the hub, the value of α was found to be nearly 60° on the suction surface and 30° on the pressure surface of the blade. Basing our assumption on this, α is assumed to vary linearly from 45° at the hub to zero at the tip (fig. 13). This enabled evaluation of the functions $\zeta(r)$ and $\xi(r)$ (eqs. (30) and (31)) in equation (34). The variations of these functions with radii are plotted in figure 13.

The predicted values of relative tangential velocity at the trailing edge obtained from equation (34), using estimated values of $F(r)$, $F'(r)$, $\zeta(r)$, and $\xi(r)$ (figs. 12 and 13), are plotted in figure 14. The boundary condition assumed for the solution of the differential equation (34) is that the tangential velocity ($\overline{W_\theta}$) at the midradius is the same as that of design. The predicted values are in good agreement with the values derived from stationary probe measurements at station 5.[5]

The effect of neglecting the inertial terms due to radial velocity gradients (i.e., functions $\zeta(r)$ and $\xi(r)$ in equation (34)) is also shown in figure 14. The inertial terms due to radial velocity gradients in the radial equilibrium equation seem to have very little effect on the predicted values of $\overline{W_\theta}$. Even though the acceleration components due to radial velocity gradients are small, their influence in increasing the frictional losses cannot be ignored. Hence, in conclusion, it can be said that the acceleration component due to radial velocity gradients can easily be neglected in predicting the relative tangential velocity distribution from the radial equilibrium equation. But the influence of radial velocities on axial velocity profile at the exit cannot be ignored.

In deriving equation (34) from the generalized radial equilibrium equation (eq. (4)), it was assumed that the term $W_z(\partial W_z/\partial r)$ is very small. Its influence on the predicted values of $\overline{W_\theta}$ is evaluated by using the

---

[5] It should be remarked here that the loss coefficient (λ_R) derived in this paper is based on the measurements carried out at one-seventh to one-ninth blade chord (refs. 15, 17, and 18) downstream of the trailing edge. Hence, these loss correlations include mixing losses. To be consistent, only the measurements carried out at station 5, which approximately corresponds to the measuring stations of references 15, 17, and 18, is compared with the predicted values.

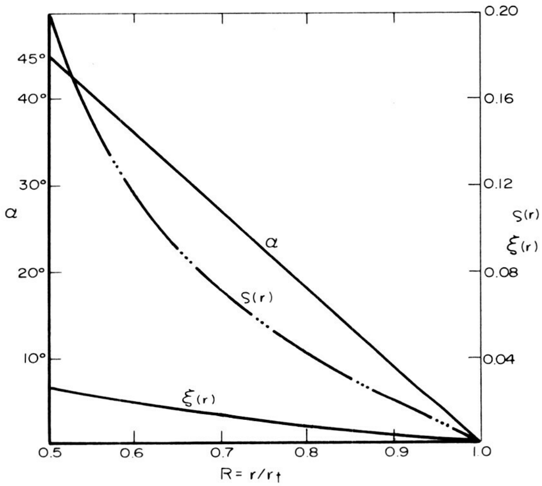

FIGURE 13.—*Radial variation of* ζ(r) *and* ξ(r) *(eqs. (30) and (31)) and assumed* α.

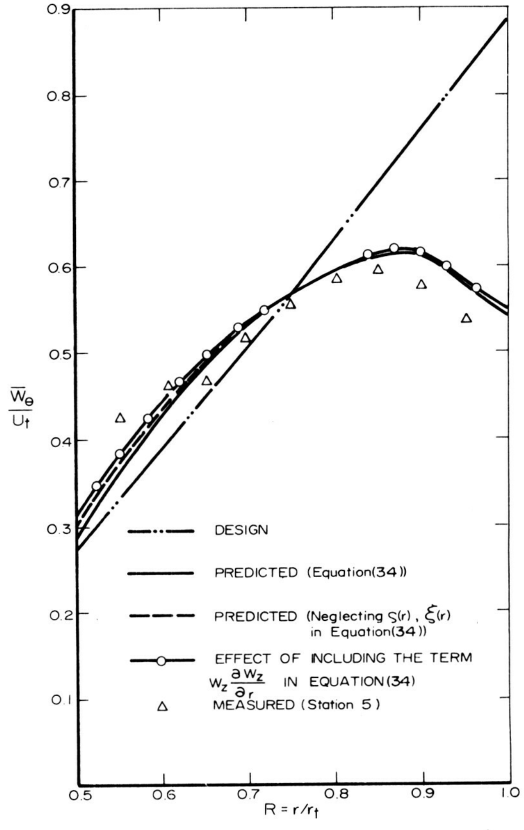

FIGURE 14.—*Predicted and measured relative tangential velocity.*

experimental values of $W_z(\partial W_z/\partial r)$ (fig. 16) and the following modified equation

$$\overline{W_\theta}\,\frac{\partial \overline{W_\theta}}{\partial r}\,(1.015+2F(r))+\frac{\overline{W_\theta}^2}{r}\,(1.015+rF'(r)-\zeta(r))+\overline{W_z}\,\frac{\partial \overline{W_z}}{\partial r}=2\Omega\overline{W_\theta}(1-\xi(r)) \qquad (35)$$

The effect of neglecting the axial velocity gradient term in equation (34) is evident from figure 14. The effect of this term on the predicted values of $\overline{W_\theta}$ seems to be appreciable only near the hub (where the axial velocity gradients are large) and negligibly small at other radial positions.

The predicted tangential velocity components of the absolute flow $(U-\overline{W_\theta})$ are plotted and compared with experimental values, derived from stationary probe measurements[6] at station 5, in figure 15. The agreement between the predicted and experimental values is good. The inclusion of the axial velocity gradient term $W_z(\partial W_z/\partial r)$ in equation (34) seems to bring the predicted values of $\overline{V_\theta}$ closer to the experimental values only near the hub.

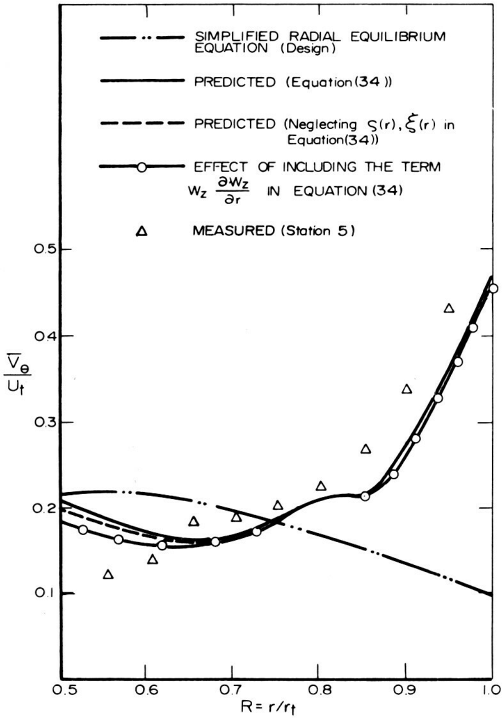

FIGURE 15.—*Predicted and measured values of absolute tangential velocity.*

---

[6] See footnote 5.

The effect of neglecting the radial velocity gradients $\zeta(r)$ and $\xi(r)$ in equation (34) is shown in figure 15. It is evident that the friction loss term in the radial equilibrium equation (eq. (7)) has a very appreciable effect in changing the tangential velocity gradient in the radial direction.

The tangential velocity distribution derived from hot-wire probe and stationary probe measurements, carried out very close to the trailing edge (station 3A), is compared in figure 17. There is a slight discrepancy between the two measurements. This may be due to error in measuring the fluctuating (with reference to stationary probe) stagnation pressure close to the trailing edge.

Axial Velocities at the Exit

The measured radial distribution of axial velocities at various axial stations is plotted in figure 16.

Immediately downstream of the inducer (stations 3 and 4), the minimum velocity occurs at the midradius. This seems to suggest that radial migration inside the blade boundary layer is very large from midradius to tip as compared to that from hub to midradius. At station 3, where the hub flow is still under the influence of blade, the blockage effects are large. Sandercock et al. (ref. 17) and Soltis et al. (ref. 18) concluded earlier that the inducers operating at low flow coefficients have separated flow near the hub. These conclusions are based on measurements taken far downstream. The present investigation seems to suggest that such flow separation takes place downstream of the inducer due to considerable flow redistribution. It should be remarked here that large radial velocities exist

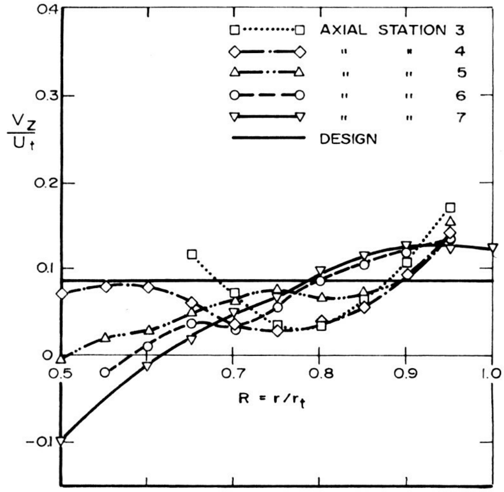

FIGURE 16.—*Radial variation of axial velocity at various axial locations.*

in the blade wakes of the inducer. This accounts for large changes in axial and tangential velocities and stagnation pressures measured downstream (figs. 11, 16, and 18).

Far downstream of the inducer (stations 5, 6, and 7), the minimum axial velocity occurs near the hub, and in fact shows a tendency to separate at station 5. Downstream of the inducer, the radial velocities inside the blade wakes are outward near the hub, whereas the wake interactions near the tip produce an inward flow. The net effect is a migration of the mass flow toward the midradius. This effect can be clearly seen at stations 5 and 6. Thus, there is a substantial improvement in axial velocity distribution near the midradius and a deterioration near the hub. Furthermore, the extent of back flow is observed to grow continuously as the flow proceeds downstream and occupies nearly 20 percent of the annulus far downstream (station 7, fig. 16). In a pumping unit where the inducer is an integral part of the main pump, the back flow may be absent if aerodynamically designed blade sections are used. It is not clear whether this is true for flat plate inducers, since measurements close to the trailing edge are not available for such units. Inside the blade passages, the perturbation in axial velocity is due to:

(1) Radially varying blade thickness and hence blockage

(2) Radial flow inside the blade boundary layers. This is by far the most important cause of the change in axial velocities from hub to tip.

The perturbations in downstream flow are predominantly due to radial velocities in the three-dimensional wakes.

The prediction of axial velocity distribution should take into consideration the detail flow structure, including the radial velocities inside blade boundary layers, inside such inducers. The boundary layer in a rotating helical channel, currently under investigation at Pennsylvania State University, should provide the urgently needed information for the accurate prediction of axial velocity distribution. Thus, considerably more theoretical and experimental work is necessary before the observed flow can be regarded as rationally explained.

It should be emphasized here that the flow redistribution downstream of the inducer (caused by the radial velocities in the three-dimensional blade wakes) is considerable and extreme caution should be exercised in evaluating the performance of an inducer from the measurements obtained far downstream.

The average values of the axial velocities derived from the hot-wire probe measurements very close to the trailing edge are shown plotted and compared with stationary probe measurements in figure 17. This seems to confirm the trend in axial velocity discussed earlier; i.e., very low axial velocities at midradius.

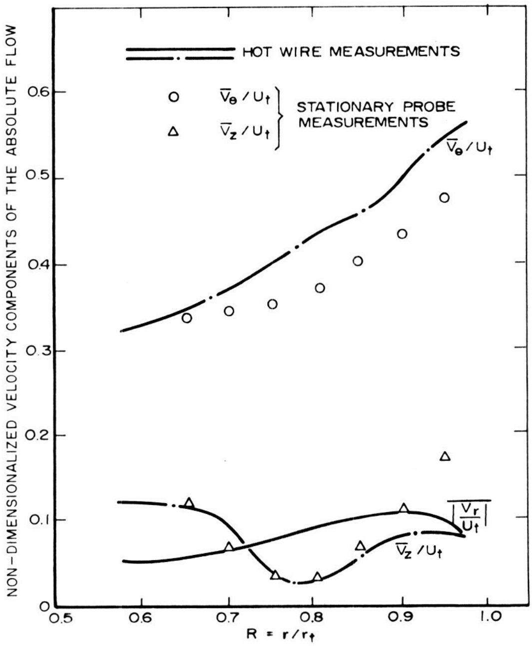

FIGURE 17.—*Comparison of the absolute velocity components measured by the hot wire and stationary probe at station 3A.*

Radial Velocities at Exit

The radial distribution of average radial velocities ($\overline{|V_r|}$) derived from the hot-wire measurements is plotted in figure 17.[7]

It should be remarked here that the hot-wire probe senses only the magnitude and not the direction of the radial velocity. Near the inducer tip, radial *inward* flow exists due to boundary layer interactions. Thus, the algebraic average of radial velocities across the passage is likely to be different from $\overline{|V_r|}$, especially near the tip.

It is evident from figure 17 that the radial velocities are of the same order of magnitude as axial velocities, with values increasing monotonically toward the tip. The maximum average radial velocity occurs a small distance away from the tip (fig. 17) and this location corresponds to the maximum inward flow region.

These measurements confirm the earlier conclusion that radial velocities in such low flow coefficient and high solidity inducers are large. For the eventual flow analysis, it is essential to know the detail blade-to-blade variation of radial velocities including the extent of radial inward flow.

---

[7] Discrepancy between the hot-wire results reported in reference 21 (unpublished) and this paper is due to the fact that earlier results are based on $K=0$ in equation (26).

Stagnation Pressure Coefficient at Exit

The radial variation of stagnation head coefficient at various axial stations is shown plotted in figure 18 and compared with design values. These plots are typical of inducers tested earlier (refs. 17 and 18). The pressure coefficients near the tip are two to three times the corresponding design values. Strong real fluid effects from midradius to tip are thus evident. The performance of the inducer is similar to a "shear force pump" or "drag pump," where shear forces are utilized to exchange kinetic energy between fluid and solid bodies. Thus, the sections near the tip operate predominantly as a shear force pump, whereas the pressure rise near the hub is largely due to flow turning effects.

The stagnation head decreases continuously as the flow proceeds downstream of the trailing edge. Major changes occur between stations 3 and 4, especially near the hub. Comparing the corresponding axial velocities at stations 3 and 4 in figure 16, it is evident that the major effects come from the axial velocity changes. The wake mixing losses also contribute to the change in stagnation head. These effects are dominant from midradius to tip. The tip sections experience considerable pressure losses as the flow proceeds downstream despite the fact that axial velocity changes (fig. 16) are small. The presence of large mixing losses is thus evident in these regions.

An attempt is made to estimate the stagnation pressure or head rise coefficient and losses on the basis of the analysis indicated in the preceding section (Approximate Theoretical Analysis). The knowledge of the

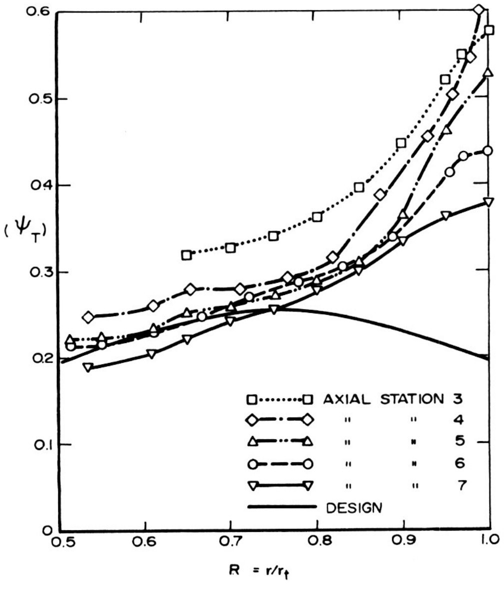

FIGURE 18.—*Radial variation of absolute stagnation pressure coefficient* (ψ_T) *at various axial locations.*

relative velocities derived from the theory outlined earlier (see Tangential Velocities at Exit and fig. 15) enables an estimate of the energy losses to be made from equation (11). The loss coefficients so derived are shown compared with the measured losses in figure 19 for station 5.[8] Reasonably good agreement between the estimated and measured losses confirms the validity of an empirical correlation such as equation (11) for estimating the energy losses associated with friction.

Since the theoretical values of Euler head ($\psi_E = 2RV_\theta/U_t$) are known from the predicted values of V_θ (fig. 14), the actual head rise can be estimated from the equation $\psi_T = \psi_E - \psi_{\text{loss}}$.

The value of ψ_T thus estimated is shown plotted and compared with measured values at station 5 in figure 19. Here again, the agreement is reasonably good and large gradients in stagnation head near the tip are estimated qualitatively.

Static Pressure Coefficient at the Exit

The static pressure coefficients derived at various axial locations are plotted and compared with design values in figure 20.

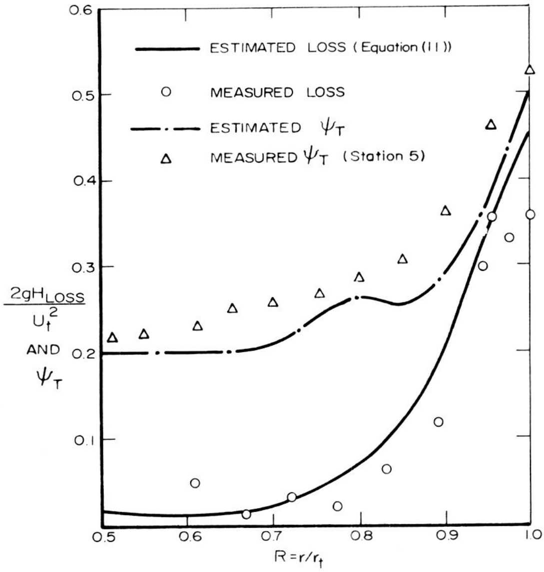

FIGURE 19.—*Estimated and measured friction losses and stagnation pressure coefficient* (ψ_T).

---

[8] See footnote 5.

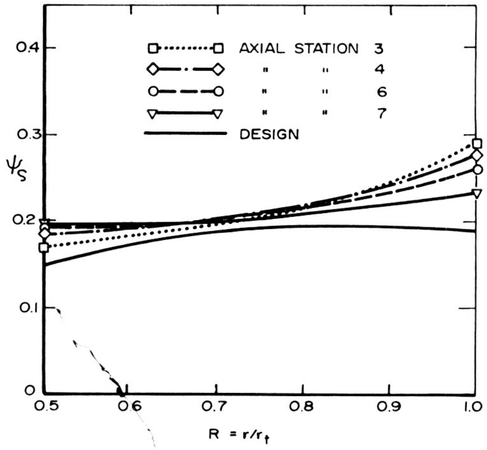

FIGURE 20.—*Radial variation of ψ_S at various axial locations.*

Near the tip, the measured pressure gradients are found to be large compared to those of the design. This is in conformity with the radial equilibrium requirements since tangential velocities at these locations are very large. It should be remarked here that the hub flow at station 3 is still under the influence of the rotor and hence the increase in ψ_S observed between stations 3 and 4. There is appreciable loss in static pressures as the flow proceeds downstream.

SUMMARY AND CONCLUSIONS

(1) A new friction loss coefficient applicable to inducers operating in the range of flow coefficients $\phi=0.065$ to $\phi=0.2$ is defined and derived from the inducer data available in the literature. This empirical friction loss coefficient is found to increase exponentially toward the blade tip. For the Penn State inducer, the radial variation of frictional losses estimated from this newly derived empirical loss coefficient agrees closely with the measured values.

(2) A circumferentially averaged radial equilibrium equation is used to predict the relative and absolute tangential velocities. The analysis is based on suitable assumptions for the radial and mainflow velocity profiles (based on the existing three-dimensional turbulent boundary layer data available) and the loss coefficients explained above. The agreement between theory and experiment is reasonably good. Hence it is evident that, if the frictional effects are known either empirically or analytically, the flow properties at the exit of the inducer can be predicted quite accurately. The stagnation head rise estimated from the predicted tangential velocities and the stagnation pressure losses (item (1)) agree qualitatively with the measured values.

(3) The test inducer, designed approximately for uniform head distribution over its discharge area (assuming ideal flow), actually produces a nonuniform head. Near the tip, the actual head of the absolute flow was found to be two to three times that at hub and midradius. This nonuniform head distribution can be explained qualitatively by real fluid effects and is in agreement with the observations of other investigators. The stagnation pressures are found to decrease continuously as the flow proceeds downstream. The wake mixing losses combined with large change in axial velocity distribution are the major causes of this.

(4) The expected radial motions within the blade passages have been qualitatively confirmed by hot-wire measurements and appear to be quite strong at all radii. The radial velocities are found to be of the same order of magnitude as axial velocities and increase continuously towards the tip.

(5) Measurements carried out several stations downstream indicate that the axial velocity profiles undergo marked changes as the flow proceeds downstream. The back flow region develops after the flow has left the rotating hub and grows continuously as the flow proceeds downstream. The minimum velocity occurs near the midradius, immediately downstream of the trailing edge, whereas, far downstream, the hub locations have minimum axial velocity.

(6) The absolute tangential velocities are substantially higher than the design values, except near the hub. These are consistent with the stagnation pressure rise observed. There is a large change in tangential velocities as the flow proceeds downstream. This is caused by mass flow redistribution and mixing losses that occur downstream of the inducer.

(7) The measured static pressure gradients are found to be large compared to those of design, especially near the tip. There is appreciable loss in static pressures in the tip flow as the flow proceeds downstream.

ACKNOWLEDGMENT

The author wishes to thank G. F. Wislicenus, who initiated this research and was largely responsible for the design of the test inducer. Acknowledgment is also made to several individuals who participated in various phases of the research program. Among these are C. A. Gorton, N. F. Wood, and C. E. Mothersbaugh.

LIST OF SYMBOLS

d_h	Hydraulic mean diameter (equation (9))
F	Frictional force per unit mass
$F(r), \zeta(r), \xi(r)$	Functions defined in equations (33), (30), and (31)

H	Stagnation head rise (in absolute flow)
H_E	Head rise derived from Euler's Equation (UV_θ/g)
H_{loss}	$H_E - H_m$
H_m	Measured stagnation head rise (in absolute flow)
H_{sv}	Net positive suction head, ft
h	Static head
L	Blade chord length
N	Rotative speed, rpm
n	Number of blades
P	Static pressure
P_0	Stagnation pressure
ΔP_0	Stagnation pressure loss due to friction
Q	Flow rate, gpm
R	r/r_t
R_{ht}	Hub/tip ratio
R_N	Reynolds number, $\overline{W}\, d_h/\nu$
r, θ, z	Radial, tangential, and axial coordinates
$2S$	Width of the passage measured normal to blade surface
SS	Suction specific speed, $N\sqrt{Q}/H_{sv}{}^{3/4}$
s	Blade spacing
U	Blade speed
V	Resultant absolute velocity
W	Resultant relative velocity
x, y	Coordinates parallel to and perpendicular to blade camber line and lying on a cylindrical surface (fig. 7)
α	Angle between limiting streamline and x direction (fig. 7)
β	Blade angle measured from axial direction
β'	Air angle measured from axial direction
η	y/S
$\Delta\eta$	Distance between the mean streamline and camber line normal to blade chord
λ	Blasius friction coefficient defined in equation (8)
λ_R	Friction coefficient for a rotating channel defined by equation (11)
ν	Kinematic viscosity
ρ	Density
ϕ	Flow coefficient, $W_z/\Omega r_t$
ψ_E	$2gH_E/U_t^2$
ψ_{loss}	$2gH_{\text{loss}}/U_t^2$
ψ_S	$2gh/U_t^2$ (static head rise coefficient)
Ω	Angular velocity
ψ_T	Stagnation head coefficient, $2gH/U_t^2$

Subscripts

h	Hub
m	Values at midpassage
RMS	Root-mean-square value
r, θ, z	Components along r, θ, z directions
t	Tip
x, y	Components along x, y directions (fig. 7)
1	Inlet
2	Outlet

Superscript

$\bar{}$	Averaged over the passage

REFERENCES

1. Acosta, A. J., An Experimental Study of Cavitating Inducers. *Proc. Second Symposium on Naval Hydrodynamics* (Washington, D.C.), August 25, 1958.
2. Arcand, L., *The Performance of Two Axial Flow Water Jet Pumps.* ASME Symposium on Pumping Machinery for Marine Propulsion, May 1968.
3. Poncet, A., and B. Lakshminarayana, *Investigations and Analysis of Flow Phenomona in Axial Flow Inducers.* NASA CR 107267, October 1969.
4. Poncet, A., and B. Lakshminarayana, *Investigations of Three-Dimensional Flow Characteristics in a Three Bladed Rocket Pump Inducer.* NASA CR-2290, 1973.
5. Lakshminarayana, B., A. Jabbari, and H. Yamaoka, Turbulent Boundary Layer on a Rotating Helical Blade. *J. Fluid Mech.*, Vol. 51, p. 547, 1972.
6. Wislicenus, G. F., *Fluid Mechanics of Turbomachinery.* Dover, Inc., 1965, Chapter 29.
7. Wislicenus, G. F., and B. Lakshminarayana, *Design of a Test Inducer.* Progress Report, NASA Contract NSG 537, March 1964.
8. Ackeret, Contribution to the Layout of Closely Spaced Cascade of Vanes. *Schweizer Bauzeitung,* Vol. 120, No. 9, August 1942.
9. Cooper, P., and H. Bosch, *Three-Dimensional Analysis of Inducer Fluid Flow.* NASA CR 54836, TRW ER 6673A, February 1966.
10. Ruden, P., *Investigations of Single-Stage Fans.* NACA TM 1062, April 1944.
11. Smith, L. H., The Radial Equilibrium Equation of Turbomachinery. *Trans. ASME,* Ser. H, Vol. 88, 1966, pp. 1–12.
12. Mager, A., *Generalization of Boundary Layer Momentum Integral Equation to Three-Dimensional Flows Including Those of Rotating System.* NACA TR 1067, 1952.
13. Spannhake, W., *Proc. Nat. Conf. Ind. Hydraulics,* Vol. 8, October 1944.
14. Ludwieg, H., *Ing. Arch.*, Vol. 19, No. 296, 1951.
15. Mullan, P. J., *An Investigation of Cavitating Inducers for Turbopumps.* M.I.T., Gas Turbine Lab Report 53, May 1959.
16. Bosch, H. B., et al., *Advanced Inducer Study.* ER-5288, NASA Document N63–21124, TRW, Inc., May 1963.
17. Sandercock, D. M., et al., *Cavitation and Noncavitation Performance of an 80.6° Flat Plate Inducer.* NACA TN D1439, November 1962.

18. Soltis, R. F., et al., *Investigation of the Performance of a 78° Flat Plate Helical Inducer.* NACA TN D1170, March 1962.
19. Vavra, M. H., *Aerothermodynamics and Fluid Flow in Turbomachines.* John Wiley and Sons, Inc. (New York), 1960, p. 123.
20. McCafferty, H. G., *Errors in Measuring the Fluctuating Flow at the Discharge of an Inducer.* M.S. thesis, Dept. Aerospace Eng., Penn State U., June 1967.
21. Lakshminarayana, B., *Investigations and Analysis of Flow in Axial Flow Inducer.* NASA CR 103291, June 1969.
22. Smith, L. H., *Three-Dimensional Flow in Axial Flow Turbomachinery.* Johns Hopkins U., Report I–14, November 1953.
23. Schwarz, W. H., and C. A. Friehe, *Deviations from Cosine Law for Yawed Cylindrical Anemometer Sensors.* ASME Paper 68–WA/APM–16.
24. Lakshminarayana, B., Visualization Study of Flow in Axial Flow Inducer. *J. Basic Eng.,* Dec. 1972, p. 777–787.

DISCUSSION

G. F. WISLICENUS (Tucson, Arizona): I am very happy to discuss this paper, as I was connected for a considerable length of time with the work on which this paper reports.

Our friends from NASA will recall that we had no illusions about the inherent difficulties of this investigation at the time it was proposed. As I recall it, we stated in this proposal that real-flow effects were expected to extend over the *entire* flow field. In other words, we expected to find a mess, and this expectation was certainly fulfilled. The objective we had in mind was not only to learn something about rocket pump inducers, but equally to learn how to deal with such a complex and theoretically almost hopeless flow problem. It may be understandable why an old engineer like myself might want to get involved in such a problem. But it commands my respect when a younger engineer and scientist like Dr. Lakshminarayana is willing to struggle for years with this type of investigation, and even more so if he finally comes up with results that seem to make sense. I can assure you that while I was still at Penn State I found hardly any time to contribute to this often frustrating work. And now I am completely out of it, which has given Dr. Lakshminarayana the opportunity to pursue his investigation in a more undisturbed fashion.

I do not feel qualified to discuss the author's theoretical investigations except for the observation that some of the comparisons between his theoretical and experimental results impress me as much closer than I personally would have expected. But if it is really true, as stated in conclusion (2), that frictional effects in inducers are now predictable, then it is our obligation to put this knowledge in a form that can be used by the practical designer. After all, if friction effects double or triple the head generated in the tip regions, then their consideration is a plain necessity in the design process.

There is only one point I should like to discuss in a little more detail; i.e., that according to figures 11 and 18 the angular momentum of the flow *seems* to decrease with increasing distance from the impeller. The statement that this is due to "mass flow redistribution" might not be a sufficient explanation for some old-fashioned engineers like myself. It seems to me that this situation could be cleared up by plotting the circumferential velocity component (V_θ) against the stream function of the (circumferentially averaged) meridional flow, as the local angular momentum transport is, after all, proportional to the local mass flow. If such a plot still shows a decrease in angular momentum, this decrease must be explained by a circumferentially nonuniform mass and momentum exchange between the positive flow region and the backflow region.

In passing, I should like to ask whether the axial velocity curves shown in figure 16 satisfy the condition of continuity. To check this, it might be interesting to plot the same curves against r^2, considering the backflow areas as negative. It illustrates the measuring problem before us if we mention that under such complex conditions of flow measurement any check on the validity on the results obtained is most welcome.

It worries me just a little that the simple throttle valve which I suggested to use might have an upstream effect that could influence the separation at the hub downstream of the inducer. This possibility could be checked with relative ease.

J. E. CROUSE (NASA Lewis Research Center): The author and investigators associated with this project should be congratulated on the depth of their research work. It is encouraging to see some "in depth" studies among the large number of papers published these days.

In the paper, considerable effort was made to construct models of velocity profiles and loss mechanisms. The data essentially confirms that suspected significant radial profiles near the blade surfaces do indeed exist. One of the more interesting results of the work is the small effect these radial components have on the predicted energy addition as evidenced by the $\overline{V_\theta}/U_t$ profiles of figure 15 with and without the radial velocity terms.

The important empirical term in the author's flow prediction equation is the term representing the loss gradient. Especially for low flow coefficient turbomachines, such as inducers, a good flow prediction method is highly dependent on an accurate representation of the loss gradient. The source of the losses is not important for the prediction method itself, but knowledge of the source of the losses can be rather important in setting up a reasonable loss model. The author chose to correlate all the losses associated with the flow through an inducer into a pipe-type friction parameter for the relative flow channel.

The experimental data of figure 9 for several rotors, according to the author's suggested correlation, is indeed somewhat better than that of figure 8, which is the same data by another correlation. The better correlation of loss data should be considered one of the most important results of this work.

J. H. HORLOCK (Cambridge University): To one who has attempted to predict the averaged flow in conventional axial flow turbomachines, this is a fascinating paper in that the method of attack has to be entirely different for several reasons.

(1) The axial velocity term in the radial equation of motion $W_z(dW_z/dr)$ is neglected because of the high stagger of the blade.

(2) Prediction of the tangential velocity distribution $W_\theta(r)$ instead of $W_z(r)$ is attempted.

(3) Variations of velocities across the pitch due to viscous effects are important.

(4) The radial loss distribution is dominant (although this is also important in axial-flow compressors at low flow coefficients).

I have followed B. Lakshminarayana's work with interest and discussed it with him. But there are still several aspects of the investigation that are not clear to me.

(1) On what basis is it justifiable to neglect $\partial W_z/\partial r$ compared with $\partial W_r/\partial z$?

(2) In the region near the blade in the outer half of the rotor, I think the magnitude of the radial body force due to viscous loss should be estimated. It is of order of magnitude $[\tan \alpha\, \partial(\Delta P_0/\rho)/\partial x]$ and may not be negligible.

(3) Why is the loss correlation improved by including the flow coefficient ϕ? I would expect it to be related to $(\phi-\phi_{\text{design}})$ but not simply as inverse of ϕ.

(4) The change in $\overline{V_\theta}(r)$ with r (fig. 11) is mysterious. Is it possible to measure the torque on the rotor and compare it with the change of tangential velocity across the rotor, in order to see if there are errors in the measurement of the latter.

Undoubtedly this work will be of use to designers of other turbomachines, especially in the prediction of performance at low ϕ. Has the author any recommendations on how the design of the inducer may be modified to allow for the observations of this paper? Can the large increase in loss with radius be avoided, and is the operation of the outer part as a drag pump inevitable? Or should the inner part be designed inviscidly and the outer part as a drag pump?

P. COOPER (Case Western University and TRW Inc.): Dr. Lakshminarayana's work makes one aware of the strong three-dimensional effects that serve to alter the expected performance of an inducer. He has made us aware of heretofore unexplained radial flows and other effects of the highly frictional flow that exists in an inducer. That he has been able to predict the outlet tangential velocity distribution by using his new loss scheme is especially encouraging.

I would like to inquire about the flow process connected with his predicted shift in this tangential velocity distribution from that of design. The author suggests that the flow action near the inducer tip is like that of a shear force pump. Is there a way that he could illustrate this more fully? One possible explanation for this phemonenon at the tip is that the much higher loss there would result in too low a pressure—were it not for the action of the blades in maintaining radial equilibrium. Accordingly, the outlet tangential velocity component becomes quite large at the tip in an effort by the machine to produce more work there to offset this loss. Now, regardless of the blade-to-blade and hub-to-shroud velocity profiles, is not this process the result of guidance by the blades? Is the tip axial velocity component still connected with the tangential component through the blade angle there?

F. F. ANTUNES (Ingersoll Rand Inc.): Since the testing was done as a free impeller (without a stator or guide vanes), there is some question as to whether the three-dimensional effects are greatly exaggerated from that of an inducer with stator downstream. It is suggested that a reasonable stator be added and velocities remeasured.

LAKSHMINARAYANA (author): I would like to thank the discussors for their helpful comments and criticisms.

Professors Wislicenus and Horlock have commented on the mysterious effect; i.e., large change in angular momentum as the flow proceeds downstream. The author explained that this is due to large redistribution of mass flow that occurs downstream of the inducers. This can be explained from the following calculations. To check the accuracy of the measurements, area averaged axial velocity $\overline{V_z}$ and mass averaged $\overline{V_\theta}$ are computed at the measuring stations using the following equations.

$$\frac{\overline{V_z}}{U_t}=\frac{2}{1-R_h^2}\int_{R_h}^{1}\frac{V_z}{U_t}R\,dR$$

$$\frac{\overline{V_\theta}}{U_t}=\frac{\displaystyle\int_{R_h}^{1}\frac{V_\theta}{U_t}\frac{V_z}{U_t}R\,dR}{\displaystyle\int_{R_h}^{1}\frac{V_z}{U_t}R\,dR}$$

The values of $\overline{V_z}/U_t$, $\overline{V_\theta}/U_t$ at various measuring stations (see fig. 10) are shown in table D–I.

As can be seen from table D–I, the accuracy of V_z measurements, which is within 4 percent, is better than expected in such a flow. The change in mass averaged $\overline{V_\theta}$ is small compared to local changes observed at various stations (compare fig. 11 and table D–I). This confirms the author's conclusions that local V_θ changes are brought about mainly by flow redistribution. The mass averaged V_θ shows a consistent trend in that it decreases continuously downstream, the decrease being small

TABLE D–I.—*Values of* $\overline{V_z}/U_t$, $\overline{V_\theta}/U_t$ *at Various Stations*

Station number	4	5	6	7
$\frac{\overline{V_z}}{U_t}$	0.076	0.0775	0.0745	0.0775
$\frac{\overline{V_\theta}}{U_t}$	0.346	0.326	0.306	0.26

everywhere except between stations 6 and 7. The reasons for this are mentioned by Wislicenus. Some of the discrepancy in $\overline{V_\theta}$ may also be due to experimental inaccuracy in measuring the flow in the backflow region, whose extent extends up to 20 percent of annulus at station 7.

To check whether a simple throttle valve used in these experiments has any effect on inducer flow, especially in inducing backflow at the hub region, measurements were carried out with a properly designed throttle as shown in the insert in figure D–1. The tests were carried out with a *three-bladed inducer,* since this geometry was readily available. Please note that all the measurements reported in this paper are carried out in a *four-bladed inducer* and *hence velocity profiles plotted in figures D–1 and 16 are for different solidity inducers.* The results shown in fig. D–1 indicate that the throttle has no effect on flow separation at the blade trailing edge and its influence is felt only beyond station 6, which is far downstream of the inducer. Thus, it is concluded that the throttle has no effect on flow separation observed at stations 3, 4, and 5, even though the extent of backflow is somewhat reduced at station 6.

The author agrees with Mr. Crouse with regard to the source of the losses. Knowledge of the source of losses is extremely important in the design of inducers where incorporation of viscous effects is a necessity. The group at Penn State is now engaged in understanding the various sources of losses. This would lead to an analytical model which recognizes various mechanisms responsible for flow departure and losses.

In regard to Professor Horlock's comment on the magnitude of the body force term due to viscous losses, I have proved below that its magnitude is extremely small and its neglect in the equations of motion is justified.

Since the radial equilibrium equation used in this paper is passage averaged, it is necessary to find the average (blade to blade) of the body force term due to viscous losses. This term is thus equal to

$$\overline{F_{d_r}} = \int_0^1 \frac{\partial}{\partial x}\left(\frac{\overline{\Delta P_0}}{\rho}\right)\frac{W_r}{W_x}\,d\eta \tag{36}$$

$$\simeq\frac{1}{3}\tan\alpha\,\frac{\partial}{\partial x}\left(\frac{\overline{\Delta P_0}}{\rho}\right) \tag{37}$$

(from equation (13)).

In deriving equation (37), it is assumed that the streamwise gradient of local loss in P_0 is nearly the same as the corresponding gradient of average loss in P_0. Using equation (21), it can be proved that

$$\overline{F_{d_r}}\sim\frac{1}{3}\lambda_R\overline{W}\,\frac{\partial\overline{W}}{\partial x}\tan\alpha \tag{38}$$

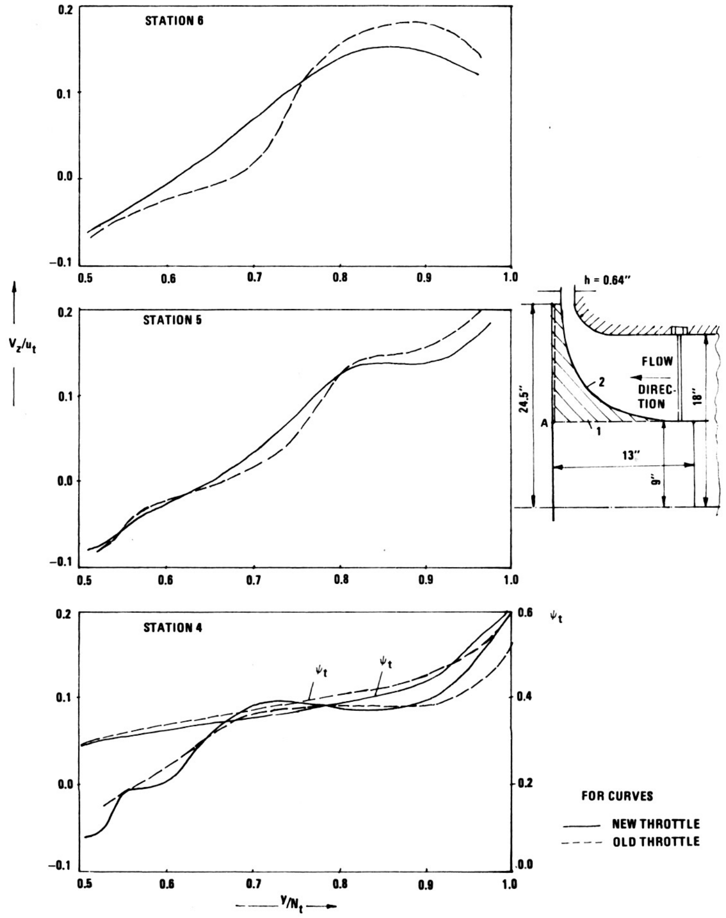

FIGURE D–1.—*Radial variation of* V_z/U_t *and* ψ_t *at various axial stations with simple (old) and aerodynamically designed (new) throttle (three-bladed inducer).*

since

$$\frac{L}{d_h} \sim \frac{1}{\cos\beta}$$

and

$$\frac{\partial}{\partial r}\left(\frac{\overline{\Delta P_0}}{\rho}\right) \sim \frac{\lambda_R}{r_t}\,\overline{W}\,\frac{\partial \overline{W}}{\partial R} + \frac{\overline{W}^2}{2r_t}\,\frac{\partial \lambda_R}{\partial R} \tag{39}$$

Hence the ratio of the two terms is

$$\frac{\overline{F_{d_r}}}{\frac{\partial}{\partial r}\left(\frac{\overline{\Delta P_0}}{\rho}\right)} = \frac{r_t\lambda_R \frac{\partial \overline{W}}{\partial x} \tan\alpha}{3\left(\lambda_R \frac{\partial \overline{W}}{\partial R} + \frac{\overline{W}}{2}\frac{\partial \lambda_R}{\partial R}\right)} \tag{40}$$

This ratio is evidently very small as illustrated in this example (using measured values).

At $R=0.8$, $\tan\alpha=0.36$ (from fig. 13)

$\lambda_R=0.19$, $\frac{\partial \lambda_R}{\partial R}=2.1$ (from fig. 9)

$\overline{W}=0.6U_t$, $\frac{\partial \overline{W}}{\partial R}=0.6U_t$ (from fig. 14)

$\frac{\partial \overline{W}}{\partial x}=\frac{-0.05U_t}{r_t}$ (fig. 9 and eq. (27))

Substituting these values in equation (40), we get

$$\frac{\overline{F_{d_r}}}{\frac{\partial}{\partial r}\left(\frac{\overline{\Delta P_0}}{\rho}\right)} \simeq 1.5\times 10^{-3}$$

Hence the body force term neglected in my analysis is extremely small compared to $\partial/\partial r(\overline{\Delta P_0/\rho})$ and its neglect is certainly justified. Even at the tip, where $\partial \overline{W}/\partial R$ is negative, the ratio is extremely small since $\partial \lambda_R/\partial R$ is very large and α is very small.

The other comment by Professor Horlock concerns the choice of the parameter ϕ in the loss correlation. The physical reasoning behind this choice is that at lower ϕ (which means larger stagger angles) narrower blade passages result and thus the flow in these passages becomes fully developed sooner and hence viscous effects become larger. I don't agree with Professor Horlock that $\phi - \phi_{\text{design}}$ should be the parameter. Unlike a compressor aerodynamicist, an inducer hydrodynamicist is faced with the dilemma of evaluating the losses even at the design conditions where the frictional losses are several orders of magnitude higher than those in a compressor. It is the intention of the author to understand the design flow first and then attempt to correlate the flow losses at off-design conditions.

The physical flow process occurring within the inducer is more complex than explained by Dr. Cooper. Larger increase in V_θ and absolute head rise is not due to guidance of the blade. The flow deviation angles are found to be large at every radial location. As explained in this paper, the radial velocities are large and are of the same order of magnitude as the axial components. Under these circumstances, the inducer should be treated as a mixed flow pump. The meridional component (in the viscid flow) through the inducer can be divided into axial and radial components. The axial component can be treated in the manner described by Dr. Cooper, but the radial component of the flow makes the inducer behave as a shear force pump. The author is presently investigating the possibility of predicting the flow by this approach.

With regard to the comment by Mr. Antunes, it is very doubtful that a stator or guide vane would improve the flow through the inducer. On the other hand, large flow redistribution that occurs downstream of the inducer may be controlled, to some extent, by means of a stator. From physical and mathematical considerations, it is very hard to see how a stator would change the three-dimensional viscous character of the flow inside the inducer.

Prediction of Pump Cavitation Performance

ROYCE D. MOORE

NASA Lewis Research Center

A method for predicting pump cavitation performance with various liquids, liquid temperatures, and rotative speeds is presented. Use of the method requires that two sets of test data be available for the pump of interest. Good agreement between predicted and experimental results of cavitation performance was obtained for several pumps operated in liquids which exhibit a wide range of properties. Two cavitation parameters which qualitatively evaluate pump cavitation performance are also presented.

Cavitation in turbopumps is usually undesirable because it can produce vibrations, flow instabilities, and blade structural damage, as well as losses in head rise. However, in some cases, it is advantageous to operate with cavitation present. For example, the overall structural weight of rocket vehicles can generally be reduced if the turbopump is operated with a controlled degree of cavitation. This type of operation can permit greater pump speeds or lower propellant tank pressures; either can reduce vehicle weight, thereby allowing increased payload. These size and weight advantages offered by increased rotative speed are not limited to space applications.

Rocket engine pumps generally employ an inducer ahead of the main pump rotor. The inducer, by virtue of its design, can operate satisfactorily with a considerable amount of cavitation present on the suction surface of the blades. Because cavitation is a vaporization process which involves heat and mass transfer, the properties of the pumped liquid and its vapor and the flow conditions can affect the cavitation performance of the inducer. These combined effects of fluid properties, flow conditions, and heat transfer—termed thermodynamic effects of cavitation—can improve cavitation performance. For example, cavitation studies have shown that for certain liquids and liquid temperatures the net positive suction head (NPSH) requirements can be significantly less than that obtained in room temperature water (refs. 1 to 3). The accurate prediction of the thermodynamic effects of cavitation and its relation to the NPSH requirements is therefore essential to an optimum design of a cavitating flow system.

This paper presents a method for predicting the cavitation performance of pumps and inducers. The method presented is based on, and is an extension of, the method discussed in references 4 and 5 for Venturis. Two parameters which qualitatively evaluate the cavitation performance are also presented.

ANALYSIS

The method for predicting pump cavitation performance presented here is detailed in reference 6. The method is based on Venturi cavitation results (refs. 5, 7, and 8). Use of the prediction method requires that two sets of appropriate test data be available for the pump and operating conditions of interest.

Assumptions

A prerequisite to the prediction method developed for Venturis is that similarity of the cavitating flow be maintained for all conditions to which the method is applied. For a given inducer design, similarity of cavitating flow is assumed to exist under the following conditions:

(1) Constant flow coefficient. The flow is entering the blades at a constant incidence angle.

(2) Constant head-rise coefficient ratio. The cavity on the suction surface of the blades and thus the vapor volume corresponding to a specific cavitating-to-noncavitating head-rise coefficient ratio is essentially constant irrespective of liquid, liquid temperature, or rotative speed.

(3) The same or geometrically scaled inducers. The inducer should have similar velocity and pressure distribution along the blade surfaces.

Thermodynamic Effects of Cavitation

The differences in pump cavitating performance are generally attributed to the thermodynamic effects of cavitation which reflect the varying degrees of evaporative cooling that accompany vaporization of the particular liquid being pumped. In situations where evaporative cooling is significant, the cavity pressure and the vapor pressure of the liquid adjacent to the cavity are reduced by an amount corresponding to the reduced local temperature. This reduction in cavity pressure retards the rate of further vapor formation, thereby allowing satisfactory operation of the inducer at lower values of net positive suction head than would otherwise be possible.

The magnitude of thermodynamic effects of cavitation Δh_v can be estimated by setting up a heat balance between the heat required for vaporization and the heat drawn from the liquid surrounding the cavity. The heat balance has been derived in references 4, 6, and 7. Thus, only the resulting equation is presented. All symbols are defined at the end of this paper.

$$\Delta h_v = \left(\frac{\rho_v}{\rho_l}\frac{L}{C_l}\frac{dh_v}{dT}\right)\left(\frac{\mathcal{V}_v}{\mathcal{V}_l}\right) \tag{1}$$

The vapor-to-liquid volume ratio $(\mathcal{V}_v/\mathcal{V}_l)$ in any real flow situation is not known nor can it be measured directly. However, from the Venturi cavitation studies (refs. 4 and 5), the following equation, which estimates the volume ratio relative to a reference value, was developed.

$$\left(\frac{\mathcal{V}_v}{\mathcal{V}_l}\right) = \left(\frac{\mathcal{V}_v}{\mathcal{V}_l}\right)_{\text{ref}}\left(\frac{\alpha_{\text{ref}}}{\alpha}\right)\left(\frac{V}{V_{\text{ref}}}\right)^{0.8} \tag{2}$$

For the experimental case where a value of Δh_v is known, the corresponding reference value of $\mathcal{V}_v/\mathcal{V}_l$ can be determined from equation (1). Then values of $\mathcal{V}_v/\mathcal{V}_l$ for other liquids, liquid temperatures, and flow velocities are estimated by equation (2). With the predicted value of $\mathcal{V}_v/\mathcal{V}_l$, determination of the corresponding value of Δh_v is possible using equation (1).

Similarity Relations

For the Venturi studies, a cavitation parameter $K_{c,\text{min}}$ was shown to be a constant for similarity of cavitating flow. In terms of pump parameters, the cavitation parameter can be expressed as

$$K_{c,\text{min}} + 1 = \frac{\text{NPSH} + \Delta h_v}{(V^2/2g)} \tag{3}$$

Because $K_{c,\text{min}}$ is constant for geometrically similar cavities in a given flow device, it follows that

$$\frac{\text{NPSH} + \Delta h_v}{\text{NPSH}_{\text{ref}} + (\Delta h_v)_{\text{ref}}} = \left(\frac{V}{V_{\text{ref}}}\right)^2 \tag{4}$$

where the subscript ref denotes a reference value which must be determined experimentally. Equation (4) may be used to predict the required NPSH for a particular pump operated at a fixed flow coefficient and head-rise coefficient ratio, but with changes in liquid, liquid temperature, and rotative speed.

For pumps, direct measurement of $(\Delta h_v)_{\text{ref}}$ needed for use in equation (4) is not feasible. However, it is possible to estimate Δh_v without measuring cavity pressure directly. This requires that two sets of experimental data be available at the flow coefficient and head-rise coefficient ratio of interest. Although these experimental data do not have to be for the same liquid, liquid temperature, or flow velocity, one set of data must yield measurable thermodynamic effects of cavitation. Measured values of NPSH and V from one of the test conditions are arbitrarily chosen as the reference value. Since both Δh_v and $(\Delta h_v)_{\mathrm{ref}}$ are unknown, an iterative solution of equations (1), (2), and (4) is required to determine $(\Delta h_v)_{\mathrm{ref}}$. With the value of $(\Delta h_v)_{\mathrm{ref}}$ once determined, the required NPSH can be predicted for other liquids, liquid temperatures, and flow velocities.

RESULTS AND DISCUSSION

The prediction method has been applied to several axial-flow inducers and centrifugal pump impellers. These rotors were operated in several different liquids at various liquid temperatures. The rotors were tested at various rotative speeds and flow coefficients.

Liquid Temperature Effects

The cavitation performance for an 84° research inducer (fig. 1) is presented in figure 2. The data are for liquid hydrogen at temperatures from 27.5° R to 36.6° R (15.3 K to 20.3 K) and for a constant rotative speed of 20 000 rpm (ref. 3). The flow coefficient is also constant. The data are plotted in terms of head-rise coefficient ratio ψ/ψ_{NC} as a function of NPSH. For a given value of ψ/ψ_{NC}, the required NPSH decreased rapidly with increasing liquid temperature. The performance results obtained at 27.5° R and 31.7° R (15.3 K and 17.6 K) were arbitrarily chosen as the reference data to predict the NPSH requirements for

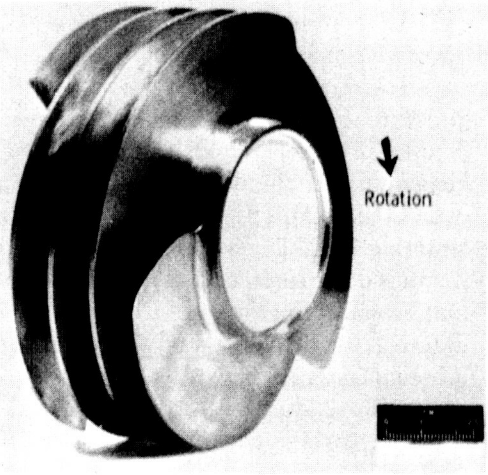

FIGURE 1.—*84° flat-plate helical inducer. Tip diameter, 4.986 inches (12.66 cm); hub diameter, 2.478 inches (6.29 cm); number of blades, 3.*

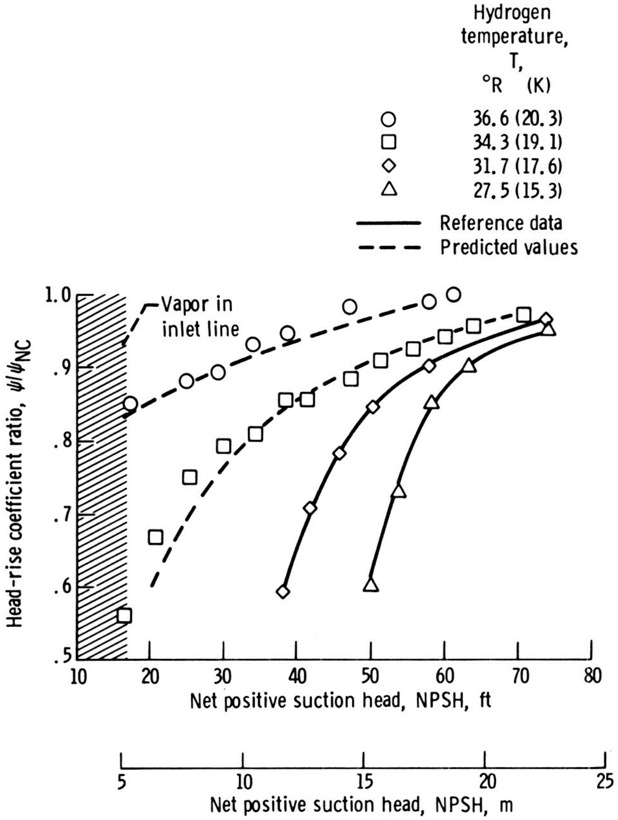

FIGURE 2.—*Effect of liquid temperature on cavitation performance of 84° inducer. Rotative speed, 20 000 rpm.*

hydrogen at 34.3° R and 36.6° R (19.1 K and 20.3 K). The predicted NPSH requirements (dashed lines of fig. 2) agree reasonably well with the experimental results.

The static pressure in the inlet line of a pump is less than the inlet total pressure as a result of the flow velocity. However, the inlet total pressure is used in defining NPSH. Thus, at some relatively low value of NPSH, depending on the design and mode of operation, a condition is reached where the static pressure at the pump inlet equals the pressure of the entering fluid. The fluid in the inlet line is therefore in a boiling state. Any further decrease in NPSH will cause more vapor to be generated; and this vapor will be ingested by the pump. For the inducer performance data of figure 2, this condition of boiling in the inlet line occurs at an NPSH of about 17 feet (5.2 m), as noted by the vertical line. The data for 36.6° R (20.3 K) show that the test inducer was capable of pumping boiling hydrogen while it maintained 0.85 of the noncavitating head rise.

The present prediction method applies to two-phase flow (cavitation) within the blade passages of a pump or inducer. However, when a boiling liquid is pumped, two-phase flow also exists in the inlet line ahead of the pump (shaded area of fig. 2, for example). The condition of a vapor-liquid mixture in the inlet line presents an added complication to the prediction of cavitation performance; the present prediction method does not apply to this condition.

The magnitude of the thermodynamic effects of cavitation realized for this inducer at a rotative speed of 20 000 rpm and ψ/ψ_{NC} of 0.7 is shown in figure 3. The Δh_v values increased rapidly with increasing temperature.

Liquid Effects

The measured and predicted NPSH requirements for three small commercial pumps that were operated in water, methyl alcohol, butane, and Freon-11 at various temperatures are compared in table I. The measured NPSH values listed are taken from previously reported results (refs. 1 and 2). All values are for a cavitating-to-noncavitating head rise of 0.97 and for a speed of about 3550 rpm. The two reference values of NPSH listed for each pump (denoted by a) were arbitrarily chosen as the

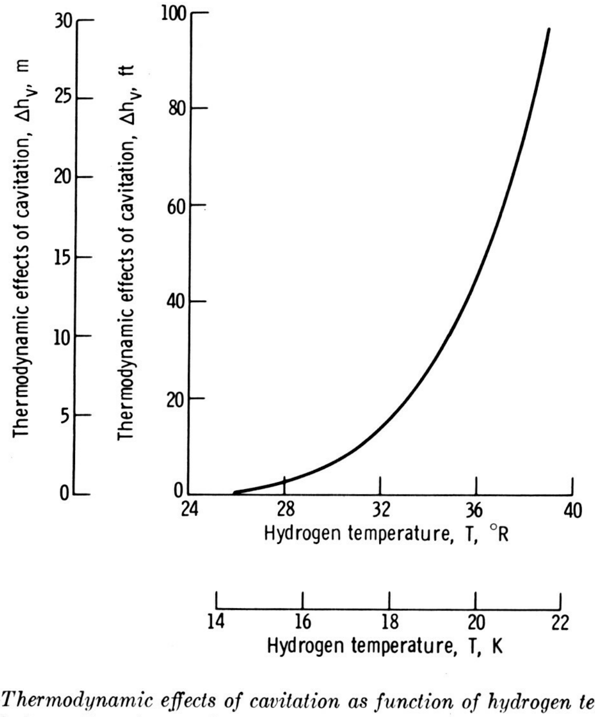

FIGURE 3.—*Thermodynamic effects of cavitation as function of hydrogen temperature for 84° inducer. Rotative speed, 20 000 rpm; head-rise coefficient ratio, 0.70.*

reference test data for use in the prediction method. The predicted NPSH values are in good agreement with experimental results. In fact, except for the 756° R (420 K) water data for pump 1 the predicted values are within the experimental accuracy of measured NPSH values. For pump 3 operated in 870° R (483 K) water, the predicted NPSH value is zero, which from previous discussion implies that this particular pump should have been capable of satisfactory operation (3-percent loss) at an NPSH value sufficiently low to cause vapor to form in the inlet line. As stated in reference 1, there were indications that flashing in the inlet line did occur at rated flow; consequently, the pump was operated at a less-than-design flow rate and the resulting measured NPSH was extrapolated to design conditions. This last set of data further illustrates that, because of the thermodynamic effects associated with cavitation, it may have been possible to pump this liquid under boiling conditions satisfactorily.

The magnitudes of the thermodynamic effects of cavitation realized with these various commercial pumps are also listed in table I. For each liquid, the Δh_v values increase with increasing temperature. It should also be noted that the Δh_v values for the same temperature liquid vary with the various pumps.

Rotative Speed Effects

Liquid hydrogen cavitation data were also obtained for a small research centrifugal pump impeller (fig. 4) operated at various rotative speeds (ref. 6). The experimental and predicted cavitation performance are compared in figure 5. The data were obtained for four rotative speeds at a constant temperature and flow coefficient. The performance curves

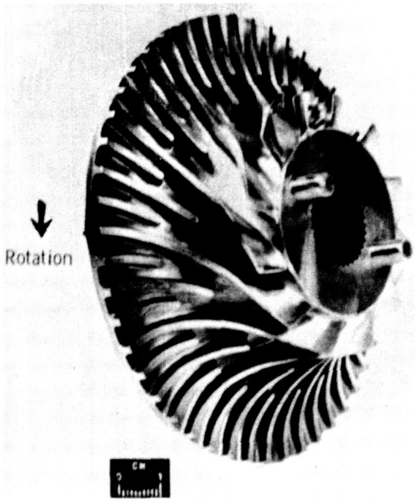

FIGURE 4.—*Centrifugal pump impeller. Overall diameter, 4.56 inches (11.58 cm); number of blades, 12; number of splitter vanes, 36; inlet tip blade angle, 71.3° (from axial direction).*

TABLE I.—*Effect of Liquid and Liquid Temperature on Pump Cavitation Performance*

[Nominal rotative speed, 3550 rpm; head-rise coefficient ratio, 0.97.]

Pump	Liquid	Temperature, T		Net positive suction head, NPSH				Thermodynamic effects of cavitation, Δh_v	
		°R	K	ft		m			
				Measured (±0.5 ft)	Predicted	Measured (±0.2 m)	Predicted	ft	m
I (ref. 2)	Water	534	297	17.5[1]	------------	5.3[1]	------------	0	0
		600	333	17.5	17.5	5.3	5.3	0	0
		670	372	17.5	17.4	5.3	5.3	0.1	0
		710	394	17.0[1]	------------	5.2[1]	------------	0.5	0.1
		735	408	16.0	16.5	4.9	5.0	1.0	0.3
		756	420	13.3	15.6	4.1	4.8	1.9	0.5
	Methyl alcohol	560	311	17.5	17.4	5.3	5.3	0.1	0
		611	339	16.7	16.8	5.1	5.1	0.7	0.2
		641	356	15.5	15.3	4.7	4.7	2.2	0.6
		663	368	13.5	13.3	4.1	4.1	4.2	1.2

II (ref. 1)	Water	530	294	12.3	11.8	3.7	3.7	0	0
		710	394	11.0[1]		3.4[1]		0.8	0.3
		760	422	8.6	8.7	2.6	2.7	3.1	1.1
	Butane	495	275	9.8	10.2	3.0	3.1	1.6	0.5
		515	286	8.8[1]		2.7[1]		3.0	0.9
		540	300	5.1	5.6	1.6	1.7	6.2	1.9
		550	306	3.5	3.4	1.1	1.0	8.4	2.6
	Freon-11	545	303	10.2	10.5	3.1	3.2	1.3	0.4
		580	322	8.4	8.1	2.6	3.7	3.7	1.1
III (ref. 1)	Water	530	294	12.0[1]		3.7[1]		0	0
		750	417	9.5[1]		2.9[1]		2.5	0.8
		785	436	6.0	6.0	1.8	1.8	6.0	1.9
		870	483	2.0[2]	0	0.6	0	12.0	3.7

[1] Reference test data.

[2] Estimated accuracy of 2.0 ft (0.6 m).

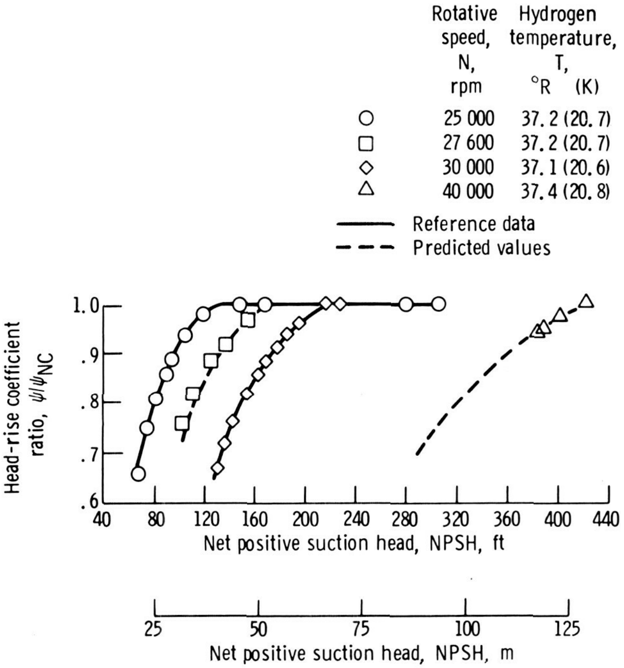

FIGURE 5.—*Effect of rotative speed on cavitation performance of centrifugal pump impeller.*

obtained at 25 000 rpm and 30 000 rpm (solid curves) were used as reference test data to predict the NPSH requirements for 27 600 rpm and 40 000 rpm (dashed lines). The predicted and experimental results are in good agreement. The predicted magnitude of the thermodynamic effects of cavitation for this pump operated in 37.2° R (20.7 K) liquid hydrogen is shown in figure 6. The Δh_v values increase with increasing rotative speed. For the data of figure 5, the pump NPSH was sufficiently large that the condition of boiling in the inlet line was not encountered.

Flow Coefficient Effects

The prediction method was also used to predict the cavitation performance of a 80.6° inducer (fig. 7) operated in liquid hydrogen at a rotative speed of 30 000 rpm (refs. 9 to 12). The required NPSH for a ψ/ψ_{NC} of 0.7 is plotted as a function of flow coefficient in figure 8. For each liquid temperature, the required NPSH increases with increasing flow coefficient. The performance curves for 31.0° R and 34.1° R (17.2 K and 18.9 K) hydrogen were used as the reference data. The predicted and experimental values are in good agreement. The predicted magnitude of the thermodynamic effects of cavitation is shown in figure 9. For each

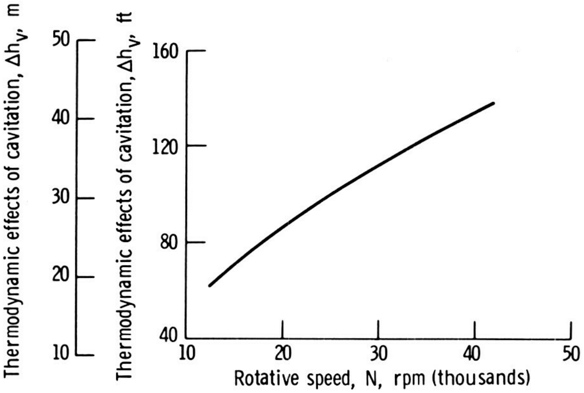

FIGURE 6.—*Thermodynamic effects of cavitation as function of rotative speed for centrifugal pump impeller. Hydrogen temperature, 37.2° R (20.7 K); head-rise coefficient ratio, 0.70.*

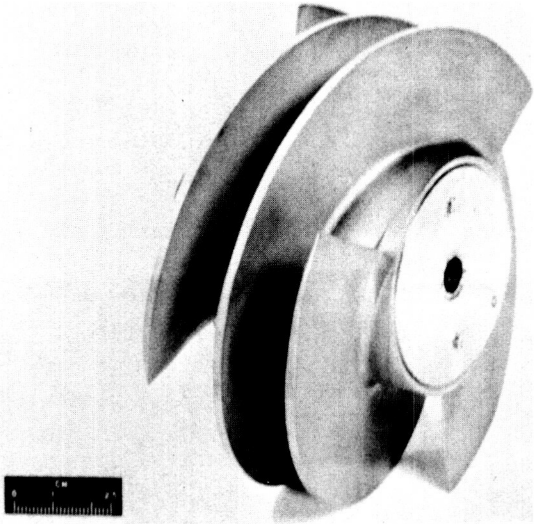

FIGURE 7.—*80.6° flat-plate helical inducer (Inducer A). Tip diameter, 4.980 inches (12.65 cm); hub diameter, 2.478 inches (6.29 cm); number of blades, 3.*

temperature above the triple point temperature, Δh_v decreased with increasing flow coefficient. As was the case with the other inducer and pumps, Δh_v increased with increasing liquid temperature.

Cavitation Parameters

As shown here and in references 3, 6, and 9 to 14, both the required NPSH and the magnitude of the thermodynamic effects of cavitation vary with liquid, liquid temperature, rotative speed, flow coefficient and inducer or pump design. Thus, when values of NPSH and Δh_v are given, they must be accompanied by each of these variables.

A more convenient way to express the cavitation performance is to express equation (3) as

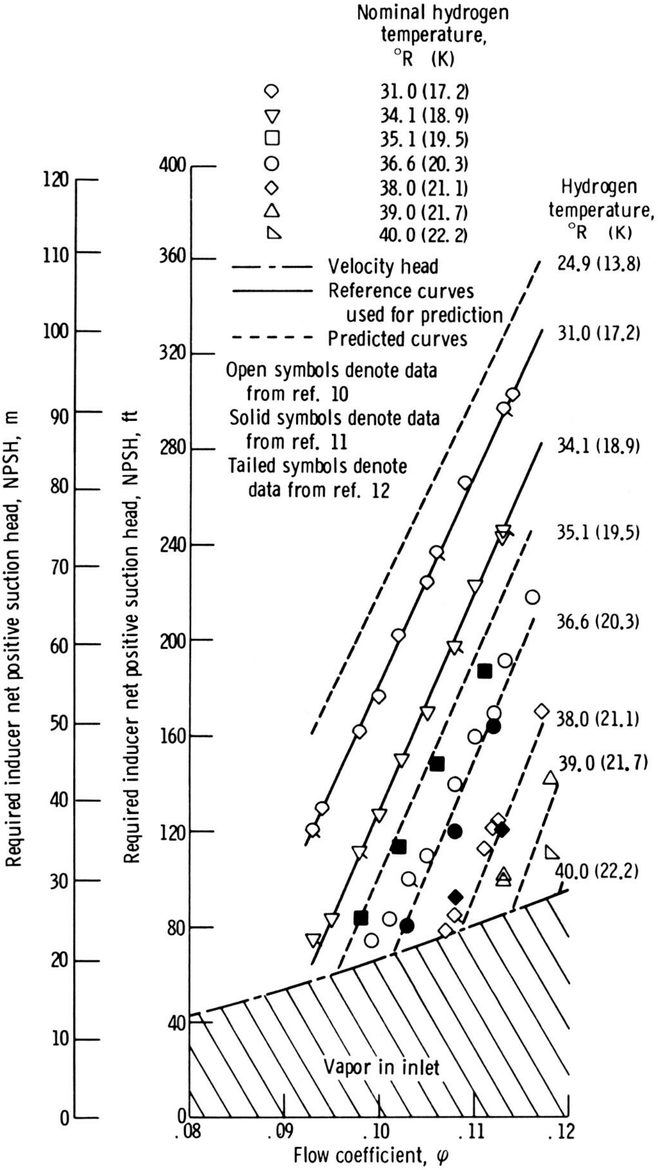

FIGURE 8.—*Effect of flow coefficient on cavitation performance of 80.6° inducer (Inducer A). Rotative speed, 30 000 rpm; head-rise coefficient ratio, 0.70.*

$$K\text{-factor} = K_{c,\min} + 1 = \frac{\text{NPSH} + \Delta h_v}{(V^2/2g)} \tag{5}$$

With the K-factor known, the cavitation performance of an inducer operated in a liquid without thermodynamic effects can be evaluated. The greater K-factor will result in the greater required NPSH.

Another way to evaluate the thermodynamic effects of cavitation is to express the reference values in equation (2) as

$$M\text{-factor} = \left(\frac{\mathcal{V}_v}{\mathcal{V}_l}\right)_{\text{ref}} (\alpha_{\text{ref}}) \left(\frac{1}{V_{\text{ref}}}\right)^{0.8} \tag{6}$$

With the substitution of equation (6), equation (2) will become

$$\left(\frac{\mathcal{V}_v}{\mathcal{V}_l}\right) = M\text{-factor} \left(\frac{1}{\alpha}\right) (V)^{0.8} \tag{7}$$

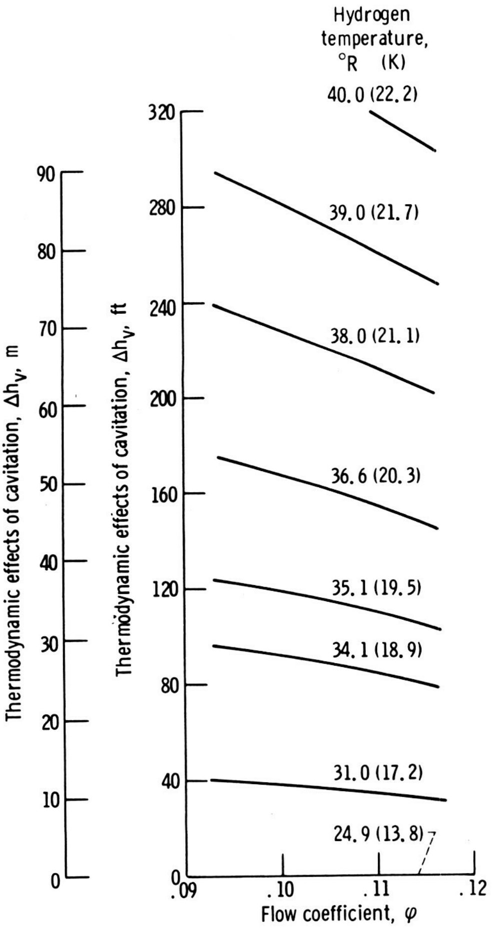

FIGURE 9.—*Thermodynamic effects of cavitation as function of flow coefficient for several hydrogen temperatures for 80.6° helical inducer (Inducer A). Rotative speed, 30 000 rpm; head-rise coefficient ratio, 0.70.*

Equation (7) can then be used in conjunction with equation (1) to determine the value of Δh_v for the condition of interest. Thus only the M-factor has to be known to qualitatively evaluate which inducer (or pump) will have the most thermodynamic effects of cavitation. When the same temperature liquid is being pumped at a particular speed, the inducer with the greater M-factor will have the greater thermodynamic effects.

Blade Leading Edge Thickness Effects

To evaluate the effect of blade leading edge thickness on the cavitation performance of an inducer, the 80.6° inducer (fig. 7) was tested with three different fairings. The leading edges of the blades were faired as shown in figure 10. The results from those tests (refs. 9, 13, and 14) are summarized in figure 11 where the cavitation parameters, M-factor and K-factor, are

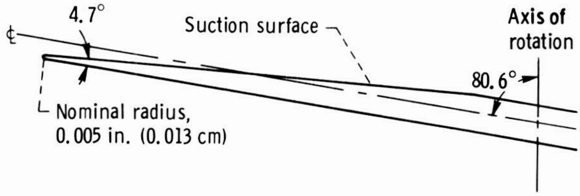

a.—*Inducer* A.

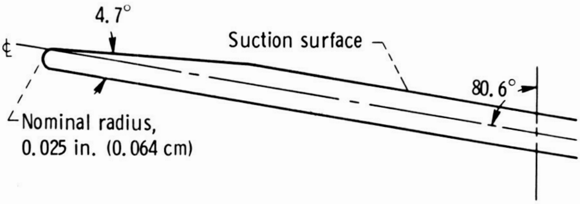

b.—*Inducer* B.

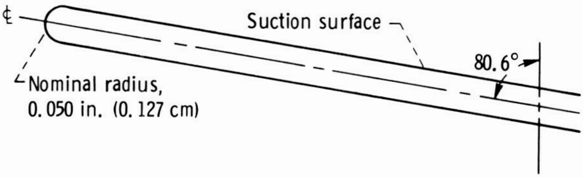

c.—*Inducer* C.

FIGURE 10.—*Blade leading edges for three 80.6° helical inducers.*

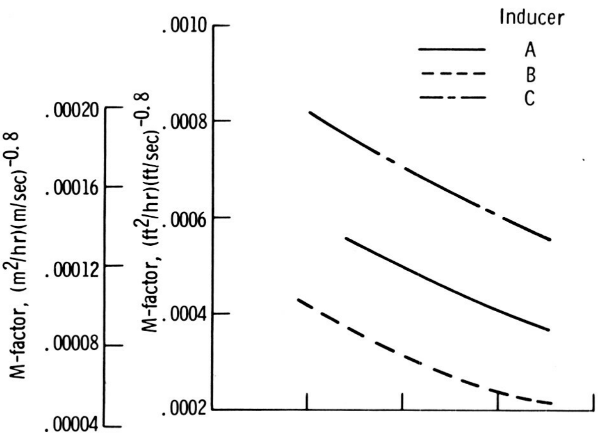

a.—M-*factor.*

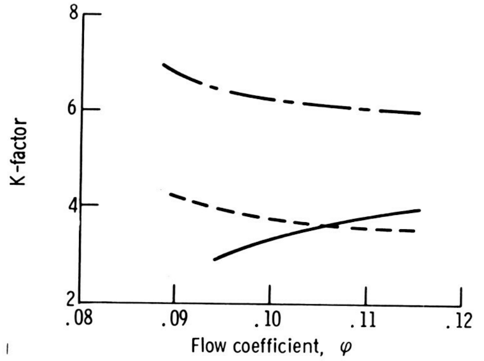

b.—K-*factor.*

FIGURE 11.—*Effect of blade leading-edge thickness on cavitation parameters for 80.6° helical inducer in hydrogen. Head-rise coefficient ratio, 0.70.*

plotted as a function of flow coefficient. Inducer *A* is the same as that shown in figure 7.

Although Inducer *C* has the greatest thermodynamic effects of cavitation (indicated by the greatest *M*-factor), that inducer does not necessarily have the best cavitation performance (indicated by the highest *K*-factor). Depending on liquid temperature, the increase in Δh_v gained by blunting the blades may not be large enough to overcome the increase in NPSH requirements. Thus, compromises in blade fairing must be made in order to optimize the inducer design over a temperature range.

The values of Δh_v and NPSH can be obtained for each inducer from the cavitation parameters, *M*-factor (eq. (6)) and *K*-factor (eq. (5)). For example, the *M*-factor for Inducer *A* will yield the Δh_v-values shown on the curves of figure 9. The *K*-factor for Inducer *A* can be used to calculate the required values of NPSH shown in figure 8 for liquid hydrogen at 24.9° R (13.8 K). The values of Δh_v obtained from the *M*-factor are then subtracted from the required NPSH at 24.9° R (13.8 K) to obtain the required NPSH at other liquid temperatures (fig. 8).

CONCLUDING REMARKS

A method for predicting the cavitation performance of pumps was developed. The prediction method, formulated from theoretical and supporting experimental studies, provided good agreement between predicted and experimental results for several inducers and pumps handling liquids of widely diverse physical properties. The use of the method requires that two appropriate sets of test data, not necessarily for the same liquid, liquid temperature, or rotative speed, be available for the pump of interest. From these reference tests, the cavitation performance for the pump can then be predicted for any liquid, temperature, or rotative speed provided that flow similarity is maintained. The method also has useful application in the generalization of experimental data obtained with liquids that exhibit substantial thermodynamic effects of cavitation. For example, pump cavitation studies that use a particular liquid need not be conducted at predetermined precise values of temperature and rotative speed since, through the use of the cavitation parameters, the data can be normalized.

Because of the large thermodynamic effects of cavitation for liquid hydrogen, it is possible to pump hydrogen in a boiling state with relatively small losses in pump performance. The net positive suction head requirements will depend on the combination of fluid properties and on the flow conditions.

LIST OF SYMBOLS

C_l	Specific heat of liquid, Btu/(lbm)(°R); J/(kg)(K)
dhv/dT	Slope of vapor pressure head to temperature curve, ft of liquid/°R; m of liquid/K
g	Acceleration due to gravity, ft/sec^2; m/sec^2
ΔH	Pump head rise based on inlet density, ft of liquid; m of liquid
Δh_v	Decrease in vapor pressure because of vaporization (magnitude of thermodynamic effect of cavitation), ft of liquid; m of liquid
$K_{c,\min}$	Developed cavitation parameter based on minimum cavity pressure
k	Liquid thermal conductivity, Btu/(hr)(ft)(°R); J/(hr)(m)(K)
L	Latent heat of vaporization, Btu/lbm; J/kg
N	Rotative speed, rpm
NPSH	Net positive suction head, ft of liquid; m of liquid
U_t	Blade tip speed, ft/sec; m/sec

V	Average axial velocity at inducer inlet, ft/sec; m/sec
$\mathcal{V}_l$	Volume of liquid involved in cavitation process, in.^{3}; cm^3
$\mathcal{V}_v$	Volume of vapor, in.^{3}; cm^3
α	Thermal diffusivity of liquid, $k/\rho_l C_l$, ft^2/hr; m^2/hr
ρ_l	Density of liquid, lbm/ft^3; kg/m^3
ρ_v	Density of vapor, lbm/ft^3; kg/m^3
φ	Flow coefficient, V/U_t
ψ	Head-rise coefficient, $g\Delta H/U_t^2$
ψ/ψ_{NC}	Cavitating-to-noncavitating head-rise-coefficient ratio

Subscripts

NC	Noncavitating
ref	Reference value obtained from experimental tests

REFERENCES

1. Salemann, Victor, Cavitation and NPSH Requirements of Various Liquids. *J. Basic Eng.*, Vol. 81, No. 2, June 1959, pp. 167–180.
2. Spraker, W. A., The Effects of Fluid Properties on Cavitation in Centrifugal Pumps. *J. Eng. Power*, Vol. 87, No. 3, July 1965, pp. 309–318.
3. Meng, Phillip R., *Change in Inducer Net Positive Suction Head Requirement With Flow Coefficient in Low Temperature Hydrogen (27.9° to 36.6° R).* NASA TN D–4423, 1968.
4. Ruggeri, Robert S., *Experimental Studies on Thermodynamic Effects of Developed Cavitation.* International Symposium on the Fluid Mechanics and Design of Turbomachinery, Penn State U., August 31–September 3, 1970.
5. Moore, Royce, D., and Robert S. Ruggeri, *Prediction of Thermodynamic Effects of Developed Cavitation Based on Liquid-Hydrogen and Freon-114 Data In Scaled Venturis.* NASA TN D–4899, 1968.
6. Ruggeri, Robert S., and Royce D. Moore, *Method for Prediction of Pump Cavitation Performance for Various Liquids, Liquid Temperatures, and Rotative Speeds.* NASA TN D–5292, 1969.
7. Gelder, Thomas F., Robert S. Ruggeri, and Royce D. Moore, *Cavitation Similarity Considerations Based on Measured Pressure and Temperature Depressions in Cavitated Regions of Freon-114.* NASA TN D–3509, 1966.
8. Moore, Royce D., and Robert S. Ruggeri, *Venturi Scaling Studies on Thermodynamic Effects of Developed Cavitation of Freon-114.* NASA TN D–4387, 1968.
9. Moore, Royce D., and Phillip R. Meng, *Thermodynamic Effects of Cavitation of an 80.6° Helical Inducer Operated in Hydrogen.* NASA TN D–5614, 1970.
10. Meng, Phillip R., and Royce D. Moore, *Cavitation Performance of 80.6° Helical Inducer in Liquid Hydrogen.* NASA TM X–1808, 1969.
11. Moore, Royce D., and Phillip R. Meng, *Cavitation Performance of Line-Mounted 80.6° Helical Inducer in Hydrogen.* NASA TM X–1854, 1969.
12. Meng, Phillip R., and Royce D. Moore, *Hydrogen Cavitation Performance of 80.6° Helical Inducer Mounted in Line With Stationary Centerbody.* NASA TM X–1935, 1970.

13. Meng, Phillip R., and Royce D. Moore, *Hydrogen Cavitation Performance of 80.6° Helical Inducer With Blunt Leading Edges.* NASA TM X–2022, 1970.

14. Moore, Royce, D., and Phillip R. Meng, *Effects of Blade Leading Edge Thickness on Cavitation Performance of 80.6° Helical Inducer in Hydrogen.* NASA TN D–5855, 1970.

DISCUSSION

P. COOPER (TRW Inc. and Case Western Reserve University): Mr. Moore presents conclusive evidence in support of a theory that is the result of careful application to pumps of fundamental discoveries made at NASA with regard to cavitating flows. Basic to the theory presented is the discovery of the relationship between the NPSH and other relevant quantities that exists for similarly appearing flow configurations. That this relationship furnishes a pump cavitation performance map is emphasized if one approaches the problem of predicting such performance by using the classical methods of dimensional reasoning.

In outlining the problem in this way, we must distinguish between the *dynamic similarity* to which dimensional reasoning is applied and the *flow configuration similarity* that is basic to the theory presented by Mr. Moore. For the former, we first write, in terms of the quantities evidently involved, the physical equation for pump performance:

$$\Delta H=f\left(V, \Omega, r, \rho_l, \rho_v, \frac{dt}{dh_v}, C_l, L, \alpha, g\text{NPSH}, m, \{G_i\}\right) \qquad \text{(D–1)}$$

where Ω is the angular speed; r, the pump inlet tip radius; $\{G_i\}$, the set of geometrical lengths that describe the pump shape; m, another independent quantity or combination of quantities implied as being involved by the discoveries made; and the other symbols are those defined by the author. Recognizing the dimensions of these quantities and the combinations of them that appear in the theory, we obtain a dimensionless functional equation for pump performance:

$$\frac{\Delta H}{\Omega^2 r^2}=f_1\left(\frac{V}{\Omega r}, \frac{g\text{NPSH}}{(V^2/2)}, \frac{dt}{dh_v} \frac{C_l}{L} \frac{\rho_l}{\rho_v} \frac{V^2}{2}, \frac{rV}{\alpha}, \frac{m}{r^{4/5}V^{1/5}}, \left\{\frac{G_i}{r}\right\}\right) \qquad \text{(D–2)}$$

or, abbreviating these dimensionless groups,

$$\psi=f_1(\phi, k, \theta, P_e, \hat{m}, \{\hat{G}_i\}) \qquad \text{(D–3)}$$

Here, ψ can be replaced by ψ/ψ_{NC}, since ψ_{NC} is a constant of the problem. (ϕ is fixed, and noncavitating Reynolds number effects are apparently ignored.) ϕ is the flow coefficient; k is a cavitation number; θ is essentially the parameter presented in an earlier NASA-sponsored inducer study (ref. D–1)[D–1]; and P_e is a Peclet number.

[D–1] There the parameter is developed as $H \simeq dt/dh_v \; C_l/L \; \rho_l/\rho_v \; \Omega^2 r^2 = 2\theta/\phi^2$.

Now, Mr. Moore's theory embodies the method of solution of equation (D–3), and it is in that solution that we see the independent parameter $\hat{m}$ involved. The relationships given by him in his equations (1), (2), and (3) (with his equation (2) modified by the addition of the size effect D/D_{ref} from equation (11) of NASA TN D-5292 (ref. 6) may be combined and written as follows:

$$k+\frac{\hat{m}P_e}{\theta}-1=K_{c,\mathrm{min}} \tag{D–4}$$

$K_{c,\mathrm{min}}$ and m, where

$$m=\hat{m}r^{4/5}V^{1/5}=\frac{\mathcal{V}_v}{\mathcal{V}_l}\,\frac{r^{4/5}V^{1/5}}{P_e}=\frac{\mathcal{V}_v}{\mathcal{V}_l}\,\frac{\alpha}{V^{4/5}r^{1/5}}$$

are constants for fixed values of the dependent parameter ψ/ψ_{NC}, ϕ, and the shape $\{\hat{G}_i\}$.

From the standpoint of the rationalist who must evolve equation (D–1), it is unfortunate that the constant dimensional quantity m is unknown. It must be some combination of the known quantities that are involved, such as surface tension, viscosity, etc., just as

$$\frac{dt}{dh_v}\,\frac{C_l}{L}\,\frac{\rho_l}{\rho_v}$$

is another such combination. This is to be expected because, among other possibilities, no Reynolds number appears explicitly in the analysis.

Mr. Moore's method has made it unnecessary for us to know m from the beginning; he merely asks that two tests be run to determine it, together with $K_{c,\mathrm{min}}$. This points up another attribute of m, at least for the cavity-type flow configuration: It is independent of the fluid used and depends only on the quantities ψ/ψ_{NC}, ϕ, and $\{\hat{G}_i\}$. Apparently m is some compensating combination of physical properties and some of the other independent quantities listed in equation (D–1) such that it can have this constancy character.

The quantity $K_{c,\mathrm{min}}$ is not an independent parameter of the functional performance equation (D–3), but rather is a function of the independent dimensionless parameters that turns out to be constant under the given conditions for similarly appearing flow configurations of the type assumed to exist in cavitating pumps. Since m is also constant under these conditions, the parameter $\hat{m}$ could be a combination of more independent parameters that might have different influences in a basically different flow structure.

The flow of vapor and liquid in an inlet line is an example of a situation with which is associated a flow configuration fundamentally different from the cavity type basic to the prediction method presented by Mr.

Moore. If, as was done in the earlier inducer study already noted, one assumes such a flow to be fog-like (i.e., a homogeneous variable-density continuum consisting of many small bubbles in equilibrium with the surrounding liquid), $\hat{m}$ and P_e are eliminated from equation (D–3). Furthermore, the solution of the entire resulting compressible flow field can be sought using an equation of state for the mixture density ρ:

$$\rho=\frac{\rho_l}{1+\Theta C_{pv}} \tag{D–5}$$

This was applied wherever the pressure depression coefficient $C_{pv}=(p_v-p)g/(\rho_l\Omega^2r^2)$ exceeded zero, p_v being the initial vapor pressure of the fluid and p_v-p being the vapor pressure depression (since p is then the local vapor pressure).

This fog-flow approach was applied to inducers. The assumption of a cavity on the suction side of each blade is well substantiated by Mr. Moore for the operating conditions investigated. However, at complete head breakdown, or near such a condition with vapor in the inlet line, the blades are unloaded, and the fog-flow approach might more closely describe the flow, especially in the inlet region. Such an analysis applied to an 83.8° inducer yielded dimensionless NPSH results for this limiting situation over an Θ-range of 10 to 1000 that agree qualitatively with those indicated in figure 2 for the 84° inducer of figure 1 of Mr. Moore's paper. His range of the parameter Θ was from 46 to 1260 for the corresponding LH_2 temperature range of 36.6° R to 27.5° R at 20 000 rpm—the lower values of Θ corresponding to the greater thermodynamic effects of cavitation. Of particular interest is the fog-flow performance calculation, which indicated no head breakdown for the 83.8° inducer at $\Theta=10$. There the NPSH was zero, and there was vapor in the inlet line.

Attention has been called to these fog-flow calculations as an indicator of the ideal for which the cavitation performance predictor strives; namely, the analytical description of cavitating flow fields under all possible conditions. Obviously a successful description, complete with losses, is a long way off. Thus there seems no doubt that the procedure presented by Mr. Moore will serve as the prediction method for a long time. His empirical determination of pump cavitation performance from two sets of test results shows excellent correlation of experiment and theory for all practical pump flows.

H. G. PAUL: The method for predicting thermodynamic effects of cavitation described by Mr. Moore has been used at the Marshall Space Flight Center (MSFC) for the past several years to predict the suction performance of cryogenic propellant pumps. It is our experience that the effect of pump speed and fluid temperature on suction performance can be predicted accurately. However, attempts to predict cavitation performance of a pump when several fluids were involved have not always been completely satisfactory. The following data for the J-2 rocket engine fuel pump are cited as an example of the problem encountered. In this assessment, it is assumed that water has negligible vapor pressure depression and all NPSH deviations from the similarity laws in cryogenic liquids are due to thermodynamic effects. The data are

Fluid	LH_2	LN_2[D-2]	H_2O[D-3]
Speed, rpm	27 100	7590	6320
Temperature, °R	38	140	530
NPSH @ ref head loss, ft	80	12.5	12.2

If the water and hydrogen data are used to predict the vapor pressure decrease in LN_2 for the above conditions, a value of 2.5 ft is calculated compared to a value of 5.0 ft obtained from the nitrogen and water data. Similarly, if the water and nitrogen data are used to predict the vapor pressure depression in LH_2 at the above conditions, a value of 245 ft is calculated compared to a value of 145 ft obtained directly from the water and hydrogen data. From this result, it is concluded that some caution should be exercised when using these methods to predict cavitation performance of a pump in a fluid other than that fluid for which test data exist.

An additional point which merits comment is the capability to satisfactorily pump two-phase fluids under certain circumstances as discussed by Mr. Moore. This capability is of considerable interest as an operational mode for space vehicle pumping systems. Cryogenic liquids used in these applications are stored at close to saturation conditions under zero "g" conditions. In order to supply NPSH for pump operation, a vent and pressurization cycle is required. This complicates the system operation and is costly from a weight standpoint because of the requirement for stored pressurization gas. "Zero tank NPSH" operation, which implies two-phase operation at the pump inlet, has the potential for eliminating the vent and pressurization cycle and is therefore viewed as a highly desirable capability.

MOORE (author): I would like to thank Mr. Cooper and Mr. Paul for their comments. Mr. Cooper has presented an interesting discussion of the theory. Dimensionless parameters involving, V, α, and r might have been found had a model different from the conduction model been chosen. I agree that any and all theories should be examined in an effort to develop an analytical description which can predict cavitation performance under all conditions.

[D-2] Reference D–2.

[D-3] Reference D–3.

It is realized that large errors can occur when the predicted speed is several times greater than the reference value as is the case with Mr. Paul's example for hydrogen. Examination of the similarity equation (eq. 4) will show that any measurement errors occurring at the lower speed will increase by the speed squared at the higher speed. It is felt that prediction for various speeds should be limited to about a 2-to-1 change in speeds. A study made by C. F. Braun & Company, under NASA contract, indicated that pump similarity parameters were reasonably accurate to only a 2-to-1 change in speed.

REFERENCES

D–1. Cooper, P., Analysis of Single- and Two-Phase Flows in Turbopump Inducers. *Trans. ASME*, Ser. A, Vol. 89, No. 4, October 1967, pp. 577–588.

D–2. *Hydrodynamic Testing (in LN_2) of Mark 15F Pump.* North American Aviation, Inc., Internal Letter TAMM 3115–2011, July 12, 1963.

D–3. *Test Results of a 7.25″ D and a 7.8″ D, J–2 Fuel Inducer (Mark 15F) in Water.* North American Aviation, Inc., Internal Letter TAMM 4115–77, July 2, 1964.

SESSION VII

Turbomachinery for Marine Propulsion

Chairman: **R. E. HENDERSON**

An Introduction to the Design of Marine Propulsors

Robert E. Henderson

The Pennsylvania State University

This paper is intended to serve as an introduction to the area of marine propulsor design by presenting a brief summary of current design methods. In addition, a list of reports dealing with the design of open propellers, ducted propellers or pumpjets, and waterjets is presented together with a discussion of some of the major problems facing today's marine propulsor designer.

The propulsion of a marine or waterborne vehicle represents one of the earlier applications of turbomachinery design. For the past 100 years, ships have been propelled by the open screw propeller while in more recent times the ducted propeller or pumpjet, the waterjet, and various novel forms of the open screw propeller have been employed. The similarities which exist between these marine propulsors and the axial-flow compressors of the modern aircraft engine or the liquid pumps employed in today's space rockets are obvious. One would think, therefore, that the methods employed in the design of these types of turbomachinery would be similar.

Indeed, the principles employed and the problems encountered in the designing of these turbomachines are similar. However, the design methods employed are many times quite different. It is hoped that, through this symposium on design methods, not only can data on methods for the design of improved marine propulsors be presented, but there can be an exchange of the design methods used for various types of turbomachinery, and this will provide solutions in common problem areas.

The design of a marine propulsor, like the design of any turbomachine, can be separated into four distinct steps. Each of these steps must be carried out in the indicated order to arrive at a final configuration which will provide the desired propulsive performance. These steps are

(1) A preliminary or one-dimensional design analysis to determine the design parameters at which the particular propulsor is to operate.

This step ensures compatibility between the propulsor and the power-transmitting machinery and performance characteristics of the marine vehicle on which it is to be operated. This step results in the selection of the type of propulsor to be employed (i.e., open propeller, pumpjet or waterjet).

(2) The determination of the flow field which results when the selected propulsor produces the desired performance characteristics. This includes the prediction of velocity distributions at the leading and trailing edges of the rotating element, usually based on an inviscid theory. Of primary importance in this step is a knowledge of the flow field on the vehicle in which the propulsor is to operate. This flow field, together with the desired performance characteristics, determines the spanwise and axial distribution of energy addition to the fluid.

(3) The determination of the shape and size of the blade, i.e., the camber, thickness, and angle distributions required to produce the desired performance characteristics. This step must consider the chordwise variations in flow over the individual blades and include effects of viscosity and cavitation. With regard to cavitation, the design must either avoid its occurrence, as in a subcavitating propulsor, or account for the influence of its presence, as in a supercavitating propulsor.

(4) The specification and description of the blades for manufacture and to comply with the stress requirements of the application. The involvement of the designer in the specification of the blades for manufacture is essential in ensuring that the final product faithfully reproduces the design surfaces.

The completion of all of these steps, in the order indicated, is necessary to complete a marine propulsor design. Each of the steps involves a considerable amount of detail and, in the following, each will be discussed briefly in relation to present-day design procedures.

THE PROCEDURE OF DESIGN

Preliminary Analysis

The preliminary or one-dimensional analysis of a propulsor is a very important step. It is from this step that the designer selects the type of propulsor which is to be employed and matches its performance parameters to those of the vehicle in question. In order to conduct this step, the designer must have a knowledge of the flow field of the subject vehicle; i.e., its drag and the velocity distribution on its surface, the characteristics of its power-transmitting machinery, and the desired operating characteristics of the propulsor-vehicle combination. Assuming that these data are accurately known (although this is sometimes not the case) the designer must select the optimum form of propulsor based on the thrust, efficiency, and cavitation performance together with its weight, size, and unsteady-force-producing characteristics.

This selection can still involve a great deal of "art" based on the designer's experience. Several attempts (refs. 1, 2, 3, 4, and 5) have been made to correlate this information in a manner similar to that employed in the selection of classical pumping machinery (ref. 6). This correlation is done in terms of a power factor, B_p, or the related thrust specific speed, n_{sf}. While some experimental data have been correlated on this basis (refs. 3 and 5), considerably more are required to provide the designer with a complete spectrum of propulsor performance.

Determination of Propulsor Flow Field

On completion of the preliminary analysis of the propulsor performance, the designer has determined the type, size, and operating characteristics of the propulsor to be employed. It is then necessary, as in the design of any turbomachine, to mathematically represent the action of this propulsor and determine the flow field through the propulsor in the process of producing the desired propulsive force. In particular, this is necessary at the inlet and exit of the blades in order that their shapes can be determined.

Historically, marine propulsor designers have employed vortex methods to represent the action of the propulsor and thus to determine the flow field. These representations of the blade action are based on finite wing theories and have progressed from lifting line to lifting surface representations. An excellent review of vortex design methods as applied to open propeller design is presented in reference 7. As discussed in this reference, vortex methods and, in particular, lifting surface methods have been developed to give a very accurate representation of the action of subcavitating propellers within the limits of the assumptions employed. These assumptions are an inviscid flow, no curvature of the streamlines or existence of radial pressure gradients, and axisymmetric inflow. With these methods, the effect of radial and chordwise variations in loading, radial variation of inflow velocity, finite blade effects, and skew of the blade surface can be considered accurately.

While vortex representations have also been employed in the design of ducted propellers and pumpjets (ref. 8), these propulsors have also employed streamline curvature or through-flow analysis in their design (refs. 9, 10, 11, and 12). These latter methods allow for the inclusion of streamline curvature effects and, empirically, the effects of viscosity. The extension of present-day propeller design methods to include these effects may be possible by combining the vortex methods and those of reference 10 or 11. Since the methods for including streamline curvature are iterative in their solutions, the vortex theory can be used as an initial or starting solution. In addition to the effects of radial pressure gradients, the effects of viscosity and, in particular, wall boundary layers and secondary flows can be included (ref. 13).

Determination of Blade Shape

With the determination of the flow field at the inlet and exit to the rotating blades, the designer must determine the shape of the blades which will produce this flow field. This includes the determination of the camber, thickness, and pitch distribution. In addition to the desired propulsive action, the cavitation performance and required strength characteristics must be considered.

As in the design of any turbomachine, this step is conducted using two-dimensional data with appropriate corrections to include the effects of the three-dimensionality, viscosity, and finite-blade effects. The effects of viscosity obtained from experimental data are included as inviscid corrections in the lifting surface or through-flow analysis. Reference 14 presents a tabulation of these inviscid corrections derived from lifting surface theory for a NACA ($a=0.8$) mean camber line.

The use of an existing camber line and thickness distribution implies the specification of a particular chordwise pressure distribution. The design of a blade to minimize the occurrence of cavitation can be hindered by such an approach. Thus, the design of a blade shape to give a specific pressure is desirable and can be accomplished by the mean streamline method (ref. 6). This method is based on two-dimensional experimental data with the necessary corrections for three-dimensionality, viscosity, and thickness.

Cavitation in a marine propulsor is avoided by the selection of the proper chordwise and radial loading distribution. In addition, the designer must consider blade end effects which result in tip vortex or leakage cavitation (refs. 15, 16, and 17). A survey of the effects of cavitation in propulsors and pertinent design data is presented in reference 18.

Specification of the Blade for Manufacture

Once the designer has completed the determination of a propulsor configuration which will provide the desired propulsion action, the propulsor must be converted to actual hardware. While this does not appear to be a design step, it is important that the designer concern himself with the process if the final hardware is to perform satisfactorily. The manufacture of hardware can result in variations in blade shape and contour which result in major deviations from the design performance and greatly affect the cavitation performance of the propulsor (refs. 19 and 20).

To ensure that the hardware produced is a replica of what the designer has specified, computer graphic techniques (refs. 21 and 22) and numerical machining of master hardware are being used. In this way, the blade can be accurately represented to the manufacturer and a detailed interpretation of the design configuration for use in different manufacturing processes can be provided.

SOME PROBLEMS IN MARINE PROPULSOR DESIGN

The marine propulsor designer is faced with many problems requiring additional research. These include (1) minimization of unsteady forces, (2) the effects of viscosity in design, (3) the design of propulsors with cavitation, (4) the design of heavily loaded propellers, and (5) the prediction of off-design performance.

In the area of unsteady forces, considerable effort has been devoted to the prediction of the unsteady forces which exist on a given propulsor operated in a known time-varying environment (refs. 23 and 24). As in the design of axial flow compressors and liquid pumps, these predictions must be supplemented by methods which will allow the designer to choose that configuration of blade geometry which will minimize the generation of unsteady forces. Such data would be similar to those currently available for the selection of blade geometries to minimize the occurrence of cavitation.

Present-day methods of calculating the flow field through a propulsor must be extended to include heavily loaded propellers and the effects of streamline curvature and radial pressure gradients. Possibly, this could be done by employing a combination of the existing vortex lifting-surface methods and the streamline curvature of through-flow analysis used in axial-flow compressor design. The combination of these two methods will also allow viscous and secondary flow effects to be included. In addition, the area of the prediction of off-design performance must be considered.

The design of supercavitating propulsor blades (i.e., the design for the presence of cavitation) is far from being complete (ref. 25). At present, only one-dimensional and empirical methods of design are available. The methods for the design of supercavitating propellers are undergoing the same development as the subcavitating design methods experienced in the early 1950's. This development must be continued in light of high-speed vehicle development.

Current two-dimensional experimental data relating blade-section performance lags the design requirements of blade solidities, stagger angle, and chordwise loading. Therefore, additional data must be obtained. These should include higher solidities, higher blade stagger angles, the effects of turbulence, and changes in axial velocity through the blades.

SUMMARY

This review is very brief and certainly does not, by itself, present a complete description of marine propulsor design. It is hoped, however, that together with the included references and, in particular, those review papers indicated, it will provide an introduction to the area and, together with the other papers in this session, will serve as a basis for the discussion of marine propulsor design. (Refs. 26–33 are sources of information utilized in addition to those specifically referred to in the preceding text.)

REFERENCES

1. Wislicenus, G. F., *Pumping Machinery for Marine Propulsion.* ASME Symposium on Pumping Machinery for Marine Propulsion, May 1968.
2. Wislicenus, G. F., Hydrodynamic and Propulsion of Submerged Bodies. *J. Am. Rocket Soc.*, Vol. 30, No. 12, December 1960, pp. 1140–1148.
3. Van Manen, J. D., The Choice of the Propeller. *Marine Technology,* Vol. 3, No. 2, April 1966.
4. Van Manen, J. D., and M. W. C. Oosterveld, *Analysis of Ducted-Propeller Design.* SNAME, Presented at Annual Meeting, November 1966.
5. Oosterveld, M. W. C., *Model Tests With Decelerating Nozzles.* ASME Symposium on Pumping Machinery for Marine Propulsion, May 1968.
6. Wislicenus, G. F., *Fluid Dynamics of Turbomachinery,* Vols. I and II. Dover Publications, 1965.
7. Cox, G. G., State-of-the-Art for Subcavitating Propeller Design Methods. *International Touring Tank Committee Report, Appendix II,* September 1969.
8. Morgan, W. B., and E. B. Caster, *Comparison of Theory and Experiment on Ducted Propellers.* Seventh ONR Symposium on Naval Hydrodynamics (Rome), 1968.
9. Henderson, R. E., J. F. McMahon, and G. F. Wislicenus, A Method to Design Pumpjets. *Underwater Missile Propulsion,* Compass Publications, 1967.
10. Smith, L. H., S. C. Traugott, and G. F. Wislicenus, A Practical Solution of a Three-Dimensional Flow Problem of Axial-Flow Turbomachinery. *Trans. ASME,* Vol. 75, No. 5, 1953.
11. Treaster, A. L., *Computerized Application of the Streamline Curvature Method to the Indirect, Axisymmetric Turbomachine Problem.* Ordnance Research Lab Technical Memorandum 514.2491–16, October 31, 1969.
12. Bruce, E. P., W. S. Gearhart, J. R. Ross, and A. L. Treaster, *The Design of Pumpjets for Hydrodynamic Propulsion.* Turbomachinery Symposium, Penn State U., 1970.
13. Marsh, H., *The Through-Flow Analysis of Axial Flow Compressor.* Cambridge U., Eng. Dept. Report CUED/A/–Turbo/TR11, January 1970.
14. Morgan, W. B., G. Silovie, and S. B. Denny, Propeller Lifting Surface Correction. *SNAME,* Vol. 76, 1968.
15. Gearhart, W. S., Tip Clearance Cavitation in Shrouded Underwater Propulsors. *AIAA J. Aircraft,* Vol. 3, No. 2, 1966.
16. English, J. W., *One-Dimensional Ducted Propeller Theory—Influence of Tip Clearance on Performance.* National Physical Laboratory, Ship Division Report 94, May 1967.

17. McCormick, B. W., J. J. Eisenhuth, and J. Lynn, *A Study of Torpedo Propellers, Parts I and II.* ORL UNCL External Reports Nos. 16597–5 and 13, 1956.

18. Morgan, W. B., and J. Z. Lichtman, *Cavitation Effects on Marine Devices.* ASME Symposium on Cavitation State of Knowledge, 1969.

19. Moechel, G. P., *The Effect of Distortion of Subcavitation Foil Contours on Cavitation-Inception Velocity. J. Ship Res.*, December 1966.

20. Holl, J. W., and G. F. Wislicenus, Scale Effects on Cavitation. *Trans. ASME*, Series D, Vol. 83, 1961.

21. Davis, R. F., *Marine Propeller Blade Section Definition.* ORL UNCL TM 512.3531-04, February 14, 1969.

22. Davis, R. F., *Marine Propulsor Blade Lofting.* ORL UNCL TM 512–03, Aug. 3, 1970.

23. Tsakonas, S., W. R. Jacobs, and P. H. Rank, Jr., Unsteady Propeller Lifting-Surface Theory with Finite Number of Chordwise Modes. *J. Ship Res.* Vol. 12, No. 1, 1968.

24. Jacobs, W. R., and S. Tsakonas, A New Procedure for the Solution of Lifting-Surface Problems. *AIAA J. Hydronautics*, Vol. 3, No. 1, 1969.

25. Cox, G. G., State-of-the-Art for Supercavitating Propeller Design Methods. *International Towing Tank Committee Report, Appendix IV*, September 1969.

26. Brandau, J. H., *Aspects of Performance Evaluation of Waterjet Propulsion Systems and a Critical Review of the State-of-the-Art.* Paper No. 67–360, AIAA/SNAME Advance Marine Vehicles Meeting, May 1967.

27. Gearhart, W. S., and R. E. Henderson, Selection of a Propulsor for Submersible System. *AIAA J. Aircraft*, Vol. 3, No. 1, 1966.

28. Thurston, S., and R. C. Amsler, *A Review of Marine Propulsor Devices.* Paper No. 65-482, AIAA 2nd Annual Meeting, July 1965.

29. Weissinger, J., and L. Maass, *Theory of the Ducted Propeller: A Review.* Seventh ONR Symposium on Naval Hydrodynamics (Rome), 1968.

30. Lerbs, H. W., Moderately Loaded Propellers With Finite Number of Blades and an Arbitrary Distribution of Circulation. *SNAME*, Vol. 60, 1952.

31. Pien, P. C., Calculation of Marine Propellers Based on Lifting Surface Theory. *J. Ship Res.*, Vol. 5, No. 2, 1961.

32. Kerwin, J. E., *The Solution of Propeller Lifting Surface Problems by Vortex Lattice Methods.* MIT Naval Architecture Dept. Report, 1961.

33. Nelson, D. M., *A Lifting Surface Propeller Design Method for High Speed Computers.* NAVWEPS Repoht 8442 NOTS, 1964.

Application of Theory to Propeller Design[1]

G. G. Cox and William B. Morgan

Naval Ship Research and Development Center

Subcavitating propeller design theory has been developed to the extent that theoretically designed propellers perform as predicted. Such design procedures depend heavily on the availability of high-speed digital computers for making lifting-line and lifting-surface calculations. In spite of these developments, many aspects of propellers remain an art.

Supercavitating propeller design theory has also been developed, but the computer programs necessary for application are still under development. Of necessity, the design of these propellers follows semiempirical procedures.

The various theories available to the designer are reviewed. Emphasis is given to the key design decisions which face the designer.

INTRODUCTION

Purpose of the Paper

During recent years, the availability of high-speed digital computers has provided the stimulus for the formulation of improved propeller design procedures. Much more adequate mathematical models can be used to represent the hydrodynamic action of a marine propeller than was hitherto possible. A further outcome of using a computer is that the designer, released from the drudgery of performing laborious computations, is better able to exercise critical design judgments and to practice his "art." The major purpose of this paper is to emphasize the art of contemporary propeller design, as seen by the authors, and to discuss propeller theory and computational procedures mainly from the viewpoint of available techniques.

---

[1] The authors are indebted to Mr. Robert J. Boswell for review and to Mrs. Shirley Childers for preparation of the manuscript.

Development of Subcavitating Design Procedures

For many years, the design of subcavitating propellers depended to a large extent on experimental series data and a number of extensive series have been developed (e.g., Taylor, Troost, and Gawn, refs. 1, 2, 3, and 4). These series are still very helpful for preliminary design studies, but they are seldom applied to a specific propeller design today, since the propeller must be constrained to a specific geometry. This geometry may be unsatisfactory for reasons of cavitation and/or vibration, particularly for propellers which operate in a wake.

More recently, most design methods depended on lifting-line theory of one form or another with finite-width effects being considered in an empirical, semiempirical, or approximate manner (e.g., Schoenherr, ref. 5; Lerbs, ref. 6; Hill, ref. 7; Van Manen, ref. 8; McCormick, ref. 9; and Eckhardt and Morgan, ref. 10). Two common "approximations" were use of Goldstein factors and camber correction factors, to allow for effects of blade number and aspect ratio, which were not strictly applicable to the propeller being designed. These approximations were necessary before the advent of high-speed digital computers, due to the computational effort required by the more rigorous solutions. Today, with computers, both lifting-line and lifting-surface calculations can be performed in sufficient detail to make rigorous theoretical design calculations feasible and desirable.

Development of Supercavitating Propeller Design Procedures

Initial attempts at the David Taylor Model Basin (DTMB) to formulate a design method were made by Tachmindji and Morgan (ref. 11). This method essentially grafted two-dimensional supercavitating design theory data onto a subcavitating design method (ref. 10) then in current use at DTMB. This method used conventional subcavitating lifting-line theory (i.e., Goldstein factors) and involved the use of lifting-surface corrections which did not account for cavity interaction effects. Test results for models designed by this method are described by Hecker, Peck, and McDonald (ref. 12) who showed that these model propellers did not generally perform as predicted.

Posdunine (see reference 13 for a list of this Russian author's references) pointed out that the blade cavities affect propeller performance in ways other than that due to two-dimensional supercavitating hydrofoil characteristics. Cavity-blade interference and cavity thickness effects can lead to major differences between noncavitating and supercavitating propeller performance. Currently used design methods include approximate recognition of these effects. The Naval Ship Research and Development Center (NSRDC, formerly DTMB) makes use of current subcavitating lifting-line and lifting-surface methods, with cavity-blade interference effects accounted for by superimposing an estimated cavity thickness onto the lifting-surface calculations. Hydronautics (ref. 13) also makes use of subcavitating propeller lifting-line theory and corrects for lifting-surface effects by use of camber correction factors (ref. 14). In addition, cavity-blade interference effects are approximated by use of data derived from a study of a two-dimensional supercavitating hydrofoil in proximity to a free surface. More recently, Titoff, Russetsky, and Georgiyevskaya (ref. 15) and Davis and English (ref. 16) described the problems associated with actual applications of their design methods. In this respect, a very detailed description of a supercavitating propeller strength investigation is given in reference 16.

Attempts are continuing to develop more adequate supercavitating propeller design methods based on a correct recognition of the effects of the blade cavities. English (ref. 17) has formulated a lifting-line supercavitating propeller theory, based on an extension of Goldstein's work for a subcavitating finite-bladed propeller (ref. 18), with modified boundary conditions to allow for the effect of the cavities. Cox (ref. 19) has devised lifting-line and lifting-surface theory for the determination of induced velocities (the central problem of theoretical design). The effect of the blade cavities is accounted for by use of pressure source singularities. Laurentiev (refs. 15 and 20) has also formulated a propeller lifting-surface solution based on a similar model. No numerical results or design calculations and model test results are available for these new theories.

Only limited experimental series data are available for supercavitating propellers (e.g., Newton and Rader, ref. 21, and Georgiyevskaya, ref. 22). One reason that more series data are not available is that a supercavitating propeller operates efficiently over only a small range of advance coefficient. At advance coefficients much higher than design, pressure-side cavitation occurs and the performance falls off and at advance coefficients much lower than design, the suction-side cavity becomes very large since the section is operating at a relatively high angle of attack and the performance also falls off. Thus, for a good performing supercavitating propeller series, it is not sufficient to have a simple variation of pitch but it is necessary to vary the blade-section shape for different advance coefficient ranges. This necessity makes obtaining data for a series of good performing supercavitating propellers very expensive. To furnish data for use in design, Caster (ref. 23) developed a theoretical "design-point" series for supercavitating propellers based on the method of Tachmindji and Morgan (ref. 11). The experimental series work of Newton and Rader (ref. 21) furnishes limited data but has its main application for a speed range where the cavitation may not be fully developed; i.e., 50 knots or less.

The Advantages and Disadvantages of Theoretical Design

The use of a design method based on a rational theory permits the designer a free choice with respect to the following features: (1) number of blades, (2) hub size, (3) radial blade loading, (4) chordwise blade loading, (5) blade shape and size, (6) blade skew, and (7) wake adaption. All of these features, with the possible exception of hub size, can play a major role in minimizing ship vibration and/or cavitation problems. The proper recognition of propeller blade strength requirements can only be *conveniently* satisfied within the framework of a theoretical design method, and the strong interdependency between efficiency and strength for a supercavitating design makes the use of a theoretical design method mandatory for most applications.

With the possible exception of the so-called optimum subcavitating propeller in uniform inflow, a high-speed digital computer is essential to perform the very laborious and complex computations associated with present-day lifting-line and lifting-surface theories for marine propellers. This is an obvious disadvantage since the programs and computing facilities may not be readily available. Also, even the most keen proponent of computerized lifting-line and lifting-surface computations has to be aware of a very serious drawback of this approach. Such design calculations are very prone to undetected numerical mistakes, and the detection and elimination of these mistakes requires great care in use and understanding of the computer programs.

For the case of subcavitating propeller design, the theoretical design procedures are generally quite adequate. However, in the case of supercavitating propeller design, the theoretical design procedures, mainly due to lack of computer programs, have not been adequately developed. At the same time, the more approximate approaches are not satisfactory even for power performance, whereas for the subcavitating propeller, these approximate approaches are often adequate for this purpose.

DESIGN CONSIDERATIONS

Phases of Design

Basically, there are five separate phases in the design of a propeller; namely

(1) Preliminary design analysis to determine the design parameters for which the propeller is to be designed in order that the propeller be compatible with the ship, installed propulsion machinery, and transmission from the standpoint of efficiency and vibration. In addition, for supercavitating operation, it is necessary to ensure that the design

parameters are chosen to permit the blades to operate in a supercavitating regime.

(2) Determination of the desired radial load distribution, together with the radial hydrodynamic pitch angle; i.e., lifting-line calculations. The theory is for inviscid flow but the viscous drag can be taken into account suitably by a strip theory analysis. For the sake of convenience for supercavitating operation, blade cavity pressure drag is considered in association with blade viscous drag.

(3) Determination of the blade shape, area, and thickness distribution from the standpoint of cavitation and strength. For subcavitating propellers, cavitation erosion and thrust breakdown should not occur at the design conditions. For supercavitating propellers, blade pressure-side cavitation should not occur and the suction-side cavity should completely enclose the suction side of the blade at the design conditions.

(4) Determination of the final camber and pitch distributions from lifting-surface calculations.

(5) A strength check for the final configuration.

Methodical series data can play a useful role during preliminary design analysis; i.e., phase (1). The main emphasis of theoretical propeller design calculations is concerned with lifting-line and lifting-surface calculations; i.e., phases (2) and (4), respectively. Phase (3) is concerned with design of the propeller from the standpoint of both cavitation and strength for subcavitating propellers and both strength and efficiency for supercavitating propellers. Phase (5) makes use of detailed intermediate results determined during the design procedure.

Ship Propulsive Performance and Basic Propeller Design Considerations

As already mentioned, the propeller designer attempts to select design parameters to achieve effective ship propulsion characteristics; i.e., minimize delivered power P_D to the propellers for a given ship operating speed V or maximize ship operating speed for a given delivered power. These simple objectives often have to be compromised to some degree in order to meet constraints imposed by ship and appendage geometry, machinery and gearing, minimization of vibration and cavitation erosion, and, last but not least, ship construction costs. The propeller designer cannot usually exercise a choice regarding number of propellers, shaft inclination, maximum diameter, and shaft and hub size. He will nearly always have to meet the required propulsion characteristics within a narrow range of rpm.

The design conditions are characterized by the thrust loading coefficient C_{T_h} (or power coefficient C_P), and advance ratio λ. For the selected ship speed, their specification involves the thrust T the propeller has to deliver (or power P to be absorbed), diameter D, propeller revolutions n, and speed of advance V_A. The determination of these parameters usually involves model basin tests of the appended hull,

$$C_{T_h}=\frac{T}{(\rho/2)\pi R^2 V_A{}^2} \qquad C_{T_h}=\frac{T}{(\rho/2)\pi R^2 V^2} \quad \text{(wake adapted)}$$

$$C_P=\frac{P}{(\rho/2)\pi R^2 V_A{}^3} \qquad C_P=\frac{P}{(\rho/2)\pi R^2 V^3} \quad \text{(wake adapted)}$$

$$\lambda=\frac{V_A}{\pi n D} \qquad \lambda=\frac{V}{\pi n D} \quad \text{(wake adapted)}$$

both with and without "stock" propellers to measure the resistance, thrust, torque, and rpm. From these measurements the effective horsepower P_E, delivered horsepower P_D, thrust deduction t, and effective wake w (derived from propeller open-water curves) and, hence, propulsive efficiency are determined approximately:

$$\eta_D=\frac{P_E}{P_D}=\eta_B\eta_H=\eta_B\,\frac{(1-t)}{(1-w)}$$

where η_H is hull efficiency and η_B is propeller behind efficiency.

Every towing tank has its own approach for correcting the various elements of the propulsive efficiency to allow for model/ship correlation. The important thing to note is that the thrust deduction factor and the wake fraction are dependent on the choice of the stock propeller, which is chosen to approximate the final propeller design with regard to diameter, pitch-to-diameter ratio P/D, blade area, and number of blades Z, diameter being the most important parameter. A different final choice for diameter, especially when the propeller operates substantially in a wake, requires a new estimate for the affected components.

In some cases, where self-propulsion tests are not available, it may be necessary to estimate the thrust deduction and effective wake. The work of Harvald (ref. 24) and Todd (ref. 2), and the work on the Series 60 (refs. 25 and 26) can be used for making this estimate. Also, Beveridge (ref. 27) has shown that it may be possible to calculate the thrust deduction from theoretical considerations.

During this stage of design, the velocity field in the plane of the propeller is determined by making wake measurements on the model to determine the inflow velocities to the propeller. If wake measurements are not made, an estimate of these wake velocities must be made. The work of Hadler and Cheng (ref. 28) can be used for estimation purposes. From these measurements, not only is the spatial flow pattern obtained, but also the circumferential average of the inflow velocities. The circumferential averaged velocities are a necessary input to the propeller design so that the propeller can be designed for the desired radial load distribution. The so-called "optimum" load distribution (Troost, ref. 29, and Morgan and Wrench, ref. 30) can usually be specified unless other considerations such as cavitation and vibration are important. Many propellers have been designed for load distributions radically different from "optimum" without a significant loss in propeller efficiency. This is due to the fact that the optimum load distribution is usually only concerned with minimum induced drag. If a load distribution is specified, it should ensure that maximum blade load is carried in the vicinity of midblade. Placing maximum load toward the extreme blade root or tip can result in an appreciable loss of efficiency.

Subcavitating propeller efficiency is not strongly dependent on blade number, provided that flow choking does not occur near the hub. If it is necessary to consider a large number of blades, then the hub-to-propeller diameter ratio must be increased. Experience has shown that it is quite safe to consider five blades with a hub-to-propeller diameter ratio of 0.2, except for very low pitch ratios. Supercavitating propeller efficiency is strongly dependent on the number of blades. Off-design efficiency of these propellers can deteriorate due to the proximity of a blade cavity to the pressure side of a neighboring blade. The greater the blade number, the greater is this effect.

It is at this stage that the decision is made whether the design should be for a subcavitating or a supercavitating propeller. The decision is based on the local cavitation number of the blade sections. Criteria (ref. 11) indicate that the design should be a supercavitating one if the local cavitation number at 0.7 radius, $\sigma_{0.7}$, is less than 0.05, and a subcavitating one if $\sigma_{0.7}$ is greater than 0.1. Figure 1 presents the desired operating regions for subcavitating and supercavitating propellers in terms of cavitation number σ and advance coefficient J. Lines 1 and 2 indicate $\sigma_{0.7}$ values of 0.1 and 0.05, respectively. If the operating region falls between Lines 1 and 2, the decision concerning type of design will depend on the application. It should be pointed out the use of cavity "ventilation" can effectively reduce the local cavitation number of the blade sections, which can mean that an operating condition originally between Lines 1 and 2 can be moved below Line 2.

Vibration

Propeller-associated vibration comes from two sources: (1) the unsteady bearing forces which are associated with the propeller blades operating in a spatially varying wake field and unsteady forces being introduced through the shaft and (2) the pressure forces which are associated with the rotation of the propeller past the hull. Both can be controlled to some extent by the propeller design. To minimize unsteady

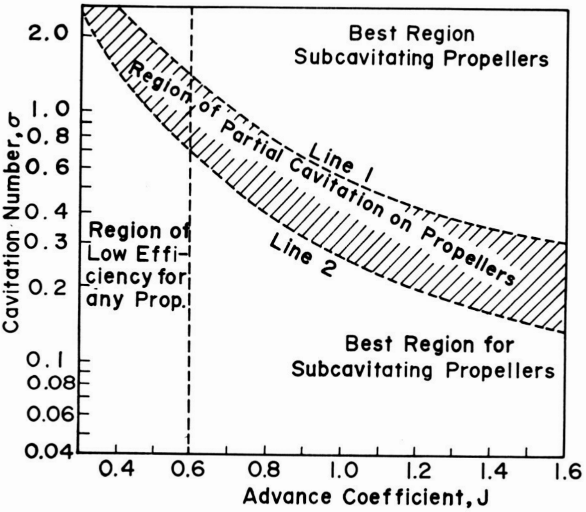

FIGURE 1.—*Propeller design ranges from considerations of cavitation.*

bearing forces, it is necessary to avoid coincidence of blade number, or blade number ±1, with strong wake harmonics (ref. 28). A Fourier series analysis of the spatially varying flow into the propeller will provide excellent guidance in the selection of the number of blades. Also, in the selection of number of blades, it is essential to avoid exciting a main hull resonance at normal operating speeds. By changing the blade number, it is often possible to alter the blade-rate excitation of hull resonance to an unimportant speed.

The propeller pressure forces are dependent on the clearances between the ship and the propeller, the blade thickness, and the blade loading. The clearances should be selected with care. If the clearances are too small, vibration will be a problem, and if too large, arrangement problems may arise. A number of criteria have been developed to help select the

TABLE I.—*Effect of Thickness Distribution on Section Modulus for Typical Airfoil Sections*

Section	C_s
NACA 16 series	0.0890
NACA 65–A series	0.0775
NACA 66 series	0.0848
TMB–EPH section	0.0899

clearance (refs. 31, 32, 33, and 34). The proper clearance will usually be the factor which controls the propeller diameter.

Blade rake and skew may be used to help minimize vibration. Blade rake (i.e., angular displacement of the blade centerline in the propeller axis plane) is often used for propellers which work in an aperture to increase the distance between the blades and the hull and appendages forward of the propeller. Blade skew (i.e., differential displacement of chords along helical reference lines) permits a more gradual entry of the blade into a high wake region. Skew also increases clearance between the blades and the hull and appendages forward of the propeller.

Strength

A propeller blade must contain enough material to keep the stresses within the blade below a certain predetermined level. This level depends on the material properties with regard to both steady-state and fatigue strength and both mean and unsteady blade loading. The material selection controls the allowable stress level and the blade chord and thickness are the main parameters which control this stress level. The maximum stress for subcavitating propellers normally occurs at the point of maximum blade thickness unless the blade is unusually distorted. Without consideration of the centrifugal forces and blade rake and skew, the required maximum blade thickness-chord ratio, t/c, for subcavitating propellers, can be approximated by the following equation:

$$\frac{t}{c}=\left(\frac{M_{x_o}}{C_s C_c c^3 \sigma_a}\right)^{1/2}$$

where M_{x_o} is the bending moment about the blade chord (obtained from lifting-line calculations), σ_a is the allowable blade stress, C_s is a coefficient dependent on the chordwise thickness distribution (given in table I), C_c is a coefficient dependent on the chordwise camber distribution, and c is the section chord. The coefficients C_s and C_c were derived from Milam and Morgan (ref. 35) by Barr (ref. 36). McCarthy and Brock (ref. 37) in their measurements of propeller stress indicate that the principal axes follow almost along the section meanline. This means that for subcavitating propellers C_c should be assumed equal to 1.

The maximum thickness for supercavitating propellers cannot be derived on such a simple basis (refs. 37 and 38). In fact, the design of these propellers from the standpoint of stress is unsatisfactory.

All propellers should be designed considering both mean and unsteady loads acting on the blade. These must be considered together since the allowable unsteady stress decreases as mean stress increases. A simple equation for the allowable stress level can be derived from the Goodman diagram (ref. 39) for both the mean and unsteady load. This equation is known as the equation for the Goodman safe region

$$\sigma_f = \frac{\sigma_{\max}(2-R_s)}{3}$$

where

R_s	ratio of minimum stress to maximum stress during a cycle
σ_f	fatigue stress for a given number of cycles, single amplitude (table II)
$\sigma_{\max}$	maximum stress for a given number of cycles.

In principle, the unsteady forces on a blade can be calculated theoretically (Tsakonas, Breslin, and Miller, ref. 40). The available theoretical procedures are not yet in a form which can be used easily; as an approximation, the method of McCarthy (ref. 41) can be used for unsteady loading at the blade root.

The calculation for t/c is made at each radius to obtain the blade thickness distribution. For practical application, certain limitations are usually applied for minimum thickness and judicious fairing is used. For instance, the thickness at the tip, for fairing purposes, is often assumed to be 0.003 times the propeller diameter. From the standpoint of stress, it is always better to have the blade slightly too thick than too thin.

The simple formulation presented is for the initial check on stress. Once the design is completed and the geometry of the propeller is known, a strength check which includes the effect of centrifugal force and blade rake and skew must be made. Unfortunately, the theory is not adequately developed to make what would be considered to be a satisfactory calculation. McCarthy and Brock (ref. 37) have shown that simple beam theory gives a good approximation to the maximum stress for a wide-bladed, unskewed, subcavitating propeller, but Boswell (ref. 42) has

TABLE II.—*Fatigue Strengths (psi) in Seawater, 10^8 Cycles*

Material	σ_a
Manganese bronze	6 000
Nickel-manganese bronze	6 000
Nickel-aluminum bronze (Ni–Bral)	12 500
Manganese-nickel-aluminum bronze (Superston 40—Grade 5)	9 000
CF–4 stainless steel	6 500 (20 000 with cathodic protection)

shown that it is not adequate for blades with large amounts of skew. McCarthy and Brock also conclude that present procedures are not adequate for determining the stress in a supercavitating propeller. Similar results have also been shown by Davis and English (ref. 16).

Cavitation

The designer must try to ensure that a propeller designed for subcavitating operation does not suffer from thrust breakdown and is not prone to erosion due to cavitation (Morgan and Lichtman, ref. 43, and Newton, ref. 44). Initially, during the preliminary design stages, the minimum expanded area ratio (EAR) should be determined to ensure freedom from thrust breakdown for the maximum power condition. The Burrill chart (ref. 45), or equivalent (ref. 46), is probably sufficient for this purpose.

The detailed procedure for performing a check to ensure freedom from blade cavitation is carried out after the lifting-line calculations. This check relies on the results of experimentally observed cavitation inception data (ref. 47), or theoretically predicted data (refs. 48, 49, and 50) for sections of prescribed thickness to chord ratio t/c, and meanline cambered for a design lift coefficient C_{L_i}. Figure 2 shows an example of such data for a range of angles of attack against local cavitation number σ_r with t/c as a parameter. The insides of the "buckets" are cavitation-free regions with the top and bottom of the buckets indicating leading-edge suction-side (back) and pressure-side (face) cavitation, respectively. A study of these curves will immediately reveal a tradeoff choice; namely, that by selection of t/c it is often possible to achieve increased latitude against leading-edge

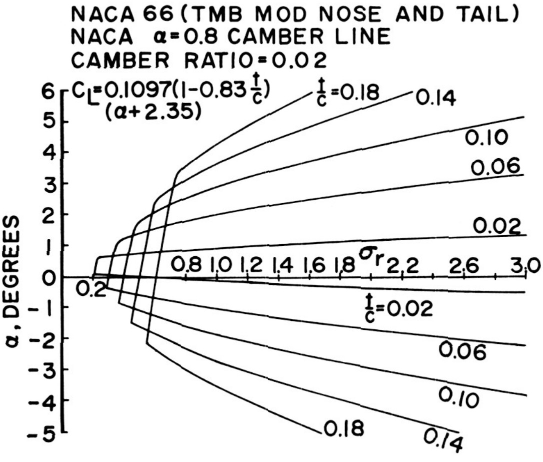

FIGURE 2.—*Typical cavitation inception diagram for a two-dimensional section.*

cavitation due to fluctuating angle of attack at the price of earlier onset of back bubble cavitation at shock-free entry. The type of information shown in figure 2 can easily be derived for any desired meanline and basic thickness form by the method of linear superposition (ref. 51). Such data can easily be condensed into a more convenient form for design use (refs. 49 and 50).

Figure 3 shows the wake for one radius value at the propeller position for a typical single-screw merchant ship. At 0.8 radius, the flow angle varies about the mean from -8 degrees to $+2$ degrees during each revolution. Hence, for a propeller which has to operate in a wake, it is necessary to obtain measurements or a good estimation of the inflow into the propeller. Both circumferentially averaged flow angles $\beta(r)$ and maximum positive and negative variations in flow angle about the mean are required for the operating condition under investigation. In order to obtain an engineering estimate for the effective variations in flow angle, an adaptation of the method described by Lerbs and Rader (ref. 52) can be used. This makes use of the concept of "effective aspect ratio" for each section of a propeller blade. The wake shown in figure 3 would result in an effective angle of attack variation of somewhat less than $+8$ degrees to -2 degrees.

If, in the use of the cavitation diagrams, the thickness ratio is smaller than required for stress and the cavitation diagrams indicate that thicker

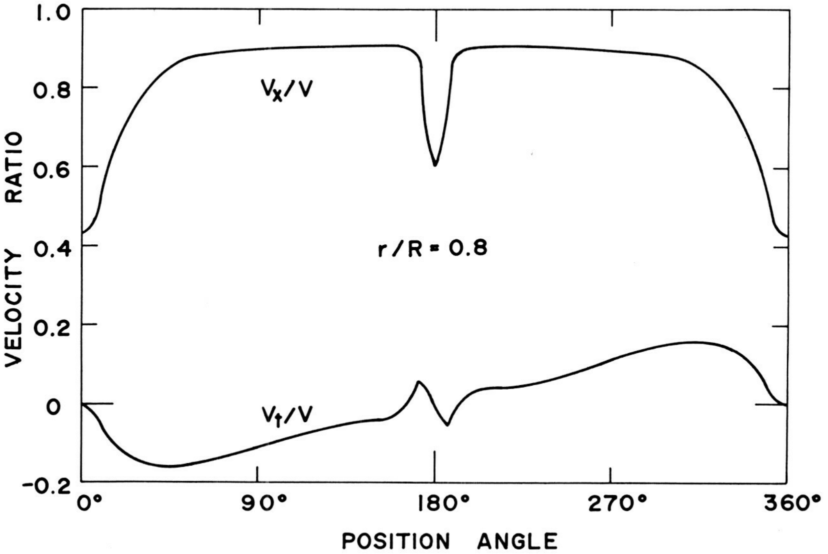

FIGURE 3.—*Representative velocity distribution in plane of propeller for single-screw ship.*

sections will cavitate, the section chords should be increased and the calculations repeated until a balance is achieved between cavitation and strength criteria.

For the uncommon situation where cavitation is absolutely no problem, the section chord and thickness are chosen for minimum drag and to meet the strength criteria. For frictional drag, the chord should be as short as possible, but if the thickness-chord ratio is too large, separation will occur on the foil and the form drag will increase. Although a precise maximum value of the thickness-chord ratio cannot be given, it is probably best to limit the maximum value to 0.18 to 0.22. This value may also depend on the lift of the foil.

A common situation is one in which the angle of attack variation is so great and/or the cavitation number is so low that it is impossible to pick a section shape which will not cavitate. If the cavitation number is sufficiently low, then a fully cavitating propeller should be designed. In those instances where this is not possible, and where cavitation arises mainly from an angle of attack variation, it is desirable to use the cavitation diagrams to minimize the occurrence of cavitation. How a particular subcavitating propeller which falls into this category is designed depends on the particular ship's operating characteristics. The cavitation and strength calculations are usually carried out at the maximum power condition. If cavitation is unavoidable at this condition and the ship operates generally at some lower speed, say a cruise speed, then the selection of blade chord should be based on the cruise condition or some higher speed if possible. The strength is always based on the maximum power condition. For most ships, there is little change in the thrust and power coefficient between cruise and maximum speed; therefore, this speed change can be accounted for by multiplying the cruise cavitation number by the ratio of the two speeds squared (for the lower speed the cavitation number will be higher). Thus, in essence, the blade thickness-chord ratio is selected to give the maximum cavitation-free speed. Care must be exercised that sufficient blade area is provided to prevent thrust breakdown at the maximum speed. Model tests, of course, should be conducted to help ensure that cavitation erosion will not occur. In this regard, any bubble cavitation on the blade should be avoided.

In general, the approach outlined when the propeller is operating in a wake field will result in sections with higher thickness-chord ratios than if the propeller is designed as if it were operating in a steady flow. The thicker sections are less susceptible to cavitation caused by angle of attack variations but are more susceptible to cavitation if no angle of attack variation occurs.

It will not be necessary to repeat the lifting-line calculations after the thickness and cavitation calculations are made unless large changes are made in the chord ratio. This will influence the section viscous drag and the importance of this drag is dependent on the lift coefficient and the propeller hydrodynamic pitch.

In addition to blade area and thickness, the designer possesses considerable freedom of choice in number of blades, blade shape, and radial and chordwise load distribution to minimize the occurrence of cavitation. None of these parameters, within reasonable limits, has a strong effect on propeller efficiency for a subcavitating propeller, and a considerable choice is offered to delay cavitation.

If it is considered necessary to avoid the impingement of tip and hub vortex cavitation on rudders, it is possible to delay this type of cavitation by unloading the blade tip and root. As already pointed out, nonoptimum radial load distributions have very little effect on efficiency.

Any selected blade outline should have a shape without kinks or points of inflection such that its rate of change with respect to radial position is smooth and moderate. Experience has indicated that a kink in the leading-edge outline is often the origin of cavitation. It is good design practice for a subcavitating propeller to have the maximum chord position in the vicinity of maximum blade loading. Root chord should be selected on the basis of number of blades and amount of flow inclination due to the stern shape and shaft angle, bearing in mind the danger of root cavitation. For a supercavitating propeller blade, it is usual to select a blade shape which has maximum chord near the root in an attempt to maintain effective blade strength. A comprehensive family of blade shapes is given by Cox (ref. 14) who defines formulae for blade size and shape in terms of number of blades, expanded area ratio, position of maximum chord and ratio of root chord to maximum chord.

The choice of chordwise load distribution should be based on avoidance of cavitation in the case of a subcavitating design and minimizing induced cavity drag in the case of a supercavitating design. In the past, designers often favored constant chordwise loading, which corresponds to the NACA$(a=1.0)$ two-dimensional meanline loading. Due to viscous effects, such loading cannot be sustained toward the trailing edge. This has been demonstrated by two-dimensional foil tests which indicated that the NACA$(a=1.0)$ meanline realized only 74 percent of its theoretical lift (ref. 51). Since theoretical propeller design methods can only account for viscous effects by use of simple strip-theory methods, the use of a theoretical design procedure with some form of semiempirical corrections is necessary when a constant load meanline is used. If one wishes to design a propeller by a completely theoretical procedure, it is necessary to use a chordwise load distribution for which there is good agreement between potential flow and experimental lift, at least in two dimensions. An excellent choice, backed by experimental two-dimensional and propeller model tests, is that equivalent to a NACA$(a=0.8)$ meanline loading; i.e., constant load from the leading edge to 80-percent chord, followed by a linear decrease to zero at the trailing edge. Such type of loading, of course, involves an ideal angle of attack.

Another type of chordwise loading which may offer considerable advantages in the case of avoidance of leading-edge cavitation due to fluctuations in flow angle from operating in a wake is a "roof-top" type loading; i.e., symmetrical about midchord and increasing linearly from zero at the leading edge to a certain percent of chord, and thence constant to some other percent of chord, followed by a linear decrease to zero at the trailing edge (refs. 49, 53, and 54). Such a loading has not been investigated experimentally.

Interaction Between Strength and Performance in a Supercavitating Propeller

The difficulty in the design of supercavitating propellers, besides cavity interference, is the interaction which occurs between performance and strength. For the subcavitating propeller, there is essentially no such interaction, as the section drag coefficient is independent of the blade thickness for the sections usually used in marine propellers. For supercavitating propellers, there is an inverse relationship between efficiency and strength. The blade material is placed between the camberline and the cavity on the suction side. For low cavity drag, the blade section should be highly cambered and have a thin cavity which means a thin, highly stressed blade. To decrease the blade stress, the blade must be thicker, especially at the leading edge. To accommodate this increased thickness the cavity is made thicker by decreasing the camber and increasing the angle of attack. A considerable increase in the section drag will result and the propeller will be less efficient.

The design calculations not only involve the approximation of the induced velocities due to both loading and thickness, but an iteration must be carried out to obtain the maximum efficiency at the safe stress level in the blade. Coefficients for the section modulus have been derived for a number of sections (Morgan, ref. 38), and the change in cavity drag can be approximated theoretically (ref. 13). How the cavity drag is affected by the three-dimensionality of the flow is not known.

During the design of the supercavitating propeller, not only are the camber and angle of attack varied but also the section chord. This will have an effect on both the drag and the strength. Because of the sharp leading edge generally necessary for low-drag supercavitating sections, the sections cannot take a negative angle of attack during a revolution of the blade without severe pressure-side cavitation occurring at the leading edge. To offset this cavitation problem, it is often necessary to design the section for a higher angle of attack than for minimum drag or strength. Thus, the requirement of operating in a wake field will often have an adverse effect on the performance. During the design of supercavitating propellers, it is necessary to examine closely the wake field in which the propeller must operate and ensure, if necessary by redesign of the hull or appendage system in front of the propeller, that the propeller sections do not operate at negative angles of attack.

Another way the stress of fully-cavitating propellers has been decreased is by adding a thickness distribution to the section, usually parabolic (ref. 55). This can give a lower stress level with less drag penalty than using angle of attack. However, it does not improve the section performance when there is a varying angle of attack.

THE FOUNDATIONS OF THEORETICAL PROPELLER DESIGN

The distinct and important roles played by lifting-line and lifting-surface theory have already been pointed out. Satisfactory numerical procedures now exist for inclusion in subcavitating propeller design methods. Unfortunately, this is not yet the case for supercavitating propeller design methods. The historical development of these theories and identification of the significant contributions in this field was reported during 1969 by Cox (ref. 56).

Propeller Lifting-Line Theory

Propeller lifting-line theory follows from Prandtl's mathematical treatment of the lifting-line theory as applied to wings of finite length. This model cannot account for chordwise effects but can recognize spanwise (radial) effects. Thus, now that it has been extensively developed for moderately loaded propellers, it provides a very satisfactory and powerful tool.

The lifting-line theory of propellers is described as follows. It is assumed that each propeller blade can be replaced by a lifting line and that the circulation varies along the propeller radius. From vortex theory, it follows that free vortices are shed from the lifting line and, in a coordinate system which rotates with the propeller, these free vortices form a general helical surface behind the propeller. Since the free vortices follow streamlines in the rotating coordinate system, the pitch of the helical vortex sheet is taken to be dependent on the free-stream velocity, the speed of rotation of the propeller, and the velocities induced by the vortex system. For the supercavitating propeller, the pitch of the helical vortex sheet should also probably depend on the velocities induced by the blade and cavity thickness. In principle, the effect of thickness could be included in the lifting-line theory of subcavitating propellers, but the magnitude of these induced velocities from thickness can generally be ignored in this phase of the calculation, although thickness effects must be included in making lifting-surface corrections. For propellers with large numbers of blades and low blade pitches, the induced velocities from the blade thickness should be included in the lifting-line calculations.

Although the lifting-line is a very simple representation of a propeller blade, the theory has proven very useful for the design of propellers. From a combination of lifting-line theory, the Kutta-Joukowski law, and strip theory, it is possible to determine the radial distribution of hydrodynamic pitch and load which will produce the required propeller thrust and torque. In addition, detailed calculations can be made regarding efficiency, cavitation, and strength. These calculations all require the use of iteration procedures but are much simpler than performing the lifting-surface calculations.

A discussion of the details of subcavitating lifting-line theory and the associated computational procedures was given in 1965 by Morgan and Wrench (ref. 30). This work includes the significant contributions of Betz (1919), Goldstein (1929), Moriya (1933, 1942), Kawada (1936), Strscheletzky (1950), and Lerbs (1952). The lifting-line procedure of Lerbs is used in the NSRDC design procedure. No satisfactory procedure is yet available for supercavitating propellers. A recent study was presented by Cox in 1968 (ref. 19).

The main hypotheses and assumptions of the lifting-line concept are summarized as follows:

(1) The fluid is inviscid and incompressible. However, in the calculation procedure, allowance is made by the use of strip theory for the viscous drag of the blade for subcavitating propellers and viscous and cavity drags for supercavitating propellers.

(2) The free-stream velocity is axisymmetric and steady. Consequently, the propeller may be wake-adapted.

(3) Each propeller blade is replaced by a lifting line and the circulation varies along the radius.

(4) Each of the free vortices is at a constant pitch in the downstream direction, but a radial variation in pitch is allowed. This means that effects of slipstream contraction and centrifugal force on the shape of the vortex sheets are ignored.

(5) The radial velocity induced at the hub is assumed small so that the effect of the hub on the pitch of the trailing sheets is ignored. For very large hub propellers, this assumption would not be valid.

(6) For the supercavitating propeller, a pressure-source representation on the trailing vortex sheet can be used to represent the cavity thickness. The strength and length of the source distribution will then depend on the circulation and the free-stream cavitation number.

An additional assumption made is that the circulation is zero at the propeller hub. It is obvious that the circulation must go to zero at the blade tip but, at the blade hub, the assumption is justified on the basis of an argument by Wald (ref. 57). He showed that for a hub of finite length behind the propeller the circulation must go to zero at the hub for an optimum propeller and it can be inferred from this work that the circulation must always be zero at the hub for a hub of finite length. On the other hand, if the hub is of infinite length, the circulation should have a finite value at the hub for an optimum distribution (McCormick, ref. 58). Since most propellers will not be optimum and because of Wald's results, it seems reasonable to assume that the circulation will be zero at the propeller hub.

For propeller design, it is necessary only to calculate the velocity induced by the vortex system at one of the bound vortex lines. Only the axial and tangential components of this induced velocity are considered, as the radial component does not contribute to the forces on the propeller.

Propeller Lifting-Surface Theory

Lifting-line theory cannot recognize chordwise effects, and thus provides no information about how to achieve the required radial distribution of lift for the relatively broad-bladed marine propeller. It is not sufficient to insert cambered sections, of known chord and lift coefficient in two-dimensional flow, at the requisite radial stations, since they will develop much less lift once they are part of a low-aspect ratio propeller blade. In order to determine section camber, it is necessary to use a more adequate vortex theory model for the propeller blades which recognizes both chordwise and radial distribution of lift. Lifting-surface theory can be used to achieve this purpose since the known (chordwise integrated) radial circulation distribution predicted by lifting-line theory can be distributed in any desired manner in the chordwise direction. In addition, the radial pitch distribution of the lifting surface is known from the lifting-line theory. In principle, it is then possible to calculate the shape and position of the cambered meanline surface with reference to the lifting-surface position, such that the required radial and chordwise lift distribution is achieved. (Recognizing the effects of blade skew, if necessary, adds no complication to a lifting-surface procedure.)

The assumptions which have been put forward previously for lifting-line theory hold for lifting-surface theory except that now it is assumed that the bound vortices are distributed over the blade surface rather than concentrated at a lifting line and the blade is allowed to have a finite thickness. From the standpoint of the linearized theory, the loading and thickness effect can be considered separately. Also, the theory is approached from the standpoint that it is required to design a propeller to produce a certain thrust, or power, at a specified speed coefficient and not from the standpoint of determining the performance of a given propeller.

Another consequence of linearized theory is the assumption that the lifting surface lies on the free helical vortex sheets and has only a small deviation from this surface. This assumption is equivalent to the linearized theory of two-dimensional airfoils where the boundary condition is not satisfied on the profile, but on the profile chord.

Present subcavitating propeller lifting-surface procedure at NSRDC is mainly based on theoretical formulations by Pien (ref. 59) or Kerwin (ref. 60) for chordwise load effects on camber and pitch, together with the approach of Kerwin and Leopold (ref. 61) for the effects of blade thickness. The main feature of Pien's approach is that the numerical procedure is greatly simplified by subtracting out the lifting-line contribution, while Kerwin's method is based on the vortex lattice approach of Falkner (ref. 62). With regard to Pien's method, both Cheng (ref. 63) and Lerbs, Alef, and Albrecht (ref. 64) have formulated computation procedures for uniform chordwise loading, and Cheng (ref. 63) for NACA($a = 0.8$) type chordwise loading. NSRDC experience with the use of Cheng's procedure for NACA($a = 0.8$) chordwise loading, combined with Kerwin and Leopold's thickness procedure, indicates excellent comparisons with the results of model propeller tests. Various other theories and numerical approaches are due to Strecheletzky (ref. 65), Sparenberg (ref. 66), Yamazaki (ref. 67), Nelson (ref. 68), and Murray (ref. 69).

Lerbs, Alef, and Albrecht (ref. 64) present systematic lifting-surface calculation data for 48 propellers for a specific blade outline (nonskewed and skewed), optimum radial load distribution, constant chordwise load distribution, and varying number of blades, expanded area ratio, and hydrodynamic advance ratio. These results do not include blade thickness effects. More recently, Morgan, Silovic, and Denny (ref. 70) have performed a very comprehensive study of the Cheng/Kerwin and Leopold procedures and critically examined these procedures, upgraded output data by selective improvements in computational techniques, and presented a large amount of systematic lifting-surface data for a NACA ($a = 0.8$) type chordwise load distribution, varying radial load, and blade thickness distributions, several blade outlines (nonskewed and skewed), varying number of blades, expanded area ratio, and hydrodynamic advance ratio. This latter data is particularly significant since NACA ($a = 0.8$) type loading is realistic in real flow, whereas uniform chordwise loading is not, due to viscous effects. Results from these two sets of calculations, reinforced by earlier calculations of Pien, Cheng, Kerwin and Leopold, clearly demonstrate that

(1) The effect of blade skew is important and results in an ideal angle correction to the hydrodynamic pitch angle which is positive toward the root and negative toward the tip.

(2) The effect of blade thickness results in an ideal angle correction to the hydrodynamic pitch angle which is largest toward the root and diminishes toward the tip.

(3) Blade skew and thickness have a negligible effect on the chordwise distribution of blade camber.

(4) Chordwise loading which is symmetric about midchord does not result in any ideal angle correction to the hydrodynamic pitch angle.

(5) The concept of a camber correction factor is generally valid for practical design purposes. Moreover, with the use of complete lifting-surface procedures, it is feasible to define ideal angle correction factors for the effect of blade skew, thickness, and nonsymmetric loading about midchord.

Finally, and following the last conclusion, it should be mentioned that prior to the availability of complete lifting-surface procedures, finite aspect ratio effects had to be allowed for by the use of camber correction factors; i.e., a correction to the two-dimensional camber line. This type of correction factor was obtained by a limited application of lifting-surface theory which was formulated first in 1944 by Ludwieg and Ginzel (ref. 71), who had to use graphical means to obtain a limited set of results. Later Cox (ref. 14) refined their theoretical approach and produced a more comprehensive set of correction factors using a digital computer. However, these factors were only determined for constant chordwise loading and left to semiempirical methods the problem of obtaining any necessary corrections to hydrodynamic pitch angle. The recent correction factors for camber and pitch derived by Morgan, Silovic, and Denny, which were also extracted from their complete lifting-surface calculations for the realistic NACA($a=0.8$) type chordwise loading, will prove useful to the designer for several purposes; i.e., checking calculations, showing trends, back analysis, and cavitation calculations to account for operation in circumferentially varying inflow (refs. 52 and 72).

CONCLUSIONS

Based on the authors' combined experience and knowledge, it can be concluded that subcavitating propeller theoretical design procedures are generally adequate and in an advanced state of development. Present-day numerical procedures are sufficient to permit great flexibility to the designer in his choice of design parameters. Moreover, the consequences of design parameter choice are well understood. Future areas for investigation will probably tend to "off-design" performance rather than "design-point" performance.

It is concluded that the state-of-the-art for supercavitating propeller design is several years behind that for subcavitating propellers. Although existing theory is well developed, much remains to be done in the area of numerical procedures; in addition, relatively little is understood regarding choice of design parameters for supercavitating propellers. Present-day design procedures for these propellers are semiempirical, but the way is open for a rapid upgrading in the next few years.

LIST OF SYMBOLS

A_E	Expanded area ratio, $$Z\int_{r_h}^{R} c\,dr$$
A_0	Disc area, πR^2
c	Chordlength
C_c	A strength coefficient which is dependent on chordwise camber distribution
C_{L_i}	Section design lift coefficient, $$\frac{L_i}{(\rho/2)cV_r^2}$$
C_P	Propeller power coefficient, $$\frac{P}{(\rho/2)\pi R^2 V_A{}^3} \quad \text{or} \quad \frac{P}{(\rho/2)\pi R^2 V^3}$$
C_s	A strength coefficient which is dependent on chordwise thickness distribution
C_{T_h}	Propeller thrust loading coefficient, $$\frac{T}{(\rho/2)\pi R^2 V_A{}^2} \quad \text{or} \quad \frac{T}{(\rho/2)\pi R^2 V^2}$$
D	Propeller diameter
EAR	Expanded area ratio, A_E/A_0
J	Advance coefficient, V_A/nD or V/nD
M_{x_o}	Bending moment about blade chord
n	Revolutions per unit time
p	Static pressure at a reference position
p_c	Cavity pressure (or vapor pressure)
P	Power
P/D	Pitch to diameter ratio
P_D	Delivered power to propeller(s)
P_E	Effective power, RV
r	Radial distance

r_h	Propeller hub radius
R	Ship resistance or propeller radius
R_s	Ratio of minimum to maximum stress during a cycle
t	Thrust deduction factor, $R=T(1-t)$; or blade section maximum thickness
t/c	Section thickness-to-chord ratio
T	Propeller thrust
U	Reference velocity
V	Ship speed
V_A	Speed of advance of propeller
V_r	Resultant velocity to the blade section
V_t	Tangential component of ship wake
V_x	Axial component of ship wake
w	Taylor wake fraction, $V_A=V(1-w)$
Z	Number of blades
α	Angle of attack
$\beta(r)$	Advance angle, $\tan^{-1}(V_A/2\pi nr)$
η_B	Propeller behind efficiency, TV_A/P_D
η_D	Propulsive efficiency, P_E/P_D
η_H	Hull efficiency, $(1-t)/(1-w)$
λ	Advance ratio, J/π
σ	Cavitation number, $\dfrac{p_\infty-p_c}{(\rho/2)U^2}$
σ_c	Allowable blade mean stress
σ_f	Fatigue stress for a given number of cycles, single amplitude
$\sigma_{\max}$	Maximum stress for a given number of cycles

REFERENCES

1. O'Brien, T. P., *The Design of Marine Screw Propellers.* Hutchinson and Company, Ltd., 1962.
2. Todd, F. H., Resistance and Propulsion. *Principles of Naval Architecture,* Chapter 7, Soc. Naval Architects and Marine Engrs., 1967.
3. Van Lammeren, W. P. A., J. D. Van Manen, and M. W. C. Oosterveld, The Wageningen B-Screw Series. *Trans. Soc. Naval Architects and Marine Engrs.,* Vol. 77, 1969.
4. Lindgren, H., and E. Bjarne, *The SSPA Standard Propeller Family Open-Water Characteristics.* The Swedish State Shipbuilding Experimental Tank Publication No. 60, 1967.
5. Schoenherr, K. E., Propulsion and Propellers. *Principles of Naval Architecture,* Vol. 2, H. E. Rossell and L. Chapman, eds., Soc. Naval Architects and Marine Engrs. (New York), 1939, pp. 119–194.
6. Lerbs, H. W., *Applied Theory of Free Running Ship Propellers.* Admiralty Experiment Works Report 42/48 (Haslar, England), November 1948.

7. Hill, J. G., *The Design of Propellers.* Soc. Naval Architects and Marine Engrs., Vol. 57, 1949, pp. 143–170.
8. Van Manen, J. D., Fundamentals of Ship Resistance and Propulsion, Part B: Propulsion. *International Shipbuilding Progress,* Vol. 4, Nos. 30–37, 1957.
9. McCormick, B. W., *Propeller Design Procedures.* Ordnance Research Laboratory Technical Memorandum, TM 5.2400–22, 1953.
10. Eckhardt, M. K., and W. B. Morgan, A Propeller Design Method. *Trans. Soc. Naval Architects and Marine Engrs.,* Vol. 63, 1955, pp. 325–374.
11. Tachmindji, A. J., and W. B. Morgan, The Design and Estimated Performance of a Series of Supercavitating Propellers. *Proc. Second ONR Symposium on Naval Hydrodynamics,* U.S. Government Printing Office, August 1958, pp. 489–532.
12. Hecker, R., J. G. Peck, and N. A. McDonald, *Experimental Performance of TMB Supercavitating Propellers.* David Taylor Model Basin Report 1432, January 1964.
13. Tulin, M. P., Supercavitating Propellers—History, Operating Characteristics and Mechanics of Operation. *Proc. Fourth ONR Symposium on Naval Hydrodynamics,* U.S. Government Printing Office, August 1962, pp. 239–286.
14. Cox, G. G., Corrections to the Camber of Constant Pitch Propellers. *Trans. Roy. Inst. Naval Architects,* Vol. 103, 1961, pp. 227–243.
15. Titoff, I. A., A. A. Russetsky, and Ye. P. Georgiyevskaya, Principles of Cavitating Propeller Design and Development on the Basis of Screw Propellers With Better Resistance to Erosion for Hydrofoil Vessels Raketa and Meteor. *Proc. Seventh ONR Symposium on Naval Hydrodynamics,* August 1968.
16. Davis, B. V., and J. W. English, The Evolution of a Fully-Cavitating Propeller for a High-Speed Hydrofoil Ship. *Proc. Seventh ONR Symposium on Naval Hydrodynamics,* August 1968.
17. English, J. W., *An Approach to the Design of Fully-Cavitating Propellers.* ASME Symposium on Cavitation in Fluid Machinery, November 1965.
18. Goldstein, S., On the Vortex Theory of Screw Propellers. *Proc. Roy. Soc. (London),* Series A, Vol. 63, 1929, pp. 440–465.
19. Cox, G. G., Supercavitating Propeller Theory—The Derivation of Induced Velocity. *Proc. Seventh ONR Symposium on Naval Hydrodynamics.* August 1968. (See also David Taylor Model Basin Report 2166, February 1966.)
20. Yakhimenko, A. I., ed., *Problems and Methods in the Hydrodynamics of Submerged Foils and Propellers* (in Russian). Izdatel'stvo Publishing House (Naukova Dumka, Kiev), 1966.
21. Newton, R. N., and H. P. Rader, Performance Data of Propellers for High-Speed Craft. *RINA,* Vol. 103, 1961, pp. 93–129.
22. Georgiyevskaya, Ye. P., Series of Five-Bladed Cavitating Screw Propellers. *Sbornik Statez po Gidromekhanike i Dinamike Sudna,* Sudostroyeniye Publishing House (Leningrad), 1968, pp. 59–65.
23. Caster, E. B., *TMB 2, 3, and 4-Bladed Supercavitating Propeller Series.* David Taylor Model Basin Report 1637, January 1963.
24. Harvald, S. A., *Wake of Merchant Ships.* The Danish Technical Press (Copenhagen), 1950.
25. Hadler, J. B., G. R. Stuntz, Jr., and P. C. Pien, Propulsion Experiments on Single-Screw Merchant Ship Forms—Series 60. *Trans. Soc. Naval Architects and Marine Engrs.,* Vol. 62, 1954, pp. 121–178.
26. Todd, F. H., G. R. Stuntz, Jr., and P. C. Pien, Series 60—The Effect Upon Resistance and Power of Variation in Ship Proportions. *Trans. Soc. Naval Architects and Marine Engrs.,* Vol. 65, 1957, pp. 445–589.

27. Beveridge, J. L., Analytical Prediction of Thrust Deduction for Submersibles and Surface Ships. *J. Ship Res.*, Vol. 13, No. 4, December 1969, pp. 258–271.
28. Hadler, J. B., and H. M. Cheng, Analysis of Experimental Wake Data in Way of Propeller Plane of Single and Twin-Screw Ship Models. *Trans. Soc. Naval Architects and Marine Engrs.*, Vol. 73, 1965, pp. 287–414.
29. Troost, L., The Pitch Distribution of Wake-Adapted Marine Propellers. *Trans. Soc. Naval Architects and Marine Engrs.*, Vol. 64, pp. 357–374.
30. Morgan, W. B., and J. W. Wrench, Some Computational Aspects of Propeller Design. *Methods in Computational Physics*, Vol. 4, Academic Press, Inc. (New York), 1965, pp. 301–331.
31. Todd, F. H., *Ship Hull Vibration.* Edward Arnold Ltd. (London), 1961.
32. Noonan, E. F., ed., *Proc. First Conference on Ship Vibration.* David Taylor Model Basin Report 2002, August 1965.
33. *Rules and Regulations for the Construction and Classification of Steel Ships.* Lloyd's Register of Shipping (London), 1969, p. 635.
34. Viner, A. C., *Ship Vibration.* Lloyd's Register of Shipping, Publication No. 53 (London), 1966.
35. Milam, A. B., and W. B. Morgan, *Section Moduli and Incipient Cavitation Diagrams for a Number of NACA Sections.* David Taylor Model Basin Report 1177, October 1957.
36. Barr, R. A., Choice of Foil System for Optimum Performance. *Hydrodynamics of Hydrofoil Craft—Subcavitating Hydrofoil Systems*, Chapter 2, Hydronautics, Inc., Technical Report 463–1, May 1964.
37. McCarthy, J. H., and J. S. Brock, *Static Stress in Wide-Bladed Propellers.* Naval Ship Research and Development Center Report 3182, 1970.
38. Morgan, W. B., *Centroid and Moment of Inertia of a Supercavitating Section.* David Taylor Model Basin Report 1193, August 1957.
39. Timoshenko, A., and G. H. MacCullough, *Elements of Strength of Materials*, 3rd. ed., D. Van Nostrand Company, Inc. (Princeton, New Jersey), 1949.
40. Tsakonas, S., J. Breslin, and M. Miller, Correlation and Application of an Unsteady Flow Theory for Propeller Forces. *Trans. Soc. Naval Architects and Marine Engrs.*, Vol. 75, 1967, pp. 158–193.
41. McCarthy, J. H., *On the Calculations of Thrust and Torque Fluctuations of Propellers in Nonuniform Flow.* David Taylor Model Basin Report 1533, 1961.
42. Boswell, R. J., *Static Stress Measurements on a Highly-Skewed Propeller Blade.* Naval Ship Research and Development Center Report 3247, December 1969.
43. Morgan, W. B., and J. Z. Lichtman, Cavitation Effects on Marine Devices. *ASME Cavitation State of Knowledge*, 1969, pp. 195–241.
44. Newton, R. N., *Influence of Cavitation on Propeller Performance.* Convegno di Tecnica Navale, Trieste U., 1961.
45. Burrill, L. C., and A. Emerson, *Propeller Cavitation: Further Tests on 16 In. Propeller Models in the Kings College Cavitation Tunnel*, Vol. 79. North East Coast Institution of Engineers and Shipbuilders, 1962–63, pp. 295–320.
46. Keller, J., Enige Aspecten Bij Het Ontwerpen van Scheepsschroeven. *Ship and Yard*, No. 24, 1966, pp. 658–662.
47. Kruppa, C., *Methodical Cavitation Tests of Blade Sections—Three Component Forces and Cavitation Patterns.* Vosper Ltd., Report 115 (Portsmouth, England), 1963.
48. Rader, H. P., *Cavitation of Propeller Blade Sections*, Parts I and II. Admiralty Experiment Works, Reports 22/54, 32/54 (Haslar, England), 1954.
49. Cox, G. G., *A Proposed Meanline for Use With AEW Design Propeller*, Parts I and II. Admiralty Experiment Works, Technical Memoranda 16/63, 20/63 (Haslar, England), 1963.

50. Brockett, T., *Minimum Pressure Envelopes for Modified NACA Sections With NACA a=0.8 Camber and BuShips Type I and Type II Sections*. David Taylor Model Basin Report 1780, 1966.

51. Abbott, I. H., and A. E. Von Doenhoff, *Theory of Wing Sections*. Dover Publications, Inc. (New York), 1959.

52. Lerbs, H. W., and H. P. Rader, Uber der Auftriebsgradienten von Profilen im Propeller verband. *Schiffstechnik*, Vol. 9, No. 48, 1962.

53. Wirth, R. J., *A TMB Meanline Series to Delay Cavitation Inception*. David Taylor Model Basin Report 1429, May 1960.

54. Sturgeon, M. L., *Slender Airfoil Camberlines With Trapezoidal Lift Distributions*. NOTS TP 3145 (NAVWEPS Report 8092), June 1963.

55. Auslaender, J., *The Linearized Theory for Supercavitating Hydrofoils Operating at High Speeds Near a Free Surface*. Hydronautics Technical Report 001–5, 1961.

56. Cox, G. G., State-of-the-Art for Subcavitating and Supercavitating Propeller Design Methods. *Propeller Committee Report, Proc. 12th International Towing Tank Conference*, Appendices II and IV (Rome), 1969.

57. Wald, R., *The Distribution of Circulation on Propellers With Finite Hubs*. ASME Paper 64-WA/UNT-4, November 1964.

58. McCormick, B. W., The Effect of a Finite Hub on the Optimum Propeller. *J. Aeron. Sci.*, Vol. 22, No. 9, September 1955.

59. Pien, P. C., The Calculation of Marine Propellers Based on Lifting-Surface Theory. *J. Ship Res.*, Vol. 5, No. 2, 1961, pp. 1–14.

60. Kerwin, J. E., *The Solution of Propeller Lifting-Surfaces Problems by Vortex Lattice Methods*. MIT Naval Architecture Dept. Report, 1961.

61. Kerwin, J. E., and R. Leopold, Propeller Incidence Due to Blade Thickness. *J. Ship Res.*, Vol. 7, No. 2, 1963, pp. 1–6.

62. Falkner, V. M., *The Solution of Lifting-Plane Problems by Vortex-Lattice Theory*. Aeronautical Research Council, R&M No. 2591, 1947.

63. Cheng, H. M., *Hydrodynamic Aspects of Propeller Design Based on Lifting-Surface Theory*, Parts I and II. David Taylor Model Basin Reports 1802 and 1803, 1964–65.

64. Lerbs, H. W., W. Alef, and K. Albrecht, Numerische Auswertungen zur Theorie der Tragenden Flache von Propellern. *Jahrbuch Schiffbautechnische Gesellschaft*, Vol. 58, 1964, pp. 295–318.

65. Strecheletzky, M., *Hydrodynamische Grundlagen zur Berechnung der Schiffsschrauber*. Verlag G. Braun (Karlsruhe), 1956.

66. Sparenberg, J. A., Application of Lifting-Surface Theory to Ship Screws. *International Shipbuliding Progress*, Vol. 7, No. 67, 1960, pp. 99–106.

67. Yamazaki, R., On the Theory of Screw Propellers. *Fourth ONR Symposium on Naval Hydrodynamics*, 1962, pp. 3–28.

68. Nelson, D. M., *A Lifting Surface Propeller Design Method for High Speed Computers*. NAVWEPS Report 8442, NOTS TP 3399, 1964. (See also *Numerical Results From the NOTS Lifting Surface Propeller Design Method*. NAVWEPS Report 8772, NOTS TP 3856, 1965.)

69. Murray, M. T., Propeller Design and Analysis by Lifting Surface Theory. *International Shipbuilding Progress*, Vol. 14, No. 160, 1967, pp. 433–451.

70. Morgan, W. B., V. Silovic, and S. B. Denny. *Propeller Lifting-Surface Corrections*. Soc. Naval Architects and Marine Engrs., Vol. 76, 1968, pp. 309–347.

71. Ludwieg, H., and J. Ginzel, Zur Theorie der Breitblattschraube. *Aerodynamische Versuchsanstalt*, Report 44/A/08 (Gottingen), 1944.

72. Rader, H. P., Cavitation Phenomena in Nonuniform Flows. *Cavitation Committee Report, Proc. 12th International Towing Tank Conference*, Appendix II (Rome), 1969.

DISCUSSION

J. D. VAN MANEN (Netherlands Ship Model Basin): This joint paper contains a nearly complete review of the application of theory to propeller design.

One critical remark may be made with respect to the determination of the diameter, rpm, or number of blades. It is not necessary to determine these principal parameters of the propeller from series charts. In my opinion, an extension of theoretical computations with reliable drag coefficient values for the selected profiles may render fruitful, and in many cases more accurate, information for the determination of the optimum principal parameters. This procedure of determining optimum values holds not only from a viewpoint of efficiency but even from an economic or acoustic point of view.

G. E. THOMAS (Admiralty Research Laboratory): The authors are to be commended for this comprehensive review paper on propeller design.

They quite rightly suggest that a future field of investigation should be concerned with off-design performance. Equally important, however, is the need to develop experimental techniques to determine the flow field around the propeller so that adequate comparisons can be made with predictions by lifting-surface theory. A weakness at present is that the lifting-surface model is assessed on the basis of comparisons between experimental values and integrated values of thrust and torque at the design point. Until the design method is validated by satisfactory correlation between the pressure distribution as measured over the blade and that predicted by theory, is it strictly correct to refer to the $a=0.8$ meanline as being more "realistic"?

The loss of lift due to viscous effects on two-dimensional airfoils (of the order of 5 to 20 percent) has been satisfactorily explained by many authors by using the concept of displacement thickness to allow for boundary-layer growth. It is presumed that no such procedure has been incorporated in the authors' design method. It would be appreciated, therefore, if more clarification could be given by the authors as to the basis for their statement that the $a=0.8$ meanline is "more realistic."

COX AND MORGAN (authors): We wish to thank the discussors for their comments. Professor Van Manen stated that he preferred to use theoretical computation methods in preference to propeller series charts for preliminary design purposes. We are in complete agreement with this approach and regret our lack of emphasis on this point in the paper.

Mr. Thomas commented on the authors' viewpoint regarding the advantage of using NACA ($a = 0.8$) type chordwise loading as opposed to a uniform chordwise distribution. All the evidence of which we are aware for two-dimensional airfoil and propeller model tests indicates that chordwise loading of the NACA ($a = 0.8$) type meets its theoretical pressure distribution reasonably well, whereas NACA ($a = 1.0$) type loading most certainly does not. Of course, it is not maintained that $a = 0.8$ loading is necessarily the very best choice, especially for rotating flows. We are aware that a number of investigators have attempted to use the concept of displacement thickness to allow for boundary-layer growth and loss of lift due to viscous effects. However, we are not aware that this procedure has yet been successful. We prefer not to incorporate unproven yet complex techniques into a computer program when a judicious selection of the meanline pressure distribution alleviates the difficulty.

Mr. Thomas is quite correct in stating that good agreement for total thrust and torque values does not properly indicate the adequacy of the theoretical design procedures. In addition to comparing the total thrust and torque values, we always examined the cavitation patterns for the propellers we have designed. These results indicate that the radial load distribution is reasonable. We agree that this approach only gives an indication; hence, our engineers have developed techniques for measuring the pressure distribution on a propeller (ref. D-1). Pressure distributions will be obtained soon for a propeller designed by lifting-surface theory.

REFERENCES

D-1. Brandau, J. H., and J. L. Leahy, *Measurement of Marine Propeller Blade Pressure Distribution.* ASME 1970 Cavitation Forum (Detroit, Michigan), May 24-27, 1970.

The Design of Pumpjets for Hydrodynamic Propulsion

EDGAR P. BRUCE, WALTER S. GEARHART, JOHN R. ROSS, AND ALLEN L. TREASTER[1]

The Pennsylvania State University

This paper illustrates a procedure for use in the design of a wake-adapted pumpjet mounted on the aft end of a body of revolution. To this end, a pumpjet is designed for the Akron airship. The propulsor mass flow is selected to minimize kinetic energy losses through the duct and in the discharge jet. The shaft speed and disk size are selected to satisfy specified limits of cavitation performance and to provide acceptable blade loading. The streamtubes which pass through a propulsor mounted on a tapered afterbody follow essentially conical surfaces. A method is provided for defining these surfaces as a function of shroud geometry, rotor head distribution, and the energy distribution of the ingested mass flow. The three-dimensional effects to which the conical flow subjects the cylindrical blade design sections are described and a technique is presented which permits incorporation of these effects in the blade design procedure.

INTRODUCTION

This paper is written under the assumption that the analysis that is normally exercised in selecting a propulsor, based on consideration of factors such as body geometry, vehicle speed, cavitation performance, torque balance, vehicle stability and control, efficiency, noise, simplicity, and expense of manufacture, has been accomplished and the pumpjet has emerged as the best candidate. Guidance in selecting the proper propulsor for a given application is presented in references 1 and 2.

The term "pumpjet" defines a hydrodynamic propulsor which consists of a rotating vane system operating in an axisymmetric shroud or duct.

---

[1] This work was performed at the Ordnance Research Laboratory, The Pennsylvania State University, under the support of the U.S. Navy, Naval Ordnance Systems Command, NOOO 17-70-C-1407.

However, in addition to the rotating vane system, a stationary vane system is utilized at the exit to permit jet discharge through a nozzle with zero peripheral velocity.

The interest in pumpjets has resulted primarily from efforts to develop propulsor systems for both high-speed surface vehicles and submerged vehicles. The attractiveness of pumpjets for high-speed applications originates from the ability to design the propulsor to operate with velocities of smaller magnitude relative to the rotating vanes than the forward velocity of the propelled body. This feature is achieved by proper selection of rotor disk area and shaft speed with respect to the mass flow and energy input of the propulsor. When the velocities relative to the propulsor blades are reduced to a value below the forward velocity of the propelled body, the blading is less susceptible to the inception of cavitation than the body itself. This reduction in the magnitude of the velocities relative to the rotating blade system can normally be accomplished only if the shaft speed and the meridional flow velocity are both reduced. In most cases, this leads to high-torque propulsors of low shaft speeds.

High-torque, low-rotational-speed propulsors require either a stationary vane system or counterrotating rotors to provide an axial discharge jet. This eliminates the kinetic energy losses that are associated with the high circumferential velocities that would otherwise be dumped overboard in the discharge jet.

The original efforts in the design and development of pumpjets are summarized in reference 3. Much of this design philosophy is still used; however, it is the intent of this paper to present an approach that incorporates the results of recent cascade work and includes some of the techniques presently used in axial flow compressor design. This method permits the sizing and design of a pumpjet to satisfy specified performance criteria relating to (1) vehicle forward velocity, (2) available power for propulsion, (3) propulsor shaft speed, (4) vehicle size and shape, and (5) required submergence depth below which no cavitation is tolerable.

To this end, the proper mass flow through the pumpjet to provide a maximum propulsive efficiency must be determined. Once the optimum mass flow has been derived, it is necessary to determine the disk area, blade solidity, and shaft speed which will permit the design of a vane system that satisfies specified limits of resistance to flow separation and cavitation.

On completing the preliminary sizing of the propulsor, a detailed analysis of the flow properties at various stations through the pumpjet must be performed to permit the graphical design of the individual rotor and stator blade systems.

The following paragraphs outline a procedure, summarized above, which has been used with success in the design of pumpjet propulsors. Without reservation, the authors are fully aware of their indebtedness to past developments at various hydrodynamic and aerodynamic laboratories which provide a part of the basis for the design procedures presented. However, familiarity inevitably supports a tendency to emphasize one's own work. Apologies are offered for any such offense.

Vehicle Boundary Layer Velocity Profile and Drag Coefficient

The propulsor configuration and its performance are highly dependent on the hydrodynamic characteristics of the body or vehicle to which it is to be applied. Under ideal conditions, the inflow velocity to the propulsor would be uniform in the radial and circumferential directions. However, in most cases, energy distortions are present in the ingested flow due to the skin friction drag of the vehicle and/or to wakes from upstream appendages such as shroud support struts, control and stabilizing surfaces, etc.

The circumferential distortions due to upstream appendages can amount to as much as 15 percent of the free-stream velocity and are undesirable when it is considered that vane systems rotating in a circumferentially nonuniform velocity field are prone to periodic cavitation, vibration, and loss of efficiency. For these reasons, every effort should be made to minimize such distortions or mix them out prior to their arrival at the rotating vane system.

Analytical predictions of the velocity profiles near the aft end of a body of revolution are difficult to obtain since the afterbody curvature often produces a pressure gradient normal to the flow that is of the same magnitude as the gradient parallel to the flow. In many cases, existing experimental results for similar bodies can be used and corrected for variations in Reynolds number. It is often far more expedient and reliable to fabricate a scale model and obtain the necessary energy distributions and vehicle drag by either wind or water tunnel tests. A method for estimating the drag of hydrodynamic bodies is given in reference 4 and a method for estimating the velocity profile near the aft end of a body is given in reference 5.

For the illustrative purpose of this paper, a wake-adapted pumpjet has been designed for the U.S. airship Akron. Table I presents the body coordinates of the Akron and the revised coordinates used in this design exercise. Note that the only difference is over the aft 20 percent of the body length, where the contour has been altered slightly to accommodate the pumpjet installation. The necessary velocity and pressure distribution data have been taken from reference 6 which contains the results of a detailed wind tunnel test program conducted on the Akron by the NACA.

To determine the optimum mass flow with respect to minimizing kinetic energy losses dumped overboard in the discharge jet, a reference station is selected near the aft end of the body where the static pressure on

TABLE I.—*Body Coordinates for the Airship Akron and for the Akron Body Modified for Pumpjet Installation*

Percent length	Body radius-to-length ratio	
	Airship Akron	Modified body
0	0	0
1	0.0090	0.0090
2	0.0210	0.0210
3	0.0297	0.0297
4	0.0367	0.0367
5	0.0423	0.0423
6	0.0470	0.0470
7	0.0508	0.0508
10	0.0603	0.0603
15	0.0707	0.0707
20	0.0781	0.0781
25	0.0812	0.0812
30	0.0833	0.0833
35	0.0843	0.0843
40	0.0845	0.0845
45	0.0845	0.0845
50	0.0841	0.0841
55	0.0832	0.0832
60	0.0812	0.0812
65	0.0784	0.0784
70	0.0743	0.0743
75	0.0686	0.0686
80	0.0613	0.0612
85	0.0522	0.0519
90	0.0408	0.0380
95	0.0277	0.0227
99.5	0.00308	0.0117
100	0	0

the hull is equal to its value in the free stream. In addition, it is assumed that the static pressure is constant through the boundary layer at this station. This assumption is valid since the analytically determined static pressure profile at this station, including streamline curvature effects, shows only a very slight variation of static pressure with distance from the body. The velocity profile that exists at the reference station and other bare-body characteristics are shown in figure 1. It is also necessary to estimate the total drag of the vehicle, which includes bare-body drag

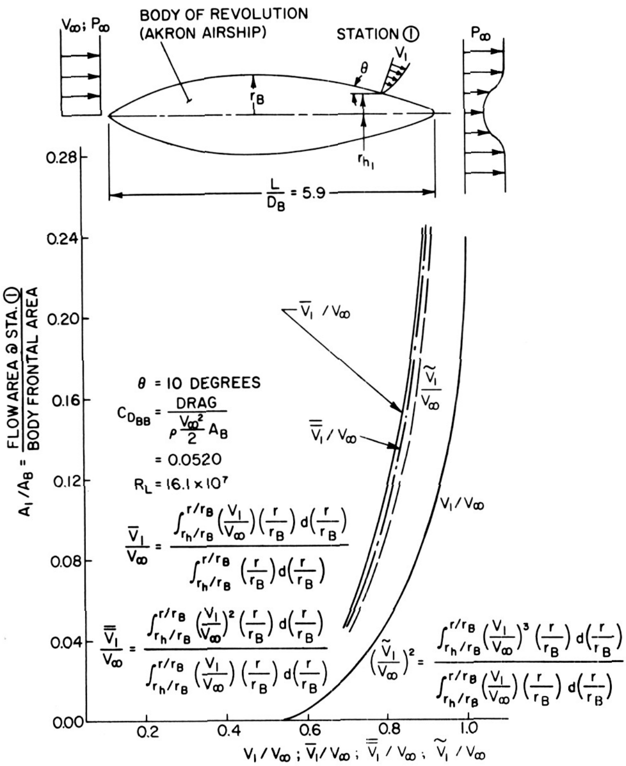

FIGURE 1.—*Velocity distributions associated with the Akron.*

plus increments due to the nacelle or shroud and control surfaces. Reference 4 provides data which is of assistance in estimating the drag increment associated with the control system. In this design example, the added drag due to control surfaces is predicted to be 6 percent of the bare-body drag.

The increment of drag attributed to the frictional effects of the shroud varies with shroud size. This effect can be estimated by referring to figure 2 and noting that, by continuity,

$$A_1\overline{V_1}=A_2\overline{V_2}$$

or

$$r_{T_2}=\left\{\left[\frac{\overline{V_1}}{\overline{V_2}}\left(r_{\psi_1}{}^2-r_{H_1}{}^2\right)\right]+r_{H_2}{}^2\right\}^{1/2} \tag{1}$$

If the wetted surface area of the shroud is approximated by

$$A_s=4\pi r_{T_2}l_s \tag{2}$$

then the nondimensional shroud drag can be written as

$$C_{D_s} = C_{D_s}' \frac{A_s}{A_B} \tag{3}$$

where C_{D_s}' is the skin friction drag coefficient based on shroud wetted surface area. After substituting equations (1) and (2) into equation (3) and adding the increments due to bare-body and control surface drag, the total thrust coefficient may be expressed as

$$C_T = C_{DBB} + 0.06C_{DBB} + 4C_{D_s}' \frac{l_s}{r_B} \left\{ \frac{\overline{V_1}}{\overline{V_2}} \left[\left(\frac{r_{\psi_1}}{r_B} \right)^2 - \left(\frac{r_{H_1}}{r_B} \right)^2 \right] + \left(\frac{r_{H_2}}{r_B} \right)^2 \right\}^{1/2} \tag{4}$$

In equation (4), preliminary values are now assigned to selected quantities as follows: $l_s/r_B = 1.00$; $r_{H_2}/r_B = 0.25$; $\overline{V_1}/\overline{V_2} = 1.15$; and $C_{D_s}' = 0.003$. The accuracy of the estimated values of these quantities will become evident from later developments. It is important to note that the above relation reflects an increase in shroud drag as ingested mass flow increases.

In this estimate, only the frictional drag of the propulsor shroud has been considered. However, it must be remembered that the pressure drag of the body, which was initially included in the bare-body drag coefficient, is substantially reduced by the addition of the propulsor. Thus, the inclusion of the full bare-body drag in all calculations tends to compensate for increases in the form drag of the pumpjet shroud.

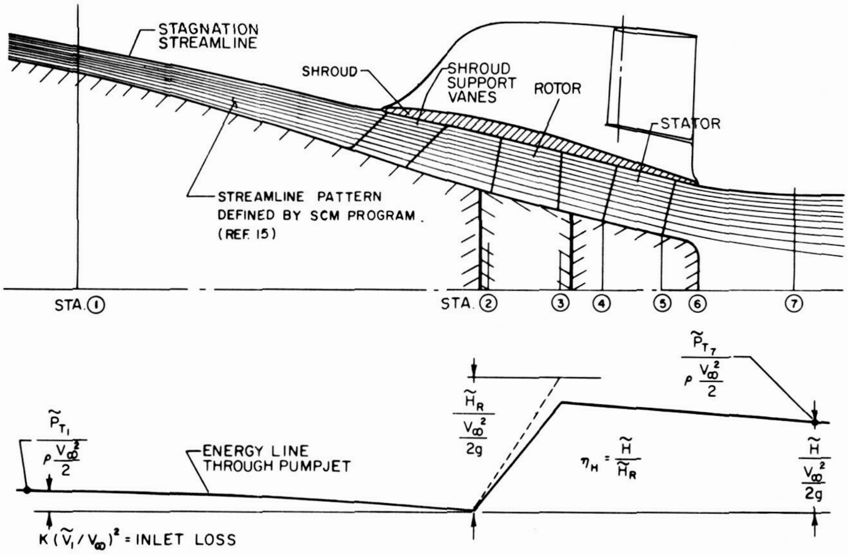

Figure 2.—*Streamlines and energy line through the pumpjet.*

Optimum Propulsor Mass Flow

When seeking an engineering design solution involving boundary-layer ingested flow, it is necessary to define three separate average velocity quantities which are a function of the boundary-layer shape at the reference station. These mean quantities are representative of the mass flow rate, the momentum, and the kinetic energy of the ingested flow. For cases where all streamlines are approximately parallel to the body surface, they are defined as follows:

$$\frac{\overline{V_1}}{V_\infty}=\frac{\displaystyle\int_{r_H/r_B}^{r/r_B}\frac{V_1}{V_\infty}\frac{r}{r_B}\,d\left(\frac{r}{r_B}\right)}{\displaystyle\int_{r_H/r_B}^{r/r_B}\frac{r}{r_B}\,d\left(\frac{r}{r_B}\right)} \tag{5}$$

$$\frac{\overline{\overline{V}}_1}{V_\infty}=\frac{\displaystyle\int_{r_H/r_B}^{r/r_B}\left(\frac{V_1}{V_\infty}\right)^2\frac{r}{r_B}\,d\left(\frac{r}{r_B}\right)}{\displaystyle\int_{r_H/r_B}^{r/r_B}\frac{V_1}{V_\infty}\frac{r}{r_B}\,d\left(\frac{r}{r_B}\right)} \tag{6}$$

$$\left(\frac{\tilde{V}_1}{V_\infty}\right)^2=\frac{\displaystyle\int_{r_H/r_B}^{r/r_B}\left(\frac{V_1}{V_\infty}\right)^3\frac{r}{r_B}\,d\left(\frac{r}{r_B}\right)}{\displaystyle\int_{r_H/r_B}^{r/r_B}\frac{V_1}{V_\infty}\frac{r}{r_B}\,d\left(\frac{r}{r_B}\right)} \tag{7}$$

For many cases, the three values given by the different definitions for the mean velocity will not differ significantly. However, the individual values are dependent on the "shape factor" of the boundary layer and for boundary-layer profiles having a ratio of displacement to momentum thickness of 1.5 or greater it is important to insert the respective values in mass flow, momentum, or energy relations. This practice will be followed in this paper even though the velocities, as defined by equations (5), (6), and (7) and plotted in figure 1, indicate little difference.

Propulsion devices depend on the principle of reaction. The impulse-momentum relation when applied in the axial direction between Stations ① and ⑦ of figure 2, where it is assumed that free-stream static pressure exists, results in

$$T=\rho A_1\overline{\overline{V}}_1(\Delta\overline{\overline{V}}_a) \tag{8}$$

where $\Delta\overline{\overline{V}}_a$ is the average change in axial velocity. This expression can be written in terms of the thrust coefficient as

$$C_T=2\,\frac{A_1}{A_B}\,\frac{\overline{\overline{V}}_1}{V_\infty}\,\frac{\Delta\overline{\overline{V}}_a}{V_\infty} \tag{9}$$

Referring to equation (9), the product $(A_1/A_B)(\overline{\overline{V}}_1/V_\infty)$ represents the nondimensionalized mass flow rate through the pumpjet and the quantity $\Delta\overline{\overline{V}}_a/V_\infty$ represents the axial acceleration of the fluid between Stations ① and ⑦. It is evident that to obtain a given thrust, the product of these two quantities must remain constant. This can be achieved with significant variations in the individual values of the mass flow rate and the acceleration. The criterion used in selecting the proper mass flow rate is based on minimizing the energy dumped overboard in the discharge jet and the energy losses in the duct inlet. The parameter normally used in defining this performance criterion is termed the propulsive coefficient (sometimes referred to as propulsive efficiency). It expresses the relative effectiveness of converting the energy placed in the fluid by the propulsor into propulsive vehicle energy. Since the propulsor is ingesting low-energy boundary-layer fluid, the selection of the optimum mass flow rate is influenced by the shape and energy of the velocity profile near the aft end of the body as discussed in references 2, 7, and 8.

The approach which is used to determine the optimum mass flow rate is based on analysis of averaged energy relations through the pumpjet, thereby eliminating the need for defining the propulsive vehicle energy. This quantity is confusing because its definition often leads to propulsive coefficients greater than unity. Referring to figure 2, the energy relation between Stations ① and ⑦ can be written

$$\tilde{P}_{T_1}=\tilde{P}_{T_7}-\gamma\tilde{H}+K\rho\,\frac{\tilde{V}_1^2}{2} \tag{10}$$

This relation is depicted graphically in figure 2. Assuming the same static pressure at both stations, the nondimensional relation defining the energy placed in the fluid can be expressed as

$$\frac{\tilde{H}}{(V_\infty{}^2/2g)}=\left(\frac{\tilde{V}_7}{V_\infty}\right)^2-\left(\frac{\tilde{V}_1}{V_\infty}\right)^2+K\left(\frac{\tilde{V}_1}{V_\infty}\right)^2$$

Since $\tilde{V}_7$ can be closely approximated by $\tilde{V}_1+\Delta\overline{\overline{V}}_m$, this expression reduces to

$$\frac{\tilde{H}}{(V_\infty{}^2/2g)}=2\,\frac{\Delta\overline{\overline{V}}_m}{V_\infty}\,\frac{\tilde{V}_1}{V_\infty}+\left(\frac{\Delta\overline{\overline{V}}_m}{V_\infty}\right)^2+K\left(\frac{\tilde{V}_1}{V_\infty}\right)^2 \tag{11}$$

where $\Delta\overline{\overline{V}}_m/V_\infty$ is obtained from equations (4) and (9) with consideration of the local body geometry. The variation of $\Delta\overline{\overline{V}}_m/V_\infty$ with amount of ingested mass flow is shown in figure 3. The last term in equation (11) represents the energy loss in the shroud inlet. A typical value of the loss coefficient for this type of inlet, $K=0.13$, was used in this case.

The hydraulic efficiency of a turbomachine is defined as the ratio of the energy placed in the fluid to the shaft energy. The energy placed in the fluid could be determined from an averaged total head traverse fore and aft of the rotor-stator system and the shaft energy could be determined from the shaft speed and torque. Over the range of flows to be investigated here, it has been assumed that the hydraulic efficiency, defined by the ratio

$$\eta_H=\frac{\tilde{H}}{\tilde{H}_R} \tag{12}$$

remains constant at 0.89, a value typical of axial-flow pumps. This estimate of the hydraulic efficiency can be evaluated later in the design exercise by using the final spanwise loading and flow characteristics and the technique described in reference 9.

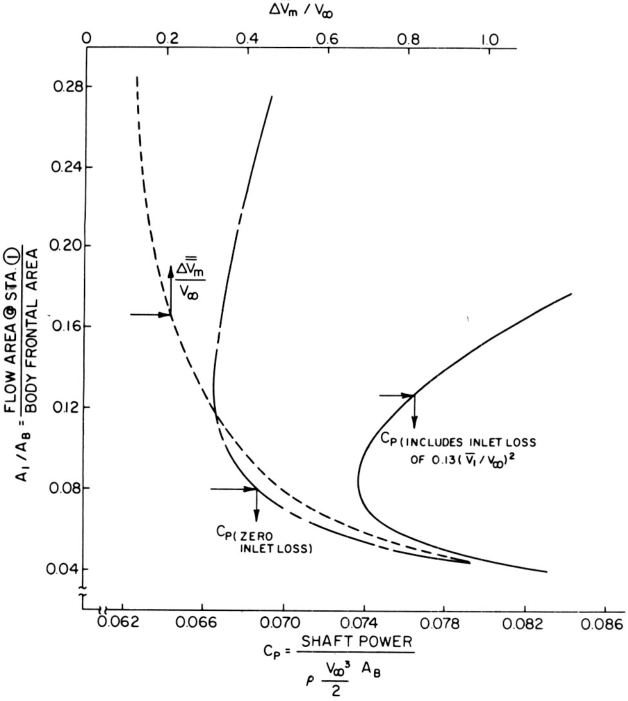

FIGURE 3.—*Power requirements and meridional velocity change as a function of flow area at Station 1.*

A nondimensional shaft power coefficient can now be defined.

$$C_P = \frac{P}{\frac{1}{2}\rho V_\infty{}^3 A_B} = \frac{\tilde{H}_R}{(V_\infty{}^2/2g)}\,\tilde{C}_m \tag{13a}$$

where

$$\tilde{C}_m = \frac{A_1}{A_B}\,\frac{\tilde{V}_1}{V_\infty} \tag{13b}$$

Substituting equations (11), (12), and (13*b*) in equation (13*a*) gives

$$C_P = \frac{1}{\eta_H}\left[2\,\frac{\Delta\overline{\overline{\overline{V}}}_m}{V_\infty}\,\frac{\tilde{V}_1}{V_\infty} + \left(\frac{\Delta\overline{\overline{\overline{V}}}_m}{V_\infty}\right)^2 + K\left(\frac{\tilde{V}_1}{V_\infty}\right)^2\right]\frac{A_1}{A_B}\,\frac{\tilde{V}_1}{V_\infty} \tag{14}$$

By substituting the velocity ratios at given values of A_i/A_B as indicated by figure 1, a plot of the shaft power coefficient can be obtained as shown in figure 3. The optimum mass flow with respect to minimizing required shaft power corresponds to $A_1/A_B = 0.10$, $\tilde{V}_1/V_\infty = 0.78$, and $\Delta\overline{V}_m/V_\infty = 0.39$. The optimum was chosen slightly above the predicted value to ensure staying above that portion of the power curve where adverse C_P gradients occur.

The magnitude by which the inlet loss affects the performance of the propulsor is illustrated in figure 3 by the plot of the power coefficient associated with zero inlet loss. The advantage of boundary-layer intake for this propulsor configuration should also be emphasized. The increased performance associated with boundary-layer intake can be illustrated by considering an alternate propulsor configuration that is strut-mounted at a distance from the hull sufficient to permit ingesting fluid of free-stream dynamic energy. The power required for this configuration is found by substituting $\tilde{V}_1/V_\infty = 1$ into the previous equations and is 15-percent greater than that associated with the propulsor that takes advantage of boundary-layer intake.

CAVITATION PERFORMANCE

The problem of propulsor cavitation is largely dependent on the degree to which cavitation has to be avoided. It has been well established that limited cavitation occurring within the blade passages of pumps, propellers, or pumpjets does not affect the propulsor performance or efficiency. However, strongly developed cavitation can lead to complete performance breakdown and falloff in shaft torque. The problem of cavitation is considerably complicated when it is necessary to avoid local, incipient cavitation at specified vehicle speeds and depths. In this case, the propulsor must operate with a minimum of cavitation-induced noise, vibration, and erosion, all of which can be introduced with only minute sporadic cavitation.

The parameter used to describe the cavitation performance of pumping machinery is suction specific speed. An analogous parameter, which has been used by various hydrodynamic laboratories, is termed a cavitation index. The use of the latter cavitation parameter permits describing the cavitation performance of either a rotating or stationary element of the hydrodynamic machine. The suction specific speed parameter, by definition, involves a shaft speed and has generally been used to describe the overall cavitation performance of the entire shrouded rotor-stator system. A discussion indicating the relation of these two cavitation parameters is found in reference 3.

The cavitation index will be used in this paper as the cavitation performance parameter. It is defined as the ratio of the difference between the ambient static pressure at the centerline of the vehicle and the vapor pressure to the dynamic head of the free-stream fluid as shown below.

$$\sigma=\frac{h_{\mathrm{sub}}+h_{\mathrm{atm}}-h_V}{(V_\infty^2/2g)}=\frac{h_{\mathrm{sub}}+32.0}{(V_\infty^2/2g)}=\frac{p_\infty-p_V}{\frac{1}{2}\rho V_\infty^2} \tag{15}$$

The critical cavitation index, σ_{cr}, relates the unique conditions of depth and forward velocity at which cavitation inception occurs. Referring to figure 2, the energy relation expressed between Stations ① and ② has the form:

$$\frac{p_2-p_\infty}{\frac{1}{2}\rho V_\infty^2}=\left(\frac{\tilde{V}_1}{V_\infty}\right)^2-\left(\frac{\tilde{V}_2}{V_\infty}\right)^2-0.13\left(\frac{\tilde{V}_1}{V_\infty}\right)^2 \tag{16}$$

The minimum pressure coefficient along the blade profile at the tip can be defined as

$$C_b=\frac{p_2-p_{\mathrm{min}}}{\frac{1}{2}\rho W_2^2} \tag{17}$$

The relative velocity, W_2, at the rotor blade tip is used in this relation since the velocity at the tip is a maximum, making this region most critical with respect to cavitation.

By utilizing equations (15), (16), and (17) and letting p_{min} equal the vapor pressure of the fluid, the following relation defining the critical cavitation index is obtained.

$$\sigma_{\mathrm{cr}}=C_b\left(\frac{W_2}{V_\infty}\right)^2-\left(\frac{\tilde{V}_1}{V_\infty}\right)^2+\left(\frac{\tilde{V}_2}{V_\infty}\right)^2+0.13\left(\frac{\tilde{V}_1}{V_\infty}\right)^2 \tag{18}$$

The average values of the quantities indicated in equation (18) will be used to obtain values of cavitation performance for preliminary selection of disk area and shaft speed. On this basis, with

$$\frac{\tilde{V}_2}{V_\infty}=\frac{\tilde{V}_1}{V_\infty}\frac{A_1}{A_2} \tag{19a}$$

and with

$$\left(\frac{W_2}{V_\infty}\right)^2=\left(\frac{\tilde{V}_2}{V_\infty}\right)^2+\left(\frac{U_T}{V_\infty}\right)^2 \tag{19b}$$

we have

$$\sigma_{\text{cr}}=C_b\left[\left(\frac{\tilde{V}_1}{V_\infty}\right)^2\left(\frac{A_1}{A_2}\right)^2+\left(\frac{U_T}{V_\infty}\right)^2\right]+\left(\frac{\tilde{V}_1}{V_\infty}\right)^2\left(\frac{A_1}{A_2}\right)^2-0.87\left(\frac{\tilde{V}_1}{V_\infty}\right)^2 \tag{20}$$

This relationship can be expressed nondimensionally in terms of the advance ratio, rotor hub and tip radii, and mass flow rate coefficient by noting that

$$J=\frac{V_\infty}{nD_B} \tag{21a}$$

$$\frac{U_T}{V_\infty}=\frac{\pi}{J}\frac{r_T}{r_B} \tag{21b}$$

$$\frac{A_2}{A_B}=\frac{(r_T/r_B)^2-(r_H/r_B)^2}{\cos\theta} \tag{21c}$$

By inserting these expressions and equation (13*b*) into equation (20), a very useful relation is obtained that permits the selection of values of disk area and advance ratio which satisfy specified limits of cavitation performance.

$$\sigma_{\text{cr}}=C_b\left\{\tilde{C}_m{}^2\left[\frac{\cos\theta}{(r_T/r_B)^2-(r_H/r_B)^2}\right]^2+\left(\frac{\pi}{J}\right)^2\left(\frac{r_T}{r_B}\right)^2\right\}$$
$$+\tilde{C}_m{}^2\left\{\left[\frac{\cos\theta}{(r_T/r_B)^2-(r_H/r_B)^2}\right]^2-0.87\left(\frac{A_B}{A_1}\right)^2\right\} \tag{22}$$

To illustrate the use of equation (22), it has been solved as a function of r_T/r_B for various advance ratios by substituting the quantities $\tilde{C}_m=0.078$, $A_1/A_B=0.100$, and $\tilde{V}_1/V_\infty=0.780$ obtained from optimum conditions indicated by solution of equation (14). The tip section minimum pressure coefficient C_b was set equal to 0.3, which is representative for thin airfoil sections at zero incidence. The quantity r_H/r_B is, in most cases, dictated by the geometry of the tail-cone and limited by the mechanical design of the aft bearings and shafting. In this case, r_H/r_B was taken equal to 0.25. The angle θ, which is also specified by the tail-cone geometry as shown in figure 1, was equal to 13° in this case. The results of substituting these values for the various parameters into equation (22) are plotted in figure 4. The curves indicate that, for a given disk area, as advance ratio is increased (shaft speed decreased) the cavitation performance improves. Conversely, for a given advance ratio, as the disk area is increased (or as greater diffusion of the flow is permitted between Stations ① and ②), the cavitation index also improves. However, efficient operation over the complete range of these two design variables is not possible since extremely low shaft speeds require such high blade loadings that flow separation will occur on the blades themselves. By the same reasoning, the flow from Station ① to Station ② can be decelerated only a certain amount before separation on the hull can be expected. For these reasons, the disk area and advance ratio indicated as the design point in figure 4 were selected for this design exercise. At this point, there is approximately 15-percent diffusion of the flow between Stations ① and ②. Little is gained in terms of increased cavitation performance by further diffusion since the curve is starting to obtain a gradual slope. In

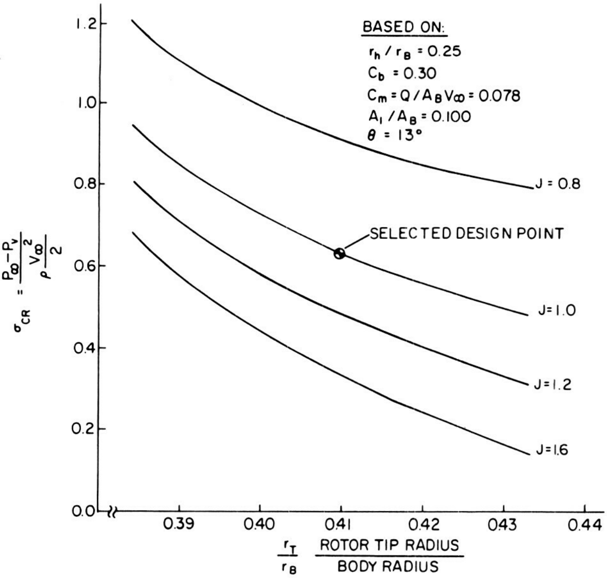

FIGURE 4.—*Critical cavitation index as a function of rotor tip radius and advance ratio.*

addition, this amount of diffusion does not significantly risk flow separation on the hull. It is recommended that the sizing of the shroud inlet be based on the studies of reference 10 which indicate the amount of prediffusion that can be obtained efficiently with nonuniform energy flows. This approach provides a preliminary estimate of disk size. A more detailed evaluation of the flow properties at Station ②, obtained from a computerized solution of the flow field within the duct, will be presented later.

To proceed with the design example, it is now assumed that operational conditions require a forward speed of 50 knots at a cavitation-free depth of 40 feet. It is also assumed that the shaft speed is unrestricted and can be selected at the designer's discretion. Using the relation given as equation (15), it is found that these conditions correspond to a critical cavitation index of 0.650. Referring to figure 4 shows that this value of cavitation index is compatible with the values of r_T/r_B and J selected previously. The predicted cavitation performance is approximate since average values of velocities were used; however, it is representative and final predictions cannot be made until the blade sections are designed. The blade design procedure and the resulting critical cavitation indices are presented in a later section.

It must be emphasized that the preceding design considerations have been directed toward predicting the onset of blade surface cavitation. A second form of cavitation occurs in shrouded propulsors due to the presence of secondary flows such as tip clearance leakage flow. This flow generates cavitation in the clearance gap itself. After proceeding through the gap, this fluid rolls up into a tip vortex of low core pressure. The leakage flow also impinges on the tip of the stator system, causing periodic cavitation. It is usual in pumpjets to find that the cavitation resulting from secondary flows occurs before blade surface cavitation. However, research described in references 11, 12, and 13 provides design criteria which, if properly applied, will give overall propulsor cavitation performance within the limits previously described.

Blade Geometry and Loading Distribution

Satisfying the cavitation requirements of the blading does not imply that flow separation will not occur from excessive blade loading, especially near the root section where relative flow velocities are low. Flow separation leads to high energy losses and creates large wakes which promote both cavitation and vibration.

The magnitude of the average rotor head $\tilde{H}_R/(V_\infty^2/2g)$ was evaluated previously using equations (11) and (12). It is now necessary to obtain a radial distribution of this rotor head which also satisfies established limits of blade loading.

By Euler's equation, the rotor head can be equated to the mass averaged integrated value at the rotor exit, assuming that there is no peripheral velocity component in the flow at the rotor inlet.

$$\frac{\tilde{H}_R}{\dfrac{V_\infty^{\,2}}{2g}} = 2\,\frac{\displaystyle\int_{r_H/r_B}^{r_T/r_B} \frac{V_{m_3}}{V_\infty}\,\frac{U}{V_\infty}\,\frac{V_{\theta_3}}{V_\infty}\,\frac{r}{r_B}\,d\left(\frac{r}{r_B}\right)}{\displaystyle\int_{r_H/r_B}^{r_T/r_B} \frac{V_{m_3}}{V_\infty}\,\frac{r}{r_B}\,d\left(\frac{r}{r_B}\right)} \tag{23}$$

The selection of the radial distribution of V_{θ_3}/V_∞ requires an iterative procedure since many distributions would satisfy this condition, including the free vortex distribution shown in figure 5. However, near the hub the free vortex loading requires, in many cases, an absolute peripheral component of velocity greater than the peripheral wheel speed. This is undesirable since turning the relative flow past the axial direction is not recommended for reasons of separation (see ref. 14). The free vortex loading is also undesirable since kinetic energy losses are minimized in a discharge jet whose velocity is uniform and approaches the vehicle velocity in magnitude. A uniform discharge jet cannot be obtained with free vortex loading since boundary layer fluid is ingested. This condition can be more closely approached with a forced vortex loading. The forced vortex V_{θ_3}/V_∞ distribution shown in figure 5 was selected after several iterations and was used as input to the Streamline Curvature Method

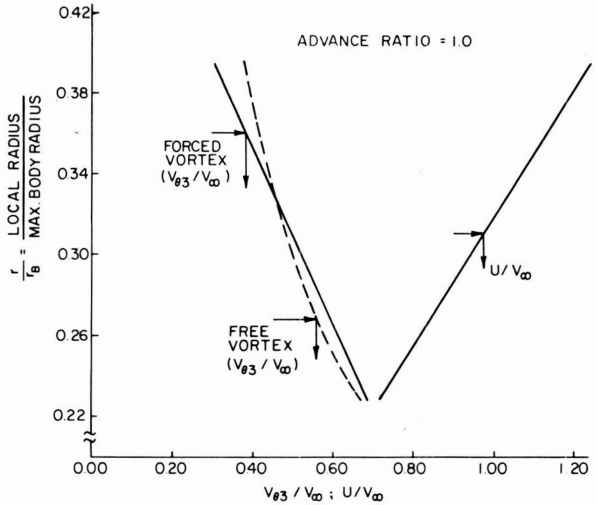

FIGURE 5.—*Rotor velocity and load distribution.*

(SCM) computer program of reference 15. This program provides a solution to the axisymmetric flow field from which the detailed flow properties at various stations through the pumpjet can be obtained. A general discussion of a computerized version of this method, its operation and application, is presented in Appendix I. To obtain a solution, the coordinates of the vehicle hull are used as input and are spline fit to describe the inner contour of the pumpjet. The outer contour is defined by passing a spline curve through points corresponding to the coordinates of the stagnation streamline at Station ①, the shroud inlet, the rotor tip, and the shroud exit. The shroud exit is sized to reflect the "vena contracta" of the discharge jet as discussed in reference 16. This geometric information, in addition to the energy and velocity profiles at Station ① and the radial distribution of rotor head at Station ③, is the information required as program input data.

The velocity and energy profiles obtained as SCM program output at the rotor inlet and exit and at the stator inlet and exit are shown in figures 6 and 7. Using these velocity distributions and an established separation criterion such as the Diffusion Factor described in reference 17, the blade solidity necessary to prevent separation can be obtained. The diffusion factor, *D*, is defined below for rotor blades. For trailing edge loaded blades it is suggested that a value of 0.5 or less be maintained.

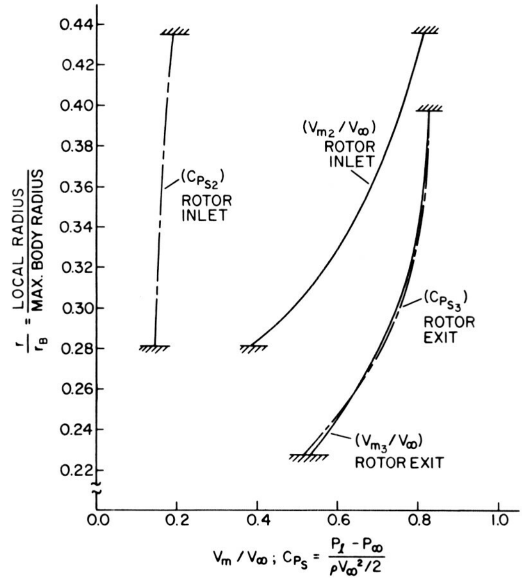

FIGURE 6.—*Velocity and static energy profiles at rotor inlet and exit.*

$$D=1+\frac{1}{2}\frac{V_{\theta 3}}{W_2}\frac{t}{c}-\frac{W_3}{W_2} \tag{24}$$

For preliminary design, the length of the chord can be computed from the projected view of the blade system shown by figure 2 and the vector mean of the velocities relative to the blade at inlet and exit. The diffusion factor and lift coefficient are plotted in figure 8 as a function of r/r_B for a 13-bladed rotor system and a 9-bladed stator system.

Before leaving the discussion regarding the selection of the spanwise loading distribution on the rotor, it must be emphasized that wake-adapted vane systems such as the propeller and pumpjet have an unparalleled potential for the generation of secondary flows. To create secondary flows in blade passages, the primary requirement is an upstream component of vorticity normal to the relative flow at the blade inlet. It is obvious that with boundary-layer intake this condition is amply satisfied and, in contrast to axial-flow compressors where only a fraction of the blade span is subjected to a wall shear flow, the blading of a wake-adapted propulsor is subjected to these flows over the entire blade span. In reference 18, this secondary flow problem has been investigated both analytically and experimentally. Based on this reference, the following physical reasoning is presented with regard to the origin of the secondary flow.

The vane turns the fluid because of the pressure difference between the suction and pressure surfaces. If this pressure differential varies from one

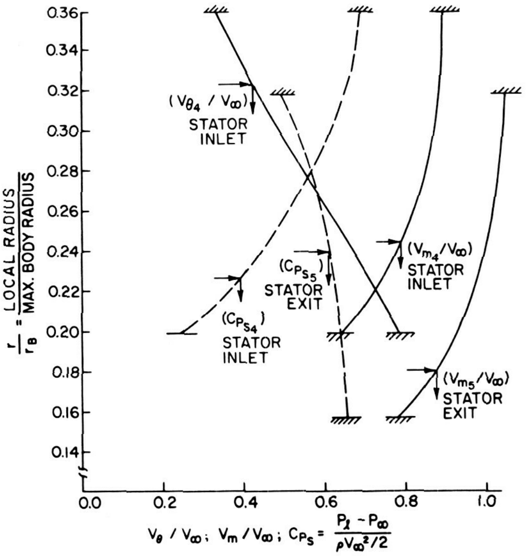

FIGURE 7.—*Velocity and static energy profiles at stator inlet and exit.*

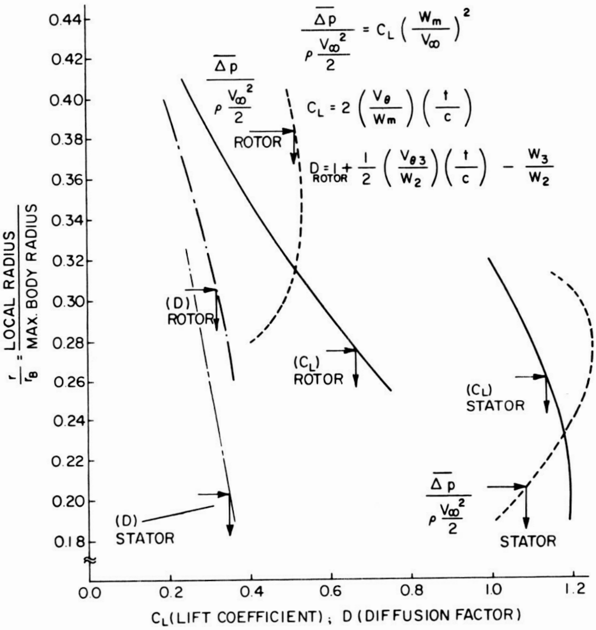

FIGURE 8.—*Spanwise distribution of lift coefficient, diffusion factor, and average pressure differential.*

spanwise location to the next, a spanwise pressure gradient will exist causing spanwise velocities which contribute to the secondary flow. This spanwise pressure gradient is represented by the radial distribution of $\overline{\Delta p}/(\frac{1}{2}\rho V_\infty{}^2)$ plotted in figure 8. It is obvious that the loading distribution could be improved in the aspect of reducing secondary flows. However, to obtain a uniform radial distribution of average pressure differential requires excessive fluid turning at the rotor hub sections. It is evident from this brief discussion that the relative magnitude of the loss in both efficiency and cavitation performance associated with minimizing secondary flows, avoiding excessive fluid turning, or discharging a jet having relatively high shear and kinetic energy losses must be considered in the selection of the loading distribution.

In summary, this phase of the preliminary design required several iterations to obtain a distribution of rotor head and blade solidity that satisfied propulsive energy requirements and blade cavitation and separation criteria. The blade solidity was chosen somewhat higher than necessary to ensure that the cavitation characteristics of the blading would be more critical with respect to the velocity of the relative flow than the blade loading. In the next section, additional consideration is given to these matters and to the detailed design of typical cylindrical blade sections for the rotor and stator.

MEAN STREAMLINE METHOD OF BLADE DESIGN

The design of blade sections requires the use of a method general enough to accommodate practical applications in which the blade sections are subjected to a flow which, in most cases, is not two dimensional. Most available methods contain a high degree of mathematical and computational complexity and, therefore, require a lengthy period of detailed study before they can be applied successfully. It appears to be impossible for the average designer to become familiar with a sufficient number of methods to be able to correct and modify the two-dimensional solutions to reflect the typical three-dimensional flows normally encountered. Even when automatic computation is used and programs are available, the designer must have a full understanding of the method of solution used.

Consequently, it is desirable for a designer to be familiar with a method that is not too complicated but which is still generally applicable. On this basis, the mean streamline method of reference 14 has been used at the Ordnance Research Laboratory for the blade design of a number of axial-flow pumps. This method of blade design, applicable to the indirect problem, has several very attractive features. Among the most important are

(1) It permits the designer to derive a blade shape of arbitrary thickness and chordwise loading distribution while providing a specified amount of fluid turning.

(2) It provides the capability to account for three-dimensional flow effects, such as changes in the axial velocity along the blade chord and changes in total energy relative to the blade row from leading edge to trailing edge.

Evaluations of the performance of axial-flow pumpjet designs, as determined in wind tunnel and water tunnel tests at the Ordnance Research Laboratory, have indicated values of blade thickness and loading distributions with satisfactory resistance to cavitation. The loading distribution clearly shows characteristics prevalent with trailing edge loaded blades, while the thickness distribution shows that the leading edge as well as the trailing edge should be kept thin. The thin forward portion of the blade, in conjunction with the loading distribution described above, desirably reduces the local blade surface velocities in the vicinity of the leading edge. This is important since this is the region that is most susceptible to the inception of cavitation.

As an illustration of the application of the mean streamline method of blade design, rotor and stator cylindrical blade sections have been designed for the Akron pumpjet at values of r/r_B equal to 0.345 and 0.265, respectively. These blade sections are located near the midspan position of each blade system.

The basic input data required to initiate the blade design procedure are the vehicle geometry and the flow properties at the rotor and stator inlet and exit stations. The change in the flow properties across a single element of the propulsor—for example, the rotor—is related to the average pressure change across the element by the impulse-momentum relation. Figure 9 depicts the basic geometric characteristics, velocity components, and flow directions for a rotor blade cylindrical section of axial length l located at a distance r from the centerline of a vehicle of maximum radius r_B. The meridional and peripheral velocity components at the inlet and exit stations are V_{m2}, and V_{m3} and $V_{\theta 3}$, respectively. Due to the taper of the body and the effect of the rotor, the streamline that enters the rotor at the radius r exits from the rotor at a radius less than r. The manner in which this nonaxial character of the flow influences the blade design procedure is described in the paragraphs that follow.

The development of a portion of the cylindrical section of radius r and thickness Δr is shown in figure 10. The rotation of the rotor at the angular velocity ω gives rise to the blade peripheral velocity, $U = r\omega$, as shown. The average pressure, $\overline{\Delta p}$, represents the uniform pressure which, when applied over the incremental area $l(\Delta r)$ in the time increment Δt produces a change in the peripheral momentum of the flow equal to $m(\Delta V_\theta)$. Thus the

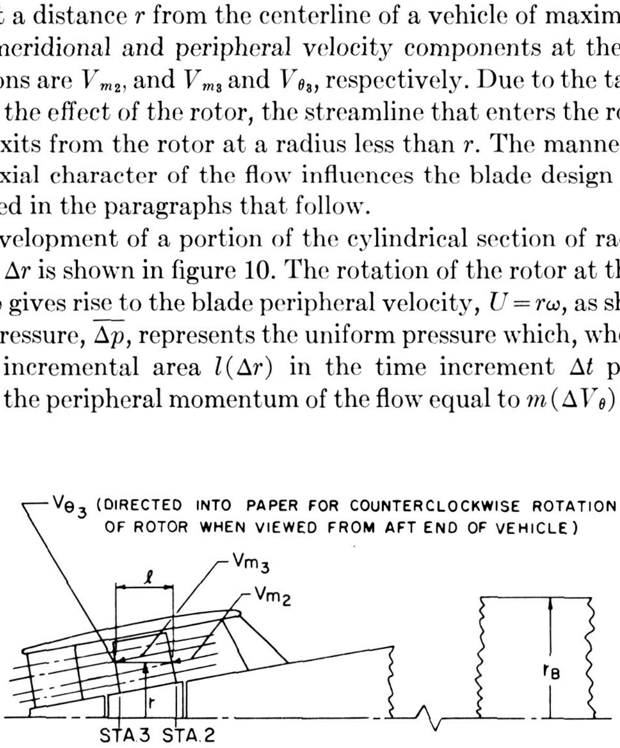

FIGURE 9.—*Basic geometric and flow characteristics.*

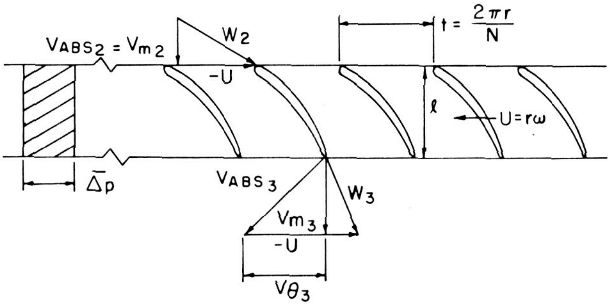

FIGURE 10.—*Rotor cylindrical section development.*

impulse-momentum relation, when applied in the peripheral direction, is

$$F(\Delta t) = m(\Delta V_\theta) \tag{25}$$

where

$$F = N(\overline{\Delta p})l(\Delta r)$$

$$\frac{m}{\Delta t} = 2\pi\rho V_m r(\Delta r)$$

$$\Delta V_\theta = V_{\theta_3} - V_{\theta_2}$$

Combining these with $V_m = \frac{1}{2}(V_{m_2} + V_{m_3})$ and $V_{\theta_2} = 0$ leads to the relation

$$\overline{\Delta p} = \frac{\pi\rho r}{Nl}(V_{m_2} + V_{m_3})V_{\theta_3} \tag{26}$$

By dividing this expression by the quantity $\frac{1}{2}\rho V_\infty^2$, the useful nondimensional expression presented as equation (27) is obtained.

$$\frac{\overline{\Delta p}}{\frac{1}{2}\rho V_\infty^2} = \frac{2\pi r_B}{Nl}\left(\frac{V_{m2}}{V_\infty} + \frac{V_{m3}}{V_\infty}\right)\frac{V_{\theta_3}}{V_\infty}\frac{r}{r_B} \tag{27}$$

The uniform pressure $\overline{\Delta p}$ is related to the actual axial pressure distribution $\Delta p = \Delta p(l')$ by the expression

$$\overline{\Delta p} = \frac{1}{l}\int_0^l \Delta p(l')\, d(l') \tag{28}$$

where l' denotes axial position along the rotor cylindrical section. The $\Delta p/(\frac{1}{2}\rho V_\infty^2)$ distributions and the level of the quantity $\overline{\Delta p}/(\frac{1}{2}\rho V_\infty^2)$ used in the design of the rotor and stator blade sections for the Akron propulsor are shown on the right in figures 11 and 12, respectively.

As defined by equation (27), the average pressure change is proportional to the total change in the peripheral velocity component. For the rotor, the variation of V_θ across the blade section from $V_\theta = 0$ at the inlet to $V_\theta = V_{\theta_3}$ at the exit would be a linear function of l' if $\overline{\Delta p}$ represented the actual loading distribution; i.e., if $\Delta p \neq \Delta p(l')$. However, since this is not the case, it is necessary to relate the variation of V_θ with l' to the variation of Δp with l'. This is achieved by dividing the loading distribution into segments and noting that

$$\left(\frac{V_\theta}{V_\infty}\right)_{l'=al} = \left(\frac{V_{\theta_3}}{V_\infty}\right)_{r_{3_{l'}}/r_B} \frac{\int_0^{l'} \Delta p\, d(l')}{\int_0^{l} \Delta p\, d(l')} = \left(\frac{V_{\theta_3}}{V_\infty}\right)_{r_{3_{l'}}/r_B} K_{aR} \tag{29}$$

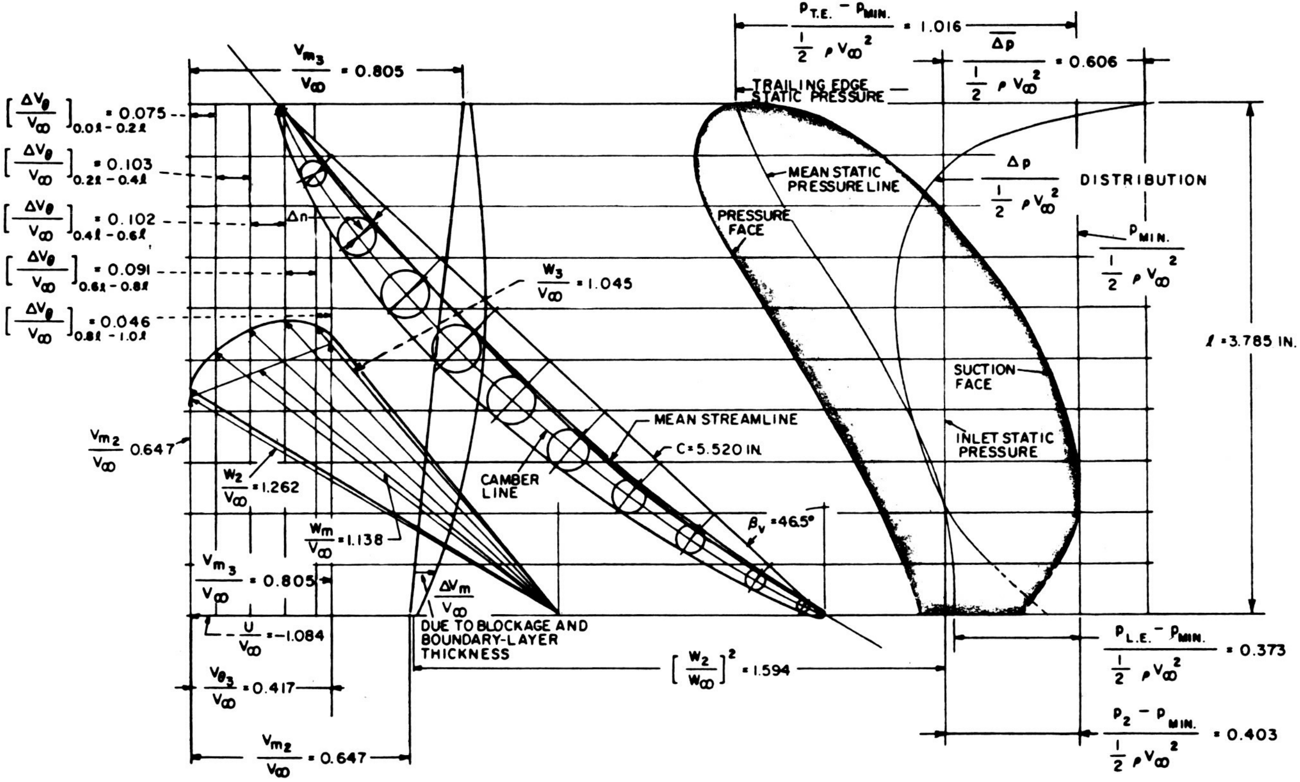

FIGURE 11.—*Rotor cylindrical design section at* $r/r_B = 0.345$.

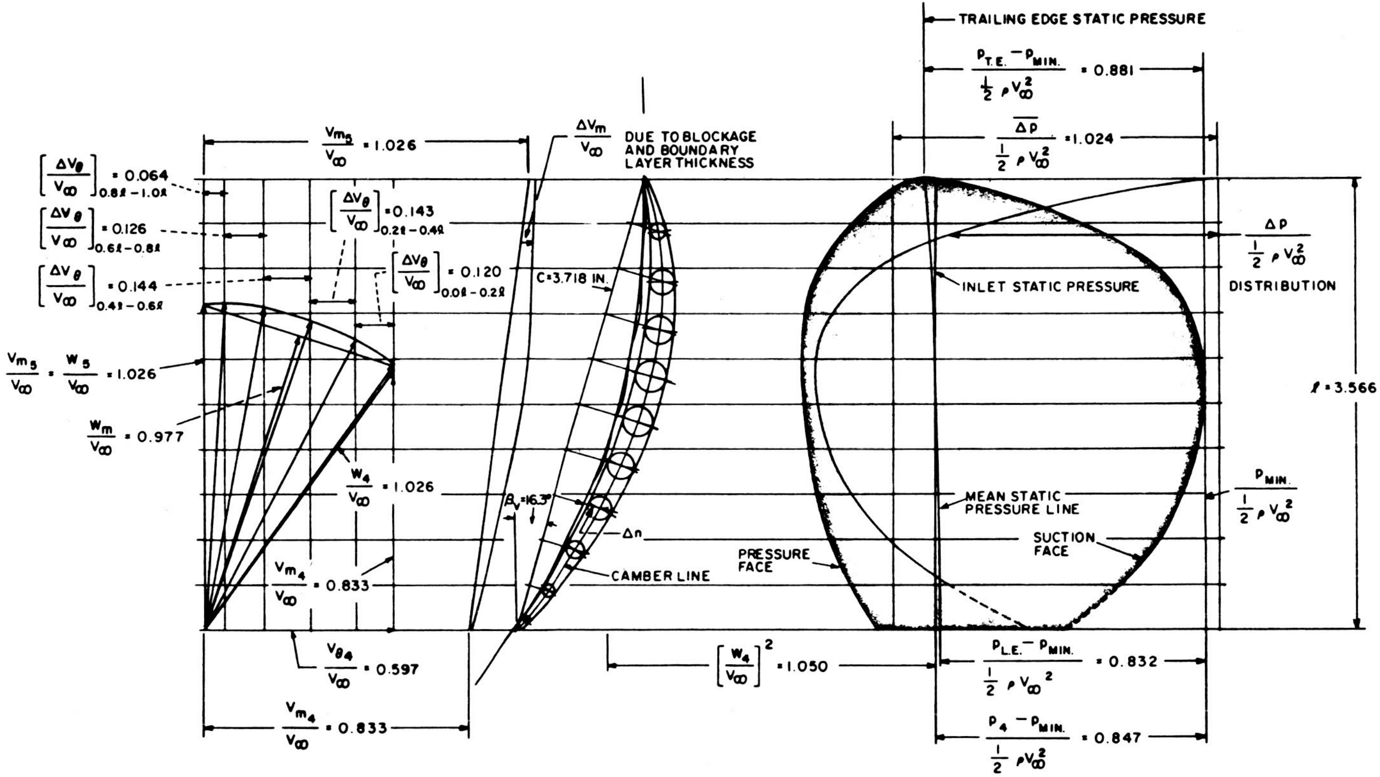

FIGURE 12.—*Stator cylindrical design section at* $r/r_B = 0.265$.

where $a=0, 0.2, 0.4, \ldots, 1.0$; $(V_{\theta 3}/V_\infty)_{r_{3_{l'}}/r_B}$ is the value of the peripheral velocity at the rotor trailing edge on the streamline that passes through the rotor cylindrical section at l'; and K_{aR} is a function of l'/l alone for a given loading distribution. The quantity $\int_0^{l'} \Delta p \, d(l')$ represents the area under the Δp versus l' curve between the points 0 and l' and $\int_0^{l} \Delta p \, d(l')$ represents the total area.

It is important to note that equation (29) as written applies to cases in which the propulsor element imparts a peripheral velocity component to flow that had only a meridional component at the inlet. In the case of the stator, the inflow contains both a meridional and a peripheral velocity component. The function of the stator is to reduce the peripheral component to zero at the trailing edge. Thus, for the stator, $K_{a_s}=1-K_{aR}$ where K_{aR} is the value given by inserting the stator loading distribution and the appropriate values of $(V_{\theta_4}/V_\infty)_{r_{4_{l'}}/r_B}$ into equation (29).

Examination of figures 2 and 9 reveals that the flow streamlines are inclined at an angle to cylindrical blade sections, and reference to figures 5 and 7 reveals that V_θ is a function of r at the rotor exit and at the stator inlet. Consideration of these factors has led to the following procedure for selection of the values of $(V_{\theta 3}/V_\infty)_{r_{3_{l'}}/r_B}$, or $(V_{\theta_4}/V_\infty)_{r_{4_{l'}}/r_B}$, to be used in equation (29). Referring to figure 2, and restricting consideration to the rotor, locate the points $l'=al$ along the line of length l determined by the intersection of the particular rotor cylindrical section under consideration with the plan view of the rotor. Streamlines passing through the points along l denoted by increasing values of l' can then be approximated and the radial position, denoted by $r_{3_{l'}}$, where these streamlines exit from the rotor can be determined. The flow along these streamlines enters the rotor with no peripheral velocity and must exit from the rotor at $r_{3_{l'}}$ with the peripheral velocity $(V_{\theta 3}/V_\infty)_{r_{3_{l'}}/r_B}$ given by entering the $V_{\theta 3}/V_\infty$ curve in figure 5 at $r_{3_{l'}}/r_B$. Thus the peripheral velocity at a point l' on a rotor blade cylindrical section is given by the product of the exit peripheral velocity associated with the streamline that intersects the cylindrical section at l' and the fraction of the loading that is concentrated between the leading edge and l'. Similar reasoning, when applied to the stator, leads to the conclusion that the peripheral velocity at a point l' on a stator blade cylindrical section is given by the product of the inlet peripheral velocity associated with the streamline that intersects the cylindrical section at l' and the fraction of the loading that is concentrated between the point l' and the trailing edge.

At this point, it is possible to construct a portion of the relative flow velocity diagrams shown on the left in figures 11 and 12. For the rotor section, with $r/r_B=0.345$ and $J=1.0$, $U/V_\infty=1.084$ by equation (21*b*). From figures 5 and 6, $V_{m2}/V_\infty=0.647$, $V_{m3}/V_\infty=0.805$, and $V_{\theta 3}/V_\infty=0.417$. The direction and magnitude of the inlet and exit relative velocity vectors W_2/V_∞ and W_3/V_∞ are given by vector addition of the components

$-U/V_\infty$ and V_{m2}/V_∞, and $(-U/V_\infty)+(V_{\theta 3}/V_\infty)$ and V_{m3}/V_∞, respectively. The mean relative velocity vector, W_m/V_∞, is also defined, as described in reference 14, since it terminates on the midpoint of the line connecting the end points of the inlet and exit relative velocity vectors. Application of the technique described above also defines the incremental changes $\Delta V_\theta/V_\infty$ associated with 20-percent length increments along l; thus vertical lines can be constructed based on the magnitude of these increments. If the blade section had no thickness and no boundary layer, the end points of the internal mean flow relative velocity vectors would be defined by the points of intersection of the vertical lines denoting the internal values of V_θ/V_∞ with the line joining the end points of the inlet and exit relative velocity vectors. However, since each blade has both physical thickness and a boundary layer, both of which act to reduce the flow area, the internal meridional velocity component must increase because of blockage. The mean streamline method of blade design requires that a guess be made, at this point, of the magnitude of the incremental change in V_m/V_∞ within the blade passage due to these factors. This permits construction of a curved line above the portion of the velocity diagram already constructed whose shape and level reflect the estimated change in the meridional velocity component. The points of intersection of this curved line with the vertical lines denoting the internal V_θ/V_∞ values then locate the end points of the relative velocity vectors as shown in figure 11. These relative velocity vectors thus denote the estimated magnitude and direction of the relative velocity at points on the cylindrical section corresponding to $0.0l$, $0.2l$, $0.4l$, $0.6l$, $0.8l$, and $1.0l$. The estimated increments in V_m/V_∞ at $0.0l$ and at $1.0l$ are due to the fact that the actual blade surface extends slightly forward of the $0.0l$ line and to the fact that the boundary-layer displacement thickness represents blockage at $1.0l$. Identical reasoning applied to the stator cylindrical section at $r/r_B=0.265$ permits construction of the relative velocity diagram shown on the left in figure 12. Note that in figures 11 and 12 the basic construction is made over a background of horizontal lines that subdivide l into 10 equal increments.

The mean streamline development is initiated by constructing a continuous line made up of segments extending from $0.0l$ to $0.1l$, $0.1l$ to $0.3l$, $0.3l$ to $0.5l$, $0.5l$ to $0.7l$, $0.7l$ to $0.9l$, and $0.9l$ to $1.0l$, respectively. The line segment extending from $0.0l$ to $0.1l$ is constructed parallel to the $0.0l$ relative velocity vector. The next segment in this line is then drawn, in the region from $0.1l$ to $0.3l$, by constructing a line segment parallel to the $0.2l$ relative velocity vector. The remaining segments are constructed by repeated application of this process and the mean streamline is developed by passing a spline curve through the points on this line at $0.0l$, $0.2l$, $0.4l$, $0.6l$, $0.8l$, and $1.0l$.

The blade cylindrical section is then specified by definition of the blade chord, the blade camber line, and the blade maximum thickness and thickness distribution. The steps required in this development are as follows:

(1) The approximate length of the blade chord is given by the length of the straight line that joins the points where the mean streamline intersects the $0.0l$ and $1.0l$ lines.

(2) The blade camber line is displaced from the mean streamline and is constructed by

(*a*) Determining the maximum value of the departure of the camber line from the mean streamline, $(\Delta n)_{\max}$, by use of equation (30).

$$(\Delta n)_{\max}=\left(\frac{\Delta n_1}{C}\right)_{\max} C\,C_L \tag{30}$$

In equation (30), $(\Delta n_1/C)_{\max}$, the maximum value of the ratio of the camber line departure from the mean streamline for unit lift coefficient to the chord length, is given in reference 14 as a function of β_V the vane chord angle measured from the axial direction. The lift coefficient is given by equation (31) where t, the blade-to-blade spacing, is given by $2\pi r/N$.

$$C_L=2\,\frac{V_\theta}{W_m}\,\frac{t}{C} \tag{31}$$

(*b*) Determining the variation of the departure of the camber line from the mean streamline as a function of position along the blade chord. In reference 14, the variation of $\Delta n/(\Delta n)_{\max}$ with distance from the blade leading edge in percent chord length is given as a function of the type of blade loading distribution. The values of $\Delta n/(\Delta n)_{\max}$ presented in table II have been used in recent propulsor designs at the Ordnance Research Laboratory. These values are identical to those presented in reference 14 except in the leading edge region where the magnitudes have been reduced in an attempt to reduce the susceptibility to leading edge suction face cavitation. Multiplication of these ratios by $(\Delta n)_{\max}$ as calculated above defines the variation of Δn with distance along the chord.

(*c*) Constructing lines perpendicular to the chord line at the chordwise points where Δn has been evaluated. Points on the camber line are then defined by locating points on these perpendiculars that are Δn units from the mean streamline. The camber line is then defined by passing a spline curve through these points.

(3) The blade thickness is distributed symmetrically about the camber line. The thickness is determined by the product of the ratios $(T/T_{\max})(T_{\max}/C)$ where $T/T_{\max}$ is expressed as a function of distance from the blade leading edge in percent chord length and $T_{\max}/C$ expresses the ratio of the maximum thickness to the chord length. Recent Ordnance

Research Laboratory designs have been based on the $T/T_{\max}$ distribution listed in table III and $T_{\max}/C = 0.065$. Specification of the blade cylindrical section is completed by (1) constructing lines perpendicular to the camber line at the chordwise points where the blade thickness has been defined, (2) defining points on the blade surface by locating points on these perpendiculars that are $T/2$ units on either side of the camber line, and (3) defining the blade contour by matching the end points of spline curves passed through these blade surface points to elliptical sections drawn symmetrically about the camber line end points.

TABLE II.—*Deviation of Camber Line from Mean Streamline*

Percent chord	$\Delta\eta/(\Delta\eta)_{\max}$
0	0.125
10	0.510
20	0.770
30	1.025
40	1.200
50	1.370
60	1.500
70	1.540
80	1.420
90	0.970
100	0

TABLE III.—*Blade Thickness Distribution*

Percent chord	$T/T_{\max}$
0	0
3	0.271
10	0.411
20	0.583
30	0.740
40	0.878
50	0.967
60	0.999
70	0.954
80	0.796
90	0.519
99	0.194
100	0

The blade section defined by this process represents a first approximation only since its construction was based on an estimate of the internal changes in V_m due to blockage and since the length of the chord was approximated by the length of the line joining the end points of the mean streamline. The chord length is defined as the length of the line that connects the end points of the camber line.

A second application of the mean streamline method of blade design should be made at this point. In this application, the internal changes in V_m can be calculated by utilizing values of the blade thickness measured normal to the meridional direction, taken from the initial approximation of the blade cylindrical section, and estimated values of the boundary-layer displacement thickness. In addition, the blade chord can be constructed by applying the value of Δn calculated for the zero-percent chord position in the initial approximation at the point where the revised mean streamline intersects the $0.0l$ line to locate the approximate true end point for the revised chord.

The calculation of the blockage correction to the meridional velocity is based on the following reasoning. As the flow proceeds through the blade passages, the meridional velocity is affected by blockage due to the blade thickness and to the boundary-layer displacement thickness. Thus, to satisfy the continuity equation, the local meridional velocity must increase above the base value which would exist in the absence of these factors. Base values of the meridional velocity for the Akron blade sections were obtained by assuming a linear variation of V_m with l' as indicated in figures 11 and 12. If the local base value of the meridional velocity is designated as $V_{ml'}$, then reference to figure 13 permits definition of the required correction $\Delta V_{ml'}$. Considering a cylindrical section of height Δr, the continuity equation becomes

$$\rho V_{ml'} t(\Delta r) = \rho(V_{ml'} + \Delta V_{ml'})(t - \tau)(\Delta r) \tag{32}$$

which reduces to

$$\frac{\Delta V_{ml'}}{V_\infty} = \frac{V_{ml'}}{V_\infty} \frac{\tau}{t - \tau} \tag{33}$$

where τ is the sum of the local blade thickness, measured normal to the meridional direction, and the total local boundary-layer displacement thickness. A rational estimate of the displacement thickness can be obtained by the method outlined in reference 16. This method requires the selection of a skin friction factor and a form factor representative of a turbulent boundary layer that has been subjected to an adverse pressure gradient.

Past experience has shown that two applications of the mean streamline method of blade design are generally sufficient. Exceptions have been

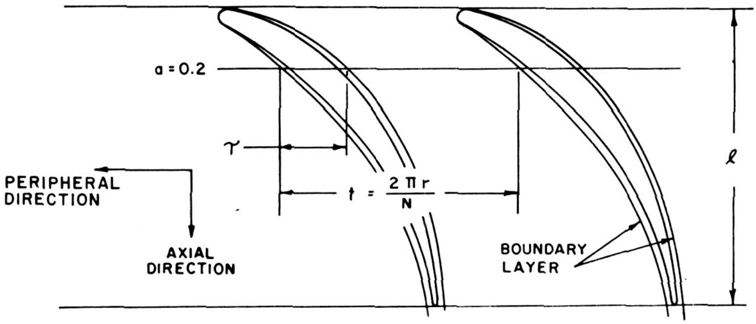

FIGURE 13.—*Cylindrical section development illustrating meridional flow blockage.*

noted in cases where a particularly poor initial guess of the blockage effects has been made; however, it is safe to say that this iterative design procedure converges very rapidly. The blade sections shown in figures 11 and 12 are based on three applications of the design method. For these sections, the differences between the blade profiles obtained in the second and third approximations were negligible.

The blade section pressure distributions shown in figures 11 and 12 were determined by (1) calculating the variation of the mean pressure, $p_{l'}$, with position along the axial length and (2) constructing the blade pressure diagram about the mean pressure line by dividing the $\Delta p/(\frac{1}{2}\rho V_\infty^2)$ distributions shown on the right in figures 11 and 12 between the suction and pressure sides of the blades in a two-thirds/one-third distribution.

The mean pressure variation was found by writing Bernoulli's equation to relate flow conditions on a streamline at the inlet to flow conditions at the point where the streamline crosses the blade cylindrical section. For the rotor, if the subscripts 2 and l' refer to points at the inlet and on l, then

$$p_2+\tfrac{1}{2}\rho V_{m_2}{}^2=p_{l'}+\tfrac{1}{2}\rho V_{ml'}^2+\tfrac{1}{2}\rho V_{\theta l'}^2-\frac{l'}{l}\,(\Delta P_T)-\rho U V_{\theta l'}$$

where ΔP_T represents the difference in total pressure at the inlet between streamlines that intersect l at $l'=0$ and at $l'=l$, and $\rho U V_{\theta l'}$ represents the pressure increment associated with development of the rotor head H.

Nondimensionalizing these relations by the factor $\frac{1}{2}\rho V_\infty{}^2$ leads to equation (34) which is the desired form for the variation of the mean static pressure as a function of l' for rotor blade cylindrical sections.

$$\frac{p_{l'}-p_2}{\frac{1}{2}\rho V_\infty{}^2}=\left(\frac{V_{m2}}{V_\infty}\right)^2-\left(\frac{V_{ml'}}{V_\infty}\right)^2-\left(\frac{V_{\theta l'}}{V_\infty}\right)^2+\frac{l'}{l}\,\frac{\Delta P_T}{\frac{1}{2}\rho V_\infty{}^2}+2\,\frac{U}{V_\infty}\,\frac{V_{\theta l'}}{V_\infty} \qquad (34)$$

Equation (35) was derived on the basis of similar reasoning and represents the variation

$$\frac{p_{l'}-p_4}{\frac{1}{2}\rho V_\infty^2}=\left(\frac{V_{m_4}}{V_\infty}\right)^2+\left(\frac{V_{\theta_4}}{V_\infty}\right)^2-\left(\frac{V_{ml'}}{V_\infty}\right)^2-\left(\frac{V_{\theta l'}}{V_\infty}\right)^2+\frac{l'}{l}\,\frac{\Delta P_T}{\frac{1}{2}\rho V_\infty^2} \qquad (35)$$

of the mean static pressure with l' for stator blades.

The basis for the two-thirds/one-third distribution of the static pressure change between the suction and pressure sides of the blade is empirical and is based on examination of the NACA cascade test results. An experimental cascade program is in progress at the Ordnance Research Laboratory at present, one of whose objectives is a critical evaluation of available theoretical and empirical blade design methods. A summary of this program is presented in Appendix II. Results from this program will be used as they become available to verify and/or modify the mean streamline method of blade design.

Values of the cavitation index σ and of the diffusion factor D, defined by equation (15) with $p_V=p_{\min}$, and by equation (24), respectively, are presented in the following table for the rotor and stator blade sections. These values are well below the maximum design values, $\sigma=0.650$ and $D=0.500$.

Blade Section	σ	D
Rotor at $r/r_B=0.345$	0.244	0.273
Stator at $r/r_B=0.265$	0.314	0.304

The design of individual cylindrical blade sections for the rotor and stator of the Akron pumpjet has been described in detail. An adequate design of the rotor and stator blading would require the design of additional cylindrical sections at values of r/r_B both above and below the values selected here for illustrative purposes.

LIST OF SYMBOLS

A	Area
A_B	Frontal area of body
A_s	Wetted surface area
a	Fractional portion of projected chord length
C_{DS}	Shroud frictional drag coefficient based on body frontal area
C'_{DS}	Shroud frictional drag coefficient based on shroud wetted surface area
C_T	Thrust coefficient
C_{DBB}	Bare-body drag coefficient
C_b	Blade pressure coefficient

C_P	Power coefficient
C_m	Mass flow coefficient
C_L	Lift coefficient
C	Chord length
D_B	Maximum body diameter
D	Diffusion factor
g	Gravitational constant
H	Head (fluid energy)
H_R	Head (shaft energy)
h_{sub}	Submergence depth in feet
h_{atm}	Atmospheric head in feet
J	Advance ratio
K	Inlet loss coefficient
K_{a_R}	Rotor load distribution factor
K_{a_S}	Stator load distribution factor
l	Projected length of chord in peripheral direction
l'	Fractional distance of l defined by $l' = al$
l_s	Shroud chord length
N	Number of blades
n	Rotor shaft speed
$(\Delta n)_{\max}$	Maximum departure of camber line from mean streamline (normal to chord)
P_T	Total pressure
p	Static pressure
r	Local radius
r_B	Maximum body radius
r_T	Tip radius
r_H	Hub radius
$r_{3_{l'}}$	Radial position at rotor trailing edge of the streamline that passes through the rotor cylindrical section at l'
$r_{4_{l'}}$	Radial position at stator leading edge of the streamline that passes through the stator cylindrical section at l'
r_{ψ_1}	Radial location of stagnation streamline at Station ①
T	Blade thickness normal to camber line
t	Blade pitch, defined as $t = 2\pi r/N$
U	Peripheral blade velocity
V	Absolute velocity
W	Relative velocity
W_m	Mean relative velocity
β_v	Vane angle between chord line and axial direction
γ	Volumetric density
θ	Angle between meridional and axial direction
η_H	Hydraulic efficiency
ρ	Mass density

σ	Cavitation index
ω	Angular velocity
Δ	Incremental difference

Subscripts

1, 2, 3, 4, 5, 6, 7	Flow stations of figure 2
a	Axial component
m	Meridional component
θ	Peripheral component
∞	Ambient free-stream conditions

Superscripts

$-$	Average value of quantity based on mass flow rate
$=$	Average value of quantity based on momentum
$\sim$	Average value of quantity based on energy

APPENDIX I. Computerized Streamline Curvature Method

The indirect turbomachine design problem entails the specification of a blade geometry to produce a set of desired performance characteristics. Within the limits of the current development, the solution of the indirect problem requires the determination of the inlet and exit velocity profiles produced by a specified peripheral velocity distribution at the blade boundary planes and any associated variation in total pressure through the blade passage.

Simple radial equilibrium theory has often been used to gain a first approximation of the velocity distributions; however, this method neglects the effects of the meridional curvature of the streamlines and is rather limited in the variety of situations to which it is applicable. When the effects of the meridional radius of curvature are included in the radial equilibrium equation, the calculation process is termed the streamline curvature method. Smith, Traugott, and Wislicenus in reference 19 presented a detailed analysis which included these streamline curvature effects.

Historically, attempts to accurately employ the streamline curvature method have been hampered by the necessity of physically measuring the geometric input data and by the tedious iterations required for a solution. The current development of the streamline curvature method as an accurate design procedure has been made possible by the use of digital computers to perform the iteration processes and by the advent of the so-called spline functions (ref. 20) for data specification.

The spline function is a mathematical model of a thin elastic beam used to represent a draftsman's plastic spline. The importance of the spline function is its ability to accurately produce valid and continuous values of a function, and of its first and second derivatives. Thus, by employing spline functions to specify the flow parameters and stream patterns, it is no longer necessary to rely on physical measurements of slopes and radii of curvature. These properties can be calculated directly from the spline functions.

The current development of the computerized solution of the indirect axisymmetric turbomachine problem by the streamline curvature method relied heavily on the work of Novak in reference 21. A detailed development of the basic equations of motion and of the computer program (SCM I) is presented in reference 15, where the problem to be solved is stated as follows: Given the geometry of the flow boundaries, the reference pressure and velocity profiles, and the desired blade performance (i.e., the peripheral velocity distribution at the blade exit planes), determine the streamline pattern and the associated pressure and velocity distributions for the axisymmetric flow through the blade system.

Essentially, the program computes an iterative solution using the cylindrical form of the equations interrelating (1) continuity, (2) conservation of angular momentum, (3) constant total pressure along a streamline in the absence of any energy sources, and (4) radial equilibrium. The following assumptions have also been included in the analysis:

(1) The flow is axisymmetric and free of secondary flows.

(2) The fluid is inviscid and incompressible.

(3) The flow processes occur under steady-state conditions and at a constant temperature.

(4) All pressure losses along the streamlines are neglected.

A typical flow field to be analyzed is illustrated by the geometry in figure 2, where the velocity and pressure distributions at Station ① are assumed to be known from experimental or theoretical data and where the peripheral velocity distributions at the exit planes of the rotor and stator have been specified. The axial station locations are chosen so that they accurately describe the geometry of the flow field and are in locations of desired data output.

Spline curves are passed through the input data as a function of radial distance at the appropriate stations. At the reference station, Station ① the streamline location is derived based on equal increments of mass flow rate coefficient between streamlines. The first approximation of the streamline pattern at the remaining stations is formed in proportion to the flow area at the respective station. Spline curves are passed through this streamline pattern and the necessary geometric properties are calculated. The total pressure coefficient is specified as a constant along a given streamline from the reference station to the rotor inlet; at the rotor exit the total pressure is incremented by the rotor head and specified as a constant at the new value for the remaining stations.

The appropriate equations and required data from the spline curves are employed to determine the meridional velocity profiles for all stations other than the reference station. This entails an iteration process between the assumed value of meridional velocity at the midstreamline and the continuity equation. These newly formed profiles are integrated to determine a new streamline pattern which is then adjusted according to the procedure suggested by Horlock in reference 22. Spline curves are then developed to define these new streamline shapes as a function of axial position. The entire process is repeated until the difference in streamline location for two successive passes through the program is within a specified limit for all streamlines at all stations. When this static condition is reached, the program has defined the final solution.

The program then enters the output phase. Geometrically, the output data at each station may be specified along a line at any specified angle with respect to the centerline. At each station the program outputs the x and y coordinates of the streamline pattern and the corresponding values of meridional velocity ratio, peripheral velocity ratio, static pressure coefficient, total pressure coefficient, local flow angle, and the meridional radius of curvature of the streamline. Also included in the output are the evaluations of the mean rotor head and torque coefficient.

The results of the program have agreed very well with alternate axisymmetric solutions such as the graphical technique described by Gearhart in reference 23. In general, the agreement between experimental data and that presented by the SCM I computer program is good; the differences are thought to result from real fluid effects not included in this perfect fluid solution. It is planned to incorporate an empirical estimate of the streamwise and spanwise energy losses in the near future.

APPENDIX II. ORL Cascade Research Program

Success in performing fundamental turbomachinery research using the subsonic cascade tunnel as the basic experimental tool is exemplified by the results of the research effort at the University of Liverpool which are summarized in reference 24.

With a subsonic porous wall tunnel not only can two-dimensional flow be obtained, but the capability of varying the axial velocity ratio exists and it is possible to obtain cascade performance data over a range of axial velocity ratios. With such capability, the blade boundary-layer growth and secondary flows can be modeled and studied in detail. Blade end wall losses and blade separation limits can also be established. Efforts at the

Ordnance Research Laboratory directed toward the development of hydrodynamic blading having surface velocities of minimum magnitude near the blade leading edge, thereby providing maximum resistance to cavitation, have required the design, fabrication, and operation of a cascade flow facility as shown by figures 14 and 15.

The initial tests in this facility are being directed toward clarifying two problems which remain regarding the application of the mean streamline method of design.

(1) A risk is encountered when using trailing edge loaded blades which create steep, adverse pressure gradients near the trailing edge. The degree of adversity of a pressure gradient can only be decided by cascade tests which can show whether a design load distribution over a blade is satisfactory or unsatisfactory. Use of a trailing edge loaded blade implies that an adverse pressure gradient on the forward portion of the blade has been intentionally reduced to provide increased cavitation resistance while the pressure gradient at the aft end has been made more adverse to permit carrying the same total load as a forward loaded blade. Concerning blade losses (not cavitation resistance), the NACA has developed trailing edge loaded profiles of acceptable performance as reported in reference 25. In a similar manner, through cascade tests, the Ordnance Research Laboratory must produce similar performance curves for their profiles which have different thickness and loading distributions.

(2) The mean streamline method of design, reference 14, is semi-empirical in that the deviation of the blade camber line from the mean streamline is based on offsets derived from existing NACA cascade data. Generating similar cascade data for blading having an extended range of

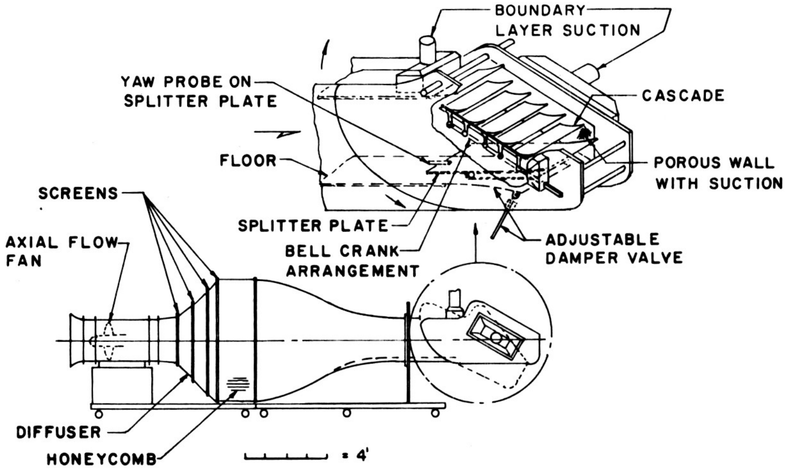

FIGURE 14.—*Schematic of subsonic cascade tunnel.*

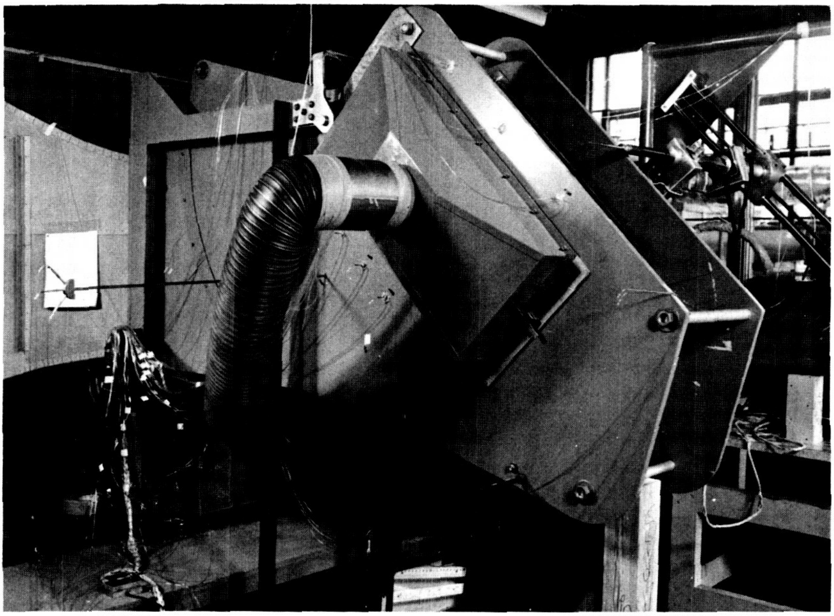

FIGURE 15.—*Test section of cascade tunnel.*

solidities ($c/t > 1.5$), and with alternate thickness and loading distributions will further strengthen an already proven design method.

On this basis, a series of two-dimensional blade geometries utilizing the table III thickness distribution and the loading distributions of figures 11 and 12 have been designed and fabricated to permit an experimental evaluation of their pressure distributions and loss characteristics. Concurrently, a theoretical analysis of these cascade geometries is being conducted. Successful prediction of the pressure distribution of the tested blade geometries using the theoretical analysis will permit many geometries to be analyzed theoretically with only periodic experimental verification to ensure that the limitations of the potential solution have not been exceeded.

The theoretical solution selected for use in this program is outlined in reference 26. This reference also lists the computer program for use on an IBM 7090. The terminology in the reference is somewhat different from that commonly used in NACA compressor cascade reports. The program has been rewritten for use on the IBM 360 digital computer and the geometry of the cascade has been redefined in the more common cascade terminology. Application of this analysis to various cascade geometries and a listing of the program for use on the IBM 360 digital computer is given in reference 27. In this reference, it is shown that the comparison between the pressure diagrams obtained analytically and those obtained experimentally by the NACA for the same cascade geometries is quite good, even for blades operating far from zero incidence. As might be expected, the analytical solution predicts more turning of the flow than is obtained experimentally. This difference is thought to be due to viscous effects which are neglected in the analytical solution.

An effort has been initiated which will permit including real fluid effects in the potential solution. The revised method will require using the potential flow pressure distribution to obtain the boundary-layer displacement thickness along the pressure and suction surfaces of the blade. This thickness will then be added to the blade thickness and the resulting cascade geometry will be reinserted in the Douglas Neumann program of reference 27 to obtain corrected fluid deflection data.

The experimental results which have been obtained from the cascade program to date are reported in reference 28. A summary is also presented in this reference of the test procedures, operating characteristics, and capabilities of the cascade test facility.

REFERENCES

1. Brandau, John H., *Aspects of Performance Evaluation of Waterjet Propulsion Systems and a Critical Review of the State-of-the-Art.* NSRDC Report 2550, October 1967.
2. Gearhart, W. S., and R. E. Henderson, Selection of a Propulsor for a Submersible System. *J. Aircraft,* Vol. 3, No. 1, January-February 1966.
3. Wislicenus, G. F., and L. R. Smith, *Hydraulic Jet Propulsion and Incipient Cavitation.* Internal Flow Research Report I-6, Part A, Johns Hopkins U. Mech. Eng. Dept., March 21, 1952.
4. Brooks, J. D., and T. G. Lang, Simplified Methods for Estimating Torpedo Drag. *Underwater Missile Propulsion,* L. Greiner, ed., Compass Publications, Inc. (Arlington, Virginia), 1967, pp. 117–146.
5. Mayer, A., and F. J. Hill, *On a Rapid Estimate of Inlet Velocity Distribution for a Pumpjet Operating in a Prediffused Turbulent Boundary Layer of an Axially Symmetric Body.* NOTS Report TM 671.
6. Freeman, *H. B., Measurements of Flow in the Boundary Layer of a 1/40 Scale Model of the U.S. Airship Akron.* NACA Report No. 430, 1932.
7. Wislicenus, G. F., Hydrodynamics and Propulsion of Submerged Bodies. *J. Am. Rocket Soc.,* Vol. 30, 1960, pp. 1140–1148.
8. Thurston, S., and M. S. Evanbar, *The Efficiency of a Propulsor on a Body of Revolution Inducting Boundary Layer Fluid.* AIAA Paper No. 65–234, presented at the Marine Systems and ASW Conference (San Diego), March 1965.
9. Schlichting, H., Application of Boundary Layer Theory in Turbomachinery. *Trans. ASME, J. Basic Eng.,* Series D, Vol. 81, 1959, pp. 543–551.
10. Eskinazi, S. J., C. D. Flagle, J. R. Ruetenik, and J. R. Weske, *A Problem in Retardation of a Turbulent Boundary Layer.* Inst. Cooperative Res., Johns Hopkins U., Report I–6, Part B, March 1952.
11. Rains, D. A., *Tip Clearance Flows in Axial Flow Compressors and Pumps.* Cal. Tech., Report 5, June 1954.

12. MITCHELL, A. B., *An Experimental Investigation of Cavitation Inception in the Rotor Blade Tip Region of an Axial Flow Pump.* ARL Report ARL/R1/G/HY/11/2, August 1958.
13. GEARHART, W. S., Tip Clearance Cavitation in Shrouded Underwater Propulsors. *J. Aircraft,* Vol. 3, No. 2, March–April 1966.
14. WISLICENUS, G. F., *Fluid Mechanics of Turbomachinery,* Volumes 1 and 2. Dover Publications, Inc. (New York), 1965.
15. TREASTER, A. L., *Computerized Application of the Streamline Curvature Method to the Indirect, Axisymmetric Turbomachine Problem.* ORL TM 514.2491–16, October 31, 1969.
16. HENDERSON, R. E., J. F. MCMAHON, AND G. F. WISLICENUS, A Method for the Design of Pumpjets. *Underwater Missile Propulsion,* L. Greiner, ed., Compass Publications, Inc. (Arlington, Virginia), 1967, pp. 117–146.
17. LIEBLEIN, S., F. C. SCHWENK, AND R. L. BRODERICK, *Diffusion Factor for Estimating Losses and Limiting Blade Loading in Axial Flow-Compressor Blade Elements.* NACA RM53D01, June 1953.
18. SMITH, L. H., *Three Dimensional Flow in Axial-Flow Turbomachinery,* Parts I and II. Reports I–14 and I–16, Inst. Cooperative Res., Mech., Eng. Dept., Johns Hopkins U., November 1953.
19. SMITH, L. H., S. C. TRAUGOTT, AND G. F. WISLICENUS, A Practical Solution of a Three-Dimensional Flow Problem of Axial-Flow Turbomachinery. *Trans. ASME,* Vol. 75, No. 5, July 1953.
20. DAVIS, R. F., *Spline Curve Fit Functions, Their Derivation and Use.* ORL TM 512.3531–02, July 23, 1968.
21. NOVAK, R. A., *Streamline Curvature Computing Procedures for Fluid Flow Problems.* ASME Paper 66–WA/GT–3, November 27, 1966.
22. HORLOCK, J. H., *Axial Flow Turbines.* Butterworth Scientific Publications (London), 1966.
23. GEARHART, W. S., *Graphical Analysis of Incompressible Axisymmetric Flow.* ASME Symposium on Pumping Machinery for Marine Propulsion (Philadelphia), May 6, 1968.
24. HORLOCK, J. H., Some Recent Research in Turbo-Machinery. *Proc. Inst. Mech. Engrs.,* Vol. 182, Part I, No. 26, 1967–68.
25. ERWIN, J. R., M. SAVAGE, AND J. C. EMERY, *Two-Dimensional Low-Speed Cascade Investigation of NACA Compressor Blade Sections Having a Systematic Variation in Mean-Line Loading.* NACA TN 3817, November 1956.
26. GIESING, J. P., *Extension of the Douglas Neumann Program to Problems of Lifting Infinite Cascades.* U.S. Department of Commerce Report No. LB31653, AD605207, Revised July 2, 1964.
27. ROSS, J. R., AND L. E. ESKAY, *The Application of the Douglas Neumann Computer Program to the Analysis of Blade Cascade Geometries.* ORL TM 506.2491–31, January 31, 1969.
28. GEARHART, W. S., AND J. R. ROSS, *A Subsonic Cascade Test Facility, an Aid to Hydrodynamic Blade Design.* ORL TM 506–02, March 13, 1970.

DISCUSSION

L. MEYERHOFF (Eastern Research): Obtaining a ducted propeller design for operation in a boundary layer at the rear of a body is a difficult task. It is a nonpotential (rotational) problem, often approximated in the literature without substantive justification by a combination of potential and nonpotential methods. In the broad sense, it is necessary to contend with the effects of radially varying boundary-layer velocities, body shape, duct shape, and propulsor-body-flow interaction. To this is added the additional complication of obtaining cavitation delay for the blading and duct surfaces.

The authors present a rational approach to the problem, showing the important techniques they have developed. The discussion which follows relates mainly to the first part of the authors' paper, on the initial performance study, and, in particular, to the problem of determining where the inflow station ahead of the propulsor is to be located.

The initial performance study begins with the flow picture shown in figure 2. Here, the upstream inflow station (Station ①) is seen, as well as the propulsor which adds a total pressure rise to the flow and, finally, the issuing jet at Station ⑦. In general, all flow quantities at all stations will be radially varying. The significance of the inflow station is that its location determines the initial velocity and static pressure profiles needed for calculating both the overall propulsion design parameters and the final flow field.

It would seem that the inflow station should be defined as the first axial location ahead of the propulsor where the bare-body flow is not affected by the propulsor operation. Aft of this location, the mutual interaction of body and propulsor flows will alter the bare-body flow. Clearly, it is a difficult analytical problem to determine such a location.

How important are these considerations from the viewpoint of a practical initial performance prediction? Some preliminary information on this question follows.

In the authors' paper, the inflow is taken at a location about 82 percent back from the body nose; at this station, the bare-body static pressure coefficient is zero. Boundary-layer velocities are given in reference 6 of the authors' paper.

Eastern Research Group (ERG) has obtained corresponding performance results using three other nearby inflow stations which bracket the authors' 82-percent location.

Figure D–1 shows these velocity profiles of reference 6 at 67.9-percent, 77.5-percent, and 86.9-percent axial body stations; body static pressure coefficients at these stations are about −.075, −.025, and +.030, respectively.

These flow velocities were inserted as input data for a computer program developed at ERG. Since the radial variation of static pressure at the inflow stations is not available in reference 6, this will be taken as radially constant but at one-half the values given previously. (The authors take a zero value.)

The thrust equation used by ERG is

$$\text{Thrust} = \int (V_7 - V_1 \cos\theta)\, d(\text{mass flow}) - \int (p_1 - p_7)\, dA_1$$

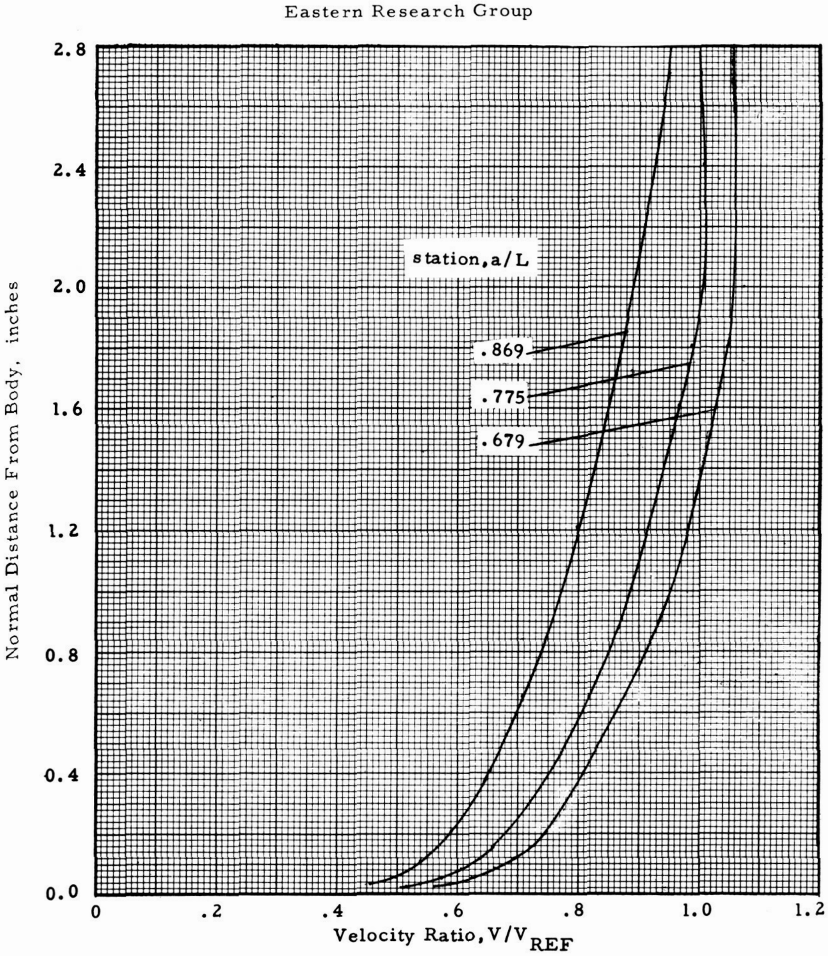

FIGURE D–1.—*Akron boundary-layer profiles.*

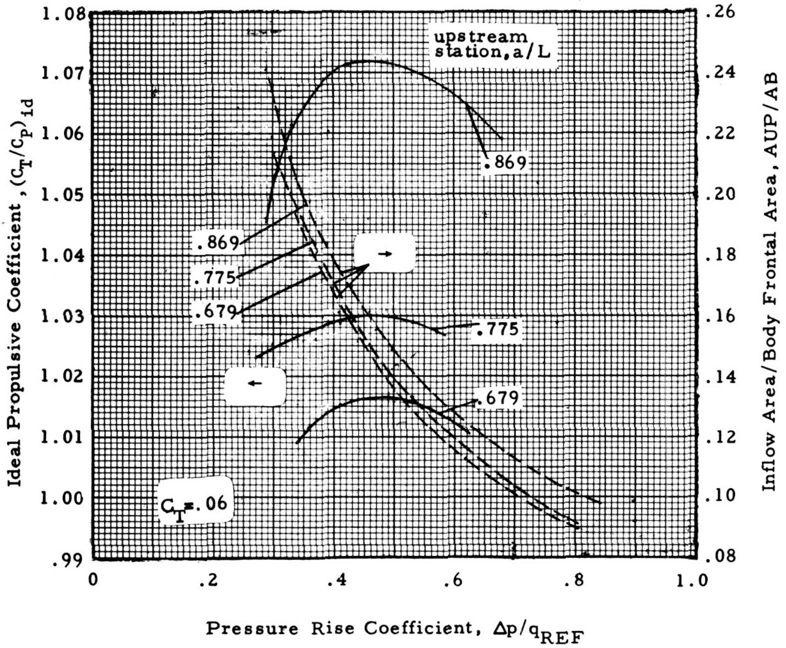

FIGURE D–2.—*Ideal efficiency and inflow area versus required propulsor pressure rise.*

where p_7 is assumed to be the static ambient value at the body centerline. The need for the static pressure term is avoided in the authors' paper by choosing an inflow station where the pressure is ambient and assuming, as in the ERG equation, that the jet static pressure is at the ambient value.

Figure D–2 shows the effect of inflow station location on ideal efficiency[D-1] defined by $(C_T/C_p)_{id}$ and inflow area ratio A_1/A_B. This ideal efficiency does not contain blading efficiency or duct inflow loss. The thrust coefficient is $C_T = .06$. The abscissa of figure D–2 is the total pressure rise coefficient needed to produce $C_T = .06$, and is taken as radially constant; q_{REF} is the free-stream dynamic pressure. Efficiencies are seen to progressively increase as the inflow station is moved back from the body nose. A maximum 6-percent difference is seen between the 67.9-percent and 86.9-percent stations. The total pressure rise required at maximum

---

[D-1] Propulsive coefficient (P.C.) is generally defined as RV/power; where R is bare-body resistance, V is vehicle speed, and power is that delivered to the rotor. The relation between P.C. and the ideal efficiency $(C_T/C_P)_{id}$ of figure D–2 is P.C. = $(C_T/C_P)_{id}\ (1 - t)\eta$, where η is the conventional blading efficiency and $1 - t$ is the naval architect's thrust factor; i.e., required net thrust equals [bare-body resistance/$(1 - t)$] + duct drag (with rotor operating). The authors' paper assumes $t \sim 0$; see the sixth paragraph of the section on optimum propulsor mass flow.

efficiency appears to be independent of inflow location. Inflow area ratios, A_1/A_B, shown in figure D–2 are seen to increase with distance back along the body.

Figure D–3 shows the effect of inflow station on the local velocity ratio at the stagnation line radius of Station ① (fig. 2 of authors' paper). This velocity is seen to change significantly with inflow station location. The differences in velocity ratios in figure D–3 can be of importance for rotor blade cavitation inception.

Figure D–4 shows the jet radius and mass flow coefficient corresponding to the data in figure D–2 and D–3. The jet radius appears to be independent of inflow station location and this may be peculiar to the body velocity profiles used. It is interesting to observe that the jet radius is

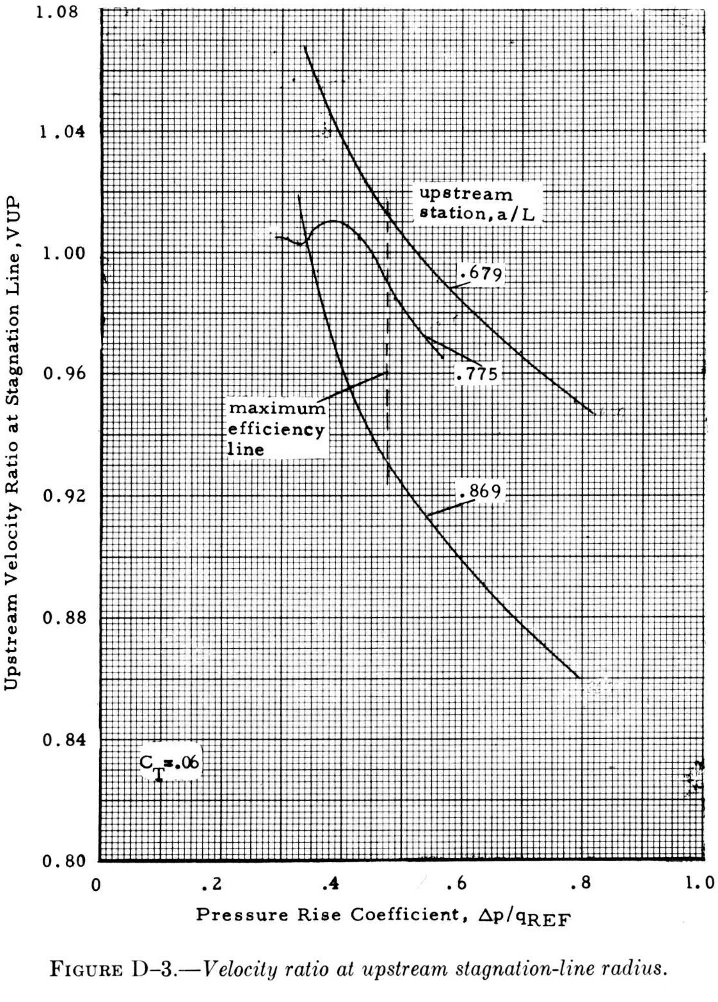

FIGURE D–3.—*Velocity ratio at upstream stagnation-line radius.*

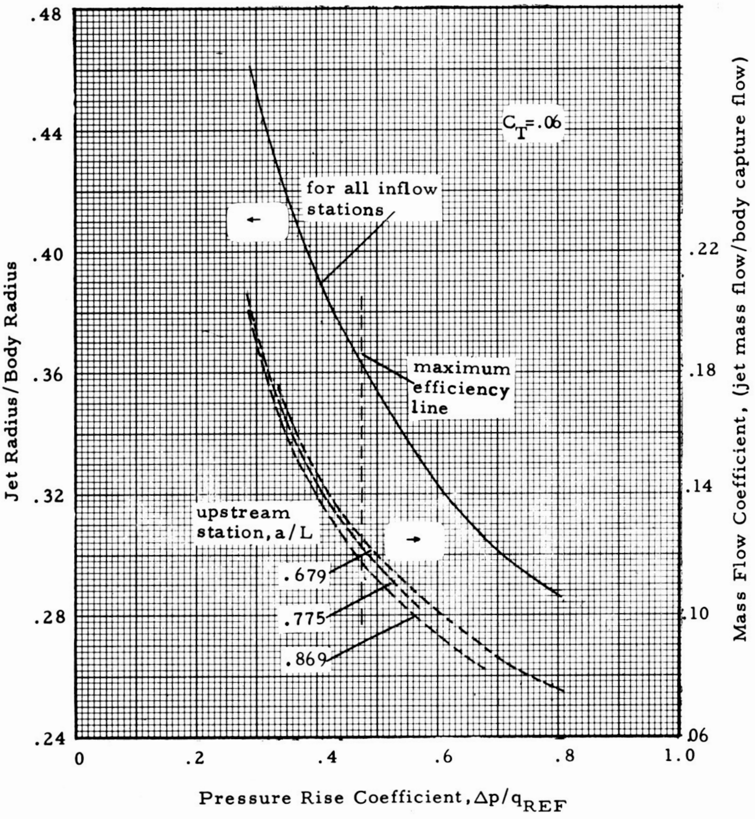

FIGURE D–4.–*Jet radius and mass flow.*

about 36 percent of the maximum body radius for peak ideal efficiency. Mass flow changes in figure D–4 are seen to have a relatively small change with inflow station.

It can be concluded that the selection of the inflow location may have a significant effect. The choice of the inflow location appears to affect the efficiency, upstream velocity, and inflow streamtube area. Still unresolved is the effect of inflow station on the detailed flow field.

Finally, there appear to be differences in results between the averaged flow method of the authors' paper and the direct integration approach as used by ERG. At the maximum efficiency point for the 82-percent station, these differences are

(1) Inflow area ratio is about 0.12 (fig. 3) versus 0.19 in figure D–2.

(2) Stagnation line velocity at ① is about 0.90 (figs. 1 and 3) versus 0.97 in figure D–3.

W. B. MORGAN (Naval Ship Research and Development Center): I have two comments. The first is in regard to the performance obtained using this procedure. How well do you predict the shaft horsepower?

The other question has to do with the optimum mass flow. I take exception to the word optimum if I understand correctly what you mean. We want to design for given speed or given cavitation characteristics and it really is not quite clear how we select the duct in the sense of its length. Also, it seems that the use of just the optimum mass flow does not properly take into consideration the drag of the duct, the induced drag about the duct, the interaction between the duct and the hull, and the interaction between the impeller and hull. These really are not all considered, and I wonder, when you talk about the optimum diameter using optimum mass flow, how close that is.

BRUCE, GEARHART, ROSS, AND TREASTER (authors): The comments of Dr. Meyerhoff with regard to the care that must be exercised in selecting the location of the upstream reference station are highly pertinent. This is particularly true if one is considering the flow to be inviscid downstream of this station. The momentum and energy relations which are subsequently utilized to predict the overall performance of the propulsor are quite dependent on the reference station flow characteristics. In addition, the induced effects of the shroud on the reference station flow characteristics must be considered. A potential solution indicates that the upstream induced flow effects from a cascade of blade profiles are negligible one chord length upstream. On this basis, the authors' practice has been to select a reference station at least one shroud length upstream of the shroud inlet.

In the paper, the drag coefficient was not held constant as ingested mass flow changed, but was varied in a manner that reflected the inlet losses and the added frictional drag on the shroud. This is felt to be more realistic than the approach used in the analysis of the discussor and could account, to some degree, for the deviations in the results. From Dr. Meyerhoff's analysis, he reaches the conclusion that neither rotor total pressure rise nor pumpjet mass flow varies with choice of reference station, which implies that required shaft power does not depend on choice of reference station. This effect is felt to be artificial due to the fact that shroud drag was held constant in his calculations.

Dr. Morgan inquired about the degree of success that had been experienced in applying the design approach of the paper. A number of pumpjet propulsors have been designed over a relatively wide spectrum of advance ratios and ingested mass flow coefficients. Model tests of these units indicate that predicted and measured shaft torque at a given shaft speed can be matched within 3 to 4 percent. Cavitation performance has been found to generally exceed those values predicted by the methods outlined.

Several units have been tested which provided overall cavitation indices less than 0.5.

With regard to the comments on the method for selecting the optimum mass flow, consider a ring shroud moving forward along a line parallel to its axis of revolution and its similarity to an infinite airfoil. In steady flow there are no vortices shed since there are no circumferential changes in circulation. Therefore, there is no induced drag. In addition, the rotation in the far wake of the jet is zero and the associated pressure drag is zero since the stator system has provided an axial discharge jet. Thus the increment of added drag normally experienced by a shrouded propeller without a stator system or by a single open propeller is nonexistent when the pumpjet is considered. If the shroud is nonseparating, it is felt that a rational approximation of the shroud drag is obtained by combining the frictional losses on the wetted surface area and the energy losses at the shroud inlet. These considerations have been included in the analysis leading to the selection of the optimum mass flow, thereby minimizing the overall power coefficient of the propulsor for a given vehicle.

Page intentionally left blank

Theory of One-Element Pumps for Propulsion[1]

Joseph Levy

Aerojet-General Corporation

The development of conventional pumps has been aimed mainly at increasing the pressure of the pumped fluid. For propulsion applications, however, the desired output is in the form of kinetic energy rather than pressure. Propulsion pumps may therefore assume configurations considerably different from those of conventional pumps. They may, for instance, consist of one element only—i.e., an impeller without a stationary casing (as in the ordinary ship's propeller). The discharge from this type of pump contains a whirl component that cannot be used for propulsion and must therefore be considered a loss. This loss is balanced by the elimination of other losses, such as those due to disk friction, diffusion, seals, and leakage.

This paper develops a basic theory for one-element propulsion pumps, and does so without reference to internal details of a particular design. It establishes a limit to the attainable efficiency and indicates relationships among pump-performance parameters that result in the greatest efficiency. It shows that the peripheral velocity of the pump is directly related to ship speed and develops some relationships between performance parameters and pump geometry. An example of this family of pumps is described.

Development efforts for normal, conventional pumps have been aimed primarily at increasing the pressure of the pumped fluid in order to raise the fluid to a higher elevation, to force it into a pressure vessel, or to make up for pipeline losses. This objective requires that the impeller be enclosed in a stationary pump casing, which becomes part of a closed conduit system. The pump casing also serves to convert kinetic energy into pressure by diffusion and (in the case of centrifugal or mixed-flow pumps) to collect the flow from the entire periphery of the impeller and pass it

---

[1] This research was sponsored by the General Hydromechanics Research Program of the Naval Ship Research and Development Center under Naval Ship Systems Command Subproject SR 009 01 01 (ONR Contract No. N00014–66–C0014).

into the discharge pipe. The casing and contained water constitute most of the bulk and weight of conventional pumps.

In seagoing propulsion applications, however, the desired output is in the form of kinetic energy (and not pressure), because water is taken from the ocean essentially at atmospheric pressure and is returned at the same pressure, but with a higher velocity. In addition, the propelling jet is discharged freely into the atmosphere, and it is therefore unnecessary to collect the outflow from the impeller. Peripheral discharge is equally acceptable.

Propulsion pumps may thus assume configurations that are very different from those of conventional pumps. They may, in fact, consist of one element only—i.e., an impeller without a stationary casing. The ordinary ship's propeller can be viewed as such a pump. If the flow enters a pump of this type, without prerotation, the discharge contains a whirl velocity component that is not useful for propulsion. The kinetic energy associated with that velocity must therefore be viewed as a loss chargeable to the pump. This loss, which does not occur in normal pumps, is counterbalanced by other factors that favor the one-element pump. These are

(1) Elimination of all the losses that occur in the stationary casing of normal pumps (e.g., disk friction, diffusion, leakage)

(2) Absence of the stationary casing, making this type simpler and more compact than normal pumps

(3) Operation at higher rotative speeds than conventional pumps, as a rule, thus further reducing the size required for a given task.

The losses in a pump of this type may be divided into (1) those due to viscosity (real-fluid effects), which may include boundary-layer friction, losses due to separation of the flow from a solid boundary, and energy-conversion losses (e.g., diffusion losses), and (2) the energy represented by the whirl component.

It is obviously desirable, for the sake of efficiency, to reduce losses of both types to the greatest degree possible. They cannot be eliminated altogether, however, because all hydraulic processes involve losses due to real-fluid effects and because a one-element pump accomplishes its function only by introducing whirl.

It thus becomes necessary, if one-element pumps are to have acceptable efficiency and be compact, to seek out all processes susceptible to optimization and to determine the conditions required for optimum performance. The designing of pumps generally is a complex process that leans heavily on empirical data, but such data are largely lacking for designs that differ substantially from conventional patterns. It therefore becomes necessary to inquire whether there are any simple, easily derived relationships that govern the performance of such pumps and are useful as guidelines for their design. Specifically, the following questions suggest themselves:

(1) Are there identifiable relationships between the relative magnitude of the whirl component and the efficiency of the pump?

(2) Is there an optimum relationship between the whirl-component loss and the friction loss?

(3) Is the ratio of peripheral speed of impeller to ship speed fixed, or is it open to choice?

(4) Are simple relationships available for use in calculating the blade angles of the impeller?

This paper covers an analytical investigation of the performance of one-element pumps for propulsion, insofar as this can be predicted from theory, and represents one aspect of a more general study reported in reference 1. It deals only with pumps that conform strictly to the limitation to one element; i.e., those that do not have guide vanes ahead of the impeller for the introduction of prerotation and do not have stationary casings surrounding or following the impeller. Propellers are not dealt with explicitly; however, as stated above, they may be considered as members of this family of pumps.

The overall performance of a one-element pump may be effectively investigated without reference to the internal details of the particular design—i.e., the impeller may be viewed as a black box. Impeller action on the water is then represented by velocity diagrams at the inlet and outlet, while internal losses are represented by a single loss coefficient. Existing pump theory is next applied to predict the overall performance and to answer some of the questions listed above. The results thus obtained are then used to establish guidelines for impeller design.

The efficiency of paramount importance in propulsion applications is the overall propulsive efficiency, η. It is defined as the ratio of thrust horsepower (THP) to shaft horsepower (SHP), where THP is the power required to move the ship through the water at a given speed (equivalent to towline power, if the ship were towed), while SHP is the power provided to the propulsion system by the prime mover. This efficiency is a function of several factors including pump efficiency. As shown in the next section, however, overall propulsive efficiency is directly proportional to pump efficiency. For the present study it is therefore sufficient to consider pump efficiency alone. The problem of matching the pump to the ship's requirements is discussed only with regard to its effect on the rotational speed of the pump.

RELATIONSHIP BETWEEN PUMP EFFICIENCY AND PROPULSIVE EFFICIENCY

The following expression, a modified version of equation (7) of reference 2 and derivable by combining equations (7) and (18*b*) of that reference, relates the pump efficiency and the overall propulsive efficiency of a waterjet system.

$$\frac{\eta}{\eta_\pi}=\frac{2k}{(1+k)^2(1+K_D)-1} \tag{1}$$

where

η overall propulsive efficiency (THP/SHP)
η_π pump efficiency
K_D duct-loss coefficient, including all internal losses, except those occurring in the pump
k jet-velocity ratio, $(V_j-V)/V=\Delta V/V$
V speed of advance of ship
V_j velocity of propelling jet relative to ship

The subscript π on η is used to distinguish the particular kind of pump efficiency considered here—i.e., one in which the energy of the whirl component is taken as a loss chargeable to the pump. The term K_D is defined by

$$H_D=K_D\frac{V_j^2}{2g}=K_D\frac{V^2}{2g}(1+k)^2 \tag{2}$$

where H_D is the head loss in ducting, elbows, and nozzles, and g is the acceleration of gravity.

Equation (1) shows that the propulsive efficiency is strongly affected by the choice of the jet-velocity ratio (k) and the value of the duct-loss coefficient (K_D). Given a pair of values for k and K_D, however, the overall propulsive efficiency is directly proportional to the pump efficiency.

ATTAINABLE EFFICIENCY

Basic Expression

The analysis that follows applies to all types of pumps (from axial to radial) in which the whirl component is not recovered, as well as to the ordinary ship's propeller, which may be viewed as a pump.

Because the type of pump under consideration does not require a stationary casing, the shaft torque (neglecting seal and bearing friction) is utilized fully to change the moment of momentum of the fluid passing through the impeller. The action of the impeller on the fluid is represented by velocity diagrams at the inlet and outlet, as shown in figure 1, for either an axial- or a radial-flow impeller. Equating the shaft torque (T_s) to the time rate of change of moment of momentum,

$$T_s = \rho Q (V_{w2} r_2 - V_{w1} r_1) \tag{3}$$

where

Q	volume flow rate
V_w	tangential velocity
r	radial position
ρ	fluid density

If the flow enters the impeller without prerotation,

$$V_{w1} = 0$$

and

$$T_s = \rho Q V_{w2} r_2$$

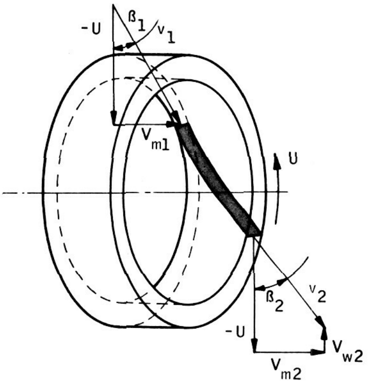

a.—*Axial-flow impeller.*

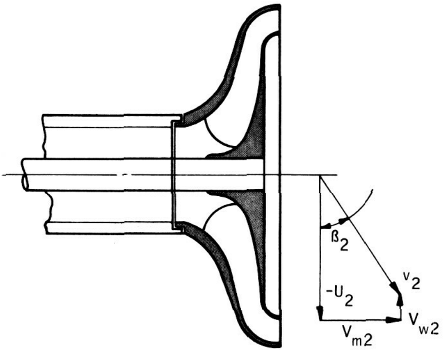

b.—*Radial-flow impeller. (Velocity design corresponds to impeller discharge radius.)*

FIGURE 1.—*Velocity diagrams.*

The power input (P_i) is

$$P_i = T_s\omega = \rho Q V_{w2}\omega r_2$$

where ω is the rotational speed of the impeller.
Because

$$\omega r_2 = U_2$$

it is possible to write

$$P_i = \rho Q V_{w2} U_2 \tag{4}$$

The input head, H_i (also called ideal head), or energy, may be written as

$$H_i = \frac{P_i}{\rho g Q} = \frac{V_{w2} U_2}{g} \tag{5}$$

We may define an input-head coefficient (ψ_i) based on peripheral velocity, by writing

$$H_i = \psi_i \frac{U_2^2}{2g} \tag{6}$$

Comparison of equations (5) and (6) shows that

$$\frac{V_{w2}}{U_2} = \frac{1}{2}\psi_i \tag{7}$$

The useful output head (H_π) is equal to the input head minus two losses: (1) that due to impeller friction (H_f) and (2) that due to nonrecovery of the whirl component (H_w). These may be expressed, respectively, as

$$H_f = K_f \frac{v_2^2}{2g} \tag{8}$$

and

$$H_w = \frac{V_{w2}^2}{2g} \tag{9}$$

where K_f is a friction-loss coefficient based on v_2, the relative velocity. Thus, the output head is

$$H_\pi = \frac{2V_{w2}U_2 - K_f v_2^2 - V_{w2}^2}{2g} \tag{10}$$

The pump efficiency is the ratio of the output head to the input head:

$$\eta_\pi = \frac{2V_{w2}U_2 - K_f v_2^2 - V_{w2}^2}{2V_{w2}U_2} \tag{11}$$

Ideal-Fluid Efficiency

For an ideal, frictionless fluid ($K_f=0$), equation (11) reduces to

$$(\eta_\pi)_i=1-\frac{1}{2}\frac{V_{w2}}{U_2} \tag{12}$$

and, using equation (7), this may be written

$$(\eta_\pi)_i=1-\tfrac{1}{4}\psi_i \tag{13}$$

It is thus evident that the efficiency in the frictionless case is a simple function of the input-head coefficient. When pumping a real fluid, the maximum attainable efficiency will be less than $(\eta_\pi)_i$. Therefore, one-element pumps must be designed to operate with low values of input-head coefficient if they are to have acceptable efficiency; in other words, as indicated by equation (7), they should operate at relatively high peripheral velocities.

Efficiency With a Real Fluid

The real-fluid efficiency is given by equation (11), which involves three velocity components. Before attempting optimization, a functional relationship must be established between the relative velocity (v_2) and the whirl component (V_{w2}). It is convenient also to reduce all velocity components to nondimensional ratios by dividing each by the peripheral velocity (U_2). The velocity diagram on the discharge side of the impeller (fig. 1) may now be labeled as shown in figure 2, recalling that $V_{w2}/U_2=\tfrac{1}{2}\psi_i$. The functional relationships are

$$\tfrac{1}{2}\psi_i=1-k_v\cos\beta \tag{14}$$

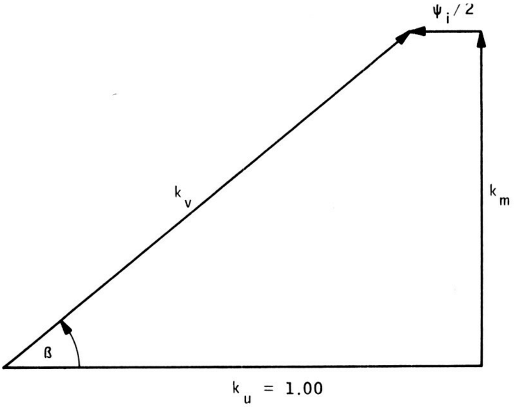

FIGURE 2.—*Dimensionless velocity diagram.*

and

$$k_m = k_v \sin \beta \tag{15}$$

where β is the relative flow angle measured from the tangential direction.

Equation (11) may now be written in terms of the velocity ratios as

$$\eta_\pi = \frac{\psi_i - K_f k_v^2 - \frac{1}{4}\psi_i^2}{\psi_i} \tag{16}$$

Each term, when multiplied by $U_2^2/2g$, represents a head (ideal input, friction loss, and whirl loss, respectively). Using equation (14) to substitute for ψ_i in equation (16), we obtain

$$\eta_\pi = \frac{2(1-k_v \cos \beta) - K_f k_v^2 - (1-k_v \cos \beta)^2}{2(1-k_v \cos \beta)} \tag{17}$$

which may be reduced to

$$\eta_\pi = \frac{1}{2}\left[\frac{1-k_v^2(K_f + \cos^2 \beta)}{1-k_v \cos \beta}\right] \tag{18}$$

Optimization with respect to β yields

$$K_f k_v^2 = \tfrac{1}{4}\psi_i^2 \tag{19}$$

which shows that the efficiency would be a maximum when the friction loss and the whirl-component loss have equal magnitudes.

Optimization with respect to k_v results in

$$K_f k_v^2 = \frac{1-\psi_i}{1+\psi_i}\left(\tfrac{1}{4}\psi_i^2\right) \tag{20}$$

which shows that the efficiency would be a maximum when the friction loss is somewhat less than the whirl-component loss.

The preceding two equations are satisfied simultaneously only when $\psi_i = 0$ (i.e., when the pump is doing no work and when the friction loss is zero), in which case the efficiency would be unity. Because useful pumps operate with positive values of ψ_i, the efficiency of a one-element pump has only one theoretical limit, which is the one derived for the ideal-fluid case as expressed in equations (12) and (13). The real-fluid efficiency will be less than that, and its magnitude will depend on the minimum friction loss that can be achieved with a given pump configuration.

It is interesting to examine the maximum efficiency that results when either of the two foregoing equations is used separately. Equation (14) may be used in combination with either one to make substitutions in equation (17) so as to express the efficiency in terms of ψ_i only. When equation (19) is used, the result is

$$(\eta_\pi)_{\max,1} = 1 - \tfrac{1}{2}\psi_i \tag{21}$$

while equation (20) yields

$$(\eta_\pi)_{\max,2} = \frac{1}{1+\frac{1}{2}\psi_i} \tag{22}$$

When ψ_i is small in comparison with unity, these equations give substantially the same result. However, when ψ_i is not very small, the two efficiencies are quite different. The maximum efficiencies, and the corresponding loss distributions, of equations (19) and (21) are plotted in figure 3*a*, while those of equations (20) and (22) appear in figure 3*b*. The efficiency is greater in plot *b*, but its attainment requires that the friction loss be smaller than shown in plot *a*. That smaller friction may be difficult to achieve in practice, especially when ψ_i approaches either 0 or 2. On the other hand, when ψ_i is not small, it should be possible to achieve friction losses below those shown in figure 3*a*.

It may therefore be said that practical designs should be aimed for efficiencies that fall between the values shown in plots *a* and *b*. These two lines of (so-called) maximum efficiency are replotted in figure 4. For propulsion we require pumps of high efficiency (e.g., at least 80 percent). The region of practical interest is thus the shaded portion of this figure, preferably in the upper end of that portion.

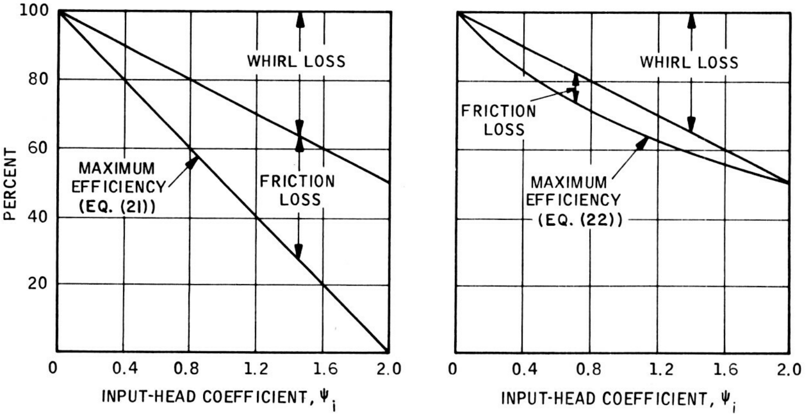

a.—*Equations (19) and (21).* b.—*Equations (20) and (22).*

FIGURE 3.—*Maximum efficiencies and loss distributions.*

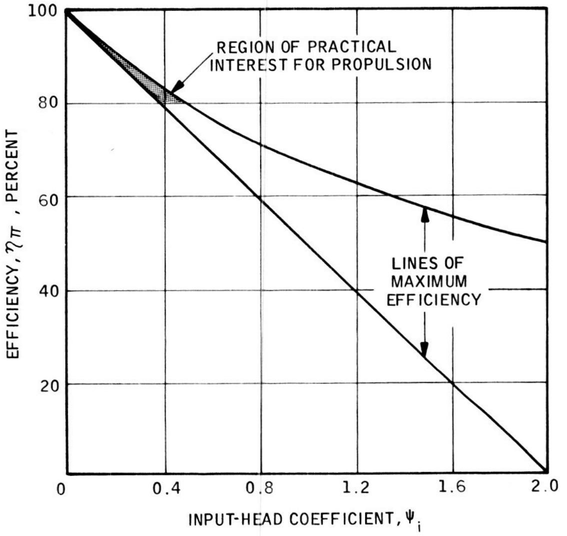

FIGURE 4.—*Efficiency range for practical design.*

RELATIONSHIPS BETWEEN EFFICIENCY AND IMPELLER GEOMETRY

Certain guidelines for the design of impellers for one-element pumps may be derived from the foregoing expressions for maximum efficiency and from the geometrical relationships represented by velocity diagrams (fig. 1). The results that follow pertain only to the terminal stations. Subscript 1 refers to the inlet to the impeller vanes, while subscript 2 refers to the station where the propelling jet is discharged freely from the impeller. The pump designer must provide transitions between these stations. The efficiency to be used hereafter is the lower value of maximum efficiency, that of equation (21).

The conditions prescribed here for the impeller outlet apply to the station at which the flow is discharged into the atmosphere in the form of free, thrust-producing jets. The angle β_2 gives the relative-flow direction, which differs somewhat from the geometrical blade angle in some cases. In some arrangements, especially with centrifugal or mixed-flow impellers, the radial position of the jet discharge may be different from that of the outlet end of the working blades (as in the Hydrocket® propulsion unit described in a succeeding section as an example of a one-element pump). In these cases, the product UV_w remains constant in the flow between the blades and the nozzles that form the jets, although all the velocity components may change magnitude.

Centrifugal and Mixed-Flow Impellers

Combining equations (21) and (7),

$$(\eta_\pi)_{\max}=1-\frac{V_{w2}}{U_2} \tag{23}$$

Substituting

$$V_{w2}=U_2-v_2\cos\beta_2$$

and

$$U_2=U_1\frac{r_2}{r_1}=v_1\cos\beta_1\frac{r_2}{r_1}$$

in equation (23) yields

$$(\eta_\pi)_{\max}=\frac{r_1v_2\cos\beta_2}{r_2v_1\cos\beta_1} \tag{24}$$

The relative-velocity ratio (v_2/v_1) in this equation may be replaced with the flow-area ratio (r_1b_1/r_2b_2) by making the following substitutions:[2]

$$v_1\cos\beta_1=\frac{V_{m1}}{\tan\beta_1}$$

and

$$v_2\cos\beta_2=\frac{V_{m2}}{\tan\beta_2}$$

From continuity,

$$V_{m1}=\frac{Q}{2\pi r_1b_1}$$

and

$$V_{m2}=\frac{Q}{2\pi r_2b_2}$$

where Q is the volume flow rate and b is the width of the flow passage at each station. Equation (24) may now be rewritten as

$$(\eta_\pi)_{\max}=\frac{r_1^2b_1\tan\beta_1}{r_2^2b_2\tan\beta_2} \tag{25}$$

Axial-Flow Impellers

For the usual type of axial-flow impeller (i.e., cylindrical hub and casing, noncavitating), $r_2=r_1$, $b_2=b_1$, and $V_{m2}=V_{m1}$. Equation (25) may

---

[2] Editor's Remarks: The author does not distinguish between the mass averaged radii used hitherto and the arithmetic averaged radii used in the next four equations. The error involved in equating these two averages is of the order of 5 percent for a hub/tip radius ratio of 0.5. In view of the death of the author, the editors felt impelled not to modify the analysis.

therefore be simplified to read

$$(\eta_\pi)_{\max} = \frac{\tan \beta_1}{\tan \beta_2} \tag{26}$$

or, from Equation (24),

$$(\eta_\pi)_{\max} = \frac{v_2 \cos \beta_2}{v_1 \cos \beta_1} \tag{27}$$

In some special types of axial pumps (e.g., supercavitating or superventilated), the meridional velocities (V_{m1} and V_{m2}) are not equal. However, the relative velocities (v_1 and v_2) are very nearly equal, and we may write

$$v_2 = k_b v_1$$

where k_b is nearly unity. Equation (27) then becomes

$$(\eta_\pi)_{\max} = \frac{k_b \cos \beta_2}{\cos \beta_1} \tag{28}$$

RELATIONSHIP BETWEEN PERIPHERAL SPEED AND SHIP SPEED

It can be shown that the peripheral speed of a one-element pump has a definite relationship to the design speed of a ship that is to be propelled by a pump of this type. This is done by equating the useful head developed by the pump to the head required for propelling the ship.

The head developed by any pump may be expressed in terms of the peripheral velocity (U_2), the input-head coefficient (ψ_i), and the pump efficiency (η_π), as follows:

$$H_\pi = \frac{U_2^2}{2g} \psi_i \eta_\pi$$

It may be assumed that, at the design ship speed, the pump will be operating at its best efficiency, and that (for one-element pumps) the best efficiency and the input-head coefficient are related. We may therefore use equation (21) to replace ψ_i by its equivalent, $2(1-\eta_\pi)$. The pump-output head then becomes

$$H_\pi = \frac{U_2^2}{g} (\eta_\pi - \eta_\pi^2)$$

The pumping head required to propel a ship at a speed V, with a jet-velocity ratio of $k = \Delta V/V$, and having a duct-loss coefficient K_D, can be shown (see, for instance, eq. (12) of ref. 2) to be

$$H_\pi = \frac{V^2}{2g}\left[(1+K_D)(1+k)^2-1\right]$$

Equating the two expressions for H_π and rearranging,

$$\frac{U_2}{V} = \left[\frac{(1+K_D)(1+k)^2-1}{2(\eta_\pi-\eta_\pi{}^2)}\right]^{1/2}$$

This expression is plotted in figure 5 for several values of pump efficiency and duct-loss coefficient.

DESCRIPTION OF A ONE-ELEMENT PUMP

One arrangement of a one-element pump with a centrifugal impeller is shown in figure 6. It was conceived by Mr. C. A. Gongwer (formerly of

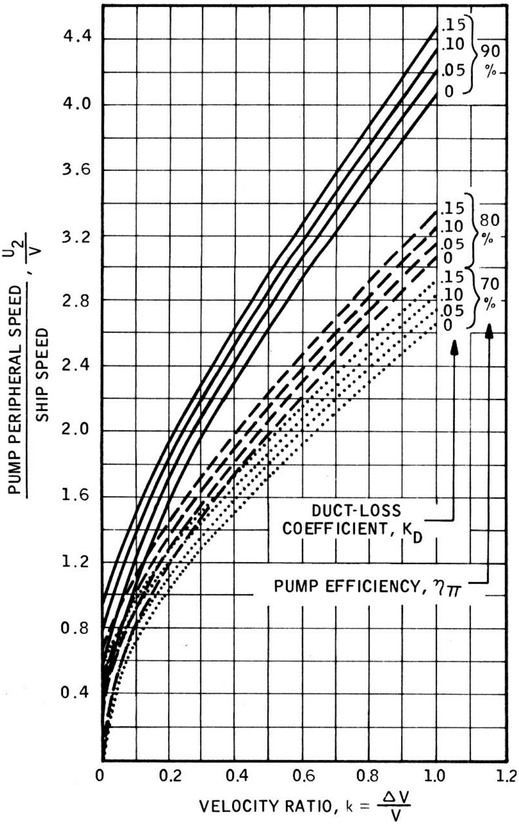

FIGURE 5.—*Peripheral-speed ratio versus jet-velocity ratio.*

Aerojet-General Corporation) for the propulsion of pleasure craft—as well as large ships—and was named the Hydrocket® propulsion unit.

The Hydrocket unit consists of an impeller (either radial-flow or mixed-flow), similar to a conventional pump impeller except for modifications at the periphery. The conventional impeller is open at the periphery, and its flow discharges radially into the pump casing. The Hydrocket impeller terminates in a gallery that is closed, except for a ring of nozzles, and turns the flow from the radial to the axial direction before discharging it through the nozzles. The gallery and nozzles are integral parts of the impeller and rotate with it. The nozzles are canted in a direction opposite to the peripheral velocity, making the angle β_2 with the impeller face, so that the absolute velocity of the jet is nearly in the meridional, or thrust, direction but does have a small whirl-velocity component (V_{w2}).

Several boats, including an 18-ft hydrofoil, were equipped with Hydrocket propulsion systems and were operated successfully for several years.

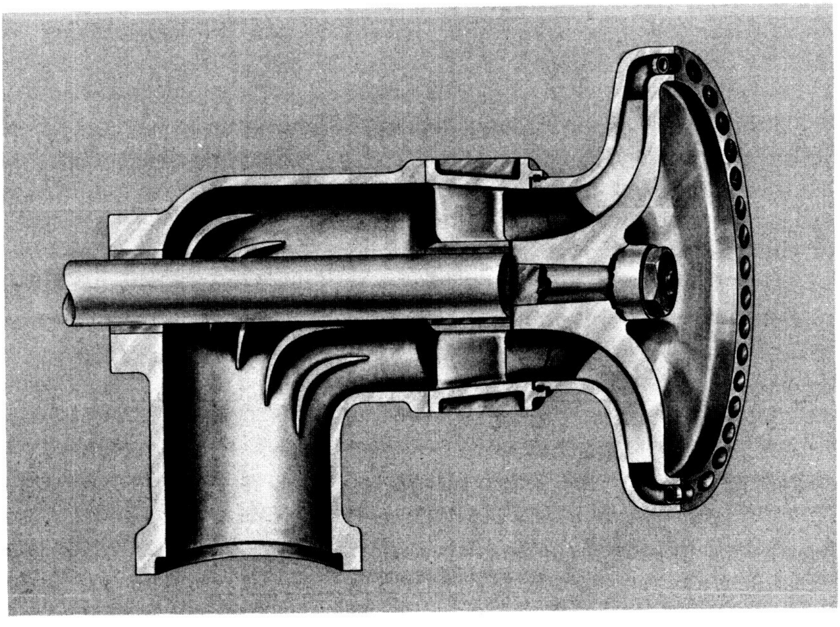

FIGURE 6.—*Hydrocket® propulsion unit (artist's drawing).*

CONCLUDING REMARKS

The relationships developed in this paper provide preliminary design guidelines for a wide range of one-element pumps for propulsion, although they prescribe only the conditions at the pump inlet and outlet. Blade shapes and shrouds may be sketched in, to provide smooth transitions between the prescribed terminal conditions, and internal-loss coefficients may then be estimated. Pumps of this general type can have acceptable efficiency and are more compact and simpler than conventional pumps.

REFERENCES

1. Levy, J., and S. Davis, *Analytical Study of Unconventional Pumps for Waterjet Propulsion.* Aerojet-General Report No. 3522 (final report under Office of Naval Research Contract No. N00014-66-C0014), March 1968.
2. Levy, J., The Design of Water-Jet Propulsion Systems for Hydrofoil Craft. *Marine Technology,* Vol. 2, No. 1, January 1965.

DISCUSSION

G. F. WISLICENUS (Tucson, Arizona): The paper discloses the competence in the hydrodynamic propulsion field for which its author is well known. Therefore, the writer of this discussion will limit his remarks to a few questions and only one general comment.

It is not clear to this discussor why a one-element propulsion pump can run under the same operating conditions at a higher speed of rotation than a conventional pump. This statement is made in the third paragraph of the introduction, item (3). It would seem that generally a single-element pump would be limited to the same suction specific speed as a conventional pump. Is it that the author feels single-element pumps can be operated with fully developed cavitation or ventilation, and the conventional pump cannot? This contention would have to be justified.

Equations (20) and (22) and figure 3*b* are not clear to this discussor as to their *physical* origin and meaning. Some explanatory comments by the author as to *why* this must be so would be helpful.

This discussor has never understood why the inventor of the Hydrocket (Calvin Gongwer) separated the discharge nozzle ring of his ingenious device from its pump vane system. Either a reason for this arrangement, or a statement that this separation is not necessary, perhaps not even desirable, would be very instructive.

This brings this discussor to his general comment: The Hydrocket (or any one-element pump) can be reasonably efficient only with low ψ_i values; i.e., low ratios of the circumferential discharge velocity component to the peripheral velocity of the runner. Standard centrifugal pumps are reasonably efficient only if ψ_i is in the vicinity of 1 or this velocity ratio in the vicinity of $\frac{1}{2}$. For a one-element propulsion pump such values would lead, according to equations (12) and (13) of the paper to *ideal* pump efficiencies in the neighborhood of 0.75, which is unacceptable. The reason why one-element pumps of the type of the Hydrocket can be operated with much lower ψ_i values than conventional pumps (and therefore with acceptable efficiencies) is the fact that the exterior of the Hydrocket rotor is exposed to air, not to water. This reduces the so-called disc-friction losses radically, thus removing the reason why ψ_i values cannot be much lower than unity. It seems that the recognition of this difference between the Hydrocket and a conventional centrifugal pump was essential for making the Hydrocket a practical possibility.

This discussor believes that further consideration of fluid friction losses in rotating vane systems will be necessary for arriving at optimum designs for the Hydrocket.

F. GILMAN (Worthington): As I looked at this paper, I was struck with the idea of a single element and the need for a jet, and to me a single element and a jet is a Pelton wheel. Now if one could collect the fluid from the sea with relatively low velocity and direct it into a nicely formed rearward jet by some means, using a very low-specific-speed machine such as a Pelton wheel, I think that we would have very low friction within the unit, and we would have no loss due to a whirl component. I've been quite interested in what a nice jet can be formed, for instance, with a spoon under the kitchen tap, and I think that something the reverse of the Pelton wheel might be constructive.

LEVY (author): The author wishes to thank Dr. Wislicenus for having reviewed the paper and for raising some penetrating questions. There are five separate questions (although some are interrelated) as follows:

(1) Why can a one-element pump run at a higher speed of rotation than a conventional pump operating under the same conditions? Perhaps the term speed of rotation was used too loosely in the paper. Most one-element pumps must operate at higher peripheral speeds than their conventional counterparts, as shown by equations (5) and (23). This implies a higher speed of rotation in those cases where impeller diameters are approximately equal. The problem of suction specific speed does apply to one-element pumps, although it was not treated in the paper.

(2) Does the author feel that one-element pumps can operate with fully developed cavitation or ventilation, whereas conventional pumps cannot? Both types of pumps may operate in this manner, and, in this respect, the Hydrocket is subject to the same considerations as normal pumps. However, other types of one-element pumps may discharge into the atmosphere without throttling the flow. Therefore, cavitation or ventilation voids do not have to close or collapse within the impeller. This eliminates the problems of cavitation erosion and of reentrant jets and the associated turbulence that results from the collapse of voids in liquid flows.

(3) What is the *physical* origin and meaning of equations (20) and (22) and of figure 3*b*? It should be noted that the same question could be asked with regard to equations (19) and (21) and figure 3*a*. The results obtained (in both cases) are due to the restrictions imposed by the mathematical process of partial differentiation, in which it is assumed that we can change one independent variable without affecting any of the others. This may not be achievable in the physical world. Equations

(19) and (21) (and fig. 3a) may appear to be more credible (as pointed out by Dr. Wislicenus in the oral discussion following presentation of the paper) because the result is similar to that obtained in other cases, wherein efficiency is a maximum when two types of losses (in this case whirl component and friction) are of equal magnitudes. Nevertheless, this result should also be questioned, as may be seen from the following example. Let us assume that ψ_i has the value 1.00; the whirl component loss ($\frac{1}{4}\psi_i^2$) would then have the value 0.25. In the absence of friction (i.e., $K_f=0$), the pump efficiency would be 0.75, as given by equation (13). Equation (16) states that, in the presence of friction, the efficiency would be lower than 0.75 by the amount $K_f k_v^2$. Thus, for instance, the efficiency would be 0.65, if $K_f k_v^2$ had the value 0.10. However, equations (19) and (21) and figure 3a state that, for this example, the maximum attainable efficiency is 0.50 and that this occurs when $K_f k_v^2=0.25$. Now, there is no physical reason for accepting this limitation. It may be said, in conclusion, that the limitation expressed by equation (13) is a hard ceiling; that is, the real efficiency will always be lower than that. How much lower will depend on the magnitude of the smallest friction loss that can be achieved in the real case.

(4) Why is the Hydrocket (or any one-element pump) efficient only if ψ_i has low values, while a normal centrifugal pump is efficient when ψ_i is in the vicinity of unity? It should be recalled that the theory presented in the paper is based on analysis of the velocity diagram at final discharge into the atmosphere. Velocity diagrams inside the impeller may be quite different. Let us examine the case of a normal centrifugal impeller that is converted into a one-element pump, as was done for the Hydrocket shown in figure 6. In a normal pump, the impeller shrouds would end where the vanes end in this figure; the discharge from the impeller would be radial, and it would flow against the back pressure imposed by the pump casing and the discharge pipe; the relative velocity (v) and the meridional velocity (V_m) would be small by comparison with the peripheral velocity (U); the energy added by the impeller would be partly pressure and partly kinetic energy. Conversion to a one-element pump is achieved (in this case) by extending the shrouds, first turning the flow toward the axial direction and then discharging it through nozzles that make some angle (β) with the face of the impeller. The nozzles perform a number of different functions. Some of these could, perhaps, be eliminated or achieved by other means. These functions are

(*a*) To throttle the flow so that velocities inside the impeller are kept within reason, thereby reducing internal losses.

(*b*) To convert pressure energy into kinetic energy.

(*c*) To guide the flow into the desired direction.

(*d*) To return energy to the impeller.

The conversion of energy and the guidance result in substantial increases in the relative velocity (v) and the meridional velocity (V_m) and in a reduction in the magnitude of the whirl component (V_w). It should be recalled that, at final discharge, V_m must be greater than ship speed (V) in order to achieve a positive thrust; also that V_w must be small in order to achieve good pump efficiency.

The nozzle ring, in the arrangement shown in figure 6, acts as a turbine; i.e., some of the energy added by the impeller vanes helps to drive the impeller. The energy (per unit time or per pound of water) input by the shaft is less than the energy added by the vanes. This input is equal to the sum of the kinetic energies of the two components of the absolute velocity at final discharge, and result in acceptably small internal loss. Many arrangements are possible; however, the author was not at liberty to describe them in this open publication.

In reply to Mr. Gilman's question, if we stipulate that there be no loss due to a whirl component, we imply that this component should be oriented in the direction of the thrust vector. This is precisely the mode of action of the paddle wheel. If such a wheel could be designed to produce "a nicely formed rearward jet," it would indeed be an efficient propulsor, although it might be very large and complex. Since (in this case) the whirl component is not lost, such devices are not in the class of turbomachines discussed in the present paper.

INDEX OF AUTHORS AND DISCUSSORS*

• Italic page numbers indicate first page of paper.

☆ U.S. GOVERNMENT PRINTING OFFICE: 1974 —507-499